R-08-94

Bedrock transport properties Laxemar
Site descriptive modelling
SDM-Site Laxemar

James Crawford, Magnus Sidborn
Kemakta Konsult AB

November 2009

Svensk Kärnbränslehantering AB
Swedish Nuclear Fuel
and Waste Management Co

Box 250, SE-101 24 Stockholm
Phone +46 8 459 84 00

ISSN 1402-3091
SKB Rapport R-08-94

Bedrock transport properties Laxemar
Site descriptive modelling
SDM-Site Laxemar

James Crawford, Magnus Sidborn
Kemakta Konsult AB

November 2009

Keywords: Transport properties, Laxemar.

This report concerns a study which was conducted for SKB. The conclusions and viewpoints presented in the report are those of the authors and do not necessarily coincide with those of the client.

A pdf version of this document can be downloaded from www.skb.se.

Preface

This report consists of several parts for which different authors have contributed material in a collaborative effort. A short description of the main contributors and the relevant parts of this report that they have been involved with follows:

James Crawford, Kemakta Konsult AB (Chapters 1–3, 5–7, Appendices A–F).

Magnus Sidborn, Kemakta Konsult AB (Chapters 1–3, 6).

Eva Selnert, Johan Byegård, Henrik Widestrand, Seje Carlsten, Christin Döse, Geosigma AB (Chapter 4).

Eva-Lena Tullborg, Terralogica AB (Chapter 4).

Martin Löfgren, Kemakta Konsult AB (Co-author of Appendix D).

The helpful comments of Prof. Ivars Neretnieks are also gratefully acknowledged with regard to the descriptions of saline mixing contained in Appendix A.

Editors: James Crawford and Magnus Sidborn.

Summary

This report contains a detailed account of the work that has been carried out within the final stage of site descriptive modelling of Laxemar (SDM-Site Laxemar) with regard to bedrock transport properties evaluation.

A quantitative assessment is made of flow-related transport properties (the F-factor and advective travel time) within different rock volumes comprising the Laxemar local model volume. In this evaluation, the hydrodynamic controls on transport are calculated with the aid of models and data supplied by Hydrogeology. Particle tracking simulations have also been made using an equivalent continuous porous medium (ECPM) representation of the Laxemar bedrock where the different hydraulic rock domains, deterministic deformation zones, and shallow bedrock aquifers are combined with a set of topologically determined hydraulic boundary conditions.

Material properties of the rock governing solute retention as measured in the transport properties laboratory programme have been used to parameterise a semi-quantitative retardation model for Laxemar. The effective diffusivity of the rock matrix as given by the formation factor is found to be very similar for different rock types and no strong quantitative basis can be found for distinguishing between different rock types at the site. Although the sample sizes are typically small, there appears to be no systematic difference between the sorptive properties of the different, (hydrothermally unaltered) rock types. The apparent variation of sorptive properties appears to be more strongly related to groundwater composition than to the subdivision of the bedrock. There are also indications that altered material adjacent to fracture surfaces and deformation zone materials may have sorptive and diffusive retention properties that are enhanced relative to that of the unaltered rock matrix away from the fracture. Fracture coatings of secondary minerals are thought to have significantly enhanced retention properties relative to the rock matrix owing to the high specific surface area and generally high porosity of the former.

Simulations have also been made of solute transport where material property descriptions are combined with flow-related transport properties to estimate typical residence times for transported radionuclides. Additionally, it is found that transport models accounting for diffusion from narrow flow channels to effectively stagnant regions of a flowing fracture may increase radionuclide residence times substantially. Channelised flow therefore may have an overall beneficial effect when fully considered in transport modelling.

Confirmatory tracer tests have been performed in the form of dipole, and single well injection-withdrawal (SWIW) tracer tests. The evaluation of the results gives clear indications of diffusive and sorptive retention processes consistent with the conceptual understanding of solute transport at the Laxemar site. Further analysis suggests that while the retardation of sorbing tracers appears to be governed principally by direct diffusive and sorptive interactions with fracture surface coatings, the retardation of non-sorbing tracers may be more strongly influenced by hydrodynamic effects that have not been fully accounted for in the data evaluation and modelling performed. These additional effects, however, are not thought to be relevant for radionuclide transport at safety assessment timescales.

Sammanfattning

Denna rapport utgör en detaljerad beskrivning av det arbete som utförts inom det avslutande stadiet av den platsbeskrivande modelleringen av Laxemar med inriktning mot utvärdering av bergets transportegenskaper.

En kvantitativ bedömning av flödesrelaterade egenskaper (F-faktorer och advektiv transporttid) utförs för de olika bergvolymer som tillsammans utgör den lokala modellvolymen i Laxemar. Hydrodynamiska parametrar av vikt för transport beräknas med hjälp av modeller och data som levererats av Hydrogeologi. Partikelspårningssimuleringar där berget i Laxemar representeras av ett ekvivalent kontinuerligt poröst medium (ECPM) har också utförts. I denna representation kombineras de olika hydrauliska bergdomänerna, deformationszonerna och ytliga vattenbärande akviferer med en uppsättning av topologiskt bestämda hydrauliska randvillkor.

Uppmätta materialegenskaper hos berget som bestämmer lösta ämnens retention har använts för att parameterisera en semikvantitativ retardationsmodell för Laxemarområdet. Den effektiva diffusiviteten i bergmatrisen som ges av formationsfaktorn har visat sig skilja mycket litet mellan olika bergartstyper och någon kvantitativ grund för att särskilja olika bergartstyper i området har inte kunnat påvisas. Även om antalet bergprover vanligtvis är begränsade verkar det inte finnas någon systematisk skillnad i sorptionsegenskaper mellan de olika (hydrotermiskt oförändrade) bergartstyperna. Den märkbara variationen i sorptionsegenskaperna verkar vara närmare relaterad till grundvattensammansättningen än till bergartstypernas klassificering och sammansättning. Hydrotermalt omvandlade zoner associerade med sprickor, material från deformationszoner, och beläggningar av sekundära mineral på sprickytor uppvisar förhöjda sorptiva och diffusiva retentionskapaciteter jämfört med den ostörda oomvandlade bergmatrisen.

Transportsimuleringar har utförts där material- och flödesrelaterade transportegenskaper kombineras för att beräkna uppehållstiden för transport av radionuklider längs typiska flödesvägar. Det har visat sig att radionuklidernas beräknade uppehållstid ökar ansenligt om transportmodeller används som tar hänsyn till diffusion från smala kanaler till zoner med stillastående vatten i flödande sprickor. Kanalbildningseffekter inkluderade i transportmodeller kan därför ha en gynnsam effekt.

Spårämnesförsök i form av dipol- och enhålstester (SWIW) har utförts med syfte att stärka och verifiera den konceptuella förståelsen av diffusiva och sorptiva retentionsprocesser. Utvärderingen visar tydligt att resultaten stämmer överens med den konceptuella förståelsen av dessa processer i Laxemar. Utökade analyser tyder på att retardationen av sorberande spårämnen verkar bestämmas av direkt diffusiv och sorptiv interaktion med ytbeläggningar i sprickorna medan retardationen av icke-sorberande spårämnen kan påverkas mer av hydrodynamiska effekter som ej har tagits hänsyn till i utvärderingen av data och utförd modellering. Dessa ytterligare effekter bedöms dock inte ha betydelse för radionuklidtransport i de tidsperspektiv som är relevanta för säkerhetsanalysen.

Contents

1 Introduction

1.1 Background

The Swedish Nuclear Fuel and Waste Management Company (SKB) is conducting site investigations at two different locations in Sweden (the Laxemar and Forsmark areas) for the purpose of siting a deep geological repository for spent nuclear fuel. The results from the investigations at the sites are used as a basic input to the site descriptive modelling.

A Site Descriptive Model (SDM) is an integrated description of the site and its regional setting, covering the current state of the biosphere as well as ongoing natural processes of importance for long-term safety. The SDM summarises the state of knowledge of the site at the conclusion of the complete site investigation (CSI). It also provides parameters and models to be used in further analyses within Safety assessment (SA), Repository Design, and Environmental Impact Assessment. The present report is produced as the main (level II) reference for the concluding stage of the site descriptive modelling of the Laxemar area (henceforth, SDM-Site Laxemar). The hierarchy of various reports comprising SDM-Site Laxemar are shown in Figure 1-1.

1.2 Scope and objectives

This report provides a detailed account of modelling that has been performed in support of bedrock transport property assessment for SDM-Site Laxemar. The transport site descriptive model presented in this report incorporates both a detailed account of retardation parameters and flow-related transport properties of the rock. The integration of material property data and flow-related aspects of radionuclide transport allows the prediction of characteristic transport times for typical transport paths from hypothetical repository depth to the near surface.

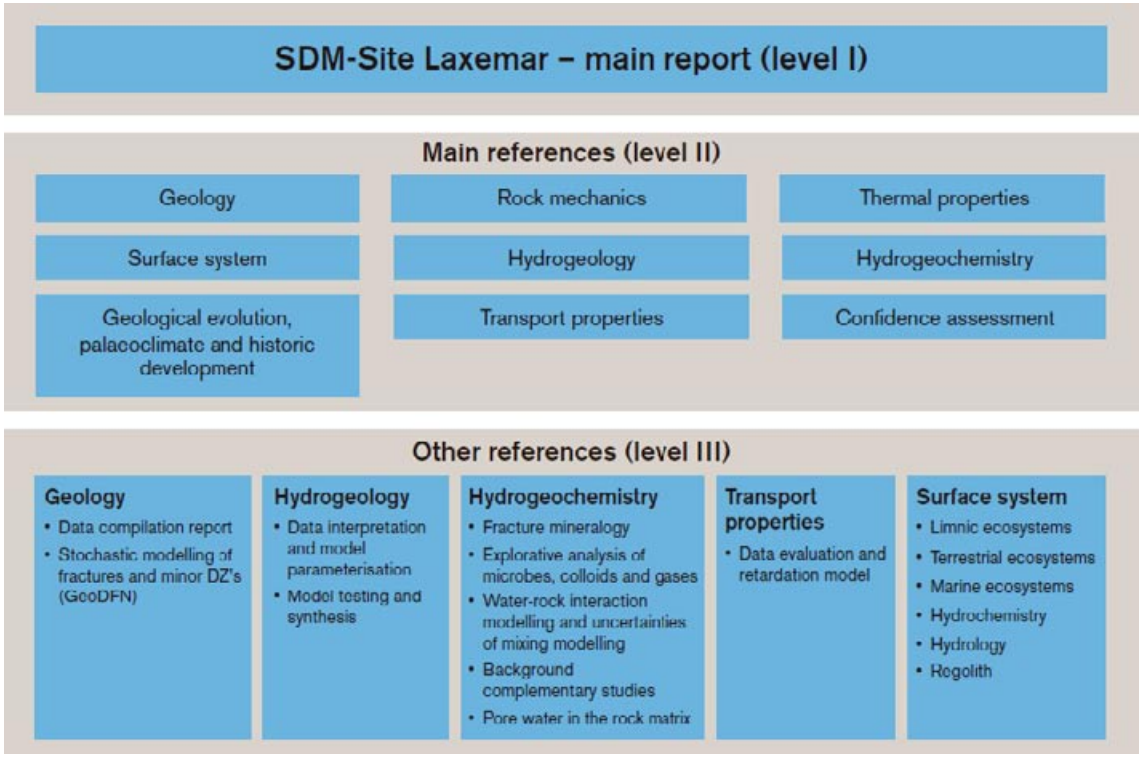

Figure 1-1. *Hierarchy of background reports feeding into the SDM-Site Laxemar main report.*

The primary objectives of the work are to:

- outline the conceptual understanding of transport processes within the rock encompassing both material property and hydrodynamic aspects controlling solute transport in Laxemar;
- provide a summary of quantitative material property data and supporting evidence used to parameterise a retardation model describing the rock matrix as well as typical fracture types and deformation zones encountered in the rock in Laxemar;
- make estimates of the hydrodynamic transport resistance (advective travel time and flow-wetted surface to flow ratio, or F-factor) for typical flowpaths in the target rock volume in Laxemar using data and models supplied by Hydrogeology;
- make estimates of travel times for specific solutes investigated in the transport properties laboratory programme for typical flowpaths in the rock in Laxemar without any specific considerations of repository layout or radionuclide release scenarios;
- describe and interpret results of field-scale tracer tests performed in Laxemar which are made in support of the site descriptive transport modelling.

A secondary objective is to make a systematic attempt to explain the possible role of channelised flow on the transport of solutes of interest. This includes analyses of the possible impact of channelling phenomena on data interpretation (*inverse modelling*) as well as possible impacts upon solute migration when considered in flow and transport modelling (*forward modelling*).

1.3 Hydrogeological and geological setting

The Laxemar area is situated in north-eastern Småland within the municipality of Oskarshamn, about 300 km south of Stockholm. The setting of the Laxemar-Simpevarp regional model area and the Laxemar local model area are indicated in Figure 1-2. Figure 1-3 illustrates the candidate area and the location of drill sites and boreholes from which data were available for SDM-Site Laxemar.

The regional model volume is divided into 9 major rock domains denoted RSM[A-P] based on their respective geological characteristics. The rock domain code RSM[A-P] is followed by an alphanumeric identifier for each continuous region. The locations of the rock domains in the regional model volume are shown in Figure 1-4.

The Laxemar local model volume consists of rock domains RSMA01, RSMD01, RSMM01, RSMP01, and RSMP02. A detailed illustration of deterministic deformation zones of high and medium confidence is shown in Figure 1-5 where they intersect the surface. The rock is also divided into a number of additional compartments referred to as fracture domains, hydraulic rock domains, and hydraulic conductor domains. These are discussed in more detail in Chapter 2 with regard to flow related transport properties.

The present regional groundwater flow at the Laxemar site is principally influenced by topography with a gradient extending from elevated areas in the west towards the Baltic Sea in the east. The flow patterns are largely governed by the connected system of large deformation zones transecting the site. The topography also results in localised areas of groundwater recharge/discharge which represent groundwater circulation cells of varying depth and extent and consequently, also different groundwater ages. There is a diminishing effect of groundwater circulation down to a depth of about 1,000 m and below 1,200 m the groundwater is thought to be effectively stagnant /Rhén et al. 2008, Rhén et al. 2009/.

Groundwater recharge is generally associated with high altitude areas, whereas groundwater discharge is located in low altitude areas (valleys, watercourses and depressions). From the particle tracking analyses documented in /Rhén et al. 2009/, recharge and discharge locations have been identified at the site. These are illustrated in Figure 1-6. All the major islands (Äspö, Ävrö and Hålö) together with the Simpevarp peninsula act as recharge areas, as do the central parts of the Laxemar subarea. A number of recharge areas that influence the Laxemar subarea are located in the hills several kilometres to the west and southwest. Generally, the discharge areas for groundwaters from deeper levels in the bedrock are located predominantly in the valleys to the south and north of Laxemar and along the Baltic coast shoreline.

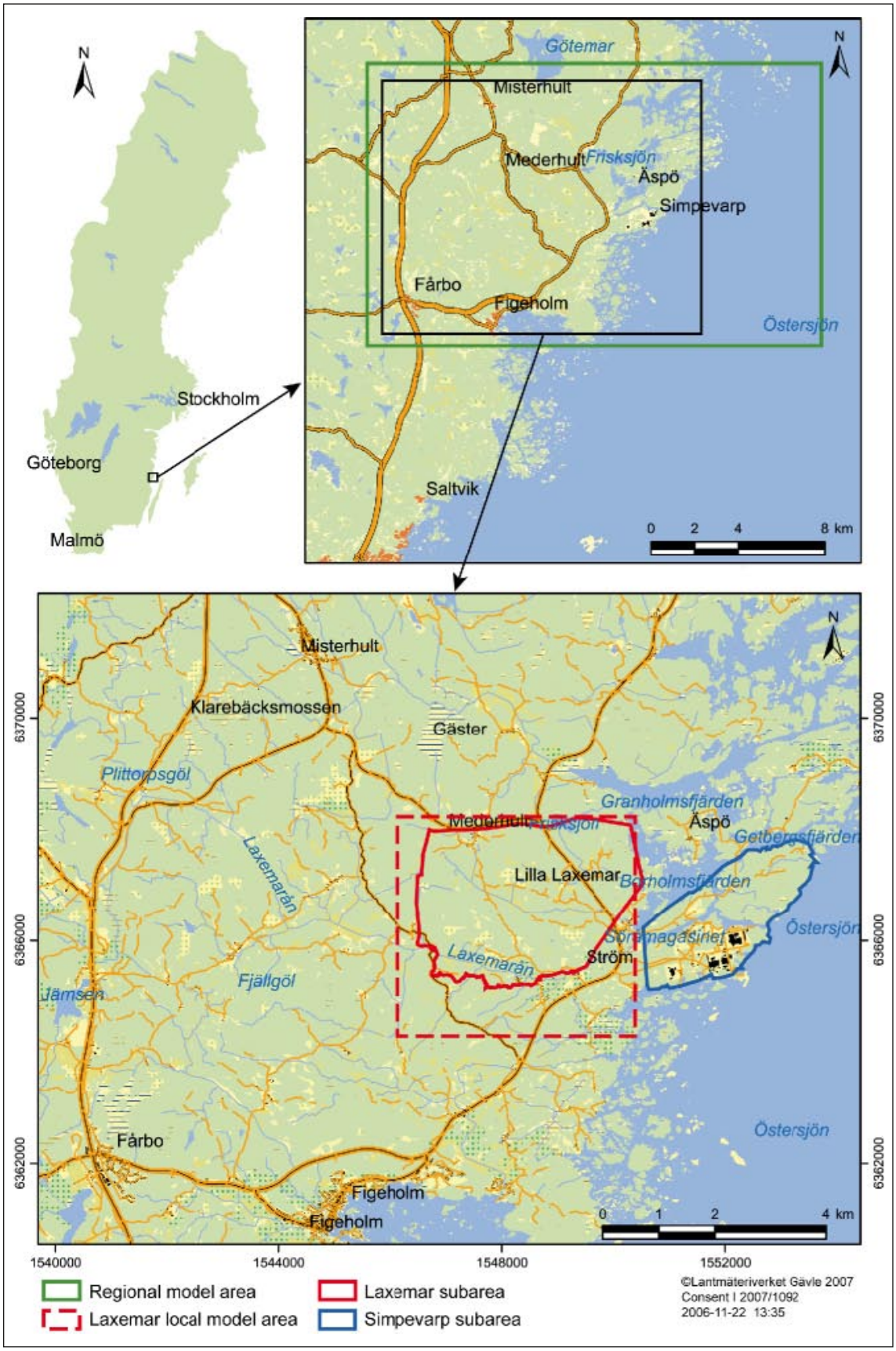

Figure 1-2. *Setting of the Laxemar-Simpevarp regional model area and Laxemar local model area. The black rectangle in the top-right inset shows the spatial extension of the enlarged map.*

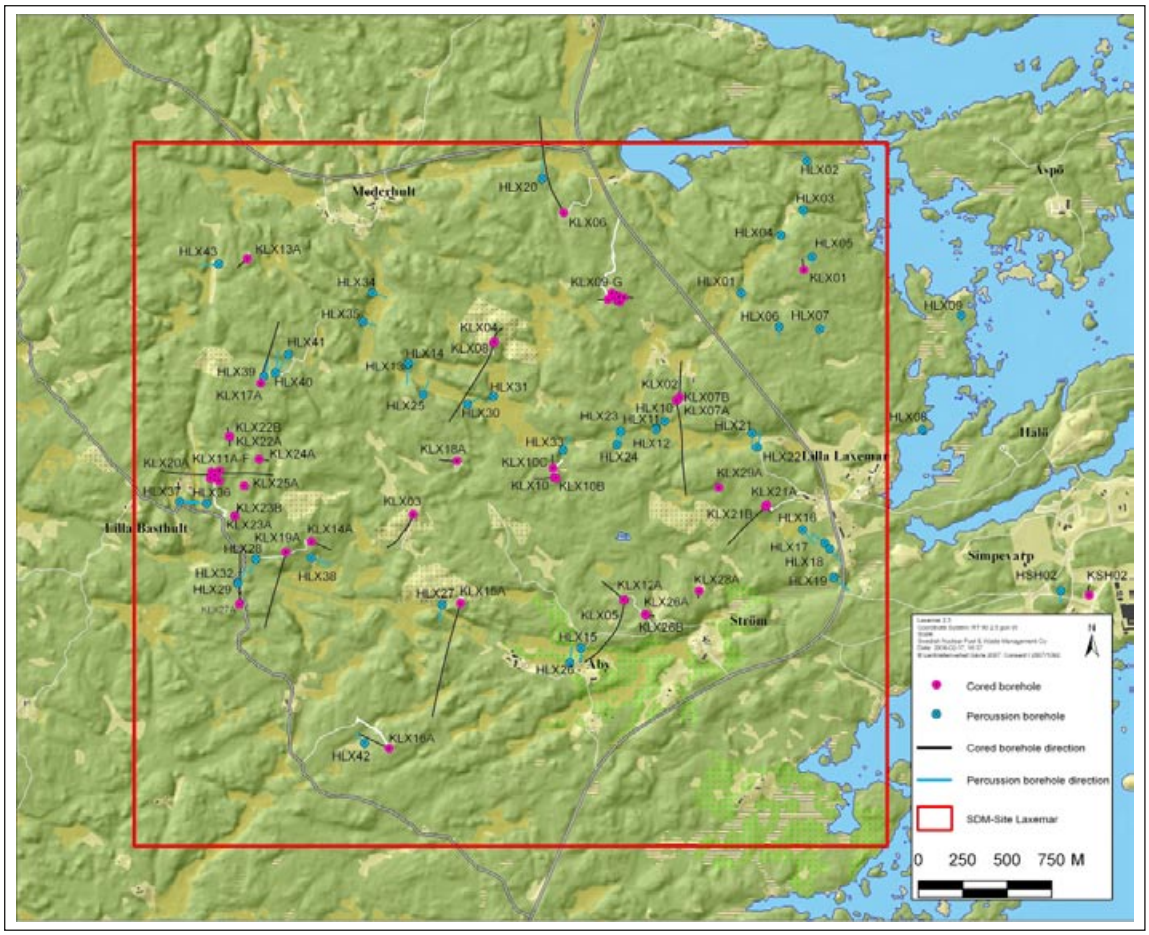

Figure 1-3. *The Laxemar local model area showing the location of drill sites and boreholes from which data were available for SDM-Site Laxemar /Hakami et al. 2008/.*

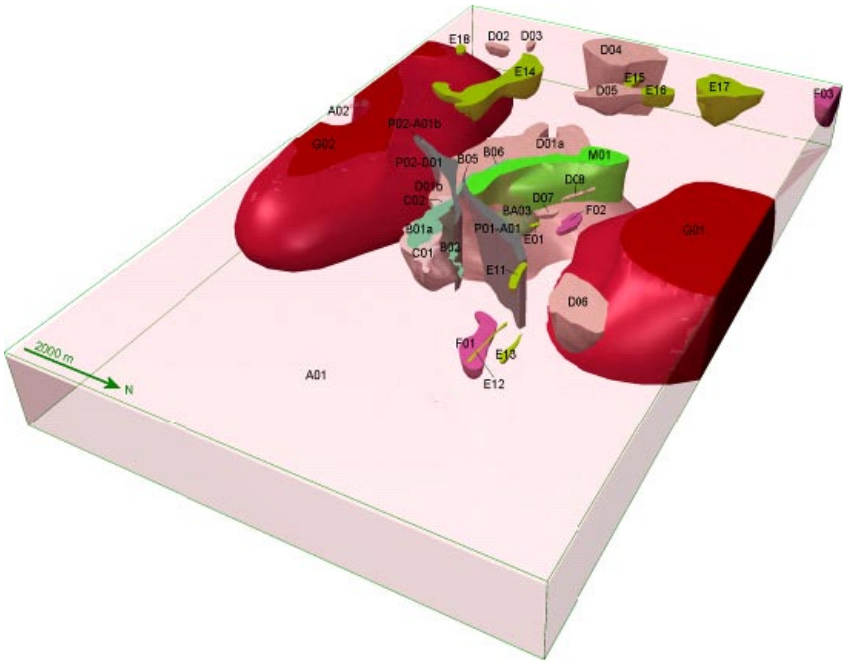

Figure 1-4. *Rock domains visualised in 3D, bounded by the regional model area. Ävrö granite (RSMA) is made transparent to highlight the 3-dimensional structure of the rock domains /Wahlgren et al. 2008/.*

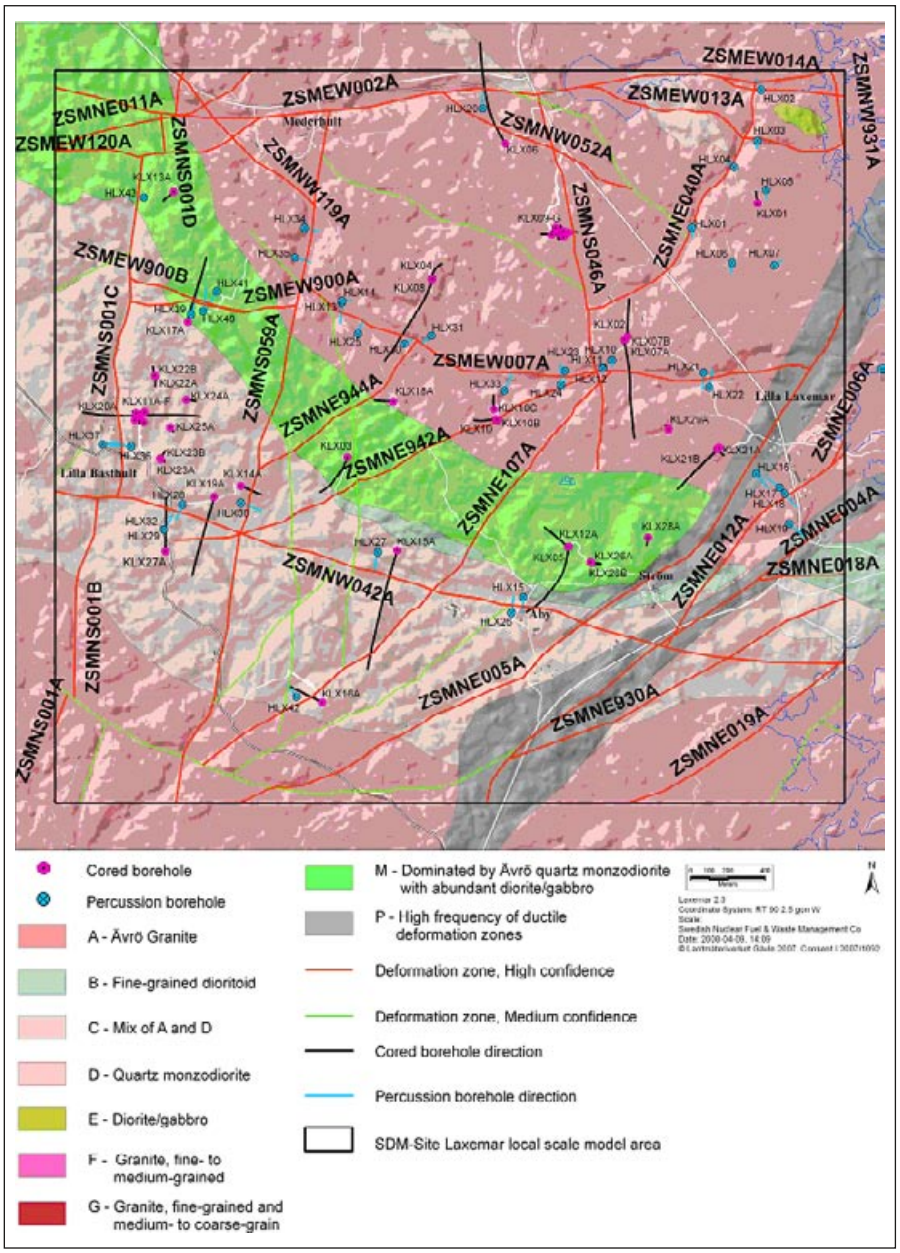

Figure 1-5. *Rock domains and deformation zones within the Laxemar local model area /Wahlgren et al. 2008/.*

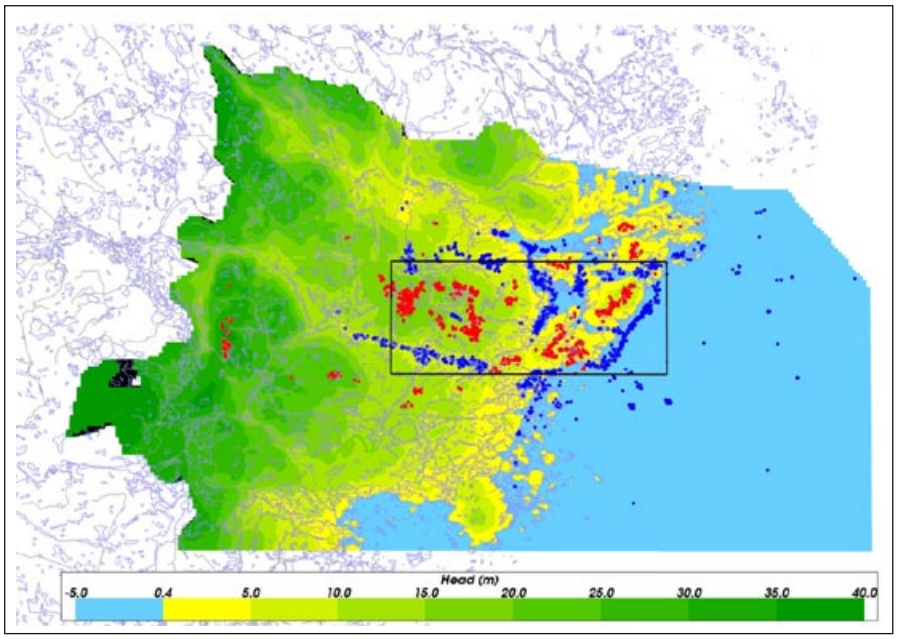

Figure 1-6. *Illustration of some prominent groundwater recharge locations (red markers) and discharge locations (blue markers) identified at the Laxemar site by following particles released in the flow field calculated for the regional hydrogeological model under contemporary conditions. The recharge points are the upstream starting points for flow paths passing through the particle release area (black rectangle) whereas the discharge points are the correspond downstream exit points /Rhén et al. 2009/.*

1.4 Hydrogeochemical characteristics of the Laxemar site

The groundwater types represented in Laxemar are distinguished largely by way of their salinity, ^{18}O oxygen isotopic content, magnesium, and chloride-bromide ratios. The major water types identified in Laxemar are referred to as: *Fresh, Brackish Glacial, Brackish marine, Brackish Non-marine, Saline, and Highly Saline* /Laaksoharju et al. 2009/. In addition, two other so-called "transitional" groundwater types were included to accommodate important mixing processes identified to be important for observed hydrochemical compositions. These additional groundwater types consist of a shallow, near-surface *Mixed-Brackish* type (a mix of fresh and brackish-glacial groundwater sometimes with a weak marine component) and a deeper *Transitional* groundwater type (a mix of brackish glacial or brackish non-marine groundwater mixed with a brackish marine component).

In the hydrogeochemical site descriptive model /Laaksoharju et al. 2009/ the current groundwater types to be found at the site are described in terms of their perceived main origin as can be discerned from hydrochemical analysis and modelling interpretation. The so-called "end members" which define the main groundwater types by origin are described in detail by /Gimeno et al. 2009, Gurban 2009/. The present groundwaters have compositions which have been substantially altered by mixing and chemical reactions within the rock although their chemical signatures are still such that it is possible to understand their origin and follow their evolution over long periods of time.

Past climate changes are recognised as being one of the major driving forces for long term hydrogeochemical changes over periods from hundreds to many thousands of years. The understanding of these changes is therefore of fundamental importance for understanding the evolution and present state of the groundwater within the Fennoscandian crystalline bedrock. Several of the groundwater end members can be associated with past climatic events in the later Pleistocene (i.e. from roughly 100 ka to 10 ka before present) including inter-glaciations, glaciations, de-glaciations, and associated shore level displacements in connection with marine/non-marine transgressions and regressions. Among these, the last glaciation and post glacial period is thought to be the most important for the current groundwater state, especially in terms of land uplift, shore-level displacement, and the development of the Baltic basin. In spite of this the hydrogeochemistry of the Laxemar groundwaters cannot be satisfactorily explained without including older relict components remaining from previous glacial and interglacial periods.

Primary end members are /Gimeno et al. 2009, Gurban 2009/:

Altered meteoric: a dilute groundwater ultimately originating from atmospheric precipitation (rainwater) during temperate periods although more particularly during the current interglacial. The composition of this water is influenced by chemical reactions with, for example, calcite and biogenic components accumulated during its movement through surface quaternary deposits.

Glacial: a dilute groundwater originating from the melting of retreating glaciers at the conclusion of the most recent glaciation (18,000–8000 BC). This end member is substantially depleted with respect to the heavy isotopes of oxygen (^{18}O) and hydrogen (^{2}H, Deuterium) indicating a cold climate origin. This end member is defined by analogy with present day glacial melt-waters which have a very low content of dissolved solids (even lower than meteoric water). The end member represents the chemical composition of the water prior to the water rock interaction processes occurring during infiltration into the bedrock. It should be noted that since the glacial water is drastically modified by mixing with waters of other origins, there are essentially no undisturbed glacial melt-water remnants within the bedrock that can be considered as pure glacial mixing components modified only by water-rock interactions.

Littorina: a brackish, marine groundwater component originating from the period 4500–3000 BC and characterised by a salinity (6,500 mg/l Cl) about twice that of the present day Baltic Sea and a relatively high Mg content.

Deep Saline: The chemical composition of this end-member corresponds to the deepest and more saline waters sampled at Laxemar. This water has a salinity of 47,200 mg/l Cl with a predominantly Ca-Na-Cl composition and deviates significantly from the GMWL (Global Meteoric Water Line) in $\delta^{18}O$ vs. $\delta^{2}H$ plots. Although there is some uncertainty concerning the ultimate origin of this water type, the great age of the water (in excess of 1.5 Ma) as estimated from ^{36}Cl data suggests that it is likely to be close to equilibrium with the minerals comprising the bedrock.

Figure 1-7 shows some of the more recent stages of importance for understanding groundwater chemistry in Laxemar. As mentioned in the caption of Figure 1-7, two different scenarios are illustrated. The upper series of images represents areas not covered by the Littorina Sea and shows from left to right; 1) the groundwater situation prior to the last deglaciation, 2) the groundwater situation during the last deglaciation accompanied by intrusion of Late Wechselian meltwater, 3) meteoric recharge during the Holocene, and 4) the present groundwater situation. The lower series of images represents areas submerged by the Littorina Sea for a period long enough to influence the groundwater. This series shows from left to right the same evolutionary sequence as the top series with the exception of panel 3) which shows the intrusion of brackish marine (Littorina Sea) water and panel 4) which shows the present groundwater situation following on from the preceding brackish marine intrusion.

Based on the prevalence of different fracture minerals and distributions of redox sensitive elements within the investigation boreholes it is thought that the redox front in Laxemar generally resides at a depth of about 15–20 m. Although accurate measurements do not exist to draw very specific conclusions about groundwater redox conditions in the near surface 20–250 m of the bedrock, uranium decay-series analysis of fracture minerals indicate a gradual transition from mainly uranium removal (oxidising conditions) to uranium deposition (reducing conditions) occurring in the upper 100 m of the bedrock. The Eh values measured in groundwater in the Laxemar-Simpevarp area (at depths greater than about 150 m) generally lie between –200 and –310 mV although the Eh values do not seem to follow any systematic depth trend /Laaksoharju et al. 2009/. The presence of Fe(II) bearing minerals in the fracture fillings obtained from all depths indicates that past oxidising events have not exhausted the reducing capacity of the fracture minerals even in the shallowest part of the system. This together with the significant Fe(II) content of both the unaltered and altered (red-stained) wall rock indicate that a non-trivial redox buffering capacity remains in the rock. Sulphur isotope ratios in the dissolved sulphate indicate that sulphide has been produced in the system and that microbial sulphate reduction is ongoing. The presence of sulphate-reducing bacteria has been identified at all depths sampled although with large variations in population levels.

Colloid concentrations in Laxemar groundwaters are comparable to those found in other granitic environments and are composed mostly of aluminium, silica, iron, and sulphur. The range of colloid concentrations found in Laxemar varies from approximately 5 µg/l to 90 µg/l with an average concentration of about 27 µg/l /Laaksoharju et al. 2009/. An apparent decrease in colloid concentration with increasing depth is also indicated by the measurement data, although there are large differences between concentrations measured in different boreholes.

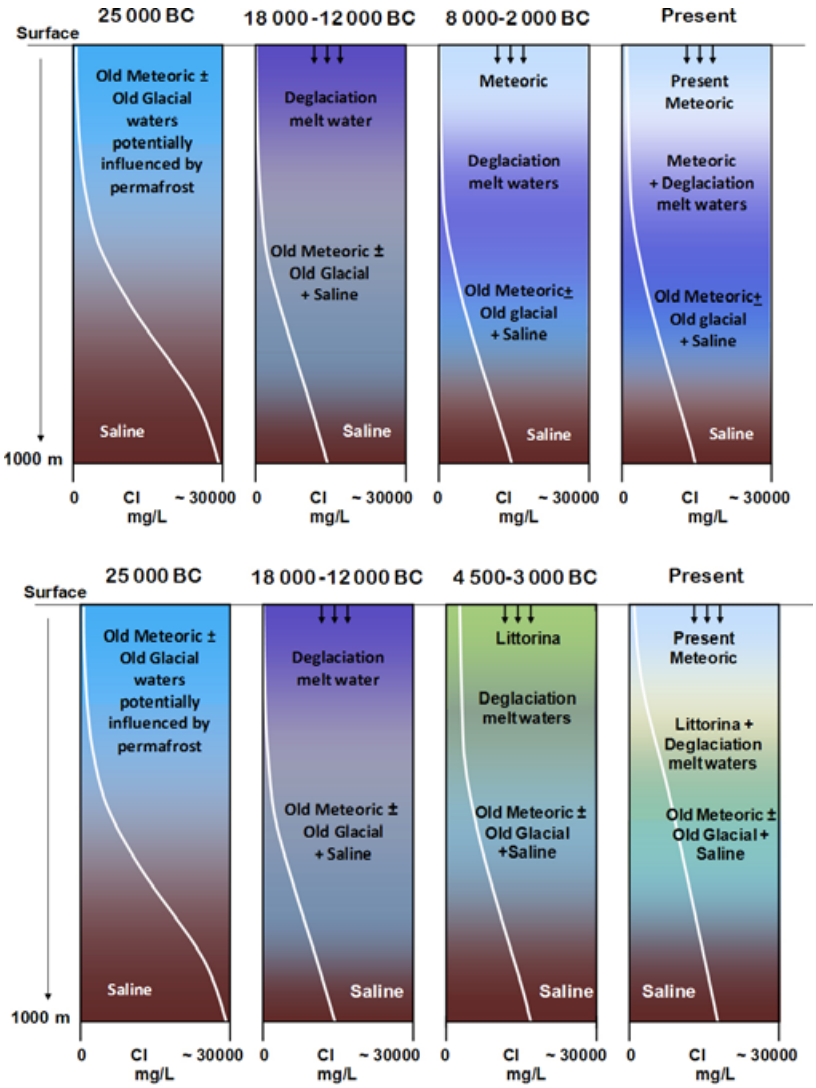

Figure 1-7. *Schematic overview of the current conceptual understanding of late Pleistocene-Holocene groundwater evolution at the Laxemar site showing approximate salinity and groundwater-type distribution versus depth for hydraulically transmissive zones in the Laxemar sub-area. Two different scenarios are illustrated; the upper series representing areas not covered by the Littorina Sea, and the lower series representing areas submerged by the Littorina Sea for a period long enough to influence the groundwater. See text for explanation. (Image taken from /Laaksoharju et al. 2009/).*

1.5 Relationship to safety assessment

In this report the main goal is to provide a comprehensive account of site specific transport properties for Laxemar. The broad intention is that this should not only function as an input to safety assessment, but also as an aid to explaining past and predicting future rock-groundwater interactions of relevance to other disciplines such as Hydrogeochemistry and Hydrogeology. The site specific transport properties are also used as an aid to understanding and quantifying features and processes observed during confirmatory testing.

It is acknowledged that processes active over timescales relevant for safety assessment which can encompass timescales of 0.1 to 1 Ma (or perhaps longer) are often difficult to observe and quantify in a meaningful manner during field scale tracer tests with a duration of at most a few thousand hours and highly unusual hydraulic boundary conditions. In a practical sense this means that while data derived from interpretation of field tests can be used to corroborate process understanding in a general sense, the transport properties sampled may not always be appropriate for application within safety assessment which is associated with different spatial-temporal scales and boundary conditions.

The description of the solute transport characteristics of a site is an intermediate step between site characterisation and safety assessment. It represents a diverse mix of site data and partially generic modelling which is used to interpret the consequences of the interactions between hydrogeological and chemical reactive processes in the rock as well as underlying uncertainties. For safety assessment purposes, the modeller is interested in reducing the complexity of the system description sufficiently that well-reasoned estimates of radiological risk can be made. This entails capturing the main physical and chemical properties of the geological formation while seeking to place conservative bounds on processes and parameters that cannot be adequately quantified in a defensible manner. Highly detailed descriptions of transport properties, while useful from the point of view of qualitative process understanding and palaeo-hydrogeochemical reconstruction, are less relevant for safety assessment purposes. The procedures and methods used for interpretation and abstraction of salient process parameters from field observations are not always easy to reconcile with safety assessment requirements and this report attempts to strike a balance between the requirements of these different, and at times conflicting, modes of analysis.

1.6 A roadmap to this report

This report is divided up into a number of major sections. To assist the reader, a broad description of the content of each of these sections is briefly described below:

Chapter 1 contains a short background description to the work and the principal aims of this report. In addition, an overview of Laxemar including its hydrogeological, geological, and hydrogeochemical setting is given.

Chapter 2 gives a summary of the different mechanisms and processes which influence the transport of solutes within fractured rock. It contains a description of the different phenomena of interest for evaluation of flow related transport properties as well as an account of the main chemical and diffusive transport mechanisms which lead to retention of radionuclides in the microporous structures of the rock matrix and consequently retards their transport by flowing groundwater along paths existing in the fracture system. It is in this chapter that the major processes of interest are outlined. Descriptions are given of how these processes are modelled, and what process-descriptive simplifications are necessary in order to establish an internally consistent and accurate model for the purposes of safety assessment.

Chapter 3 contains an account of modelling carried out to determine the flow-related transport properties of the system. It is here the concept of the flow-wetted surface to flow ratio is elaborated and calculations are made to assess its magnitude. This is one of the key parameters influencing the extent of the retardation effect experienced by radionuclides transported with the groundwater and is central to the description of the transport properties of fractured rock.

Chapter 4 contains a description of the material properties of the rock which govern the retention of radionuclides of interest in safety assessment. Different parameters which describe the retention properties of the rock including sorption, diffusion, and porosity are discussed and measurement data from the site descriptive modelling laboratory programme are presented. The chapter concludes with a retardation model describing the retention parameters related to different rock types, fracture types, and various other structural sub-elements in the rock which can be used in a modular fashion to synthesise a model for simulating the transport of radionuclides.

Chapter 5 contains an account of transport modelling which has been carried out with the aim of establishing typical transport times for a selection of radionuclides of interest. It is here the description of flow-related transport properties is brought together with the retardation model in an integrated transport properties model which is used to make predictions of transport times.

Chapter 6 contains an account of a number of field scale tracer tests which have been carried out with the aim of partially validating the existence of postulated retardation mechanisms and models used for their description. This chapter describes each test in detail including major results and discusses the evidence in support of specific retention mechanisms underlying the apparent retardation of tracers transported within the fractured rock.

Chapter 7 contains a broad summary of what has been learned during the process of site descriptive modelling and important conclusions of importance for continued safety assessment studies concerning Laxemar. The main conclusions regarding site specific transport properties are also outlined in this chapter. In addition, consequences of various sources of uncertainty and phenomena which can have a strong impact upon the retardation of radionuclide transport are discussed.

As an aid to the reader at the conclusion of each major chapter, a short summary is given of the main findings of interest for the site descriptive model, principal uncertainties identified, and what significance these might have for safety assessment.

1.7 Previous model versions

Laxemar 1.2 /SKB 2006c/ was the first site descriptive model for the Laxemar subarea, although it inherited many of the features from the Simpevarp 1.1 /SKB 2004/ and 1.2 /SKB 2005/ model versions.

The main uncertainty of the previous Simpevarp 1.1 and 1.2 model versions was identified to be the lack of site specific transport data. In Simpevarp 1.2, site specific formation factors based upon both laboratory resistivity measurements for all major rock-types and in situ measurements were available. Sorption coefficients, however, were derived based on data from the Äspö Hard Rock Laboratory (Äspö HRL). Due to inconsistencies identified in the parameterisation of data, which was based upon geochemical analogy between Äspö diorite and all major Simpevarp rock types, a different approach was adopted in the Laxemar 1.2 version. Instead of importing Äspö HRL data, sorption coefficients were derived based upon an assumed correlation of sorption properties with the measured surface area of mineral grains.

In the Laxemar 1.2 model version, flow related transport properties and material properties were only partially integrated. The integration of these two aspects of transport was not based on large scale hydrogeological simulations. This decision was principally based upon perceived difficulties in communicating the difference between the transport resistances and advective travel times obtained from large scale flow models used in the Simpevarp 1.2 site description to those obtained from high-resolution flow models including a repository layout developed by safety assessment.

In the Laxemar 1.2 model version, the retardation of radionuclide migration in the hydraulic conductor domains, HCD, was neglected owing to a lack of supporting information required both for the parameterisation of suitable retardation models as well as for estimation of the flow-wetted surface of these features.

2 Overview of conceptual aspects on flow and solute transport properties

The conceptual model underlying the transport properties evaluation in SDM-Site Laxemar is based upon a description of solute transport in discretely fractured rock. Specifically, the fractured rock is viewed as consisting of mobile and immobile zones. The mobile zones are regions within fractures and deformation zones where groundwater flow and advective transport take place. The immobile zones include the rock mass itself as well as stagnant regions within or immediately adjacent to flowpaths where solutes can be retained (i.e. removed temporarily or permanently from the mobile water) /Berglund and Selroos 2004/.

In the conceptual model, advection is the dominant process for moving solutes in the transport direction, whereas the main role of diffusion is to remove the solutes from the mobile water and transport them within the immobile zones.

The conceptualisation outlined above implies that solute transport takes place along flow paths consisting of connected, hydraulically conductive "sub-paths" in fractures and deformation zones of different sizes. The fractures and deformation zones reside in rock domains which can contain one or more different rock types. Rock domains are defined in /Wahlgren et al. 2008/ as rock volumes that show specifically similar composition, grain size, texture, degree of bedrock homogeneity, and degree and style of ductile deformation. Similar subdivisions of the rock are also made to give various hydraulic domains and fracture domains although these are based upon hydrogeological and fracture-statistical premises.

The following sections summarise the conceptual description of flow and solute transport in the Laxemar bedrock and how it relates to the various domains as defined by Geology and Hydrogeology.

2.1 Flow related transport properties

In this section the hydrodynamic properties of the hydraulically conductive regions of the rock are discussed. In the site descriptive model, the groundwater system is divided into three different hydraulic domains. These are defined in the hydrogeological background report /Rhén et al. 2008/ as

- HSD, or Hydraulic Soil Domain. This domain comprises the quaternary deposits or soil overlying the bedrock;
- HCD, or Hydraulic Conductor Domain. This domain comprises the deterministically defined deformation zones as classified by Geology;
- HRD, or Hydraulic Rock Domain. This domain comprises the fractured bedrock outside of the deformation zones and may include so-called minor deformation zones which are not modelled deterministically. As discussed in the following sections, these are also related to the fracture domains which reflect different fracture frequency and orientation characteristics in different rock volumes.

The hydraulic domains are illustrated in Figure 2-1.

The bedrock is divided up into different domains according to geological, fracture-statistical, and hydrogeological characteristics. Since the definitions of these structures are based on different properties of the bedrock they should not be considered to be true subsets of each other.

As described in Section 1.3, the bedrock is divided up into different geological rock domains denoted RSM[A-P]. Both the HCD and HRD domains are hosted within the geological rock domains although, being hydrogeological constructs, they do not necessarily comply with the geological boundaries defining the RSM subdivisions. The bedrock is further sub-divided into a number of fracture domains that represent rock volumes with similar fracture frequency characteristics (denoted FSM*x* where *x* represents an additional alphanumeric identifier). The fracture domains are defined on the basis of the single-hole interpretation work and the statistical treatment of fracture populations. Since the fracture domain subdivisions are based upon fracture characteristics, they too do not necessarily comply with the geological boundaries defining the RSM subdivisions.

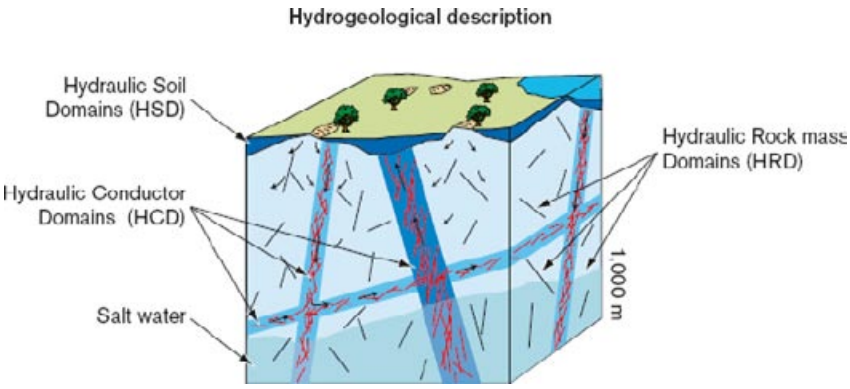

Figure 2-1. *Illustration showing the division of the crystalline bedrock and superficial quaternary deposits into hydraulic domains. Within each domain, the hydraulic properties are represented by equivalent values, or by spatially distributed statistical descriptions /Rhén et al. 2003/.*

Fracture domains are, by definition, considered to be separate entities to the deterministic deformation zones comprising the HCD, although a single fracture domain can be transected by one or more of these zones. The HRD domains can consist of one or more fracture domains. In the bedrock transport properties evaluation, focus is primarily given to the properties of the HCD and HRD. The transport properties of the HSD are handled separately within SDM-Site by the Surface Systems sub-discipline.

2.1.1 Conceptual description of the HCD

The Hydraulic Conductor Domain, HCD, consists of the set of local major and local minor deformation zones, the orientation, extent and properties of which have been described deterministically in the geology background report /Wahlgren et al. 2008/. A deformation zone is a general term referring to an essentially 2D structure along which there is a concentration of brittle, ductile or combined brittle and ductile deformation. A brittle deformation zone is further classified as a fracture zone if no specification is given as to whether there has been a shear sense of movement along the zone. A fracture zone that shows a shear sense of movement is referred to as a fault zone. Although it is possible to find small deformation zones intercepted in the drill core that show exclusively ductile deformation, on the larger scale of the Laxemar local model volume, all local, major and regional deformation zones that have a ductile origin can also be considered to have been subjected to multiple phases of later brittle reactivation.

The Laxemar regional model volume contains a total of 209 deterministically modelled deformation zones, of which 70 are located within the local model volume. Most of these deterministic zones are referred to as ZSM[*Strike*][*Id*], where [*Strike*] (NS, NE, EW, or NW) provides an indication of the strike of the zone, and [*Id*] is an additional alphanumeric identifier specific to individual zones. A subset of the deterministic zones are interpreted based on single-hole observations and inferred zone thicknesses greater than 10 m and are not associated with surface lineaments or corroborated by observations in other boreholes. To facilitate traceability, these zones are referred to by the borehole name and a zone identifier, i.e. KLX*xx*_DZ*xx*. They are modelled as discs with a 564 m radius, a value based on an area equivalent to a 1×1 km^2 square. This area is roughly estimated from an inferred zone thickness of 10 m by a power-law relationship described in the geology background report /Wahlgren et al. 2008/. Since this standard geometry is applied even when the inferred zone thickness is significantly greater than 10 m, it should be noted that this method does possibly lead to the zones' equivalent area being systematically underestimated. Given the variability of deformation zone thicknesses, however, it could also be argued that there is a reasonable chance of underestimating deformation zone area. It should also be noted that although these deformation zones centred on boreholes are high confidence in terms of existence, the confidence levels of the majority of other associated descriptors are medium or low.

Generally, the deformation zones in Laxemar are further classified according to size. Based on their length, they are referred to as regional (>10 km), major (1–10 km), and minor deformation zones, or MDZ (10 m–1 km). The regional and major deformation zones in Laxemar are modelled deterministically, whereas the MDZ and brittle structures with a length less than 1,000 m are handled statistically as part of the stochastic fracture network.

Although modelled as 2D structures, deformation zones are generally made up of swarms of fracture clusters, fracture splays, "stepovers" and other features that are interpreted *en echelon*[1] to link up into large heterogeneous structures of common tectonic origin as shown schematically in Figure 2-2. They are identified and modelled on the basis of aerial, surface, and core-borehole geophysical measurements as well as observations at ground surface and in the cored-boreholes.

In the conceptual model outlined by /Munier et al. 2003/ deformation zones are depicted as consisting of a heavily fractured core for the most part filled with annealed fractures, breccias and low permeability mylonitic features. Outside the core lies a region of rock with a higher frequency of open fractures than the core zone and a consequently higher permeability. Flanking the outer core region is a transition zone with a fracture frequency somewhere in between that of typical rock featuring "background" fracturing and that of the outer core. Deformation zones are typically formed during repeated cycles of tectonic activity over geological timescales and contain many of the same structures as the HRD although intensely localised along a specific geometric orientation in 3D that defines the deformation zone.

The heterogeneous geological structure of deformation zones implies heterogeneous hydrogeological properties and zones typically exhibit considerable complexity in their flow characteristics. The void space characteristics of individual joints and fault segments comprising the zone, their interconnectivity, and orientation to prevailing stresses are overwhelmingly important for the overall hydraulic properties of the zone. This picture is further complicated by the existence of secondary mineralisations formed during ancient hydrothermal events and contemporary mineral precipitation-dissolution processes. Tectonic processes within deformation zones lead to rock fabric alteration which typically results in the formation of mylonite and cataclasite. The latter of these two is commonly associated with fault breccias (particulate) and gouge material (generally cohesive) that can have a strong influence on the local hydraulic properties of conductive elements comprising the zones.

The transmissivity in individual deformation zones generally decreases with depth. It is also expected that that most flowing features are concentrated to the outer core region of deformation zones or even concentrated to the outer core/transition zone boundary /Rhén et al. 2008/. In some cases the inner core of deformation zones behaves as an effective hydraulic barrier owing to its low permeability. An example of this is deformation zones associated with dolerite dykes, observed in e.g. ZSMNS001C, ZSMNS059A and KLX19_DZ5-8_dolerite /Rhén et al. 2008/. These deformation zones are assumed to have a fractured but yet impermeable dolerite core with a permeable wall rock along the dolerite. The continuity of these impermeable cores and conductive flanks is however uncertain.

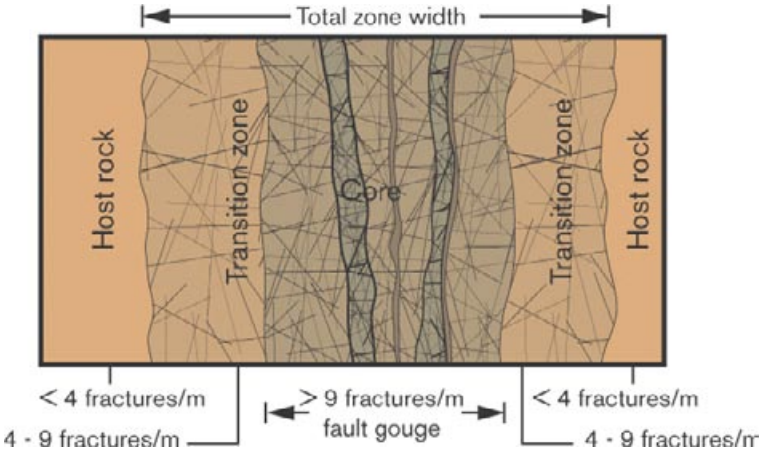

Figure 2-2. *Schematic illustration of the structure of a brittle deformation zone /Munier et al. 2003/.*

[1] The geological term "en echelon" is used to describe parallel or subparallel, closely-spaced, overlapping, or step-like minor structural features in rock, such as faults and tension fractures, that are oblique to the overall structural trend.

2.1.2 Conceptual description of the HRD

The Hydraulic Rock Domain (HRD) is the name given to the relatively sparsely fractured bedrock outside the interpreted deterministic deformation zones and is also taken to include minor deformation zones (MDZ) which are not modelled deterministically. The hydraulic rock domains are defined on the basis of the spatial distribution of hydraulic properties.

As mentioned previously, the bedrock in the Laxemar local model volume is sub-divided into six different fracture domains (denoted FSM_[*Id*], where [*Id*] represents an additional alphanumeric identifier). This sub-division is based upon fracture frequency characteristics /La Pointe et al. 2008/. However, it also reflects the fact that different parts of the rock have different hydrogeological properties. Therefore, the partitioning of the rock volume into hydraulic rock domains as shown in Figure 2-3 and Figure 2-4 differs only slightly from the fracture domain sub-divisions.

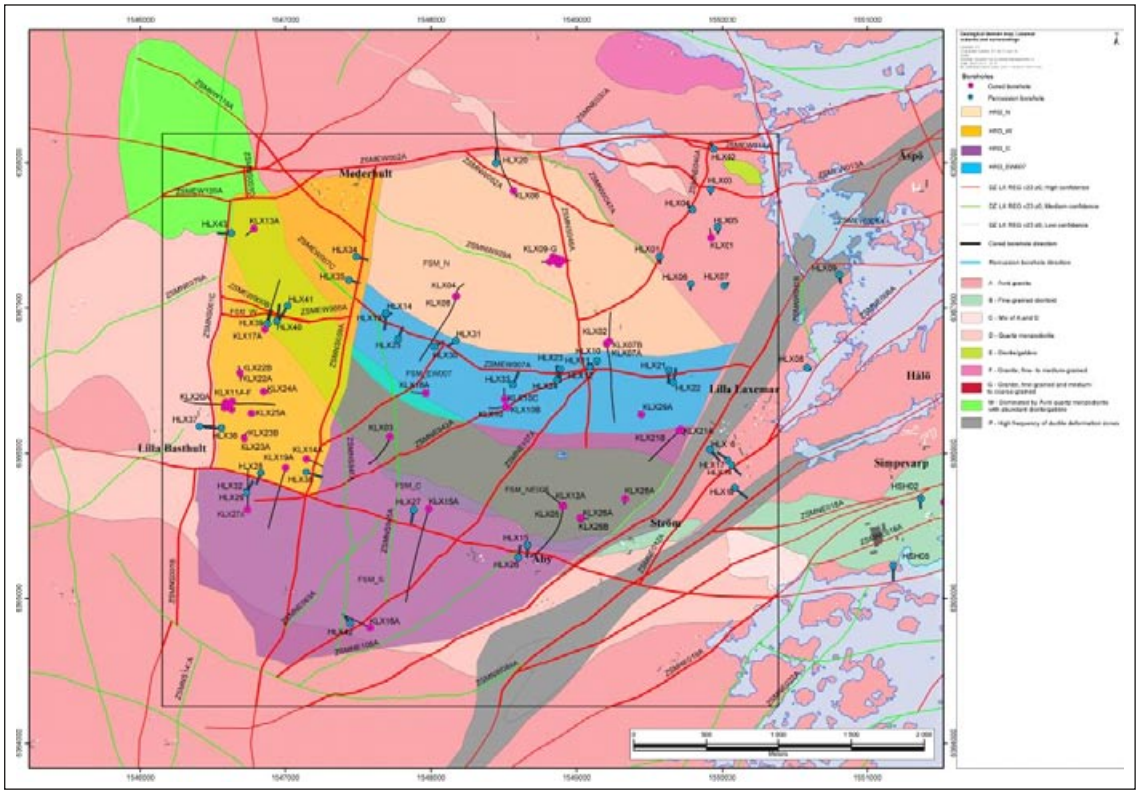

Figure 2-3. *Illustration of the SDM Site Laxemar Hydraulic Rock Domain Model /Rhén et al. 2008/.*

Figure 2-4. *Illustration of the SDM Site Laxemar Hydraulic Rock Domain Model, vertical section from south (left) to north at Easting X=154,800 m /Rhén et al. 2008/.*

The HRD contains many fractures; some open and hydraulically connected to the wider fracture network, some are open although hydraulically isolated, while others may be closed – either tightly sealed by surface asperity contact or annealed by precipitation of minerals. Annealed fractures may be the result of precipitation from saturated hydrothermal fluids or contemporary low temperature groundwater. Annealed fractures may also be reactivated at different times by tectonic stresses.

In the Geology site descriptive model it is hypothesised that the frequency of fractures is correlated with size by way of a power law (Pareto) distribution which implies scale-invariant behaviour. Although a series of alternative models are presented in the geology background report, the power law distribution is judged to be most geologically consistent with the available data /La Pointe et al. 2008/. Larger features are rarely individual fractures and may be considered as linked sets of smaller fractures and minor deformation zones.

Fractures undergoing stress induced shear can interact in complex ways to form minor deformation zones (MDZ). They tend to link up in an en-echelon geometry over a wide range of scales. The so-called, stepover zones where fault fractures interact tend to be locally very fractured and can form efficient conduits for fluid flow in a perpendicular direction to the shear direction. The permeability of these features may be modified by the precipitation of secondary minerals thereby reducing potential for flow. It is generally thought that the direction of increased permeability in overlapping regions of the en-echelon fractures is oriented in the direction of intermediate principal stress unless completely filled by mineral precipitates /NRC 1996/. Deformation zones larger than 1,000 m radius are modelled deterministically in the SDM and are therefore consigned to the HCD. The most likely target volume for the hypothetical repository resides in hydraulic rock domains HRD_C, HRD_W, and HRD_EW007.

2.1.3 Channelised flow phenomena

In fractured crystalline rock it is generally thought that flow is heterogeneously distributed and occurs along preferential flowpaths within fractures and deformation zones. This phenomenon is commonly referred to as flow channelling.

In SDM-Site Laxemar (and Forsmark), six principal types of flow channelling have been identified as having relevance for the bedrock transport properties evaluation. These are:

1. Network-scale flow channelling;
2. In-plane flow channelling;
3. Flow channelling at fracture intersections;
4. Flow channelling at geological interfaces;
5. Flow channelling within foliations;
6. Flow channelling within fault stepovers, shears and fracture jogs.

Other, more exotic flow channelling effects are referred to in various discussions in this report. These, however, are considered to be special sub-types of the above listed categories and are not treated explicitly as separate phenomena. Examples are low temperature erosion pipes in calcite (or possibly laumontite) annealed fractures, and wormhole-like flow pipes lined with hydrothermal precipitates (e.g. quartz or epidote) as might be found within fault zones that have been subject to aggressive hydrothermal activity.

In the following sections, each of the identified six principal types of flow channelling are examined and how they might influence the flow properties of the Laxemar bedrock is discussed. It is noted already here, however, that many aspects of flow channelling are difficult to fully resolve from a surface-based site investigation and may not be possible to properly quantify until the construction of an underground tunnel where more detailed hydrogeological information can be obtained.

Network-scale flow channeling

This type of flow channelling refers to the tendency of heterogeneous fracture networks to exhibit poor hydraulic connectivity and form preferential flowpaths on the scale of the fracture network itself.

When there are large contrasts between transmissivities of individual fractures comprising the network, fluid flow will tend to seek out the path of least hydraulic resistance. If the fracture network is sufficiently poorly connected, this may also give rise to flow compartmentalisation and fractal behaviour. Here, the term fractal is used strictly to describe the spatial distribution of flowing features rather than other scale independent properties such as power law fracture size distributions. Network-scale flow channelling processes of this kind are taken to include both regional flow channelling within linked major deformation zones in the HCD as well as on the scale of local fracture clusters within individual deformation zones and the HRD.

For flowing features within the rock to exhibit this behaviour does not necessarily require the fracture network itself to conform to a fractal spatial distribution as this flow characteristic can arise spontaneously in Poissonian fracture networks when close to the percolation threshold /e.g. Follin et al. 2006/. The impact of fracture network connectivity upon the flow and transport properties of the rock is discussed in more detail in Chapter 3.

In-plane flow channelling

This type of flow channelling refers to the tendency for preferential flowpaths to develop within the plane of individual fractures. It arises due to the variable aperture of the void space between opposing fracture surfaces which results in a spatially variable transmissivity field across the fracture plane.

Although visualised as planar structures, fractures in crystalline rock are typically rough and have highly irregular surfaces. Dilating fractures initially have open, although very slight apertures owing to normal displacement of opposing surfaces. Initially mated, opposing surfaces of such fractures can become mismatched at some length scale due to shear movement relative to the plane of the fracture. When this occurs a somewhat larger void space may emerge where there are regions in which the surfaces are in direct physical contact and regions in which the fracture has a non-negligible aperture /NRC 1996/. Under compression a certain degree of surface asperity contact is usually necessary owing to the need for the fractures to transmit stress. An exception is if the fluid pressure is sufficiently high that the fracture is held completely open. This, however, is highly unusual and such fractures will tend to close again unless held open by mineral precipitates or other detritus in the enlarged void space.

The variable aperture of fractures and the degree of surface asperity contact is dependent upon the effective normal stress perpendicular to the fracture plane. As the hydraulic resistance of a fracture arises due to the viscous forces between the flowing water and the fracture surface, the aperture distribution and the existence of flow constrictions and flowpath tortuosity have a very strong influence upon the effective transmissivity of individual fractures.

The aperture and asperity contact area of a fracture tends to vary with applied stress in a complicated fashion. Generally, surface asperity contact area increases approximately linearly with increasing effective normal stress as the rock deforms elastically /e.g. Glover et al. 1998/. The effective transmissivity of single fractures, however, is known to decrease roughly exponentially with increasing normal stress /NRC 1996/. Substantial shear movements, on the other hand, may cause destruction of asperities and give rise to slickenside striations running parallel to the shear direction. Repeated loading-unloading cycles and shear reversal as might occur during glaciation-deglaciation also tend to result in hysteresis effects for the relation between transmissivity and stress /NRC 1996/. The overall picture of the effect of in situ stress on fracture transmissivity and flow channelling is thus complicated and varies significantly among individual fractures with different tectonic histories. Although the relationship between fracture normal stress and transmissivity is well known for reconfined single fractures described in the scientific literature, it is very difficult to ascertain any universal relationships that are generally applicable for heterogeneous fracture populations. The Laxemar site is no exception in this respect.

A significant concern for flow modelling is that if substantial fractions of fracture surface are in direct physical contact, flow channels may be very narrow and sparsely distributed within individual fractures. In such cases it has been suggested that the frequency of flowing features in the rock may be severely underestimated during flow logging owing to the limited extent of the flow channels and

the low probability of intersection with a borehole. A secondary concern is whether the transmissivities of identified flowing features have been assessed correctly given that flow may be strongly channelised over the radius of influence of the measurement. These concerns have been addressed in the present report by way of generic scoping calculations which are described in more detail in the corresponding background report for transport properties at the Forsmark site /Crawford 2008/.

Flow channelling at fracture intersections

Flow channels arising at the intersection of crossing or terminating fractures have been suggested as possible conduits for fast flow and transport in fractured rock /NRC 1996/. Observations of increased flow at fracture intersections in tunnels constructed in crystalline rock have been reported in the literature /e.g. Abelin et al. 1990, Abelin et al. 1991, Abelin et al. 1994, Neretnieks 1994/. Such features are referred to in this report as fracture intersection zones, or FIZ (using the terminology introduced by /Dershowitz and Klise 2002/). This channelling phenomenon is predicted to occur on the basis of the theoretically reduced viscous resistance for flow parallel to fracture intersections.

For the Laxemar site descriptive modelling, three possible sub-types of flow channels formed at fracture intersections are considered. These are:

A. Simple flow conduits formed at crossing or terminating fracture intersections;

B. Enlarged flow conduits formed due to displacement of block discontinuities;

C. Enlarged flow conduits formed at fracture intersections with enhanced aperture due to spheroidal weathering processes.

These sub-types are illustrated schematically in Figure 2-5.

Flow channels characterised as sub-type A for crossing or terminating fracture intersections are ubiquitous within the rock and will exist wherever there is an intersection between two open fractures. From flow modelling of smooth fracture intersections it has been found that the Darcy flux at fracture intersections can be as much as 2–4 times greater than that within the flanking fracture planes if surface roughness is neglected and the applied hydraulic gradient is parallel to the line of fracture intersection (See /Crawford 2008/). The enhanced Darcy flux at the intersection will, however, probably not be as great as this in the presence of rough fracture edges, discontinuities and filling materials. Even so, it is possible to discount the influence of such flow channels by consideration of the overall flow. This is discussed in more detail in /Crawford 2008/.

Intersection sub-type B is possible where free rock blocks, as might exist in deformation zones, are rotated by shear movement giving rise to an enhanced aperture. In this case it is also possible for stress concentrations at the contacting edges to predispose the corners of the blocks to breakage thereby further enhancing the effective mechanical aperture /Bruines 2003/.

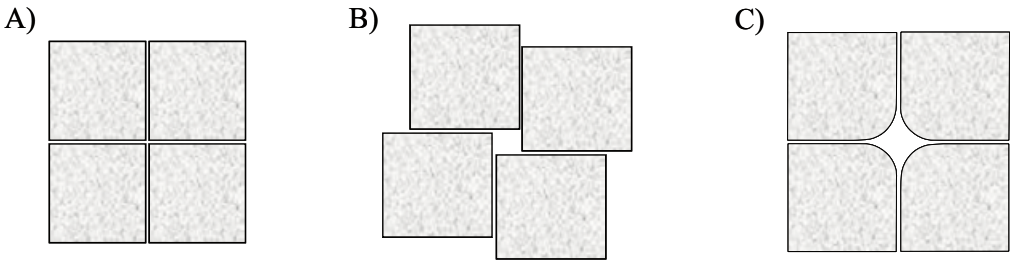

Figure 2-5. *Sketch of different sub-types of flow channelling phenomena potentially occurring at fracture intersections.*

Flow conduits of sub-type C can arise in fractures initially of sub-type A or B as a result of subsequent spheroidal weathering processes. This occurs during geochemical weathering of granitic rock when the formation of secondary minerals in the alteration rim of the fracture weakens its structure. This is particularly the case for oxidative weathering processes where alteration products such as ferric oxy-hydroxides have higher specific volumes than the minerals initially present in the rock matrix. At fracture intersections and block discontinuities weathering is more intense as it can proceed from two adjacent surfaces simultaneously. The combined effect is a tendency for fracture intersections to evolve towards cuspoid geometry with a substantially enhanced aperture. These types of features are more likely to be found in transmissive deformation zones where hydrothermal alteration has occurred most intensely. In Laxemar, the majority of the cored borehole intervals within deformation zones exhibit visible signs of oxidative alteration. This seems to be particularly extensive and characteristic of the dominating E-W striking deformation zones, ZSMEW002A, ZSMEW007A, and ZSMNW042A. Within the fracture domains, only faint to weak oxidative alteration affects approximately 10–25% of the rock volume indicating that a large proportion of the oxidative alteration has been restricted to the HCD.

Flow channels corresponding to sub-types B and C present very little viscous resistance to flow and it is possible for very high flow rates to exist in such features. In these cases, fault gouge and fracture filling materials as well as the hydraulic resistance of entry and exit points are the only entities likely to limit flow. In such cases, aperture based analyses of flow resistance may be inaccurate and relations for flow in packed beds of particulates (e.g. the Blake-Kozeny relation /Bird et al. 2002/) may be more appropriate.

Owing to their limited width, it is very difficult to observe such features in boreholes and it is only possible to infer the possibility of their existence from geological argumentation. Although one cannot estimate the spatial frequency or flow properties of these features directly from observational data in boreholes, it is feasible to make scoping calculations of the impact that they may have on flow and transport of solutes under different limiting assumptions. This is discussed in more detail in Section 3.4.2.

Flow channelling at geological interfaces

Here, flow channels that may occur in the vicinity of dykes and other igneous intrusions in the rock are considered. This includes fractures parallel to dykes and similar geological features, although in this report the definition is extended to also include regions in the rock where penetration of aggressive hydrothermal fluids has rendered the rock matrix locally more permeable.

An example of such a geological interface is the N-S striking dolerite dykes, found in the western parts of the local model area in Laxemar. These intrusions are associated with extensional opening in an E-W direction /Wahlgren et al. 2008/ and follow, at least in part, pre-existing deformation zones, which were reactivated in connection with the intrusion. Their probable extensions, based on magnetic field data /Triumf 2007/, are illustrated in Figure 2-6 (green lines), along with other lineaments deemed possible with respect to dolerite content (red lines). It should be noted that the uncertainty in the prediction of the possible intrusions of dolerite is high, due to the similarity in magnetic data to fracture zones and ductile to brittle-ductile shear zones in general. The probability of the existence of dolerite dykes in ZSMN001C and ZSMN059A is higher, supported by several observations in boreholes intersecting these deformation zones. Flow channelling in these dolerite dykes along with other geological features that are associated with deformation zones are internalised as part of the description of structures comprising the HCD and, although acknowledged, are not given special treatment in this report.

Flow channelling associated with foliations

During ductile deformation, potential flow channels can be created within dilational fractures. These fractures typically form parallel to the notional plane of foliation (i.e. analogous to bedding planes in sedimentary rock) and in the direction of the intermediate stress component /Bruines 2003/. Additional dilational fractures may also form perpendicular to the foliation plane in the convex part of the folding structure /NRC 1996/. These features may occur wherever ductile deformation and foliation occurs although are principally thought to be a feature of the HCD.

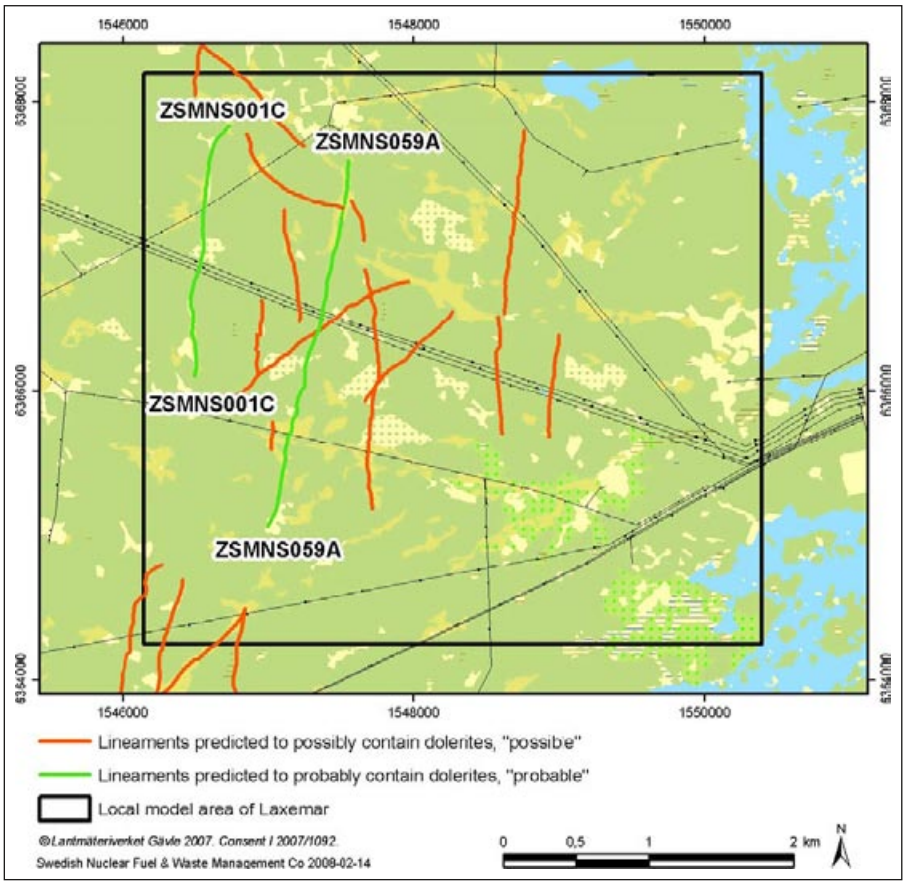

Figure 2-6. *Lineaments deemed probable (green lines) and possible (red lines), regarding their potential content of dolerite in the Laxemar local model area. The probable dolerite dykes coincide with the deformation zones ZSMNS001C and ZMNS059A. Figure taken from /Triumf 2007/.*

Flow channelling within fault stepovers, shears and fracture jogs

Overlapping regions of extensional faults or en-echelon fault zones typically host linking structures including fault stepovers, Riedel shears, crush zones, etc. that are known to form open conduits for flow that can be oriented in a direction parallel to the intermediate stress vector associated with the formation of the fault /NRC 1996/. These conduits may consist of conductive dilating fractures, fracture clusters, and structural sub-elements such as FIZ (principally sub-type B and C with enlarged apertures). The hydraulic properties of such features are complex and not well understood, although they can potentially host highly transmissive flow channels of limited extent.

Precipitates of secondary minerals such as calcite and quartz from past hydrothermal events can modify the permeability of the flow channels, sometimes effectively propping open the hydraulic aperture to resist subsequent closure during altered stress regimes. The cementation of the flow pore space with precipitates and aggregated breccias can also have consequences for the possibility of detecting such features from borehole investigations as they may be wormhole like (similar in many respects to karstic porosity) and hydraulically isolated from nearby open fractures. This is further complicated by the slip of the fault surfaces themselves which can lead to the formation of highly impermeable structures near the core of the deformation zone that can hinder the detection of such features. Low permeability bands can also develop in fault gouge materials subjected to shear /Zhang and Tullis 1998, Zhang et al. 1999/.

Many of the deformation zones at Laxemar are characterised by the occurrence of fault rocks. Cataclasites are most common but breccias and fault gouge occur as well /Wahlgren et al. 2008/. Although such flowing features are probably more likely to occur in the large deformation zones comprising the HCD, similar but less transmissive flow channels could also be hosted in en-echelon, overlapping fractures undergoing dilation (“fracture jogs”) or within minor deformation zones present in the modelled HRD.

Flow conduits of this type within fault stepovers are thought to be very likely in the HCD and the reduced permeability adjacent to these features resulting from diagenetic processes cannot be ruled out as a potential problem for the detection of these features from boreholes drilled from the surface. On the other hand, it is not clear whether flow conduits in the possibly simpler minor deformation zone (MDZ) structures hosted in the HRD should be more, or less easy to detect than "normal" in-plane, fracture flow channels identified from borehole hydraulic testing. Although beyond the scope of what was possible to achieve during this investigation, information contained in the geological Site Descriptive Model could be used to make estimates of the possible biasing effect this might have upon statistics of flowing features identified in the HRD.

2.2 Solute transport

In this section the transport properties of the rock are described. Although the mechanisms and processes that influence transport have relevance for many different environmental solutes, particular emphasis is placed on the migration of radionuclides from a hypothetical repository to the ground surface.

In crystalline rock such as granite, all long range transport is postulated to occur by way of advectively channelised flow. Owing to the low permeability of the rock, the water residing in the porosity of the rock matrix is considered to be immobile and long range transport through the rock mass itself can be neglected over the timescales relevant for safety analysis. There are a number of processes which act to retard the transport of solutes in such a way that they are transported at a slower rate than the groundwater within which they are carried. These processes are described in the following sections.

2.2.1 Fractured rock microstructure and the conceptual understanding of solute transport

In the event of deposition canister failure, radionuclides may escape and migrate to the surrounding rock through the bentonite buffer or backfilling material surrounding the canister emplacement. The radionuclides may then be transported into fractures intersecting the deposition hole, into the disturbed zone around the excavated volume, and into fractures intersecting the tunnels.

Radionuclides that reach the rock volume are transported by the groundwater flowing in fractures within the rock. Certain radionuclides may sorb on the surface of the fractures through which they are transported. From the fractures they may also migrate into the rock matrix by molecular diffusion. As flow is commonly channelised, there may be regions of effectively stagnant water within the fractures into which nuclides can migrate by molecular diffusion and then subsequently migrate into the rock matrix. The interior of the rock matrix contains stagnant "porewater" and micro-surfaces upon which the radionuclides can sorb.

An illustration of a typical open fracture likely to be found in the Laxemar fracture domains is shown in Figure 2-7. Open, water bearing fractures generally feature a thin coating of secondary mineralisation typically consisting of chlorite, calcite, and mixed layer clay minerals. Smaller amounts of other minerals such as hematite, prehnite, epidote, and individual pyrite mineral grains may also be present (see Section 4.2.1). It is frequently found that the mineral coatings exhibit a discontinuous structure rather than forming distinct layers. Single mineral phases such as calcite can therefore be found in direct contact with both the fracture surface and flowing water in the fracture and are interspersed with, for example, chlorite in a patchwork like arrangement. There may be an alteration rim of limited thickness, which may or may not be made visible by red staining (due to the presence of hematite micro-precipitates), adjacent to the fracture surface and extending a short distance into the rock. A small, although statistically non-trivial number of open fractures have been identified at the Laxemar site that lack surface mineralisations possibly indicative (although not necessarily) of geologically recent formation. These are discussed in more detail in Chapter 4.

Fractures may have been formed at different times, been reactivated, and undergone both hydrothermal and low temperature alteration processes giving rise to different fracture filling materials. In borecores taken from the Laxemar site, younger fractures containing filling materials are frequently seen to transect older fractures annealed with filling materials of different hydrochemical origin allowing relative chronological sequences of formation events to be catalogued (referred to as "cross-cutting" relations in /Wahlgren et al. 2008/).

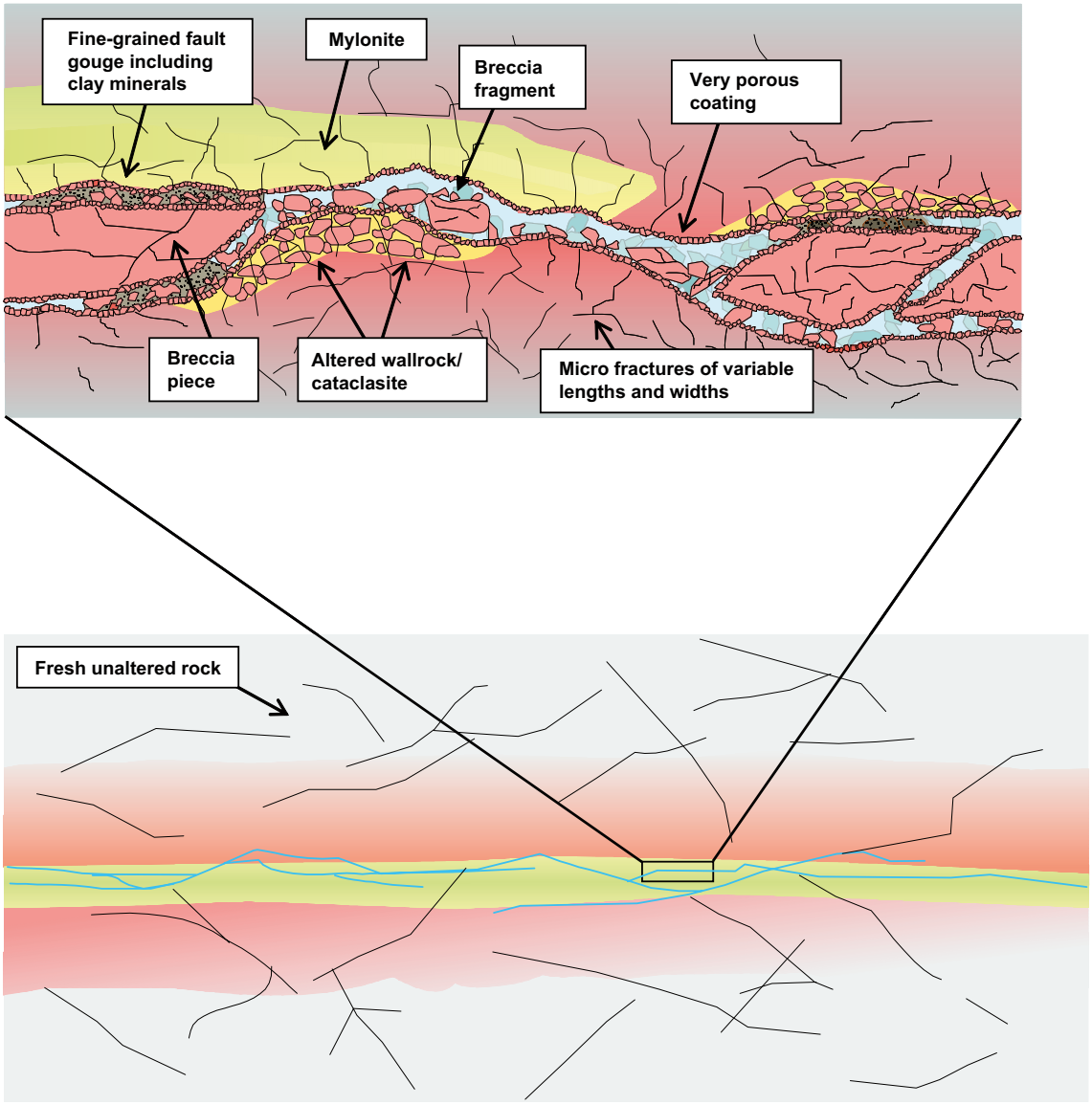

Figure 2-7. *Schematic illustration of a transport path in cross-section. The pathway is characteristic of a typical complex fracture possibly belonging to a minor deformation zone. Based on conceptual model taken from /Andersson et al. 2002/.*

Nine different fracture types have been identified in Laxemar. These differ only in the types of secondary minerals present in the fracture coating and the estimated thickness of the alteration rim. The classification is based partly upon the different historical epochs of alteration that are thought to have occurred at the site, and partly upon the potential for the different secondary minerals to influence transport processes. The different fracture types are discussed in more detail in Section 4.2.1.

The fractures comprising deformation zones are conceptualised to be similar to the background fractures in the fracture domains, although with added microstructural complexity and with different proportions of the nine, abovementioned "type"-fractures. Fractures within deterministic deformation zones comprising the HCD are considered to have layers of hydrothermal and sometimes tectonic alteration that extend from the fracture surface to some distance within the host rock. In some cases, the rock between successive fractures is completely altered leaving no intervening unaltered rock whatsoever. During the evolution of the rock, the fractures may have been sealed by secondary mineral precipitates and reactivated in different cycles. The fracture coatings therefore are not necessarily distributed evenly on both surfaces of the fracture.

In the conceptual model, advection within flow channels is the dominant process for long range transport, whereas the main role of diffusion is to remove the radionuclides from the mobile zone and transport them within the immobile zones where they may sorb on mineral surfaces and be sequestered in the water filled porosity of the rock matrix. In the following sections these processes will be discussed in more detail.

It should be noted that this conceptual model and the methodology for site descriptive modelling in general are, to a large extent, based on previous experience from experiments at Stripa /e.g. Birgersson et al. 1992/ as well as from the Äspö Hard Rock Laboratory (HRL). The conceptual model illustrated in Figure 2-7 is derived primarily from the TRUE project /Winberg et al. 2000, Poteri et al. 2002/ carried out at the Äspö HRL, although is considered applicable to the transport conditions in the Laxemar-Simpevarp area.

Matrix diffusion

Matrix diffusion is considered to be a major mechanism for the transport retardation of radionuclides released from a repository /Neretnieks 1980/. Put simply, it describes the tendency for solutes to be transported by random molecular movement from regions of high concentration to regions of low concentration within the immobile zone. Diffusion in the rock matrix takes place within the connected microporosity of the rock. The microporosity consists mainly of grain boundary pores and micro-fractures. Additional pore types that can exist are sheet silicate pores (the inter-layer regions of clay minerals) and solution pores or fluid inclusions /Möri et al. 2003/.

Autoradiograph measurements of core sample impregnation with ^{14}C-labelled poly-methylmethacrylate (^{14}C-PMMA) /Penttinen et al. 2006/ reveals that grain boundary porosity is the most abundant pore type in unaltered samples with low porosity (<1%) in Laxemar. Altered rock matrix samples featuring high porosities (3–20%), on the other hand, are often dominated by intragranular porosity (i.e. micro-fractures).

It is difficult to obtain fully representative samples from drill cores owing to stress relaxation and mechanical damage sustained during core excavation and sample preparation. This generally results in dilation of the existing pore spaces and the formation of additional micro-fractures that increases the porosity of samples used in laboratory measurements. Using triaxial compression in the laboratory it is possible to make estimates of the changes in sample porosity with increasing stress magnitudes. By means of this technique, core samples obtained from Laxemar boreholes are typically found to have slightly higher porosities in the laboratory relative to in situ conditions owing to the abovementioned effects /Hakami et al. 2008/. From the measurement of microcrack volume strain, however, it is concluded that the additional porosity imparted by micro-cracking probably accounts for a small proportion of the total porosity as established by water resaturation measurements. Laboratory through-diffusion and electrical resistivity measurements are typically made on core samples 1–3 cm in length which is significantly smaller than the 13 cm long samples used in the triaxial compression measurements. The results obtained for samples of different length generally show reasonable agreement, although artefacts related to damage and stress-release cannot be entirely ruled out.

It has been hypothesised /Löfgren 2004/ that grain boundary pores should be ubiquitous throughout the rock mass. The reasoning for this is as follows: When rock magma crystallises at great depths, the grain boundary porosity is virtually non-existent and individual crystals are as closely packed as possible. As the rock is uplifted (which occurred during Proterozoic times in the case of the Fennoscandian shield), the temperature decreases, mineral grains become increasingly rigid and the pressure decreases. As different minerals have different thermal expansion coefficients and bulk moduli of expansion, some grains expand while others contract during this process. This uneven change in mineral volume gives rise to a void surrounding individual grains. Above a certain temperature, void creation is likely to be counteracted by re-crystallisation and other processes associated with metamorphism. At some point during the uplift, metamorphism ceases due to low temperature conditions. Uplift from these depths may create the grain boundary porosity observed today within the rock matrix around repository depth. The differential expansion of mineral grains may also induce strains that result in intragranular micro-fracturing as an additional mechanism for the formation of porosity.

The process of grain boundary expansion is such that one might expect connectivity of grain boundary pores to extend throughout the entire rock mass in a pervasive manner. It should be remembered, however, that this is purely a hypothesis at present and would need to be confirmed by microscopic characterisation and thermal modelling. It is also possible that the constant pressure field in situ does not allow for the relatively small thermal expansion differences to manifest beyond the vicinity of the fracture zones and in the form of micro-fractures. This could also mean that grain boundary pores may only occur in de-stressed core samples where significant decompaction of the mineral crystals forming the rock matrix has occurred.

Studies of in situ rock resistivity, as described in Section 4.3 (and Appendix D), lend strong support to the concept of matrix pore connectivity over large distances into the rock matrix. The existence of diffusive exchange over many tens of metres and very long time scales is also strongly supported by the signatures of palaeo-hydrochemical markers found in the porewater of the rock matrix at the Laxemar site /Laaksoharju et al. 2009/. Specifically, the fact that sampled matrix porewater many metres distant from the nearest identifiable flowing fracture contains relict groundwater signatures is a strong indication of an essentially unlimited matrix penetration depth aside from how fast the process is postulated to occur.

Matrix diffusion is customarily considered to involve diffusion in the stagnant pore water that saturates the microporous system of the rock matrix. Diffusion from flowpaths to stagnant water volumes, however, can also occur in fault gouge, fracture coatings and in effectively stagnant water lying within the fracture plane itself. Diffusion in water-bearing, although hydraulically non-conductive fractures which incidentally intersect advective transport paths may also be significant for retention if the fracture frequency is sufficiently high. Diffusion within the in-plane stagnant zones of an advective fracture as well as subsidiary stagnant water-filled fractures may have important consequences for solute transport when consideration is also given to the additional matrix surface area potentially available for solute interaction /Neretnieks 2006a/.

The rate of diffusive transport in the rock matrix is (in addition to the concentration gradient) determined by:

- The intrinsic diffusivity of the solute species in the pore water;
- Sorption reactions (discussed in the following subsection);
- The geometry of the porous system (the formation factor);
- Non-partitioning interactions between solutes and mineral surfaces (e.g. anion exclusion and the possibly enhanced diffusion of certain cations in the electrical double layer).

Often the diffusivity of a species in the porewater is approximated as the diffusivity of the species at infinite dilution. This is inexact and in certain circumstances additional consideration needs to be given to multicomponent effects and the possible influence of the electrical double layer (EDL) within the limited pore space of the rock matrix. For very dilute solutes multicomponent effects can be largely neglected, although they may be of some importance when consideration is given to the transport of major solutes that determine the porewater chemistry (e.g. salt transport). Electrical double layer effects may need to be considered during different scenarios of repository evolution where anion exclusion and EDL-mediated surface diffusion may have a non-negligible impact upon the effective diffusion properties of the rock matrix. The intrinsic diffusivity of solutes is also influenced by the temperature of the porewater which varies with depth from the ground surface. The effect, however, is small and relatively simple to correct for.

Partitioning is discussed in the following subsection although it can be mentioned already here that the immobilisation of solutes at mineral surfaces within the rock matrix decreases their apparent diffusivity (i.e. depth of penetration). On the other hand, it also enables greater amounts of solutes to be transported into the rock matrix as free concentrations in the pore water are kept low for longer periods of time thereby substantially enhancing transport retardation.

There are four main entities associated with the geometry of the porous system that affect the diffusive transport. These are; the porosity, the constrictivity, the tortuosity, and the pore connectivity. The combined effect on the effective diffusivity from the porosity, tortuosity, and constrictivity is internalised in the formation factor. As transport can only occur in the pore water and generally not

through mineral lattices themselves, the volume available for transport is restricted. The connected porosity (also called the storage porosity) can be divided into transport porosity and "dead-end" porosity. Non-connected porosity, such as fluid inclusions, is believed to be of no importance for matrix diffusion.

Sorption

The term "sorption" is a broad concept that describes the processes by which dissolved solutes are sorbed (adsorbed or absorbed) on or in another substance /IUPAC 1997/. Although sorption can also include Van der Waals interactions, in the context of radionuclide transport, adsorption to mineral surfaces by way of electrostatic and covalent chemical bonding is mainly considered. In this report, the terms sorption and adsorption are used interchangeably.

Sorption can take place on the external fracture surfaces in contact with flowing water or within the micro-porous structure of the rock matrix itself. Since the diffusion-accessible mineral surface area within the rock matrix can be orders of magnitude greater than that of the external fracture surfaces in contact with flowing water, the sorption of radionuclides can give an enormously increased retardation effect over that of matrix diffusion alone.

Transported radionuclides are usually in the form of ionic, charged species and will tend to sorb upon mineral surfaces that possess a net charge of opposite sign. Such interactions are well described in the scientific literature /e.g. Stumm and Morgan 1996/ and the most important mechanisms for this interaction are thought to be ion-exchange and surface complexation. The surface charge of minerals is usually described as having a *permanent* component which is independent of solution composition, and a *variable* component which changes with the solution composition /Langmuir 1997/. Permanent charge arises due to so-called isomorphous substitutions within mineral crystal lattices as well as lattice imperfections or defects. This is a negative charge as elements within the crystal lattice are replaced by elements with a higher number of valence electrons (e.g. Al^{3+} replaced by Fe^{2+} or Mg^{2+}). The variable charge largely occurs at crystal edges where broken bonds remain as reactive ligands and can interact with various aqueous species present in solution.

For phyllosilicate minerals, which includes biotite, chlorite, and smectite clay minerals, the charge is dominated by the permanent component and there is only minor variation with solution composition. For non-phyllosilicate minerals (such as silica, hematite, and feldspar minerals), the charge is dominated by the variable component. The variable surface charge is sensitive to the pH of the solution since it derives from ionisation or reaction of surface oxide groups. These processes give rise to surface "functional groups" such as O^{2-}, OH^{-}, OH^{2+} which possess charge. From the surface chemistry literature /e.g. Stumm and Morgan 1996/ it is evident that most of the minerals that comprise granitic rock will have negatively charged surfaces at all reasonable groundwater pH values.

Figure 2-8 illustrates the principle of the association of ionic solutes with a charged mineral surface.

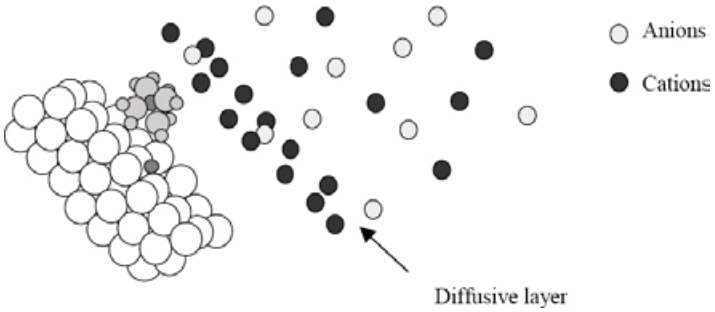

Figure 2-8. *Conceptual illustration of solutes at a mineral surface. Image taken from /Löfgren and Neretnieks 2002/ and adapted from /Stumm and Morgan 1996/. The negatively charged mineral surface is shown to the left of the image (white spheres), while the solution containing ionic solutes are shown to the right (shaded spheres).*

Non-hydrated cations form so-called “inner-sphere” surface complexes and are thought to be covalently bound to the functional groups at the mineral surface (the inner sphere complex is indicated as a single grey sphere at the surface in Figure 2-8). These are considered so closely bound to the surface that they are immobile. Inner sphere complexes do not generally balance the entire negative surface charge of mineral surfaces and as a result there are other hydrated cations bound by electrostatic forces to the surface as “outer-sphere” complexes (shown by the grey sphere surrounded by water molecules in Figure 2-8). Although less strongly bound than inner sphere complexes, due to their close proximity to the mineral surface they are considered to be more or less bound to specific functional groups and their mobility is considerably reduced.

In many cases, the inner and outer sphere complexes cannot completely balance the total negative charge of the surface and therefore other cations in solution are attracted towards the surface. At some distance the more closely bound cations shield the residual charge of the surface from less closely bound cations to such an extent that only the potential gradient normal to the surface limits the movement of the less closely bound cations. For these cations, transport parallel to the surface is relatively unhindered while movement normal to the surface is restricted by electrostatic forces. The volume these cations occupy is referred to as the diffuse double layer or electrical double layer (EDL) /Stumm and Morgan 1996/.

Whereas surface complexing solutes associate with reactive functional groups at the mineral surface, exchangeable solutes reside at the mineral surface in close association with permanently charged sites. This interaction is purely electrostatic in nature. Different solutes have different hydrated charge densities and therefore can associate more or less closely with these charged sites thereby giving rise to different affinities for association amongst different solution components. Although they are treated differently in surface complexation sorption models, it is noted that outer sphere complexes are identical to, and are generally considered to be, ion exchangers /e.g. Bradbury and Baeyens 2005/. Ion-exchange in the context of solute transport in geological media refers to the tendency of certain cations to replace others electrostatically bound to charged sites at the mineral surface due to the differences in sorption affinity.

2.2.2 Modelling approach

In the safety assessment framework that provides the basis for identification of retention parameters in the site descriptive models, retention is assumed to be caused by diffusion and equilibrium sorption /e.g. Berglund and Selroos 2004/. For modelling purposes these processes are usually assumed to be reversible and linear. In safety assessment modelling, diffusive transport of solute within the rock matrix is typically characterised by an effective diffusivity, D_e that can vary spatially depending upon the local micro-structural properties of the rock. The effective diffusivity of specific solutes in the rock depends upon the geometric structure and connectivity of the rock matrix porosity which as already discussed can consist of both micro-fractures and grain boundary pores. The effect of pore space geometry, specifically the tortuosity and constrictivity of the pores, is formalised in the definition of the formation factor, F_f which is independent of the identity of the diffusing species (see /Crawford 2008/). Additional effects such as anion exclusion which can act to reduce the effective diffusivity of specific solutes are typically internalised in the effective diffusivities used in safety assessment calculations by way of an additional correction factor.

The sorption of specific solutes on mineral surfaces is characterised by a linear partitioning coefficient, K_d that describes the equilibrium relation between sorbed and aqueous solute concentrations. While the effective diffusivity is relatively insensitive to the identity of the diffusing species, the sorptivity of different solutes can vary over many orders of magnitude, ranging from very weak sorption in the case of certain ion-exchanging solutes to very strong sorption in the case of trivalent actinides and lanthanides. Some solutes such as tritium, Cl^- and I^- have little or no perceptible sorption at all and their rate of uptake to the rock matrix is governed by the effective diffusivity and storage porosity of the rock matrix.

The sorption of solutes on specific rock types is related to the distribution of minerals in the rock as different solutes exhibit varying affinities for different mineral phases. This is connected to both the surface area and site density of permanent charge and surface reactive groups on individual mineral grains. Sorption is strongly influenced by the composition of the groundwater. The ionic strength,

pH, Eh (redox), and presence of various complexing agents can all modify the strength of sorption and have a very strong influence on the mobility of specific solutes. It is frequently the case that the apparent sorptive variability between different rock types is less than that observed within rock types due to the acute sensitivity of sorption for minute changes in groundwater composition and experimental conditions between different experiments.

All sorptive variability is internalised in the K_d values and uncertainty ranges used in safety assessment by measuring the sorption of radionuclides of concern on different representative rock types in contact with site specific water compositions selected to mirror the likely groundwater chemistry to be found at the site over the relevant timescales.

It is thought that radionuclides will principally be transported via a sequence of pathways featuring successively increasing flow in the HRD until they encounter flowpaths in the HCD from where they may be transported to the near surface. Implicit in this conceptual model is the conjecture of transport in a dual porosity system where there is a clear demarcation between advective and diffusive domains. This is a modelling simplification. In reality, a hierarchy of scales exist for transport within the rock which results in a continuum of behaviours spanning the different size realms.

The use of a Fickian model for solute diffusion in combination with a linear model of sorption (as implied by the K_d concept) are modelling simplifications of what is in reality a complex, coupled reactive transport process. Generally, such simplifications are justified on the basis that the transported radionuclides are considered to be extremely dilute, trace components within the groundwater. There is a broad scientific consensus, however, that provided appropriate parameter values are selected for the prevailing conditions the use of these modelling simplifications is adequate for the goals of safety assessment (see /e.g McKinley and Scholits 1993, NEA 1999, Alexander et al. 2003/). With regard to sorption, the use of a constant K_d value is contingent upon the following conditions being fulfilled /Crawford 2006/:

- The modelled process is a true equilibrium sorption process;
- The water chemistry, mineralogy, and physical state of the rock are identical to those used in partitioning coefficient data acquisition and do not vary in time and space;
- The solute concentration range encountered along the transport path (for the radionuclide of interest) must not invalidate the fundamental assumption of sorption linearity.

The mechanisms by which radionuclides are postulated to interact with the rock matrix (i.e. diffusion and sorption) are also applicable to the transport of other solutes dissolved in the groundwater and are considered to be part of the suite of chemical reactive processes that affect groundwater composition. For groundwater constituents that are present in sufficiently high concentrations that they themselves exert an influence upon the groundwater hydrogeochemistry, simplifications such as those outlined above cannot be used and more sophisticated reactive transport models must generally be employed.

2.2.3 Alternative processes and process models

Alternative conceptual models for transport could involve additional processes or more refined descriptions of the presently considered processes. In the Laxemar transport properties site descriptive model presented in this report, a number of additional mechanisms have been included in the transport modelling of specific radionuclides that have not been considered in previous site descriptive model versions or safety assessments made by SKB. Specifically, the impact of diffusion into in-plane stagnant zones from narrow flow channels has been considered as well as the consequences of diffusive uptake into the rock matrix in a 2D radially symmetric mode rather than a 1D linear mode as is typically assumed in safety assessment modelling. In the case of stagnant zone diffusion, the scoping calculations made incorporating reasonable assumptions give indications that substantial enhancement of radionuclide transport retardation is possible (see Chapter 5) if these mechanisms were to be fully considered in safety assessment.

For radionuclide retention, consideration of more refined representations of radionuclide sorption (process-based, thermodynamic sorption models) and additional retention processes (e.g. precipitation and coprecipitation) are of particular interest. Modelling activities involving process-based models of sorption have been initiated and are ongoing /SKB 2007/. Although not intended to

supersede the use of simplified linearised approaches for transport modelling in the short to medium term, they will play an increasingly significant role in the selection of K_d data appropriate for specific scenarios and partial validation of modelling simplifications used in safety assessment modelling.

Similarly, more detailed consideration of surface mediated transport processes such as anion exclusion and surface diffusion of cations is envisaged as an aid to selection of appropriate data for matrix diffusivities in future safety assessment. Although anion exclusion is an important phenomenon which may decrease uptake of anionic species to the rock matrix, enhanced diffusion of cations in the electrical double layer is currently thought to be of relevance only for very weakly sorbing solutes (more specifically, cations that sorb by ion-exchange). The possibility of more detailed models of matrix diffusion incorporating multiple rates of mass transfer in heterogeneously distributed porosity, and possibly also process based descriptions of diffusion (i.e. Maxwell-Stefan) are possible avenues for future work, although it is not yet clear whether they will provide significantly improved models and insights for safety assessment applications.

3 Flow related transport properties model

As mentioned in preceding sections, solute transport in fractured rock occurs primarily along advective flow paths hosted within fractures and deformation zones. Matrix diffusion coupled with sorption has also been identified as the main retardation process that limits the rate at which solutes are transported along these flowpaths. In general, the greater the surface area in contact with flowing water (the so called "flow-wetted surface", or FWS) for a given water flowrate, the greater the interaction will be with both the fracture surface itself and the rock matrix. Within SDM-Site the flow-wetted surface to flow ratio (FWS/q) is referred to as the "F-factor" /Andersson et al. 1998/ or "hydrodynamic transport resistance". The F-factor is a key parameter governing the transport of radionuclides within fractured rock.

The conceptual understanding and modelling of channelised flow within the rock are central for the prediction of radionuclide transport retardation. In this chapter, the analysis of hydrodynamic controls on radionuclide transport is presented. Here, this takes the form of a simplified conceptual model for transport from a canister position to the near surface via flowpaths of sequentially increasing transmissivity and complexity. The focus is upon identifying the flow related transport properties of typical flowpaths within the bedrock. Using the data and models supplied by Hydrogeology for the focused volume in Laxemar, predictions of F-factors and advective travel times are made according to this conceptual model and a set of assumed boundary conditions. The estimated F-factors and advective travel times are then used as the basis for calculations presented in Chapter 5 where the transport times of representative radionuclides are estimated for site specific conditions at Laxemar.

3.1 Overall modelling strategy

The repository siting concept includes a respect distance of a minimum of 100 m between any given canister emplacement and regional deformation zones with a surface trace length in excess of 3,000 m /Munier and Hökmark 2004/. These are primarily avoided for mechanical protection, although it may be noted that such features also typically have a high transmissivity. One consequence of the respect distance requirement is that zones of high transmissivity that may provide fast transport paths to the biosphere are therefore avoided. In addition to this, the locations of individual canister holes are chosen both to avoid fractures along which sufficient seismic-induced movement can occur that would jeopardise canister integrity as well as to minimise the possibility of buffer erosion from the deposition hole during potential post glacial episodes of increased water flow. The fractures which are likely to intersect a canister position may therefore not be representative of the HRD as a whole and thus should be treated separately in any consideration of typical flowpaths from the repository to the near surface.

In the modelling work presented in this report, transport is conceptualised to occur along advective flowpaths in a multi-compartment system. This is illustrated schematically in Figure 3-1. The three compartments assumed in the transport model are:

1. The non-engineered near field (NNF);
2. The immediate far field (IFF);
3. The distant far field (DFF).

In this model, the non-engineered near field (NNF) is assumed to comprise approximately the first 10 m, or so from a canister position intersected by one or more low transmissivity fractures to the nearest large conductive structure within the HRD. The distance of 10 m is arbitrary although thought to be not an unreasonable order of magnitude estimate of the average distance for a "typical" transport path in the NNF.

The immediate far field (IFF) is assumed to comprise the first 100 m, or so in the HRD. This distance is also arbitrary, although motivated by consideration of the respect distance as described above. Here, the choice of 100 m is intended largely for illustrative purposes and may not necessarily

coincide with forthcoming repository layout designs. Since fractures featuring high transmissivities are likely to be avoided when selecting canister deposition holes, typical flowpaths within the IFF should, on average, have higher transmissivities than flowpaths within the NFF.

The distant far field in the present context is taken to comprise the deformation zones residing in the HCD. In all, some 209 deformation zones located within the Laxemar-Simpevarp regional model domain have been modelled deterministically in the Hydrogeology SDM for Laxemar /Rhén et al. 2008/. Out of these 209 zones, 70 are located within the local model domain. Some of the larger deterministically modelled deformation zones within the local model volume are visualised in Figure 1-5.

The description of transport in the HCD is simplified by considering only those deformation zones in the analysis that are thought to have the most dominant role in forming flowpaths from a repository to the near surface. Some examples of what could be considered to be potential pathways are illustrated in Figure 3-2.

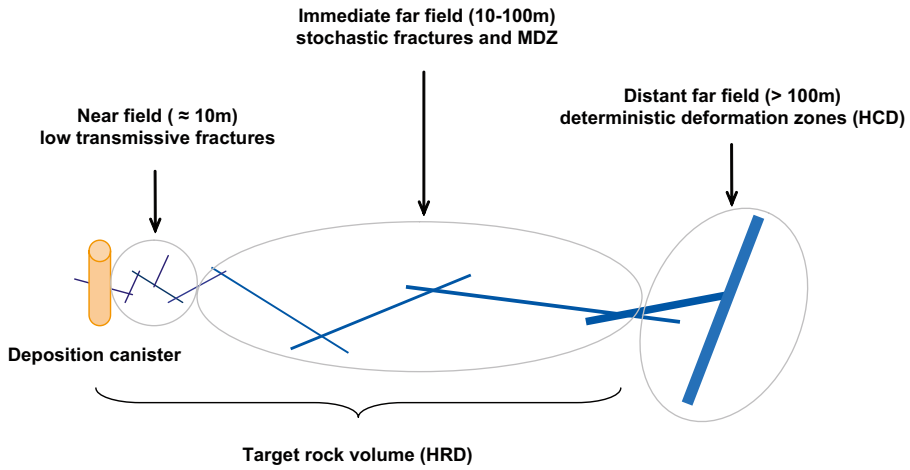

Figure 3-1. *Illustration of a potential flowpath from a hypothetical repository to the near surface. Transport is conceptualised to occur along a sequence of flowpaths featuring increasing transmissivity.*

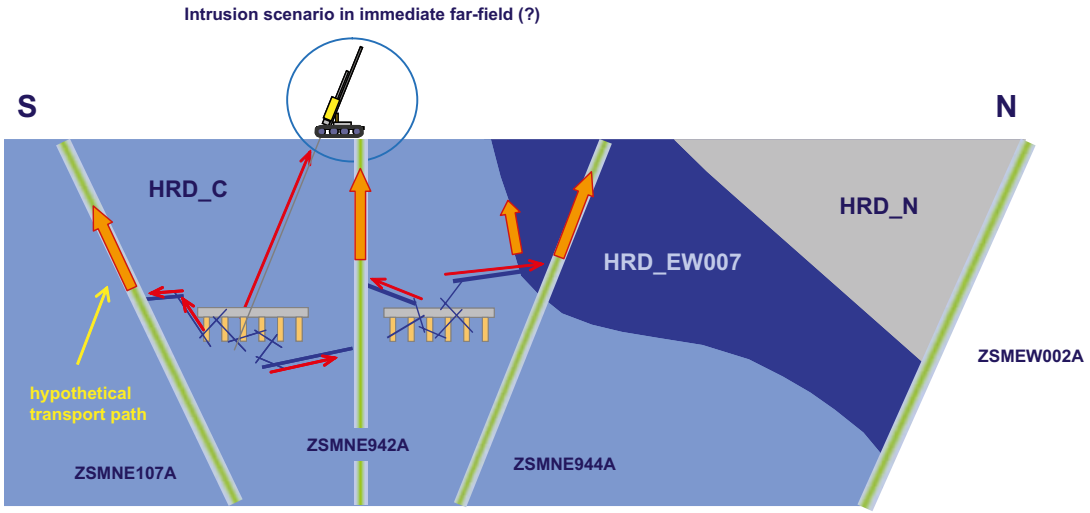

Figure 3-2. *An illustration of some potential flowpaths through the HCD considered likely for transport from a hypothetical repository. The vertical section running from south to north at Easting X = 154,800 m is based upon the illustration of the SDM Site Laxemar hydraulic rock model given in /Rhén et al. 2008/.*

Although issues concerning the specific layout of the repository are not considered within the SDM transport properties evaluation, it is assumed that the bulk of a hypothetical repository would most likely lie in the central part of the local model volume in the vicinity of some of the steeply-dipping deformation zones such as (although not necessarily) ZSMNE944A and ZSMNE107A, and the subvertical-dipping zone ZSMNE942A as illustrated in Figure 3-2. For the analyses of hydrodynamic transport resistance presented here, transport is considered from a hypothetical repository at elevation –500 m to the near surface which is taken to be at an elevation of –100 m. Most of the hydrodynamic transport resistance is encountered at greater depths within the HCD, so the neglect of the highly transmissive features in the upper 100 m, or so of the bedrock does not substantially influence the estimated F-factors.

Within safety assessment, alternative scenarios of radionuclide transport are considered. One of these is the possibility of a deliberate or accidental anthropogenic intrusion as illustrated in Figure 3-2. In such a situation, transport via the HCD may be bypassed completely. Also, in a safety assessment setting it may be necessary to consider scenarios where transport occurs in the backfilled tunnels leading from the repository to the surface. In this report there are no specific calculations made for such migration paths as these are considered to be more of a Safety assessment character and not strictly part of an SDM.

In the overall modelling strategy, F-factor estimations are made for each sub-compartment of the hypothetical transport path assuming a pre-defined set of reference conditions. In the calculations presented in this chapter, a local hydraulic gradient of 1% is assumed as a reference condition for each sub-compartment. This allows comparisons to be made of the relative importance of different compartments given different scenarios for the local hydraulic gradient.

The cumulative F-factor for the complete transport path is given by:

$$F = \left(\frac{i_0}{i_{NNF}}\right) F_{NNF_0} + \left(\frac{i_0}{i_{IFF}}\right) F_{IFF_0} + \left(\frac{i_0}{i_{DFF}}\right) F_{DFF_0} \qquad \text{(Eq. 3-1)}$$

Here, the terms F_{NNF_0}, F_{IFF_0} and F_{DFF_0} refer to the F-factor (yr/m) calculated for each compartment under the reference hydraulic gradient, i_0 (m/m). As the F-factor is inversely proportional to the hydraulic gradient, the numeric value for each compartment can then be easily rescaled for different scenario-specific values i_{NNF}, i_{IFF}, and i_{DFF} (m/m).

It should be noted that the calculation procedure represented by Equation 3-1 makes no a priori consideration of flowpath persistence /e.g. Painter and Cvetkovic 2005/ which may need to be considered if realistic distributions of F-factors are to be estimated for the multi-compartment system. Flowpath persistence specifically refers to the tendency of fast flowpaths in one compartment to be associated with fast flowpaths in subsequent compartments. In this report the sum of median F-factors obtained for each compartment are considered to be approximately representative of the composite transport path and estimates of the overall F-factor are made based on this premise. The demarcation of the transport system into a three-stage compartment is used here purely for illustrative purposes and for making scoping calculations to account for where the main hydrodynamic transport resistances are encountered in the rock. In SR-Site, the hydrogeological models comprising the HRD and HCD are used directly in an integrated model where flowpath persistence arises naturally.

3.2 Overview of input from Hydrogeology

The main source of input data used as a basis for the calculations presented in this chapter is the hydrogeology background report /Rhén et al. 2008/. The overall approach to modelling the site specific hydrogeological properties combines a deterministic representation of the major deformation zones residing in the HCD with a stochastic representation of the less fractured rock outside these zones residing in the HRD. For the fracture domains comprising the HRD, the stochastic description is based upon a Discrete Fracture Network (DFN) representation conditioned to borehole observational data. In SDM-Site this is referred to as the Hydrogeological DFN. The description of the HCD, on the other hand, is based upon a 2D or 3D representation of deformation zone structures incorporating a simplified model of lateral and depth dependent transmissivity variation, also conditioned to borehole observational data.

The various models and input data supplied by Hydrogeology are described in the following sections.

3.2.1 Hydrogeological data

A detailed account of the hydrogeological input data gathered for the Laxemar Hydrogeology SDM is given in /Rhén et al. 2008/ and only a brief overview is given here.

The methods used for hydraulic characterisation of the bedrock differ according to the drill technique employed. The shallow, percussion-drilled (HLX) boreholes are 140 mm in diameter and typically less than 200 m deep. These are investigated using the HTHB method which combines pumping and impeller flow logging. HTHB measurements generally have a measurement threshold corresponding to a fracture transmissivity of about 10^{-6} m^2/s and therefore can only be used to characterise structures featuring relatively high flow rates.

For the core-drilled (KLX) boreholes, both the Posiva Flow Log (PFL) and Pipe String System (PSS) methods have been used for hydraulic characterisation. The PFL method can be used in two different modes (PFL-s and PFL-f) as described in /e.g. Rouhiainen et al. 2005/. In this report, however, PFL-f measurements are generally the focus of the discussions since such measurements are intended to detect individual fractures on a dm scale spatial resolution. The measurements are made at steady state flow conditions after roughly a week of pumping the entire borehole at different drawdowns. The flow itself is measured by a thermal pulse or thermal dilution method for a packed off section of 0.5 m length sealed with rubber discs. The probe is winched in increments through the borehole to obtain a detailed map of borehole inflows. By measuring the ratio of flows at two different drawdowns, the background head can be calculated and, assuming approximately radial flow conditions, the transmissivity can be estimated. The quantitative transmissivity threshold for the measurement method varies depending upon the field conditions, although typically it is on the order of 10^{-9} m^2/s in Laxemar. Qualitative indications of flow can be found at transmissivities nearly an order of magnitude less than the quantitative limit.

The PSS measurement system is based upon a constant head, double-packer injection method. In this case, the packed section is pressurised (i.e. rather than pumping the entire borehole as in PFL) and the transient flow vs. time curve is interpreted to give a best estimate transmissivity in addition to an assumed steady state value obtained after 20 minutes of injection. The PSS method has a measurement threshold of roughly 6.7×10^{-10} m^2/s which is lower than PFL-f although the interpretation is complicated by the possibility of transient effects in isolated fracture clusters which are not easily discernible from connected fractures of low transmissivity. Locally connected fractures short circuiting with the borehole above or below the packed-off section can also give false indications of hydraulic connectivity. For these reasons, the Hydrogeological DFN produced by Hydrogeology is largely based upon PFL-f measurement data. The consequences of this are discussed in the hydrogeology background report /Rhén et al. 2008/ although is also discussed in Section 3.6.1 in the context of low transmissive fractures intersecting individual canister positions.

3.2.2 Hydrogeological description of the HRD

Fracture set orientations

In the Geology SDM, fractures are classified into different sets based upon similar strike and dip as measured from core-borehole intercepts. Classifying the observed fractures into different sets allows the anisotropy of preferred orientation to be represented in a relatively straight-forward manner. The SDM-Site Laxemar geological DFN orientation model uses global fracture orientation sets across all fracture domains although the fracture intensity and size distribution are treated as fracture-domain and fracture-set specific properties /La Pointe et al. 2008/. The global fracture sets are parameterised using a univariate Fisher hemispherical probability distribution /Fisher 1953/, which models the distribution of fracture poles as a Gaussian cluster around a specific preferred orientation. It is the equivalent of the symmetrical, bivariate normal distribution mapped to a spherical surface. The resulting discrete fracture network (DFN) model represents a synthesis of data from all boreholes and is intended to represent the average properties of the fractured rock within the investigated rock volume.

In the DFN model produced for SDM-Site by Hydrogeology, the membership of fracture sets is determined on the basis of “hard sector” divisions where fractures are clearly demarcated into specific sets depending upon whether they fall within or outside predefined boundaries in a stereonet plot of projected fracture poles. The DFN model produced by Geology, on the other hand differs slightly in that it represents a mixture of hard and so-called “soft sector” sets and thus there is some overlap of the fracture pole clusters.

Fracture intensity

The volumetrically normalised total area of fracture planes in the rock volume is called the fracture intensity or P_{32} (m^2/m^3) and can be estimated from the borehole fracture intersection frequency, P_{10} (m^{-1}) after correction for orientation bias in the observational data /Terzaghi 1965/. Details of the correction procedure can be found in the hydrogeology background report /Rhén et al. 2008/.

Whether or not a fracture is mapped as open or closed in the geological interpretation does not say a lot about its hydraulic aperture. Fractures that are hydraulically closed by surface asperity contact although non-sealed (i.e. that physically part the borecore) will be mapped as open if the fracture is judged to be genuine. Since fracturing can occur during drilling and bore core extraction, this is a judgment that relies on physical examination of the borecore fracture surface. As the evidence is frequently ambiguous, the interpretation is assigned a confidence level in the SICADA database (open-certain, open-probable, open-possible).

By and large, only completely sealed fractures that do not part the bore core or sealed fractures that have clearly been broken open during drilling and core extraction are mapped as closed-certain in the geological interpretation. Most sealed fractures that have been broken during drilling are mapped as closed-probable or closed possible which reflects the uncertainty of actually determining if they are pre-existing or incurred during drilling.

Fractures are mapped as partly open if there is clear evidence for open sections within an unbroken borecore. These are typically fractures that only partly penetrate the borecore or sealed fractures that host visibly permeable structures. In the Hydrogeological DFN model, the fracture intensity (P_{32}) is estimated on the basis of open and partly open fracture statistics within the core boreholes. The geological DFN, on the other hand, considers all fractures both open and closed. An implicit assumption in the hydrogeological modelling is that the fractures are assumed to be either geologically open across their full extent, or closed (annealed) across their full extent. The validity of this assumption is discussed later in the context of channelling effects although it can be noted already here that it is an assumption that is central to the estimation of the flow wetted surface within the rock.

Fracture size distributions

Although the open fracture areal intensity (P_{32o}) in the rock can be readily estimated from 1-dimensional statistics of fracture-borehole intersection, the distribution of fracture sizes within the rock is a much more difficult parameter to quantify. In the geology SDM, statistics of fracture trace length on surface outcrops are measured for fractures on the scale of metres to tens of metres. In addition to this, there is also information available for lineaments on the scale of 1 km to several kilometres. A significant problem is that there is a substantial gap in the data for fractures in the size range, from tens of metres to 1 km (i.e. side length).

There are a number of different alternative models that can be used to represent the distribution of fractures sizes, including the lognormal, exponential, gamma, and power law distributions /e.g. Bonnet et al. 2001/. Some of these are discussed in the geology discrete fracture modelling background report /La Pointe et al. 2008/ and the geological SDM strategy documents /Munier 2004/. A commonly used assumption is one of a mode of fracturing that spans all scales in a continuous manner (the so-called "tectonic continuum" hypothesis). In keeping with this hypothesis, each fracture set in the Hydrogeological DFN is assigned a frequency-size distribution that is modelled as a power law (Pareto) distribution which is inherently scale invariant. The key parameters for the power law distribution are the so-called shape parameter, k_r (the power law exponent) and the location parameter, r_0 (essentially the smallest fracture size considered in the model).

For the purposes of synthesising a Hydrogeological DFN model, it is thought that trace lengths on surface outcrops are not relevant for parameterising the fracture network at repository depth owing to differences in the mechanisms of their formation. An alternative procedure is therefore used for estimating the appropriate fracture parameters, r_0 and k_r. The method employed is based upon an iterative simulation procedure coupled with an analysis of open fracture connectivity and is described in the following sections.

Spatial distribution of fractures

Although fractures within the HRD at first glance appear to be distributed in a random fashion, this is not always the case and the variation of fracture intensity and preferred orientation can vary as a function of depth, lithology, influence of tectonic processes, or other geological factors. A large proportion of the variability is accounted for by the division of the rock into different fracture domains. For the Hydrogeological DFN, additional sub-divisions within fracture domains are proposed in order to account for depth variation of hydrogeological properties. Even after accounting for these coarse scale variations, there are frequently regions that show indications of spatial clustering.

If the locations of fracture centroids are completely independent, constant, and uniform (isotropic) over a rock volume, then the system is said to be random /Munier 2004/ and the spatial distribution is described as being Poissonian. A direct and testable consequence of a Poissonian spatial structure is that the frequency of fracture intercepts observed in a borehole should be approximately constant (i.e. showing no trend or structure) and their spacing should follow an exponential distribution. Using different geostatistical methods, this analysis can also be extended to fracture trace centres identified on surface outcrops as described in /Munier 2004/ and the geology SDM /La Pointe et al. 2008/.

For a Poissonian distribution of fracture centres one would expect the fracture intensity to scale with the Euclidean dimension; double the volume of the rock, for example, and the total number of fractures should also double. On the other hand, for a system which exhibits fractal clustering, where fracture centroids exhibit a non-random spatial structure, this may not be the case. In the spatial variability evaluation in the geological DFN report for Laxemar /La Pointe et al. 2008/, the observational data were found to reasonably consistent with a Euclidean scaling regime, and it was suggested that a Poissonian spatial model is probably the most self-consistent model for fracturing at Laxemar over all scales of interest.

As the Hydrogeological DFN produced by Hydrogeology is based exclusively upon cored borehole data, there is not sufficient data to argue convincingly in favour of a fractal spatial distribution or indeed any other kind of spatial model. The simplest spatial model, however, is Poissonian and on the basis of the geological argumentation in favour of this, it has been assumed in the hydrogeological modelling work. It should be noted that this does not imply that the distribution of flowing features also exhibits a Poissonian spatial structure. As discussed previously in Section 2.1.3, fractal clustering of flowing features can arise spontaneously in a Poissonian fracture system if it is close to the percolation threshold /Follin et al. 2006/.

Resultant Hydrogeological DFN model

The modelling procedure used for obtaining Hydrogeological DFN parameters for each of the fracture domains comprising the HRD is described in detail in the Hydrogeology background report /Rhén et al. 2008/. The main steps required in constructing such a model are illustrated in Figure 3-3.

A key assumption in the Hydrogeological DFN modelling work is the hypothesis of a correlation between fracture size and transmissivity. The reasoning behind the hypothesis of a size-transmissivity relation is two-fold. Firstly, one can infer the existence of a correlation owing to the fact that large joints and fault fractures are also commonly associated with larger dilation and shear movement than smaller features. Indeed, the strategy for identifying and avoiding deposition positions in unfavourable locations is based upon an inferred relationship between fracture size and potential for shear movement during deglaciation (see /e.g. Munier and Hökmark 2004, Cosgrove et al. 2006/).

It is not unreasonable to anticipate therefore that the mean hydraulic transmissivity of such features is also correlated with size. The second argument relates to the fact that deformation zones are often comprised of a number of smaller elements interpreted en-echelon as a single feature. Larger fractures and minor deformation zones are also more likely to feature greater microstructural complexity than smaller single fractures in the rock. For this reason one can also suspect that larger features have greater potential for hosting fast flow channels of greater transmissivity than smaller features.

As it is not possible to observe these correlations in a quantitative fashion directly in the field, three different size-transmissivity models have been used in the Hydrogeological DFN modelling. These three models are thought to represent the approximate range of possibilities applicable to Laxemar. As discussed in /Rhén et al. 2008/, two extreme assumptions are to assume either a direct correlation between fracture size and transmissivity or to assume there is no correlation. These are referred to as

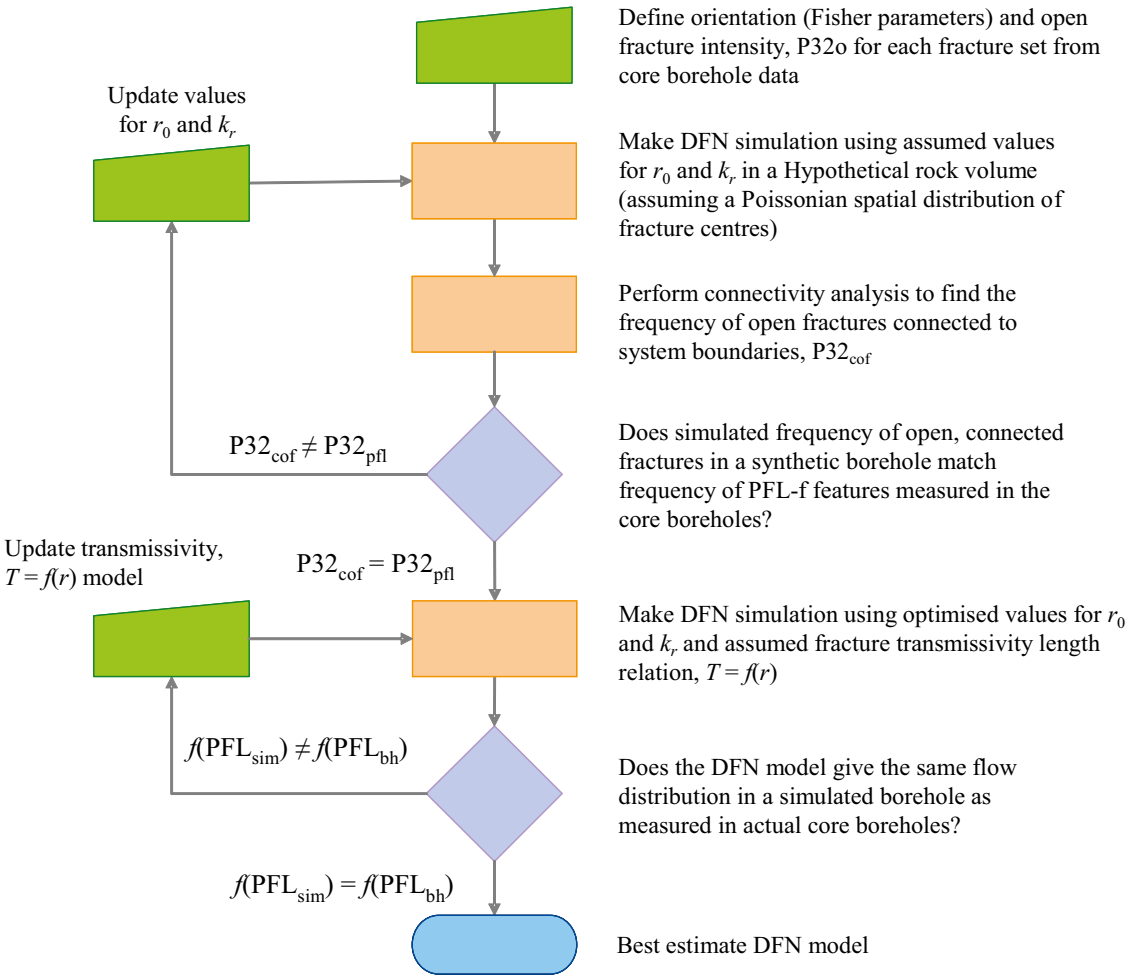

Figure 3-3. *Flowchart showing procedure for obtaining optimised Hydrogeological DFN parameters using an iterative simulation fitting procedure.*

the correlated (or fully correlated, FC) and uncorrelated (or non-correlated, NC) cases, respectively. A third possibility, the semi-correlated case (SC), assumes a partial correlation between fracture size and transmissivity with a stochastically distributed variation around a size-correlated mean value. This is thought to be the most realistic scenario as one would almost always expect some stochastic variation in a heterogeneous system. It is noted that there are other alternatives that have not been explored such as a uniform log-normal or a stochastic power law distribution (see /e.g. Gustafson and Franson 2006/). The choice of models actually used in the Hydrogeological DFN modelling work, however, is thought to be reasonable given the sparsity of data and should reproduce the flow characteristics of the system with realistic efficacy. Details of the three transmissivity models are given in Table 3-1.

Table 3-1. Different transmissivity models used in Hydrogeological DFN modelling /Rhén et al. 2008/. The variable T (m^2/s) is the transmissivity; adjustable parameters in the various models are a, b, μ, and σ; the symbol $R_n(0,1)$ represents a normal random deviate with mean zero and variance of unity.

Type	Description	Relation
Semi-correlated (SC)	lognormal distribution about a power-law correlated mean	$\log_{10} T = \log_{10}(a) + b\log_{10}(r) + \sigma R_n(0,1)$
Correlated (FC)	1:1 power-law relation	$\log_{10} T = \log_{10}(a) + b\log_{10}(r)$
Uncorrelated (NC)	lognormal distribution about a constant mean	$\log_{10} T = \mu + \sigma R_n(0,1)$

It should be noted that the modelling procedure outlined above does not directly consider flow channelling phenomena apart from network scale flow channelling effects which arise naturally due to fracture connectivity issues. There therefore exists the possibility that there are inbuilt biases in the resulting Hydrogeological DFN. There are a number of issues that need to be considered in relation to this. These are discussed in more detail in Section 3.11.

A complete listing of the Hydrogeological DFN input parameters for hydraulic rock domains HRD_C, HRD_W, HRD_EW007, and HRD_N at different depth intervals can be found in /Rhén et al. 2008/. In the present report, scoping calculations are made for the depth interval –650 m to –400 m (i.e. m.a.s.l. relative to sea level) and consider only the so-called OPO Hydrogeological DFN models which include open or partly open fractures. These domains and intervals may be considered to represent the focused volume for the proposed repository in Laxemar and are summarised in Table 3-2 to Table 3-5. Model variants referred to as OPO-CP (open or partly-open fractures with certain or probable confidence) in /Rhén et al. 2008/ are not included in this report as they are deemed to give a less realistic representation of the hydrogeological properties of the HRD.

Table 3-2. Hydrogeological DFN parameters for HRD_C (OPO) in the depth interval –650 to –400 m.a.s.l. with fixed r_0 = 0.038 m /Rhén et al. 2008/.

Elevation zone (m.a.s.l.)	Fracture set name	Orientation set pole: (trend, plunge), conc.	Size model, power-law (k_r,r_0) (-,m)	Frac. intensity, P_{32} (m^2/m^3)	Transmissivity model, T (m^2/s) Semi-correlated (SC): (a,b,σ) Correlated (FC): (a,b) Uncorrelated (NC): (μ,σ)
–650 to –400	ENE	(155.1, 3.4), 9.6	(2.80, 0.04)	0.38	SC: (5×10^{-7}, 0.5, 0.5) NC: (2×10^{-6}, 0.8) FC: (3×10^{-8}, 0.7)
	WNW	(204, 1.6), 12	(2.50, 0.04)	0.74	SC: (2×10^{-8}, 0.6, 0.4) NC: (1×10^{-7}, 0.9) FC: (3×10^{-9}, 0.9)
	NS	(270.2, 8.4), 7.8	(2.90, 0.04)	0.47	SC: (1×10^{-8}, 0.4, 0.4) NC: (8×10^{-8}, 0.4) FC: (1×10^{-8}, 0.5)
	SubH	(46.3, 84.7), 12	(2.90, 0.04)	0.58	SC: (3×10^{-7}, 0.6, 0.6) FC: (2×10^{-6}, 0.9) NC: (1.5×10^{-7}, 0.9)

Table 3-3. Hydrogeological DFN parameters for HRD_W (OPO) in the depth interval –650 to –400 m.a.s.l. with fixed r_0 = 0.038 m /Rhén et al. 2008/.

Elevation zone (m.a.s.l.)	Fracture set name	Orientation set pole: (trend, plunge), conc.	Size model, power-law (k_r,r_0) (-,m)	Frac. intensity, P_{32} (m^2/m^3)	Transmissivity model, T (m^2/s) Semi-correlated (SC): (a,b,σ) Correlated (FC): (a,b) Uncorrelated (NC): (μ,σ)
–650 to –400	ENE	(340.3, 1.2), 15	(2.80, 0.04)	0.17	SC: (3×10^{-9}, 0.6, 0.5) NC: (2×10^{-9}, 0.5) FC: (1×10^{-9}, 0.6)
	WNW	(208.9, 2.2), 10.9	(2.55, 0.04)	0.33	SC: (3×10^{-8}, 0.6, 0.5) NC: (2×10^{-7}, 0.3) FC: (2×10^{-8}, 0.7)
	NS	(272.8, 12), 11.5	(2.55, 0.04)	0.30	SC: (3×10^{-8}, 0.4, 0.4) NC: (2×10^{-7}, 0.3) FC: (1×10^{-8}, 0.6)
	SubH	(277.1, 84.3), 11.1	(2.65, 0.04)	0.38	SC: (5×10^{-7}, 0.4, 1.0) NC: (1.5×10^{-5}, 1.2) FC: (1.2×10^{-7}, 1.2)

Table 3-4. Hydrogeological DFN parameters for HRD_EW007 (OPO) in the depth interval –650 to –400 m.a.s.l. with fixed r_0 = 0.038 m /Rhén et al. 2008/.

Elevation zone (m.a.s.l.)	Fracture set name	Orientation set pole: (trend, plunge), conc.	Size model, power-law (k_r,r_0) (-,m)	Frac. intensity, P_{32} (m^2/m^3)	Transmissivity model, T (m^2/s) Semi-correlated (SC): (a,b,σ) Correlated (FC): (a,b) Uncorrelated (NC): (μ,σ)
–650 to –400	ENE	(162.8, 1.4), 10.7	(2.95, 0.04)	0.69	SC: (3×10^{-8}, 0.4, 0.4) NC: (3×10^{-8}, 0.6) FC: (3×10^{-8}, 0.4)
	WNW	(25.3, 0.2), 16.4	(2.50, 0.04)	1.43	SC: (1×10^{-7}, 0.3, 0.3) NC: (2×10^{-7}, 0.5) FC: (1×10^{-7}, 0.3)
	NS	(88.9, 3.9), 8.8	(2.95, 0.04)	0.64	SC: (3×10^{-7}, 0.4, 0.4) NC: (1×10^{-6}, 0.6) FC: (3×10^{-7}, 0.4)
	SubH	(138.7, 81.3), 9.7	(2.95, 0.04)	0.92	SC: (3×10^{-8}, 0.6, 0.4) NC: (1×10^{-7}, 0.8) FC: (3×10^{-8}, 0.6)

Table 3-5. Hydrogeological DFN parameters for HRD_N (OPO) in the depth interval –650 to –400 m.a.s.l. with fixed r_0 = 0.038 m /Rhén et al. 2008/.

Elevation zone (m.a.s.l.)	Fracture set name	Orientation set pole: (trend, plunge), conc.	Size model, power-law (k_r,r_0) (-,m)	Frac. intensity, P_{32} (m^2/m^3)	Transmissivity model, T (m^2/s) Semi-correlated (SC): (a,b,σ) Correlated (FC): (a,b) Uncorrelated (NC): (μ,σ)
–650 to –400	ENE	(342.2, 0.2), 15.8	(2.60, 0.04)	0.26	SC: (1×10^{-7}, 0.5, 0.7) NC: (6×10^{-6}, 1.1) FC: (2×10^{-7}, 0.8)
	WNW	(209.8, 1.6), 14.6	(2.40, 0.04)	0.36	SC: (1×10^{-7}, 0.5, 0.5) NC: (3×10^{-7}, 0.7) FC: (2×10^{-7}, 0.5)
	NS	(271.3, 3.8), 10.3	(2.60, 0.04)	0.25	SC: (5×10^{-8}, 0.3, 0.3) NC: (2×10^{-7}, 0.5) FC: (5×10^{-8}, 0.3)
	SubH	(238.9, 81.5), 12.7	(2.70, 0.04)	0.41	SC: (5×10^{-8}, 0.4, 0.4) NC: (5×10^{-8}, 0.3) FC: (3×10^{-8}, 0.4)

3.2.3 Hydrogeological description of the HCD

In the Hydrogeology background report /Rhén et al. 2008/ a large amount of hydrogeological data is presented relating to interpreted borehole intercepts with deterministically modelled deformation zones. The data correlates individual sets of deformation zones with elevation (of borehole measurement intervals) and measured transmissivity or hydraulic conductivity. The individual sets of deformation zones are deduced based on defined criteria, such as ductility, brittleness, size, orientation in the horizontal plane, dip, and combinations of these. Details of the transmissivity and conductivity depth dependence for these different sets of deformation zones are given in the above reference. The measurement data indicate a substantial depth trend as shown in Figure 3-4, based on data for all deformation zones in the local model volume. In /Rhén et al. 2008/, two different models describing the depth dependence were proposed; an exponential trend model and a power-law trend model describing the depth dependence of transmissivity. The model equations for the transmissivity can be written in terms of the elevation, z (m.a.s.l.) as:

$$T(z) = a(-z)^b \quad \text{(power-law trend model)} \qquad \text{(Eq. 3-2)}$$

$$\log_{10} T(z) = a + b \cdot z \quad \text{(exponential trend model)} \qquad \text{(Eq. 3-3)}$$

The same equation forms are used to model the depth dependence of hydraulic conductivity with the variable K (m/s) used in place of T (m^2/s). It should be noted that the formulation of the exponential (decay) trend model in $\log_{10}$ space rather than natural log space is slightly different to the corresponding model used in the Forsmark transport SDM /Crawford 2008/.

The *a* parameter in the linear trend model is the expected value of the $\log_{10}$ transmissivity at zero elevation, and *b* is the slope for the line of best fit to the data when plotted on semi-logarithmic axes (as in Figure 3-4). For the power-law trend model, on the other hand, *a* is an empirical fitting parameter and *b* is obtained from the slope of the line of best fit to the data when plotted on log-log axes. The hypothesis of an approximately exponential decay of transmissivity with increasing depth is generally supported by other studies in the literature (see for example, the meta-analysis by /Stober and Bucher 2007/) and it is also consistent with the way in which transmissivity of single fractures is thought to vary with the increasing normal stress at greater depths.

In the hydrogeological description of deformation zones which is common to both Forsmark and Laxemar a distinction is made between two different kinds of lateral heterogeneity (although these are not referred to as such in /Rhén et al. 2008/ they are discussed in /Follin et al. 2007/ and are also implicit in the Laxemar hydrogeological site description):

Intra-category lateral heterogeneity, concerning the differences in transmissivity observed between all deformation zones belonging to a particular category, e.g. all deformation zones with a certain orientation;

Intrinsic lateral heterogeneity, concerning the spatial variability in transmissivity observed within a single (specific) deformation zone and elevation.

In most cases there are not enough measurement data for individual deformation zones to differentiate properly between intra-category and intrinsic lateral variability. Such deformation zones are assumed to have a similar depth dependency relation and consequently, a dominant intrinsic lateral variability component. This is a simplification that is used in the present report to make estimates of flow related transport properties that are partially generic in nature (i.e. they can apply equally well to all deformation zones of a particular class).

It is possible that by lumping the hydrogeological properties of different deformation zones together in this fashion, a bias may be introduced whereby the modelled properties represent the central tendency of the aggregate data set while failing to represent local extremes of behaviour. For the calculations presented in this report, the data set was considered sufficiently sparse that it was not possible to consider individual deformation zones separately in a rigorous fashion with the exception of ZSMEW007A where a relatively detail-rich data set was available. Even this zone, however, is characterised by a relatively large number of conductive features identified in the upper 200 m of the bedrock while there is only very sparse data coverage at greater depths.

It should be noted, however, that in the regional hydrogeological modelling for SDM-Site Laxemar a procedure of local conditioning was used to assign transmissivity-depth trends for specific deformation zones /Rhén et al. 2009/ to give agreement with borehole observations (principally natural groundwater heads as well as drawdowns in single-hole hydraulic tests and multiple-hole hydraulic interference tests).

In /Rhén et al. 2008/ only a weak depth dependency is observed for the intrinsic lateral heterogeneity of individual deformation zones (i.e. standard deviation of deformation zone transmissivity at a given elevation) which is also modelled as an exponential decay trend.

In the scoping calculations presented in this report, only the mean transmissivity trend data are considered and lateral heterogeneity is not given special consideration. It was previously demonstrated in /Crawford 2008/ that provided the flow channels are well connected in space (which is implicit in the customary formulation of deformation zones as mildly heterogeneous 2D planar features or as a 3D porous medium), lateral intrinsic heterogeneity should only play a minor role and can be neglected in scoping calculations. If, on the other hand, the sampled flow channels represent hydrogeologically compartmentalised flow systems, the most transmissive features potentially represent fast and persistent flowpaths within the deformation zones. This scenario was previously described using the stochastic multi channel model, or MCM in /Crawford 2006/ where the concept was applied to describe the flow related transport properties of the hydraulic rock domains in Laxemar.

In an approach similar to that adopted in /Crawford 2008/, F-factors are calculated for the flowpath representing the mean parameter depth trend (i.e. transmissivity or hydraulic conductivity) in the data set for the local Laxemar model volume. To take account of the possibility of fast, persistent

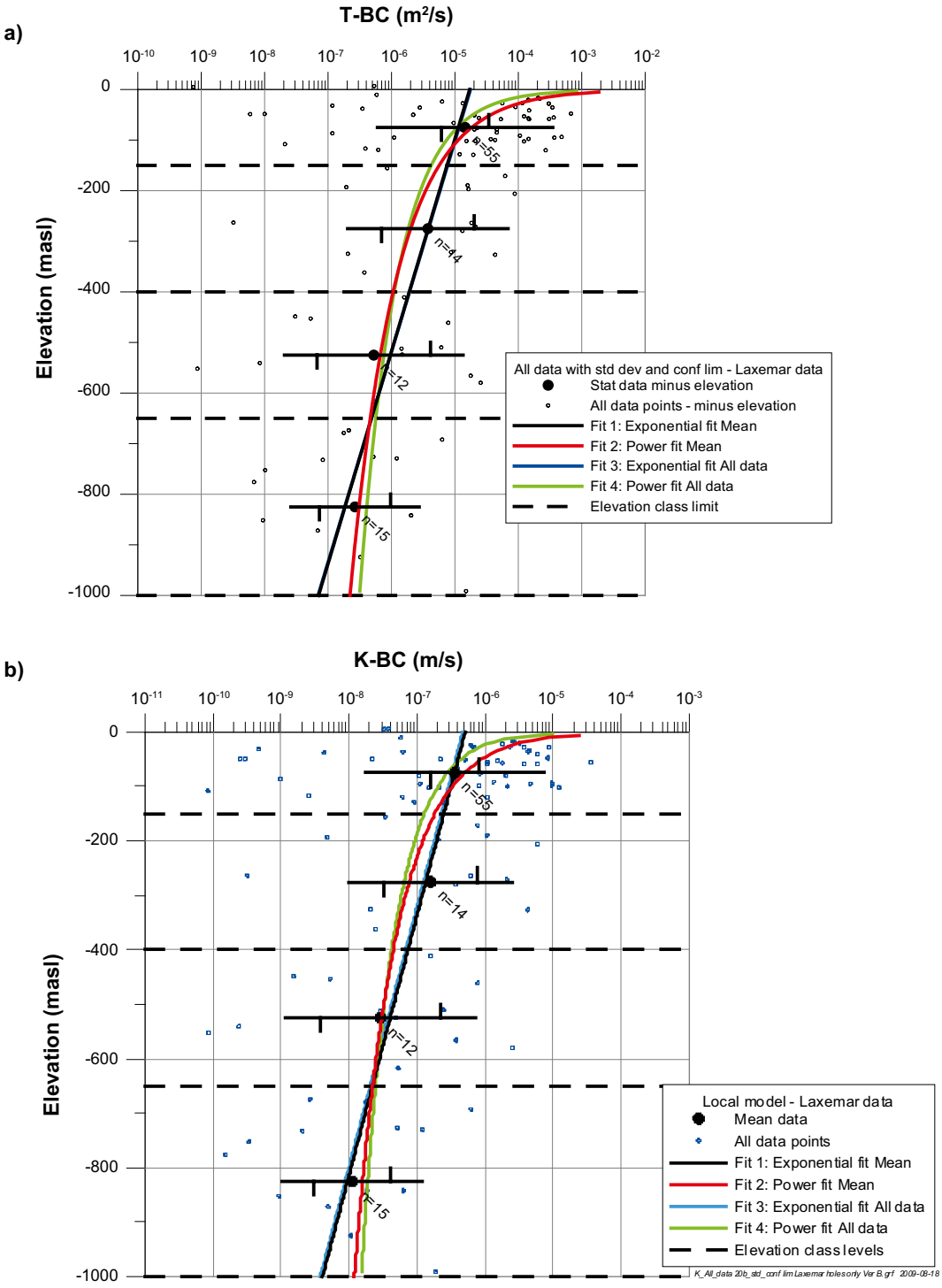

Figure 3-4. *a) Transmissivity T (m^2/s), and b) hydraulic conductivity K (m/s), plotted as a function of elevation for deformation zones in the Laxemar local model volume. For the elevation intervals indicated by broken horizontal lines, the geometric mean (circle markers) ± 1 standard deviation (horizontal lines) are plotted. The confidence limits for the mean value are indicated by vertical notches on the horizontal lines. Exponential (blue) and power-law (green) fitted curves based on all data are also shown. Figures taken from /Rhén et al. 2008/.*

flowpaths as described above, two limiting cases are also included for the transmissivity model. These correspond to the maximum (T_{max}) and minimum (T_{min}) expected transmissivity trend for individual flow channels in an MCM representation where the extreme values are assumed to be shifted (± 1.96 standard deviations of the maximum lateral intrinsic heterogeneity) relative to the mean depth trend model (T_{mean}). The maximum standard deviation of the $\log_{10}$ transmissivity reported in /Rhén et al. 2008/ is approximately 1.41 in the Laxemar local model volume. The physical meaning of this particular modelling representation is illustrated in Figure 3-5.

In order to calculate F-factors using a 3D porous medium approximation (modelled here as a stream tube), both hydraulic conductivity data and an estimate of the specific flow-wetted surface, a_R (m^2/m^3) must be given. In /Rhén et al. 2008/, the Terzaghi corrected intensity of flowing features, $P_{10,corr}$ (1/m) identified using PFL measurements is given by:

$$P_{10,corr}(z) = a + b \cdot z \quad \text{(linear trend model)} \qquad \text{(Eq. 3-4)}$$

The specific flow-wetted surface can be estimated by assuming approximately random flow channel orientation in the deformation zones, in which case:

$$a_R(z) \approx 4P_{10,corr}(z) \qquad \text{(Eq. 3-5)}$$

In the 2D planar representation of a deformation zone, only the transmissivity distribution is necessary for the calculation as the flow-wetted surface is implicitly defined by the modelled geometry. Generally, the 2D planar representation can be expected to underestimate the available flow-wetted surface for a given amount of fluid flow since this represents the physical minimum for two bounding surfaces enclosing a heterogeneous flow field. The simplified stream tube model, on the other hand, most likely overestimates the specific flow-wetted surface since it assumes that the flow evenly samples the available flow-wetted surface in an uncorrelated manner which may not be true in a strongly channelised flow system.

A summary of the parameter values used for transport modelling calculations presented in this report for generic deformation zones are given in Table 3-6.

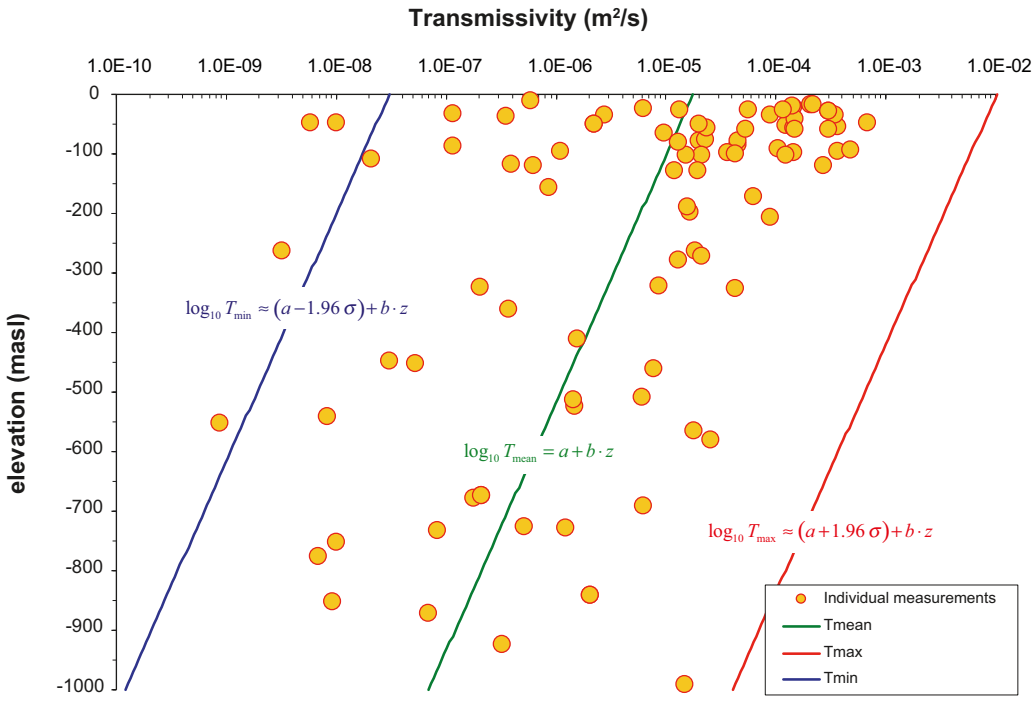

Figure 3-5. *Variation of transmissivity with depth for deformation zones in the Laxemar local model volume. Data points are plotted for individual transmissivity measurements (orange markers) while the approximate range of possible transmissivities for "potential" fast flowpaths is given by the area bounded by the blue and red curves (assumed to be limiting cases and defined as ±1.96σ relative to the mean depth trend). The mean transmissivity vs. depth trend is shown as the green curve.*

Table 3-6. Deformation zone property parameters used in transport calculations for generic deformation zones presented in this report /Rhén et al. 2008/.

Model ID	Depth trend model	Parameter (units)	a	b
DZ-L-1	Power-law	Transmissivity (m^2/s)	4.099×10^{-3}	–1.37208
DZ-L-3	Exponential	($\log_{10}$) Transmissivity (m^2/s)	–4.754	2.405×10^{-3}
DZ-L-K5	Power-law	Conductivity (m/s)	2.50×10^{-5}	–1.0095
DZ-L-K7	Exponential	($\log_{10}$) Conductivity (m/s)	–6.3646	1.87×10^{-3}
HCD-L-P1	Linear	$P_{10,corr}$ (PFL) (1/m)	1.01984	9.36×10^{-4}

It is noted here that hydraulic conductivity and corrected PFL intensity data specific for deformation zones were not compiled in the Forsmark Hydrogeology SDM /Follin et al. 2007/ and therefore only calculations assuming the 2D planar representation of deformation zones were presented in /Crawford 2008/. The inclusion of a 3D stream tube representation of deformation zone hydrogeological properties is therefore a novel feature of SDM-Site Laxemar.

For deformation zone ZSMEW007A there is a sufficient quantity of data available that calculations can be made for zone specific conditions. A summary of the depth trend data available for this deformation zone is given in Table 3-7.

In /Rhén et al. 2008/ parameters are only supplied for the transmissivity depth trend of ZSMEW007A. In order to make calculations using the streamtube representation, the hydraulic conductivity of the deformation zone is estimated as the deformation zone transmissivity divided by the zone thickness which is assumed to be approximately 80 m.

Plots of individual measurements of the deformation zone hydraulic conductivity, local values for the specific flow-wetted surface (estimated using Equation 3-5), and the associated depth trend models specified in Table 3-7 are given in Figure 3-6.

3.3 Model volume description and boundary conditions

For modelling the flow related transport properties of the HRD, a hypothetical cubic volume of rock (or "voxel") with dimensions 100 m × 100 m × 100 m is considered. The layout of the modelled rock volume relative to the hypothetical repository, the HCD, and an assumed local hydraulic gradient is illustrated schematically in Figure 3-7. The general modelling procedure is broadly similar to that used previously in /Crawford 2006/ as well as in /Outters 2003, Cvetkovic et al. 2004, Painter 2006/ for generic modelling of fractured rock transport properties.

As a first approximation, a local hydraulic gradient applied parallel to the simulation axes is assumed. To account for directional anisotropy in the hydrogeological properties of the HRD, calculations are made for a hydraulic gradient applied over different directions corresponding to the three principal axes of the model (i.e. North-South, East-West, and Vertical).

Table 3-7. Deformation zone property parameters used in transport calculations for ZSMEW007A presented in this report (based upon data contained in /Rhén et al. 2008/).

Depth trend model	Parameter (units)	a	B
Exponential	($\log_{10}$) Transmissivity (m^2/s)	–3.996	2.158×10^{-3}
Exponential [(1)]	($\log_{10}$) a_R (m^2/m^3)	0.639	1.824×10^{-3}
Linear [(1)]	a_R (m^2/m^3)	3.161	4.262×10^{-3}

[(1)] note: depth trend parameter values for the specific flow-wetted surface, a_R (m^2/m^3) are estimated using linear regression from raw data tabulated in /Rhén et al. 2008/.

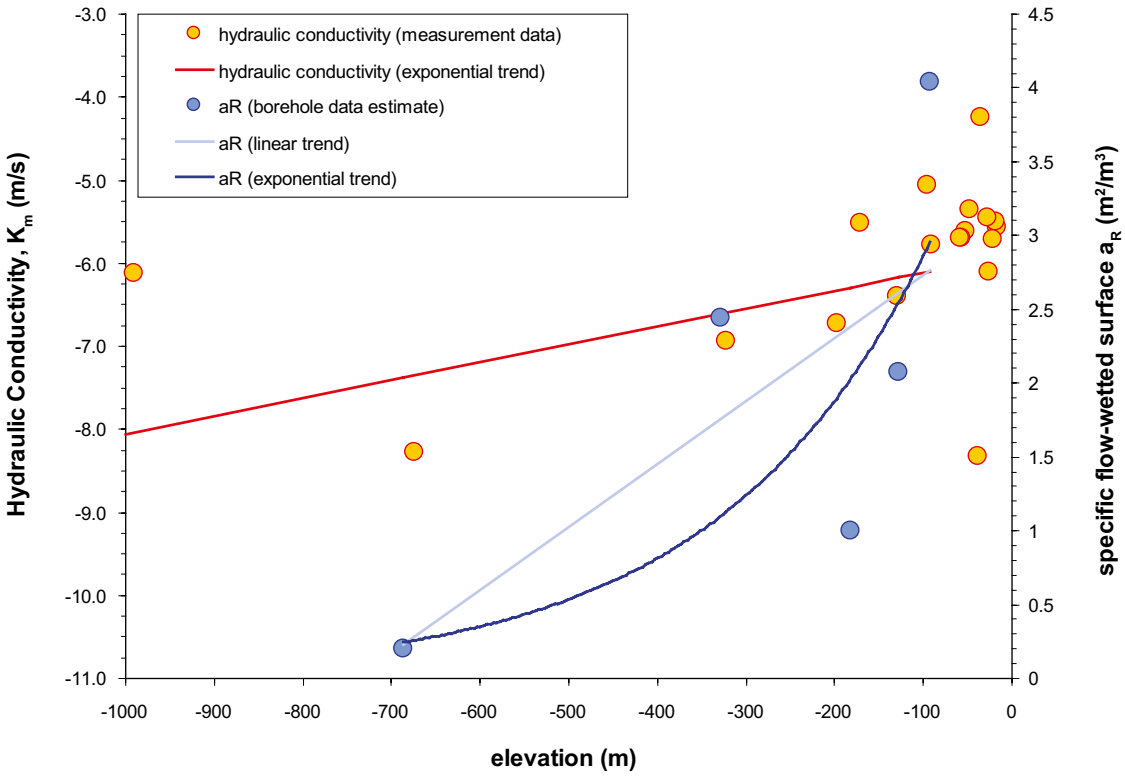

Figure 3-6. *Variation of hydraulic conductivity (orange markers) and specific flow-wetted surface (blue markers) with depth for deformation zone ZSMEW007A. An exponential depth trend model for hydraulic conductivity is shown as a red curve along with two different depth trend models for specific flow-wetted surface (light and dark blue curves).*

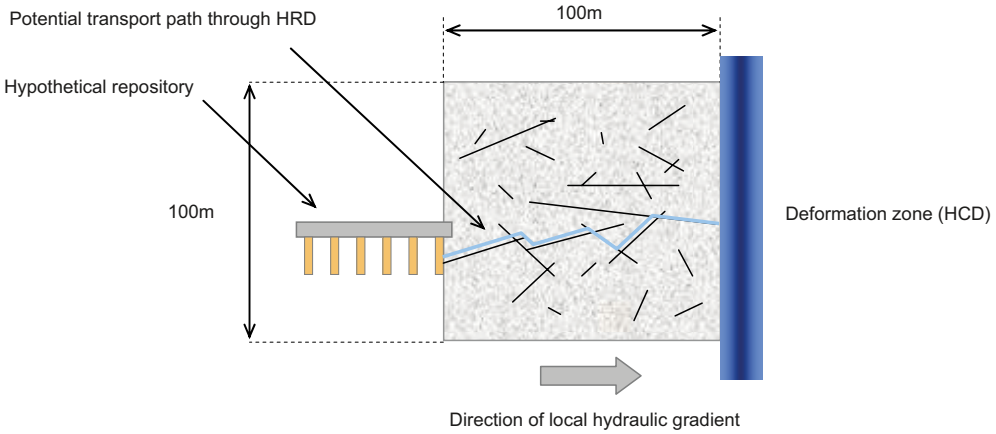

Figure 3-7. *Illustration of HRD model volume showing the relation between the hypothetical repository, a steeply dipping deformation zone in the HCD, and the prevailing local hydraulic gradient.*

The continental hydraulic gradient in Sweden is taken to be roughly the height of the tallest features within the Scandinavian mountains (≤ 2,500 m) over the average distance to the Baltic sea (~400–500 km). Although only a very rough estimate, it gives an idea of the order of magnitude of the continental hydraulic gradient. The hydraulic gradient calculated in this fashion is in the range 0.5%–0.6% (0.005–0.006 m/m). On a regional scale and based upon the landscape topography, a groundwater hydraulic gradient on the order of about 4% (0.04 m/m) is estimated. This corresponds to a difference in groundwater surface elevation of about 40 m over a 1 km distance from elevated areas inland to the Baltic coast at Laxemar. Additional complicating factors are site scale, lateral and depth dependent variations in salinity and temperature which have the potential to influence flow patterns by way of buoyancy effects. Generally there is a consistent depth dependent variation of both of these parameters within the local model area /Sundberg et al. 2008, Laaksoharju et al. 2009/ and any lateral variations appear to be sufficiently small that they should not have an appreciable impact upon contemporary hydraulic gradients.

In any case, given the uncertainty in assigning an appropriate representative hydraulic gradient based upon topographical considerations, the assumption of 1% (0.01 m/m) is considered a reasonable estimate in the transport properties evaluation. This is the reference hydraulic gradient used for subsequent calculations of flow related transport properties. Furthermore, it must be remembered that the estimates provided in this report are only indicative. A comprehensive assessment of flow paths and flow magnitudes from the actual repository layout is to be made within the framework of long term safety assessment (e.g. SR-Site).

A large number of in situ measurements of flow under approximately background hydraulic conditions have been made in Laxemar as part of the site investigation. Some of these have been performed in permanently instrumented boreholes /Thur and Gustafsson 2007, Thur 2008/ while others have been performed in conjunction with tracer tests for the purpose of characterising individual flowing features /Gustafsson and Nordqvist 2005, Gustafsson et al. 2006, Thur et al. 2007a, b/. These tests are based upon a tracer dilution method, where the groundwater flow is fitted to the measured decrease in tracer concentration with time using a mixed tank reactor model. The method is extremely sensitive and can measure flow rates substantially lower than that possible using standard flow logging methods thus enabling the method to be used to measure flow under relatively natural (i.e. non-pumped) conditions.

By combining these measurements with the estimated transmissivities of the specific borehole sections obtained independently, the apparent background hydraulic gradient can be estimated. A compilation of the site specific data is given in Figure 3-8 (data compiled by /Nordqvist et al. 2008/) where the apparent gradient is plotted as a function of fracture transmissivity and measurement elevation.

As can be seen from the figure there is a large spread in the measurement data and most points appear to lie above the estimated reference hydraulic gradient (horizontal broken line). In spite of the large variability in the data, there does appear to be a non-negligible inverse correlation with transmissivity as indicated by the power law regression curve in the Figure (orange line). The regression curve is, however, very poorly constrained by the data set and cannot be taken to indicate a clear-cut relation between hydraulic gradient and transmissivity. Although there is a qualitative prevalence of more transmissive features at shallower depths and less transmissive features at greater depths, there does not appear to be a strong relation between hydraulic gradient and depth.

The existence of the inverse correlation between gradient and transmissivity is qualitatively consistent with expectations based upon flow modelling calculations described in /Crawford 2008/. The magnitude of the apparent background hydraulic gradient, on the other hand, appears to be considerably greater than what seems reasonable in comparison to the estimated reference gradient for the site. In Figure 3-8 the empirically derived, apparent local gradients are up to three orders of magnitude higher than the reference level. This apparent discrepancy has also been remarked in a more detailed analysis of the Forsmark site data by /Nordqvist et al. 2008/ and is also discussed in /Crawford 2008/.

Since it is suspected that the magnitude of the estimated hydraulic gradient is an artefact, the authors recommend against use of the power law indicated in Figure 3-8 for directly assigning local hydraulic gradients to the different compartments in the flow related transport properties model. In the calculations presented in the following sections for the NFF, hydraulic gradients in the range 0.1%–10% are assumed which is thought to be more reasonable for the site. In order to examine the

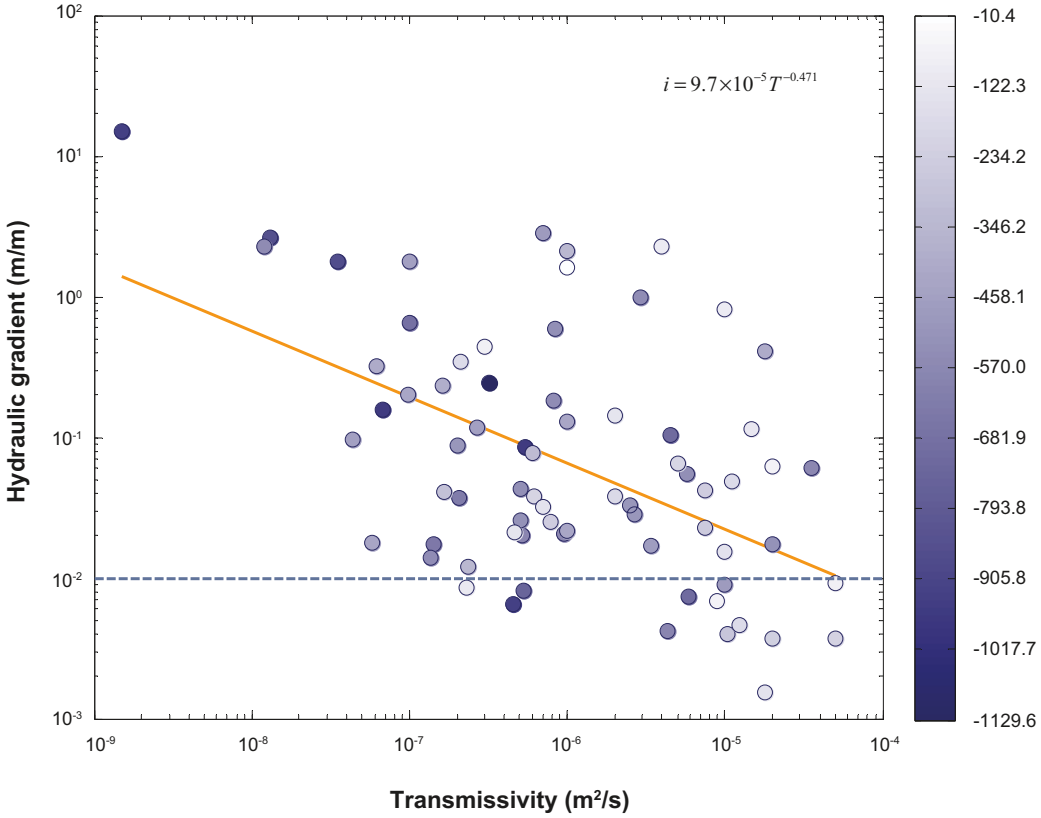

Figure 3-8. *Apparent hydraulic gradients measured at the Laxemar site as a function of fracture transmissivity (x-axis) and measurement elevation (shading). The horizontal broken line corresponds to the reference hydraulic gradient of 1%. The orange line represents a linear regression curve for the power law given in the figure. The colourbar to the far right indicates elevations (m.a.s.l.) corresponding to the shading of markers in the figure. Data are taken from /Nordqvist et al. 2008/.*

impact of possible inverse correlation between transmissivity and hydraulic gradient, calculations are additionally made assuming a power law relation with the same exponent as in Figure 3-8, although with magnitude reduced by a factor of 100. This modification gives a maximum gradient of slightly less than 10% for the least transmissive fractures.

The above discussions notwithstanding, it should be clearly emphasised that the estimation of local hydraulic gradients for the purpose of making multi-compartment scoping calculations does not affect larger regional scale simulations where the topographically driven hydraulic boundary conditions are well characterised. In such simulations and those to be used in safety assessment, spatially variable local gradients arise naturally due to the distribution of differently conductive elements in the hydrogeological model and do not need to be considered explicitly.

3.4 Modelling strategy for the HRD

3.4.1 The non-engineered near field (NNF)

For the non-engineered near field (NNF), the focus is upon assessing the F-factor for the first cluster of connected, low-transmissive background fractures that connect a typical deposition hole with a typical major flowpath within the HRD. If relatively transmissive features (however this is defined) are actively avoided during repository construction, one could speculate that many canister positions will probably be located sufficiently distant from such features that they can be discounted from contributing significantly to radionuclide fluxes in the far-field. Although this may be the case for a large proportion of canister positions, it is still necessary to make estimates of F-factors for "typical" flowpaths. The question then becomes; what would a typical distance be for radionuclide transport from a canister position to a major flowpath?

Here, a number of issues need to be considered. Firstly, a typical distance in this context does not necessarily imply average distance since a damaged canister in close proximity to a major flowpath can be expected to have a much greater impact upon far-field radionuclide release rates than a damaged canister located further away, all other things being equal. One also must consider what respect distance is to be applied for large fractures that, although not actually intersecting the deposition hole, may be sufficiently close to cause concern with regard to radionuclide transport potential. It is likely to be canister positions with closest proximity to these features that have the greatest potential to influence the far field release. An additional consideration is the possibility that the repository itself, including the excavation damaged zone (EDZ) will connect and activate flowpaths that otherwise would be isolated in the bedrock.

Most of these considerations, however, are strongly coupled to repository layout and design criteria and as such are more of a safety assessment character. For this reason, and owing to the dominant role of canister positions in close proximity to major flowpaths, the assumption is made of an approximately 10 m transport distance for the NNF. Here it is assumed that large conductive features lying closer than this to individual canister positions will likely be identified from geophysical measurements and other geological evidence and therefore be avoided. Large, relatively transmissive features lying 10 m or more away from a canister hole might not be seen and therefore could well exist somewhere in the repository volume. These features and the canister deposition holes in closest proximity will then probably dominate the radionuclide flux from the repository. It is noted, however, that the assumption of 10 m transport distance is likely to be pessimistic and could be considered as more, or less a worst case scenario for the NNF.

For a single hypothetical pathway connecting a deposition hole with a major flow path in the HRD, the F-factor is given by /SKB 2006b/:

$$F = \frac{2L_p}{Ti} \qquad \text{(Eq. 3-6)}$$

Where, L_p (m) is the flowpath length, T (m^2/s) is the flowpath transmissivity, and i (m/m) is the hydraulic gradient.

If it is assumed that flow bearing fractures in the transmissivity interval 10^{-8} to 10^{-10} m^2/s are allowed to intersect canister positions, then approximately representative F-factors for the NNF can be estimated. Since the calculations consider local pathways rather than an entire rock volume, it is also necessary to carefully consider an appropriate hydraulic gradient for such a flowpath. Owing to this uncertainty, estimates of the F-factor were made for possible hydraulic gradients in the range 0.1%–10% as well as for the special case where the local hydraulic gradient is simply correlated with transmissivity in a similar fashion to the empirically derived result in Figure 3-8.

3.4.2 The immediate far field (IFF)

As discussed in Section 3.3, the immediate far-field is simulated as a 100 m×100 m×100 m voxel with a hydraulic potential difference applied over opposing faces. To account for directional anisotropy in the Hydrogeological DFN model, simulations are also made along the different axes of the model. Consideration is therefore given to transport parallel to the x-axis (EW direction), y-axis (NS direction), and z-axis (vertical direction).

The aim of the simulations is not to model the actual F-factor distribution for transport of radionuclides from an individual canister position, but rather to give an indication of F-factors associated with typical flowpaths in the HRD. This is important to bear in mind as an individual canister hole presents a cross-sectional area considerably less than the 10,000 m^2 face of the simulation volume. Transport from any particular canister location is therefore strongly dependent upon additional considerations of local fracture network connectivity and represents a sub-sampling of the typical F-factor distributions calculated for the rock volume as a whole. In addition to F-factors for typical flowpaths in the rock, an assessment is also made as to the relative frequency with which they can be expected to occur. This is an important measure of transport potential in different HRD volumes as it reflects directly upon the number of canister positions that are expected to be in near contact with major flowpaths.

In the scoping calculations presented in this report, two complementary methods have been used to illuminate the flow related transport properties of the HRD. These are described in the following sections.

Primary modelling strategy

As an initial modelling step for the different fracture domains comprising the HRD, 100 stochastic DFN realisations were generated using the Hydrogeological DFN parameters given in Table 3-2 to Table 3-5 and subjected to a connectivity analysis using graph theory. Owing the relatively high fracture intensity, the fracture radius (size) distribution was truncated to the range of 10–560 m and the connectivity analysis was performed for different boundary plane separation distances in the range 10–100 m, and along the three principal axes of the simulation volume (see Figure 3-9). The aim was to identify candidate realisations that exhibit potential hydraulic connectivity between boundary planes within the simulated rock volume and how this connectivity can be expected to vary with hypothetical distance (i.e. respect distance between a hypothetical repository and the HCD). The fractures were generated in a volume significantly larger than the simulation volume in order to avoid edge truncation effects and fracture network thinning at the system boundaries.

For each realisation found to be hydraulically connected, the Hydrogeological DFN was converted to an equivalent pipe network representing the connectivity of individual fractures comprising the network. In this approximate method, midpoints of fracture intersections are considered to be mixing nodes and pair-wise pipe connections are made between nodes residing in individual fracture planes. The conductance of individual pipe elements within a fracture plane is proportional to the transmissivity of the fracture hosting the connection and the distance between the mixing nodes. In this fashion, the hydraulic connectivity and relative transmissivity of different pathways through the system can be honoured. The overall approach is a similar although simplified version of that used in the PAWorks package for flow simulation in discrete fracture networks /Dershowitz et al. 2004/.

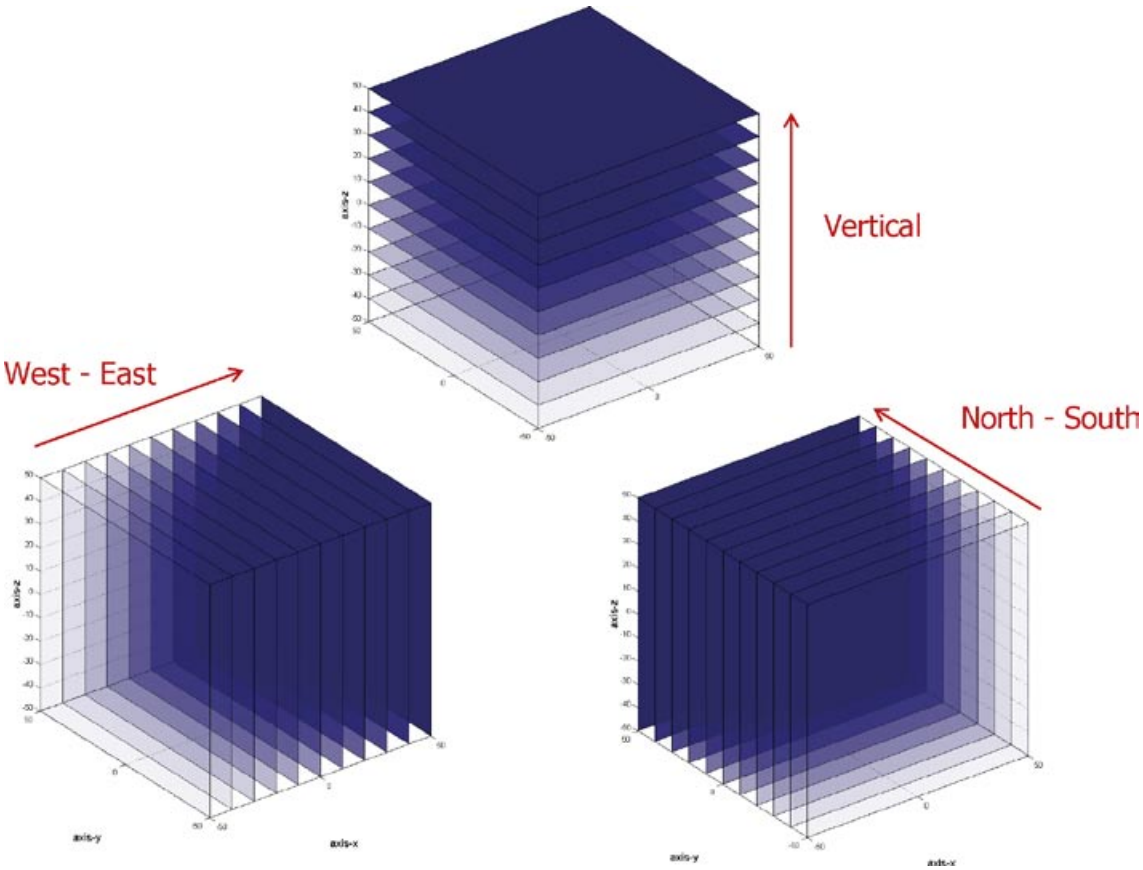

Figure 3-9. *Illustration of modelling strategy A. The connectivity of individual DFN realisations was assessed for different hypothetical transport distances in the range 10–100 m and along the different principal axes of the simulation volume. Hypothetical boundary planes for the different transport distances are depicted as shaded polygons in the figure.*

Although this approximation gives an acceptable representation of the hydraulic properties of the rock (hydrological responses), the transport pathways are not altogether realistic as the model does not capture the intricacies of mass transfer interactions between interconnected flow channels in the plane of fractures. For this reason particle tracking methods have not been used to calculate solute transport as this would likely give physically non-meaningful results. Instead, the weighted adjacency matrix of the resultant pipe network is used to calculate a hypothetical path of least transport resistance (PLTR) using graph theory. From the known lengths and conductances of individual pipe elements comprising the PLTR a notional F-factor for this pathway can be calculated in a relatively straight forward manner for an assumed hydraulic gradient. The method is based upon a Matlab version of Dijkstra's algorithm /e.g. Cormen et al. 2001/ as implemented within the Boost Graph Library /Gleich 2006/. Since a substantially larger volume of rock is considered for the IFF than that contemplated for the NNF, the assumption of the regional hydraulic gradient of 1% is probably not unreasonable as a boundary condition for this calculation. The implications of this will need to be fully investigated within safety assessment using detailed simulations of radionuclide transport from the repository to the HCD.

Using an equivalent pipe network representation of the fracture network makes it possible to investigate the impact of hydraulically conductive fracture intersection zones (FIZ) in a rudimentary fashion. For systems with neutrally conductive FIZ, there is little tendency for flow to occur along the line of fracture intersection. Equivalent pipe connections made between the midpoints of fracture intersections can therefore be taken to represent an approximate, average trajectory for fluid flow in the system. For highly conductive FIZ (Type B and C as illustrated in Figure 2-5), on the other hand, there is a strong tendency for flow to occur along the path of least resistance which includes the line of fracture intersection. In the limiting case of zero hydraulic resistance in the FIZ, pipe connections are made between the points of closest approach of the fracture intersection line segments. This scheme is illustrated in Figure 3-10 below.

The treatment of conductive FIZ in this fashion represents a worst case scenario for the transport modelling as no account is made of filling materials, discontinuities and roughness in the fracture intersections that would reduce the potential for preferential flow to occur. The F-factor estimates for the Hydrogeological DFN incorporating conductive FIZ therefore constitute an approximate upper bound for the detrimental impact that such features can have upon the transport resistance in the system, all other things being equal.

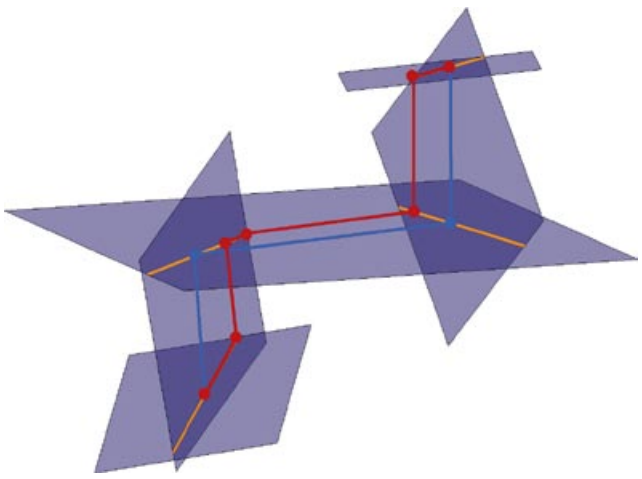

Figure 3-10. *Illustration of equivalent 3D pipe network concept for the case of neutrally conductive FIZ (blue nodes and pipes connecting fracture intersection midpoints) and for highly conductive FIZ (red nodes and pipes connecting fracture intersection points of closest approach). Fractures are visualised as blue polygons and fracture intersections are indicated as orange line segments.*

Using the simulation technique described above, the PLTR was calculated for the limiting cases of neutrally- and highly conductive FIZ and the different size-transmissivity models described in Section 3.2.2. Although the DFN connectivity analysis considers 10 m intervals in the range 10 m to 100 m, F-factor estimates were made only for 25 m, 50 m, 75 m, and 100 m transport distances owing to the numerically intensive nature of the calculations.

In the calculations, the same hydraulic gradient was applied in each case. For the 100 m transport distance, for example, the hydraulic potential difference was 1 m. In a similar fashion for the 25 m, 50 m, and 75 m cases, the hydraulic potential difference was set to 0.25 m, 0.5 m, and 0.75 m respectively. The results reported for each transport distance therefore represent individually applied boundary conditions rather than an F-factor reported at a check-point (control plane) within a larger simulation.

The reason for performing the calculation in this way is because the heterogeneous population of single penetrating fractures and fracture network clusters exhibit different connectivity characteristics over different length scales. Given that the Hydrogeological DFN also incorporates length transmissivity relations for fractures it is reasonable to expect that the transmissivity of typical flowpaths is also a function of boundary plane separation. By applying the same hydraulic gradient in each case, it was possible to quantify the properties of typical flowpaths for different distances separating the notional boundary planes in a comparable fashion. Although no specific calculations concerning intrusion scenarios have been made in this report, these comparisons are also relevant for scoping estimation of the flow related transport properties for short transport distances between a hypothetical repository and an intruding borehole.

A more detailed account of the modelling procedure can be found in /Crawford 2008/.

Complementary modelling strategy

In this modelling strategy, flow and transport simulations are made using the Napsac/ConnectFlow program /Serco Assurance 2007/. In these cases, the Hydrogeological DFN was implemented directly in the program using the parameters given in Table 3-2 to Table 3-5. For these cases, realisations were made for each transport direction and size-transmissivity model considering transport distances of 25 m, 50 m, 75 m, and 100 m. As previously, the fracture radius distribution was truncated to the range of 10–560 m and a total of 20 DFN realisations were made for each case. It should be noted, however, that a proportion of the fracture networks generated exhibited zero connectivity and the statistics for the F-factors of typical flowpaths are therefore not always based upon a full complement of 20 realisations.

Napsac calculates flow using a finite element method applied directly to the fracture network in 3D. F-factor estimates were made for each connected DFN realisation using the particle tracking algorithm in Napsac. Unlike the F-factor estimates using the primary modelling strategy, the results here represent the ensemble average for 1,000 released particles. As particles can take different routes through the system, a distribution of F-factors is obtained in each individual realisation.

3.5 Modelling strategy for the HCD

Although in many instances deformation zones comprising the HCD are notionally assumed to be planar structures, it is emphasised that there is no particular requirement for flowing features comprising deformation zones in the HCD to be planar and in reality it is possible to expect a very complex system of preferential flowpaths that follow a convoluted path in three-dimensional space. The individual flow path elements comprising the zones may be short and highly interconnected, long and poorly interconnected or some combination in between. In cross-section, a deformation zone may look something like that illustrated schematically in Figure 3-11.

In /Rhén et al. 2008/ data are given which enable the parameterisation of models for the HCD based upon the representation of deformation zones as both planar features and as a 3D porous medium. In this report both representations are used to make independent, complementary estimates of F-factors typical of flowpaths within the HCD.

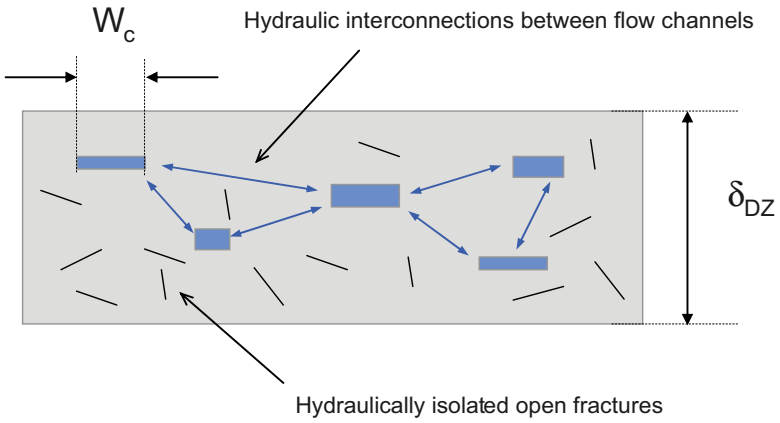

Figure 3-11. *Cross section of a hypothetical deformation zone viewed perpendicular to its strike with flow channels oriented into the plane of the page. The flow channels may have varying widths (W_c) and hydraulic apertures and follow convoluted pathways through the interpreted deformation zone of thickness δ_{DZ}. Although typically modelled as a planar feature there is no strict requirement for this to be the case.*

In the case of the 2D planar representation, only the distribution of measured flow transmissivities is needed. This is because both the flow-wetted surface and the flow in individual channels comprising the heterogeneous flow system can be shown to be proportional to the channel width. When calculating the ratio of these variables (see Equation 3-6) the unknown channel width is then cancelled out and therefore does not need to be considered explicitly. It is noted that the 2D planar representation implicitly assumes two bounding surfaces representing the interface between flowing water and the rock matrix. This may be considered to be a lower bound for the true flow-wetted surface.

In the 3D porous medium representation, on the other hand, an additional estimate of the specific flow-wetted surface is necessary to make an assessment of the F-factor along a flowpath. In this report the 3D case is handled using a streamtube approximation as described in /RETROCK 2004/.

Although both the planar and streamtube models are known to be physically inaccurate descriptions, the authors feel that the description is reasonable since both models represent two conceptual extremes for how flow could be distributed over the available wetted surface area bounding the flow channels (all other things being equal). The 2D planar representation will tend to overestimate flowpath connectivity and possibly underestimate the available flow wetted surface for a given flowrate through the zone. This would result in what, for all practical purposes, can be regarded as a lower limit for the F-factor. The 3D streamtube approximation, on the other hand, assumes that the entire available flow-wetted surface is sampled by the total flowrate in an uncorrelated manner which should thereby give an upper estimate for the F-factor.

The accuracy of this conjecture, however, depends upon whether the transmissivity of individual flow channels (or the hydraulic conductivity of the zone and the flow channel frequency) is properly assessed from borehole data. Since the surfaces of natural open fractures are not ideal flow channels, both the transmissivity and flow-wetted surface of the flow channels can differ from that implicit in the above model formulations.

If an approximately planar structure is assumed for deformation zones in the HCD, it is possible to formulate the transport problem for a zone of arbitrary orientation and dip as shown in Figure 3-12.

The magnitude of flow through the zone is dependent upon the effective transmissivity (or hydraulic conductivity) of the system over the length of the applied hydraulic head differential. Using either of the models for deformation zone transmissivity described in Section 3.2.3, the effective transmissivity of the zone is calculated as:

$$T_{eff} = \frac{1}{\frac{1}{L}\int_0^L \frac{1}{T(\xi)} d\xi} \qquad \text{(Eq. 3-7)}$$

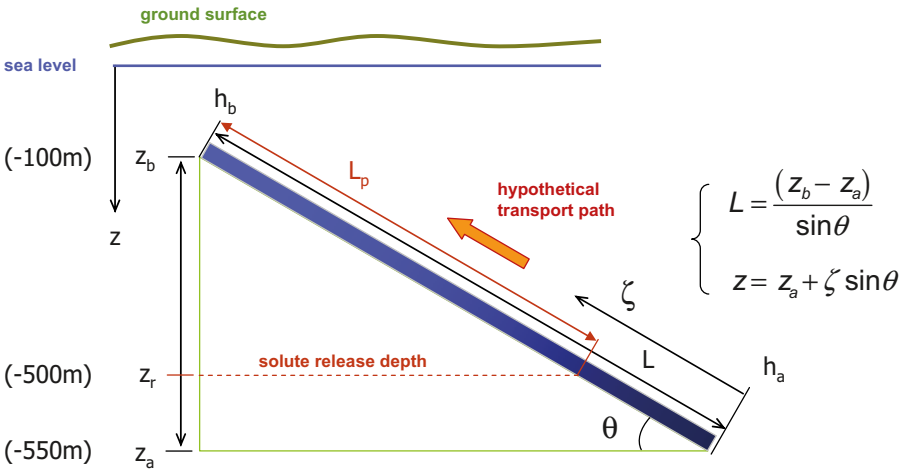

Figure 3-12. *Conceptual illustration of transport within a deformation zone of arbitrary orientation and dip (θ). A hydraulic gradient is assumed to exist across the zone that causes flow from depth to the surface through flow channels of steadily increasing transmissivity. In the hypothetical scenario for transport, the applied hydraulic gradient is assumed to extend from –550 m to –100 m elevation with solute release at –500 m.*

And consequently, the F-factor can be shown to be:

$$F = \frac{2L_p}{T_{eff} i} = \frac{2L_p}{i\,L} \int_0^L \frac{1}{T(\xi)} d\xi \qquad \text{(Eq. 3-8)}$$

The advective travel time is given by the ratio of flow volume and flowrate:

$$t_w = \frac{V}{Q} = \frac{L_p \bar{\delta}_t}{T_{eff} i} = \frac{1}{L i} \left(\int_{L-L_p}^{L} \delta_t(\xi) d\xi \right) \int_0^L \frac{1}{T(\xi)} d\xi \qquad \text{(Eq. 3-9)}$$

Where, the flowpath transport aperture, δ_t is given by the power law:

$$\delta_t = a T^b \qquad \text{(Eq. 3-10)}$$

The values for *a* and *b* in Equation 3-10 for the relation between transport aperture and transmissivity are not well known. In /Crawford 2008/ estimations of the advective transport time were made using a macroscopic cubic law (MCL) based upon the Hagen-Poiseuille equation for flow in a parallel plate slit as well as a macroscopic quadratic law (MQL) based upon a previous study by /Uchida et al. 1994/. Two further variants have been proposed in /Rhén et al. 2008/ based upon site specific data for Laxemar as well as previous work described in /Rhén et al. 1997/. These additional variants are referred to in this report as the Laxemar power law, LPL1 and LPL2 to distinguish them from the MCL and MQL models.

Table 3-8. Transport aperture, δ_t (m) correlation parameters used for calculation of advective transport times in this report (Transmissivity has units m²/s).

Description	a	b	Reference
Macroscopic cubic law (MCL), 12°C	0.0115	0.333	/Bird et al. 2002/
Macroscpic quadratic law (MQL)	0.5	0.5	/Uchida et al. 1994/
Laxemar power law #1 (LPL1)	1.43	0.52	/Rhén et al. 1997/
Laxemar power law #2 (LPL2)	0.705	0.404	/Rhén et al. 2008/

For the streamtube approximation, the effective hydraulic conductivity can be calculated in a similar fashion:

$$K_{eff} = \frac{1}{\frac{1}{L}\int_0^L \frac{1}{K(\xi)} d\xi} \quad \text{(Eq. 3-11)}$$

The average specific flow-wetted surface for transport from the release location to the near surface is given by:

$$\overline{a}_R = \frac{1}{L_p}\int_{L-L_p}^{L_p} a_R(\xi) d\xi \quad \text{(Eq. 3-12)}$$

For a streamtube, the F-factor can then be shown to be:

$$F = \frac{\overline{a}_R L_p}{K_{eff} i} = \frac{1}{L i}\left(\int_{L-L_p}^{L_p} a_R(\xi) d\xi\right)\int_0^L \frac{1}{K(\xi)} d\xi \quad \text{(Eq. 3-13)}$$

In this case, the advective travel time is given by:

$$t_w = \frac{V}{Q} = \frac{1}{L i}\left(\int_{L-L_p}^{L_p} a_R(\xi)\delta_t(\xi) d\xi\right)\int_0^L \frac{1}{K(\xi)} d\xi \quad \text{(Eq. 3-14)}$$

Equations 3-8 and 3-13 can be used to give independent estimates of the F-factor for transport according to the model and boundary conditions illustrated in Figure 3-12. Similarly, Equations 3-9 and 3-14 can be used to make estimates of the advective travel times corresponding to each of these cases. The results of this analysis are given in Section 3.7.

3.6 Transport properties of the HRD

3.6.1 The non-engineered near field (NNF)

The F-factor for a single pathway in the non-engineered near field (NNF) was calculated as a function of flowpath transmissivity using Equation 3-6. The flowpath transmissivity was taken to be approximately the same as the assumed tolerable range for flowing fractures intersecting canister positions. The results of these calculations are shown in Figure 3-13 for an assumed transport distance of 10 m and different hydraulic gradients.

As can be seen from the figure, the assumed hydraulic gradient can have a large impact upon the results particularly if an inverse correlation is assumed between fracture transmissivity and local hydraulic gradient. If there is no relation between gradient and transmissivity one would expect canister positions intersected by low transmissivity fractures to not contribute appreciably to the radionuclide release rate. If, on the other hand, there is an inverse relation of the kind postulated in Section 3.3, the low transmissive fractures may play a more important role than initially suspected. This possibility must be investigated more fully within safety assessment.

It should also be noted that the hydraulic gradient correlation used in the calculations shown Figure 3-13 is purely speculative since the pre-factor in the power law expression is reduced by two orders of magnitude relative to that which was estimated on the basis of the empirical data analysis presented previously in Figure 3-8. The rationale for this is given in Section 3.3 and the results shown in the figure above are intended to be interpreted only as a tentative, “what if” analysis.

3.6.2 The immediate far field (IFF)

The results of the connectivity analysis for HRD_C (–650 m to –400 m) are shown in Figure 3-14 where the percolation probability is plotted as a function of the boundary plane separation distance in the simulations. The results are based upon the probability of existence of at least one percolating structure spanning the modelled domain for 100 stochastic realisations of the Hydrogeological DFN considering fractures in the size range 10 m to 560 m.

The results of the connectivity analysis indicate that the probability of forming a hydraulically connected fracture cluster over the respect distance of 100 m from the repository is high although

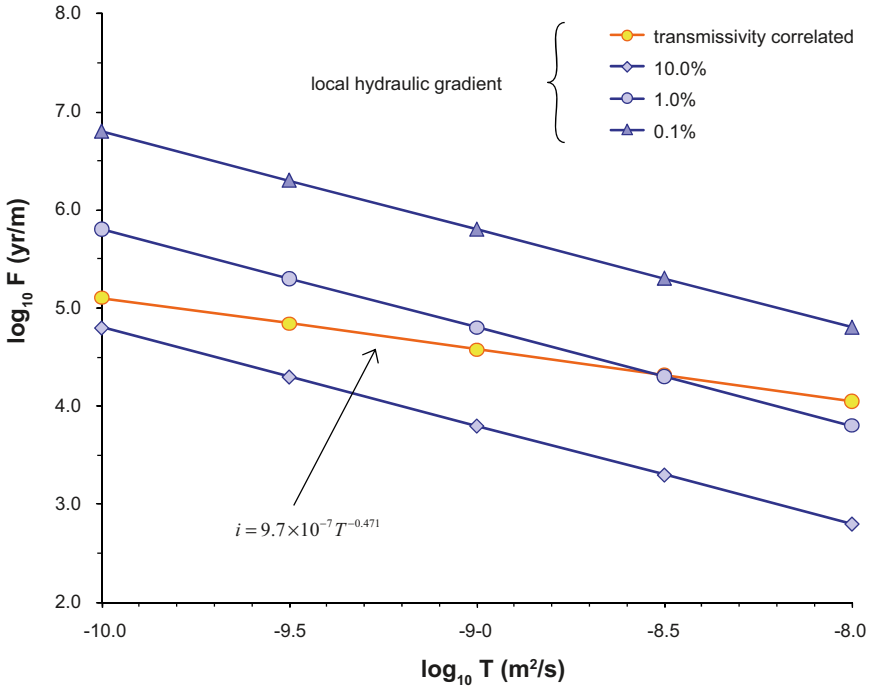

Figure 3-13. *F-factors for typical flowpaths as a function of flowpath transmissivity in the non-engineered near field (NNF). The calculations consider a transport distance of 10 m and a range of hypothetical hydraulic gradients (blue curves). F-factors corresponding to the special case of an inverse correlation between transmissivity and hydraulic gradient is also shown (orange curve).*

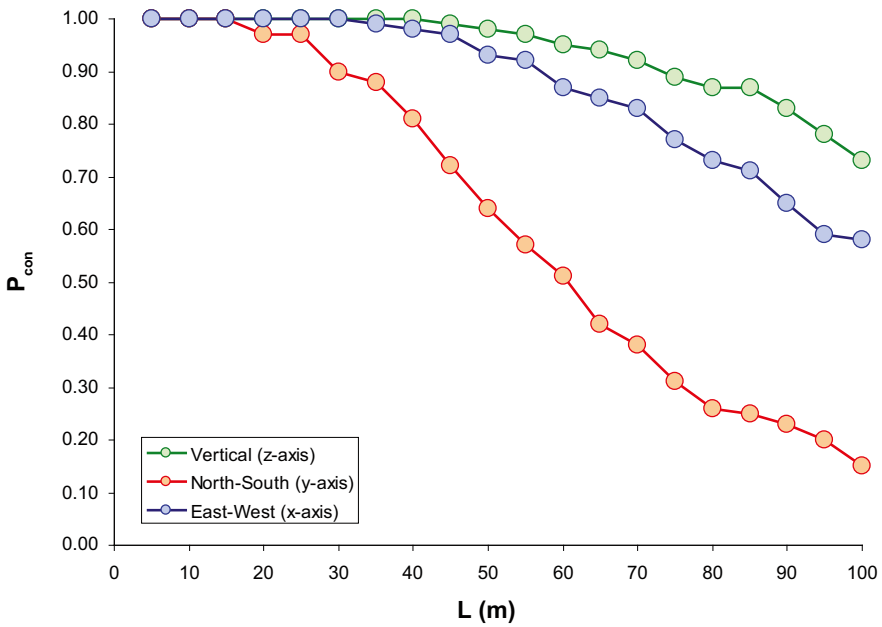

Figure 3-14. *Results of connectivity analysis for HRD_C (–650 m to –400 m) based upon 100 stochastic realisations of the Hydrogeological DFN model based upon open and partly open fractures (OPO). The percolation probability is plotted as a function of distance for the three principal axes of the model.*

there appears to be strong anisotropic effects. The probability of an individual realisation exhibiting connectivity in a NS direction appears to be considerably lower (15%) as compared to the EW (58%) or the vertical directions (73%).

For the realisations that are connected in a NS direction over a 100 m transport distance, about 12% include at least one single fracture that penetrates the entire simulation volume. The corresponding figures for the EW and vertical directions are 20% and 14%, respectively. Most realisations exhibiting connectivity, however, consist of multiple fracture clusters of varying size that span the simulation volume boundary planes. This is not necessarily true for shorter boundary plane separation distances and the percentage of realisations featuring at least one single spanning fracture generally increases with decreasing boundary plane separation distance. This, however, is expected behaviour based upon consideration of the fracture population size distribution.

Hydraulically connected DFN realisations were converted to an equivalent pipe network and the path of least transport resistance, PLTR was calculated for each realisation using Dijkstra's algorithm /e.g. Cormen et al. 2001/ for the case of neutrally conductive FIZ as well as highly conductive FIZ.

A full account of the modelling procedure can be found in /Crawford 2008/ and detailed simulation results can be found in Appendix B. An example of typical F-factor ranges calculated using this method, however, is given in Figure 3-15 for a 1% hydraulic gradient applied along the three principal axes assuming the semi-correlated (SC), fracture size-transmissivity model and a 100 m transport distance.

Summary statistics for the PLTR cases shown in Figure 3-15 are given in Table 3-9.

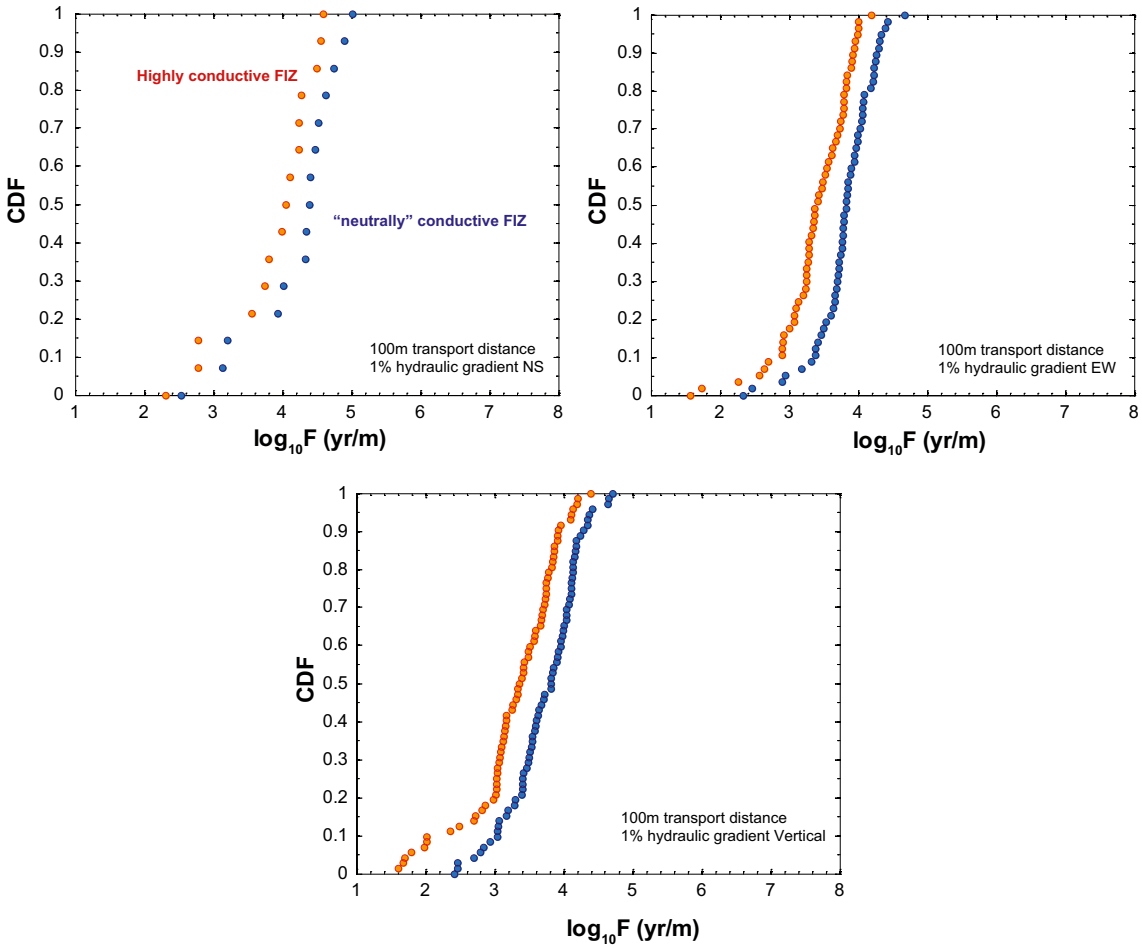

Figure 3-15. *Typical F-factor ranges for paths of least transport resistance, PLTR in the immediate far-field (IFF) based upon the results of 100 realisations of the Hydrogeological DFN for HRD_C (–650 m to –400 m). The calculations consider a 100 m transport distance and a semi-correlated fracture length-transmissivity (SC) model for the boundary conditions indicated in the figure. Results are given for the case of neutrally conductive FIZ (blue markers) and for highly conductive FIZ (orange markers) and are plotted as cumulative distribution probability curves.*

Table 3-9. Summary statistics for the F-factor (yr/m) corresponding to the path of least transport resistance (PLTR) estimated for HRD_C (–650 m to –400 m) for a nominal transport distance of 100 m along the three principal transport directions (EW, NS, V) and a hydraulic gradient of 1%. Results are given for the neutrally-conductive and highly conductive FIZ cases where the semi-correlated (SC) fracture size-transmissivity model is assumed. Data are given in log_{10}-units.

FIZ model	Neutrally-conductive			Highly-conductive		
Gradient direction	EW	NS	V	EW	NS	V
Mean	3.80	4.17	3.72	3.37	3.84	3.26
Median	3.83	4.40	3.82	3.39	4.06	3.36
5th percentile	2.92	2.69	2.72	2.39	2.43	1.71
10th percentile	3.34	3.13	3.02	2.76	2.78	2.02
25th percentile	3.66	3.96	3.41	3.14	3.60	3.03
75th percentile	4.07	4.60	4.11	3.79	4.27	3.75
90th percentile	4.29	4.89	4.30	3.94	4.56	3.93
95th percentile	4.37	4.98	4.41	4.00	4.58	4.14
Std. deviation	0.44	0.70	0.52	0.52	0.70	0.70
Variance	0.19	0.49	0.27	0.27	0.49	0.49
Min value	2.33	2.54	2.42	1.57	2.31	0.85
Max value	4.67	5.01	4.71	4.19	4.59	4.40
Fraction connected (%)	58	15	73	58	15	73

It should be remembered that the F-factor distributions given in Table 3-9 represent the aggregate data set of 100 realisations and therefore should be interpreted as a probability distribution for the singular F-factor corresponding to the path of least transport resistance in each realisation. This should not be confused with the ensemble average F-factor distribution for transport in an individual DFN realisation with particle tracking where consideration is also given to advective dispersion processes within the fracture network.

Some results from the complementary analysis of this fracture domain using the particle tracking capabilities of the Napsac/ConnectFlow program /Serco Assurance 2007/ are illustrated in Figure 3-16. Since it is not possible to simulate highly-conductive FIZ in any simple fashion using Napsac/ConnectFlow, the results consider only the base case of neutrally-conductive FIZ.

Summary statistics for the particle tracking cases are given in Table 3-9. The summary statistics represent a pooling of all particle tracking results depicted in Figure 3-16. The F-factor distributions should therefore not be seen as a true distribution of values for solute transport within the rock volume, but interpreted rather as a probability distribution for typical transport paths within the rock. The F-factor for transport from any given canister location would then correspond to a sub-sampling of these distributions.

More detailed results for the intermediate transport distances (i.e. 25 m, 50 m, and 75 m) are given in Appendix B along with full sets of results for the other hydraulic rock domains investigated (i.e. HRD_W, HRD_EW007, and HRD_N).

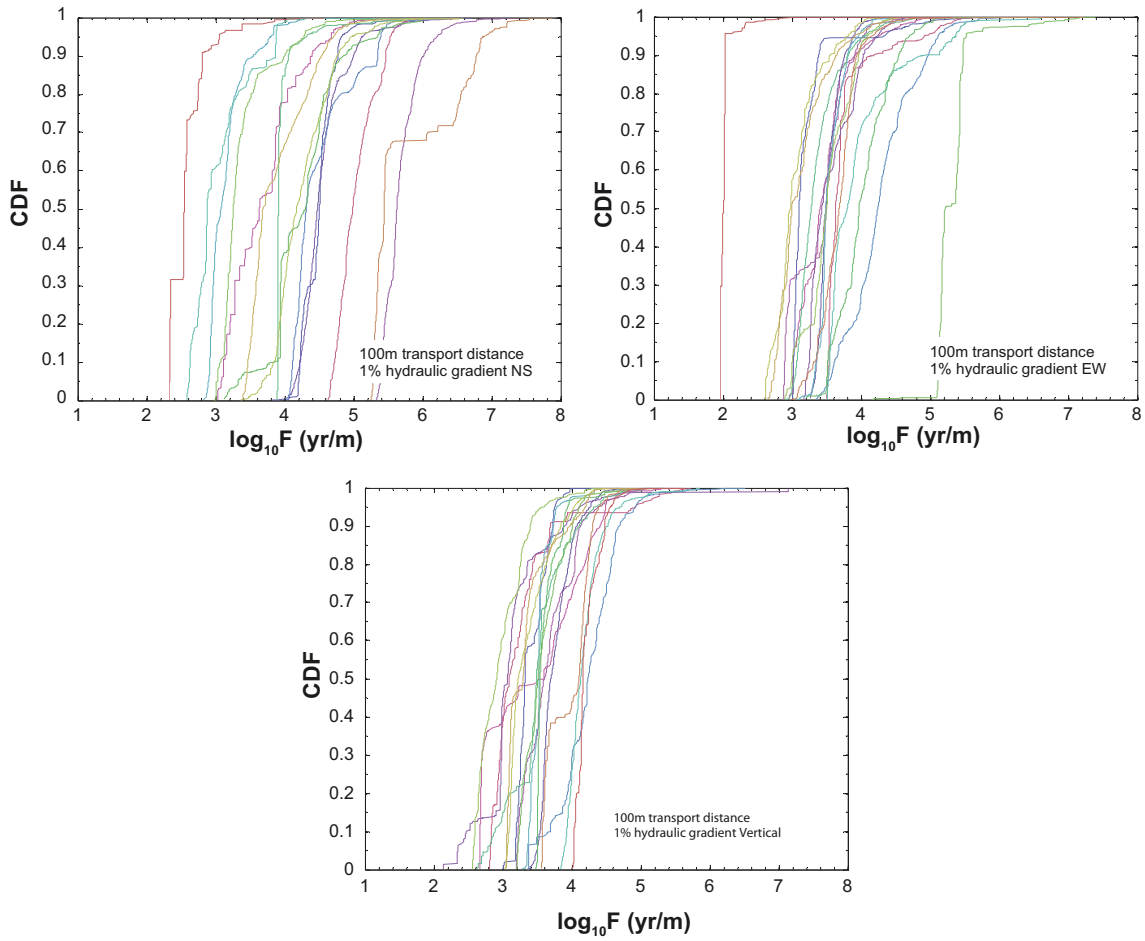

Figure 3-16. *Typical F-factor distributions obtained using particle tracking for HRD_C (–650 m to –400 m). The calculations consider a 100 m transport distance, boundary conditions as indicated in the figure, and the semi-correlated fracture length-transmissivity (SC) model. Results are given for the case of neutrally conductive FIZ only and are plotted as cumulative distribution probability curves for 20 individual Hydrogeological DFN realisations generated by Napsac/ConnectFlow.*

Table 3-10. Summary statistics for the F-factor (yr/m) calculated for HRD_C (–650 m to –400 m) using particle tracking and assuming neutrally conductive FIZ, a nominal transport distance of 100 m, and a hydraulic gradient of 1%. Results are given for the three principal transport directions (EW, NS, V) and the semi-correlated (SC) transmissivity model. The statistics consider the entire set of particles recovered in 20 stochastic simulations of the Hydrogeological DFN using Napsac/ConnectFlow (1,000 particles released in each simulation). Data are given in $\log_{10}$-units.

Gradient direction	EW	NS	V
Mean	3.58	4.16	3.61
Median	3.52	4.14	3.55
5th percentile	2.02	2.59	2.72
10th percentile	2.89	2.89	2.98
25th percentile	3.18	3.38	3.24
75th percentile	3.87	4.74	4.01
90th percentile	4.53	5.45	4.26
95th percentile	5.17	5.70	4.46
Std. deviation	0.74	0.97	0.53
Variance	0.55	0.95	0.28
Min value	1.96	2.33	2.13
Max value	7.40	7.87	7.14
# recovered particles	17,000	14,970	16,922

3.7 Transport properties of the HCD

Using the analytical models described in Section 3.5 (Equation 3-8 and 3-13), F-factors for typical flowpaths within the HCD have been calculated for an assumed hydraulic gradient of 1%. Calculations have been made both for deformation zones of "generic" type as well as calculations using data specific to ZSMEW007A. The F-factor as estimated by Equation 3-8 and 3-13 was calculated analytically with the aid of Mathematica[2] using the parameter values supplied in Table 3-6.

Results for a 2D planar representation of generic deformation zones are given in Table 3-11 for three different hypothetical dip angles. As can be seen from the results, the dip angle has essentially no bearing on the magnitude of the effective transmissivity of the zone although a small effect on the F-factor owing to somewhat increased flow-wetted surface encountered in more gently dipping zones. If the mean depth trend is taken to represent the "average" hydrogeological properties of the zone, a mean F-factor on the order of 10^3 yr/m does not seem unreasonable. If, on the other hand, the estimated maximum and minimum transmissivity trend lines (as illustrated in Figure 3-5) represent individually compartmentalised fast and slow flowpaths, the F-factor of such flowpaths could vary from as little as approximately 2 yr/m to as much as 10^6 yr/m.

Results for a 3D porous medium (streamtube) representation of generic deformation zones are given in Table 3-11 for three different hypothetical dip angles. The results are qualitatively similar to those obtained for the 2D planar representation although with a tendency to higher F-factor estimates in the range of 4×10^4 yr/m to 7×10^4 yr/m.

Using the deformation zone specific data in Table 3-7 F-factors have been estimated for transport within ZSMEW007A assuming the same boundary conditions for flow and solute release as used in the generic deformation zone calculations. The results of this analysis are given in Table 3-13.

Deformation zone ZSMEW007A has a dip angle of roughly 44° /Rhén et al. 2008/ which makes it roughly comparable to the far right hand data columns in Table 3-11 and Table 3-12. Comparison of these results suggests that the F-factor for transport in ZSMEW007A is likely to be about an order of magnitude lower than that calculated for the 2D generic case and about 4–5 times lower for the 3D generic case. The difference appears to be largely due to the higher transmissivity of ZSMEW007 relative to the generic deformation zone example.

Table 3-11. Flow related transport properties of the HCD (generic deformation zones) calculated using the 2D analytical model described in Section 3.5 and an assumed 1% hydraulic gradient. The effective transmissivity and F-factor is additionally calculated for the maximum and minimum trend line in the exponential transmissivity model case (see Figure 3-5).

Deformation zone dip (deg.)	90°	70°	45°
Flow distance, L (m)	450	479	636
Transport distance, L_p (m)	400	426	566
Effective transmissivity, T_{eff} (m^2/s)			
	(exponential depth trend model with max/min ranges, DZ-L-3):		
Maximum trend	1.32×10^{-3}	1.32×10^{-3}	1.32×10^{-3}
Mean trend	2.28×10^{-6}	2.28×10^{-6}	2.28×10^{-6}
Minimum trend	3.92×10^{-9}	3.92×10^{-9}	3.92×10^{-9}
	(power law depth trend model, DZ-L-1):		
	1.41×10^{-6}	1.41×10^{-6}	1.41×10^{-6}
Log_{10} F-factor (yr/m)			
	(exponential depth trend model with max/min ranges, DZ-L-3):		
Maximum trend	0.28	0.31	0.43
Mean trend	3.05	3.07	3.20
Minimum trend	5.81	5.84	5.96
	(power law depth trend model, DZ-L-1):		
	3.26	3.28	3.41

[2] Wolfram Research, Inc. Mathematica, Version 7.0, Champaign, IL (2009).

Table 3-12. Flow related transport properties of the HCD (generic deformation zones) calculated using the 3D analytical model described in Section 3.5 and an assumed 1% hydraulic gradient.

Deformation zone dip (deg.)	90°	70°	45°
Flow distance, L (m)	450	479	636
Transport distance, L_p (m)	400	426	566
	Effective conductivity, K_{eff} (m/s)		
(exponential depth trend model, DZ-L-3)	9.16×10^{-8}	9.16×10^{-8}	9.16×10^{-8}
(power law depth trend model, DZ-L-1)	7.28×10^{-8}	7.28×10^{-8}	7.28×10^{-8}
	Log_{10} F-factor (yr/m)		
(exponential depth trend model, DZ-L-3)	4.61	4.64	4.76
(power law depth trend model, DZ-L-1):	4.71	4.74	4.86

Table 3-13. Flow related transport properties of ZSMEW007A calculated using the 2D and 3D analytical models described in Section 3.5 and an assumed 1% hydraulic gradient. The range of F-factor values obtained for the 3D streamtube model reflects whether an exponential model (lower F-factor estimate) or linear model (upper F-factor estimate) for the a_R depth trend is used in the calculation.

	2D planar model	3D streamtube model
Flow distance, L (m)	648	648
Transport distance, L_p (m)	576	576
Effective transmissivity, T_{eff} (m^2/s)	1.64×10^{-5}	
Effective conductivity, K_{eff} (m/s)		2.28×10^{-6}
Log_{10} F-factor (yr/m):	2.35	4.09–4.22

3.8 Advective transport times for typical flowpaths

One of the parameters of interest for safety assessment is the advective transport time for the network of fractures forming conductive pathways from the repository to the near surface. This is also referred to as the water residence time in the scientific literature /e.g. Neretnieks 1980/. The advective transport time can be important for the transport of colloids and non-sorbing solutes in flowpaths featuring very low F-factors. Generally, for sorbing solutes the advective transport time is very small in comparison to the matrix retention time and can be neglected in radionuclide transport calculations if the F-factor is sufficiently high /Neretnieks and Moreno 2003, Cvetkovic et al. 2004/.

Using the three relations for the dependency of transport aperture on transmissivity (i.e. the MCL, MQL, and LPL assumptions) it is possible make scoping estimates of advective travel times under the same conditions assumed for the estimation of F-factors presented previously. The results of this analysis are presented in Section 3.8.1 for the HRD and in Section 3.8.2 for the HCD.

Owing to the computationally demanding nature of the ConnectFlow simulations, and in the interest of reducing the amount of superfluous detail, the results for the HRD only consider the case of the MQL transmissivity-aperture relation. The calculations for the HCD, however, consider all three transmissivity-aperture relations to provide an indication of the variability arising due to modelling assumptions concerning the transport aperture and its correlation with fracture transmissivity.

3.8.1 Advective travel times in the HRD

Advective transport times have been calculated for the particular Hydro DFN realisations detailed in Section 3.6.2. The calculations are based upon the particle tracking simulations made using ConnectFlow and assume the MQL transmissivity-aperture relation as a basis for the calculations. Results for individual realisations are plotted in Figure 3-17 for HRD_C. Summary statistics for the pooled ensemble of particle tracking data are given in Table 3-14.

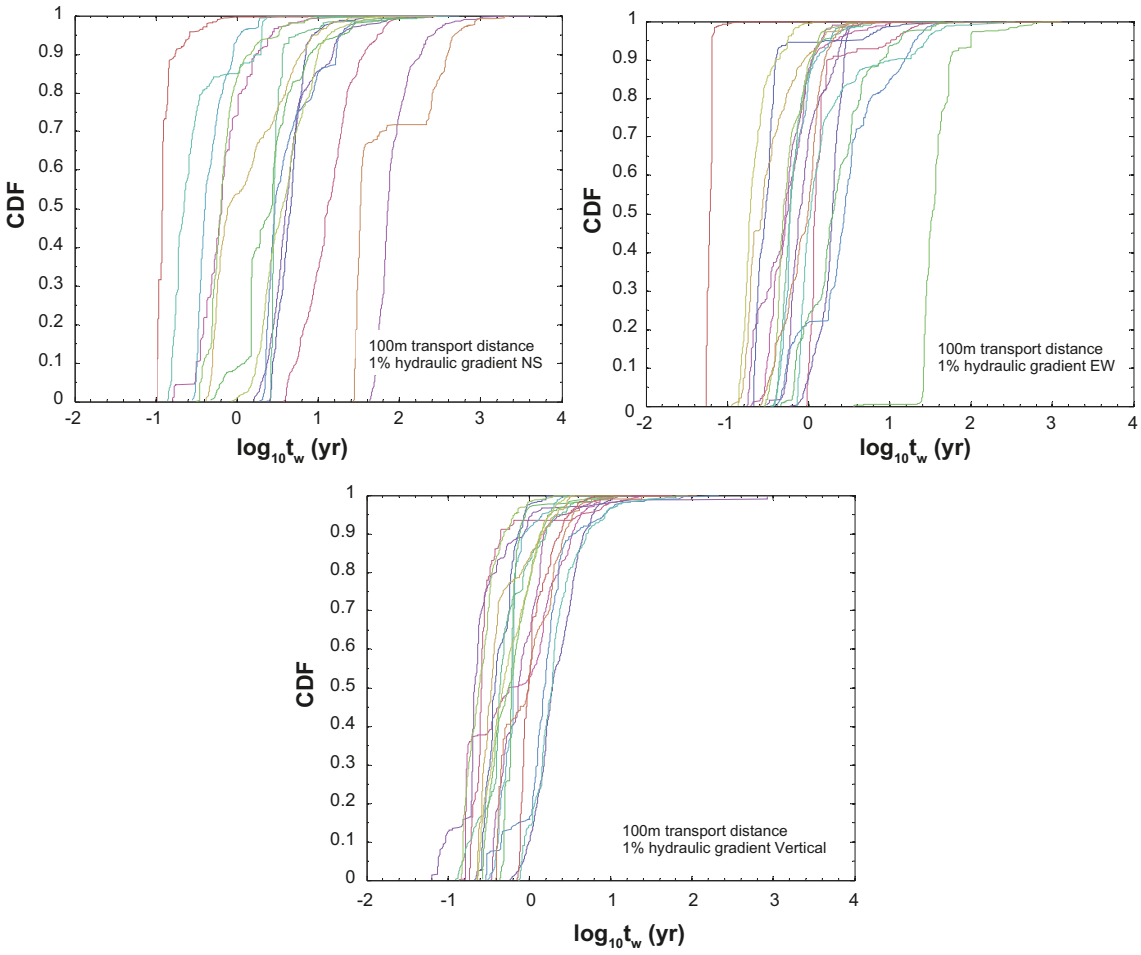

Figure 3-17. *Typical advective travel time distributions obtained using particle tracking for HRD_C (–650 m to –400 m) shown for an ensemble of realisations assuming the MQL transmissivity-aperture relation. The individual residence time distributions shown in the figure correspond to the matching F-factor distributions previously described in Section 3.6.2.*

Table 3-14. Summary statistics for the advective travel time, t_w (yr) calculated for HRD_C (–650 m to –400 m) for the Hydrogeological DFN realisations shown in Figure 3-17 and are based upon a pooling of the particle tracking data from individual runs. Data are given in $\log_{10}$-units.

Gradient direction	EW	NS	V
Mean	–0.06	0.43	–0.17
Median	–0.14	0.44	–0.22
5th percentile	–1.19	–0.87	–0.76
10th percentile	–0.73	–0.65	–0.66
25th percentile	–0.43	–0.24	–0.48
75th percentile	0.20	0.86	0.11
90th percentile	0.68	1.61	0.37
95th percentile	1.44	1.88	0.55
Std. deviation	0.64	0.83	0.42
Variance	0.41	0.69	0.18
Min value	–1.25	–0.99	–1.20
Max value	3.12	3.65	2.93
# recovered particles	17,000	14,970	16,922

Detailed results can be found in Appendix B for the other hydraulic rock domains investigated (i.e. HRD_W, HRD_EW007, and HRD_N).

3.8.2 Advective travel times in the HCD

Advective travel times for typical flowpaths within the HCD (calculated using Mathematica) are given in Table 3-15 for a 2D planar representation of generic deformation zones and in Table 3-16 for the 3D streamtube representation. In these calculations all three transmissivity-aperture relations described previously in Section 3.5 (i.e. MCL, MQL, LPL1, and LPL2) have been used to give estimates of likely advective transport times.

Based upon mean hydraulic properties, the advective travel time in generic deformation zones is predicted to lie in the approximate range 0.1–4 yr depending upon deformation zone orientation and which model is used to relate transport aperture and transmissivity. If, on the other hand, the measurement data represents a sampling of compartmentalised fast and slow flowpaths (as represented by the maximum and minimum transmissivity regression line), the advective travel time could vary anywhere from as little as 0.001 yr to as much as 160 yr. Generally it is found that the most transmissive flowpaths are associated with the shortest advective travel times, whereas the least transmissive flowpaths have the longest advective travel times.

Table 3-15. Advective travel times, t_w (yr) for typical flowpaths within the HCD (generic deformation zones) calculated using the 2D analytical model described in Section 3.5 and an assumed 1% hydraulic gradient. Four different relations for transport aperture–transmissivity dependency have been assumed in the calculations (referred to here as MCL, MQL, LPL1, and LPL2). Data are given in arithmetic (i.e. non-log) units.

Deformation zone dip (deg.)	90°	70°	45°
Macroscopic cubic law (MCL):			
	(exponential depth trend model with max/min ranges, DZ-L-3)		
Maximum trend	0.0014	0.0015	0.0020
Mean trend	0.098	0.10	0.14
Minimum trend	6.8	7.3	9.6
	(power law depth trend model, DZ-L-1)		
	0.13	0.14	0.18
Macroscopic quadratic law (MQL):			
	(exponential depth trend model with max/min ranges, DZ-L-3)		
Maximum trend	0.022	0.024	0.031
Mean trend	0.54	0.57	0.76
Minimum trend	13	14	18
	(power law depth trend model, DZ-L-1)		
	0.64	0.68	0.91
Laxemar power law (LPL1):			
	(exponential depth trend model with max/min ranges, DZ-L-3)		
Maximum trend	0.056	0.060	0.080
Mean trend	1.2	1.3	1.7
Minimum trend	25	27	36
	(power law depth trend model, DZ-L-1)		
	1.41	1.50	2.00
Laxemar power law (LPL2):			
	(exponential depth trend model with max/min ranges, DZ-L-3)		
Maximum trend	0.056	0.060	0.079
Mean trend	2.5	2.65	3.52
Minimum trend	111	118	156
	(power law depth trend model, DZ-L-1)		
	3.16	3.36	4.47

Table 3-16. Advective travel times, t_w (yr) for typical flowpaths within the HCD (generic deformation zones) calculated using the 3D analytical model described in Section 3.5 and an assumed 1% hydraulic gradient. Four different relations for transport aperture–transmissivity dependency have been assumed in the calculations (referred to here as MCL, MQL, LPL1, and LPL2). Data are given in arithmetic (i.e. non-log) units.

Deformation zone dip (deg.)	90°	70°	45°
Macroscopic cubic law (MCL):			
(exponential depth trend model, DZ-L-3)	7.42	7.89	10.5
(power law depth trend model, DZ-L-1)	7.63	8.12	10.8
Macroscopic quadratic law (MQL):			
(exponential depth trend model, DZ-L-3)	41.2	43.9	58.3
(power law depth trend model, DZ-L-1)	38.3	40.8	54.2
Laxemar power law (LPL1):			
(exponential depth trend model, DZ-L-3)	92.1	98.0	130
(power law depth trend model, DZ-L-1)	84.6	90.0	120
Laxemar power law (LPL2):			
(exponential depth trend model, DZ-L-3)	190	202	269
(power law depth trend model, DZ-L-1)	187	199	265

Similarly to the results for the F-factor, it is found that the 3D streamtube model gives advective travel time estimates significantly larger than the 2D planar model. Here, the advective travel time is predicted to vary from less than 10 yr up to approximately 270 yr depending upon deformation zone orientation and which transport aperture model is assumed in the calculation. Using the deformation zone specific data for ZSMEW007A, advective travel times have been estimated assuming the same boundary conditions for flow and solute release as used in the generic deformation zone calculations. The results of this analysis are given in Table 3-17.

The 2D calculations for ZSMEW007A suggest advective travel times in the range 0.04 yr to 1.1 yr depending upon which transport aperture relation is assumed in the calculation. For the 3D streamtube calculations, the advective travel times are found to range from about 4.5 yr to 170 yr depending on the underlying modelling assumptions. The assumed functional relation between specific flow-wetted surface, a_R and elevation used in the streamtube calculations seems to only have a minor impact on the advective travel time. Since the calculated average specific flow-wetted surface is only marginally different in each calculation case, this is not unexpected.

Table 3-17. Advective travel times for typical flowpaths within ZSMEW007A calculated using the 2D and 3D analytical models described in Section 3.5 and an assumed 1% hydraulic gradient. Four different relations for transport aperture–transmissivity dependency have been assumed in the calculations (referred to here as MCL, MQL, LPL1, and LPL2). The range of t_w (yr) values obtained for the 3D streamtube model reflects whether an exponential model (lower t_w estimate) or linear model (upper t_w estimate) for the a_R depth trend is used in the calculation.

	2D planar model	3D streamtube model
Macroscopic cubic law (MCL):		
	0.037	4.45–5.82
Macroscopic quadratic law (MQL):		
	0.28	34.7–44.6
Laxemar power law (LPL1):		
	0.64	80.8–104
Laxemar power law (LPL2):		
	1.07	132–171

3.9 Direct estimation of the F-factor from borehole measurement data

To evaluate the soundness of F-factor ranges obtained from detailed hydrogeological modelling, it may be possible to use borehole hydraulic data directly to give an order of magnitude estimate of representative F-factors characterising the HRD and HCD. One way of making such an estimate is to focus on the level of individual flowing features identifiable from borehole hydraulic measurements. Here, one might consider what the theoretical transport resistance would be if the flowing feature sampled in a borehole were to correspond to a typical flowpath. For this purpose, the most appropriate conditions for comparison with safety assessment conditions would be those corresponding to the natural background hydraulic gradients at the site.

As already discussed in Section 3.3, there are a large number of in situ measurements of flow under approximately background hydraulic conditions which could, in principle, be used to make such a calculation. These measurements take the form of tracer dilution tests performed in permanently instrumented boreholes /Thur and Gustafsson 2007, Thur 2008/ and borehole sections used in conjunction with SWIW tests /Gustafsson and Nordqvist 2005, Gustafsson et al. 2006, Thur et al. 2007a, b/.

In order to use these measurements to derive a raw-data based estimate of a site specific F-factor, it is necessary to make the following assumptions:

1. The hydraulic conditions are representative for the undisturbed background hydraulic gradient and are similar to those that would be encountered under safety assessment conditions;
2. The flow measured in a tracer dilution test, after correction for distortion of flow caused by the borehole, is representative of a flowpath of width at least equal to the borehole diameter, W_{bh};
3. The flowpath length, L_p is the same as that used for the calculation of F-factors (with the hydrogeological model) upon which the comparison is based, i.e.:
   ~100 m for the HRD (i.e. same as for the voxel calculations described previously)
   ~400 m to ~600 m for deformation zones comprising the HCD;
4. The flow-wetted surface of the sampled flowpath is equal to, or greater than twice the product of borehole diameter and flowpath length;

Based upon these assumptions, the F-factor can be defined as:

$$F \approx \frac{2W_{bh}L_p}{Q_{bh}/\alpha_{corr}} \geq \frac{4W_{bh}L_p}{Q_{bh}} \qquad \text{(Eq. 3-15)}$$

With regard to assumption 1, it can be stated that although tracer dilution tests are carried out in the absence of pumping in the measurement borehole itself, it is known that there is often considerable hydraulic interference from other activities occurring at the site. Consequently, assumption 1 described above is not reliable and measured flowrates are therefore probably not representative of the undisturbed hydraulic gradient. In all likelihood this would mean a bias towards higher measured flowrates and consequently lower F-factors than would be representative of the true background gradient.

The flow distortion introduced by the borehole depends on the permeability of the borehole section itself (effectively infinite) relative to that of the surrounding aquifer including any disturbed zone. In the interpretation of tracer dilution tests, a value for the correction factor of $\alpha_{corr} = 2$ is generally assumed in calculations /Nordqvist 2008/. This is what would be expected for a simple fracture aligned orthogonally to the borehole. Since the actual geometry and complexity of the flowing feature is not known accurately, this should be considered to be only a rough estimate. A fracture inclined at an angle of 45° to the borehole, for example, would give a correction factor roughly 1.4 times greater.

The presence of a zone of altered permeability, referred to as a skin zone, may give greater or less distortion than that predicted purely by consideration of the fracture orientation relative to the borehole. The borehole skin may be positive thereby indicating a decreased permeability near the borehole, or negative, indicating an increased permeability near the borehole. Positive skin may arise due to clogging of the fracture with infill material (giving a correction factor less than 2), while negative skin may reflect local erosion of fracture infill material or redistribution of stress near the borehole (giving a correction factor greater than 2). Also, /Bidaux and Tsang 1991/ investigated

the impact of an excess fracture permeability assumed to decay exponentially with distance from a borehole (referred to as a "complex skin"). In that study it was found that the correction factor could be as great as 10 or more for a range of negative skin factors depending upon the assumed radius of penetration of the increased permeability zone from the borehole.

Provided assumption 2 (above) is reasonable, then the result given by the right-hand side Equation 3-15 should constitute a lower bound for the F-factor. For flow correction factors greater than 2 and increased flow channel widths, the F-factor may therefore be larger than this simple estimate suggests. In /Rhén et al. 2008/ a cumulative distribution of skin factors is compiled for Laxemar based upon 444 PSS measurements in 5 m test sections. Roughly 60% of the tested borehole sections gave indications of skin factors equal to or less than zero with about 30% having skin factors less than –2.5 thereby suggesting that Equation 3-15 will tend to underestimate the effective F-factor of the sampled flow path for such features if the measured flow rate is deemed representative.

Since the F-factor is not a directly measurable quantity, it is perhaps more informative to recast Equation 3-15 to give the hypothetical flowrate required to attain a specified F-factor since this can then be compared directly with the borehole measurement data. Scoping calculations detailed in /Crawford 2008/ suggest that borehole flowrates on the order of 10^{-11} m^3/s and less would be required to obtain F-factors of 10^5 yr/m or greater over a 100 m flowpath length using Equation 3-15.

In the methodological description for tracer dilution tests /Gustafsson 2002/, the detection limit is given in terms of the Darcy velocity as being in the range 4×10^{-11} to 6×10^{-12} m/s if an error margin of up to 10% is acceptable. This limit is based upon consideration of the flow rate where the rate of advective transport is only 10 times greater than the hypothetical rate of transport by diffusion into a stagnant water-filled fracture. For a 1 m borehole section, this would correspond to a flowrate in the approximate range of 10^{-11} to 10^{-12} m^3/s. This, however, is a best case for a short borehole section with a small mixing volume. In reality, many of the tested borehole sections are significantly longer than 1 m. For the permanently instrumented boreholes, for example, it is not uncommon for the tested sections to be anywhere from 5 m to as much as 57 m in length (one instance in KLX08). Even with volume reducer inserts, such long borehole intervals contain significant dead volumes and therefore can be expected to have considerably higher detection limits.

The actual flows measured in Laxemar using the tracer dilution method (referred to in this report as "background flows" for non-pumped conditions) are shown in Figure 3-18 below.

It is difficult to make comparisons between Hydrogeological DFN simulation results for the HRD and F-factors estimated using Equation 3-15 since there are only a few data measurement points available for the HRD at repository depth (–400 m to –600 m). The flowrates measured within deformation zones and possible deformation zones, however, seem to be roughly in the same range as that required to give the F-factors predicted by the analytical models described in Section 3.7.

As can be seen from Figure 3-18, the flowrate magnitudes measured in the local model volume appear to imply F-factors of at most 10^4 yr/m. This is roughly in the middle range of the F-factor distributions calculated using the Hydrogeological DFN (see Section 3.6.2) where typical F-factors of 10^3 to 10^5 yr/m were calculated.

Although the differences between the empirically derived estimates and those simulated using the Hydrogeological DFN do not appear to be excessively large, it is possible that the empirically derived F-factors still might be unreasonably low due to probable biases inherent in the analysis. It is also plausible that flow dilution tests have only been made in borehole sections featuring relatively high flowrates that may not be fully representative of the site in general. It therefore cannot be ruled out that there are flows in non-tested borehole sections that are at or below the detection limit of this method and therefore the plotted values may represent a biased snapshot of flow statistics for the rock volume at repository depth.

In addition, there are indications from the Hydro DFN modelling work that point-sampled hydrogeological properties used to make estimates of the F-factor according to Equation 3-15 may not be fully representative of the flowpath integrated F-factor obtained by considering hydrodynamic transport properties along an entire particle trajectory. This is discussed in /Crawford 2008/ where it is concluded that further analysis is needed to identify the source of this apparent discrepancy.

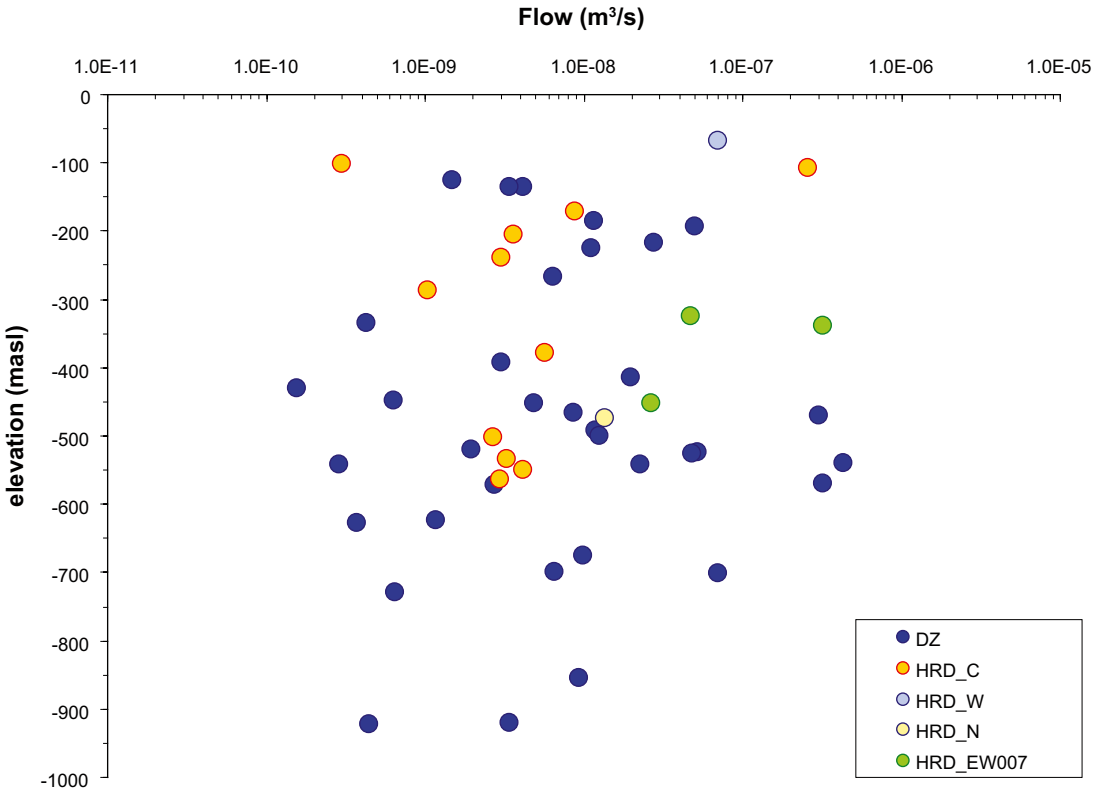

Figure 3-18. *Background flowrates measured in hydraulically conductive borehole sections using the tracer dilution method. The data are categorised according to whether the measurements were made within specified hydraulic rock domains (HRD), or deformation zones (DZ).*

3.10 ECPM simulations of the regional flow model

Within the Hydrogeology site descriptive modelling, flow and transport simulations were carried out with the intention of testing the hydrostructural model developed for the Laxemar candidate area against site scale measurement data including environmental "point-water heads" and drawdowns obtained during hydraulic interference tests. An additional aim of this work was to increase the understanding of palaeo-hydrogeochemical conditions and reconstruction of groundwater evolution during the Holocene. The model implemented in ConnectFlow takes the form of an equivalent continuous porous medium (ECPM) representation of the site including both the local and regional scale hydrogeological models. The work is extensively detailed in the background report by /Rhén et al. 2009/.

Within the hydrogeological modelling work, an additional analysis was also carried out involving particle tracking from a hypothetical repository layout at an elevation of –500 m in the rock within each of the three candidate hydraulic rock domains (HRD_C, HRD_W, and HRD_EW007). One aim of this particular calculation was to ascertain potential radionuclide release locations as an input for surface systems modelling and for safety assessment.

The following sub-sections of this chapter contain a detailed account of these particle tracking results. The aim here is to compare the simulation results with the scoping calculations presented in previous sections in order to gain a greater understanding of the flow-related transport properties of the target volume. The main difference in the calculations presented here is that the hydraulic head boundary conditions are defined implicitly by the topography of the site and the different hydrogeological elements comprising the HRD and HCD are integrated whereas in previous sections they were considered separately.

3.10.1 Flow related transport properties for solute release at –500 m

A particle tracking simulation was made using the ConnectFlow program and the Base Case flow model developed by Hydrogeology and described in the report by /Rhén et al. 2009/. The ConnectFlow simulations are based upon an equivalent continuous porous medium (ECPM) representation of the combined HRD and HCD hydrostructural models. The geometry of the particle release areas and number of released particles were identical to those used in the Hydrogeology site descriptive modelling. The particle tracking simulations consider a flow field taken from the final time step of the palaeo-hydrogeochemical simulations and "frozen" in time. This means that although the flow field is not strictly in a steady state configuration, it is assumed constant for the purposes of the particle tracking simulations. Consequently, the shoreline displacement and distribution of salinity in the system are also assumed to be constant for the duration of the particle tracking simulations which may not be strictly accurate for the very long advective transport times predicted.

The particle release areas were defined to conform to the footprints of the different hydraulic rock domains at –500 m elevation with gaps where HCD features transect the HRD rock volume. Although particle tracking was performed for HRD_C, HRD_W, and HRD_EW007, only the particle tracking results corresponding to HRD_C are described in this report owing to the protracted time required for the in-depth analysis. A total of 1253 particles were released on a regular grid with a 40 m spacing between particle release locations with spaces in locations where the hydraulic domain is transected by deterministic deformation zones. The particle release and surface exit locations are shown in Figure 3-19.

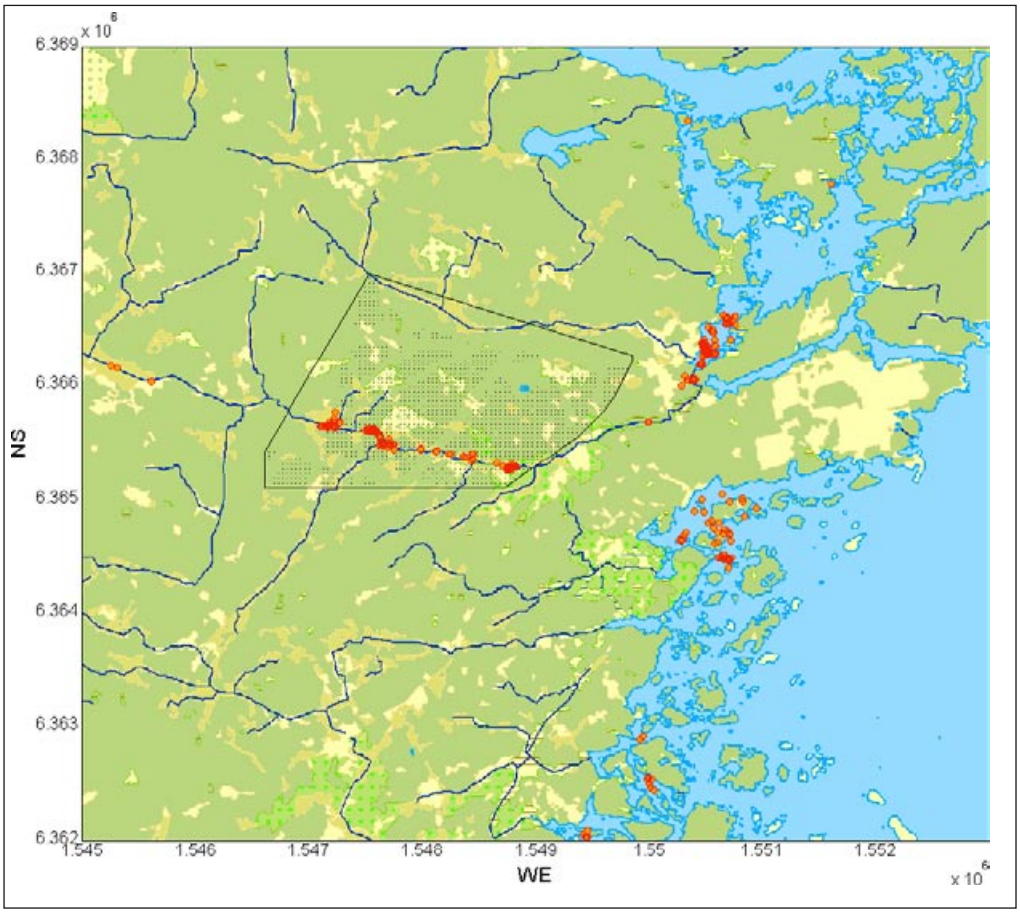

Figure 3-19. *Visualisation of particle release area for HRD_C (dark polygon outline) and surface exit locations (red orange circular markers). The small grey markers inside the release area indicate individual particle release locations with gaps corresponding to deterministic deformation zones transecting the footprint of the hydraulic domain.*

The transported particles tend to fall into two categories with one group following relatively long transport paths in an easterly direction with exit locations predominantly along the Baltic coast. These particles initially tend to track horizontally or even downwards through the HRD before encountering deterministic deformation zones which provide conduits to the surface. Other particles follow a near-vertical trajectory through the HRD before encountering deterministic deformation zones in the upper 100–200 m of the bedrock.

The distribution of F-factors for particles released in HRD_C is given in Figure 3-20 for the particles which arrived at the surface exit locations. The corresponding distribution of advective travel times and the transport distance from release location to surface exit points are given in Figure 3-21 and Figure 3-22, respectively.

A cross-plot of the F-factor vs. advective travel time as well as F-factor vs. travel distance can be found in Figure 3-23 and Figure 3-24.

Summary statistics for the F-factor, advective travel time, and transport path length are given in Table 3-18. As can be seen from Table 3-18, the mean F-factor for particle transport from the release locations in HRD_C to the surface exit locations is on the order of about 2.6×10^6 yr/m while the mean advective travel time is slightly less than 2700 years. The mean transport distance associated with these pathlines is about 2000 m. In comparison with the scoping calculations, these F-factors and advective travel times seem very high. The mean F-factor is roughly 2 orders of magnitude higher than what was taken to be a reasonable average value in the calculations presented in previous sections for typical transport paths in the immediate far field of HRD_C. The advective travel time is also at least a couple of orders of magnitude higher than expected based upon the summed HRD and HCD advective travel times for the transport scenario envisaged in Section 3.1.

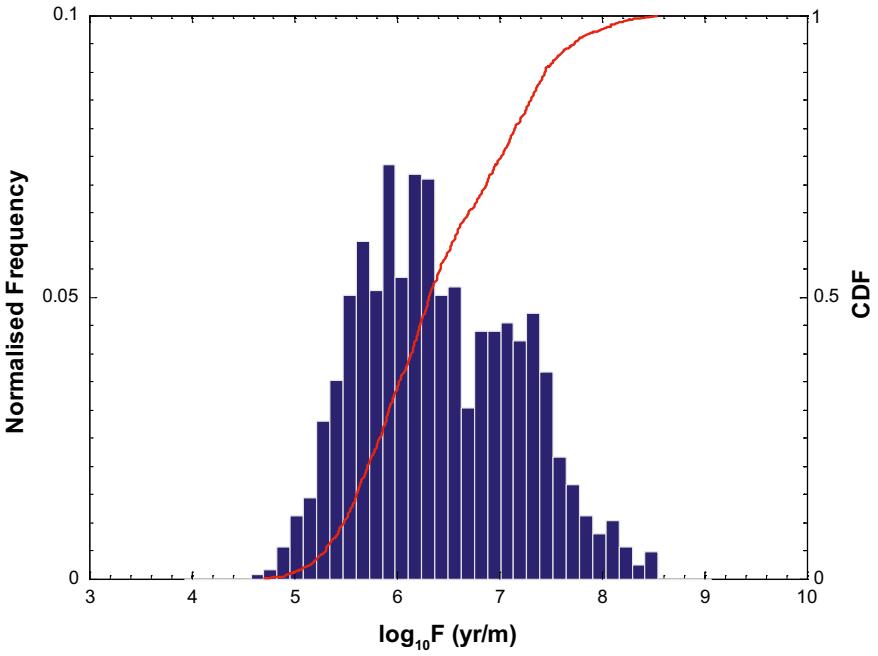

Figure 3-20. *F-factor (yr/m) distribution at release locations calculated with ConnectFlow for solute release at –500 m elevation within HRD_C. The simulated data are shown as a histogram and as an empirical cumulative distribution function (CDF).*

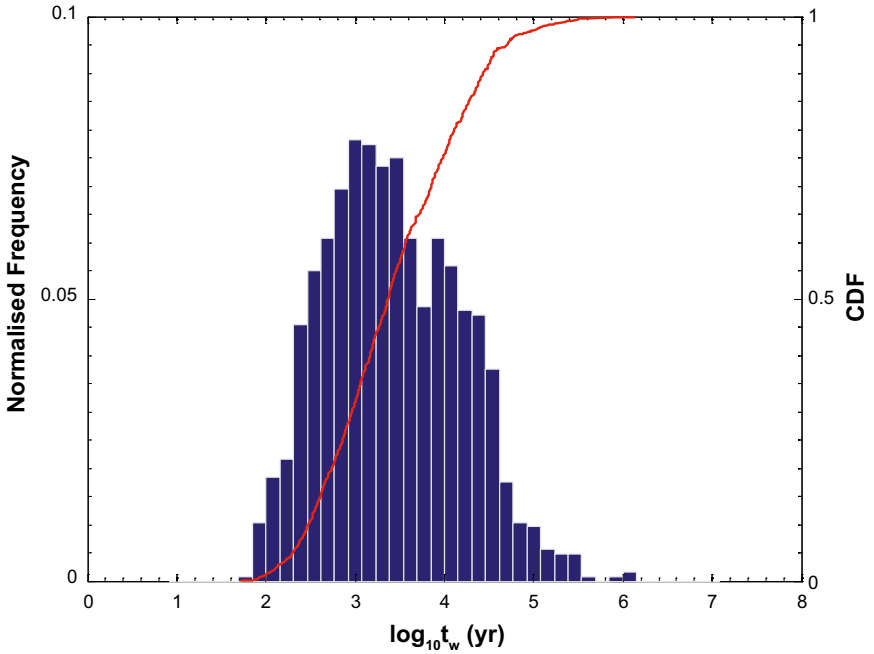

Figure 3-21. *Advective travel time, t_w (yr) at release locations calculated with ConnectFlow for solute release at –500 m elevation within HRD_C. The simulated data are shown as a histogram and as an empirical cumulative distribution function (CDF).*

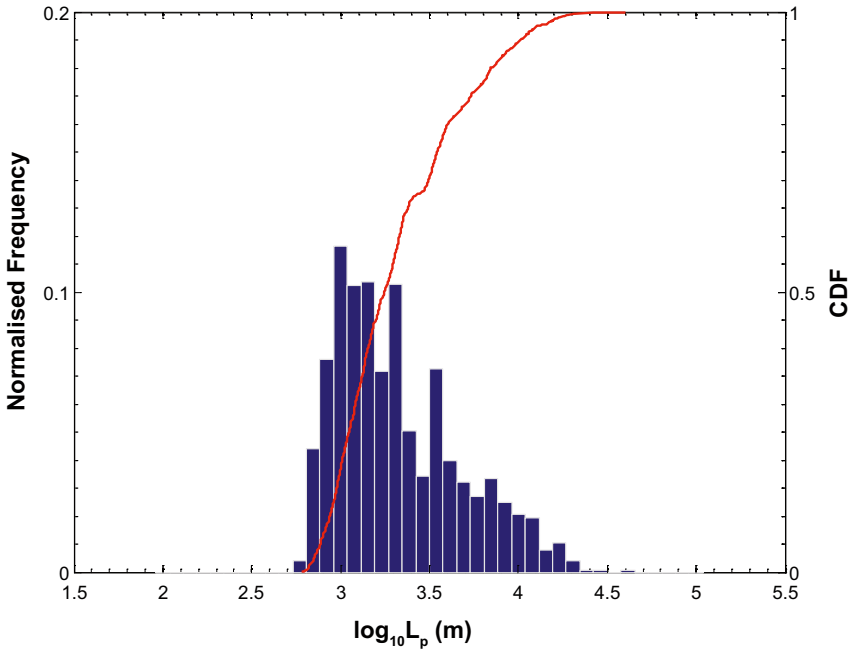

Figure 3-22. *Travel distance, L_p (m) distribution calculated using ConnectFlow for solute release at –500 m elevation within HRD_C. The simulated data are shown as a histogram and empirical cumulative distribution function (CDF).*

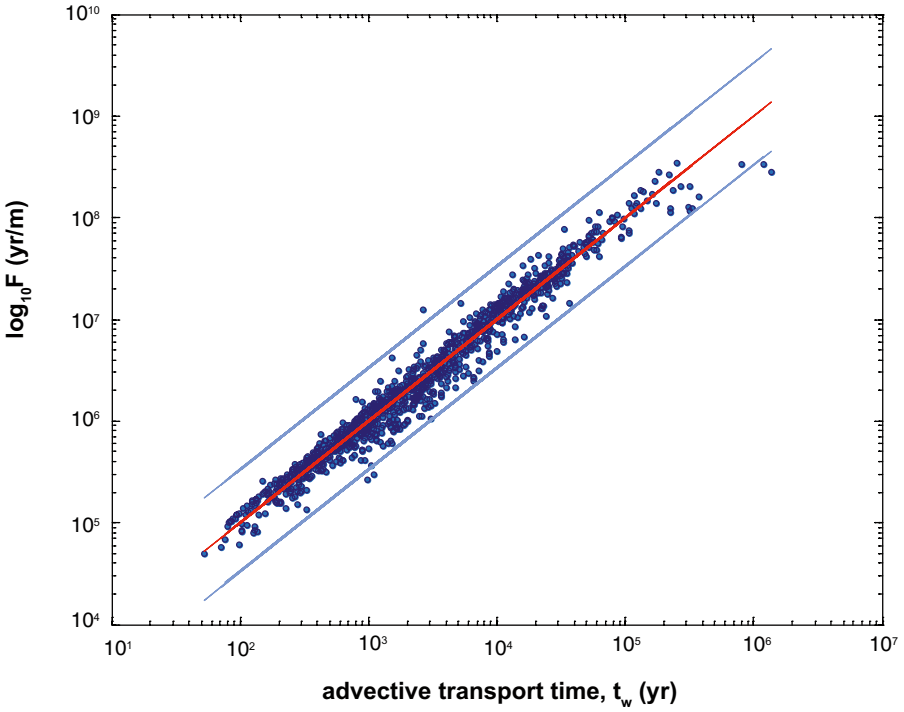

Figure 3-23. *Cross plot showing the correlation between F-factor and advective travel time calculated using ConnectFlow for solute release at –500 m elevation within HRD_C. The red trend line shows the relation between F-factor and advective travel time for an average transport aperture of 2 mm. The upper and lower trend lines bounding the data correspond to transport apertures of 0.6 mm and 6 mm, respectively.*

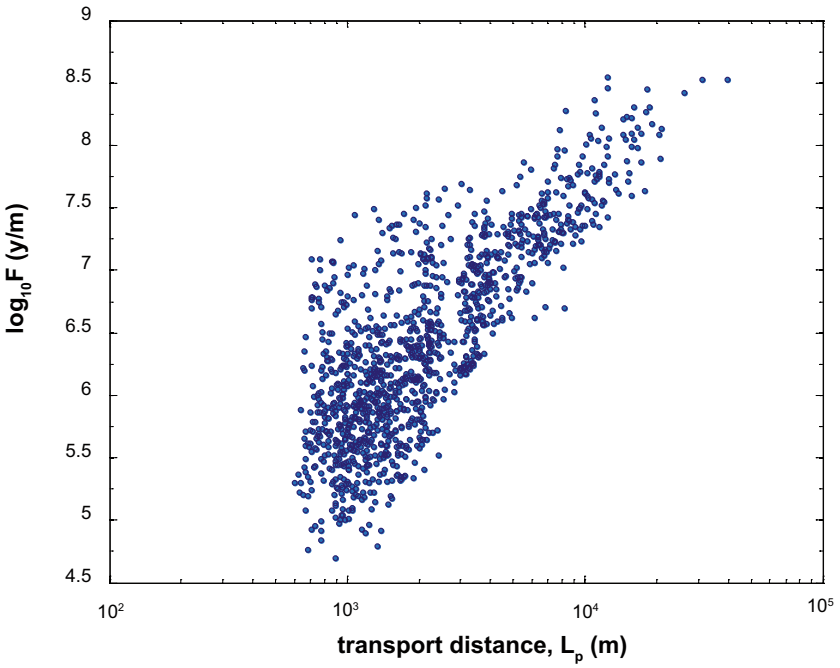

Figure 3-24. *Cross plot showing the correlation between F-factor and transport distance calculated using ConnectFlow for solute release at –500 m elevation within HRD_C.*

Table 3-18. Summary statistics for flow related transport properties calculated using ConnectFlow for solute release at –500 m within HRD_C.

Parameter	$\log_{10}F$ (yr/m)	$\log_{10}t_w$ (yr)	$\log_{10}L_p$ (m)
Mean	6.42	3.43	3.32
Median	6.31	3.37	3.25
5th percentile	5.31	2.30	2.89
10th percentile	5.49	2.48	2.94
25th percentile	5.83	2.86	3.05
75th percentile	7.02	3.98	3.54
90th percentile	7.45	4.44	3.85
95th percentile	7.73	4.70	4.01
Std. deviation	0.76	0.76	0.35
Variance	0.58	0.57	0.12
Min value	4.70	1.72	2.78
Max value	8.54	6.14	4.60
Skew	0.32	0.34	0.80
Kutosis	2.41	2.69	2.92
# Released particles	1253	1253	1253

For the ECPM simulations described in /Rhén et al. 2009/, the Laxemar power law (LPL2) relating transport aperture and transmissivity of the underlying Hydrogeological DFN model was used for the assignment of kinematic porosity. In agreement with previous investigations, the cross-plot of F-factor against advective travel time shows a strong positive correlation whereas the cross-plot of F-factor against transport distance exhibits a somewhat weaker correlation. Since the advective travel time is equal to the product of the F-factor and average transport half-aperture (i.e. $t_w = F \times \overline{\delta}_t / 2$) along individual pathlines this correlation is expected. This relationship is also demonstrated clearly in the trend lines drawn in Figure 3-23. In a similar fashion, the F-factor is approximately proportional to the path length since the total flow-wetted surface encountered by individual particles scales roughly linearly with increasing transport distance. In this case, however, the correlation is weaker since the average flowrate encountered by the particles along different migration paths varies much more strongly and therefore has a larger overall impact on the magnitude of the F-factor. It should also be noted that the path length to the surface cannot physically be less than the vertical distance to the surface from the release location which explains the left-hand truncation of the scattered data in Figure 3-24.

3.10.2 Detailed profile of a typical migration path

The migration path for an individual particle exiting to the surface along the Baltic coast is shown in Figure 3-25 (identified here as particle, p855). Although this is a slightly longer transport path than for those particles that follow a vertical trajectory exiting above HRD_C, it is a pathway that is most similar to the conceptual model of transport used in the scoping calculations described in previous sections. A number of other "typical" migration paths are detailed in Appendix C.

The cumulative F-factor as a function of transport path length is shown in Figure 3-26 while the corresponding cumulative advective travel time is shown in Figure 3-27.

In the case of this specific particle release location, most of the hydrodynamic resistance appears to be encountered within the HCD accounting for roughly 80% of the total F-factor accumulated along the transport path. A large part of the accrued F-factor, however, occurs at depths below the release location where the HCD exhibits relatively lower hydraulic conductivity. Many other particles that migrate via near vertical migration paths only encounter HCD structures in the top 100–200 m of the bedrock where the hydraulic conductivity is generally very high. In these cases, the bulk of the F-factor is accumulated within the HRD and the near surface HCD structures make a negligible contribution to the cumulative F-factor for the migration path.

As can be seen in Figure 3-27, the advective travel time for the particle is dominated by transport in the HCD with only about 10%–20% attributable to transport in the hydraulic rock domains. Since the advective travel time is equal to the product of the F-factor and transport half-aperture along the migration path, the close correspondence between the appearance of Figure 3-26 and Figure 3-27 is expected.

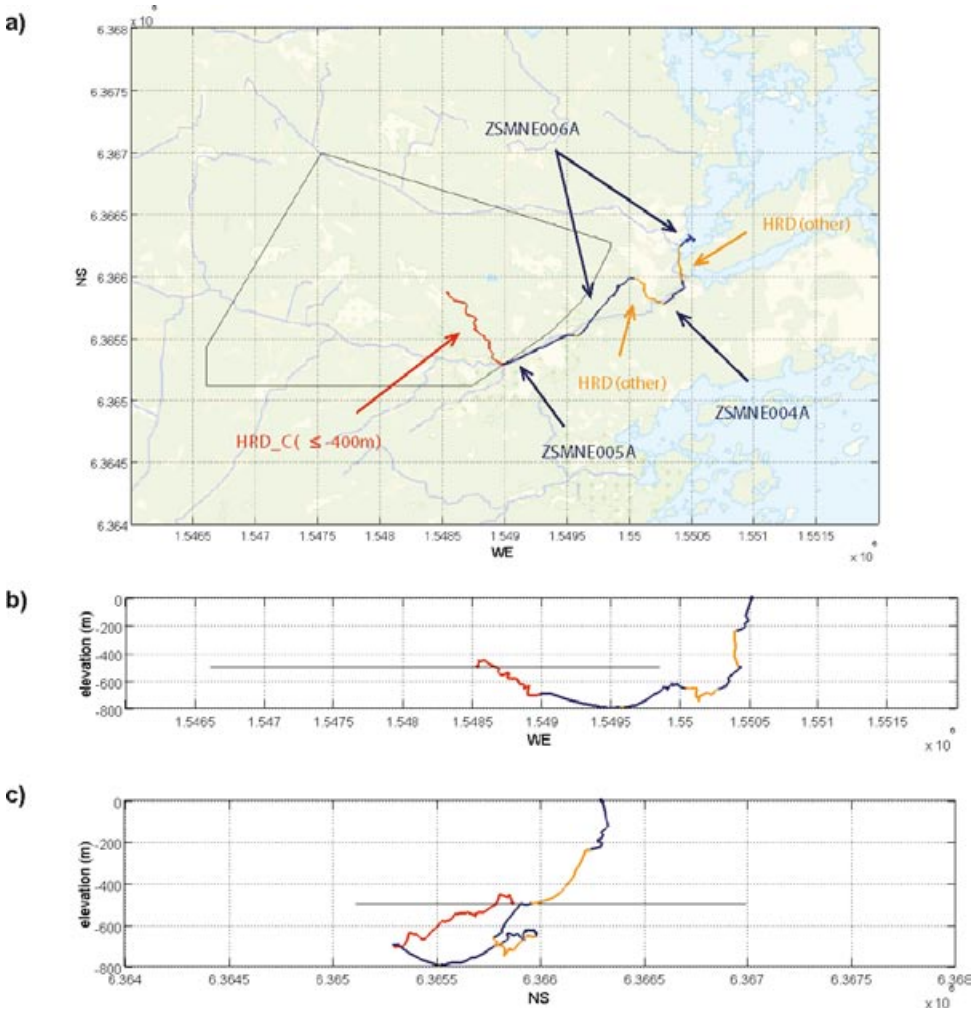

Figure 3-25. *The transport path taken by a single particle seen from above (a) as well as a cross-sectional view from a vantage point facing South (b) and facing West (c). The pathline is coloured with regard to structural elements encountered by the particle on its way to the surface exit location, i.e. red for HRD_C (≤ –400 m), dark blue for deterministic deformation zones, and orange for subsidiary HRD volumes as defined in the ECPM model. The outline of the particle release area is shown as a polygon at –500 m elevation.*

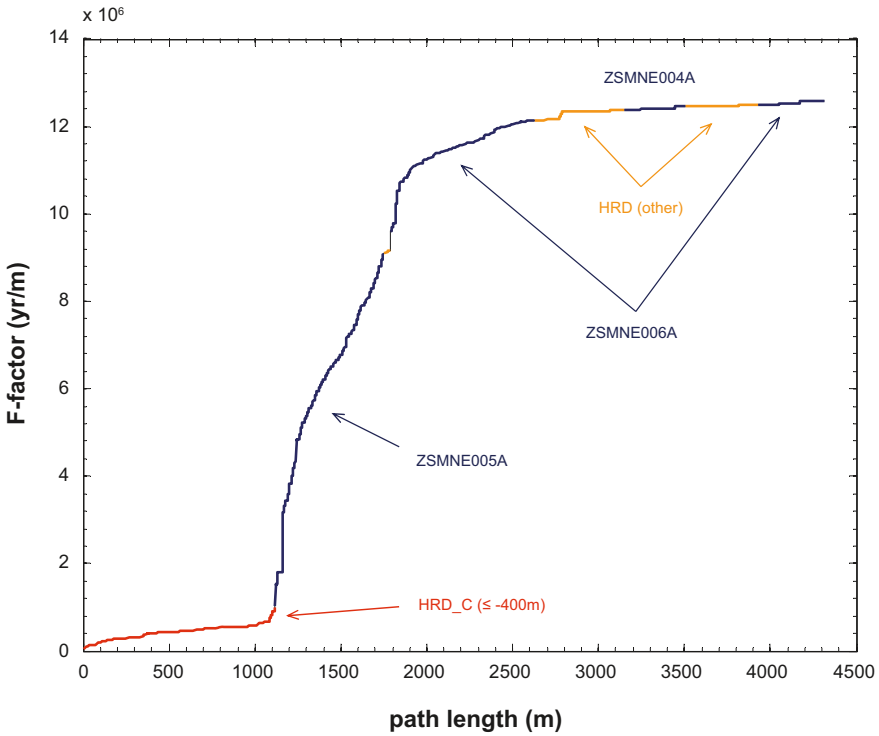

Figure 3-26. *Cumulative F-factor as a function of migration path length for a typical particle exiting to the surface along the Baltic coast. Different structural elements encountered by the particle along its migration path are colour-coded and labelled in the figure.*

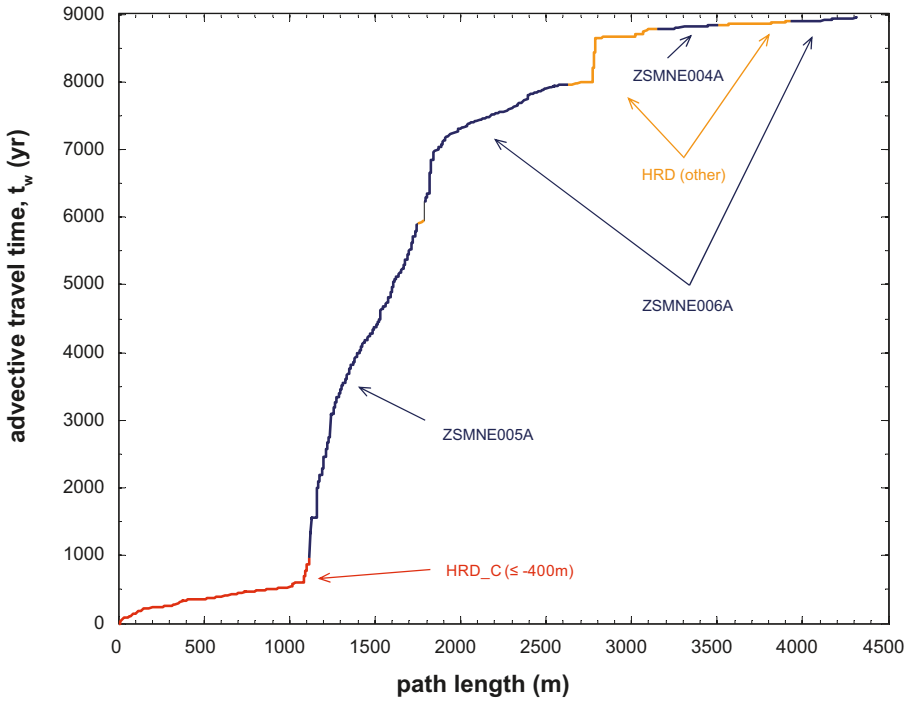

Figure 3-27. *Cumulative advective travel time as a function of migration path length for a typical particle exiting to the surface along the Baltic coast. Different structural elements encountered by the particle along its migration path are colour-coded and labelled in the figure.*

Figure 3-28 shows the local mean hydraulic conductivity encountered by the particle along its migration path plotted as a function of migration path length. Although there is considerable stochastic variation along the migration path, the particle passes through a number of distinct structures featuring steadily increasing hydraulic conductivity before reaching its surface exit location. This is in general agreement with the conceptual model of transport outlined in Section 3.1 and also illustrates well the depth dependency of hydraulic conductivity in the deformation zones encountered by the particle along its trajectory.

The local hydraulic potential gradient encountered by the particle along its migration path is shown in Figure 3-29. A cross-plot of the hydraulic potential gradient versus mean hydraulic conductivity is shown in Figure 3-30. It should be noted that the term "hydraulic potential gradient" is used here in place of hydraulic gradient since the hydraulic gradient reported by ConnectFlow does not take account of additional buoyancy effects relating to salt concentration. The gradients given in Figure 3-29 and Figure 3-30 are derived instead as the ratio of Darcy flux and hydraulic conductivity and therefore include buoyancy effects.

The markers in the cross-plot are shaded with regard to elevation in a similar fashion to the empirical data presented previously in Figure 3-8. The local hydraulic gradient is less than the maximum topographical regional hydraulic gradient (4%) and also less than that assumed in the scoping calculations (1%) for most of the migration path. On average, the hydraulic potential gradient along the pathline is slightly less than 0.3% although it rises to as much as 3.8% over a short distance of about 30 m in HRD_C.

The specific flow-wetted surface used in the ECPM calculations is plotted in Figure 3-31. The specific flow-wetted surface is estimated from the connected open fracture frequency derived from the underlying Hydrogeological DFN used to stochastically generate the hydrogeological properties of the ECPM. Implicit in the derivation of this parameter is the cut-off size for the distribution of fracture sizes assumed to contribute to advective flow, which in this case is 5.6 m.

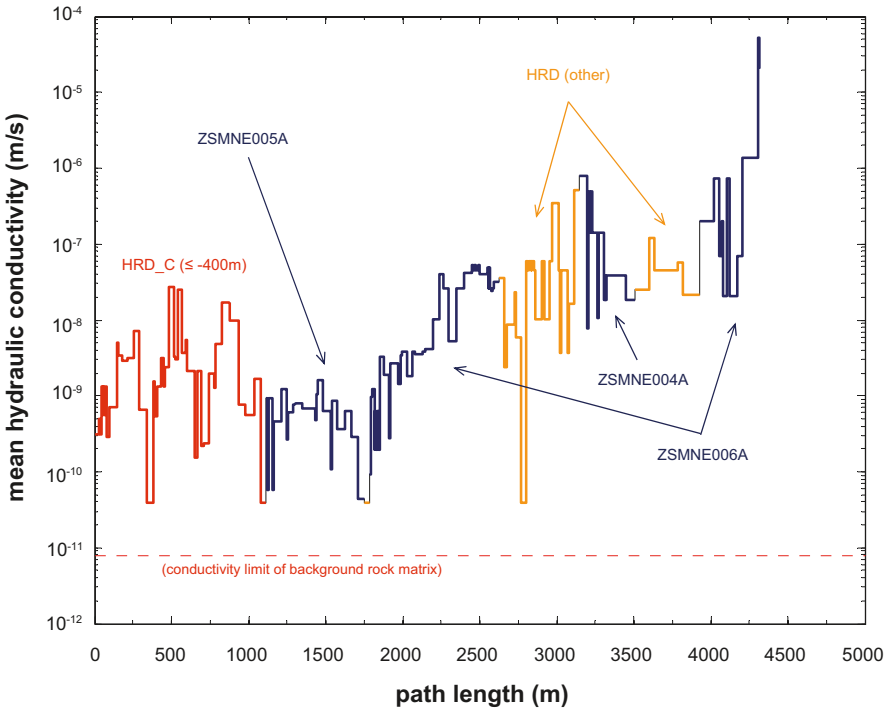

Figure 3-28. *Local mean hydraulic conductivity (m/s) as a function of migration path length. The broken horizontal line at the bottom of the figure represents the limit of hydraulic conductivity for the rock matrix itself assuming an in situ temperature of 12°C (this is defined as a permeability cut-off in ConnectFlow). Different structural elements encountered by the particle along its migration path are colour-coded and labelled in the figure. Grey coloured segments represent discontinuities in the parameter value when the particle passes from one structural feature to another.*

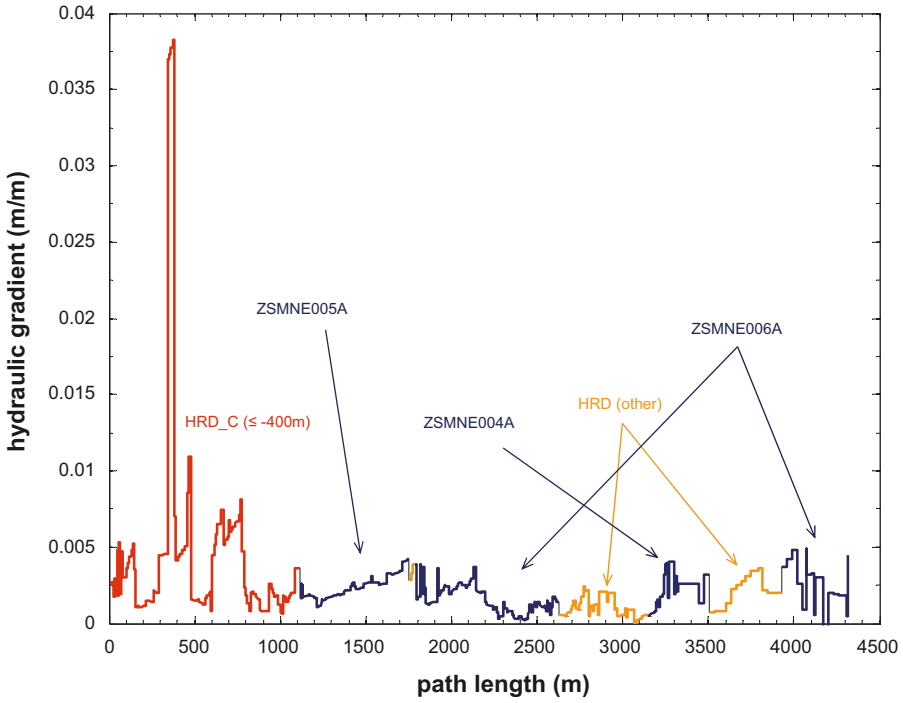

Figure 3-29. *Local hydraulic potential gradient (m/m) encountered by the particle as a function of migration path length. Different structural elements encountered by the particle are colour-coded and labelled in the figure as previously.*

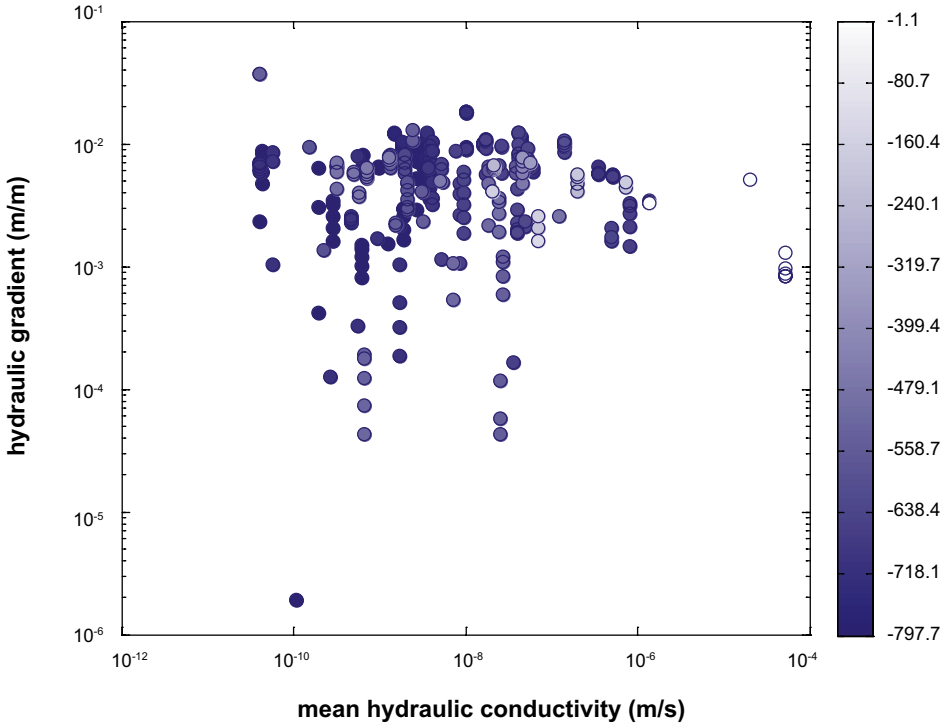

Figure 3-30. *A cross-plot of the local hydraulic potential gradient (m/m) encountered by the particle along its migration path versus the local mean hydraulic conductivity (m/s) of the rock at that location. The markers are shaded according to elevation (m) as specified by the colour bar on the right-hand side of the figure.*

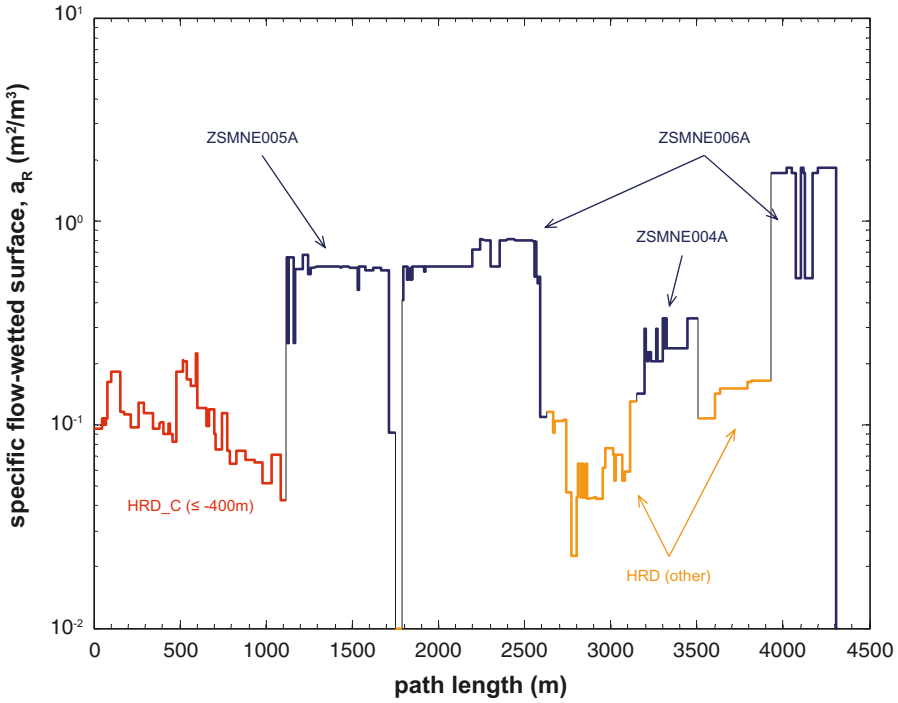

Figure 3-31. *Local specific flow-wetted surface, a_R (m^2/m^3) encountered by the particle and plotted as a function of migration path length. Different structural elements encountered by the particle are colour-coded and labelled in the figure as previously.*

3.11 Impact of flow channelling

3.11.1 General aspects relating to channelised flow

In this report, an attempt is made to characterise flow channelling in the context of both the interpretation of primary data (*inverse modelling*) as well as likely consequences when propagated forward in models (*forward modelling*). The aim is therefore to answer the following questions:

- What significance does flow channelling have for the interpretation of field data? Is there evidence, for example, that models of flow and transport contain inherent biases accrued during data acquisition owing to the inability of borehole investigations to adequately discriminate, characterise, or identify relevant hydrogeologic features in the rock?
- What significance does flow channelling have for the migration of solutes in fractured crystalline rock when included in models of flow and transport in safety assessment?

In this chapter, the first of these questions is mainly discussed whereas the second is dealt with later in Chapter 5 where the consequences of flow channelling for solute transport are investigated in more detail.

In terms of data interpretation, there are two main issues that need to be considered. One of these is whether or not the true frequency of flowing features in the rock is underestimated owing to the possibility that structures of low permeability and surface asperity contacts in fracture planes conceal them from detection by borehole hydraulic testing. This is referred to here as a "Type 1" flow censoring effect. The other issue is whether the transmissivity models used in the hydrogeological site description are somehow biased by the presence of flow channels in the rock. This is referred to here as a "Type 2" flow censoring effect. Both of these issues are, however, interrelated since the calibration of the transmissivity models for the fracture domains in the HRD is based upon conditioning to give the same numbers of flowing features (i.e. above the detection threshold) and flowrate magnitudes as observed in the field.

On the one hand there is the possibility that the true frequency of flowing features is underestimated and those detected are characterised with flowrates that might not be representative of the sampled feature. This might occur if flow is highly channelised in pipe-like features and there are significant issues relating to the permeability of the structures in which they are hosted (due to, for example, accretions of fracture filling materials). Even if hydraulic testing successfully detects the nearby presence of a flow conduit, the borehole is unlikely to intersect it directly and therefore the transmissivity of the structure may be underestimated, particularly if only steady-state flows (PFL data) are considered in the calibration procedure.

On the other hand, it is well known from previous experiences at the Äspö HRL /e.g. Black and Hodgkinson 2005/ that even very well constrained Hydrogeological DFN models appear to give greater flow connectivity and less flow compartmentalisation than what is actually observed in the field. This is particularly the case for larger features interpreted en-echelon as single structures in the Hydrogeological DFN models. Assumptions of equidimensioned fractures and stochastic generation of fractures without consideration of termination in Hydrogeological DFN models may also play a role in this.

It is difficult to predict what consequence this would have for the transmissivity models used in the Hydrogeological DFN since many of these factors may be mutually interdependent. The fact that Hydrogeological DFN models assume flow over their entire surface, for example, may introduce a bias by forcing artificially low transmissivities in the model to match the observational data. The result of this would be that both the true frequency and transmissivity of flowing channels may be higher than that estimated by inverse modelling.

Scoping calculations described in /Crawford 2008/ have shown that most flowing features should theoretically be identifiable from borehole investigations even in the presence of highly channelised flow arising due to fracture surface asperity contacts. The reason for this is that fracture planes need to support a certain level of in-plane connectivity in order for flow to exist at all in very sparsely fractured rock. This is particularly the case where fracturing is sufficiently sparse that pipe-like flow channels of limited extent such as fracture intersection zones (FIZ) or fast flow channels hosted in fault stepovers, cannot form contiguous pathways through the rock.

Furthermore, it should be considered that the most transmissive fractures are also likely to be the least compressed and should only exhibit small surface area contact fractions. The least transmissive fractures, on the other hand, are likely to exhibit greater a degree of surface contact possibly rendering their transmissivity at or below the level of instrumental detection, even if the flow space is nominally connected. This means that one would expect a larger biasing effect for fractures belonging to the lower end of the transmissivity spectrum. As such one can speculate that although Type 1 flow censoring effects are probably present, it seems reasonable to expect that they will not have a great impact on the more transmissive features to be found within the HRD.

Generalised radial flow (GRF) analysis of PSS hydraulic responses in packed off borehole sections /Rhén et al. 2008/ suggest that most flowing features (> 90%) on a 5 m test scale are associated with flow dimensions greater than 1.5. Only a very small number of tests gave indications of approximately linear flow channelling. Although it is possible that some pipe-like flow channels are missed, this result is generally consistent with the notion of a hydraulically well-connected flow space within the fractures.

In the transient analyses reported by /Rhén et al. 2008/, roughly 20% of the 5 m test sections gave indications of positive skin effects or recharge boundaries which could be interpreted as strongly transmissive flow channels embedded in less transmissive features (i.e. where the borehole happens to intersect a less transmissive region of the flow space). It is therefore not possible to strictly rule out Type 2 flow censoring effects in the available hydrogeological data set, although it appears likely that this only influences a minority of identified features.

Based on this reasoning, it is speculated that network-scale flow channelling effects probably dominate, although the other more localised flow channelling effects described above are also likely to be present in Laxemar and cannot be completely discounted. Resolution of this issue may not be possible until the construction of an underground opening since many aspects of flow channelling cannot be properly quantified from a surface based site investigation. From a tunnel, for example,

it is sometimes possible to directly observe individual flow channels and statistics of fracture trace lengths which can be used to partially validate the choice of power law slope which is treated as a fitting parameter in the Hydrogeological DFN modelling based upon borehole data. It should be noted, however, that even in situ observations are subject to substantial bias effects owing to stress redistribution and excavation damage which can have an impact on the distribution and extent of flow channelling observed in a tunnel.

Nevertheless, it is possible to approximately calculate the likely spatial distribution of different kinds of specific flow channel features from the geological information used in construction of DFN models. Simulations based upon solution of the Navier-Stokes equations for flow in crossing or terminating fracture intersections (FIZ sub-type A), for example, indicate that simple FIZ features will not contribute significantly to flow channelling phenomena in the rock /Crawford 2008/. The impact of highly conductive FIZ (sub-type B and C) has also been demonstrated by way of scoping calculations using the Hydrogeological DFN models and assuming fracture intersections with negligible flow resistance. Details of these calculations can be found in Section 3.6.2 and Appendix B. In the calculations it is shown that highly conductive FIZ features can comprise large fractions of the typical flowpaths in the HRD and still not have a significant deleterious impact upon the F-factor for transport of solutes. This, however, is contingent upon the open fracture intensity being sufficiently low that they do not form contiguous pathways through the rock and therefore this conclusion must be tested on a case by case basis for different rock volumes and transport distances.

On balance it is thought that although flow channelling might lead to the underestimation of the frequency of flow bearing features, it will probably make little difference to the order of magnitude of the hydrodynamic transport resistance provided that there is reasonable confidence in the transmissivity model for hydrologic features parameterised within the Hydrogeological DFN. Since it is thought that Type 2 flow censoring effects might only affect a small minority of PFL-tested sections, this seems a reasonable conjecture. It is also supported by cross-plot comparisons of transmissivities derived from PFL measurements and those obtained from transient PSS analysis which show reasonable order of magnitude correspondence indicating that the assumption of radial flow dimension in PFL testing does not lead to significant errors /Rhén et al. 2008/.

3.11.2 Concerning the possible existence of calcite erosion features

Although the simulations of in-plane flow channelling described in /Crawford 2008/ suggest that the flow space should be relatively well connected, it is not possible to rule out the existence of calcite erosion features in fractures containing large amounts of readily solubilised calcite precipitates. Owing to their wormhole-like structure within low-permeable features, these may not be readily detectable from borehole intersects with fracture planes. Similar features could exist in the deterministic deformation zones comprising the HCD.

Under modern environmental conditions calcite is the principal mineral which could be substantially influenced by precipitation-dissolution processes. Generally, one would expect calcite to be mobilised downwards within the fractured rock at Laxemar under the influence of infiltrating meteoric water. Indeed, this is what is seen at the Laxemar site in the upper 50–70 m of rock where there are clear indications of near surface dissolution /Drake and Tullborg 2009/. At greater depths, however, there appears to be very little variation in the amount of calcite observed in either open or closed fractures. A gradual decline in the intensity of calcite mineralization is seen below about 800 m depth which is thought to be related to the lower hydraulic conductivity at increasing depths that limits the extent of downward calcite mobilisation.

The pH buffering reactions resulting from the reaction of downward flowing meteoric water with rock minerals leads to a gradual increase in pH which can be expected to result in the precipitation of calcite. From the hydrogeochemical evaluation, however, no significant depth trends are seen and all groundwaters are found to lie within the pH interval of 7.5 to 8.6 /Laaksoharju et al. 2009/.

For downward flowing water it is also possible to predict a gradual precipitation of calcite mobilised from shallower depths owing to the increase of temperature with increasing depth at the site (since the solubility of calcite decreases with increasing temperature /Langmuir 1997/). This, however, is not possible to confirm since although there is a depletion of calcite in the near surface of the bedrock, the calcite content of fracture filling materials appears to be relatively constant with depth.

Owing to the common ion effect, calcite equilibrated water penetrating from shallower depths may become oversaturated upon encountering flowpaths containing easily solubilised gypsum thus causing localised calcite precipitation. Gypsum, on the other hand, is highly soluble and therefore tends to occur mainly in isolated locations at depths greater than about 350 m where there is less flow anyway. If substantial amounts of gypsum were to exist along fast flowpaths, these would be very quickly dissolved.

Microbial reduction of sulphate can lead to the precipitation of calcite owing to the in situ generation of carbonate when methane is oxidised. The effect can be even stronger if the sulphate reduction is accompanied by precipitation of iron sulphides (either amorphous FeS or pyrite) since this also results in an increase in pH /Stoessell 1991/. The process is limited, however, by the availability of methane and any effect on the abundance and distribution of calcite at repository depth is likely to be very slow. Evidence for this mechanism can be found in the low $\delta^{13}C$ values for fracture filling calcites at intermediate depths at Laxemar /Laaksoharju et al. 2009/ which is generally taken to be indicative of a biogenic process (i.e. isotope depletion with respect to ^{13}C in the carbonate content of calcite).

The impact of calcite dissolution and precipitation on flow channelling is difficult to predict à priori as it is highly dependent upon dissolution kinetics and diffusion in a non-linear fashion. Reaction instabilities arising due to the complicated feedback between permeability and mineral dissolution may also lead to fingering phenomena /Steefel and Lasaga 1994, Lichtner 1996, Renard et al. 1998/ which is the defining characteristic of wormhole formation by calcite erosion (in a similar process to karst formation). This is further complicated by the effects of in situ normal stresses which will attempt to close fractures as mineral precipitates lining the fracture are dissolved /Verberg and Ladd 2002/. Mineral grains at asperity contacts with high stress concentrations are thermodynamically predisposed to greater dissolution than mineral grains at lower stress locations which can lead to a redistribution of fracture minerals in a process known as pressure solution /NRC 1996/. These coupled phenomena will be particularly important if the pore space is propped open by contact bridges of secondary mineralisation. The dynamics of these processes are sufficiently complex that spontaneous switching from increasing to decreasing permeability under the influence of infiltrating fluids is not unknown /Polak et al. 2004, Yasuhara et al. 2006/.

Generally, dissolution or precipitation requires the imposition of a geochemical or thermal gradient on the system which leads to a change in mineral solubility over the length of a flowpath. Upon consideration of the contemporary situation of groundwater flow and hydrogeochemistry it appears that one should mostly expect precipitation of calcite at repository depth and thereby a slow annealing of flow bearing fractures. This process is likely to be self limiting, however, owing to the decrease in fracture transmissivity which would accompany any large scale precipitation. This might cause flow to seek out alternate routes through the fracture system over time as individual flowpaths become closed off due to calcite precipitation.

During deglaciation, however, processes can occur by which flow permeability of calcite lined fractures could potentially increase. Firstly, it is reasonable to expect that a certain percentage of annealed fractures would probably be reactivated by isostatic loading and unloading of the rock. Vestigial flow channels and newly reactivated and hydraulically connected fractures lined with calcite may then be subject to dissolution processes which reinforce flow channelling by way of the feedback processes outlined above. If very dilute glacial meltwater is forced down to repository depth, for example, calcite will tend to dissolve thereby increasing flow permeability. Even after the penetrating glacial water reaches equilibrium with respect to calcite, changes in calcite distribution may continue to occur further downstream as diffusive mixing with saline water can lead to an altered solubility of calcite.

Whether the mixing of waters of different salinity leads to a net precipitation or dissolution of calcite depends on the partial pressure of carbon dioxide (pCO_2) in the waters undergoing mixing. In situations where the salinity dependent solubility curve for calcite (generally for $pCO_2 \geq 10^{-2}$ atm) is concave downwards, mixing will lead to a net dissolution of calcite if both waters are separately in equilibrium with respect to calcite /Singurindy et al. 2004/. This means that dissolution can potentially occur during both glacial water penetration and the following saline upconing of deeper groundwater. For higher carbon dioxide partial pressures, the salinity dependent solubility curve for calcite is concave upwards which implies a precipitation of calcite. Also, owing to the non-linear solubility curve for calcite in a closed system, spatially separate water flows saturated at different carbon dioxide partial pressures can become undersaturated upon mixing /Langmuir 1997/. This is a

well-known mechanism for karst formation referred to as “mischungskorrosion” (mixing corrosion) /EPA 2002/. Although the dynamics of flow channel formation and erosion in calcite filled fractures are currently not well understood, such processes may need to be examined in greater detail in future safety assessment if they are deemed to contribute significantly to the abundance and distribution of fast and persistent flow paths in the rock.

3.12 Summary of main findings

In summary, the key findings of this chapter include:

- Transport from a repository through the geosphere to the near surface is proposed to occur via a sequence of advective pathways featuring progressively increasing flow and transmissivity. For the purpose of making scoping calculations of hydrodynamic transport resistance, the conceptual flow system was therefore sub-divided into three serially connected compartments:
  a) The non-engineered near field (NNF) comprising the network of poorly transmissive flow channels linking canister deposition holes with typical flowpaths in the HRD featuring relatively high flowrates;
  b) The immediate far-field (IFF) comprising the relatively transmissive flowpaths within the HRD which can persist for several hundred metres distance through the rock until encountering deformation zones in the HCD;
  c) The distant far field (DFF) comprising very transmissive flowpaths hosted in deformation zones within the HCD which provide fast conduits for flow to the near surface
- F-factors for the NNF are difficult to evaluate as they are highly dependent upon selection/rejection criteria for transmissive fractures intersecting the deposition holes. Typical F-factors in the range of about 10^3–10^7 yr/m are calculated for fractures in the transmissivity range from 10^{-8}–10^{-10} m^2/s depending upon the underlying assumptions, which include typical path lengths and representative hydraulic gradients.
- Scoping calculations were made to characterise F-factors for typical flowpaths within the various HRD volumes corresponding to the immediate far-field, IFF. Here the depth zonation –400 m to –650 m within HRD_C, HRD_W, HRD_EW007, and HRD_N was used as a basis for calculations. Mean F-factor ranges on the order of 10^3 – 10^5 yr/m were found to be the norm for flowpaths assuming a 100 m transport distance, a 1% reference hydraulic gradient, and different transport directions (for a semi-correlated fracture size-transmissivity relation).
- Using the exponential and power law decay models of deformation zone hydraulic transmissivity/conductivity provided by Hydrogeology it was possible to calculate a simple analytical value for typical F-factors in the HCD for a set of well-defined boundary conditions. Typical flowpaths within deformation zones are associated with F-factor ranges of roughly the same magnitude as those for the HRD (at least for the conditions simulated). The calculations assumed solute release at an elevation of –500 m with transport to the near surface, here assumed to be at an elevation of –100 m. Additional hydrodynamic transport resistance accumulated at elevations above –100 m are thought to be negligible owing to the inverse relation between transmissivity and depth.
- Particle tracking calculations for solute transport from repository depth to the surface have been made using the Base Case model developed by Hydrogeology and an ECPM representation simulated with ConnectFlow. The simulations predict mean F-factor ranges roughly 1–2 orders of magnitude higher than those calculated using the simplified scoping calculation models. Advective transport times are found to also be several orders of magnitude greater than suggested by the scoping calculations.
- The larger F-factor ranges predicted by the ECPM model are thought to be at least partly related to lower hydraulic gradients in the integrated hydrostructural model as compared with the more pessimistic assumption of a 1% hydraulic gradient in the scoping calculations. The discrepancy in advective travel times appears to be also related to this as well as a kinematic porosity possibly larger than that implicit in the scoping calculations.
- Although the scoping calculations indicate similar ranges of F-factors for typical flowpaths within the HRD and HCD, the underlying assumption is that radionuclides are transported along

principally horizontal trajectories until making contact with the HCD at –500 m elevation. In the particle tracking simulations made using the ECPM model it was found that a significant proportion of particles are transported vertically upward through the HRD owing to the trajectories of local flow cells. In such cases, the particles only make first contact with the HCD at shallow depths where the hydrodynamic transport resistance is much reduced.

- Six different sub-classes of flow channelling have been identified as being potentially important for the Laxemar site and have been considered in the analyses presented in this chapter. Flow channelling may have an impact upon interpretation of borehole data by way of censoring effects leading to the underestimation of the frequency of flowing channels within the rock. Some channels may be very narrow in width and unlikely to be intersected directly by a borehole and therefore the permeability of the surrounding fracture pore space becomes very important for identification of these features and interpretation of their hydraulic properties. The uncertainties introduced by certain forms of flow channelling can be reasonably well constrained by scoping simulations. The overall effect of flow-channelling does not appear to be sufficiently severe at present that it would cast considerable doubt on the utility of the hydrogeological models produced within SDM Site, although further justification of this will need to be made in future studies.

4 Bedrock retardation model

The bedrock retardation model is one of the key elements of the overall site descriptive model contained in this report. Essentially the retardation model is comprised of the following sub-elements:

- A qualitative identification and description of "typical" geological materials, fracture types and deformation zones to be found in Laxemar with regard to processes of relevance for transport of radionuclides and environmental solutes (i.e. naturally occurring groundwater constituents);
- quantitative data describing material properties of the different geological materials comprising the rock matrix as well as relevant alteration types and secondary minerals found in association with fractures and deformation zones;
- quantitative data concerning the relative abundance and spatial distribution of different minerals to be found in association with fractures and deformation zones;
- an abstracted model of material properties recommended for describing the transport of solutes in Laxemar. This also includes a set of "Type" fractures and structural elements of deformation zones which can be assembled in a modular fashion for application within numerical transport codes.

The methods used in the transport programme produce primary data on the retardation properties of the rock. The main parameters of interest are the immobile zone porosity, θ_m, the effective diffusivity, D_e and the linear equilibrium sorption coefficient, K_d. These retardation parameters are evaluated, interpreted and presented in the form of a retardation model. The strategy for laboratory measurements, data evaluation and development of retardation models is described by /Widestrand et al. 2003/. In the three-dimensional spatial representation of the Laxemar bedrock, the retardation model is used to parameterise the various geological elements described in the geological site-descriptive model. These elements consist of the rock mass itself containing varying proportions of different site specific rock types, key fracture classes characteristic of Laxemar, and various deformation zone microstructural components.

The retardation model combines material properties data for the major rock types and their various alteration states with a description of various fracture sub-classes and deformation zone structural elements typical for the Laxemar site investigation area. This is intended to form a basis for the parameterisation of models used within safety assessment. The integration of the material properties parameterisation with the flow-related transport properties provides a basis for solute transport modelling and scale-up of flow path retention properties.

The different methods used in the laboratory programme are described in /Widestrand et al. 2003/. The primary data evaluation is made in the transport properties evaluation background report by /Selnert et al. 2009b/. This chapter is a summary of that report.

4.1 Description of input data

The development of the retardation model relies to a large extent on interaction with other disciplines; primarily Geology and Hydrogeochemistry. Specifically, Geology provides lithological and structural models where the rock types, fractures and deformation zones are described, as well as the mineralogical compositions of intact and altered materials. Hydrogeochemical information is used as a basis for the selection of water compositions in laboratory measurements of retardation parameters. Furthermore, hydrogeochemical data together with results from mineralogical and geochemical analyses of fracture materials are important inputs to the conceptual development of the site specific retardation model and the description of the understanding of the retention processes at the site.

The input data for the retardation model consist of laboratory and in situ measurements of material properties from the transport properties laboratory programme as well as supporting information from other disciplines. The available site investigation data on transport properties are summarised in /Selnert et al. 2009b/. Transport data obtained from the laboratory programme include effective diffusivities and formation factors for diffusive solute transport in the rock matrix, matrix porosities,

specific surface areas of rock, cation exchange capacities (CEC), and sorption properties of rock in contact with synthetic groundwater of varying composition /Selnert et al. 2009a/. Field data is also available in the form of roughly 36,000 in situ measurements of the rock formation factor obtained from high resolution geophysical logging in the site investigation boreholes.

4.2 Data and models from other disciplines

Supporting descriptive data from the combined geological/hydrogeochemical interpretations of fracture mineralogy and wall rock alteration data are provided by /Wahlgren et al. 2008/ and /Eklund and Mattsson 2008/. Other geological, hydrogeological, and hydrogeochemical inputs were obtained from the relevant SDM modelling background reports as well as detailed studies of specific features (e.g. deformation zones /Viola and Venvik Ganerod 2007/).

4.2.1 Summary of supporting geological data

For the transport properties site descriptive modelling, attention has focused upon the rock domains RSMA01, RSMD01, and RSMM01 as these are volumetrically the most significant domains both in the local model volume as well as the target volume.

A full account of the proportions of different rock types and classes of alteration can be found in the SDM-Site Laxemar Geology background report /Wahlgren et al. 2008/. A brief summary of the rock types and corresponding codes referred to in this report, however, is given in Table 4-1 together with the different proportions of each rock type comprising RSMA01, RSMD01, and RSMM01.

For the purposes of parameterising the material properties of the rock, however, it is possible to say that the rock in RSMA01 is dominated by Ävrö granite (501044) with smaller amounts of subordinate rock types as indicated in Table 4-1. The most abundant type of rock alteration in RSMA01 between deterministic deformation zones is oxidation (red staining) which is mostly of faint to weak character and affects roughly 25% of the domain. Zones of saussuritization (~3%) and very sparse epidotization (< 1%) are also present.

Rock domain RSMD01, on the other hand, is dominated by quartz monzodiorite (501036). The subordinate rock types fine-grained granite (511058), fine-grained diorite-gabbro (505102), and pegmatite (501061) occur in relatively similar amounts in all boreholes. Alteration between deterministic deformation zones in RSMD01 consists of roughly equal proportions (~10% each) of faint to weak oxidation (red staining) and saussuritization. A small amount (~2%) of epidotization is also observed in this rock domain.

Table 4-1. Rock types and SKB codes for major and most common subordinate rock types found within rock domain RSMA01, RSMD01, and RSMM01. Approximate proportions (vol%) for each rock type is also given for each rock domain. The sub-division of rock type 501044 into 501046 and 501056 categories is done on the basis of density, although specific values for the proportions present in each rock domain are not specified in /Wahlgren et al. 2008/. For this reason, rock types 501045 and 501056 are given as "n/a" (not available) in the table.

Rock name	SKB code	RSMA01	RSMD01	RSMM01
Dolerite	501027	0.0	2.11	0.0
Fine-grained dioritoid	501030	3.12	0.34	0.43
Diorite/gabbro	501033	0.29	0.13	16.36
Quartz monzodiorite	501036	1.84	88.78	0.41
Ävrö granite	501044	81.69	1.1	74.79
Ävrö quartz monzodiorite	501046	n/a	n/a	n/a
Ävrö granodiorite	501056	n/a	n/a	n/a
Granite	501058	3.37	0.43	1.98
Pegmatite	501061	0.38	1.45	0.49
Fine-grained diorite-gabbro	505102	5.71	1.81	1.84
Fine-grained granite	511058	4.06	5.0	4.73

Rock domain RSMM01 contains a significantly higher proportion (~16%) of diorite/gabbro (501033) as compared to the other rock domains discussed above although Ävrö quartz monzodiorite comprises roughly 75% of the rock volume. The subordinate rock types in this rock domain are comprised of the same types and occur in similar abundance to those in RSMD01. The main alteration type is oxidation (red staining), mostly faint to weak in character, and affects roughly 14% of the rock domain. Other alteration types are saussuritization (~2%) and very sparse epidotization (< 1%).

The degree (or intensity) of alteration in the bedrock is classified as faint, weak, medium and strong. For Laxemar in general, the degree of alteration in the bedrock in between deformation zones is classified as faint to weak. It is found that up to approximately 20–25% of the bedrock is affected by alteration, although its distribution is inhomogeneous. Different alteration types mapped in the SICADA database are albitization, epidotization, oxidation (usually indicated by red staining), quartz dissolution, saussuritization, sericitization, silicification and carbonatization. The statistical occurrence of different alteration types is given in /Selnert et al. 2009b/ for the three main rock domains in the local model (RSMA01, RSMD01, and RSMM01).

Red-stained, hydrothermally altered rock is a common feature adjacent to fractures in the Laxemar area. Almost 50% of the sealed fractures in the Laxemar subarea are bounded by red-stained wall rock. Red-stained rock is commonly thought to represent a distinct zone of altered, oxidised rock although relevant analyses to verify this are infrequently performed. The main mineralogical features of the red-staining and hydrothermal alteration are:

- Pseudomorphic replacement of plagioclase by a paragenesis of albite, K-feldspar, sericite, Fe-oxide, prehnite and epidote;
- Replacement of biotite by chlorite;
- Replacement of magnetite by hematite.

Increased intragranular porosity and micro-fracturing is also frequently evident in the red-stained rock. The colour intensity of the red-staining is most prominent where hematite microprecipitates are present in porous secondary minerals, particularly in association with K-feldspar grains derived from plagioclase. It is noted, however, that the total Fe content in the altered plagioclase crystals/pseudomorphs is usually only slightly higher in the red-stained rock as compared to unaltered rock. The pseudomorphs after plagioclase in the red-stained samples are more porous than the plagioclase crystals in the unaltered samples. It has been found that the hydrothermal alteration generally extends further into the rock from the fracture surface than the red-staining would suggest (as shown by biotite and plagioclase alteration /Drake and Tullborg 2009/).

Most deformation zones exhibit red staining. This seems to be particularly extensive and characteristic of deformation zones with EW strike (especially the dominant zones ZSMEW002A, ZSMEW007A and ZSMNW042A). Most of the red stained bedrock is mapped with an intensity of weak to medium. It is emphasised, however, that the degree of intensity of red-staining may be underestimated owing to the original grey-red colour of some of the rock types which makes the alteration difficult to distinguish.

Fracture types

The majority of fractures were initiated 1.75–1.9 Ga (during the Svecokarelian to Palaeozoic period) and many show signs of later reactivation. Fractures are classified in /Drake and Tullborg 2009/ as being Generation 1–5 with regard to their chronology of formation. Based upon the characterisation of different generations of fracture mineralisations and theoretical potential for influencing transport properties, eight major fracture types have been identified. These are summarised in Table 4-2 and typical examples are shown in Figure 4-1.

Based upon detailed studies of fracture mineralogy /Eklund and Mattsson 2008/ chlorite and calcite are found to be the most frequently occurring minerals comprising fracture coatings (or filling) as well as occupying the most volume. Chlorite and calcite are frequently found together and also often in combination with other minerals.

In terms of the subdivisions defined in Table 4-2, the most common group is fracture type A (chlorite, calcite, and pyrite/chalcopyrite) and E (chlorite and calcite with or without altered wall rock).

Table 4-2. Classification of basic fracture types within retardation model.

Type	Fracture coating	Thickness	Wall rock alteration
A	Chl +Ca ± Py/CPy ± Other	0.2–1 mm	≤ 10 mm
B	**Ep and/or Pr and/or Ad** ± Chl ± Ca ± Qz	0.5–1 mm	≤ 20 mm
C	Hm ± Clay ± Chl ± Other	0.5–5 mm	≤ 50 mm
D	**Lau** ± Ca ± Chl	0.2–2 mm	≤ 20 mm
E	Chl + Ca	0.2–0.5 mm	≤ 10 mm (oxidation and saussuritisation)
F	**Clay** ± other	0.2–5 mm	≤ 50 mm
G	**Chl** ± other	~0.2 mm	≤ 50 mm
H	No mineral	n/a	≤ 10 mm (oxidation, saussuritisation, and epidotization)
I	***Ca*** ± other	~0.2 mm	≤ 10 mm

Note: Fracture mineral abbreviations are: Adularia (Ad)calcite (Ca), chlorite (Chl), chalcopyrite (Cpy), epidote (Ep), hematite (Hm), laumontite (Lau), prehnite (Pr), pyrite (Py), quartz (Qz). The specification “other” denotes any of the above minerals although quantitatively subordinate. The designation “±” means that the mineral may or may not be present while “and/or” indicates that one or several of the specified minerals must be present.

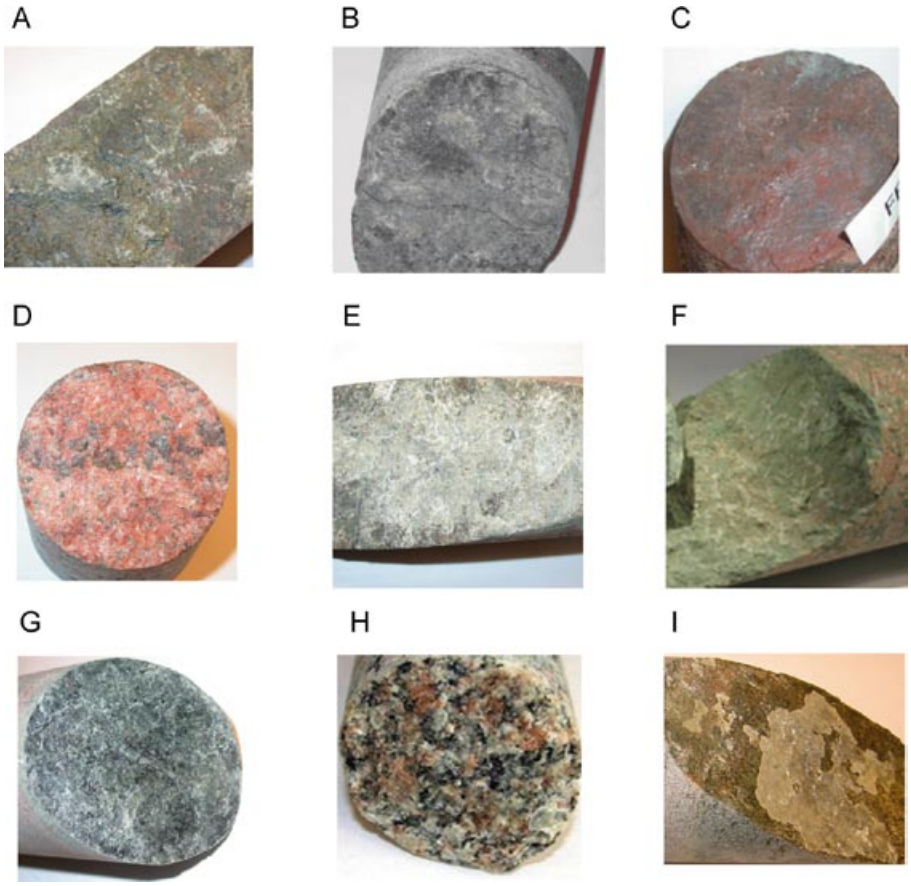

Figure 4-1. *Typical appearance of the surface coating minerals associated with the basic fracture types considered in the retardation model. The predominant mineralogy of the different fracture types is described in Table 4-2.*

About 23% of the open fractures are categorised as type E and 7% as type A. As a single mineral, calcite is present in 78% of the mapped sealed fractures and in 48% of the mapped open fractures, while chlorite is present in 76% of the open fractures and in 33% of the sealed fractures. Calcite generally covers 10–20% of the fracture surface and only rarely the whole fracture surface. Chlorite usually covers the whole fracture surface, but it is generally coated by another fracture mineral, frequently calcite /Eklund and Mattsson 2008, Wahlgren et al. 2008/.

As a single mineral, clay is found in roughly 34% of the mapped open fractures and occurs within both fracture type F (~21%) and C (~13%). This, however, may be an underestimate since according to /Wahlgren et al. 2008/ most mapped chlorite bearing fractures also contain clay. Hematite is present in about 14% of the fractures (principally fracture type C) in the Laxemar boreholes. The relative abundance of epidote, prehnite, or adularia filled fractures (fracture type B) is greater at depths below 800 m. This is partly due to the rarity of younger (Palaeozoic) fractures at greater depths and also due to older fractures in the near surface being reactivated and filled with younger mineral precipitates of a different sort. Very few fractures without visible fracture minerals or with laumontite filling have been mapped as open fractures. For the minority of open fractures without visible fracture mineralisation it is suspected that there are actually small amounts of fracture minerals, although they are present in such low quantities that they can only be identified with a microscope. An overview of the relative abundance of different fracture types is given in Figure 4-2.

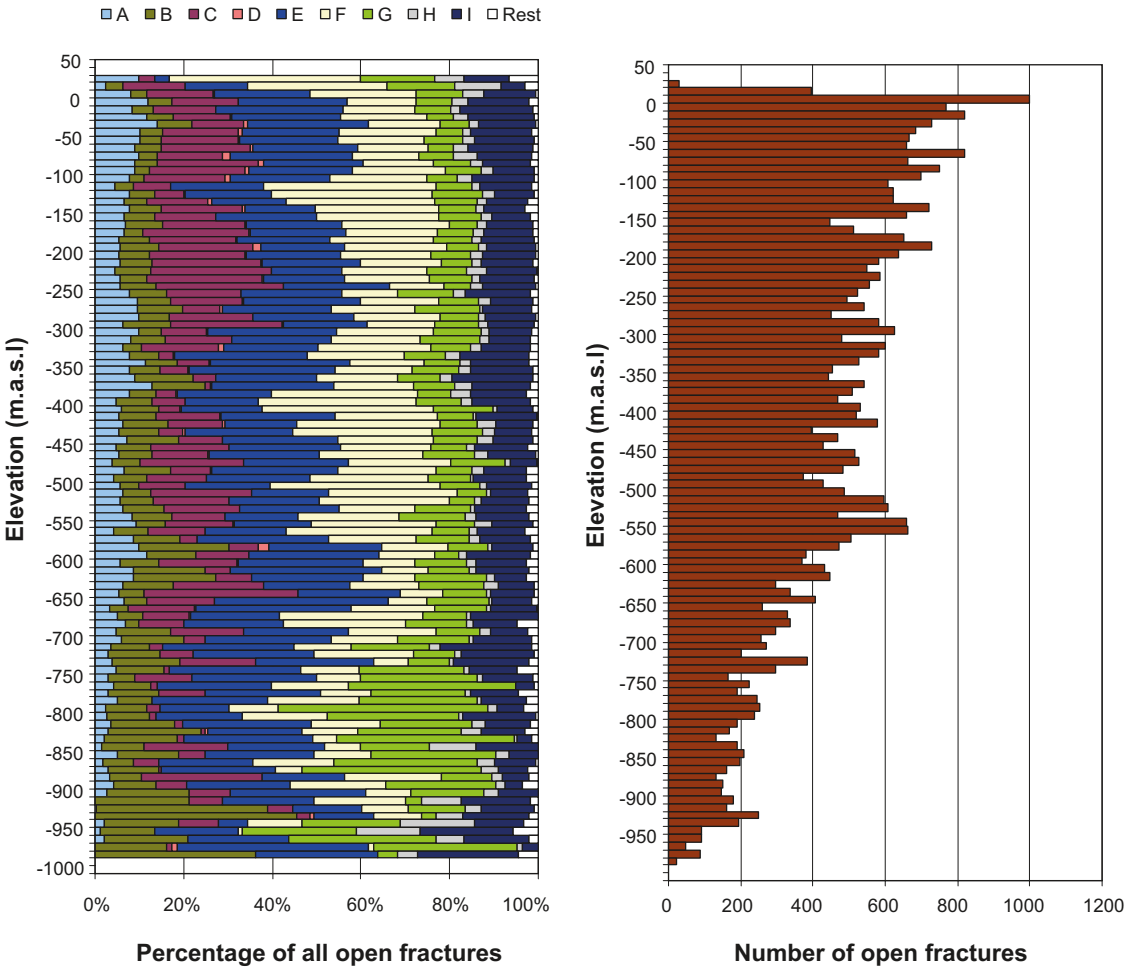

Figure 4-2. *Relative abundance of different fracture types as a proportion of open fractures (left) and open fracture frequencies (right) at various depths at the Laxemar and Simpevarp sites (based on boremap data in SICADA considering all cored boreholes).*

Only small differences are evident when comparing the relative abundances of different fracture types specific to rock domains RSMA01, RSMD01, and RSMM01. Generally the largest variations between rock domains are seen for fracture type E (chlorite/calcite) and F (clay). Similarly, a comparison of fracture mineralogy with regard to fracture domains also indicates very little overall variation. In this case, however, the most significant differences are seen in the relative abundances of fracture type C (hematite) and E (chlorite/calcite). The relative proportions of fracture types within deformation zones are different to the fracture statistics for overall relative abundances shown in Figure 4-2. The most significant differences are an increased proportion of fracture type C (hematite) and F (clay) coupled with a decreased abundance of fracture type E (chlorite/calcite).

For the retardation model, the hydraulically conductive parts of the rock are of greatest interest since these are likely to be most representative of radionuclide migration paths. As shown in Figure 4-3, the distribution of fracture types in the transmissive fractures displays a small increase in the relative abundance fracture types A, F and I compared to those shown previously in Figure 4-2 and a decrease of predominantly fracture types B, C and G.

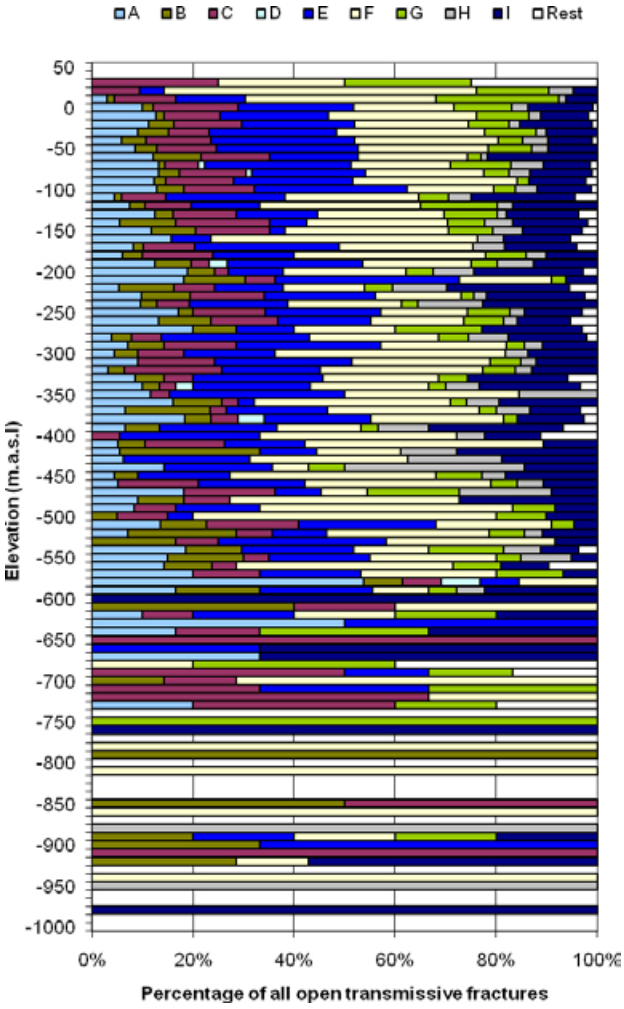

Figure 4-3. *Relative abundance of different fracture types associated with flowing features (PFL) at various depths in boreholes in the Laxemar-Simpevarp area (based on boremap data in SICADA considering all cored boreholes). It should be noted that the apparent discontinuous statistical distribution at depths > 600 m reflect a greater sparsity of data rather than a true change in the distribution of fracture types.*

Deformation zones

Deformation zones are structurally very heterogeneous and it is very difficult to exactly delineate their extent and internal structure from a small number of borehole intercepts. Figure 4-4 illustrates conceptually how a deformation zone might appear from interpretation of a borehole intercept and how the actual extent and geometrical shape of the zone may actually vary.

The transition zone can range in thickness from a few metres to several tens of meters. This part of the zone has an increased fracture frequency together with a more extensive alteration compared to the surrounding bedrock. The transition zone, however, can contain segments that are unaffected with respect to fracture frequency and alteration. The core of the deformation zone is usually thinner than the transition zone and its thickness can vary from a few centimetres to a few metres. The core has even higher fracture frequency and is often composed of sealed fractures (mainly in sealed fracture networks), fault breccia or cataclasite (often cohesive). The boundaries between the host rock, transition zone and core are commonly diffuse and difficult to demarcate.

Generally, the deformation zones in Laxemar can be divided into five distinct sets based on orientation, origin, and character. A detailed account of these can be found in the Geology site descriptive model /Wahlgren et al. 2008/. A large proportion of the possible deformation zones identified through the extended single hole interpretation (ESHI) /Wahlgren et al. 2008/ are considered to be local minor deformation zones (MDZ). These are, by definition, less than 1,000 m in length and are not modelled deterministically, although are part of the Geological and Hydrogeological DFN -models respectively. The character of minor deformation zones varies from ductile to brittle-ductile and brittle. Four subgroups of MDZ orientations have been identified of which the sub-horizontal set accounts for roughly 70%. There also appears to be a higher density of MDZ structures in the upper 150 m of the bedrock. A high proportion (~65%) of MDZ are associated with igneous intrusions such as fine-grained granite and have an increased frequency of open fractures /Wahlgren et al. 2008/.

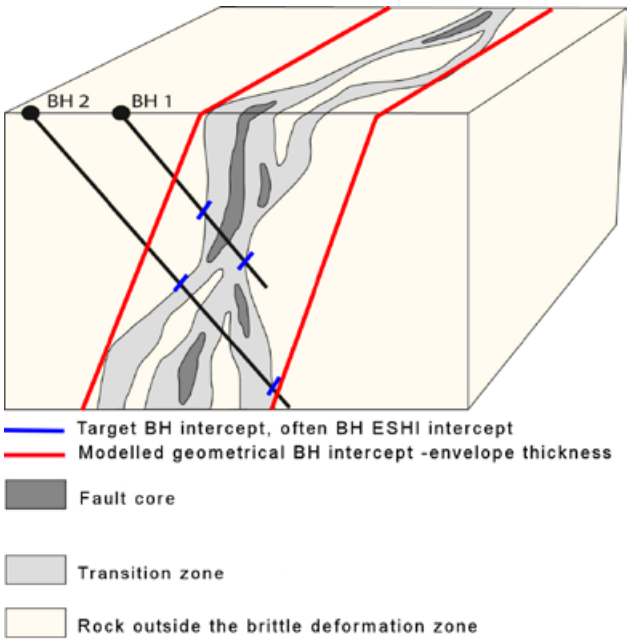

Figure 4-4. *Three-dimensional conceptual illustration of brittle deformation zone geometry typical for Laxemar (redrawn after /Caine et al. 1996/). Hypothetical borehole intercepts are indicated by the diagonal black lines in the figure.*

Structural elements characterising deformation zones

For the purposes of constructing a retardation model, five different kinds of altered bedrock have been distinguished as recurrent structural elements within, or in close association with deformation zones in addition to the single fractures described previously (Table 4-2). The recognition of these elements is based on macroscopic observations of altered parts of the retrieved drill cores during the initial phase of rock sampling for the laboratory program (discussed in Section 4.3). Furthermore, these structural elements can occur individually or together within a deformation zone and are considered as distinct from the single fracture types which also populate the deformation zones. These structural elements are described in Table 4-3.

Table 4-3. Main identified structural elements residing in deformation zones that have been included in the retardation model.

1)	**Fault rock/gouge (strongly tectonised and partly incohesive material)** Generally altered rock fragments, mineralogy partially depending on host rock together with chlorite, saussurite and clay. *Potential impact on retardation: Partly very fine-grained material which may have significantly increased surface areas available for adsorption. Increased porosity due to poor consolidation.*	
2)	**Chlorite (green gouge, primarily close to mafic rock types)** Chlorite ± corrensite *Potential impact on retardation: Partly very fine-grained material which may have significantly increased surface areas available for adsorption. Increased porosity due to poor consolidation.*	
3)	**Porous episyenitic wall rock** Prehnite, adularia, quartz, calcite ± laumontite, epidote, hematite. Quartz dissolution sometimes occurs. *Potential impact on retardation: Presumably an increased sorption capacity where hematite precipitation occurs. Increased porosity in case of a net quartz dissolution.*	
4)	**Cataclasite (with mylonitic banding)** Altered rock fragments sealed with epidote, adularia, quartz, hematite ± laumontite in various portions. *Potential impact on retardation: Increased porosity for cataclasite, increased amount of sealed fractures. Mylonitic banding may give decreased porosity with a directional dependency that may act as a barrier for diffusion.*	
5)	**Oxidized wall rock (medium to strong alteration)** Hydrothermally altered host rock, with a mineralogy related to initial rock type. Red staining due to hematite microprecipitates, K-feldspar, saussurite, plagioclase, quartz, chlorite is common in granitic variants. *Potential impact on retardation: Contains micro grains of hematite which may have an impact on adsorption of radionuclides influenced by surface complexation. Enhanced porosity in altered plagioclase grains. Increased amount of micro fractures.*	

Synthesis of a generalised model for deformation zones is difficult owing to their complexity and extraordinary spatial variability. This is further complicated by the fact that their structure is usually only known from a small number of one-dimensional borehole intercepts. Much of the complexity of deformation zones arises through cycles of reactivation during different geological events. They therefore display a wide spectrum of alteration types, as well as brittle and ductile features accumulated at different stages of their geological history.

An important concern during the modelling work has been to establish a level of appropriate microstructural detail that is both physically realistic and adequate for the purposes of safety assessment and other transport modelling. Typical questions that arose during the work /Selnert et al. 2009b/ included whether retention parameters should be given to the zone in its entirety or whether it is more appropriate to parameterise the different structural elements of the zone separately (i.e. fractures, altered bedrock, etc.) including dividing the deformation zone into high transmissive and low transmissive sub-structures. A number of different ways to deal with these questions are illustrated in Figure 4-5.

As illustrated in Figure 4-4, a deformation zone might be intersected by several boreholes and yet, exhibit dissimilar microstructural properties in each intersection. The core and transition zone in a deformation zone may contain one or more of the four structural elements described above and in Table 4-3. In addition, the fracture frequency and fracture mineralogy can be expected to vary throughout the zone as well.

As far as retention properties are concerned (i.e. for sorption, porosity, and effective diffusivity), there may be a considerable diversity between the different structural elements, single fractures and combinations thereof which comprise the complete deformation zone. It is not possible to give detailed recommendations as to which of the three alternatives depicted in Figure 4-5 is most appropriate for application in transport modelling since this must be considered on a case by case basis for different deformation zones. In the retardation model report, however, an outline of how a typical deformation zone might be parameterised is given using ZSMEW002A as an example /Selnert et al. 2009b/.

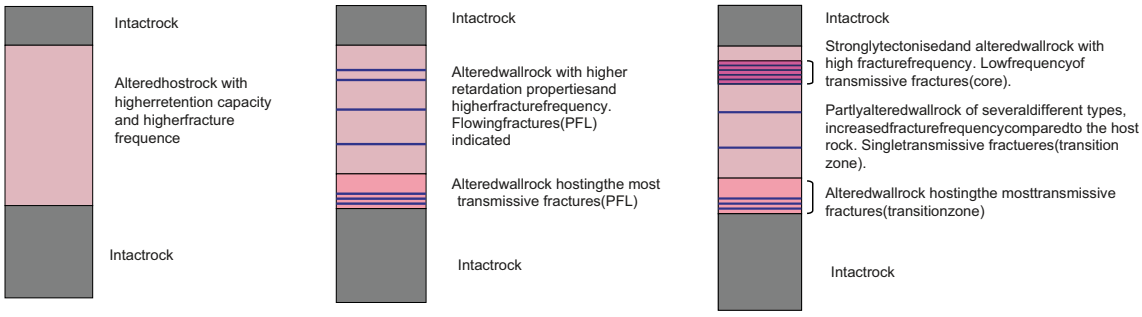

Figure 4-5. *Schematic illustration of different alternatives for describing a deformation zone retardation model; a) deformation zone considered as a single unit with higher retention capacity than the surrounding bedrock, b) deformation zone divided up into a high transmissive and a low-transmissive unit, c) variation including core and transition zone, the latter divided into a high and low transmissive unit.*

4.2.2 Summary of supporting hydrogeochemical data

The groundwater types selected for use in the laboratory measurements of sorption are intended to reflect both the present groundwater composition at repository depth as well as potential variations in groundwater chemistry at future times which may also be relevant for the transport retardation of migrating radionuclides. Based on these considerations, the following five groundwater compositions were therefore selected for use in the laboratory measurements of sorption:

I. Fresh diluted Ca-HCO_3 water; groundwater now present in the upper 100 m of the bedrock, but also a water type that can be found at greater depths during late phases of glacial periods. In Laxemar, the fresh water is predominantly of a Na-HCO_3 type. This groundwater is referred to as "Fresh" in the retardation model property tables.

II. Brackish groundwater with marine character, Na-(Ca)-Mg-Cl (5,000 mg/l Cl). This groundwater type has been found at depths of 100 to 400 m in several boreholes mainly at Äspö and beneath the Baltic Sea. This groundwater is referred to as "Marine" in the retardation model property tables.

III. Brackish groundwater of a predominantly non-marine origin Na-Ca-Cl type (5,400 mg/l Cl). This is a water with higher Ca and lower Mg compared to the Type II water and is presently found at depths below 450 to 650 m depending on location. This is a mix of Brackish Non-marine and Marine water and is of a transitional type. In the retardation model property tables this groundwater is referred to as "Saline".

IV. Brine type water of very high salinity, Ca-Na-Cl type water with Cl content of 45,000 mg/l currently found at depths greater than about 1,500 m. During a glacial period, brine type waters can be forced to more shallow levels than at present. This groundwater is referred to as "Brine" in the retardation model property tables.

V. Brackish water of non-marine Na-Ca-Cl type (2,000 mg/l Cl). This water has lower salinity than groundwaters of type II and III and is common in the Laxemar subarea at repository depth. This groundwater is referred to as "Type V" in the retardation model property tables.

In all experiments, synthetically prepared groundwaters were used to avoid the possible risk of oxidation and colloid formation which, owing to the difficulty of maintaining natural reducing conditions, would be a significant problem if actual groundwater samples were to be used. Water of salinity close to the one measured at repository depth was used for the diffusivity measurements. A water composition (described as Type II) was chosen for use in the diffusion experiments although only the major components (i.e. Ca^{2+}, Na^{+}, Cl^{-} and SO_4^{2-}) were included in the synthetic groundwater formulation. The compositions of these groundwater types are specified in Table 4-4, referring to specific sampling intervals in the boreholes.

4.3 Overview of transport property data

This section consists of two parts. The first part comprises a description of the main methods and techniques used in the laboratory programme for acquisition of transport property data (also referred to as material properties data in this report) as well as a general overview of issues related to data interpretation. The second part is a detailed description of the experimental data obtained from the laboratory investigations. These are presented in the form of material property tables for each relevant parameter and material type under specified conditions.

4.3.1 Methods and parameters

The main parameters used in the retardation model are the total storage porosity, θ_m (-), the effective diffusivity, D_e (m^2/s), and the linear equilibrium sorption coefficient, K_d (m^3/kg). The different laboratory techniques used for obtaining data and evaluating these parameters are described in the following sections.

Table 4-4. Groundwater compositions used in the transport properties evaluation laboratory programme for the Laxemar site; concentrations are given in mg/l.

	Type I (HSH02 0–200 m) Fresh water	Type II (KFM02A 509–516 m) Marine (brackish groundwater with marine character)	Type III (KSH01A 558–565 m) Saline (present groundwater at repository depth)	Type IV (KLX02 1,383–1,392 m) Brine type water of very high salinity	Type V (KLX04 510–515 m) Brackish groundwater of non-marine character
Li^+	0.016	0.051	0.58	4.85	0.0152
Na^+	127	2 120	3 230	7450	691
K^+	2.16	33.3	12.4	32.6	3.19
Rb^+	(0.0252)[A]	0.0628	0.0424	0.178	0.0424
Cs^+	(1.17×10^{-3})[A]	1.79×10^{-3}	1.37×10^{-3}	0.0186	1.37×10^{-3}
NH_4^+	(0.0947)[A]	0.04	0.04	0.56	0.0319
Mg^{2+}	1.43	232	44.7	1.2	6.9
Ca^{2+}	5.21	934	2 190	14 800	234
Sr^{2+}	0.0695	7.95	32.3	253	4.67
Ba^{2+}	(1.29)[A]	0.188	0.188	0.024	0.188
Fe^{2+}	(0.364)[C]	1.20	0.686	3.45	0.09
Mn^{2+}	0.02	2.12	0.46	1.11	0.109
F^-	3.03	0.9	0.967	(1.6)[D]	2.7
Cl^-	21.5	5 150	8 800	36 800	1 480
Br^-	(0.2)[B]	22	71	509	13.4
SO_4^{2-}	8.56	510	221	1 210	104
Si(tot)	6.56	5.2	4.7	2.6	6.63
HCO_3^-	252	124	12	42	51.4
S^{2-}	(0.01)[B]	0.05	0.05	0.05	6.0×10^{-3}
pH	8.58	7.1	7.45	6.8	7.83

A) No measurements available, data imported from KSH01, sample #5263.
B) Based on detection limit.
C) Based on the Fe-tot measurement.
D) No measurements available, data imported from KLX02, sample #2731.

Porosity

In the context of the retardation model described in this report, the porosity refers to the volume of the rock that is filled with water and available for both storage and transport of solutes (θ_m). Here, a theoretical distinction is made between the total storage porosity, θ_m of the rock and the transport porosity, θ_p which only considers the connected pore space available for diffusive through-transport.

Although very heterogeneously distributed on a microscopic to cm- or perhaps dm-scale, for the purposes of transport modelling the porosity is considered to be homogeneously distributed in the rock matrix on the macroscopic scale relevant for solute transport calculations. The porosity data used in the site descriptive transport modelling has mainly been obtained from measurements performed on rock samples intended for diffusion and sorption studies. The method used for determination of the porosity (SS-EN 1936) is a gravimetric technique based upon water re-saturation of the sample, followed by a drying step.

Estimations of the porosity for the deformation zone elements have been found to be difficult owing to the general heterogeneity of samples combined with problems of sample cohesion. For this reason, the porosity measurement based upon water saturation has been complemented with measurements based upon a PMMA-impregnation technique (Polymethylmethacrylate) /Penttinen et al. 2006/. This technique is very useful for studying the spatial distribution and modality of porosity in samples on a microscopic scale.

Effective diffusivity

The effective diffusivity is frequently given in terms of the formation factor, F_f; a dimensionless number which is defined as the ratio of the effective diffusivity, D_e of a solute in the rock to that of the solute in water at infinite dilution, D_w. Theoretically, the formation factor is a purely geometrical entity that includes the effect of transport porosity θ_p, as well as pore tortuosity, τ^2 and constrictivity δ /Löfgren and Neretnieks 2003/. Typically, it is defined as:

$$F_f = \frac{D_e}{D_w} = \theta_p \frac{\delta}{\tau^2} \qquad \text{(Eq. 4-1)}$$

The effective diffusivity can also be defined in terms of a pore diffusivity, D_p which internalises the transport tortuosity-constrictivity term in its definition:

$$D_e = D_p \theta_p \qquad \text{(Eq. 4-2)}$$

The transport porosity, θ_p should theoretically be lower than the total accessible porosity, θ_m which also includes dead-end pores that do not contribute directly to the diffusive flux. Since the transport porosity is already internalised in the measurement of the effective diffusivity (or formation factor), it is generally not necessary to evaluate this separately for the purposes of transport modelling within Safety assessment. In the Laxemar site descriptive modelling θ_p and θ_m are, for all practical purposes, considered to be identical.

Although strictly a geometrical parameter, measurement of the formation factor is influenced by other non-geometrical effects such as surface diffusion and anion exclusion. Operationally, however it is still defined as the ratio of effective and free diffusivity at infinite dilution. For this reason, laboratory measurements of the formation factor using electrical resistivity are customarily carried out on materials that have been pre-equilibrated with high ionic strength water ($\geq$ 1.0 M) so as to not be excessively influenced by surface conduction artefacts (see Appendix D for a more detailed discussion of this). From the formation factor, approximate effective diffusivities can be calculated for all solutes of interest using solute-specific, free diffusivities from the literature /Widestrand et al. 2003/.

Formation factors can be obtained by a variety of different methods. The main laboratory methods used within the Transport programme are through-diffusion tests and electrical resistivity measurements on slices of bore core samples. Through-diffusion tests are made using a two-compartment measurement cell where a tracer (tritiated water in the current laboratory programme) is allowed to diffuse through a 1–3 cm long bore core sample from a high concentration compartment to a low concentration compartment, initially free of tracer. The effective diffusivity and capacity factor are then obtained by fitting a theoretical model of diffusion to the breakthrough data for the measurement cell.

The through-diffusion tests used in the laboratory programme are based upon the use of tritiated water (HTO) as a tracer substance which, for all practical purposes, can be considered to be non-interacting. In previous investigations, uranine and iodide (I^-) were frequently used as tracers. Anion exclusion effects relating to the thickness of the electrical double layer (EDL) relative to the pore diameter, however, compromise the applicability of results obtained using these solutes for cation diffusion (although more so at low ionic strengths) and therefore they have not been used in the current site investigation. The choice of HTO as a reference tracer is motivated by the wish to obtain a quantification of the geometrical formation factor with a minimum of additional interacting processes that are strongly dependent on pore water chemistry /Widestrand et al. 2003/. Anion exclusion, however, may be important for transport processes of anions at low ionic strength in certain safety assessment scenarios.

Laboratory electrical resistivity measurements are performed also using 1–3 cm long drill core pieces and the formation factor is obtained as the ratio between the pore water resistivity and that of the (typically) brine saturated rock. This is possible owing to the analogy between diffusivity and ionic mobility as formalised in the Einstein relation /Atkins 1999/. Both alternating (AC) and direct (DC) current can be used for these measurements, although AC is frequently preferable owing to electrode polarisation effects arising when using DC methods. AC current also allows phase angle measurements to be made which can be helpful for identifying the presence of conductive minerals such as magnetite or excessive amounts of clay minerals which can lead to anomalous results /Thunehed 2005a, b, 2007a, c/.

Laboratory resistivity measurements can be performed relatively quickly, which enables testing of large numbers of samples. Thus, the majority of the laboratory formation factor data are from resistivity measurements. Electrical resistivity can also be measured by in situ methods using a resistivity logging tool /Löfgren 2004/. In laboratory measurements of resistivity, the rock samples are firstly saturated with a solution of known salinity (typically, ≥ 1 M NaCl), whereas in situ measurements rely upon accurate characterisation of the matrix porewater. This is typically done using flowing water in fractures as a proxy, although this implicitly assumes diffusive equilibrium between the matrix porewater and that sampled in the borehole. It is also possible to leach porewater from retrieved bore core samples to estimate the composition of the native porewater /Waber et al. 2009/. The in situ method can only be used for parts of the borehole where sufficiently strong saline conditions prevail that surface conduction artefacts are not an issue for result interpretation.

Sorption

The notion of sorption in the context of the site descriptive modelling relates to the adsorptive interaction of radionuclides with the surfaces of geological materials. As already discussed in Section 2.2 this occurs principally by way of the association of ionic solute species with charged mineral surfaces. In the simplified approach to sorption modelling adopted within the Site Descriptive Model, sorption processes are considered to be linear (i.e. no intrinsic concentration dependency in the range of radionuclide concentrations to be modelled) as well as being fast and reversible (chemical kinetics are not considered). The concept is the same as that described in the strategy report by /Widestrand et al. 2003/.

Within the laboratory programme the equilibrium sorption distribution coefficient, K_d is measured by batch sorption tests on crushed rock and unconsolidated fracture-filling materials. These measurements are performed in contact with different water compositions intended to cover the range of groundwater chemistries likely to be encountered by transported solutes. As the crushing of rock samples results in the formation of additional sorption surface area that may not be representative of the in situ rock, sorption data for different size fractions can be used to extrapolate estimates for the sorption coefficient for the internal surfaces of the crushed rock material.

In the original strategy for laboratory methods to be used in the transport properties evaluation /Widestrand et al. 2003/, an extrapolation technique based upon linear regression of sorption measurement data for different crushed rock size fractions was recommended for the evaluation of the sorption on internal surfaces of the rock matrix. Specifically, the evaluation technique attempts to distinguish sorption on internal and external surfaces by relating the apparent partitioning ratio, R_d (m^3/kg) to the mass-based sorption coefficient on internal surfaces, K_d (m^3/kg) and surface area normalised sorption coefficient, K_a (m) for sorption on the external surfaces of crushed particles /Widestrand et al. 2003/:

$$R_d \approx K_d + \frac{6K_a}{\rho_{bm} d_p} \qquad \text{(Eq. 4-3)}$$

The values of K_a and K_d and their error estimates can be obtained by linear regression when data for more than one particle size fraction are available if it is additionally assumed that different particle size fractions have identical surface roughness/sphericity and are not fractionated with respect to mineral content. The characteristic particle size, d_p (m) is customarily assumed to be the volumetric mean size based upon the upper and lower sieve sizes bracketing the sample /Byegård and Larsson 2004/, while ρ_{bm} (kg/m^3) is the bulk density of the rock.

Owing to problems associated with the extrapolation of data (i.e. unreasonably low, or negative K_d values owing to large regression uncertainties), this technique was found to be unreliable, and a different strategy was adopted for SDM-Site Laxemar based upon direct application of the distribution coefficient measured for the largest size fraction (1–2 mm) at the longest contact time (180 days). Since the surface areas measured for particles in this size range are reasonably close to that measured for monolithic core samples deemed representative of the in situ rock (see Section 4.4.3), this is thought to be the most appropriate alternative evaluation method at the present time.

Association of transported radionuclides with secondary minerals at the fracture surfaces is typically assumed to be sufficiently fast at safety assessment timescales that their diffusive properties do not need to be considered explicitly. These surface reactions are therefore often considered to be instantaneous, equilibrium partitioning processes. These processes are frequently described in terms of an equilibrium surface sorption coefficient, K_a (m) for the fracture coating. This is typically internalised in transport models in the form of a retardation coefficient, defined as:

$$R_a = 1 + \frac{2K_a}{\delta_t} \qquad \text{(Eq. 4-4)}$$

Where δ_t is the transport aperture governing the advective travel time within the flowing water.

Assuming fast diffusive equilibrium, the retardation coefficient for direct sorption at the fracture surface can also be defined in terms of the sorptivity (K_{ds}) of the fracture coating, its bulk density (ρ_{bs}), porosity (θ_s), and thickness (δ_{fs}) relative to the transport aperture:

$$R_a = 1 + \left(\theta_s + K_{ds}\rho_{bs}\right)\frac{2\delta_{fs}}{\delta_t} \qquad \text{(Eq. 4-5)}$$

For loose, unconsolidated particulates residing in the fracture such as fault gouge or breccia, the retardation coefficient can also be defined in terms of the corresponding material properties of the particulates (i.e. K_{dg}, ρ_{bg}, θ_g) and the relative void fraction, β_g they occupy in the fracture:

$$R_a = 1 + \left(\theta_g + K_{dg}\rho_{bg}\right)\left(\frac{\beta_g}{1-\beta_g}\right) \qquad \text{(Eq. 4-6)}$$

BET surface area and CEC

Since the sorption of radionuclides is a surface mediated process, the quantification of mineral surface area within the rock matrix and fracture coatings is a valuable proxy for understanding of sorption property variability. The sorption of many radionuclides has been observed to be strongly correlated with mineral surface area /Bertetti et al. 1996, Bertetti et al. 1998, Pabalan et al. 1998, Prikryl et al. 2001/. The correlation is expected to be quite strong for radionuclides that sorb mostly by way of a surface complexation mechanism and to some extent independent of the type of mineral phases present /Turner and Pabalan 1999/. This is thought to be because the variably charged, surface functional groups of most silicate materials are similar and consist of a mixture of amphoteric silanol and aluminol reactive sites /Bradbury and Baeyens 1997/. Sorption is not restricted to silicate minerals, however, and the different ferric oxides which may be present in the rock as oxidation products can strongly sorb cations that form surface complexes /Jakobsson 1999/. This is partly to do with their large surface area, but also due to the fact that they generally function as much stronger surface ligands than the corresponding reactive sites on silicate minerals.

For permanently charged sites that are known to be important for ion-exchange, there is also a correlation between sorptivity and surface area although the correlation is less strong owing to the fact that minerals have widely varying sorption site densities and therefore do not always sorb equally well. It is well known for example that mica minerals such as biotite and its alteration product chlorite can have a disproportionate effect upon the sorption of ion exchangers in granitic rocks /Torstenfelt et al. 1982/. The sorption of ion exchangers is therefore likely to be more closely related to the cation exchange capacity, CEC of the rock than the surface area.

The surface area of mineral phases within the rock available for sorption is measured using the BET method /Brunauer et al. 1938/ which is based upon the adsorption of gas probe molecules to a surface. Although it is difficult to establish a direct quantitative relationship between bulk surface area and sorption site density for a mixed mineral system, the results of BET surface measurements are included in the retardation model as a qualitative proxy for sorption that is useful for understanding observed sorption processes.

BET measurements have been performed on site-specific materials according to the ISO 9277 standard method. Three types of measurements have been carried out for the Laxemar site specific material. For drill core samples, crushing and sieving was performed. The particle size

fractions 63–125 μm and 2–4 mm were measured in duplicate samples for each fraction. A simple linear extrapolation technique was used to distinguish internal and external surface area in a similar fashion to that used for sorption data (analogous to Equation 4-3):

$$A_{BET} = A_{INT} + A_{EXT} = A_{INT} + \frac{6\lambda}{\rho_b d_p} \qquad \text{(Eq. 4-7)}$$

Here, A_{BET} (m^2/g) is the total surface area measured using the BET method, A_{INT} (m^2/g) is the surface area of internal microsurfaces within the particles, A_{EXT} (m^2/g) is the external surface area of the particles, and λ (m^2/m^2) is the so-called surface roughness which is an empirical factor that takes into account both the true surface roughness of the particles and deviation from sphericity ($\lambda = 1$ for a sphere). The linear extrapolation procedure implicitly assumes that the A_{INT} and λ are constant across different size fractions of the crushed material.

For natural fracture samples, surface material was abraded by scraping the fracture surfaces. The size fraction < 125 μm was then isolated by sieving of the abraded material and measured in duplicate samples. In addition to these measurements, an attempt was also made to measure the BET surface area for a small number of monolithic samples thought to be representative of the intact rock.

The method employed for CEC measurement (ISO 13536), although thought to be very reliable for soil investigations, was found to be less useful for crushed rock samples owing to their relatively low exchange capacities. For this reason, the CEC values presented in the property tables should be considered to be only semi-quantitative estimates. More details concerning these measurements can be found in /Selnert et al. 2009b/.

4.3.2 Data from the laboratory programme

The laboratory investigations have been designed with the aim of providing site-specific data for storage porosity, sorption, and diffusive properties of different rock types and geologic materials associated with fracture surfaces. Bore core samples for these measurements have been selected in accordance with the guidelines described in /Widestrand et al. 2003/ from several boreholes. Since the laboratory measurements of diffusion and sorption are very time consuming, a majority of the rock samples were collected from the first cored boreholes investigated in the Laxemar-Simpevarp area (i.e. KSH01A, KSH02, KLX02, and KLX04). The improved knowledge of the Laxemar local model volume later influenced the rock sampling by including additional boreholes in the sample collection. At the conclusion of investigations, the total sample collection consisted of about 400 rock samples from fourteen boreholes. The sample collection has been found to be representative for the target volume although it has not been possible to include all different fracture types in the laboratory measurements.

For the purpose of statistical representativity, rock samples were selected from various depths in the boreholes. For instance, in KSH01A, KSH02 and KLX02 samples were taken every 20 m. Major and minor rock types, various fracture types and altered rocks with different mode and degree of alteration in deformation zones are represented in the sample collection. In order that the material properties data reflect the properties of flowing features as far as possible, the selection of samples from open fractures was directed by indications of water flow as recorded in flow logs when available and with support from hydrogeological and hydrogeochemical expert judgement.

Sampling of materials associated with different fracture types was also dependent on the existence of a sufficient quantity of loose fracture filling material to be of use for the laboratory experiments. Sorption measurements, for example, require a minimum of about 0.5 g of material for a single batch experiment consisting of one tracer substance and one water type without replication. For some fracture types such as fracture type I (Calcite ± other), it was not possible to collect sufficient material for any measurements to be carried out.

For deformation zone structural elements, rock alteration in addition to indications of water flow were the guiding parameters for sampling. The strategy in the deformation zone sampling was to identify segments of altered rock within deformation zones that might reflect divergent characteristics relative to intact rock regarding porosity, diffusion, and sorption. A summary of the available transport laboratory data are found in Table 4-5. It is noted that the numbers given in Table 4-5 reflect the number of data points obtained using the different measurement techniques and not the originally collected number of rock samples. One original rock sample from a given location in a bore core, for example, may have been further subdivided for multiple measurements. The number of data points therefore exceeds the number of rock samples.

Table 4-5. Rock sample data included in the retardation model (i.e. the number of measurements for the respective method used in the laboratory investigations).

Method	Total number of measurements	Number of rock type measurements	Number of fracture type measurements	Number of measurements from deformation zones
Porosity (water saturation)	333	324	0	9
PMMA	3	0	1	2
Electric resistivity (lab)	42	42	0	0
Through diffusion	90	84	0	6
BET (crushed rock)	197	154	26	17
CEC	15	9	5	1
Batch sorption (crushed rock)	436	263	85	88

4.4 Material properties data

In this section the material properties data used to parameterise the retardation model are discussed.

4.4.1 Porosity

The results of the porosity measurements are summarised in Table 4-6. The detailed geological characterisation performed using a binocular microscope found several samples to have small micro fractures 3–15 mm in length and with a width of ≤ 0.5 mm, in both fresh and altered rock samples /Selnert et al. 2009b/. These are larger than intragranular micro cracks and cut through individual mineral grains. Comparison of the porosities determined for samples with and without observable micro fractures (as described in Table 4-6), indicates that such fractures give rise to an apparently higher porosity. The samples have been further categorised with respect to whether they originate in deformation zones (DZ), or from non-deformation zone sections (N), based upon the extended single hole interpretation (ESHI) data for each borehole. The results suggest very little difference between the porosity of deformation zone and non-deformation zone materials. It should be remembered, however, that this often reflects the fact that there may be large sections of non-deformed rock within borehole intervals defined as being part of deformation zones within the ESHI classification and the results should therefore be interpreted with care. The quartz monzodiorite (501036) is the only rock type that shows a clear tendency towards increased porosity in samples taken from deformation zones. This is due at least in part to the alteration of 8 out of the 10 samples used as a basis for the estimates given for deformation zone material of this rock type.

An additional classification has been made in which the visible alteration of the samples has been used as a distinguishing parameter. Here, the alteration status of individual samples was assessed by binocular microscopic inspection of individual samples. The results of this analysis are shown in Table 4-7 where alteration status is given as medium to strong alteration (M/S) or weak to absent visible alteration (W/A).

The results indicate that the majority of rock types exhibiting alteration are associated with higher porosities (for both deformation zone and non-deformation zone material). An exception is the Ävrö granodiorite (501056) samples taken from inside deformation zones where the opposite tendency is observed. It should be noted, however, that the visual assessment of alteration is more subjective and difficult for the red-coloured rock types such as Ävrö granodiorite as compared to the more greyish rock types. More detailed examination of the Ävrö granodiorite samples classified with weak to absent alteration show that they include three high porosity samples that were classified with “weak to medium alteration” (these three samples also contain sealed fractures and, in one case, observable micro-fracturing).

Porosity measurements were performed on samples representing the five different deformation zone structural elements discussed in Section 4.2.1. The results are presented in Table 4-8.

Table 4-6. Porosities (vol.%) of different rock types from the Laxemar-Simpevarp area. Data are given as the arithmetic mean (± standard deviation), median, minimum, and maximum values for the specified numbers (n) of samples involved in the study. The entries in the column labelled DZ identifies whether the corresponding rows of data are based upon deformation zone (DZ) materials or non-deformed host rock (N). A further classification is also made with regard to presence or absence of visible microfractures.

Rock type (SKB code)	DZ	microfractures	Mean ±σ	Median	Min.	Max.	n
Fine-grained dioritoid (501030)	N	no	0.19±0.22	0.12	0.00	1.49	59
		yes (all samples)	0.23±0.26	0.15	0.00	1.49	76
	DZ	no	0.13±0.11	0.09	0.04	0.41	13
		yes (all samples)	0.19±0.19	0.12	0.04	0.75	18
Diorite to gabbro (501033)	N	no	n/a	0.06	0.05	0.06	2
		yes (all samples)	n/a	0.06	0.05	0.06	2
	DZ	no	n/a	n/a	n/a	n/a	0
		yes (all samples)	n/a	n/a	n/a	n/a	0
Quartz monzondiorite (501036)	N	no	0.19±0.19	0.13	0.00	1.32	59
		yes (all samples)	0.19±0.19	0.13	0.00	1.32	61
	DZ	no	0.78±0.41	0.78	0.17	1.59	9
		yes (all samples)	0.75±0.40	0.77	0.17	1.59	10
Ävrö quartz monzodiorite (501046)	N	no	0.35±0.14	0.40	0.05	0.60	26
		yes (all samples)	0.35±0.14	0.40	0.05	0.60	28
	DZ	no	0.31±0.08	0.28	0.25	0.42	4
		yes (all samples)	0.63±0.52	0.36	0.25	1.45	6
Ävrö granodiorite (501056)	N	no	0.30±0.13	0.27	0.13	0.80	52
		yes (all samples)	0.32±0.15	0.29	0.13	0.99	58
	DZ	no	0.39±0.20	0.35	0.15	0.89	18
		yes (all samples)	0.40±0.20	0.36	0.15	0.89	19
Granite, medium- to coarse-grained (501058)	N	no	n/a	0.61	0.38	0.84	2
		yes (all samples)	n/a	0.61	0.38	0.84	2
	DZ	no	n/a	0.76	n/a	n/a	1
		yes (all samples)	n/a	0.76	n/a	n/a	1
Pegmatite (501061)	N	no	n/a	n/a	n/a	n/a	0
		yes (all samples)	n/a	0.02	n/a	n/a	1
	DZ	no	n/a	n/a	n/a	n/a	0
		yes (all samples)	n/a	n/a	n/a	n/a	0
Fine-grained diorite-gabbro (505102)	N	no	0.16±0.06	0.19	0.03	0.22	8
		yes (all samples)	0.16±0.06	0.19	0.03	0.22	8
	DZ	no	0.46±0.50	0.33	0.05	1.15	4
		yes (all samples)	0.46±0.50	0.33	0.05	1.15	4
Granite, fine- to medium-grained (511058)	N	no	0.23±0.07	0.24	0.07	0.40	23
		yes (all samples)	0.27±0.19	0.24	0.07	1.15	26
	DZ	no	0.18±0.07	0.16	0.13	0.25	3
		yes (all samples)	0.15±0.08	0.14	0.05	0.25	4

Notes: Entries given as “n/a” in the table signify data “not available”.

Table 4-7. Porosities (vol.%) of different rock types from the Laxemar-Simpevarp area. Data are given as the arithmetic mean (± standard deviation), median, minimum, and maximum values for the specified numbers (n) of samples involved in the study. The entries in the column labelled DZ identifies whether the corresponding rows of data are based upon deformation zone (DZ) materials or non-deformed host rock (N). A further classification is also made with regard to the presence (M/S) of visible medium to strong alteration or weak to absent visible alteration (W/A).

Rock type (SKB code)		All rock samples					
	DZ	Alteration	Mean ±σ	Median	Min.	Max.	n
Fine-grained dioritoid (501030)	N	M/S	0.79±0.56	0.84	0.21	1.33	3
		W/A	0.20±0.22	0.13	0.00	1.49	73
	DZ	M/S	n/a	0.47	0.19	0.75	2
		W/A	0.16±0.13	0.11	0.04	0.41	16
Diorite to gabbro (501033)	N	M/S	n/a	n/a	n/a	n/a	0
		W/A	n/a	n/a	n/a	n/a	0
	DZ	M/S	n/a	n/a	n/a	n/a	0
		W/A	n/a	n/a	n/a	n/a	0
Quartz monzondiorite (501036)	N	M/S	n/a	n/a	n/a	n/a	0
		W/A	0.19±0.19	0.13	0.00	1.32	61
	DZ	M/S	0.87±0.35	0.83	0.45	1.59	8
		W/A	n/a	0.25	0.17	0.34	2
Ävrö quartz monzodiorite (501046)	N	M/S	n/a	0.15	n/a	n/a	1
		W/A	0.36±0.14	0.42	0.05	0.60	27
	DZ	M/S	0.94±0.62	1.12	0.25	1.45	3
		W/A	0.33±0.08	0.29	0.13	0.42	3
Ävrö granodiorite (501056)	N	M/S	0.55±0.33	0.39	0.23	0.99	5
		W/A	0.30±0.10	0.28	0.13	0.58	53
	DZ	M/S	0.36±0.25	0.25	0.15	0.79	6
		W/A	0.43±0.18	0.36	0.22	0.89	13
Granite, medium- to coarse-grained (501058)	N	M/S	n/a	n/a	n/a	n/a	0
		W/A	n/a	n/a	n/a	n/a	0
	DZ	M/S	n/a	n/a	n/a	n/a	0
		W/A	n/a	n/a	n/a	n/a	0
Pegmatite (501061)	N	M/S	n/a	n/a	n/a	n/a	0
		W/A	n/a	n/a	n/a	n/a	0
	DZ	M/S	n/a	n/a	n/a	n/a	0
		W/A	n/a	n/a	n/a	n/a	0
Fine-grained diorite-gabbro (505102)	N	M/S	n/a	n/a	n/a	n/a	0
		W/A	0.16±0.06	0.19	0.03	0.22	8
	DZ	M/S	n/a	n/a	n/a	n/a	0
		W/A	0.46±0.50	0.33	0.05	1.15	4
Granite, fine- to medium-grained (511058)	N	M/S	n/a	0.64	0.12	1.15	2
		W/A	0.24±0.07	0.24	0.07	0.40	24
	DZ	M/S	n/a	n/a	n/a	n/a	0
		W/A	0.15±0.08	0.14	0.05	0.25	4

Notes: Entries given as “n/a” in the table signify data “not available”.

Table 4-8. Porosities (vol.%) of different deformation zone structural elements from the Laxemar-Simpevarp area. Data are given as the arithmetic mean (± standard deviation), median, minimum, and maximum values for the specified numbers (n) of samples involved in the study. Comments in the far right column concern PMMA porosity measurements.

Structural element	All rock samples (water saturation porosity)					PMMA porosity (description)
	Mean±σ	Median	Min.	Max	n	
DZ (Category 1) Fault rock/gouge	n/a	n/a	n/a	n/a	0	Strongly heterogeneous. Average porosity 3% (1 core sample). Low porosity rock fragments surrounded by highly porous material (clay, hematite, chlorite) with up to 18% porosity.
DZ (Category 2) Chlorite/green gouge	n/a	n/a	n/a	n/a	0	Average porosity 0.5–1% (1 core sample). Clay phases have higher porosity of up to 12%.
DZ (Category 3) Vuggy rock	n/a	6.23	4.19	8.28	2	Average porosity 0.4–0.8% (2 core samples) representing less altered parts of the rock samples. Small area fractions representing clayish phases and vugs have up to ~15% porosity.
DZ (Category 4) Catclasite	2.82±1.78	3.35	0.73	5.83	7	Average matrix porosity (material between sealed fractures) typically 0.5%. Dense mylonitic bands have porosity ≤ 0.1%. Highly porous phases in fracture minerals of up to ~40% for small areas. Average porosity for 3 whole core samples is in the range 1–6%
DZ (Category 5) Oxidised wall rock	0.68±0.43	0.75	0.15	1.59	19	Average porosity 0.3% (1 core sample).

Notes: Entries given as “n/a” in the table signify data “not available”.

4.4.2 Effective diffusivity

Through-diffusion measurements

The measurements of effective diffusivity using the through-diffusion measurement technique indicate formation factors (see Table 4-9) in the range of 5×10^{-4} to 3×10^{-5} for the major rock types classified as non-deformation zone material (N). Only very minor deviations are seen for samples designated as originating from deformation zones (DZ) which is in line with the similar observations made for porosity. Formation factors in the range of 10^{-3} to 10^{-4} are obtained for deformation zone materials in accordance with the higher porosity of the samples. The numbers of samples taken from within deformation zones are low, however, so the statistical basis for differentiating non-deformation zone and deformation zone material cannot be quantitatively established with certainty. Generally, the measured formation factor ranges tend to reflect the variation of the porosity ranges of the same rock types. Lower formation factors are found, for example, in rock of low porosity such as fine-grained dioritoid (501030) as compared to more porous rock types such as Ävrö quartz monzodiorite (501046). It should also be noted that for the minor rock types, the number of samples are low and the statistical basis for differentiating the diffusive properties of these rock types is questionable.

Drill core samples used in the laboratory experiments range from 0.5 to 5 cm in length, although roughly 60% are 3 cm (the 0.5, 1, and 5 cm lengths comprise 13% each). The 0.5–1 cm samples usually have a slightly higher diffusivity than 3–5 cm samples, although the variation within a size cohort is typically larger than the variation that can be related to sample length. The pooled results can therefore be considered to be approximately representative with only a small bias introduced due to the use of different core sample lengths.

An attempt has been made to study the influence of the porosity on the formation factor. Although there is a fair degree of correlation between the measured formation factor and porosity, the large scatter of data at low porosities (< 1%) seems to indicate that the effective tortuosity/constrictivity of the diffusion paths is highly variable and may have a dominant impact on the magnitude of the formation factor. A substantial proportion of the total porosity being in the form of dead-end pores which do not actively contribute to the diffusion of tracer could also be inferred from the results to explain the scatter in the data.

Electrical resistivity measurements

A summary of the formation factors obtained using the through-diffusion measurement technique is provided in Table 4-9. A comparison was also made where the formation factors of 42 samples, previously used for through diffusion experiments, were measured using the electrical resistivity method. The results indicate that the laboratory resistivity measurement method tends to give higher formation factors than those obtained using the through diffusion method. There are, however, large variations in the results. It is found that formation factors measured using the laboratory electrical resistivity technique are roughly double those established using through diffusion (~2.6±2.4 in the present investigation, although with a prominent positive skew). A full physical explanation for this phenomenon is not yet available, although the empirical basis for the difference has been firmly established in multiple investigations /Crawford 2008/. Further discussion concerning this can be found in Appendix D.

Comparisons have also been made between the samples used for through diffusion experiments and the nearest comparable in situ resistivity measurement. In general it is found that the in situ resistivity measurement typically gives values that are lower than those obtained using the through-diffusion method.

Formation factors which are presented in the retardation model tables (Section 4.5) in this report are based on both in situ electrical resistivity and laboratory through-diffusion measurements (as an alternative parameterisation). It should be noted that this choice is not meant to indicate a belief that the one method is more reliable than the other. It could be argued that the through-diffusion technique is the method that best simulates the actual physical process aimed to be studied (i.e. solute diffusion in the porewater) and that the electrical resistivity technique may be influenced by artefacts that are not, as yet fully understood which give rise to the empirical deviation of roughly a factor of two. A detailed discussion concerning the issues related to use of the electrical resistivity measurement technique can be found in Appendix D where the use of in situ formation factors derived from borehole resistivity logging is discussed. A large amount of data derived from the in situ measurements is also presented there and sorted according to rock type for comparative purposes.

Table 4-9. Formation factors (F_f) of different rock types from the Laxemar-Simpevarp area determined from the through-diffusion experiments. The arithmetic mean (± standard deviation), median, minimum, maximum values are given for the specified numbers (n) of samples involved in the study. The entries in the column labelled DZ identifies whether the corresponding rows of data are based upon deformation zone (DZ) materials or non-deformed host rock (N).

Rock type (SKB code)	DZ	Mean ±σ	Median	Min.	Max.	n
Fine-grained dioritoid (501030)	N	$(0.66\pm1.1)\times10^{-4}$	3.1×10^{-5}	1.1×10^{-6}	4.0×10^{-4}	19
	DZ	$(8.6\pm4.9)\times10^{-6}$	8.4×10^{-6}	1.4×10^{-6}	1.5×10^{-5}	5
Diorite to gabbro (501033)	N	n/a	n/a	n/a	n/a	0
	DZ	n/a	n/a	n/a	n/a	0
Quartz monzondiorite (501036)	N	$(1.1\pm1.2)\times10^{-4}$	6.1×10^{-4}	2.0×10^{-6}	4.7×10^{-4}	15
	DZ	$(1.8\pm1.4)\times10^{-4}$	1.4×10^{-4}	1.1×10^{-5}	3.7×10^{-4}	7
Ävrö quartz monzodiorite (501046)	N	n/a	n/a	n/a	n/a	0
	DZ	$(4.1\pm1.6)\times10^{-4}$	4.6×10^{-4}	7.5×10^{-6}	5.2×10^{-4}	9
Ävrö granodiorite (501056)	N	$(5.9\pm2.1)\times10^{-5}$	6.0×10^{-5}	3.8×10^{-5}	8.1×10^{-5}	3
	DZ	$(1.5\pm1.7)\times10^{-4}$	7.0×10^{-5}	1.3×10^{-5}	6.1×10^{-4}	20
Granite, medium- to coarse-grained (501058)	N	n/a	n/a	n/a	n/a	0
	DZ	n/a	n/a	n/a	n/a	0
Pegmatite (501061)	N	n/a	n/a	n/a	n/a	0
	DZ	n/a	n/a	n/a	n/a	0
Fine-grained diorite-gabbro (505102)	N	n/a	9.8×10^{-5}	n/a	n/a	1
	DZ	n/a	n/a	n/a	n/a	0
Granite, fine- to medium-grained (511058)	N	$(4.5\pm1.5)\times10^{-5}$	4.4×10^{-5}	2.3×10^{-5}	6.0×10^{-5}	5
	DZ	n/a	n/a	n/a	n/a	0

Notes: Entries given as “n/a” in the table signify data “not available”.

Table 4-10. Formation factors (F_f) of different deformation zone structural elements from the Laxemar-Simpevarp area determined from the through-diffusion experiments. The arithmetic mean (± standard deviation), median, minimum, maximum values are given for the specified numbers (n) of samples involved in the study. The entries in the column labelled DZ identifies whether the corresponding rows of data are based upon deformation zone (DZ) materials or non-deformed host rock (N).

Rock type (SKB code)	DZ	Mean ±σ	Median	Min.	Max.	n
DZ (Category 1) Fault rock/gouge	N	n/a	n/a	n/a	n/a	n/a
	DZ	n/a	n/a	n/a	n/a	n/a
DZ (Category 2) Chlorite/green gouge	N	n/a	n/a	n/a	n/a	n/a
	DZ	n/a	n/a	n/a	n/a	n/a
DZ (Category 3) Vuggy rock	N	1.1×10^{-3}	n/a	n/a	n/a	1
	DZ	n/a	n/a	n/a	n/a	1
DZ (Category 4) Catclasite	N	$(1.3\pm7.4)\times10^{-4}$	9.4×10^{-4}	7.6×10^{-4}	2.1×10^{-3}	3
	DZ	7.6×10^{-3}	n/a	n/a	n/a	n/a
DZ (Category 5) Oxidised wall rock	N	n/a	n/a	n/a	n/a	n/a
	DZ	$(1.5\pm1.3)\times10^{-4}$	1.4×10^{-3}	3.8×10^{-5}	3.7×10^{-4}	9

Notes: Entries given as “n/a” in the table signify data “not available”.

4.4.3 BET surface area

As described previously, drill core samples were firstly crushed and sieved and then the BET surface area of the size fractions 0.063–0.125 mm and 2–4 mm were measured in duplicate samples for each size fraction. The extrapolation technique described in Section 4.3.1 (Equation 4-7) was employed to estimate the inner surface BET area of the samples. The results of these measurements are given in Table 4-11.

Samples of loose fracture surface coatings were obtained by mechanical abrasion and the < 125 μm fraction was isolated through sieving of the collected material. The BET surface area was then measured in duplicate samples. The results of these measurements are given in Table 4-12 without extrapolation since they are already in a friable condition which is considered to be their natural state.

Comparison of the results for different rock types

The results of the BET surface area measurement are presented in Table 4-11 and Table 4-12. The major finding is the large difference between the non-altered samples compared to altered rock and fracture surfaces.

The latter group tends to be over-represented by small size fractions which, for geometrical reasons, is presumed to give higher BET surface areas. Nevertheless, comparison of the results within the smaller size fraction cohort shows that fracture filling material in several cases gives up to ~100 times higher values than the lowest value obtained for intact rock in the smallest size fraction. From these results alone it can be deduced that the rock material in or adjacent to the fractures could, if sufficiently thick, constitute a non-negligible sink for retention of radionuclides in safety assessment. This would give enhanced retardation of radionuclide transport for early solute breakthrough compared to that achieved if only the unaltered rock matrix is considered.

BET surface area vs particle size

It is thought that crushing of samples can give rise to as much as 1–2 orders of magnitude increase in surface area as compared to undisturbed rock /e.g. Crawford et al. 2006/. Since sorption is strongly related to surface area, the additional surfaces created in the crushing process may give strongly biased overestimates of the sorption capacity of the rock. One of the main purposes of the BET surface area measurements was therefore to ascertain how much new surface area is created in the crushing process that is non-representative of the intact, in situ rock.

In the laboratory strategy document /Widestrand et al. 2003/ for the batch sorption experiment, it is suggested that if the largest size fraction of crushed rock has a surface area > 75% of that of the smallest fraction, then the creation of new surfaces during crushing can be assumed to be negligible. In this case, to avoid diffusive disequilibrium effects, it is recommended the smallest size fraction is used and the solute distribution coefficient (R_d) thus obtained used directly as the K_d for the in situ rock.

If, on the other hand, the BET-measurements show the surface area of the largest size fraction is < 75% of that measured for the smallest size fraction it can be concluded that a significant fraction of the surface area of the smaller fraction is created during the crushing of the rock material and the crushed rock is therefore not representative for the intact rock. In this case, the measured solute distribution coefficient is taken to be equal to the sum of the sorption on internal surfaces (deemed relevant for in situ conditions) and sorption on external particle surfaces (not representative of intact rock).

In order to differentiate between the sorption on internal and external surfaces, it was proposed that three different size fractions should be used for the batch sorption experiment (0.045–0.090 mm, 0.25–0.5 mm, 1–2 mm) and extrapolation of the results should be made in accordance with Equation 4-3.

As can be seen in Table 4-11 and Table 4-12, there is a clear and significant increase of the total specific surface area with decreasing particle size. It appears that the increase is proportionately greater for the crushed fresh rock material than for fracture coatings and altered rock material. The increase, however, is generally lower than what would be expected for ideally spherical shaped particles since a strictly geometrical model would yield an increase of the specific surface area by a factor of roughly 32 from the 2–4 mm size fraction to the 0.063–0.125 mm size fraction. For the non-altered quartz monzodiorite rock type (501036), for example, the increase in surface area is roughly a factor of 12 which could be regarded as an indication a significant fraction of sampled surface area in the larger size fraction being in the form of "inner surfaces".

When considering the comparatively large number of samples investigated belonging to the main rock type (e.g. 501036), a large variation is nevertheless observed. This observation concerns both the measured replicate values within the individual size fractions as well as for the ratios between the two measured size fractions. Provided that the BET surface measurement procedure gives reliable values, this could be an indication of a considerable heterogeneity even within what is identified as a single rock type. The large BET-surface area measured for the deformation zone structural elements could indicate that there is an influence of alteration on the BET surface area even at levels of alteration barely observable by visual inspection.

A comparative measurement campaign was performed in which the BET surface area of crushed material in the size fractions 0.063–0.125 mm, 2–4 mm and intact drill core samples of diameter 56 mm were compared. The results described in /Selnert et al. 2009b/ indicate that, given the uncertainties, a reasonable agreement is obtained for the larger size fraction, the intact drill core, and the inner surface area extrapolated from the data for each size fraction using Equation 4-7. It is noted, however, that there appears to be a relatively larger deviation for the quartz monzodiorite rock type (501036) where the BET surface area of intact drill core samples is less than the value corresponding to the largest crushed size fraction. From this finding it is postulated that (with the possible exception of rock type 510136) the sorption measured for the largest size fraction should give results that are most representative of the intact, in situ rock assuming that the measured sorption occurs upon inner surfaces of the mineral grains accessible by diffusion.

Table 4-11. Measured BET surface area (m^2/g) of crushed rock samples for the size fractions 0.063–0.125 mm and 2–4 mm. The arithmetic mean (± standard deviation), median, minimum, maximum values are given for the specified numbers (n) of samples involved in the study. The entries in the column labelled DZ identifies whether the corresponding rows of data are based upon deformation zone (DZ) materials or non-deformed host rock (N).

Rock type (SKB code)	DZ	Size fraction	Mean ±σ	Median	Min.	Max.	n
Fine-grained dioritoid (501030)	N	0.063–0.125 mm	0.57±0.27	0.53	0.14	0.93	16
	N	2–4 mm	0.048±0.032	0.043	7×10^{-4}	0.102	17
Diorite to gabbro (501033)	N	0.063–0.125 mm	0.44±0.05	0.44	0.39	0.49	4
	N	2–4 mm	0.032±0.025	0.030	8.8×10^{-3}	0.059	4
Quartz monzon-diorite (501036)	N	0.063–0.125 mm	0.48±0.30	0.35	0.088	1.081	20
	N	2–4 mm	0.036±0.028	0.029	2.4×10^{-3}	0.098	20
Ävrö granite (501044)	N	0.063–0.125 mm	1.12	n/a	1.116	1.121	2
	N	2–4 mm	0.062	n/a	0.0576	0.066	2
Ävrö quartz monzodiorite (501046)	N	0.063–0.125 mm	0.38±0.12	0.36	0.22	0.58	10
	N	2–4 mm	0.043±0.017	0.040	0.018	0.071	10
Ävrö granodiorite (501056)	N	0.063–0.125 mm	0.25±0.14	0.27	0.04	0.44	15
	N	2–4 mm	0.033±0.022	0.039	1×10^{-4}	0.066	14
Granite (501058)	N	0.063–0.125 mm	n/a	n/a	n/a	n/a	0
	N	2–4 mm	n/a	n/a	n/a	n/a	0
Pegmatite (501061)	N	0.063–0.125 mm	n/a	n/a	n/a	n/a	0
	N	2–4 mm	n/a	n/a	n/a	n/a	0
Fine-grained diorite-gabbro (505102)	N	0.063–0.125 mm	0.78	n/a	0.77	0.80	2
	N	2–4 mm	0.079	n/a	0.072	0.087	2
Fine-grained granite (511058)	N	0.063–0.125 mm	0.69±0.69	0.35	0.25	1.83	8
	N	2–4 mm	0.094±0.064	0.079	0.015	0.212	8

Notes: Entries given as “n/a” in the table signify data “not available”.

Table 4-12. Measured BET surface area (m^2/g) of mineral coatings associated with fracture types and deformation zone material. Data are given for the crushed rock size fractions < 0.125 mm and 2–4 mm where available. For material that is initially in a disaggregated state, only the smaller size fraction is given. The arithmetic mean (± standard deviation), median, minimum, maximum values are given for the specified numbers (n) of samples involved in the study.

Description	Size fraction	Mean ±σ	Median	Min.	Max.	n
Fracture type A	< 0.125 mm	15.2±9.0	15.0	2.8	23.9	5
	2–4 mm	16.3	n/a	n/a	n/a	1
Fracture type B	0.063–0.125 mm	6.5±2.1	7.3	3.4	8.1	4
	2–4 mm	2.6±1.3	3.0	1.2	3.7	3
Fracture type C	0.063–0.125 mm	12.6±10.9	7.9	2.6	33.5	6
	2–4 mm	7.5±9.9	1.9	1.8	19.0	3
Fracture type D	0.063–0.125 mm	n/a	n/a	n/a	n/a	0
	2–4 mm	n/a	n/a	n/a	n/a	0
Fracture type E	0.063–0.125 mm	2.23	n/a	1.96	2.50	2
	2–4 mm	n/a	n/a	n/a	n/a	0
Fracture type F	0.063–0.125 mm	24.1		23.5	24.8	2
	2–4 mm	n/a	n/a	n/a	n/a	0
Fracture type G	0.063–0.125 mm	n/a	n/a	n/a	n/a	0
	2–4 mm	n/a	n/a	n/a	n/a	0
DZ (Category 1) Fault rock/gouge	0.063–0.125 mm	24.1	n/a	24.1	24.2	2
	2–4 mm	9.8	n/a	n/a	n/a	1

Description	Size fraction	Mean ±σ	Median	Min.	Max.	n
DZ (Category 2) Vuggy rock	0.063–0.125 mm	7.89		7.88	7.89	2
	2–4 mm	n/a	n/a	n/a	n/a	0
DZ (Category 3) Chlorite/green gouge	0.063–0.125 mm	13.0	n/a	12.7	13.4	2
	2–4 mm	1.8	n/a	1.4	2.2	2
DZ (Category 4) Catclasite	0.063–0.125 mm	14.8±8.2	10.1	10.0	24.3	3
	2–4 mm	6.0	n/a	5.7	6.3	2
DZ (Category 5) Oxidised wall rock	0.063–0.125 mm	0.60	n/a	0.58	0.62	2
	2–4 mm	0.10	n/a	0.09	0.10	2

Notes: Entries given as “n/a” in the table signify data “not available”.

4.4.4 Sorption

The results for the sorption coefficients selected from the large database of measurement results reported in SICADA are presented in Table 4-13 to Table 4-26. Sorption coefficients are thus presented for the different groups of geological materials, sorted according to:

- Major rock types.
- Different fracture types.
- Five different deformation zone structural elements.

Some general comments can be made concerning the results:

Values are presented as R_d (m^3/kg) values in the material property tables (i.e. Table 4-13 to Table 4-26) although as K_d (m^3/kg) values in the subsequent retardation property tables (Table 4-28 to Table 4-41). The reason for this is to emphasise that the former are best estimate (or “apparent”) values for crushed materials which may, or may not be fully representative of in situ geological materials, whereas the latter have been taken to be conditionally representative of the in situ materials for transport modelling in the preliminary assessment presented in this report. Final selection of material property data for transport modelling, however, will be performed at a later time as part of the SR-Site safety assessment.

For the Sr(II) tracer, the sorption loss from the aqueous phase can only be statistically verified for the fresh groundwater (with a few exceptions). For the other groundwater types, the high salinity promotes a strong competition for the sorption sites, giving very low adsorption. This can be seen in the minimum values which can include negative values, indicating that the sorptive effect is smaller than the standard deviation of the measurement for the blank solution.

Similarly to Sr(II), the sorption behaviour of both Ra(II) and Cs(I) was strongly influenced by the water composition. This is to be expected from their ion exchange behaviour, which results in decreasing sorptivity with increasing salinity owing to competition for sorption sites.

In the laboratory programme, Am(III) and in some cases Eu(III) were used as model substances to simulate the sorption of the trivalent actinides and lanthanides which are loosely referred to in this report as Ac-Ln(III) (this abbreviation should not be taken to specifically mean either actinium or lanthanum). These substances were found to sorb very strongly. Even in the blank sample for groundwater without any geological material present, a strong loss of the tracer can be observed which is thought to be the result of adsorption on test tube walls or possibly the formation of so-called “intrinsic” colloids (i.e. microprecipitation of hydrolysed solute species in suspension). Thorough investigations of these samples have, however, shown that in samples with rock material present, the amount of tracer associated the test tube walls is negligible compared to the sorption on the rock material.

Salinity does not appear to strongly influence the sorption of the trivalent Ac-Ln(III) tracer, the redox sensitive elements U and Np, nor Ni(II). This is expected behaviour since the major sorption mechanism for these tracers is thought to be surface complexation rather than cation exchange.

The sorption of the redox sensitive elements Np and U is comparatively low indicating the presence of the oxidized Np(V) and U(VI) species, respectively. For some of the measurements, a pronounced increase of the sorption can be found for the smallest size fraction. The increase is much higher than what should be expected from the relative BET surface areas of the different size fractions. A possible explanation for this is that minerals having enhanced reducing capacity have been enriched in the smaller size fraction during the crushing and sieving process. It is also possible that the increased surface area of the small particle size fraction results in increased rate of weathering reactions involving Fe(II)-containing silicate minerals. These processes could result in the reduction of Np and U species to Np(IV) and U(IV) in these samples. Since the redox status is not well known for these solutes in the batch sorption experiments, they are listed in the data Tables as Np(IV/V) and U(IV/VI) to make this uncertainty clear to the reader.

The time dependence of tracer loss in the aqueous phase can, in a number of cases, be potentially interpreted as the result of solute diffusion within the internal microporosity of the crushed particles. The magnitude of the tracer loss time dependency is partially consistent with a spherical diffusion model /Crank 1975/ assuming effective diffusivities similar to those predicted for the rock matrix. There are, however, additional uncertainties in the data analysis which makes this interpretation speculative. The different processes which may contribute to the apparent time dependency of solute uptake will be examined in more detail during the selection of data for SR-site.

Sorption properties of specific rock types

Table 4-13. Measured sorption coefficients, R_d (m^3/kg) for rock type 501036 (unaltered) based upon the 1–2 mm size fraction and a contact time of 180 days. The arithmetic mean (± standard deviation), median, minimum, maximum values are given for the specified numbers (n) of samples involved in the study.

Solute		Groundwater type				
		Marine	Type V	Saline	Fresh	Brine
Cs(I)	mean±σ	n/a	$(6.1\pm1.1)\times10^{-2}$	$(2.4\pm1.8)\times10^{-2}$	0.15±0.13	$(4.9\pm0.44)\times10^{-3}$
	median	n/a	6.2×10^{-2}	1.6×10^{-2}	0.14	4.7×10^{-3}
	min.	n/a	4.8×10^{-2}	7.7×10^{-3}	3.1×10^{-2}	4.6×10^{-3}
	max.	n/a	7.1×10^{-2}	4.4×10^{-2}	0.3	5.4×10^{-3}
	n	0	3	7	6	3
Sr(II)	mean±σ	n/a	$(3.1\pm1.1)\times10^{-3}$	$(2.9\pm1.7)\times10^{-3}$	$(2.5\pm0.72)\times10^{-2}$	$(-4.1\pm4.9)\times10^{-4}$
	median	n/a	2.6×10^{-3}	3.6×10^{-3}	2.6×10^{-2}	-6.4×10^{-4}
	min.	n/a	2.3×10^{-3}	-4.9×10^{-4}	1.7×10^{-2}	-7.4×10^{-4}
	max.	n/a	4.3×10^{-3}	4.5×10^{-3}	3.6×10^{-2}	1.5×10^{-4}
	n	0	3	7	6	3
Ln-Ac(III)	mean±σ	n/a	1.2±0.23	1.4±0.76	0.17±0.066	0.41±0.072
	median	n/a	1.1	1.1	0.18	4.5×10^{-1}
	min.	n/a	1.0	0.33	8.4×10^{-2}	3.3×10^{-1}
	max.	n/a	1.4	2.6	0.25	4.6×10^{-1}
	n	0	3	7	6	3
Ra(II)	mean±σ	n/a	n/a	$(7.7\pm0.39)\times10^{-3}$	0.24±0.0093	n/a
	median	n/a	n/a	7.8×10^{-3}	0.24	n/a
	min.	n/a	n/a	7.3×10^{-3}	0.23	n/a
	max.	n/a	n/a	8.1×10^{-3}	0.25	n/a
	n	0	0	3	3	0
Ni(II)	mean±σ	n/a	n/a	$(8.4\pm0.73)\times10^{-2}$	0.35±0.03	n/a
	median	n/a	n/a	8.3×10^{-2}	0.34	n/a
	min.	n/a	n/a	7.7×10^{-2}	0.32	n/a
	max.	n/a	n/a	9.1×10^{-2}	0.38	n/a
	n	0	0	3	3	0
Np(IV/V)	mean±σ	n/a	n/a	$(3.8\pm0.24)\times10^{-3}$	$(5.5\pm0.78)\times10^{-3}$	n/a
	median	n/a	n/a	2.7×10^{-3}	6.0×10^{-3}	n/a
	min.	n/a	n/a	2.7×10^{-3}	4.6×10^{-3}	n/a
	max.	n/a	n/a	4.1×10^{-3}	6.0×10^{-3}	n/a
	n	0	0	3	3	0

Solute		Groundwater type				
		Marine	Type V	Saline	Fresh	Brine
U(IV/VI)	mean±σ	n/a	n/a	$(1.2\pm0.16)\times10^{-2}$	$(5.0\pm0.78)\times10^{-3}$	n/a
	median	n/a	n/a	1.2×10^{-2}	5.4×10^{-3}	n/a
	min.	n/a	n/a	1.1×10^{-2}	4.1×10^{-3}	n/a
	max.	n/a	n/a	1.4×10^{-2}	5.5×10^{-3}	n/a
	n	0	0	3	3	0

Notes: Entries given as “n/a” in the table signify data “not available”.

Table 4-14. Measured sorption coefficients, R_d (m^3/kg) for rock type 501046 (unaltered) based upon the 1–2 mm size fraction and a contact time of 180 days. The arithmetic mean (± standard deviation), median, minimum, maximum values are given for the specified numbers (n) of samples involved in the study.

Solute		Groundwater type				
		Marine	Type V	Saline	Fresh	Brine
Cs(I)	mean±σ	n/a	$(3.3\pm0.33)\times10^{-2}$	$(2.9\pm0.27)\times10^{-2}$	0.16±0.0031	n/a
	median	n/a	3.3×10^{-2}	2.9×10^{-2}	0.16	n/a
	min.	n/a	3.0×10^{-2}	2.6×10^{-2}	0.16	n/a
	max.	n/a	3.7×10^{-2}	3.2×10^{-2}	0.17	n/a
	n	0	3	3	3	0
Sr(II)	mean±σ	n/a	$(3.7\pm0.86)\times10^{-3}$	$(2.6\pm0.7)\times10^{-4}$	$(1.9\pm0.16)\times10^{-2}$	n/a
	median	n/a	3.4×10^{-3}	2.5×10^{-3}	1.9×10^{-2}	n/a
	min.	n/a	3.0×10^{-3}	1.9×10^{-3}	1.7×10^{-2}	n/a
	max.	n/a	4.7×10^{-3}	3.3×10^{-3}	2.0×10^{-2}	n/a
	n	0	3	3	3	0
Ln-Ac(III)	mean±σ	n/a	1.1±0.47	1.5±0.31	0.15±0.006	n/a
	median	n/a	1.3	1.4	0.14	n/a
	min.	n/a	0.52	1.3	0.14	n/a
	max.	n/a	1.4	1.9	0.15	n/a
	n	0	3	3	3	0
Ra(II)	mean±σ	n/a	$(4.0\pm0.53)\times10^{-2}$	$(8.1\pm1.9)\times10^{-3}$	0.16±0.024	n/a
	median	n/a	3.8×10^{-2}	7.7×10^{-3}	0.15	n/a
	min.	n/a	3.7×10^{-2}	6.5×10^{-3}	0.14	n/a
	max.	n/a	4.7×10^{-2}	1.0×10^{-2}	0.19	n/a
	n	0	3	3	3	0
Ni(II)	mean±σ	n/a	$(5.7\pm0.18)\times10^{-2}$	$(6.6\pm0.42)\times10^{-2}$	0.37±0.066	n/a
	median	n/a	5.7×10^{-2}	6.6×10^{-2}	0.40	n/a
	min.	n/a	5.5×10^{-2}	6.1×10^{-2}	0.29	n/a
	max.	n/a	5.9×10^{-2}	6.9×10^{-2}	0.41	n/a
	n	0	3	3	3	0
Np(IV/V)	mean±σ	n/a	$(-1.7\pm2.4)\times10^{-4}$	$(3.8\pm0.24)\times10^{-3}$	$(3.3\pm0.024)\times10^{-3}$	n/a
	median	n/a	-1.8×10^{-4}	3.7×10^{-3}	3.3×10^{-3}	n/a
	min.	n/a	-4.0×10^{-4}	3.7×10^{-3}	3.3×10^{-3}	n/a
	max.	n/a	8.2×10^{-4}	4.1×10^{-3}	3.4×10^{-3}	n/a
	n	0	3	3	3	0
U(IV/VI)	mean±σ	n/a	$(3.5\pm0.29)\times10^{-3}$	$(4.0\pm0.23)\times10^{-3}$	$(2.9\pm0.043)\times10^{-3}$	n/a
	median	n/a	3.5×10^{-3}	3.9×10^{-3}	2.9×10^{-3}	n/a
	min.	n/a	3.3×10^{-3}	3.8×10^{-3}	2.8×10^{-3}	n/a
	max.	n/a	3.8×10^{-3}	4.3×10^{-3}	2.9×10^{-3}	n/a
	n	0	3	3	3	0

Notes: Entries given as “n/a” in the table signify data “not available”.

Table 4-15. Measured sorption coefficients, R_d (m^3/kg) for rock type 501030 (unaltered) based upon the 1–2 mm size fraction and a contact time of 180 days. The arithmetic mean (± standard deviation), median, minimum, maximum values are given for the specified numbers (n) of samples involved in the study.

Solute		Groundwater type				
		Marine	Type V	Saline	Fresh	Brine
Cs(I)	mean±σ	n/a	n/a	$(3.4\pm1.6)\times10^{-2}$	0.25±0.098	n/a
	median	n/a	n/a	4.2×10^{-2}	0.25	n/a
	min.	n/a	n/a	1.0×10^{-2}	0.25	n/a
	max.	n/a	n/a	4.3×10^{-2}	0.26	n/a
	n	0	0	4	3	0
Sr(II)	mean±σ	n/a	n/a	$(3.0\pm2.2)\times10^{-3}$	$(3.0\pm0.94)\times10^{-2}$	n/a
	median	n/a	n/a	4.0×10^{-3}	3.4×10^{-2}	n/a
	min.	n/a	n/a	-3.2×10^{-4}	1.9×10^{-2}	n/a
	max.	n/a	n/a	4.3×10^{-3}	3.6×10^{-2}	n/a
	n	0	0	4	3	0
Ln-Ac(III)	mean±σ	n/a	n/a	0.83±0.46	0.12±0.017	n/a
	median	n/a	n/a	0.14	0.12	n/a
	min.	n/a	n/a	8.3×10–2	0.11	n/a
	max.	n/a	n/a	0.28	0.14	n/a
	n	0	0	4	3	0

Notes: Entries given as “n/a” in the table signify data “not available”.

Table 4-16. Measured sorption coefficients, R_d (m^3/kg) for rock type 501056 (unaltered) based upon the 1–2 mm size fraction and a contact time of 180 days. The arithmetic mean (± standard deviation), median, minimum, maximum values are given for the specified numbers (n) of samples involved in the study.

Solute		Groundwater type				
		Marine	Type V	Saline	Fresh	Brine
Cs(I)	mean±σ	(1.3±0.14)×10–3	$(2.5\pm0.16)\times10^{-2}$	$(5.5\pm1.1)\times10^{-3}$	(5.3±3.9)×10–2	$(5.9\pm4.4)\times10^{-3}$
	median	1.3×10–2	2.6×10^{-2}	5.7×10^{-3}	3.5×10–2	5.1×10^{-3}
	min.	1.1×10–2	2.3×10^{-2}	4.0×10^{-3}	2.2×10^{-2}	2.0×10^{-3}
	max.	1.3×10–2	2.6×10^{-2}	6.8×10^{-3}	0.12	1.3×10^{-2}
	n	3	3	6	9	6
Sr(II)	mean±σ	(3.3±0.7)×10–3	$(3.7\pm0.26)\times10^{-3}$	$(3.9\pm7.2)\times10^{-4}$	$(1.3\pm0.89)\times10^{-2}$	$(1.5\pm2.0)\times10^{-3}$
	median	3.3×10–3	3.5×10^{-3}	3.1×10^{-4}	8.2×10^{-2}	1.1×10^{-3}
	min.	2.6×10–3	3.5×10^{-3}	-5.5×10^{-4}	7.0×10^{-3}	-1.9×10^{-4}
	max.	4.0×10–3	4.0×10^{-3}	1.7×10^{-4}	2.8×10^{-2}	5.0×10^{-3}
	n	3	3	6	8	6
Ln-Ac(III)	mean±σ	1.0±0.25	1.0±0.19	0.34±0.11	0.22±0.036	0.34±0.31
	median	0.95	1.1	0.31	0.22	0.30
	min.	0.85	0.88	0.19	0.15	5.5×10^{-2}
	max.	1.3	1.2	0.48	0.28	0.74
	n	3	3	6	9	6

Notes: Entries given as “n/a” in the table signify data “not available”.

Table 4-17. Measured sorption coefficients, R_d (m^3/kg) for rock type 511058 (unaltered) based upon the 1–2 mm size fraction and a contact time of 180 days. The arithmetic mean (± standard deviation), median, minimum, maximum values are given for the specified numbers (n) of samples involved in the study.

Solute		Groundwater type				
		Marine	Type V	Saline	Fresh	Brine
Cs(I)	mean±σ	n/a	n/a	$(1.4\pm0.053)\times10^{-2}$	(9.8±0.93)×10–2	n/a
	median	n/a	n/a	1.3×10^{-2}	9.7×10–2	n/a
	min.	n/a	n/a	1.3×10^{-2}	9.0×10^{-2}	n/a
	max.	n/a	n/a	1.4×10^{-2}	0.11	n/a
	n	0	0	3	3	0
Sr(II)	mean±σ	n/a	n/a	$(3.2\pm0.26)\times10^{-3}$	$(2.3\pm0.17)\times10^{-2}$	n/a
	median	n/a	n/a	3.2×10^{-3}	2.3×10^{-2}	n/a
	min.	n/a	n/a	3.0×10^{-3}	2.1×10^{-2}	n/a
	max.	n/a	n/a	3.5×10^{-3}	2.4×10^{-2}	n/a
	n	0	0	3	3	0
Ln-Ac(III)	mean±σ	n/a	n/a	0.82±0.16	0.11±0.023	n/a
	median	n/a	n/a	0.77	0.12	n/a
	min.	n/a	n/a	0.69	8.3×10^{-2}	n/a
	max.	n/a	n/a	1.0	0.13	n/a
	n	0	0	3	3	0

Notes: Entries given as “n/a” in the table signify data “not available”.

Sorption properties of fracture types

In the following tables the sorption properties for surface coating minerals associated with different fracture types are presented. Measurement data are available for all fracture types with the exception of fracture types D (Laumontite ±calcite ±chlorite), E (chlorite ±calcite), and G (chlorite ±other) owing to the difficulty of obtaining sufficient quantity of representative samples using the surface abrasion technique in these particular cases. The sorptive properties of fracture type H (no mineral coating) is taken to be the same as the unaltered rock in which the fracture is hosted.

Table 4-18. Measured sorption coefficients, R_d (m^3/kg) for fracture coating materials associated with Fracture Type A (KLX03A 457.4 m). Data are based upon the < 0.125 mm size fraction and a contact time of 180 days. The arithmetic mean (± standard deviation), median, minimum, maximum values are given for the specified numbers (n) of samples involved in the study.

Solute		Groundwater type				
		Marine	Type V	Saline	Fresh	Brine
Cs(I)	mean±σ	n/a	n/a	n/a	3.2	n/a
	median	n/a	n/a	n/a	n/a	n/a
	min.	n/a	n/a	n/a	3.1	n/a
	max.	n/a	n/a	n/a	3.3	n/a
	n	0	0	0	2	0
Sr(II)	mean±σ	n/a	n/a	n/a	0.16	n/a
	median	n/a	n/a	n/a	n/a	n/a
	min.	n/a	n/a	n/a	0.16	n/a
	max.	n/a	n/a	n/a	0.17	n/a
	n	0	0	0	2	0
Ln-Ac(III)	mean±σ	n/a	n/a	6.6	0.88±0.16	n/a
	median	n/a	n/a	n/a	n/a	n/a
	min.	n/a	n/a	5.6	n/a	n/a
	max.	n/a	n/a	7.6	n/a	n/a
	n	0	0	2	1	0

Notes: Entries given as “n/a” in the table signify data “not available” for single measurements, uncertainty is given as an estimate based on radiometric counting statistics.

Table 4-19. Measured sorption coefficients, R_d (m^3/kg) for fracture coating materials associated with Fracture Type B (KLX04A 951.3 m, KLX11A 509.3 m). Data are based upon the < 0.125 mm size fraction and a contact time of 180 days. The arithmetic mean (± standard deviation), median, minimum, maximum values are given for the specified numbers (n) of samples involved in the study.

Solute		Groundwater type				
		Marine	Type V	Saline	Fresh	Brine
Cs(I)	mean±σ	n/a	n/a	$(2.9\pm2.0)\times10^{-2}$	0.26±0.00723	$(1.6\pm0.009)\times10^{-2}$
	median	n/a	n/a	2.9×10^{-2}	0.26	1.6×10^{-2}
	min.	n/a	n/a	1.1×10^{-2}	0.26	1.6×10^{-2}
	max.	n/a	n/a	4.8×10^{-2}	0.27	1.6×10^{-2}
	n	0	0	6	3	3
Sr(II)	mean±σ	n/a	n/a	$(9.6\pm8.8)\times10^{-4}$	0.11±0.078	$(1.7\pm0.49)\times10^{-4}$
	median	n/a	n/a	8.8×10^{-4}	7.7×10^{-2}	2.0×10^{-4}
	min.	n/a	n/a	1.4×10^{-4}	6.2×10^{-2}	1.2×10^{-4}
	max.	n/a	n/a	2.0×10^{-3}	0.2	2.1×10^{-4}
	n	0	0	6	3	3
Ln-Ac(III)	mean±σ	n/a	n/a	1.3±0.54	0.34±0.13	0.13±0.0075
	median	n/a	n/a	1.2	0.39	0.13
	min.	n/a	n/a	0.5	0.19	0.12
	max.	n/a	n/a	1.9	0.43	0.14
	n	0	0	6	3	3

Notes: Entries given as “n/a” in the table signify data “not available”.

Table 4-20. Measured sorption coefficients, R_d (m^3/kg) for fracture coating materials associated with Fracture Type C (KSH02, 578.2 m; KLX04A, 874.5 m; KLX07A, 620.9 m). Data are based upon the < 0.125 mm size fraction and a contact time of 180 days. The arithmetic mean (± standard deviation), median, minimum, maximum values are given for the specified numbers (n) of samples involved in the study.

Solute		Groundwater type				
		Marine	Type V	Saline	Fresh	Brine
Cs(I)	mean±σ	n/a	n/a	0.19±0.18	0.35±0.05	1.1×10^{-2}
	median	n/a	n/a	0.18	0.34	n/a
	min.	n/a	n/a	2.4×10^{-2}	0.30	1.1×10^{-2}
	max.	n/a	n/a	0.39	0.41	1.2×10^{-2}
	n	0	0	6	5	2
Sr(II)	mean±σ	n/a	n/a	$(1.7\pm0.062)\times10^{-3}$	0.38±0.15	7.4×10^{-4}
	median	n/a	n/a	1.6×10^{-3}	0.39	n/a
	min.	n/a	n/a	1.6×10^{-3}	0.16	6.2×10^{-4}
	max.	n/a	n/a	1.7×10^{-3}	0.55	8.7×10^{-4}
	n	0	0	3	5	2
Ln-Ac(III)	mean±σ	n/a	n/a	0.93±0.96	0.38±0.43	0.56
	median	n/a	n/a	0.76	7.5×10–2	n/a
	min.	n/a	n/a	0.05	6.1×10^{-2}	0.44
	max.	n/a	n/a	2.2	0.87	0.67
	n	0	0	6	5	2

Notes: Entries given as “n/a” in the table signify data “not available”.

Table 4-21. Measured sorption coefficients, R_d (m^3/kg) for fracture coating materials associated with Fracture Type F (KLX03A 278.3 m). Data are based upon the < 0.125 mm size fraction and a contact time of 180 days. The arithmetic mean (± standard deviation), median, minimum, maximum values are given for the specified numbers (n) of samples involved in the study.

Solute		Groundwater type				
		Marine	Type V	Saline	Fresh	Brine
Cs(I)	mean±σ	n/a	n/a	3.0±1.5	3.2±0.47	n/a
	median	n/a	n/a	n/a	n/a	n/a
	min.	n/a	n/a	n/a	n/a	n/a
	max.	n/a	n/a	n/a	n/a	n/a
	n	0	0	1	1	0
Sr(II)	mean±σ	n/a	n/a	$(3.3\pm0.97)\times10^{-3}$	0.16±0.022	n/a
	median	n/a	n/a	n/a	n/a	n/a
	min.	n/a	n/a	n/a	n/a	n/a
	max.	n/a	n/a	n/a	n/a	n/a
	n	0	0	1	1	0
Ln-Ac(III)	mean±σ	n/a	n/a	9.3±1.9	1.2±0.22	n/a
	median	n/a	n/a	n/a	n/a	n/a
	min.	n/a	n/a	n/a	n/a	n/a
	max.	n/a	n/a	n/a	n/a	n/a
	n	0	0	1	1	0

Notes: Entries given as “n/a” in the table signify data “not available” for single measurements, uncertainty is given as an estimate based on radiometric counting statistics.

Sorption properties of deformation zone materials

In the following tables the sorption properties of different deformation zone materials are presented. Measurement data are available for deformation zone structural elements corresponding to Fault rock (1), Chlorite (2), Vuggy rock (3), Cataclasite (4), and Oxidised wall rock (5).

Table 4-22. Measured sorption coefficients, R_d (m^3/kg) for Category 1 (Fault rock) material associated with deformation zones (KLX06A, 384 m). Data are based upon the 1–2 mm size fraction and a contact time of 180 days. The arithmetic mean (± standard deviation), median, minimum, maximum values are given for the specified numbers (n) of samples involved in the study.

Solute		Groundwater type				
		Marine	Type V	Saline	Fresh	Brine
Cs(I)	mean±σ	n/a	n/a	0.6±0.027	5.1	n/a
	median	n/a	n/a	0.59	n/a	n/a
	min.	n/a	n/a	0.58	4.8	n/a
	max.	n/a	n/a	0.63	5.5	n/a
	n	0	0	3	2	0
Sr(II)	mean±σ	n/a	n/a	$(1.8\pm0.053)\times10^{-3}$	0.14	n/a
	median	n/a	n/a	1.8×10^{-3}	n/a	n/a
	min.	n/a	n/a	1.7×10^{-3}	9.6×10^{-2}	n/a
	max.	n/a	n/a	1.8×10^{-3}	0.19	n/a
	n	0	0	3	2	0
Ln-Ac(III)	mean±σ	n/a	n/a	2.6±1.7	2.5	n/a
	median	n/a	n/a	1.7	n/a	n/a
	min.	n/a	n/a	1.5	2.3	n/a
	max.	n/a	n/a	4.5	2.7	n/a
	n	0	0	3	2	0

Notes: Entries given as “n/a” in the table signify data “not available”.

Table 4-23. Measured sorption coefficients, R_d (m^3/kg) for Category 2 (Chlorite) material associated with deformation zones (KLX03A 732.6 m). Data are based upon the < 0.125 mm size fraction and a contact time of 180 days. The arithmetic mean (± standard deviation), median, minimum, maximum values are given for the specified numbers (n) of samples involved in the study.

Solute		Groundwater type				
		Marine	Type V	Saline	Fresh	Brine
Cs(I)	mean±σ	n/a	n/a	$(1.7\pm0.14)\times10^{-2}$	0.4±0.082	n/a
	median	n/a	n/a	n/a	n/a	n/a
	min.	n/a	n/a	n/a	n/a	n/a
	max.	n/a	n/a	n/a	n/a	n/a
	n	0	0	1	1	0
Sr(II)	mean±σ	n/a	n/a	$(5.1\pm2.3)\times10^{-3}$	$(3.8\pm0.46)\times10^{-2}$	n/a
	median	n/a	n/a	n/a	n/a	n/a
	min.	n/a	n/a	n/a	n/a	n/a
	max.	n/a	n/a	n/a	n/a	n/a
	n	0	0	1	1	0
Ln-Ac(III)	mean±σ	n/a	n/a	9.5±2.7	1.2±0.34	n/a
	median	n/a	n/a	n/a	n/a	n/a
	min.	n/a	n/a	n/a	n/a	n/a
	max.	n/a	n/a	n/a	n/a	n/a
	n	0	0	1	1	0
Ra(II)	mean±σ	n/a	n/a	$(2.9\pm0.29)\times10^{-2}$	1.7±0.20	n/a
	median	n/a	n/a	n/a	n/a	n/a
	min.	n/a	n/a	n/a	n/a	n/a
	max.	n/a	n/a	n/a	n/a	n/a
	n	0	0	1	1	0
Ni(II)	mean±σ	n/a	n/a	1.2±0.52	1.0±0.48	n/a
	median	n/a	n/a	n/a	n/a	n/a
	min.	n/a	n/a	n/a	n/a	n/a
	max.	n/a	n/a	n/a	n/a	n/a
	n	0	0	1	1	0
Np(V/VI)	mean±σ	n/a	n/a	$(4.7\pm0.72)\times10^{-3}$	0.21±0.0078	n/a
	median	n/a	n/a	n/a	n/a	n/a
	min.	n/a	n/a	n/a	n/a	n/a
	max.	n/a	n/a	n/a	n/a	n/a
	n	0	0	1	1	0
U(IV/VI)	mean±σ	n/a	n/a	3.5±0.27	$(4.0\pm0.18)\times10^{-2}$	n/a
	median	n/a	n/a	n/a	n/a	n/a
	min.	n/a	n/a	n/a	n/a	n/a
	max.	n/a	n/a	n/a	n/a	n/a
	n	0	0	1	1	0

Notes: Entries given as “n/a” in the table signify data “not available” for single measurements, uncertainty is given as an estimate based on radiometric counting statistics.

Table 4-24. Measured sorption coefficients, R_d (m^3/kg) for Category 3 (vuggy rock) material associated with deformation zones (KSH03A 164.8 m). Data are based upon the 1–2 mm size fraction and a contact time of 180 days. The arithmetic mean (± standard deviation), median, minimum, maximum values are given for the specified numbers (n) of samples involved in the study.

Solute		Groundwater type				
		Marine	Type V	Saline	Fresh	Brine
Cs(I)	mean±σ	n/a	n/a	0.12±0.032	0.69±0.13	n/a
	median	n/a	n/a	0.13	0.65	n/a
	min.	n/a	n/a	9.1×10^{-2}	0.58	n/a
	max.	n/a	n/a	0.15	0.83	n/a
	n	0	0	3	3	0
Sr(II)	mean±σ	n/a	n/a	$(3.9\pm1.0)\times10^{-3}$	$(6.5\pm0.13)\times10^{-2}$	n/a
	median	n/a	n/a	3.5×10^{-3}	6.5×10^{-2}	n/a
	min.	n/a	n/a	3.1×10^{-3}	6.4×10^{-2}	n/a
	max.	n/a	n/a	5.0×10^{-3}	6.7×10^{-2}	n/a
	n	0	0	3	3	0
Ln-Ac(III)	mean±σ	n/a	n/a	1.3±1.1	0.52±0.095	n/a
	median	n/a	n/a	0.85	0.53	n/a
	min.	n/a	n/a	0.54	0.42	n/a
	max.	n/a	n/a	2.5	0.61	n/a
	n	0	0	3	3	0

Notes: Entries given as “n/a” in the table signify data “not available”.

Table 4-25. Measured sorption coefficients, R_d (m^3/kg) for Category 4 (Cataclasite) material associated with deformation zones (KSH02 397.4 m). Data are based upon the 0.063–0.125 mm size fraction and a contact time of 180 days. The arithmetic mean (± standard deviation), median, minimum, maximum values are given for the specified numbers (n) of samples involved in the study.

Solute		Groundwater type				
		Marine	Type V	Saline	Fresh	Brine
Cs(I)	mean±σ	n/a	n/a	$(8.5\pm0.76)\times10^{-2}$	0.76±0.19	n/a
	median	n/a	n/a	n/a	n/a	n/a
	min.	n/a	n/a	n/a	n/a	n/a
	max.	n/a	n/a	n/a	n/a	n/a
	n	0	0	1	1	0
Sr(II)	mean±σ	n/a	n/a	$(1.0\pm0.37)\times10^{-2}$	$(3.3\pm0.4)\times10^{-2}$	n/a
	median	n/a	n/a	n/a	n/a	n/a
	min.	n/a	n/a	n/a	n/a	n/a
	max.	n/a	n/a	n/a	n/a	n/a
	n	0	0	1	1	0
Ln-Ac(III)	mean±σ	n/a	n/a	5.6±1.0	0.44±0.081	n/a
	median	n/a	n/a	n/a	n/a	n/a
	min.	n/a	n/a	n/a	n/a	n/a
	max.	n/a	n/a	n/a	n/a	n/a
	n	0	0	1	1	0
Ra(II)	mean±σ	n/a	n/a	0.19±0.021	1.9±1.1	n/a
	median	n/a	n/a	n/a	n/a	n/a
	min.	n/a	n/a	n/a	n/a	n/a
	max.	n/a	n/a	n/a	n/a	n/a
	n	0	0	1	1	0
Ni(II)	mean±σ	n/a	n/a	0.52±0.11	0.9±0.5	n/a
	median	n/a	n/a	n/a	n/a	n/a
	min.	n/a	n/a	n/a	n/a	n/a
	max.	n/a	n/a	n/a	n/a	n/a
	n	0	0	1	1	0

Solute		Groundwater type				
		Marine	Type V	Saline	Fresh	Brine
Np(V/VI)	mean±σ	n/a	n/a	(8.1±1.2)×10^{-2}	0.23±0.0085	n/a
	median	n/a	n/a	n/a	n/a	n/a
	min.	n/a	n/a	n/a	n/a	n/a
	max.	n/a	n/a	n/a	n/a	n/a
	n	0	0	1	1	0
U(IV/VI)	mean±σ	n/a	n/a	5.8±0.44	(5.9±0.26)×10^{-3}	n/a
	median	n/a	n/a	n/a	n/a	n/a
	min.	n/a	n/a	n/a	n/a	n/a
	max.	n/a	n/a	n/a	n/a	n/a
	n	0	0	1	1	0

Notes: Entries given as “n/a” in the table signify data “not available” for single measurements, uncertainty is given as an estimate based on radiometric counting statistics.

Table 4-26. Measured sorption coefficients, R_d (m^3/kg) for Category 5 (Strongly oxidised wall rock) material associated with deformation zones (KSH03A 164.8 m). Data are based upon the 1–2 mm size fraction and a contact time of 180 days. The arithmetic mean (± standard deviation), median, minimum, maximum values are given for the specified numbers (n) of samples involved in the study.

Solute		Groundwater type				
		Marine	Type V	Saline	Fresh	Brine
Cs(I)	mean±σ	n/a	(1.1±0.1)×10^{-2}	(1.7±0.13)×10^{-3}	n/a	(4.9±1.6)×10^{-4}
	median	n/a	1.1×10^{-2}	1.7×10^{-3}	n/a	5.6×10^{-4}
	min.	n/a	1.0×10^{-2}	1.6×10^{-3}	n/a	3.1×10^{-4}
	max.	n/a	1.2×10^{-2}	1.9×10^{-3}	n/a	6.0×10^{-4}
	n	0	3	3	0	3
Sr(II)	mean±σ	n/a	(4.0±0.53)×10^{-3}	(–3.3±62)×10^{-5}	n/a	(–5.3±27)×10^{-5}
	median	n/a	4.0×10^{-3}	–9.8×10^{-5}	n/a	–5.2×10^{-5}
	min.	n/a	3.4×10^{-3}	–6.1×10^{-4}	n/a	–3.2×10^{-4}
	max.	n/a	4.5×10^{-3}	6.1×10^{-4}	n/a	2.2×10^{-4}
	n	0	3	3	0	3
Ln-Ac(III)	mean±σ	n/a	1.8±0.37	0.17±0.03	n/a	0.26±0.016
	median	n/a	1.9	0.17	n/a	0.27
	min.	n/a	1.3	0.14	n/a	0.25
	max.	n/a	1.9	0.2	n/a	0.27
	n	0	3	3	0	3

Notes: Entries given as “n/a” in the table signify data “not available”.

4.4.5 Confirmatory studies of sorption

The retention data used in this model could be considered to be affected by significant uncertainties owing to the fact that the major mechanisms for radionuclide retention (i.e. diffusive uptake to the rock matrix and adsorption) are not studied interactively and are mainly addressed using crushed samples of geologic material. For partial validation of the material properties assessment it would be advantageous to be able to see if the retention parameters determined on a very small scale can be used to correctly predict radionuclide retention on larger scales.

To this end, two sets of experiments were conducted where the retention properties of intact drill core samples have been assessed.

- Studies of diffusive uptake and radionuclide sorption within intact drill cores;
- Studies of Cs(I) sorption using an electromigration technique to hasten diffusive/sorptive equilibration of the rock matrix pore space.

Generally, the results obtained in these studies confirm the understanding of retention processes which form the basis of the retardation models described in this chapter. On balance, and considering the uncertainties already addressed in the sections describing the diffusivity and sorption data, no indications of any severe deviation of the data or evidence to contradict the conceptual model of sorption can be identified at least for the spatial scales investigated. Full details concerning these complementary investigations can be found the Retardation model background report /Selnert et al. 2009b/.

4.5 Retardation model

In accordance with the general concept proposed by /Widestrand et al. 2003/, the site descriptive retardation model described in this chapter consists of tables in which the geological description is combined with selected transport parameters for each geological entity (i.e. the different geological structures where retardation of radionuclides can take place) in a fashion which allows direct application within transport models.

It is noted that the proposed conceptual model described by /Widestrand et al. 2003/ implies a description of retardation occurring in fractures where discrete layers of altered material surround the fracture. It is also implicitly assumed that these layers are of a sufficient thickness that it should be possible to take samples and make laboratory determinations of, for example, diffusivity and sorption. In general, the Laxemar site is characterised by fractures with partially cohesive fracture coatings of variable thickness and visible alteration of the wall rock.

The resulting retardation model description developed for SDM-Site Laxemar consists of three sections dealing with the major rock types, specific fracture types, and deformation zone structural elements, respectively.

The description of fracture types considers the material properties of the fracture coatings themselves as well as additional information concerning, for example, typical depths of hydrothermally altered material surrounding the fracture surfaces. Since the fractures can be hosted within different rock types (and are not necessarily specific to any given rock type), the transport properties of the fracture itself must be combined with the transport properties of the underlying rock matrix to give a full description of the transport properties of potential flowpaths through the rock comprising the HRD.

For deformation zones, the rock interspersed between the flow bearing fractures may consist of unusual fabrics and microstructures, which are not present to a great extent in the HRD. A number of typical deformation zone structural elements have therefore been described to account for differences in material properties between the rock encountered in the HRD and HCD. For the deterministic deformation zones comprising the HCD, the description of fracture types can be combined with that of the deformation zone specific materials to give a full description of transport properties of flowpaths within the HCD (noting that the fracture types are hosted in the deformation zone structural elements rather than in the unaltered rock types more common to the HRD).

In the first of the following sections (4.5.1), the prevalence of the major rock types and their “best estimate” material properties are described. The second section (4.6.2) provides a description of the retention properties of water-conducting fractures while in the third section (4.6.3) the properties of deformation zone structural elements are described. To avoid excessive repetition, data concerning the sorptivity of the various solutes investigated in the laboratory programme are referred to in the Retardation model tables by using pointers to the appropriate data tables already presented in Section 4.4.

4.5.1 Retardation properties of the rock mass

It is emphasised that the retardation model for the transport properties of the rock does not include any additional specifications or assessments coupled to the relative predominance spatial distributions of rock types in individual rock domains. Although with the aid of the geological rock domain model described in /Wahlgren et al. 2008/ it is possible to derive models which include the spatial variations of different rock types in different rock-, fracture-, and hydraulic domains, no attempt has been made to provide such a detailed specification in /Selnert et al. 2009b/ owing to the paucity of sorption data in particular.

In the Retardation model, it is implicitly assumed that the properties of flowpaths through the different rock domains can be represented in a statistical sense by consideration of the proportions of the various rock types of which the rock domains are thought to be comprised (see Table 4-1). It is noted that although this treatment does not give consideration to the possibility of preferential flowpaths involving specific rock types within the fracture domains, the approach is probably sufficiently accurate for the purposes of modelling within safety assessment since the material properties of the different rock types appear to be broadly similar (when considered together with their associated uncertainties). Further justification of this assumption may be required within safety assessment.

Representative, “best estimate” transport parameters for comparative purposes are given in Table 4-27 for the suite of rock types where a statistically significant data set exists.

Generally, it has not been possible to directly measure the diffusive properties of the (typically thin) layers of hydrothermally altered rock immediately adjacent to fracture surfaces hosted in otherwise unaltered host rock. Porosity ranges measured for hydrothermally altered materials (see Table 4-7), however, suggests only minor differences in “bulk” diffusive properties relative to the unaltered rock matrix. PMMA impregnation studies /Penttinen et al. 2006/, on the other hand, suggest a heterogeneous distribution of porosity over very short length scales and the possibility exists for increased diffusivity over a distance of some cm into the rock matrix from water bearing fractures. BET measurements indicate that the microporous surface area of altered rock could be as much as an order of magnitude higher than that of the unaltered rock, thereby suggesting an increased sorptivity in the first few cm of rock matrix immediately adjacent to fracture surfaces.

It should be noted that the possibly increased diffusivity and sorptivity of altered matrix rock adjacent to fracture surfaces is only established qualitatively at present and cannot be rigorously accounted for in the retardation model.

Table 4-27. Representative, "best estimate" transport parameters for the main rock types (> 2%) within rock domains RSMA01, RSMD01, RSMM01, and RFMBA03 intended for comparative purposes. Data are given as mean±standard deviation of measured values (where available) for porosity, formation factor, BET-surface area, and cation exchange capacity (CEC) considering non-deformation zone (N) and deformation zone (DZ) rock samples.

	501030	501033	501036	501046	501056	501058	505102	511058
Porosity (vol%), (N)								
unaltered* rock only	0.20±0.22	n/a	0.19±0.19	0.36±0.14	0.30±0.10	n/a	0.16±0.06	0.24±0.07
altered rock only	0.79±0.56	n/a	n/a	0.15	0.55±0.33	n/a	n/a	0.64
all rock	0.23±0.26	0.06	0.19±0.19	0.35±0.14	0.32±0.15	0.61	0.16±0.06	0.27±0.19
Porosity (vol%), (DZ)								
unaltered* rock only	0.16±0.13	n/a	0.25	0.33±0.08	0.43±0.18	n/a	0.46±0.50	0.15±0.08
altered rock only	0.47	n/a	0.87±0.35	0.94±0.62	0.36±0.25	n/a	n/a	n/a
all rock	0.19±0.19	0.06	0.75±0.40	0.63±0.52	0.40±0.20	0.76	0.46±0.50	0.15±0.08
Formation factor (in situ)**								
unaltered rock only	$(6.0\pm5.3)\times10^{-6}$	$(1.2\pm0.6)\times10^{-5}$	$(9.7\pm5.9)\times10^{-6}$	$(2.1\pm1.9)\times10^{-5}$	$(2.2\pm1.9)\times10^{-5}$	$(1.2\pm1.0)\times10^{-5}$	$(1.3\pm1.1)\times10^{-5}$	$(1.2\pm1.0)\times10^{-5}$
altered rock only	$(3.2\pm4.2)\times10^{-5}$	$(1.7\pm0.7)\times10^{-5}$	$(9.3\pm6.1)\times10^{-6}$	$(2.6\pm2.2)\times10^{-5}$	$(3.1\pm2.8)\times10^{-5}$	$(1.5\pm1.5)\times10^{-5}$	$(1.8\pm8.8)\times10^{-5}$	$(4.6\pm11)\times10^{-5}$
all rock	$(8.1\pm9.2)\times10^{-6}$	$(1.2\pm0.6)\times10^{-5}$	$(9.7\pm5.9)\times10^{-6}$	$(2.1\pm1.9)\times10^{-5}$	$(2.3\pm2.1)\times10^{-5}$	$(1.3\pm1.0)\times10^{-5}$	$(1.4\pm1.2)\times10^{-5}$	$(1.9\pm2.5)\times10^{-5}$
Formation factor (lab)	3.1×10^{-5}	n/a	6.1×10^{-5}	4.6×10^{-4}	7.0×10^{-5}	n/a	9.8×10^{-5}	4.4×10^{-5}
BET (m^2/g)	0.043	0.03	0.022	0.04	0.039	n/a	n/a	n/a
CEC (cmol/kg)***	1.0±0.6	n/a	1.0±0.7	0.9±0.7	< 1.0	n/a	n/a	n/a

Notes: Entries given as "n/a" in the table signify data "not available".

(*) The category "unaltered rock" in reference to porosity is defined as rock "without observation of medium or strong alteration" and therefore also includes rock with weak alteration /Selnert et al. 2009b/. For in situ Formation factors, the category "unaltered rock" specifically refers to rock defined as having no alteration of any kind as specified in the SICADA database.

(**) Formation factors derived from in situ measurements are empirically corrected for measurement bias and are for "rock matrix" (i.e. ≥ 0.5 m distant from the nearest mapped, open fracture). The data includes rock from the HRD and HCD (deterministic deformation zones) considered together.

(***) 1 cmol/kg = 1 meq/100 g.

4.5.2 Retardation properties of fractures

Retardation parameters for the identified fracture types are given in Table 4-28 to Table 4-41. Owing to a lack of data for fracture types D (laumontite), E (chlorite/calcite), and G (chlorite), data for these fracture types have been imported to the retardation model from the following sources:

- Fracture type D (laumontite) has been assigned retardation properties based upon data for the corresponding fracture type studied in the Forsmark area /Byegård et al. 2008/. The laumontite fractures at both sites have been judged by /Selnert et al. 2009b/ to be sufficiently similar that this is deemed permissible.
- Fracture type E (chlorite/calcite) has been assigned porosity data based on the detailed investigation (using the PMMA technique) of a similar fracture in the LTDE-SD experiment performed at the Äspö Hard Rock Laboratory /Widestrand 2009/.
- Fracture type G (chlorite) has been assigned retardation properties based upon data for the corresponding chlorite deformation zone element. The mineralogy of these materials have been judged by /Selnert et al. 2009b/ to be sufficiently similar that this is deemed permissible.

Table 4-28. Retardation model parameters for fracture type A.

	Fracture coating: Calcite +chlorite +Pyrite ±Chalcopyrite ±other
Thickness	0.2–1 mm
Porosity (vol%)	n/a
Formation factor	n/a
BET surface area (m^2/g)	15±9
CEC (cmol/kg)	40±13 (*)
Sorption, K_d (m^3/kg)	See Table 4-18
Percentage of all open fractures	7%
Percentage of transmissive fractures	10%
Altered rock surrounding the fracture	≤ 10 mm

Notes: Entries given as “n/a” in the table signify data “not available”.
(*) CEC value is for < 0.125 mm fraction with a BET surface area of 2.8 m^2/g.

Table 4-29. Retardation model parameters for fracture type B.

	Fracture coating: Epidote ±prehnite ±adularia ±chlorite ±quartz ±calcite
Thickness	0.5–1 mm
Porosity (vol%)	n/a
Formation factor	n/a
BET surface area (m^2/g)	6±2
CEC (cmol/kg)	n/a
Sorption, K_d (m^3/kg)	See Table 4-19
Percentage of all open fractures	8%
Percentage of transmissive fractures	5%
Altered rock surrounding the fracture	~20 mm

Notes: Entries given as “n/a” in the table signify data “not available”.

Table 4-30. Retardation model parameters for fracture type C.

	Fracture coating: Hematite +clay ±chlorite ±other
Thickness	0.5–5 mm
Porosity (vol%)	n/a
Formation factor	n/a
BET surface area (m^2/g)	13±11
CEC (cmol/kg)	12–24
Sorption, K_d (m^3/kg)	See Table 4-20
Percentage of all open fractures	10%
Percentage of transmissive fractures	9%
Altered rock surrounding the fracture	≤ 50 mm

Notes: Entries given as “n/a” in the table signify data “not available”.

Table 4-31. Retardation model parameters for fracture type D.

	Fracture coating: Laumontite ±calcite ±chlorite
Thickness	0.2–2 mm
Porosity (vol%)	n/a
Formation factor	n/a
BET surface area (m^2/g)	0.42±0.02 (*)
CEC (cmol/kg)	18±5
Sorption, K_d (m^3/kg)	n/a
Percentage of all open fractures	0.3%
Percentage of transmissive fractures	0.3%
Altered rock surrounding the fracture	≤ 20 mm

Notes: Entries given as “n/a” in the table signify data “not available”.
(*) Data imported from Forsmark retardation model /Byegård et al. 2008/.

Table 4-32. Retardation model parameters for fracture type E.

	Fracture coating: Chlorite ±calcite ±oxidised walls ±saussuritized walls
Thickness	0.2–0.5 mm
Porosity (vol%)	3–5%(*)
Formation factor	n/a
BET surface area (m^2/g)	2.2
CEC (cmol/kg)	n/a
Sorption, K_d (m^3/kg)	n/a
Percentage of all open fractures	23%
Percentage of transmissive fractures	20%
Altered rock surrounding the fracture	≤ 10 mm

Notes: Entries given as “n/a” in the table signify data “not available”.
(*) Data imported from Äspö HRL, LTDE-SD experiments /Widestrand 2009/.

Table 4-33. Retardation model parameters for fracture type F.

	Fracture coating: Clay ±chlorite ±calcite
Thickness	0.2–5 mm
Porosity (vol%)	n/a
Formation factor	n/a
BET surface area (m^2/g)	24
CEC (cmol/kg)	n/a
Sorption, K_d (m^3/kg)	See Table 4-21
Percentage of all open fractures	21%
Percentage of transmissive fractures	27%
Altered rock surrounding the fracture	≤ 50 mm

Notes: Entries given as “n/a” in the table signify data “not available”.

Table 4-34. Retardation model parameters for fracture type G.

	Fracture coating: Chlorite ±other
Thickness	~0.2 mm
Porosity (vol%)	0.9
Formation factor	n/a
BET surface area (m^2/g)	7.9 (*)
CEC (cmol/kg)	13±2 (*)
Sorption, K_d (m^3/kg)	See Table 4-23
Percentage of all open fractures	11%
Percentage of transmissive fractures	7%
Altered rock surrounding the fracture	≤ 50 mm

Notes: Entries given as “n/a” in the table signify data “not available”.
(*) Assumed to have the same properties as Catgeory 2 deformation zone material.

Table 4-35. Retardation model parameters for fracture type H.

	Fracture coating: No mineral
Thickness	n/a (not relevant for this fracture type)
Porosity (vol%)	See Table 4-27
Formation factor	See Table 4-27
BET surface area (m^2/g)	See Table 4-27
CEC (cmol/kg)	See Table 4-27
Sorption, K_d (m^3/kg)	See Table 4-27
Percentage of all open fractures	3%
Percentage of transmissive fractures	4%
Altered rock surrounding the fracture	≤ 10 mm

Notes: Entries given as “n/a” in the table signify data “not available”.

Table 4-36. Retardation model parameters for fracture type I.

	Fracture coating: Calcite ±other
Thickness	~0.2 mm
Porosity (vol%)	n/a
Formation factor	n/a
BET surface area (m^2/g)	n/a
CEC (cmol/kg)	n/a
Sorption, K_d (m^3/kg)	n/a
Percentage of all open fractures	11%
Percentage of transmissive fractures	13%
Altered rock surrounding the fracture	≤ 10 mm

Notes: Entries given as “n/a” in the table signify data “not available”.

4.5.3 Retardation properties of deformation zones

As described in Section 4.2.1, deformation zones are usually characterised as consisting of a transition zone and a core. Transmissive fractures, if they are present, are often found in the transition zone, close to the wall rock. The deformation zone core is commonly found to have substantially reduced flow permeability in a direction normal to its orientation.

Independent of which conceptual model is adopted for use in transport calculations (e.g. see Figure 4-5), there are some simplifications which constitute a basis for parameterising the transport properties of deformation zones:

- Deformation zones at Laxemar often appear to have been reactivated during different periods throughout geological history and display a wide spectrum of brittle and ductile alteration which can also vary considerably between different borehole intercepts with the same deformation zone. Consequently, it is not possible to give specific retardation properties for every single deformation zone because of their internal microstructural complexity and the fact that this is usually only known from a small number of borehole intercepts. This also limits the possibility to describe any variations between different categories of deformation zones.
- The vast majority of the sections mapped with strong or medium oxidation, are found within deformation zones. Although deformation zones are complex, varying in composition, and even can contain non-deformed rock, five categories of altered bedrock have been distinguished as recurrent structural elements within or close to deformation zones (as outlined in Table 4-3). Retardation parameters for these elements are given in Table 4-37 to Table 4-41.
- Deformation zones have an increased fracture frequency compared to the host rock (both open and sealed), which is assumed to have some effect upon their retardation properties. Statistics of fracture frequency and fracture distribution in deformation zones are available. It is possible to parameterize most of the open fracture types found within the transition zones and core regions. Retardation parameters for these fracture types (where available) have been given previously in Table 4-18 to Table 4-21.
- Both the frequency and distribution of transmissive fractures vary between different deformation zones. Notwithstanding this, the transmissivity ranges are broadly similar for all the fracture types described in the retardation model and there is little evidence of preferential flow within specific fracture types.
- Tables of retardation properties for the deformation zone structural elements are given in Table 4-37 to Table 4-41.

Table 4-37. Retardation model for Fault rock/gouge (strongly tectonised and partly incohesive material).

Mineral content	Altered rock fragments, mineralogy partly dependent on host rock. Generally chlorite, saussurite, and clay together with rock fragments.
Porosity (vol%)	3% average (strongly heterogeneously distributed porosity up to 18%) (*)
Formation factor	n/a
BET (m2/g)	24
CEC (cmo^{l}/kg)	n/a
Sorption coefficient, Kd (m3/kg)	See Table 4-22

Notes: Entries given as “n/a” in the table signify data “not available”.
(*) Determined by 14C-PMMA impregnation.

Table 4-38. Retardation model for Chlorite (primarily close to mafic rock).

Mineral content	Chlorite ±corrensite
Porosity (vol%)	12% (heterogeneous porosity from 0.5% – 12%) (*)
Formation factor	n/a
BET (m2/g)	8
CEC (cmo^{l}/kg)	13±2
Sorption coefficient, Kd (m3/kg)	See Table 4-23

Notes: Entries given as “n/a” in the table signify data “not available”.
(*) Determined by 14C-PMMA impregnation.

Table 4-39. Retardation model for Vuggy rock (porous episyenetic, wall rock).

Mineral content	Prehnite, adularia, quartz, calcite, ±laumontite, epidote, hematite (occasionally vugs from quartz dissolution)
Porosity (vol%)	6.23%
Formation factor	1.1×10–3 (*)
BET (m2/g)	13
CEC (cmo^l/kg)	n/a
Sorption coefficient, Kd (m3/kg)	See Table 4-24

Notes: Entries given as “n/a” in the table signify data “not available”.
(*) Based upon material taken from outside of a deformation zone, although classified as crush zone in boremap data.

Table 4-40. Retardation model for Cataclasite (with mylonitic banding).

Mineral content	Epidote, adularia, quartz, hematite ±laumontite (strong variations in mineralogy)
Porosity (vol%)	3±2%
Formation factor	7.6×10–3
BET (m2/g)	15±8
CEC (cmo^l/kg)	n/a
Sorption coefficient, Kd (m3/kg)	See Table 4-25

Notes: Entries given as “n/a” in the table signify data “not available”.

Table 4-41. Retardation model for oxidized (medium to strong alteration) wall rock.

Mineral content	Hydrothermally altered host rock, mineralogy related to initial rock type. Red staining from small hematite microprecipitates. K-feldspar, saussurite, plagioclase, quartz. Chlorite is also common when hosted in granite rock.
Porosity (vol%)	0.7±0.4%
Formation factor	(1.5±1.3)×10–4
BET (m2/g)	0.6
CEC (cmo^l/kg)	n/a
Sorption coefficient, Kd (m3/kg)	See Table 4-26

Notes: Entries given as “n/a” in the table signify data “not available”.

4.6 Summary of main findings

4.6.1 On retardation properties of the rock mass

The limited data available indicate that there are probably no significant differences in the retardation properties of the different rock types for which there exists data. Furthermore, the range of variation of specific material property parameters within a particular rock type is found in many cases to be larger than the apparent difference between different rock types. The minor differences that are observed can be summarised as:

- All rock types appear to have broadly similar porosities given underlying uncertainties and sample variability. The rock types for which there are more than 30 measurements, however, can be approximately ranked in order of decreasing porosity as 501056 > 501030 > 501036 (non-deformation zone samples, all alteration types).
- Ävrö quartz monzodiorite (501046) appears to have a higher formation factor than the other rock types based upon through-diffusion measurements. The data, however, may affected by a sampling bias since eight out of the total of nine samples are taken from a single, deep interval within borehole KSH01 (891.69–891.94 m). It is thought that the core boreholes established early during the site investigation (such as KSH01) may have been constructed with a less gentle drilling technique than those towards the end of the site investigation with the implication that

deep core samples from earlier boreholes may be more mechanically damaged and therefore give higher formation factors than samples taken from later boreholes (see Appendix D). Consequently, the statistical basis for the formation factor estimate of Ävrö quartz monzodiorite (501046) in Laxemar is poor if only the laboratory data are considered. It is noted that the in situ resistivity-based data which represents a substantially larger data set spread over a number of boreholes and elevations do not show any substantial differences between the formation factors of Ävrö quartz monzodiorite (501046) and Ävrö granodiorite (501056).

- All rock types investigated appear to have broadly similar sorption properties given uncertainties in the underlying data and limited statistical representatively.
- The CEC values of the major rock types are very close to each other. The uncertainty in the CEC-values, however, is roughly ±50% since the CEC is close to the detection limit for crushed rock. Any correlation with BET or sorptivity is therefore masked by the uncertainty of the CEC measurement.

It is noted that the shifting focus areas during the investigation process necessarily led to an uneven distribution of samples with regard to the ultimate focus area at the conclusion of the site investigations. Approximately half of all samples are from Simpevarp and the other half has an overrepresentation of samples from RSMA01 and fewer samples from RSMD01. However, only small differences are found in porosity between the two sites as is shown in Section 3.1.1.and Table 3-3,

4.6.2 On retardation properties of fractures

Retardation models have been produced for each of the different fracture types. A thin layer of fracture coating has been identified within all of them with the exception of fracture type H (no mineral). Due to the limited thickness of the layers and their frequently friable nature, porosity and diffusion measurements were not possible to perform on fracture coating materials.

Data from the Äspö HRL, LTDE-SD project /Widestrand 2009/ indicate that fractures categorised as type E (chlorite/calcite) exhibit an increased porosity in the surface chlorite/calcite layers of 3–5%. This is supported by PMMA-measurements which also show an increased porosity in fracture coatings /Penttinen et al. 2006/. Owing to their physical characteristics it appears likely that fracture coatings in general are characterised by a substantially higher porosity and therefore also a higher effective diffusivity (i.e. higher formation factor) than the underlying rock matrix. It therefore seems reasonable within safety assessment transport modelling to consider fracture coatings and filling materials as equilibrium storage capacities.

The measured BET surface areas of the fracture materials have been measured to be significantly higher than corresponding BET surface areas of samples from the rock mass. They vary from roughly 2 m^2/g to 24 m^2/g, which is on the order of 100–300 times higher than the corresponding ranges for unaltered rock types. This finding suggests that the fracture coatings most likely contribute positively to the overall retardation effect. The finding is supported by the 10 to 40 times higher CEC-values measured for fracture type A and C coatings as compared to the CEC values of the unaltered rock types.

As noted previously in the Forsmark site descriptive model /Crawford 2008/, the large differences found for the BET values between fracture material and intact rock are not accompanied by a 1:1 corresponding trend for sorptivity (as described by measured K_d values). The K_d for sorption of Cs(I) on clay minerals characteristic of Laxemar fracture types, for example, can be anywhere in the range 1–100 times larger than the corresponding value for the intact Ävrö quartz monzodiorite (501046). The BET surface area of the fracture filling material, on the other hand, is 100–300 times greater than that of the intact rock. In this particular case, however, the variability of the K_d values is in general agreement with the known ion-exchange behaviour of Cs(I) in association with clay minerals so this is not altogether unexpected. For solutes that sorb by way of a surface complexation mechanism, a closer agreement is expected. Although there appears to be a clear correlation between BET surface area and sorptivity generally when comparing different size fractions of crushed rock, it is very difficult to observe a consistent correlation with surface area when comparing the sorptivity of matrix rock and fracture coating materials. This is thought to be largely due to the differing mineral surfaces existing in fracture coatings and bulk of the rock which do not necessarily have the same sorption characteristics.

4.6.3 On retardation properties of deformation zone elements

The deformation zone structural elements for which retardation properties have been tabulated are all comparatively heterogeneous in their structure. The porosities are considerably higher (3–16%) than for intact rock, with the exception of oxidized wall rock which is only slightly more porous than intact, unaltered rock.

In general, it is expected that the high porosities should also be accompanied by an increased effective diffusivity (i.e. increased formation factor). This is confirmed by the formation factor ranges measured by through-diffusion for porous episyenetic wall rock and cataclasite which are about an order of magnitude larger than those of intact rock. The increase is approximately in agreement with expectations based on Archie's law where a 10 fold increase in porosity should give a roughly 40 times increase in formation factor. The formation factor range measured for these more porous materials is roughly 30–100 times greater than that of the intact rock.

BET-surface areas and sorptivities are generally slightly higher for the deformation zone materials than for intact rock. This indicates a slightly greater relative potential for retention than intact rock in the HRD.

4.6.4 Application of the retardation model

Table 4-1 and Table 4-27 provide a basis for the parameterisation of rock domains RSMA01, RSMD01, and RSMM01. This could range from the selection of a single parameter value for the dominant rock type in that domain to, for instance, flowpath averaging using data for different rock types. Generally, the data are too sparsely sampled to give material property data for individual rock types specific to particular rock domains. Nevertheless, it is thought that given the relatively small differences in material properties between different rock types, this additional classification is not motivated. The material properties of the same rock types residing in different rock domains can therefore, for all practical purposes, be considered to be identical.

The quantitative descriptions of the identified fracture types including the available retardation parameters are given in Table 4-28 to Table 4-34. The corresponding descriptions and data for deformation zones are presented in Table 4-37 to Table 4-41. It is intended that the different fracture types and deformation zone structural elements be used in a modular fashion for constructing integrated models of radionuclide transport along flow paths within the rock. For parameterisation of the HRD, fractures are considered to be hosted within the different rock types. For the most volumetrically important rock types (501036, 501046, and 501056), this would give 27 different combinatorial possibilities. Fractures within the HCD may be hosted in these rock types, although they are also likely to be hosted in one or more of the different cohesive deformation zone structural elements thereby giving even greater combinatorial possibilities.

In this chapter, the material property data are characterised in the form of simplified summary statistics (i.e. mean±standard deviation, median, minimum, maximum, and number of samples) for the measurement data which could be used as a basis for preliminary stochastic parameterisation of transport models.

This chapter should be regarded as a proposal for how to formulate a descriptive and semi-quantitative retardation model derived from the available material properties database. Recommendations for the selection of data are given, however, with acknowledgement of the qualitative and quantitative uncertainty of the retention parameters. This caveat implies that the model does not provide exact and detailed guidelines on how to "dress" the geological model with transport parameters using the retardation model tables. Nevertheless, in the opinion of the authors this is the best representation achievable with the available data. The retardation model should be viewed as an overview of the interpreted site-specific information on retardation parameters, intended to provide a basis for the formulation of alternative parameterisations or necessary simplifications within safety assessment modelling.

5 Solute transport

Coupling of the F-factor estimates from the hydrogeological modelling with the retardation model allows for the prediction of transport times for key radionuclides. As already discussed in the context of the flow related transport properties evaluation in Chapter 3, radionuclide transport in the site descriptive modelling work is conceptualised to occur in a serially connected, three compartment system consisting of the non-engineered near field (NNF), the immediate far-field (IFF), and the distant far field (DFF). In this analysis the NNF and IFF (together) are taken to correspond to the hydraulic rock domain (HRD) surrounding a repository, whereas the DFF corresponds to deterministic deformation zones comprising the hydraulic conductor domain (HCD). In this chapter, calculations are presented which have been used to quantify likely radionuclide transport times along typical transport paths from a canister deposition hole to the near surface. It is emphasised that the radionuclide transport times discussed in this chapter should be regarded as merely illustrative, showing how the interplay between hydrodynamic transport resistance and material properties affects the transport of radionuclides of varying sorptivity.

5.1 Overview of modelled solute transport processes

The transport models described in this chapter consider advectively dominated flow and transport along a flowpath where the transported solutes can diffuse into and sorb upon micro-surfaces within the rock matrix. Here, a flowpath is considered to be a simple set of serially connected flow channels within the rock. In a full hydrogeological description of the transport problem as to be used in SR-Site, however, one would expect flowpaths to bifurcate and join with other flowpaths over different length scales giving rise to a distribution of F-factors and advective transport times.

The transport model assumes that flow is fully mixed across the aperture and width of the flowpath and that hydrodynamic dispersive mixing can be neglected. This last assumption is reliant upon the observation that apparent dispersion is generally dominated by the difference in residence times of solutes transported along different flowpaths and therefore does not need to be treated on the level of individual flow channels /Neretnieks 1993/. The assumption of full mixing across the width of a flowpath depends on whether there is sufficient time for any lateral concentration differences to even out over the advective transport length. If the characteristic time for diffusion across the flowpath width is substantially smaller than the advective travel time, then fully mixed conditions can generally be assumed.

Depending upon the hydrogeological scenario under consideration, advective travel times can be expected to be on the order of a few to many tens of years. This could run to hundreds, or perhaps even thousands of years if hydraulic gradients are extremely low. For a 10 cm wide flow channel, the characteristic time for lateral diffusion will be on the order of 50–100 days and therefore full mixing can usually be assumed for flow channels of this dimension (see /Crawford 2008/) even for very short advective travel times. As the transport aperture of a flowpath is typically very small (on the order of a few mm at most), diffusive mixing across the aperture can always be assumed on safety assessment timescales.

Radionuclides transported along flowpaths leading away from the repository may mix with un-contaminated water at intersections with other flowpaths giving dilution effects. The extent of mixing will depend upon the water residence time at the flow junction and the effective surface area for diffusive mixing between adjacent water streams in which the radionuclides are being transported (assuming laminar flow). Here, the relation between the characteristic time for diffusion and stream contact time gives an indication of whether full diffusive mixing is a reasonable assumption or not. Although it is difficult to assess mixing for unknown flow intersection geometries, typically two limiting cases are considered in modelling; full mixing at flowpath intersections, and no mixing at flowpath intersections (“flowpath routing”). As the calculations presented in this chapter consider a single hypothetical flowpath, this does not need to be considered (although it is noted that the simulation of a single flowpath is conceptually indistinguishable to the assumption of transport in a multi-flowpath system with no mixing). For safety assessment calculations, however, particle tracking provides a simple means of weighting the contributions of individually traced particles to the overall radionuclide release rate in a complex, multiple-flowpath system.

Although in some cases flow channels may be described as actual physical entities in the rock (such as in the case of conductive fracture intersections or flow conduits hosted in fault stepovers), they generally are dynamic in the sense that their existence and distribution is predicated by the externally imposed flow regime /e.g. Neuman 2005/. Flow distributions in variable aperture fractures are thought to be highly channelised and effectively stagnant zones can potentially exist adjacent to these flow channels. Although the term "stagnant zone" is used frequently in this chapter it should be emphasised that truly stagnant zones, by and large, do not exist since there will always be some kind of hydraulic gradient active in a connected hydraulic system of this kind which will act as a driving force for flow. Relative to the time scales characterising advective transport in the main advective flow channels, however, very slowly flowing water in these zones can be regarded as being effectively stagnant for transport calculation purposes.

On the scale of a single fracture, variable fracture aperture provides the possibility for in-plane flow channelling although the geometry and spatial distribution of active flow channels themselves varies as a function of the applied boundary conditions. On the basis of field observations it is thought that in-plane flow channels have widths typically in the range of a few cm to some tens of cm /Abelin et al. 1991, Abelin et al. 1994, Neretnieks 2004/. For the calculations in this chapter a flow channel width of 10 cm is assumed as a main scenario.

A schematic view of the radionuclide transport problem is given in Figure 5-1. The figure illustrates the idea of advective flow through a flow channel of limited extent with stagnant zones flanking the main flowpath.

Scoping calculations (see /Crawford 2008/) indicate that for fractures with strongly variable apertures and surface asperity contacts, there could be effectively stagnant zones of substantial extent that afford additional surface area for the radionuclides to interact with the rock matrix. This is referred to as diffusion accessible surface (DAS) in the present report.

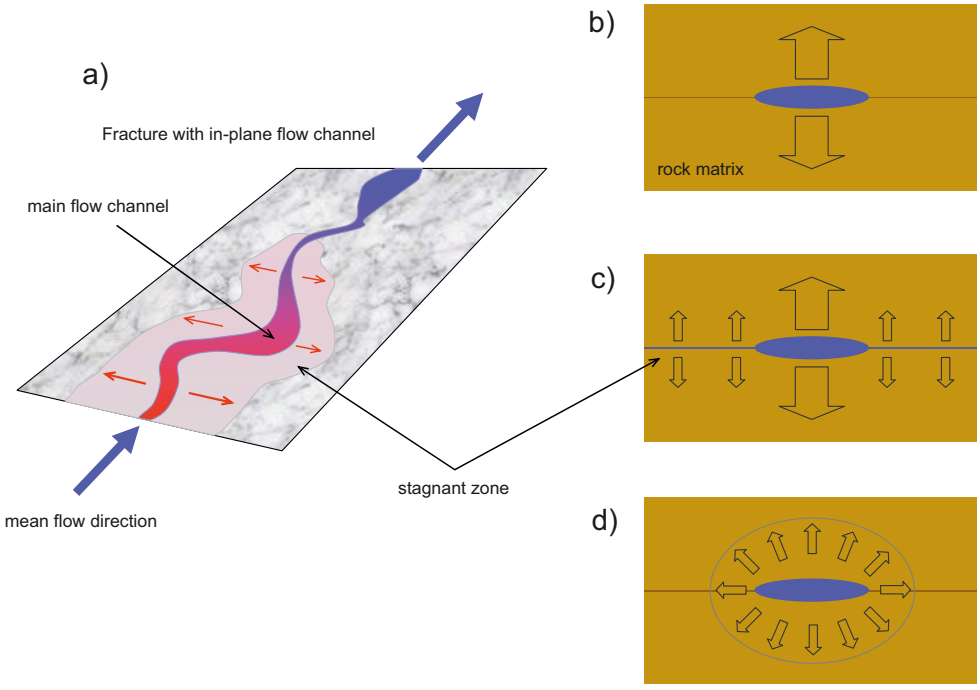

Figure 5-1. *The left-hand image (a) shows a schematic view of a fracture hosting an in-plane flow channel of limited width with stagnant zones flanking the main flowpath; The images on the right-hand side show conceptual illustrations of three different modes of mass transfer: b) diffusion directly to the rock matrix from the main flow channel; c) direct matrix diffusion coupled with diffusive uptake to the stagnant zone and subsequently into the rock matrix; d) mass transfer of solute described as a radial or pseudo-radial diffusion process when the penetration depth approaches the same size as the channel width.*

Figure 5-2 shows a typical simulation of a 10×10 m variable aperture fracture with a surface asperity contact of roughly 40% and an anisotropic, although spatially correlated aperture distribution. The open parts of the fracture have a mean aperture of 5×10^{-5} m and a standard deviation of the same size. The simulation considers a dipole line source/sink of 10 cm extent applied along the vertical (top images) and horizontal axis (bottom images) to demonstrate the dynamic nature of the flow channelling effect. As can be clearly appreciated from the figure, there are substantial regions of the fracture surface that are effectively stagnant although hydraulically accessible from the main flowpaths.

Provided flow channels are not isolated tubes hosted within annealed fractures (erosion pipes hosted within calcite filled fractures cannot be completely ruled out for the Laxemar site), these stagnant zones should be relatively well connected and accessible from the main flowpaths. It can be shown for single fractures that increasing contact of fracture surface asperities increases the degree of flow channelling significantly. Although this reduces the actual flow-wetted surface, large portions of the fracture must still stay open and be hydraulically connected for the fracture to remain conductive at all. These hydraulically accessible, although non-flowing regions correspond to the stagnant zones illustrated in Figure 5-1.

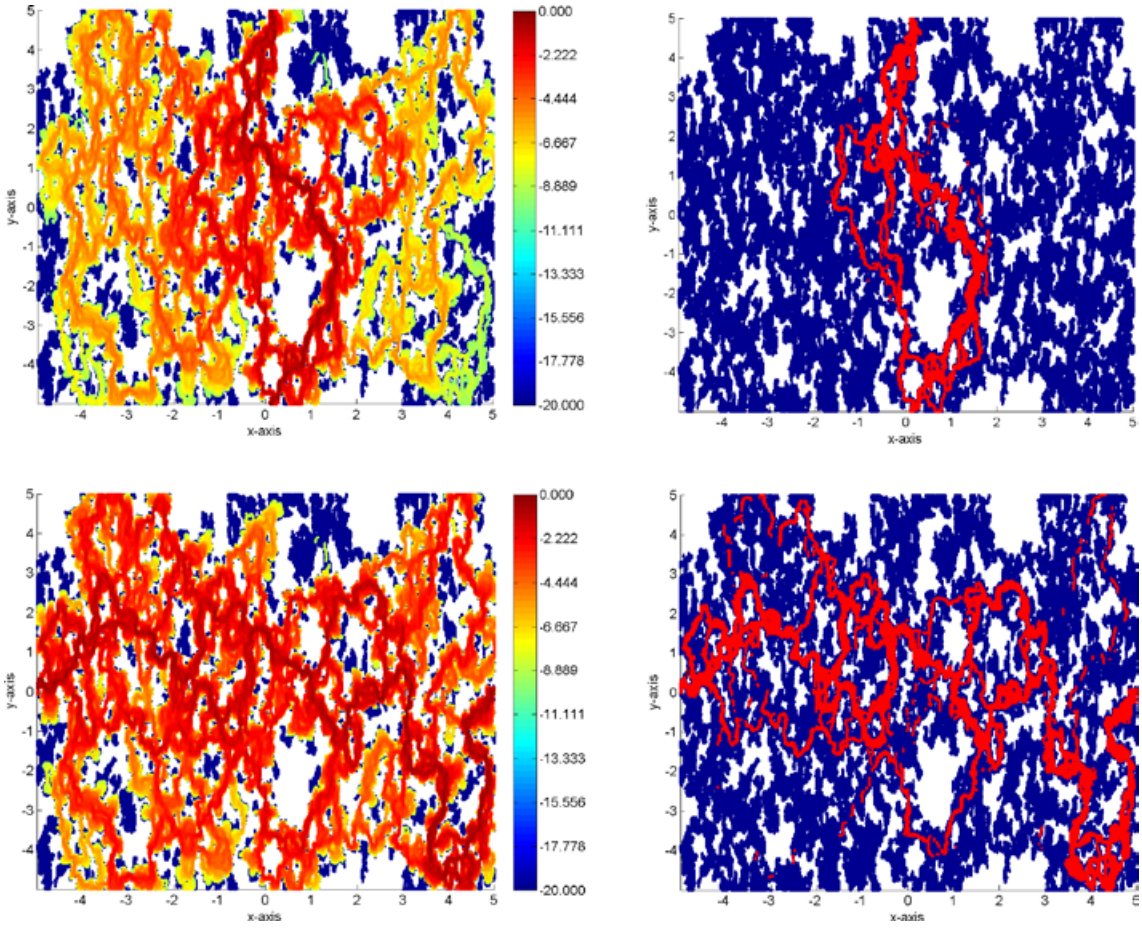

Figure 5-2. *Simulation of typical flow channels arising in a variable aperture fracture with a surface asperity contact of 40% and hydraulic gradient applied vertically (top) and horizontally (bottom) for a 0.1 m line source/sink dipole. Hydraulically inaccessible parts of the fracture are non-coloured. The left hand images indicate the actual simulated flow normalised by the maximum flow rate (log_{10}-units). The right-hand images show the dynamic nature of flow channels featuring flow > 1% (arithmetic units) of the maximum flowrate (red shading).*

In the calculations presented in this chapter a stagnant zone width roughly 10 times greater than the channel width is assumed. This is referred to as a 10:1 stagnant zone in the present report. Therefore, for a flow channel of 10 cm width, the stagnant zone would be effectively 1 m wide. For a 1 cm wide channel, on the other hand, the stagnant zone would be only 10 cm wide. Furthermore, for the purpose of the illustrative calculations made in this chapter it is assumed that the stagnant zone only exists along one flanking side of the flowpath length. If one were to assume symmetric stagnant zones flanking the main flowpath, the retardation effect could be even greater.

If flow channels are narrow as expected, the 1D description of matrix diffusion customarily used in safety assessment calculations is inaccurate and may grossly underestimate the potential radionuclide retardation. For this reason, three main scenarios for radionuclide transport are considered. These are:

A. (Base model) Advective flow coupled with 1D diffusion/sorption within the rock matrix.

B. (Model alternative 1) Advective flow in a narrow channel coupled with 1D diffusion/sorption in the rock matrix plus diffusion into a stagnant zone of limited extent and subsequent 1D diffusion/sorption within the rock matrix.

C. (Model alternative 2) Advective flow in a narrow channel coupled with 2D radial diffusion/sorption in the rock matrix.

It is emphasised that these different conceptual formulations of solute mass transfer may be considered more, or less independently of whether the flow is modelled using a Hydrogeological DFN or ECPM representation. In both situations, flow can be conceptualised to be hosted in narrow flow channels regardless of simplifications made to facilitate flow calculations. F-factor distributions calculated using either of the flow modelling approaches, for example, can be exported for use with independent codes such as, for example, MARFA /Painter and Mancillas 2007/ or FARF /Vahlund and Hermansson 2004/ (or even the numerical codes used in this chapter) to model solute transport in safety assessment. Although the three conceptual models outlined above are not strictly bound to any particular flow modelling representation, different codes incorporating combined flow and transport modelling capabilities may introduce additional constraints on the type of solute mass transfer process that can be modelled owing to software specific attributes and limitations.

Along flowpaths hosted within highly fractured rock there may be large numbers of open although stagnant fractures which intersect the flowpath. It is possible for transported radionuclides to diffuse into these regions and access additional surface area for mass transfer to the rock matrix. In the analysis of transport processes, two principal kinds of DAS can therefore be envisaged; that comprising the in-plane stagnant zones and that belonging to incident, intersecting fractures. Since the in-plane DAS by definition follows the same trajectory as the flowpath itself, this is generally the dominant type of DAS. If the intensity of open, stagnant fractures is sufficiently high, however, the additional DAS residing in incident fractures may be substantial and give an further retardation effect that is not insignificant. The impact of incident fracture DAS is somewhat complicated to describe as the mass fluxes from the different surfaces into the rock matrix will, in many cases, overlap and it is difficult to avoid double counting of the storage capacity of the rock. Further discussions concerning this issue can be found in /Crawford 2008/. In order to avoid the possibility of double counting and to improve modelling transparency, this additional effect is not considered in the transport calculations presented in this chapter.

Typical F-factors for transport from individual canister positions (i.e. the non-engineered near field, NNF) could be significantly greater than the simplified estimates in Section 3.6.1 suggest. Since there are many poorly qualified assumptions contained in the estimates of the F-factor for these initial pathways, no credit is taken for their hydrodynamic transport resistance and only the F-factors associated with typical flowpaths in the immediate far-field (IFF) are considered. As discussed previously in Chapter 3, typical flowpaths in the immediate far field are assumed to correspond to those identified in the Hydrogeological DFN models used to describe the hydrogeological properties of the HRD.

From the scoping calculations detailed in Section 3.6, typical flowpaths within the HRD are found to have mean F-factors approximately in the range 10^3–10^5 yr/m with a standard deviation implying up to an order of magnitude of variation around the mean for each ensemble of realisations studied. The cited range of mean F-factors reflects the variability arising due to the direction of the applied hydrau-

lic gradient and whether neutrally or strongly transmissive fracture intersections are considered in the calculations. Here, the elevation interval of HRD_C between –650 m and –400 m is considered as a main example and simply note that F-factor estimates for the other hydraulic rock domains (HRD_W, HRD_EW007, HRD_N) examined are very similar in magnitude at the same elevation interval.

The scoping calculations for the HCD (which comprises the distant far field, or DFF), on the other hand, also suggest mean F-factors in the range 10^3–10^5 yr/m depending upon the choice of transmissivity-aperture relation and whether a 2D planar or 3D streamtube approximation is assumed in the calculation. As the particle tracking analyses detailed in Section 3.10 and Appendix C indicate, the magnitude of the F-factor predicted for the HCD also depends upon whether radionuclides make contact with the HCD at repository depth (associated with large F-factors) or closer to the surface (associated with negligible F-factors). The large range of possible F-factors obtained for both the HRD and the HCD therefore makes it difficult to determine whether the HRD or HCD dominates the overall F-factor for transport from repository depth to the near surface.

The range of variability arising due to random variation between different realisations of specific transport cases as well as the additional variation attributable to the different assumed boundary conditions (and further modelling assumptions in the case of the HCD) give rise to large uncertainties in the flow related transport properties of the target rock volume at the Laxemar site. The results suggest that it is not possible to make a strong case for very high F-factors (i.e. much greater than 10^6 yr/m) in Laxemar based upon the current hydrogeological description. The best-estimate overall F-factor for composite transport paths from a hypothetical repository to the near surface could vary anywhere from about 10^3 yr/m to slightly higher than 10^5 yr/m.

Since most water bearing fractures in Laxemar appear to be associated with mineral coatings of various thicknesses and a region of hydrothermal alteration, it would make sense to additionally include these as part of a detailed transport model. Although the material properties of the fracture coatings and altered materials described in Chapter 4 are not as well characterised as the unaltered main rock types, the available evidence suggests that these materials will, for the most, be associated with greater diffusive and sorptive retention than the underlying, unaltered host rock.

Scoping calculations of the impact of fracture coatings and alteration layers are given in /Crawford 2006/ where it is shown that such layers can provide additional transport retardation in excess of that predicted by consideration of only the unaltered rock material. To reduce the amount of excessive detail in the transport modelling results the additional transport retardation associated with these materials is neglected and transport simulations are made where only the retention properties of simple fractures hosted in an unaltered rock matrix are considered. Although the presence of fracture coatings and hydrothermally altered rock is likely to substantially enhance the retardation of early radionuclide breakthrough, the unaltered rock matrix is expected to dominate the residence time distribution over the greater part of the radionuclide residence time distribution at intermediate to later times and gives a better picture of the overall transport properties of the site.

It is likely that the increased hydrogeological and microstructural complexity found in the HCD should, on balance, also give rise to substantially greater retardation (for the same F-factor) than that implicit in the simplified transport model. Additionally, since fracture intersection zone (FIZ) conduits are assumed to contribute insignificantly to the overall F-factor for a transport path, these are neglected and only the in-plane flow channels residing within fractures are considered. It is noted, however, that the increased complexity of the FIZ intersections with possibly large stagnant zones (relative to their dimensions) flanking the main FIZ conduit are likely to make a non-negligible contribution to retardation in spite of their substantially lower flow-wetted surface. Although the calculations presented in this chapter do not directly consider FIZ, some discussion on how solute transport within these features may be modelled is given in /Crawford 2008/.

The impact of natural colloids upon retardation properties has not been investigated in detail in this report as it is thought to be unlikely that these will exist in sufficient amounts at repository depth that they would detrimentally affect repository performance during temperate conditions /SKB 2006a/. In scoping calculations presented in Appendix E, it is shown that for the prevailing groundwater conditions at repository depth colloids should have an insignificant impact upon solute transport processes. This is, however, a phenomenon that is more fully investigated within safety assessment where scenarios can be conceived where colloids may have an unfavourable influence upon transport processes.

It has been suggested that the presence of microbial biofilms coating the fracture surfaces may detrimentally influence the retardation properties of the rock. This could occur by way of a reduced sorption capacity of the biofilm as compared to the rock matrix itself /Anderson et al. 2006, Anderson et al. 2007/, as well as by way of the presence of microbes obstructing or blocking the micropores of the rock matrix immediately adjacent to the fracture surface /Charbonneau et al. 2006/. This phenomenon is thought to have only minor significance for transport and is neglected in this report. Some further generic discussion of the role of microbial biofilms (and fracture coatings) can be found in Section 5.4 as well as /Crawford 2008/.

An additional mechanism that could reduce the effective retardation of transported radionuclides is the presence of significant amounts of strong complexing agents called siderophores which are excreted by bacteria. Bacterial siderophores are strong complexing agents released by certain bacteria, usually under oxidising conditions (i.e. when Fe(III) availability is low) by those bacteria that use the Fe(II/III) redox couple as an oxidant. These complexing agents can also bind certain radionuclides very strongly, resulting in reduced sorption on geological materials. The significance of these substances for transport processes at the Laxemar site is discussed briefly in Section 5.3.

5.2 Overview of base model with alternatives

In the calculations presented in this chapter the numerical model for advective solute transport with matrix diffusion previously described in /Crawford 2006/ is used for simulations of the conceptual base model (BM) and model alternative 1 (MA1). The model is based upon an analytical solution in Laplace space with numerical inversion to obtain the solution in the time plane. The model is generalised to handle solute transport with mass transfer to the rock matrix including an arbitrary number of alteration layers. It also includes the possibility of simulating mass transfer to stagnant zones in the fracture plane with subsequent uptake to the rock matrix. The model can simulate equilibrium or diffusive mass transfer to fracture infilling material (fault gouge and breccia) and it is also feasible to simulate solute transport in features with non-symmetrical matrix properties as may be appropriate for modelling reactivated fractures and deformation zones featuring complex rock matrix microstructures.

For the simulations, the same set of solutes considered in the site investigation laboratory programme is used. These represent a broad range of sorption strengths from mildly sorbing in the case of strontium to strongly sorbing trivalent actinides/lanthanides. As the purpose of these calculations is to estimate typical travel times for solutes of differing sorption strengths, radioactive decay is not considered. Although specific isotopes are not referred to in these calculations, it should be noted that the transport times calculated for some of the solutes are substantially greater than the half-lives of their radioactive counterparts. In this chapter the neglecting of decay is intentional as the aim is to highlight mechanistic aspects of solute transport relating to the interplay of material properties parameterisation and flow related transport properties at Laxemar. For safety assessment, on the other hand, the inclusion of radioactive decay for single solutes and decay chains for daughter nuclides is central to the estimation of far-field radionuclide release rates. The models presented here can be easily adjusted to simulate decay of single solutes and using the simplifications described by /Neretnieks 2006b/ they can be modified to simulate particular decay chains.

When considering the impact of an in-plane stagnant zone, a key variable is the ratio of diffusive surface area for uptake to the stagnant zone relative to the flow-wetted surface for diffusive uptake directly to the rock matrix. The ratio of diffusive surface area, R_s for a stagnant zone (with an effective aperture, δ_s) flanking the main flow channel is defined as:

$$R_s = \frac{\delta_s f_s}{2W_c} \qquad \text{(Eq. 5-1)}$$

For a flowpath featuring a single stagnant zone along 100% of its length, the parameter $f_s = 1$. If the stagnant zone can be assumed to be symmetrical and flanking both sides of the main flow channel, $f_s = 2$. The effective aperture, δ_s of the stagnant zone flanking the main flowpath is assumed to be 10^{-4} m in the analyses presented in this chapter. For a flow channel width of 0.1 m, this gives an R_s value of approximately 5×10^{-3} m^2/m^2 in the case of single stagnant zone. The reader should note that

this is chosen purely for the purpose of testing the consequences of the stagnant zone assumption and the "true" aperture of actual stagnant zones may be greater than or less than this assumed value.

Although intersecting stagnant fractures are not considered in this analysis, it is relevant to note that if these features were to be included, an additional stagnant zone flux term would need to be defined. This would be of most relevance for the HCD where open fractures can occur with sufficient frequency that the additional retardation effect might be non-negligible. More detailed discussion concerning the role of incident fractures can be found in /Crawford 2008/.

At very early times (i.e. in the limit as $t \rightarrow 0$), the diffusion of solute from the stagnant zone to the rock matrix can be neglected. In this case, the diffusive uptake terms can be approximated using the solution by /Crank 1975/ for diffusion into a semi-infinite slab. In the time plane and for a constant concentration boundary condition, the limiting fluxes to the rock matrix and the stagnant zone, respectively can be shown to be:

$$J_m(t) = \frac{C_0 D_e}{\sqrt{\frac{\pi D_e t}{\theta_m + K_{dm}\rho_{bm}}}} \qquad \text{(Eq. 5-2)}$$

$$J_s(t : t \rightarrow 0) \approx \frac{C_0 D_w}{\sqrt{\pi D_w t}} \qquad \text{(Eq. 5-3)}$$

Taking into account the different mass transfer surface areas for the rock matrix and stagnant zones, the overall rate of mass transfer to the stagnant zone relative to the rock matrix is then given by:

$$\frac{R_s J_s}{J_m}(t \rightarrow 0) = \frac{R_s \sqrt{D_w}}{\sqrt{D_e(\theta_m + K_{dm}\rho_{bm})}} = \frac{R_s}{\sqrt{F_f(\theta_m + K_{dm}\rho_{bm})}} \qquad \text{(Eq. 5-4)}$$

This approximation is useful for checking the results of the numerical models for very early times (Section 5.3.2) as well as for interpreting the outcome of tracer tests (see Section 6.3).

Simulations of the different model alternatives are made using the previously described Laplace space model (see also /Crawford 2008/). The 2D radially symmetric diffusion model is similar to that used for the Base Model (BM), although a different matrix uptake term is used. The modified matrix flux term is based upon a model presented in /Neretnieks 2006a/. The paper by /Neretnieks 2006a/ also contains a treatment of model alternative 1 (MA1) for a single layered rock matrix which is similar to that described in /Crawford 2006/. For the radial diffusion case (MA2) it is assumed that a flow channel of limited width, W_c and transport aperture, δ_t can be approximately modelled as a cylinder of equivalent radius, a embedded in the rock /Rasmuson and Neretnieks 1986/. For an in-plane flow channel, the equivalent transport radius can then be shown to be /Johns and Roberts 1991/:

$$a = \frac{W_c + \delta_t}{\pi} \approx \frac{W_c}{\pi} \qquad \text{(Eq. 5-5)}$$

At very early times and for low F-factors, the results predicted by the base model (BM) and model alternative 2 (MA2) are largely indistinguishable. It is only at later times when the diffusive penetration depth is roughly the same as the channel width that the results for the linear and radial cases begin to differ strongly.

5.3 Modelling results

Since sorption K_d values are highly dependent upon pore water compositions which can change significantly over time, simulation results are presented for the three transport model variants (BM, MA1, MA2) considering a range of sorption K_d values. These represent the range of sorption properties from weakly sorbing ($K_d = 10^{-5}$ m^3/kg) to strongly sorbing ($K_d = 1$ m^3/kg). To visualise the results in a enlightening fashion, a series of figures is first presented where transport times are plotted against sorption K_d, for assumed F-factors in the range of $10^3 - 10^6$ yr/m and a formation factor

of 1.1×10^{-5} which is the approximate mean value for rock within HRD_C in Laxemar as determined by in situ resistivity measurements (see Appendix D). These plots are made for a recovery fraction corresponding to 50% of recovered solute, neglecting radioactive decay and assuming a maximum matrix depth of 2 m.

In addition to the recovery time plots, full cumulative residence time distribution curves are given for the central case F-factor of 10^4 yr/m and $K_d = 10^{-4}$, 10^{-2}, and 10^{-1} m^3/kg as well as for a non-sorbing solute ($K_d = 0$) to aid interpretation of retardation mechanisms in the subsequent discussion. In this chapter results are shown for Saline (brackish, non-marine) groundwater only. Results for Fresh, Marine, Brine, and the Type V (also brackish non-marine) groundwater can be found in Appendix F.

It should be noted that the choice of 2 m matrix penetration depth is purely an arbitrary modelling convenience and should not be taken to indicate a belief that the accessible matrix depth is only 2 m. It may be appropriate in safety assessment, for example, to assume a maximum matrix penetration depth substantially less than the theoretically available penetration depth (which could be many tens of metres) owing to the need to avoid "double counting" of matrix storage capacities for closely spaced flow channels. This is discussed in more detail in /Crawford 2008/.

The results presented in the following sections generally show that saturation effects are largely absent for the range of F-factors considered here (with the exception of very late arriving solute) and the rock matrix could be assumed to be effectively infinite with little or no impact upon safety assessment calculations.

5.3.1 Typical transport times under contemporary (Type III) groundwater conditions

The Figures below show results for the BM, MA1, and MA2 transport models assuming brackish, non-marine (i.e. Type III, "Saline") groundwater chemistry and a solute recovery fraction of 50%. Transport times longer than 10^7 yr (graduated, blue background shading) are considered to be of minor interest and are only included here to illustrate the relative scaling of recovery times implied by the modelled retardation processes. In addition, to give an appreciation of the time scales involved, some significant events in Earth's geological history are indicated on the time axis (see glossary of terms at the end of this report for explanations). Since these events have taken place in the past, they are intended to be interpreted in a relative sense with regard to the estimated transport times. Approximate, illustrative time limits for quantitative (10^5 yr) and qualitative (10^6 yr) safety analysis are shown as the red, broken and unbroken, horizontal lines in the figures. These may not necessarily conform to safety assessment time limits considered in SR-Site, although are loosely based upon guidelines contained in /SSI 2005/.

To illustrate the combined impact of K_d uncertainty and model uncertainty for specific solutes, the span of transport times vs. K_d is plotted as a rectangular polygon in the figures. The lower left hand vertex is the transport time for the model giving the fastest breakthrough using the lowest reported K_d value, while the upper right hand vertex corresponds to the transport time for the model giving the slowest breakthrough time using the maximum reported K_d value. Since there are too few measurements of sorption on individual rock types to give a sufficiently reliable span of K_d uncertainty, the depicted K_d ranges consider a pooling of data for all the main rock types (501030, 501036, 501046, 501056, and 511058) compiled in Section 4.4.4.

It should be noted that the results presented in Figure 5-3 to Figure 5-5 assume constant groundwater conditions which will not necessarily be the case. Since the K_d for specific solutes is often sensitive to changes in groundwater composition, the estimated transport times shown here should be regarded as being merely illustrative.

In certain situations, colloid and possibly bacterial siderophore transport mechanisms may play a role for the release of nuclides to the biosphere. The effect is likely to be largest for the more strongly sorbing solutes (i.e. $K_d \geq 0.1$ m^3/kg) at high F-factors since under such conditions the transport of these solutes by advection and matrix diffusion is otherwise strongly retarded. For naturally occurring colloids, this will be particularly the case if sorption is deemed to be irreversible. In the case of reversible sorption, however, scoping calculations described in Appendix E indicate a negligible effect upon radionuclide transport for the natural colloid concentrations to be found in groundwater at repository depth.

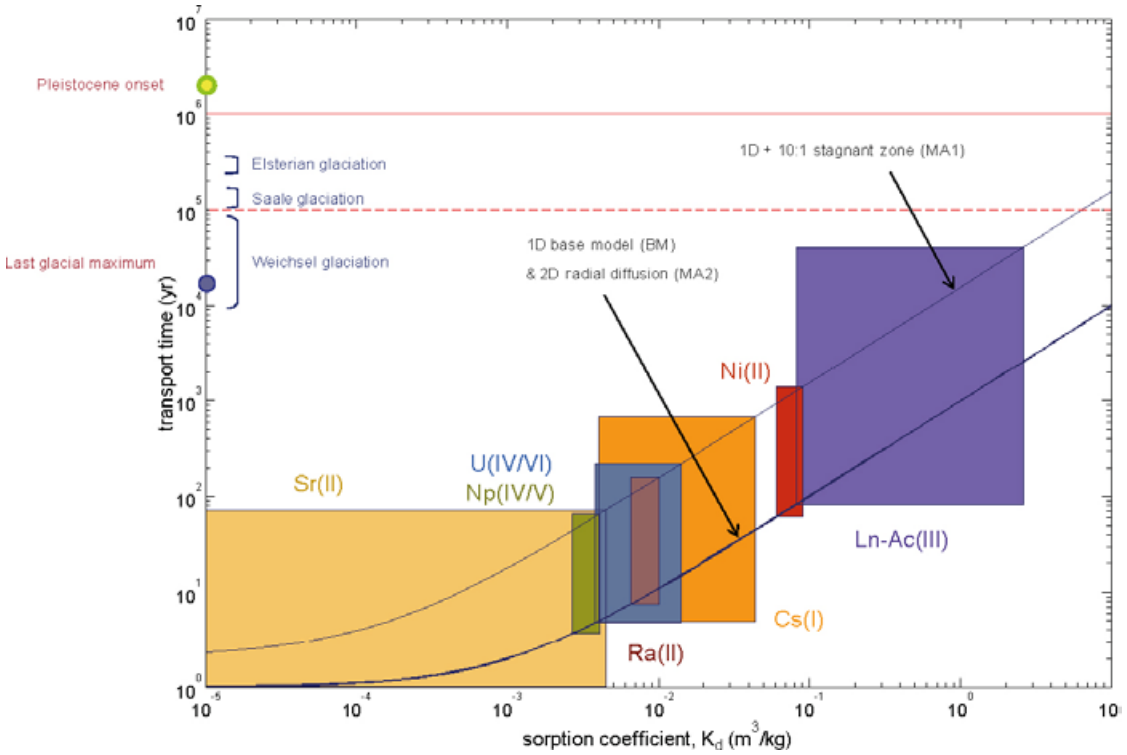

Figure 5-3. *Recovery times for solutes as a function of K_d for a recovery fraction of 50%, a fixed F-factor of 10^3 yr/m, and formation factor of 1.1×10^{-5}. The shaded polygons indicate approximate ranges of transport times for K_d values characteristic of Laxemar specific rock-types in contact with Type III groundwater (see text for detailed explanation).*

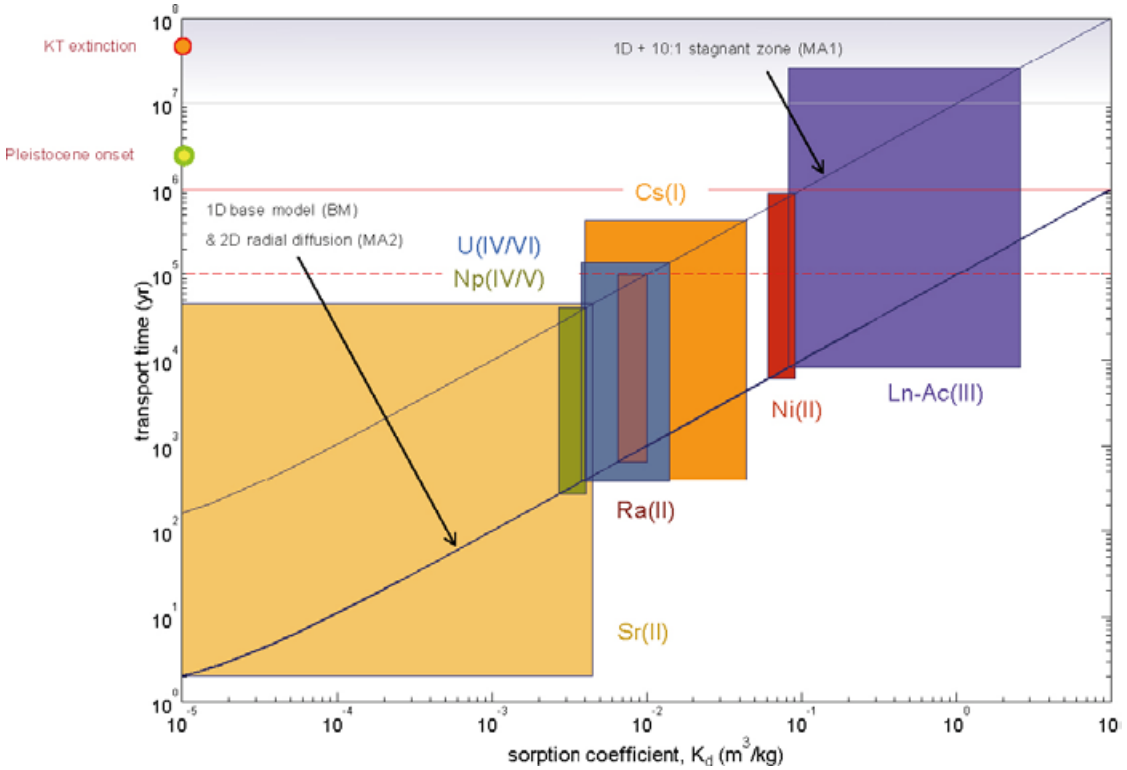

Figure 5-4. *Recovery times for solutes as a function of K_d for a recovery fraction of 50%, a fixed F-factor of 10^4 yr/m, and formation factor of 1.1×10^{-5}. The shaded polygons indicate approximate ranges of transport times for K_d values characteristic of Laxemar specific rock-types in contact with Type III groundwater (see text for detailed explanation).*

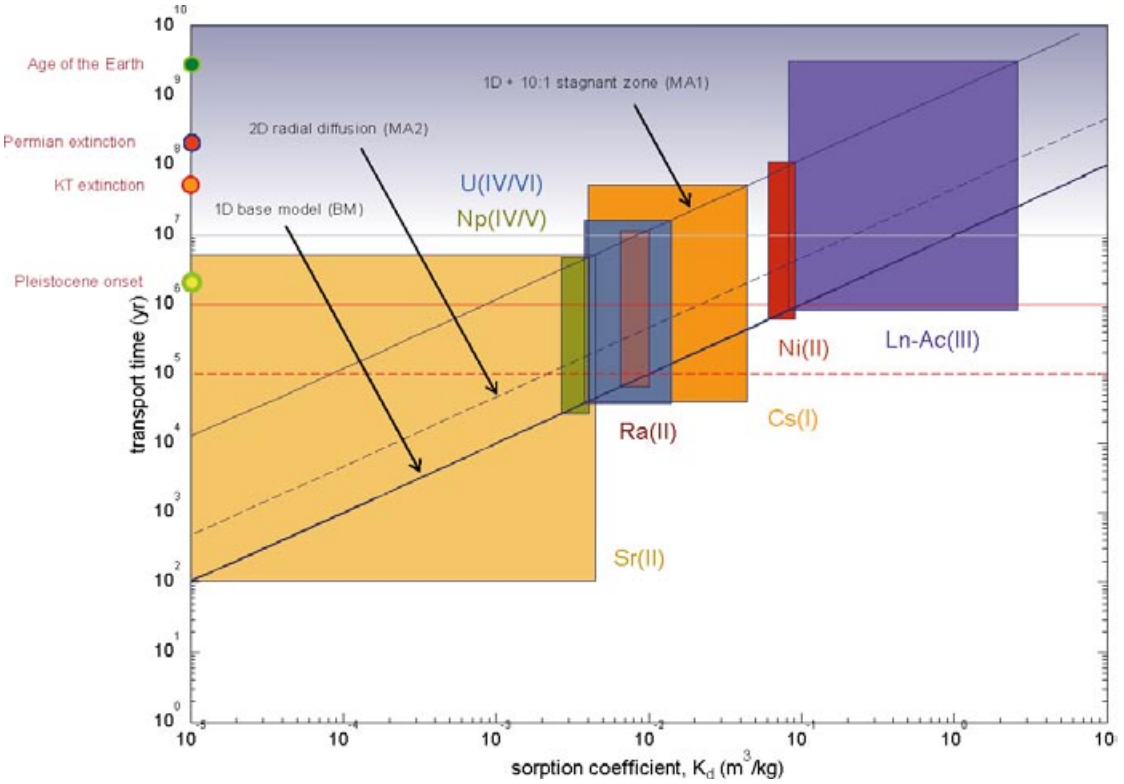

Figure 5-5. *Recovery times for solutes as a function of K_d for a recovery fraction of 50%, a fixed F-factor of 10^5 yr/m, and formation factor of 1.1×10^{-5}. The shaded polygons indicate approximate ranges of transport times for K_d values characteristic of Laxemar specific rock-types in contact with Type III groundwater (see text for detailed explanation).*

Here, by the term colloid the authors specifically mean "pseudocolloids" formed by the sorption of solutes on naturally occurring colloidal substrates. So-called "true" or "eigencolloids" formed by the microprecipitation of strongly hydrolysed actinides are not considered in the present report although may be relevant for safety assessment under certain conditions.

Bacteria capable of excreting siderophores have been cultivated from deep groundwater samples obtained at the Äspö HRL /Johnsson et al. 2006/, although it is not currently known whether there is a non-negligible background concentration of these complexing agents within the groundwater from repository depth in Laxemar (owing to the difficulty of directly identifying these by routine chemical analysis). Given that reducing conditions normally prevail at these depths, however, it is not thought that siderophores should be present in sufficient concentrations to detrimentally impact radionuclide sorption. Investigations at the Äspö HRL have confirmed that these substances are not present in the reducing groundwaters typically found at repository depth /Essén et al. 2007/.

The transport simulation results indicate a large spread in transport times for specific solutes with differing sorption properties and F-factors. For F-factors on the order of 10^3 yr/m, most solutes (including those considered to be strongly sorbing) are subjected to only trivial amounts of retardation and can be expected to be transported to the near surface within the time span of several hundred years. Under these circumstances retardation is weak or absent for K_d values less than about 10^{-2} m^3/kg, and the solute residence time is determined largely by the advective travel time which is taken to be 1 yr in the simulations described here.

Generally, if the matrix residence time is sufficiently large relative to the advective travel time, the recovery time scales linearly with regard to K_d (for a given effective diffusivity) and quadratically with respect to the F-factor. This means that one would expect transport times for an F-factor of 10^5 yr/m to be roughly 10,000 times longer than those obtained for an F-factor of 10^3 yr/m. As can be seen from the figures, this is only strictly true for K_d values somewhat higher than 10^{-2} m^3/kg and also doesn't necessarily apply for the whole residence time distribution. This is discussed in more detail in Section 5.3.2 where the full residence time distributions for a few specific cases are given.

It is interesting to note that the residence times for 50% solute recovery given by the BM (base model) and MA2 (radial diffusion) model variants are largely identical for F-factor values up to 10^4 yr/m implying relatively low effective penetration depths for this recovery fraction. The MA1 model (10:1 stagnant zone), on the other hand, exhibits enhanced retardation even at the lower F-factor of 10^3 yr/m. The enhanced retardation, however, is more pronounced in the case studies involving larger F-factors where a greater proportion of the stagnant zone participates in the mass transfer process. For an F-factor of 10^5 yr/m, a slightly enhanced retardation is obtained for the MA2 variant relative to the BM although still much less than MA1.

5.3.2 Residence time distributions for specific sorption strengths

In this section, results are given for the residence time distributions of solutes exhibiting different sorption strengths for a mid range F-factor of 10^4 yr/m which is thought to be reasonably representative of the Laxemar site. Here, a comparison is made of the transport properties of typical solutes representing the categories: non-sorbing ($K_d = 0$), weakly sorbing ($K_d = 10^{-4}$), moderately sorbing ($K_d = 10^{-2}$), and strongly sorbing ($K_d = 10^{-1}$).

Non-sorbing solutes

Figure 5-6 shows the cumulative residence time distribution for a solute characterised as non-sorbing ($K_d = 0$ m^3/kg). Results are given for the case of an infinite rock matrix as well as a rock matrix of limited depth (here taken to be 2 m).

Figure 5-7 shows the rate of solute mass transfer for different systems relative to that calculated for 1D direct uptake to the rock matrix from a flow channel. Data are shown for the uptake rate to the stagnant zone with subsequent mass transfer as well as for 2D radial mass transfer.

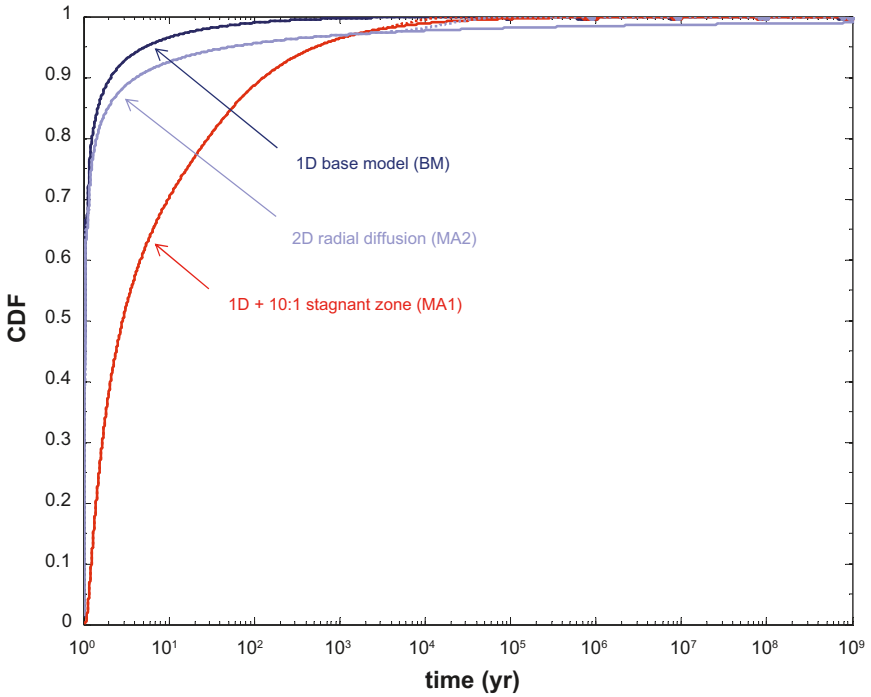

Figure 5-6. *Cumulative residence time distributions for BM, MA1, MA2 transport models for $K_d = 0$ m^3/kg (non-sorbing), a fixed F-factor of 10^4 yr/m, and formation factor of 1.1×10^{-5}. Unbroken lines show results for an infinite rock matrix, broken lines (barely visible in the figure indicating negligible impact) show results for a maximum matrix penetration depth of 2 m.*

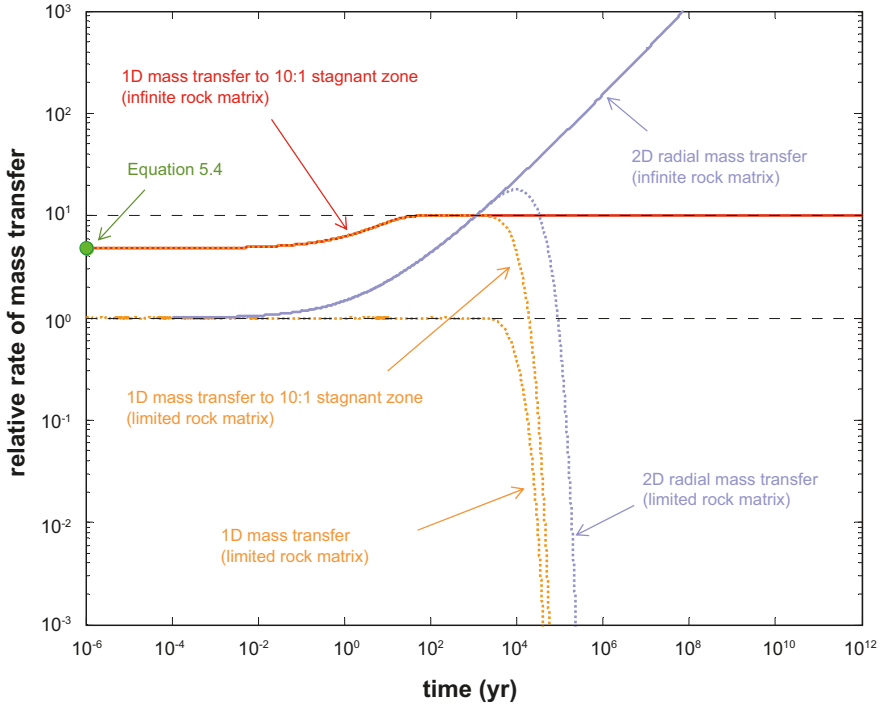

Figure 5-7. *Relative rates of mass transfer as compared to 1D direct uptake to a rock matrix of unlimited depth. The data are for K_d = 0 m³/kg (non-sorbing) and a formation factor of 1.1×10^{-5}. Unbroken lines show results for an infinite rock matrix, broken lines show results for a maximum matrix penetration depth of 2 m. The green marker indicates limiting mass transfer rate to the stagnant zone calculated using Equation 5-4.*

For the assumed flow channel width and effective stagnant zone aperture, the initial (i.e. as t→0) relative rate of mass transfer to the stagnant zone is given by Equation 5-4. For a non-sorbing solute, the limiting relative rate of mass transfer in this particular system is calculated to be 4.8 (indicated by the green marker in Figure 5-7). This means that for the specific solute modelled here, the rate of mass transfer to the stagnant zone is initially 4.8 times the rate of mass transfer directly to the rock matrix. As can be seen from the Figure, the location of the green marker agrees very closely with the limiting rate of mass transfer at early times predicted by the full numerical simulation curves.

As diffusion profiles start to develop within the rock matrix, the relative rate of mass transfer to the stagnant zone increases until it reaches its theoretical maximum where diffusive equilibrium can be assumed throughout the stagnant zone (upper, horizontal broken line). The lower, horizontal broken line indicates the limiting relative rate of mass transfer to the rock matrix from the main flow channel (which by definition is unity).

Weakly sorbing solutes

Figure 5-8 shows the cumulative residence time distribution for a solute characterised as weakly sorbing ($K_d = 10^{-4}$ m³/kg). The following Figure 5-9 contains the same data although plotted on log-log axes to accentuate detail for early breakthrough. The recovery fractions 0.01%, 1%, 10%, and 50% are indicated by horizontal broken lines in Figure 5-9. Results are given for the case of an infinite rock matrix as well as a rock matrix of limited depth (here taken to be 2 m).

Figure 5-10 below shows the rate of solute mass transfer for different systems relative to that calculated for 1D direct uptake to the rock matrix from a flow channel. Data are shown for the uptake rate to the stagnant zone with subsequent mass transfer as well as for 2D radial mass transfer.

For a weakly-sorbing solute, the limiting relative rate of mass transfer in this particular system is calculated to be 0.3 using Equation 5-4 (indicated by the green marker). This means that the initial rate of mass transfer to the stagnant zone is roughly 30% of the rate of mass transfer directly to the rock matrix. As previously, the location of the green marker coincides closely with the numerically simulated curves shown in the same figure.

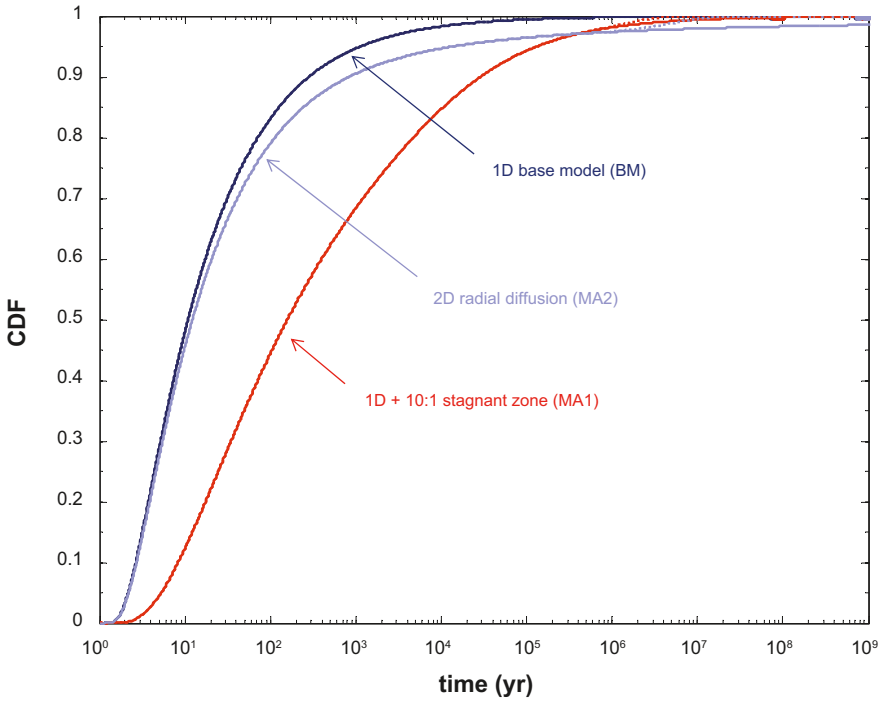

Figure 5-8. *Cumulative residence time distributions for BM, MA1, MA2 transport models for $K_d = 10^{-4}$ m^3/kg (weakly-sorbing), a fixed F-factor of 10^4 yr/m, and formation factor of 1.1×10^{-5}. Unbroken lines show results for an infinite rock matrix, broken lines show results for a maximum matrix penetration depth of 2 m.*

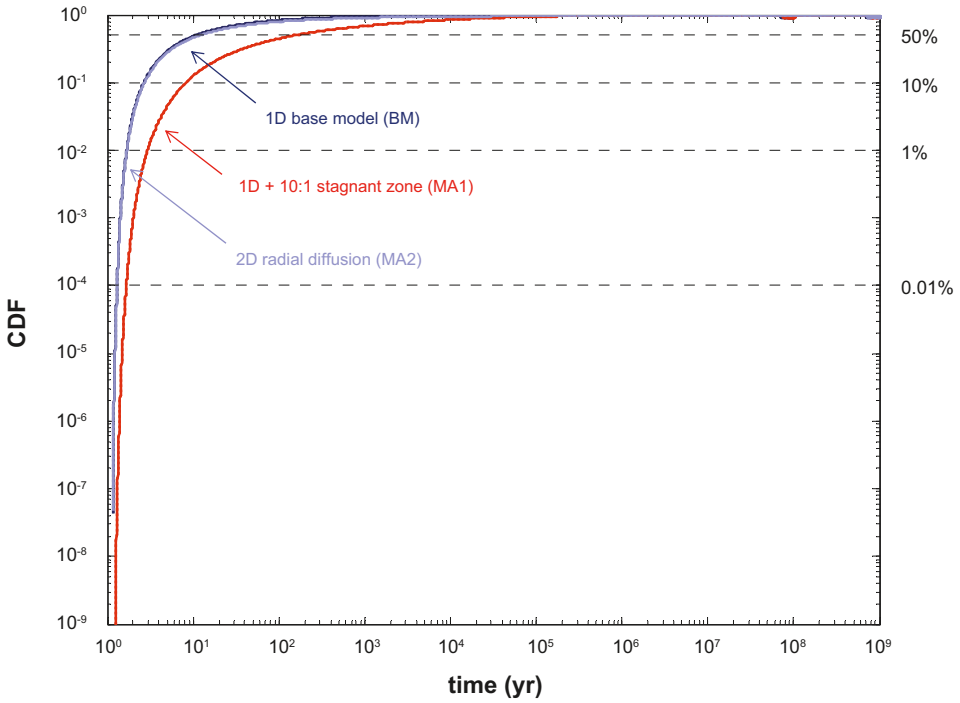

Figure 5-9. *Same results as above, although plotted on log-log axes. Horizontal broken lines indicate recovery fractions of 0.01%, 1%, 10%, and 50%.*

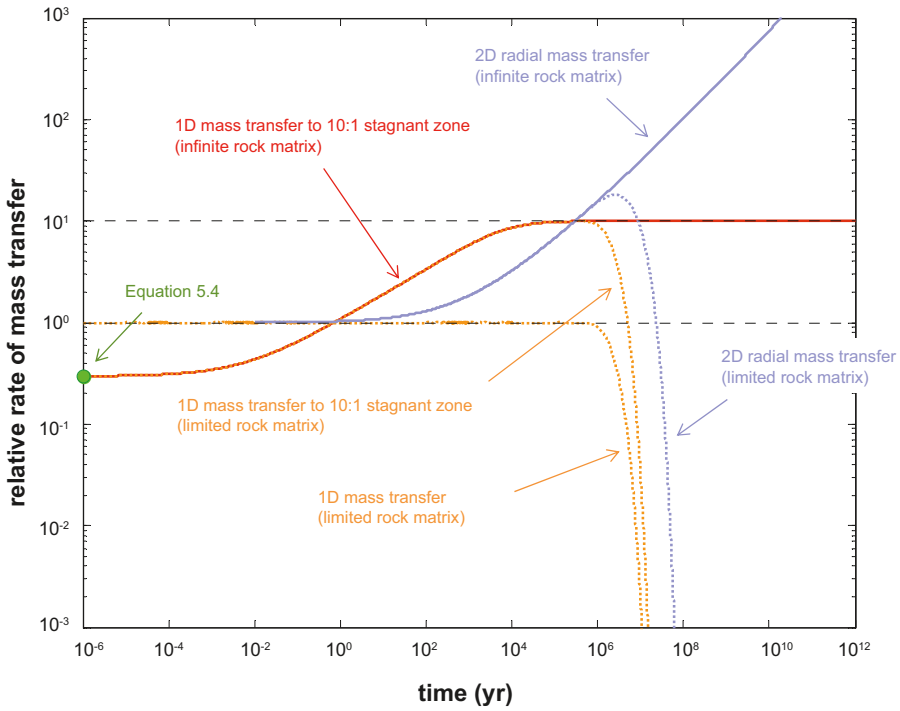

Figure 5-10. *Relative rates of mass transfer as compared to 1D direct uptake to a rock matrix of unlimited depth. The data are for $K_d = 10^{-4}$ m^3/kg (weakly-sorbing) and a formation factor of 1.1×10^{-5}. Unbroken lines show results for an infinite rock matrix, broken lines show results for a maximum matrix penetration depth of 2 m. The green marker indicates limiting mass transfer rate to the stagnant zone calculated using Equation 5-4.*

Moderately sorbing solutes

Figure 5-11 shows the cumulative residence time distribution for a solute characterised as moderately sorbing ($K_d = 10^{-2}$ m^3/kg). The following Figure 5-12 contains the same data although plotted on log-log axes to accentuate detail for early breakthrough. As previously, the recovery fractions 0.01%, 1%, 10%, and 50% are indicated by horizontal broken lines. Results are given for the case of an infinite rock matrix as well as a rock matrix of limited depth (here taken to be 2 m).

Figure 5-13 below shows the rate of solute mass transfer for different systems relative to that calculated for 1D direct uptake to the rock matrix from a flow channel. Data are shown for the uptake rate to the stagnant zone with subsequent mass transfer as well as for 2D radial mass transfer.

For a moderately-sorbing solute, the limiting relative rate of mass transfer in this particular system is calculated to be 3×10^{-2} using Equation 5-4 (indicated by the green marker). In this case, the initial rate of mass transfer to the stagnant zone is less than 2.5% of the rate of mass transfer directly to the rock matrix. As previously, the location of the green marker coincides closely with the numerically simulated curves shown in the same figure.

Strongly sorbing solutes

Figure 5-14 shows the cumulative residence time distribution for a solute characterised as strongly sorbing ($K_d = 0.1$ m^3/kg). The following Figure 5-15 contains the same data although plotted on log-log axes to accentuate detail for early breakthrough. As previously, the recovery fractions 0.01%, 1%, 10%, and 50% are indicated by horizontal broken lines. Results are given for the case of an infinite rock matrix as well as a rock matrix of limited depth (here taken to be 2 m).

Figure 5-16 below shows the rate of solute mass transfer for different systems relative to that calculated for 1D direct uptake to the rock matrix from a flow channel. Data are shown for the uptake rate to the stagnant zone with subsequent mass transfer as well as for 2D radial mass transfer.

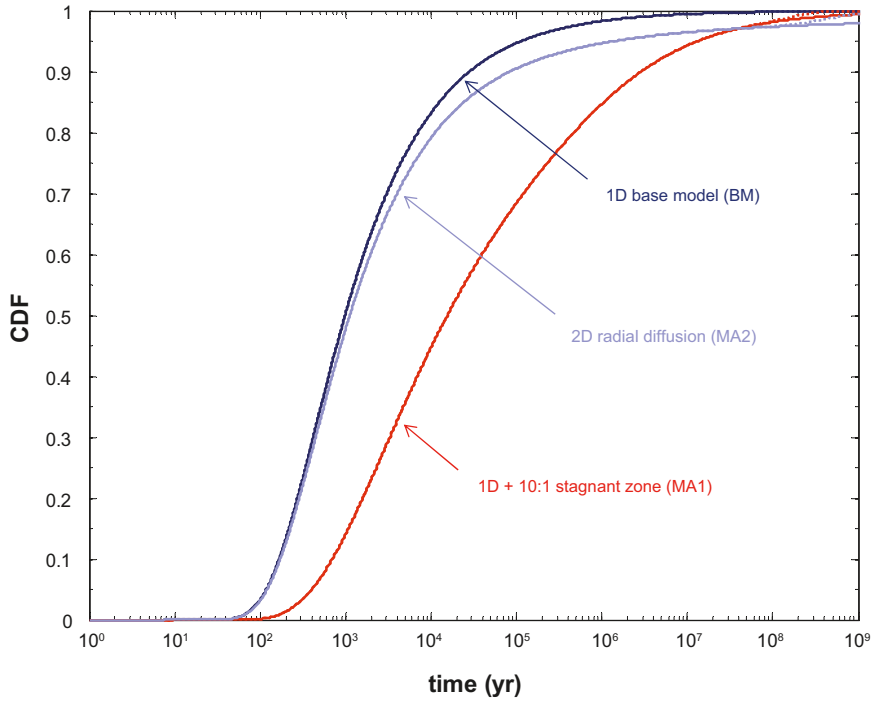

Figure 5-11. *Cumulative residence time distributions for BM, MA1, MA2 transport models for $K_d = 10^{-2}$ m³/kg (moderately-sorbing), a fixed F-factor of 10^4 yr/m, and formation factor of 1.1×10^{-5}. Unbroken lines show results for an infinite rock matrix, broken lines show results for a maximum matrix penetration depth of 2 m.*

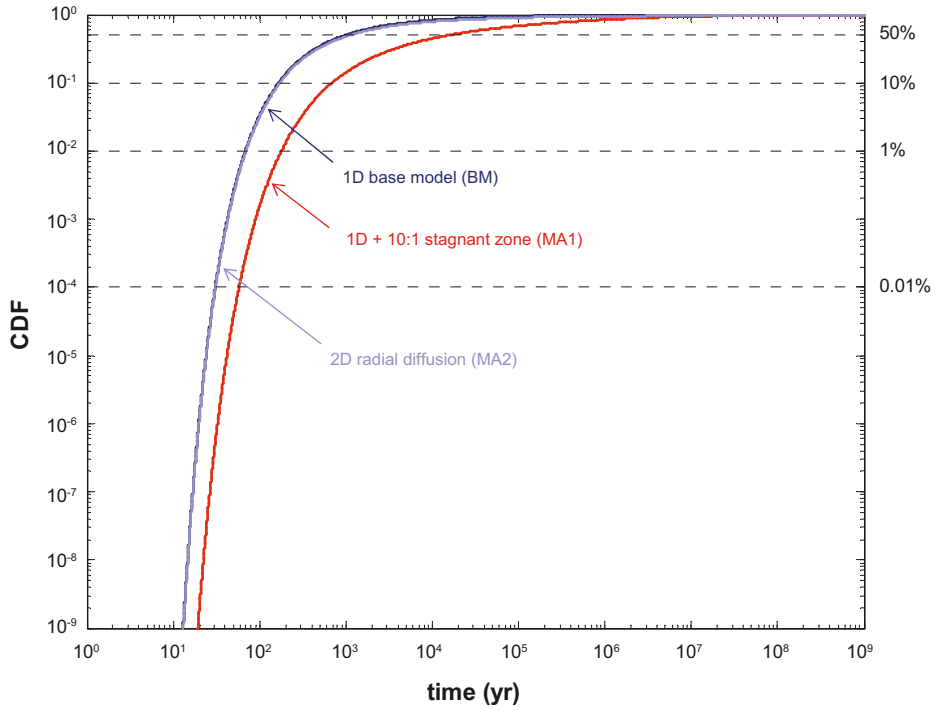

Figure 5-12. *Same results as above, although plotted on log-log axes. Horizontal broken lines indicate recovery fractions of 0.01%, 1%, 10%, and 50%.*

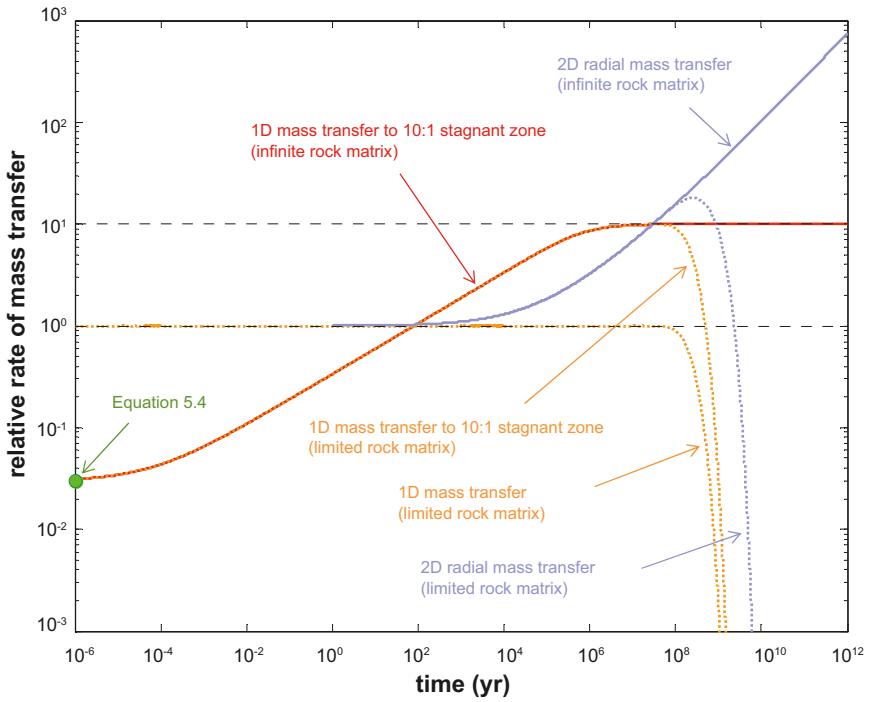

Figure 5-13. *Relative rates of mass transfer as compared to 1D direct uptake to a rock matrix of unlimited depth. The data are for $K_d = 10^{-2}$ m^3/kg (moderately-sorbing) and a formation factor of 1.1×10^{-5}. Unbroken lines show results for an infinite rock matrix, broken lines show results for a maximum matrix penetration depth of 2 m. The green marker indicates limiting mass transfer rate to the stagnant zone calculated using Equation 5-4.*

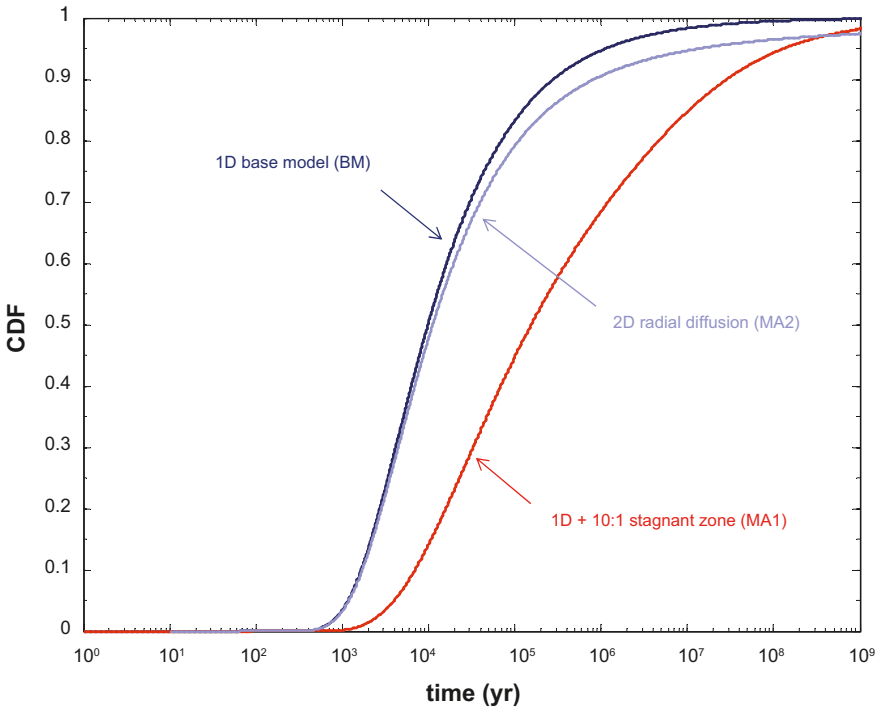

Figure 5-14. *Cumulative residence time distributions for BM, MA1, MA2 transport models for $K_d = 10^{-1}$ m^3/kg (strongly-sorbing), a fixed F-factor of 10^4 yr/m, and formation factor of 1.1×10^{-5}. Unbroken lines show results for an infinite rock matrix, broken lines show results for a maximum matrix penetration depth of 2 m.*

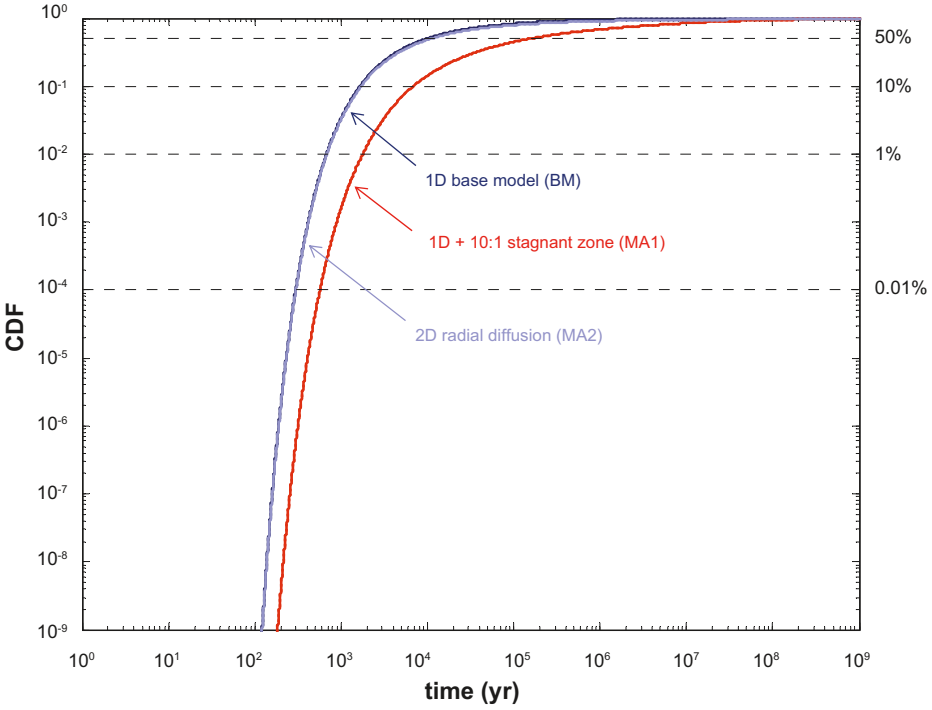

Figure 5-15. *Same results as above, although plotted on log-log axes. Horizontal broken lines indicate recovery fractions of 0.01%, 1%, 10%, and 50%.*

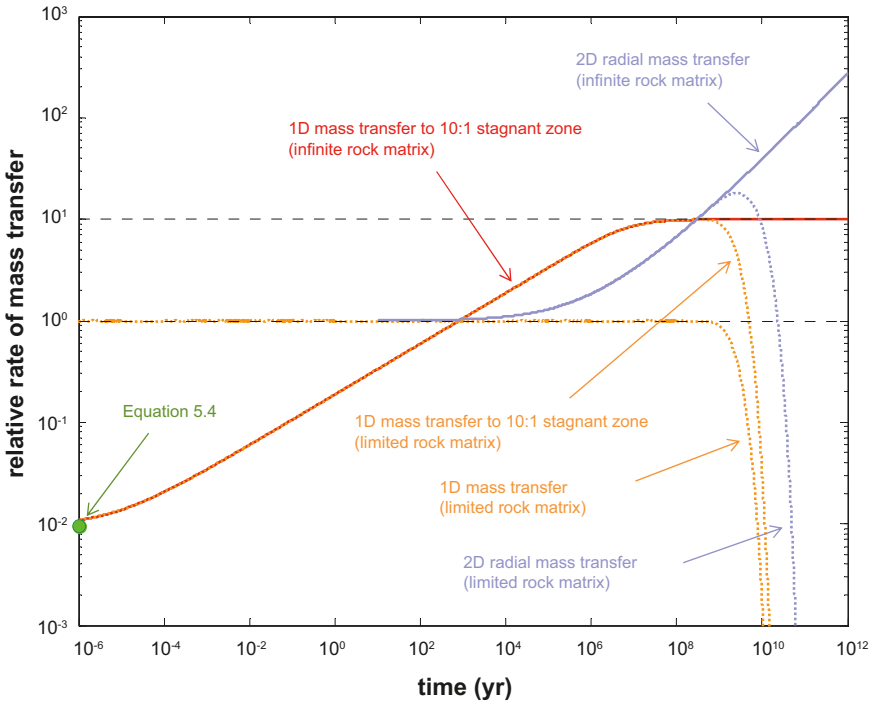

Figure 5-16. *Relative rates of mass transfer as compared to 1D direct uptake to a rock matrix of unlimited depth. The data are for $K_d = 10^{-1}$ m³/kg (strongly-sorbing) and a formation factor of 1.6×10^{-5}. Unbroken lines show results for an infinite rock matrix, broken lines show results for a maximum matrix penetration depth of 2 m. The green marker indicates limiting mass transfer rate to the stagnant zone calculated using Equation 5-4.*

For a strongly-sorbing solute, the limiting relative rate of mass transfer in this particular system is calculated to be 9.4×10^{-3} using Equation 5-4 (green marker). The location of the green marker agrees well with the numerically simulated curves, although a small discrepancy can be seen owing to the assumption that the subsequent diffusion to the rock matrix from the stagnant zone can be initially neglected.

5.4 Impact of fracture coatings and biofilms

Although a small proportion of fractures do not have identifiable coatings, most fracture surfaces are thought to be associated with secondary mineral coatings of various kinds with a thickness of typically between 0.1–5 mm. The measurement data obtained in the laboratory programme and described in chapter 4 suggests that these coatings, for the most part, have increased sorptivity and probably increased porosity as compared with the rock matrix. Owing to the difficulty of obtaining representative samples, however, there is no data concerning the effective diffusivity of these coatings. It is likely in many cases that the friable nature of these coatings may result in very high apparent diffusivities, which if considered together with the sorptivity data would suggest substantially improved retention properties compared to the rock matrix.

If one makes the assumption of a 10 times increased sorptivity and effective diffusivity within a fracture coating, it is possible to calculate the residence time distribution of a solute using the extended transport model presented in /Crawford 2006/ which explicitly accounts for diffusion in a multilayered rock matrix. It should be noted that the proposed retention enhancement factor of 10 is assumed arbitrarily here for illustrative purposes and does not necessarily correspond to the true value. Based upon the available data described in chapter 4, however, this figure does not seem at all unreasonable.

The results of this analysis are shown in Figure 5-17 and Figure 5-18 (log-log axes) assuming a fracture coating thickness of 0.1 mm and a moderately sorbing tracer ($K_d = 10^{-2}$ m^3/kg). Although results are only given for a moderately sorbing tracer it can be shown that the simulated behaviour is general for all K_d values and the residence time distribution of the solute is influenced in a proportional manner.

At this time the authors do not have an extended model for the more complex, multilayer radial diffusion problem and therefore only results for the BM and MA1 transport models are presented. The interpretation of the results, however, should apply equally well to the radial diffusion case as the thickness of the fracture coating is substantially less than typical flow channel widths and therefore radial diffusion will have a negligible impact upon the residence time distribution at very early times.

As can be seen from Figure 5-17, the presence of a 0.1 mm fracture coating with enhanced retention properties gives a small but non-negligible contribution to the "average" retardation of transported solute. The effect at shorter times, however, is much larger as can be seen in Figure 5-18 where first breakthrough of solute is increased by about an order of magnitude as compared to the cases without fracture coatings (unbroken lines).

Figure 5-19 and Figure 5-20 (log-log axes) show the corresponding results for a slightly thicker fracture coating of 1 mm and indicate an even larger enhancement of early breakthrough transport retardation. In this case, the presence of a 1 mm thick surface coating with enhanced retention gives nearly two orders of magnitude additional retardation of the first arriving solute.

The retention properties of the fracture coating can be roughly assessed by comparison of the material properties group, or *MPG* for the fracture coating as compared to the unaltered rock. The material properties group is defined as:

$$MPG = \sqrt{D_e \left(\theta_m + K_d \rho_s\right)} \qquad \text{(Eq. 5-6)}$$

Although the *MPG* does not always uniquely specify the retention properties of the rock (see discussion in /Crawford 2008/), it is still a good qualitative indicator of retention potential. Generally, a fracture coating with decreased *MPG* relative to the rock matrix gives slightly faster breakthrough for the leading edge of the solute residence time distribution, while a fracture coating with increased *MPG* gives slightly more retarded breakthrough.

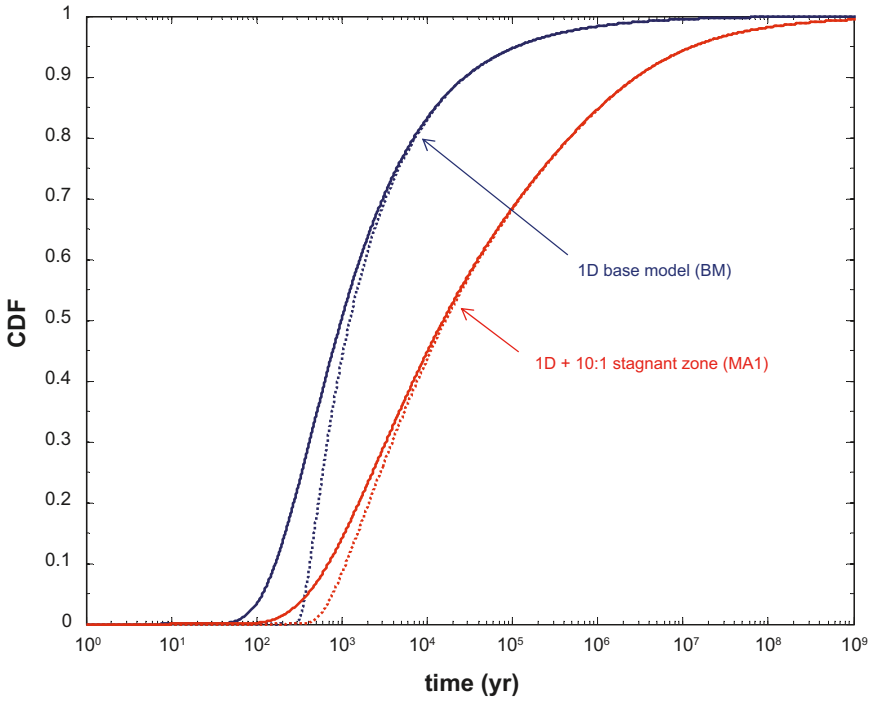

Figure 5-17. *Cumulative residence time distributions for BM and MA1 transport models for $K_d = 10^{-2}$ m³/kg (moderately-sorbing), a fixed F-factor of 10^4 yr/m, and formation factor of 1.1×10^{-5}. Unbroken lines show results for a rock matrix without fracture coating, broken lines show results for a 0.1 mm thick fracture coating with 10 times increased sorptivity and effective diffusivity.*

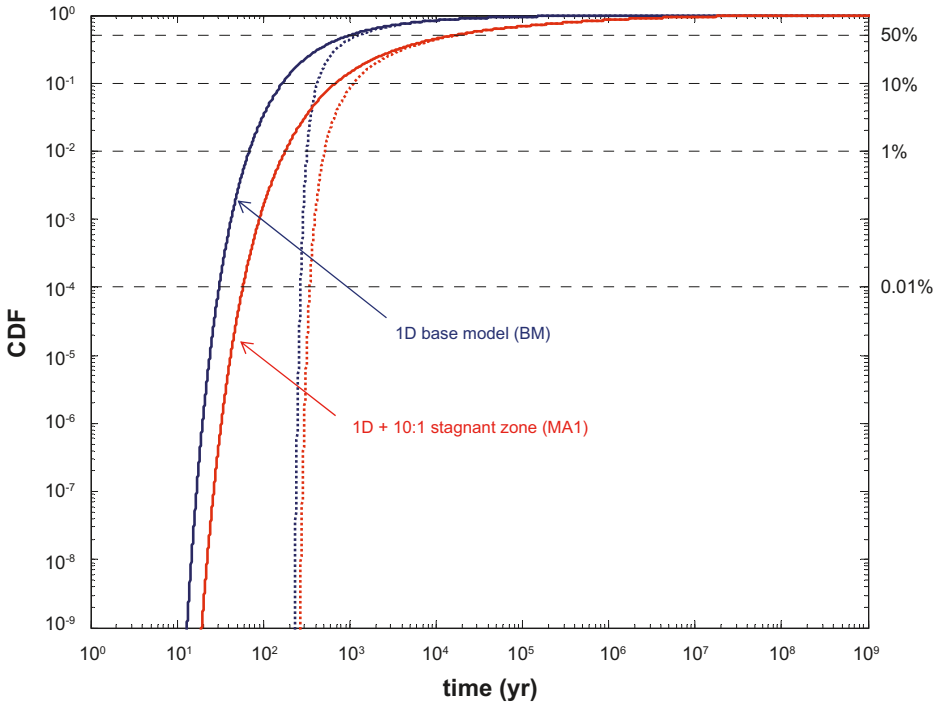

Figure 5-18. *Same results as above, although plotted on log-log axes. Horizontal broken lines indicate recovery fractions of 0.01%, 1%, 10%, and 50%.*

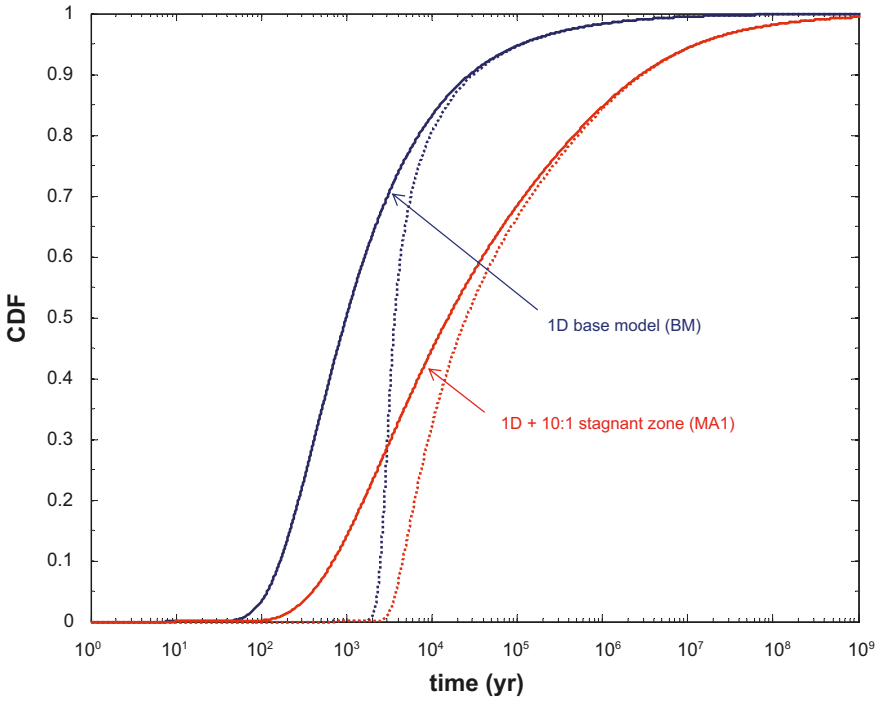

Figure 5-19. *Cumulative residence time distributions for BM and MA1 transport models for $K_d = 10^{-2}$ m³/kg (moderately-sorbing), a fixed F-factor of 10^4 yr/m, and formation factor of 1.1×10^{-5}. Unbroken lines show results for a rock matrix without fracture coating, broken lines show results for a 1 mm thick fracture coating with 10 times increased sorptivity and effective diffusivity.*

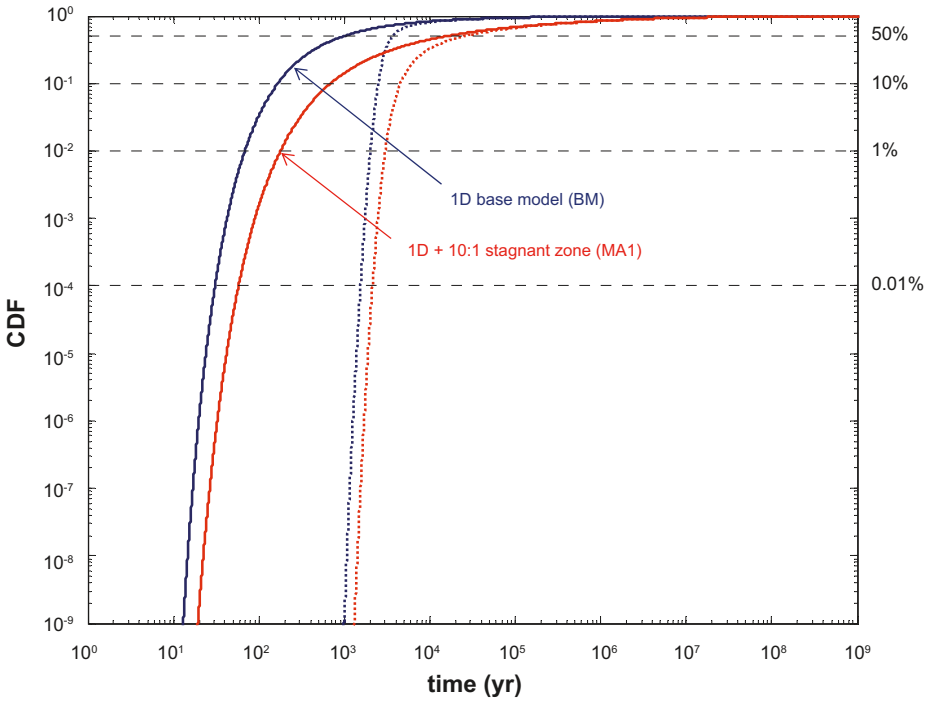

Figure 5-20. *Same results as above, although plotted on log-log axes. Horizontal broken lines indicate recovery fractions of 0.01%, 1%, 10%, and 50%.*

The simulation results indicate that for the relatively low F-factors characterising the Laxemar site, the presence of a fracture coating could potentially have a significant impact upon solute residence time distributions calculated under safety assessment conditions, particularly for the very early arrival of radionuclides.

It is also noted that the presence or absence of a fracture coating is likely to have a large impact upon tracer test results owing to the limited solute penetration depth typically achieved in such experiments. Generally it is expected that sorptive properties sampled during tracer testing, by and large, reflect the retention properties of the fracture coatings rather than the underlying matrix rock. This is discussed in more detail in Section 6.3 where the results of field scale tracer tests carried out at Laxemar are analysed and interpreted.

Figure 5-21 and Figure 5-22 show the rate of mass transfer to the stagnant zone relative to the rock matrix in model variant MA1 for a moderately sorbing and non-sorbing solute, respectively. In Figure 5-21, the relative rate of mass flux at very early times cannot be always calculated for the full 2-layer matrix formulation owing to numerical issues involving the Laplace inversion. This has been previously discussed in /Crawford 2006/. The extrapolated broken curves, however, are based upon a single layer model assuming material properties of the fracture coating and can be seen to exactly match up with the full 2-layer formulation for contact times up to about 50 minutes after which time the full 2-layer formulation is computable. It should also be noted that the data in Figure 5-21 and Figure 5-22 are independent of the F-factor since the calculation only considers the relative rate of solute uptake via the stagnant zone rather than the absolute rate of mass transfer.

It is interesting to note that the asymptotic rate of mass transfer to the stagnant zone agrees with that predicted by Equation 5-4, assuming the fracture coating to be effectively infinite in depth over the timescale of the tracer test. This feature may be of some importance for the interpretation of field scale tracer tests as is discussed later in Chapter 6.

The possibility of the existence of biofilms has also been raised in Section 5.1. Microbial biofilms in fractured rock are generally thought to consist of monolayers of bacterial cells embedded in thin, extracellular polysaccharidal matrices. Some studies have suggested that biofilms have reduced sorptivity for certain radionuclides of importance, although increased sorptivity for others /Anderson et al. 2006, Anderson et al. 2007/. Measurement of the diffusive properties of biofilms has also proven difficult owing to the very small effects measured in laboratory experiments and non-uniqueness of modelling interpretations /Charbonneau et al. 2006/. Such biofilms could exist on the external surfaces of the fractures themselves as well as within the macro-pore space of the first few μm of the rock matrix.

According to the literature /e.g. Stewart 1998/, the diffusivity of solutes in biofilms is relatively high (close to that for water) since they consist of sparsely distributed cells embedded in the volumetrically much larger extracellular matrix. Although some reductions in sorptivity have been reported for biofilms in the references above, the thickness of biofilms is thought to be sufficiently small that this would not have a great impact upon the transport properties along a flowpath.

It is considered unlikely that microbes can exist within pores smaller than themselves which would restrict such growth to pore sizes greater than ~1μm /Pedersen and Karlsson 1995/. Whether microbes present in small pores would block diffusion is not known since this depends upon the extent to which they fill the pore space and whether the limited space is conducive to respiration and growth. It has been speculated, however, that most ionic environmental solutes are excluded from the cells themselves /Stewart 1998/ which raises the theoretical possibility for some pore clogging to occur.

It is not clear what thickness such films could reach under normal growth conditions at repository depth in Laxemar as this is strongly dependent upon the availability of limiting nutrients and electron receptors. It is also not generally feasible to ascertain the presence or absence of biofilms from surface based site investigations, so in this report quantification of the impact of these can only be approached by way of scoping calculations. Further work may need to be done, however, to establish the role of pore clogging by individual microbes during the construction phase of the repository.

Since the sorptive and diffusive properties of biofilms are so poorly understood with regard to their impact on solute transport in advective flow systems it is only possible at present to make scoping calculations to assess what impact they “might” have under various bounding assumptions.

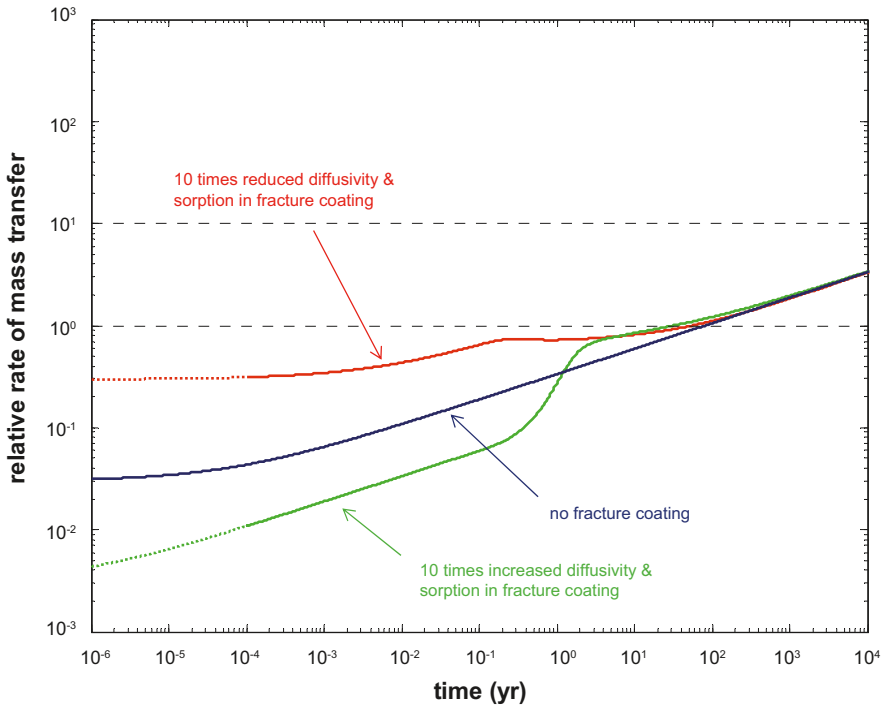

Figure 5-21. *Relative rates of mass transfer to the stagnant zone as compared to 1D direct uptake to a rock matrix of unlimited depth. The data are for $K_d = 10^{-2}$ m³/kg (moderately-sorbing) and a formation factor of 1.1×10^{-5}. Modelling results are shown for the case of no fracture coating as well as a 0.1 mm thick fracture coating with 10 times increased/decreased sorptivity and diffusivity relative to the rock matrix.*

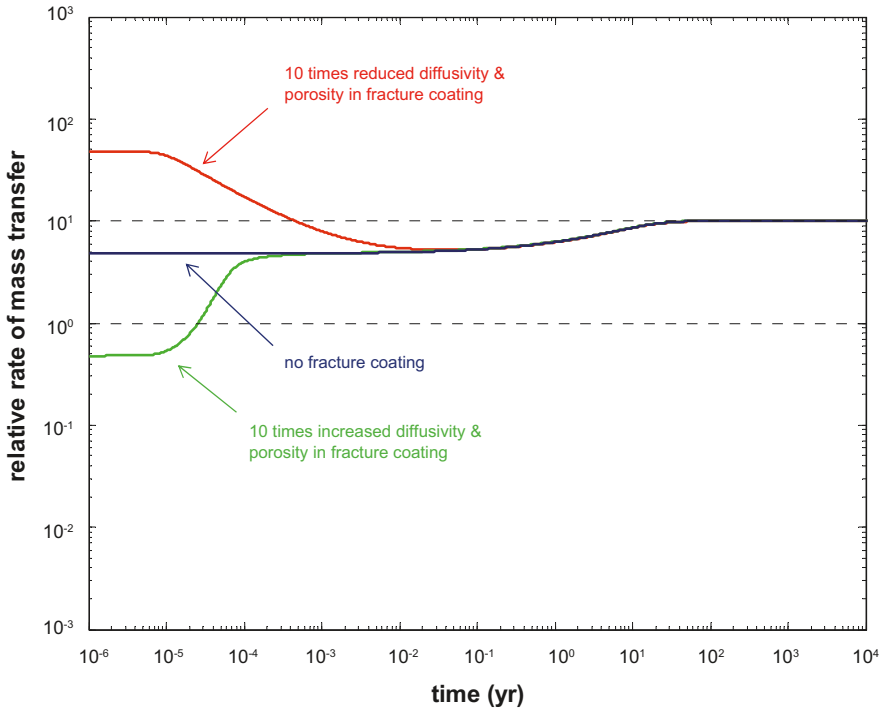

Figure 5-22. *Relative rates of mass transfer to the stagnant zone as compared to 1D direct uptake to a rock matrix of unlimited depth. The data are for $K_d = 0$ m³/kg (non-sorbing) and a formation factor of 1.1×10^{-5}. Modelling results are shown for the case of no fracture coating as well as a 0.1 mm thick fracture coating with 10 times increased/decreased storage porosity and diffusivity relative to the rock matrix.*

If one were to assume the presence of a 0.1 mm thick, continuous biofilm with a 10 times reduced sorptivity and diffusivity (owing to a hypothetical pore clogging process), the residence time distribution of a moderately sorbing solute ($K_d = 10^{-2}$ m^3/kg) might look something like that shown in Figure 5-23 and Figure 5-24 for an F-factor of 10^4 yr/m.

As can be seen from Figure 5-23 and Figure 5-24, the presence of a 0.1 mm thick biofilm (surface coating) with diminished retention has a considerable deleterious effect upon early breakthrough of solute, particularly for the early arriving fraction up to about 20–30% recovery.

This scenario, however, may not be altogether realistic since it is not known if pore clogging by microbes really does occur. For this reason an alternative case has been simulated where the biofilm has an assumed 10 times decreased sorptivity, although an effective diffusivity close to that for the solute in free solution (as suggested by /Stewart 1998/). These results are presented in Figure 5-25 and Figure 5-26.

As can be seen from the plotted residence time distribution curves, if the biofilm has an effective diffusivity much larger than the underlying rock, the effect of the biofilm is negligible even if the sorptivity of the biofilm is reduced relative to the rock. This, however, is dependent upon the value of the MPG parameter which, because of the high diffusivity of the biofilm in this case, gives a very minor enhancement of solute retardation even though the sorptivity of the biofilm is less than that of the rock.

On the basis of these results it is reasonable to conclude that the presence of a biofilm up to 0.1 mm thick with reduced sorptivity relative to the host rock should not detrimentally influence the residence time distribution of solute, provided the microbial growth does not lead to a decrease in effective diffusivity owing to pore clogging in the micropores close to the fracture surface.

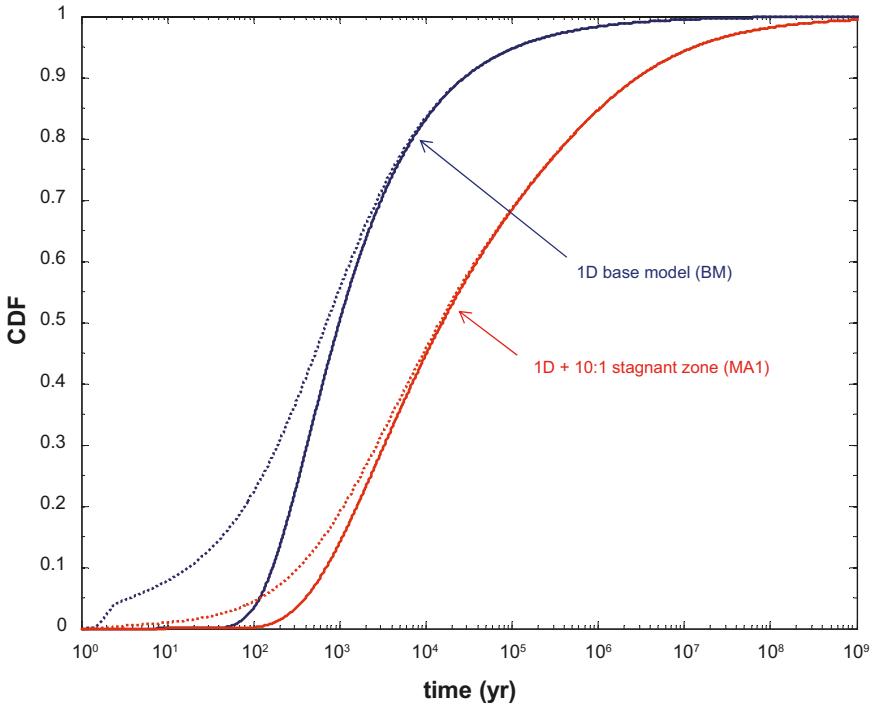

Figure 5-23. *Cumulative residence time distributions for BM and MA1 transport models for $K_d = 10^{-2}$ m^3/kg (moderately-sorbing), a fixed F-factor of 10^4 yr/m, and formation factor of 1.1×10^{-5}. Unbroken lines show results for a rock matrix without fracture coating, broken lines show results for a 0.1 mm thick fracture coating with 10 times decreased sorptivity and effective diffusivity.*

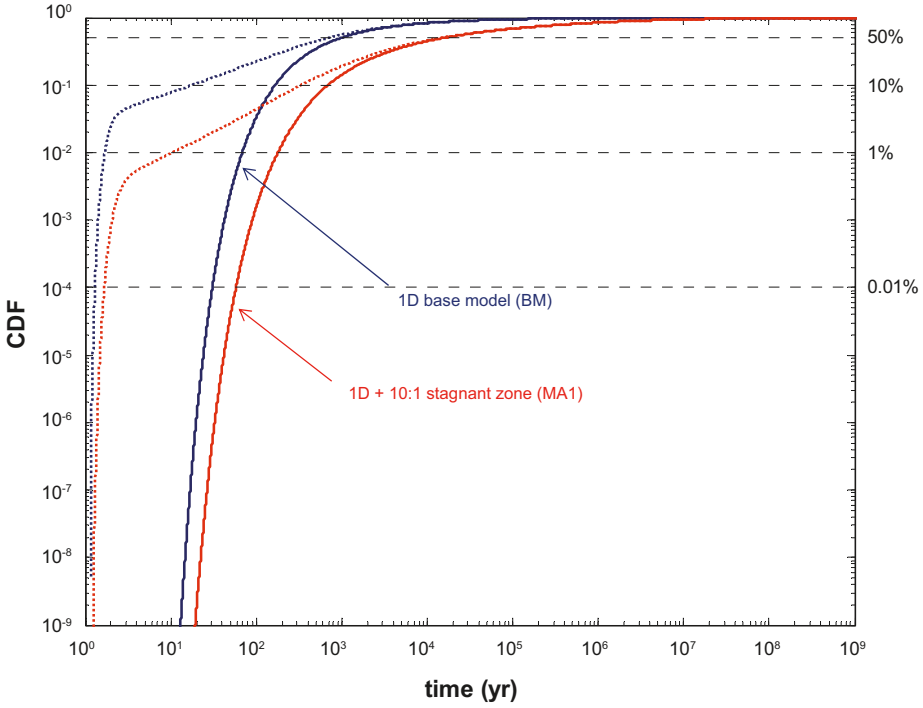

Figure 5-24. *Same results as above, although plotted on log-log axes. Horizontal broken lines indicate recovery fractions of 0.01%, 1%, 10%, and 50%.*

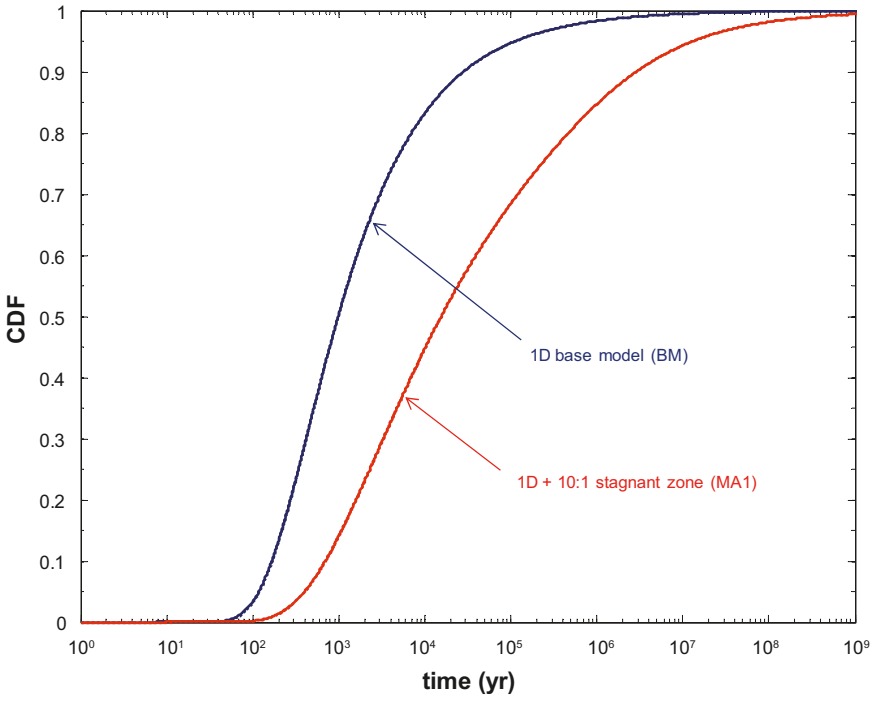

Figure 5-25. *Cumulative residence time distributions for BM and MA1 transport models for $K_d = 10^{-2}$ m³/kg (moderately-sorbing), a fixed F-factor of 10^4 yr/m, and formation factor of 1.1×10^{-5}. Unbroken lines show results for a rock matrix without fracture coating, broken lines show results for a 0.1 mm thick fracture coating with 10 times decreased sorptivity (effective diffusivity is assumed equal to free diffusivity in water).*

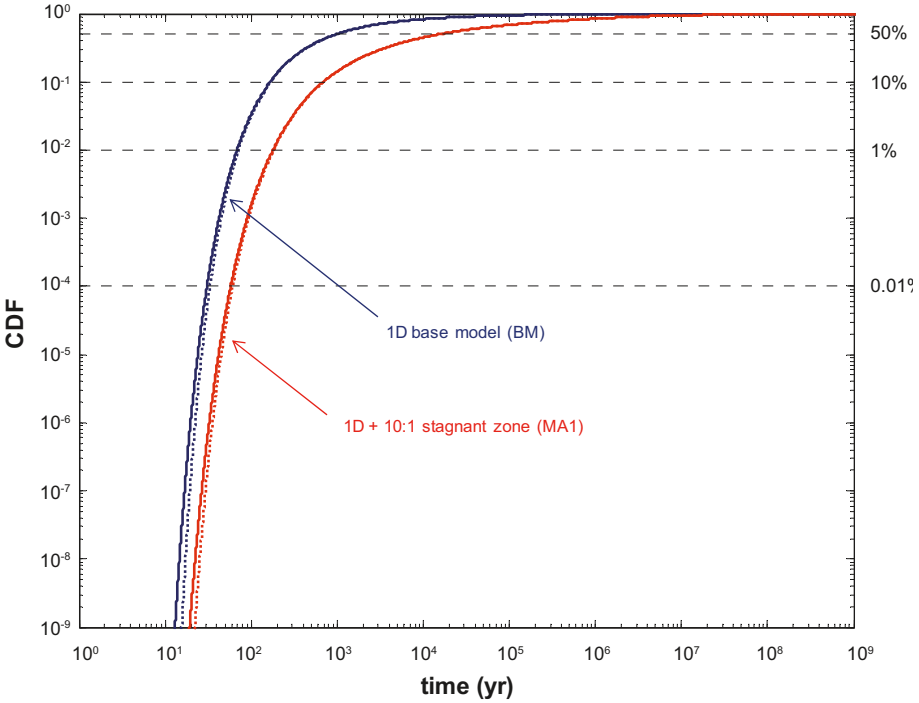

Figure 5-26. *Same results as above, although plotted on log-log axes. Horizontal broken lines indicate recovery fractions of 0.01%, 1%, 10%, and 50%.*

5.5 Discussion

The transport simulation results presented in Section 5.3 indicate a large spread in transport times for specific solutes with differing sorption properties. Generally, the transport time for a solute can be shown to be proportional to both its K_d value and the square of the F-factor for the flowpath along which it is transported for a given effective matrix diffusivity (i.e. if the rock matrix residence time is much greater than the advective travel time). A K_d value increased by a factor of 10 therefore implies a corresponding increase in the transport time. On the other hand, increasing the F-factor for a flowpath by a factor of 10 gives a 100 times increased transport time. The extent to which this can be assumed to be true, however, depends upon the magnitude of the F-factor. If the F-factor is very low, then the advective transport time cannot be neglected and the relative scaling of transport times differs somewhat from this simple heuristic rule.

The range of variability of measured K_d values for specific solutes is generally about 1–2 orders of magnitude which implies a similar range in variability of transport times for these solutes, all other things being equal. Some solutes such as Ra(II), Ni(II), and Np(IV/V) have reduced ranges of apparent variability due to the lower numbers of samples. Other solutes such as Sr(II) have poorly constrained lower K_d bounds owing to weak sorption and relatively high measurement limits. Np and U are a special case owing to their sensitivity to redox conditions and the possibility that fully reducing conditions may not have been achieved in the laboratory. As already discussed in chapter 4, this means that the lower measurement limits for U and Np may be biased by the presence of oxidised forms which may not necessarily be present under repository conditions at depth. Since the appropriate K_d values for many of these solutes are not well constrained, the transport calculations detailed in chapter 5.3.1consider a broad range of sorptivities ranging from weakly sorbing ($K_d = 10^{-5}$ m^3/kg) to strongly sorbing ($K_d = 10^{-1}$ m^3/kg).

Additional variability in estimated transport times follows if further consideration is also given to the different assumptions made during transport modelling. The three different models presented in this chapter (BM, MA1, and MA2) represent hypothetical explorations of the consequences of some different modelling assumptions related to flow channelling.

It is not clear whether the assumption of a 10:1 in-plane stagnant zone in model alternative, MA1 is a reasonable estimate of the average stagnant zone width potentially existing along typical flowpaths within the rock. If the assumption is correct, considerably increased transport times are obtained relative to the base case scenario (BM) lacking stagnant zones. When the F-factor is sufficiently high, then diffusive equilibrium can sometimes be achieved throughout the stagnant zone. As discussed in /Crawford 2008/, a direct consequence of this observation is that the transport aperture, δ_s and mass transfer surface area ratio, R_s can be neglected in safety assessment and the effect approximated by incorporating the additional diffusion accessible surface into the flow-wetted surface without introducing significant errors for most of the residence time distribution envelope. This simplification is not valid for very short times as the advectively transported solute will not have had sufficient time to diffuse fully into the stagnant zone. The residence time distribution for the MA1 case therefore converges towards that for the BM case at very short timescales, suggesting that the transport time for the very first solute arrival is given approximately correctly by the standard diffusion model (BM).

The maximum additional retardation effect that can be achieved in the case of a single 10:1 stagnant zone flanking the flowpath is therefore equivalent to that obtained by increasing the F-factor 11 times. For a matrix residence time dominated system, this translates to a 121 times increase in retarded transport time according to the abovementioned heuristic scaling rule. If roughly symmetric 10:1 stagnant zones exist on either side of the main flow channel, the total diffusion accessible surface area would be 21 times that of the flow channel, thus giving an overall increase in transport time of 441 times. For low F-factors, on the other hand, it is not possible to fully realise the theoretically available retardation enhancement since the stagnant zone is only partly equilibrated on the time scale of solute transport and increases in solute residence times are more modest.

The results in Figure 5-5 suggest diffusive equilibrium may be attainable in a 10:1 stagnant zone for F-factors in excess of about 10^5 yr/m. For the lower F-factors considered in Figure 5-3 and Figure 5-4, however, the results indicate increases in residence time that are significant although much less than the theoretical maximum. This is a good indication that the assumption of diffusive equilibrium throughout the stagnant zone cannot be applied in such cases and the full unsteady-state diffusive formulation of the stagnant zone problem needs to be solved to obtain accurate results for the residence time distribution.

For the F-factors considered here, the radial diffusion formulation (MA2) only differs slightly to the base case model (BM) at later recovery fractions when the solute penetration depth is equal to or greater than the flow channel width. For all practical purposes, the BM and MA2 models give identical results at low to intermediate recovery fractions and no advantage is conferred by this alternative model configuration.

Although in this modelling work a strict demarcation is made between flowing and stagnant water volumes, in reality there will be a heterogeneous distribution of flow across fracture surfaces with variations in local advective velocities possibly spanning some orders of magnitude. In the work flow channels are operationally defined to be pathways where “most flow” occurs. Under extreme in-plane flow channelling conditions with large portions of the fracture closed due to surface asperity contact it may be possible to find sparse flow channels and large regions of the fracture with effectively stagnant water. For less extreme flow channelling situations, flow channels may occur with a greater spatial frequency, although there will still be large variations in the magnitude of the flows and possibly regions in between the channels that are for all practical purposes stagnant although still could be considered to be flowing. Further discussion concerning some of the more generic aspects of the analysis including flowpath averaging of material properties can be found in /Crawford 2008/.

5.6 Summary of main findings

In summary, the key findings of this chapter include:

- Given the many assumptions inherent in the description of the poorly transmissive initial pathways connecting individual deposition holes with “typical” major flowpaths within the hypothetical repository volume at Laxemar, no credit was taken for the hydrodynamic transport resistance

accumulated in this part of the flow system (what in this report is termed the non-engineered near field, NNF). Only the major flowpaths in the repository volume (immediate far-field, IFF) as characterised in the Hydrogeological DFN modelling work were considered to contribute to the overall F-factor for the HRD;

- Owing to the large spread of F-factors estimated for typical flowpaths, it is not possible to determine with any certainty whether the main part of the transport resitance resides in the HRD or the deformation zones comprising the HCD. In the scoping calculations, transport resistances in the near surface aquifers are neglected and only the deeper parts of the HCD are assumed to contribute in a meaningful way to the flow related transport properties of the distant far-field;
- Given the various uncertainties inherent in the analysis, overall F-factors in the range of $10^3 – 10^5$ yr/m were considered to be cautiously realistic for the hypothetical repository volume at Laxemar and representative of the major transport paths for the transport calculations made in this chapter;
- Since advective travel times are highly uncertain, a water residence time of 1 yr was chosen as a base case. This could be considered to be at the lower end of the calculated ranges estimated for the site as described in Section 3.8 for the hypothetical repository volume at Laxemar. For the relatively low F-factors characterising the Laxemar bedrock, the advective transport time could potentially have a large impact upon radionuclide residence times in safety assessment. It should be emphasised, however, that for long lived radionuclides the uncertainty associated with the advective travel time should have little impact on safety assessment metrics for far-field dose calculations (since the range of advective transport times are effectively instantaneous on a safety assessment timescale);
- A limited rock matrix depth of 2 m was chosen for the calculations. This does not in any way reflect an assumption concerning the depth of connected rock matrix porosity and is only a modelling convenience used here to illustrate some of the effects of matrix saturation. For the ranges of F-factors studied, no matrix saturation effects of consequence were observed and the rock matrix could be assumed to be effectively infinite for safety assessment calculations without running the risk of double counting the geological storage capacity;
- Since site specific K_d values for specific solutes are not well constrained, scoping calculations of radionuclide transport have been made for a hypothetical repository at Laxemar assuming a range of K_d values ranging from non-sorbing ($K_d = 0$ m^3/kg) to strongly sorbing ($K_d \geq 0.1$ m^3/kg). The site specific formation factor of the rock matrix was assumed to be 1.1×10^{-5} which is approximately representative for the HRD_C hydraulic rock domain based upon the in situ resistivity measurement data (see Appendix D);
- Three different modelling alternatives have been considered in this chapter for the estimation of transport times for radionuclides of interest along “typical” transport paths. These were intended to explore some of the consequences of flow channelling in a forward modelling perspective; i.e. how the existence of flow-channelling can be expected to influence modelled solute transport.
  The models used in the calculations were:
  a) A standard model of advective flow coupled with 1D matrix uptake which is commonly used in safety assessment studies (referred to as the base model, BM);
  b) A model similar to the above although with the inclusion of a single, flanking stagnant zone 10 times larger in width than the narrow central flow channel. Subsequent diffusive uptake from the stagnant zone to the rock matrix is a key feature of this model (referred to as model alternative, MA1 with a 10:1 stagnant zone);
  c) A model of advective flow coupled with 2D radially symmetric matrix uptake from a flow channel of limited width (referred to as model alternative, MA2 for radial diffusion);
- Provided the F-factor is sufficiently large that the advective travel time can be neglected, the transport time of individual radionuclides is proportional to the sorption partitioning coefficient, K_d and the effective diffusivity, D_e and proportional to the square of the F-factor (if matrix saturation effects are excluded). A 10 times increase in the F-factor can then be expected to give an approximately 100 times increase in the transport time for a solute. For low F-factors on the order of $10^3 – 10^4$ yr/m where the advective travel time cannot be neglected, some departures from this general heuristic scaling rule are observed;

- The presence of stagnant zones was found to greatly increase the retardation of transported solutes when included in transport simulations. Under certain conditions, the diffusive equilibration of the stagnant zone can occur sufficiently fast relative to the solute transport time that the effect can be approximately modelled by simply upscaling the flow wetted surface to include the extra diffusion accessible surface (DAS). For the specific cases considered in this chapter, however, the increases in transport time are generally much smaller owing to lower F-factors. In such cases, transient mass transfer dynamics in the stagnant zone need to be modelled in more detail to estimate correct solute residence times;
- For high F-factors and small flow channel widths, the radial diffusion model (MA2) can sometimes give considerably greater retardation than the base case 1D model (BM). The results suggest, however, that there are only very minor differences between the predictions made by these two model variants for the range of F-factors considered in the calculations;
- Since there is currently little data concerning the presence or absence of biofilms on fracture surfaces at Laxemar, scoping calculations have been used to investigate possible effects on transport. It is found that the presence of biofilms of thickness up to 0.1 mm should not have a discernable impact upon solute travel times on safety assessment timescales when simulated using a range of arbitrarily assumed although reasonable values for reduced sorptivity and diffusivity compared to the rock matrix. However, if microbial growth occurs in such a way that partial clogging of the matrix pore space occurs in the immediate vicinity of the fracture surface, this may have a negative impact upon radionuclide transport retardation;
- Depending upon their retention properties, fracture coatings on the order of 1 mm in thickness appear to have a strongly positive impact upon solute retardation. It appears from the transport properties evaluation of site specific geologic materials described in Chapter 4 that fracture skins of secondary mineralisation are most likely to enhance radionuclide retardation for the very leading edge of the radionuclide breakthrough at early to intermediate transport times;
- Matrix saturation effects may or may not be important depending upon the permitted maximum depth of matrix penetration and transport model used. Relict porewater signatures at Laxemar /Laaksoharju et al. 2009/ imply the existence of a connected matrix porosity over at least several metres. The consideration of shorter maximum depths of penetration, however, may be necessary to avoid double counting of matrix storage capacities during safety assessment modelling. For the range of F-factors examined in the transport calculations, however, effective penetration depths for transported solutes appear to be sufficiently low that the rock matrix can be assumed to be infinite without risk of double counting the rock matrix storage capacity (with the exception of very closely spaced fractures with separation less than about 1 m);

6 Field scale tracer tests

An important element of the site descriptive modelling at Laxemar has been the integration of field scale testing within the modelling work. By "field scale" testing the authors specifically mean forms of hydrogeologic and tracer migration testing performed on site with the aim of directly characterising the properties of the system and on macroscopic scales larger than that typically considered in laboratory experiments.

These kinds of tests serve a multitude of functions for the different topic areas of interest. For Hydrogeology, the incorporation of data in the form of pressure responses in interference tests, point water heads measured in rock and soil, groundwater compositions and palaeo-hydrogeological information is instrumental in calibration of flow models and for validation of interpretations in the development of the hydrogeological site descriptive model. A large number of tracer dilution tests have also been carried out with the aim of characterising the hydrogeological properties of features with flow rates below the detection limit of direct measurement methods involving pumping such PFL and PSS. Large scale, conservative tracer tests are used to verify connectivity in the system which is used for confidence building for the flow models.

For transport properties site descriptive modelling, tracer tests are used to verify connectivity as well as to demonstrate retention and retardation of transported solutes. In this chapter the tracer tests which have been carried out within the Laxemar site investigation are discussed and an attempt is made to make interpretations of the results obtained and what these might mean for safety assessment. Here, the focus is upon the tracer tests that have most relevance for the transport properties site descriptive modelling. These consist of multiple well tracer tests and a series of single well injection withdrawal tests (SWIW). Borehole locations for tracer tests discussed in this chapter are shown in Figure 6-1. Results of tracer dilution tests are not discussed in this chapter as they have already been dealt with in Chapter 3.

6.1 Multiple well tracer tests

Three multiple well tracer tests have been performed in Laxemar, of which two have been reported at the time of preparation of this report. The first test took the form of a pumping test with non-sorbing tracer (Rhodamine WT) injection in borehole KLX02 and withdrawal in borehole HLX10 at a distance of roughly 260 m /Gustafsson and Ludvigson 2005/. The second test was carried out by non-sorbing tracer (uranine) injection in soil well SSM000228 with withdrawal pumping in borehole HLX33 /Svensson et al. 2008/ at a distance of 204 m. The third tracer test /Lindquist et al. 2008/ involved injection of various non-sorbing and sorbing tracers in KLX15A with pumping recovery in HLX27 at a distance of roughly 140 m.

A fourth, so-called "long term pumping" (LPT) test using a suite of different non-sorbing tracers injected in a number of percussion-drilled (HLX27A, HLX32, HLX37, HLX38) and core drilled (KLX11A, KLX20A) boreholes surrounding a central pumping borehole (HLX28) is currently underway in south-western Laxemar. Information from this tracer test, although not reported as part of SDM-Site Laxemar, will provide additional input to future hydrogeological modelling.

6.1.1 Tracer test between KLX02 and HLX10

In the first test, no tracer breakthrough was detected after two weeks of pumping, possibly owing to more complicated flow geometry than initially assumed. Indirect pumping responses in the injection borehole KLX02, indicated that more than one fracture/fracture zone was involved in the transport. A possible interpretation suggested that the flow path connecting the two boreholes is considerably longer than 260 m, and that a pumping period longer than two weeks would be required to obtain a breakthrough curve.

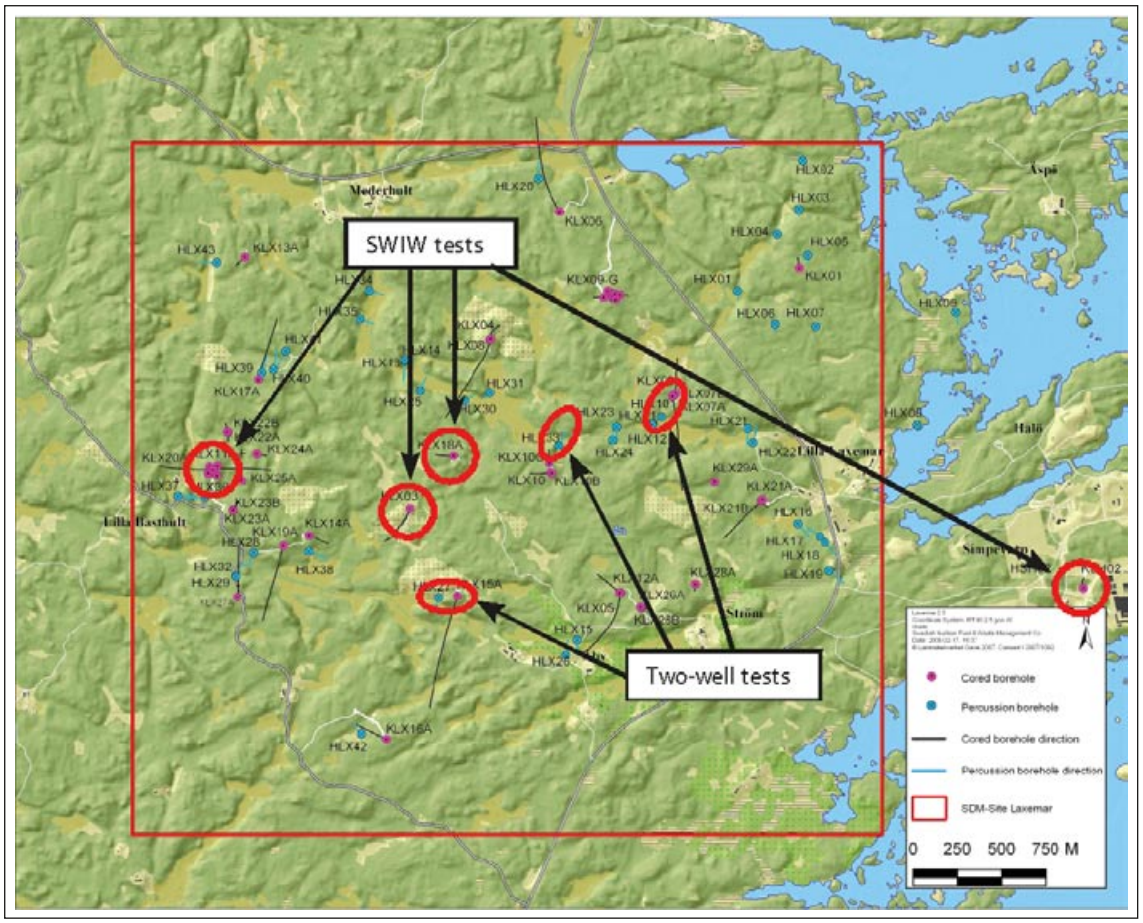

Figure 6-1. *Borehole locations for tracer tests used in the SDM-Site Laxemar transport properties evaluation.*

6.1.2 Tracer test between SSM000228 and HLX33

In the second test, a tracer (uranine) mass recovery of 33% was obtained in the withdrawal borehole HLX33 after 760 hours of sampling. The tracer recovery curve is shown in Figure 6-2. After roughly 400 hours of sampling, breakthrough data are missing for an interval of some 200 hours owing to a power failure that stopped the automatic sampler.

The tracer recovery data was evaluated using a simple one-dimensional advection-dispersion model, assuming a constant fluid velocity and negligible transverse dispersion. Model parameters were determined from a non-linear least square regression using the PAREST code /Nordqvist 1994/. The modelling results are shown in Figure 6-3.

6.1.3 Tracer test between KLX15A and HLX27

In the third test, as yet unreported, tracer mass recovery of 86% for uranine, 75% for Tb-DTPA and 77% for Li^+ were obtained after 1550 hours of sampling. No unambiguous breakthrough of Cs^+ and Rb^+ was detected during this time. Tracer breakthrough curves are shown in Figure 6-4.

The tracer recovery data was evaluated by using a simple one-dimensional advection-dispersion model (AD) coupled with sorptive retention in one and two flow pathways. Evaluation was also performed using an advection-dispersion model accounting for matrix diffusion (AD-MD). The AD-MD model evaluation results for the main test with non-sorbing tracer Tb-DTPA and Li^+ is shown in Figure 6-5. Results obtained using the AD model are shown in Figure 6-6 for Tb-DTPA and Li^+ as well as scoping simulations showing different transport retardation scenarios considered for Cs^+ and Rb^+.

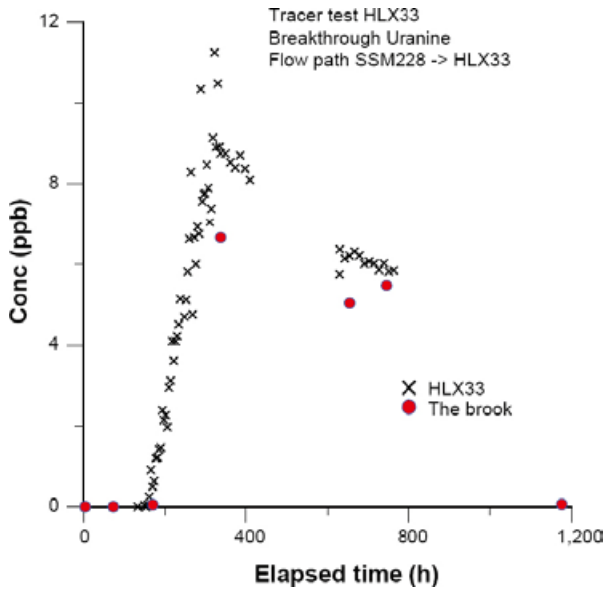

Figure 6-2. *Uranine concentrations in the discharged water from HLX33 and from the brook located just north of SSM000228. Figure taken from /Svensson et al. 2008/.*

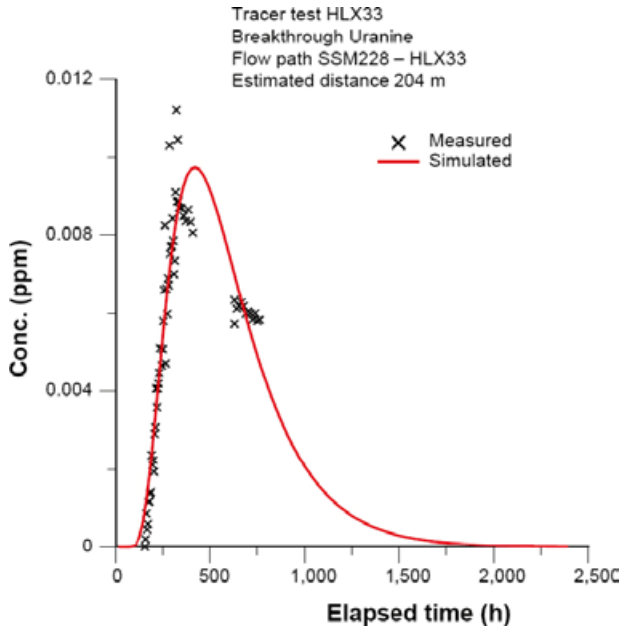

Figure 6-3. *Visualisation of model fit to experimental data using the single path, advection-dispersion model for the tracer test. Figure taken from /Svensson et al. 2008/.*

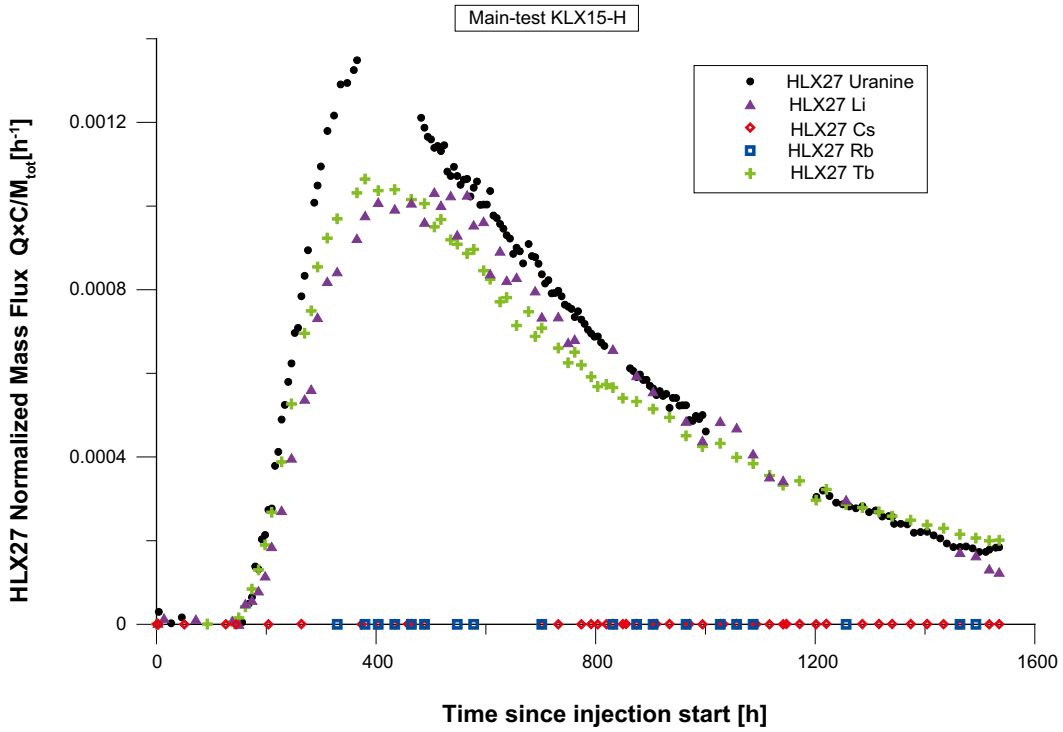

Figure 6-4. *Tracer recovery (breakthrough) curves as obtained in the discharged water from HLX27. Figure taken from /Lindquist et al. 2008/.*

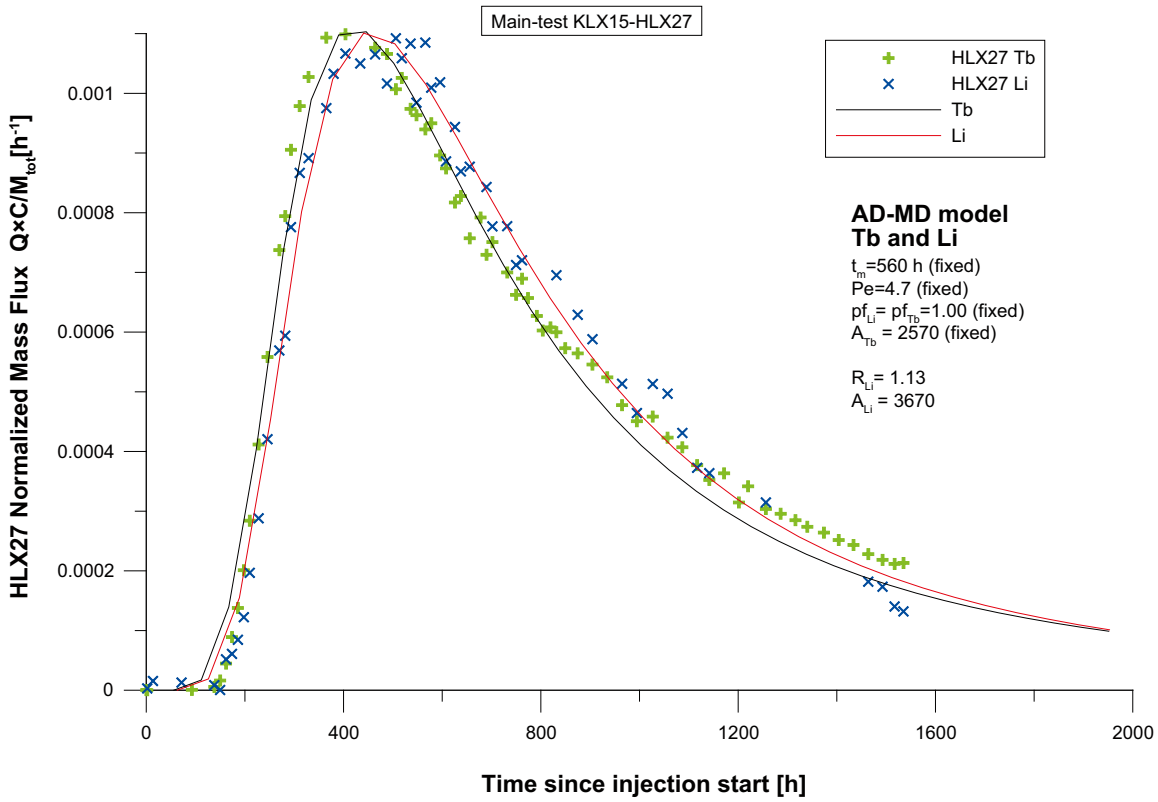

Figure 6-5. *Evaluation of tracer breakthrough data using the AD-MD model for the main tracer test. Tb-DTPA is the non-sorbing tracer and Li^+ is weakly sorbing. Figure taken from /Lindquist et al. 2008/.*

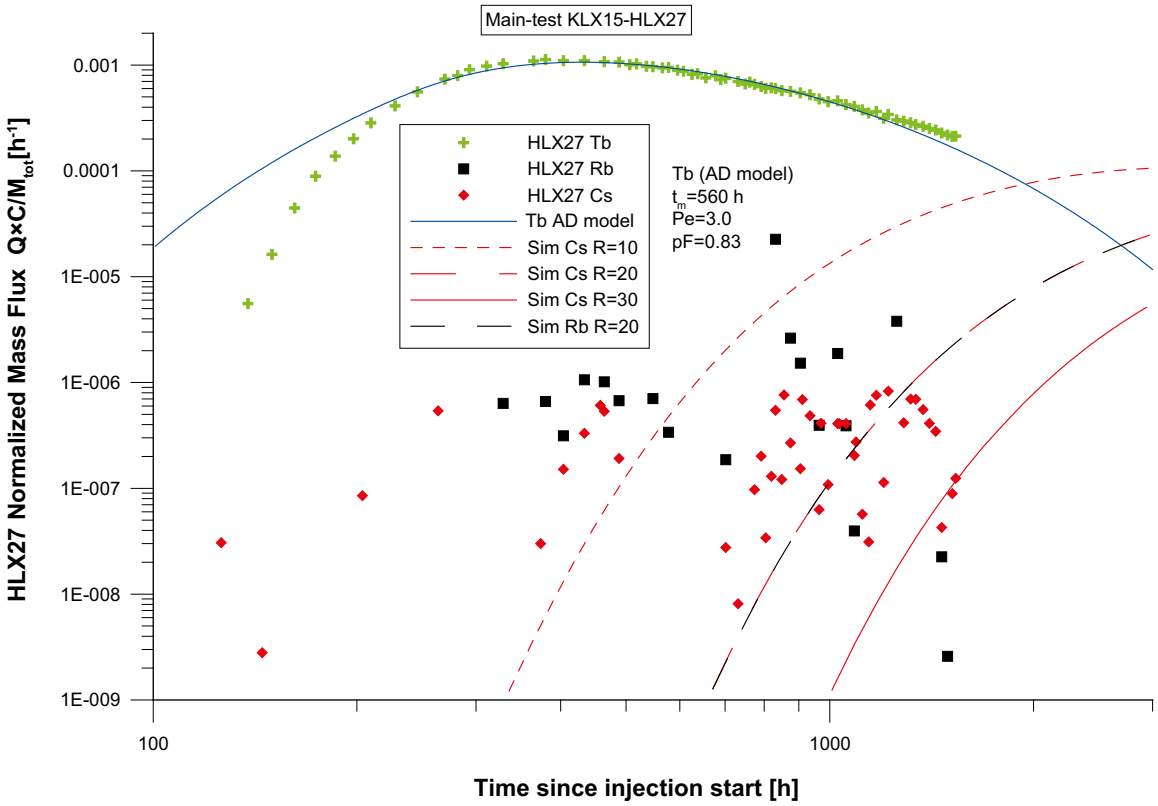

Figure 6-6. *Log-log plot of simulated tracer breakthrough using AD model and experimental data for Tb-DTPA (non-sorbing), Cs+ (R = 10, 20, 30), and Rb$^+$ (R = 20) tracer breakthrough data using the AD model. Figure taken from /Lindquist et al. 2008/.*

6.2 Single well injection withdrawal tests (SWIW)

Six single well injection-withdrawal (SWIW) tests have been performed in various borehole locations during the site investigation in the Laxemar-Simpevarp area. Four of the tests were performed inside the Laxemar local model area in boreholes KLX03, KLX18A, KLX11A, and two tests in the Simpevarp subarea in borehole KSH02. SWIW tests are also commonly referred to as "push-pull" tests in the scientific literature since the method involves a pulse injection of a tracer into a packed-off borehole section followed by pumping withdrawal in the same section. The technique is attractive for the purposes of the site investigation since it can be used to perform tracer tests within transmissive structures found at repository depth in which it would be very difficult to perform standard dipole or multiple well tracer tests from the surface. An additional advantageous feature of the SWIW technique is that the reversal of flow during the experiment theoretically reduces the impact of advective dispersion and flow dimension upon the residence time distribution of recovered tracer, thereby potentially simplifying mechanistic interpretation. The equipment used for performing the SWIW tests is illustrated in Figure 6-7.

The procedure used for the SWIW tests carried out within the site investigation is described in detail in the Oskarshamn site investigation reports /Gustafsson and Nordqvist 2005, Gustafsson et al. 2006, Thur et al. 2007a, b/ as well as in the background feasibility study reports /Nordqvist and Gustafsson 2002, 2004/. It typically comprises the following phases:

1. Pumping and storage of groundwater from the selected fracture for subsequent injection.
2. Pre-injection of accumulated water to establish steady state hydraulic conditions.
3. Active injection of one or more tracers within the packed-off borehole section (1–2 h).
4. Injection of groundwater (chaser fluid) after cessation of tracer injection (10–20 h).
5. Waiting phase, or "shut-in" period.
6. Tracer recovery phase (withdrawal of water under active pumping).

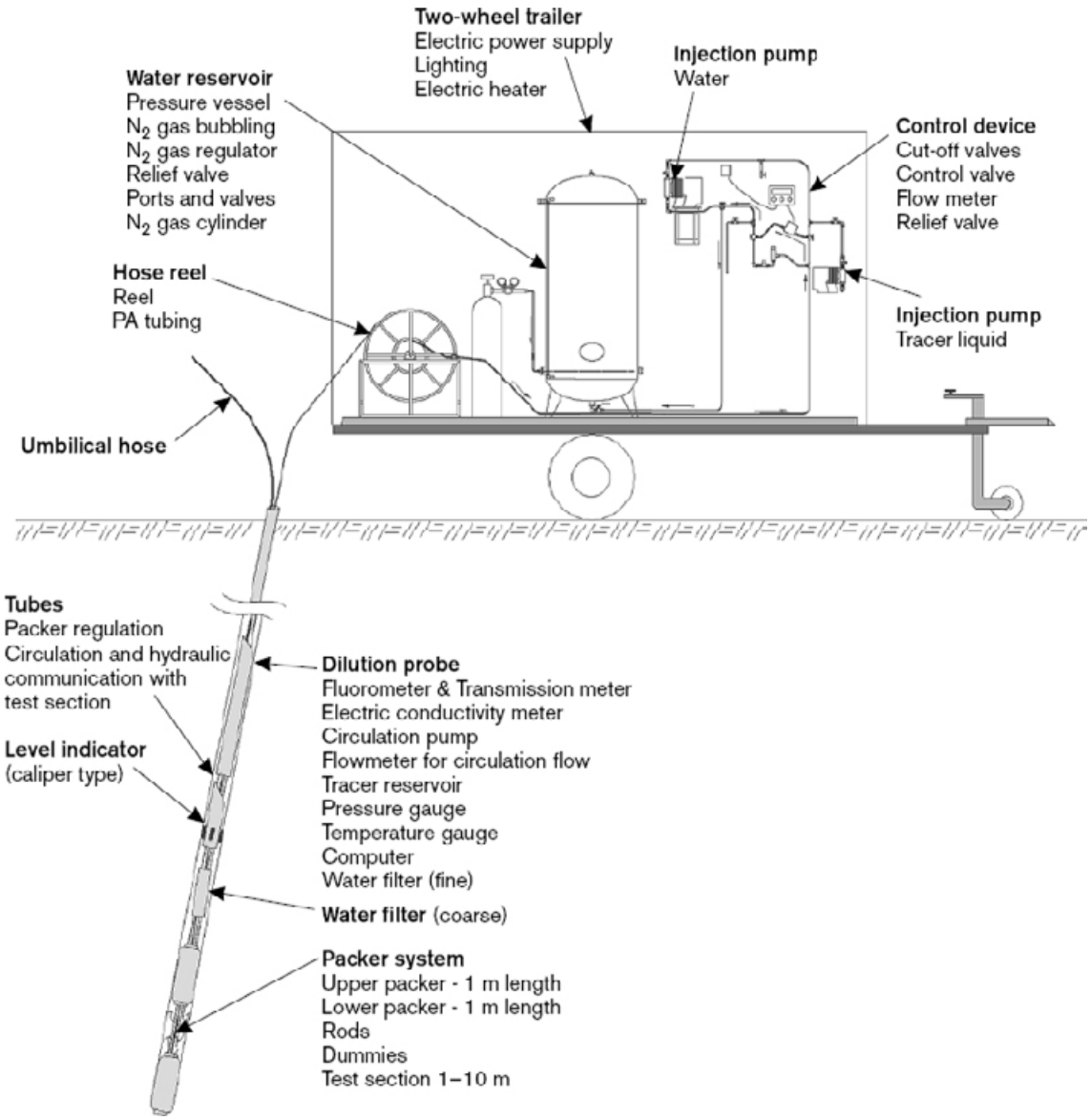

Figure 6-7. *Schematic of SWIW test equipment connected to the borehole dilution probe. Image is taken from /Gustafsson and Nordqvist 2005/.*

The tracer breakthrough data that is subsequently used in data evaluation is obtained from the recovery phase. The injection of a chaser fluid has the effect of pushing the tracer outwards in a ring in the formation surrounding the tested section /Nordqvist 2008/, the advantage being that both the ascending and descending parts of the subsequent recovery ("breakthrough") curve can then be well resolved. During the waiting phase there is no injection or withdrawal of fluid. The purpose of this is to increase the time available for diffusion and sorption within the formation so that these may be more easily evaluated from the tracer recovery data. An extended waiting period, however, suffers from the disadvantage that it increases sensitivity to background hydraulic gradients which can have a significant detrimental impact upon results.

A disadvantage of the technique as compared with multiple well tracer tests is that there is no easily discernable reference length scale associated with the test /Becker and Shapiro 2003/. In the evaluation of the test there is very little information concerning how far out into a fracture system the tracer pulse actually propagates since the arrival time of the returning pulse tends to be governed by the time schedule of the different test phases /Tsang and Doughty 2007/ rather than the flow porosity of the system as might be the case in a dipole tracer test. On the other hand, the peak concentration of the recovered tracer, its apparent spread and long-time tailing are largely dependent upon hydrodynamic dispersion (although excluding advective dispersion) and retention processes which may include diffusion and sorption.

Since the tracer arrival time does not directly depend upon the flow porosity in a SWIW test, the combined impact of dispersivity and porosity are usually not possible to separate in a rigorous fashion and it is customary to fit a dimensionless lumped dispersion parameter, τ /Gelhar and Collins 1971/. This parameter is defined as:

$$\tau = \frac{\alpha_L^2 \delta_t}{V_{inj}} \qquad \text{(Eq. 6-1)}$$

where α_L (m) is the dispersion length, δ_t (m) transport aperture, and V_{inj} (m^3) is the total injected water volume.

Based on injected volumes at Laxemar and a range of plausible transport apertures, the magnitude of the radial travel distance is estimated to be on the order of about 5–20 m assuming relatively homogenous radial flow conditions /Nordqvist 2008/. If the flow is highly fingered or channelised the penetration distance may be greater than this.

In total, six SWIW tests have been performed in the Laxemar-Simpevarp area in different types of structures, at different depths and with different transmissivity ranges with the aim of characterising the transport properties of a variety of flowing features typical of that which might be encountered in the vicinity of a repository. Four of the tests were performed in boreholes KLX03, KLX18A, and KLX11A, located inside the local model area, and two tests in borehole KSH02, located in the Simpevarp area. A summary of the individual tests is given in Table 6-1.

Numerical simulations of SWIW tests in the presence of background hydraulic gradients were previously made by /Nordqvist and Gustafsson 2002/ where it was shown that they could have a significant impact upon the shape of the tracer recovery curve. For this reason, preceding each of the SWIW tests, the ambient groundwater flow through the borehole section was measured by means of a tracer dilution test using uranine to ensure that background flows were within an acceptable range. The measured natural flowrates through the test well sections are given in Table 6-2 along with the flowrates characterising the various phases of the tests themselves.

Table 6-1. Summary of basic features of SWIW tests performed in the Laxemar-Simpevarp area.

Borehole	Elevation (m.a.s.l.)	T (m^2/s)	Type	Rock and fracture coating description
KSH02	–417	1.0×10^{-6}	1 fracture	Fine-grained dioritoid (501030) calcite coating moderately altered
KSH02	–571	5.2×10^{-7}	Deformation zone (3-4 flowing features)	Granite, fine-to medium grained (531058) calcite, chlorite coating slightly altered
KLX03	–701	4.5×10^{-6}	Deformation zone (3-4 flowing features)	Fine-grained diorite-gabbro (505102) chlorite, clay minerals coating slightly altered
KLX18A	–447	4.3×10^{-8}	Deformation zone (3-4 flowing features)	Granite to quartz monzodiorite (501044) calcite, chlorite coating 1 fracture slightly altered, 2 unaltered
KLX11A	–466	3.4×10^{-6}	2 fractures	Quartz monzonite to monzodiorite (501036) chlorite coating slightly altered
KLX11A	–542	1.4×10^{-7}	Deformation zone (2 flowing features)	Quartz monzodiorite (501036) calcite, chlorite coating slightly altered

Table 6-2. Natural background flows through SWIW test well sections (as measured by tracer dilution prior to each SWIW test) and flows characterising the different phases of the tests themselves.

Borehole	Elevation (m.a.s.l.)	Natural flow (dm^3/h)	SWIW injection flow (dm^3/h)	SWIW pumping flow (dm^3/h)	Total injected volume (dm^3)	Naural flow during "shut-in" (dm^3)
KSH02	–417	0.011	13–15(∗)	15	204	0.03
KSH02	–571	0.005	11.3–13	17.2	173.5	n/a
KLX03	–701	0.253	12.9	13.9	312.4	0.17
KLX18A	–447	0.002	2.4–2.9	2.5	111.1	n/a
KLX11A	–466	0.031	18.0–18.6	18.2	98.5	n/a
KLX11A	–542	0.001	9.2–9.7	9.4	95.3	n/a

(∗) Pump repair, during which packers were released for almost 50 hours, resulted in an estimated outflow of water of 0.55 dm^3/h.

Although the ambient flow and the rates of injection and pumping during the SWIW tests are not strictly comparable owing to the different geometry of applied boundary conditions, the assumption that background gradients did not influence the test results does not appear unreasonable from the relative magnitudes of the flows reported. The assumption could be questioned for KLX03, which showed an exceptionally large natural flow rate. The shape of the breakthrough curve for KLX03 and a simple advection-dispersion model fit, however, shows no clear indications of any deviations that could be attributed to a high natural flow rate. It should be noted that a pump failure may have affected the results from borehole KSH02 at elevation –417 m.a.s.l. as indicated in Table 6-2 and Table 6-3. The outflow of water during pump repair was estimated to 0.55 dm^3/h over a period of almost 50 hours.

The "run" parameters for each of the SWIW tests including recoveries of the different tracers are given in Table 6-3 below.

In some of the cases listed in Table 6-3, the tracer recovery was truncated due to the limited time allocated for each test and the recovery estimates are possibly lower than what would have been obtained if pumping were to continue until background values were reached. In the initial site investigation reports dealing with the SWIW tests /Gustafsson and Nordqvist 2005, Gustafsson et al. 2006, Thur et al. 2007b, a/, the recovery data were modelled using the SUTRA simulation code /Voss and Provost 2002/.

The fracture system in which the SWIW test was performed was simulated as a 2D homogeneous domain using the SUTRA simulation code /Voss and Provost 2002/. Since the code was originally designed to simulate porous media, the domain was parameterised with hydraulic properties chosen to be equivalent to the fracture being studied and centred upon a central injection and recovery well. The tracer injection at the central well was simulated as a continuously stirred tank reactor thereby giving a modified, extended tracer pulse input.

Table 6-3. Summary of run parameters for SWIW tests.

Borehole	Elevation (m.a.s.l.)	Total injected water (dm^3)	Injection + chaser duration (h)	Waiting phase (h)	Recovery (%)		
					uranine	Cs^+	Rb^+
KSH02	–417	204	61.5*	2.8	86.2	40.7	n/a
KSH02	–571	175	15.3	0	80.5	51.6	n/a
KLX03	–701	336	15.3	0.7	89.9	51.8	43.6
KLX18A	–447	122	50	0	86.8	46.4	36.7
KLX11A	–466	116	6.4	0	98	45	43
KLX11A	–542	113	11.7	0	95	72	68

* Most of the chaser injection phase in KSH02 at elevation –417 (m.a.s.l.) took place during pump repair, during which packers were released, resulting in a small outflow of water from the section.

Additional consideration was also given to sorption upon the walls of the borehole, tracer residence times in the well recirculation system including stagnant zones, and dispersion effects in the tubing between the injection section and the equipment at the surface to ensure that the modelled tracer injection was physically realistic. It was found in scoping simulations /Nordqvist 2008/ that the effect of dispersion within the tubing would have a negligible impact. This was also considered for the sampling of solute (i.e. between the test well and the surface sampling equipment) where it was found that neither the residence time nor dispersion in the sampling system should leave a significant imprint upon the solute breakthrough curve.

The modelling procedure involved making an initial simulation for the tracer injection and fluid chaser step, and then using the resulting distribution of solute within the 2D domain as the starting condition for the pumping stage of the test. In the first round of modelling which was reported in the initial site investigation P-reports dealing with the SWIW tests /Gustafsson and Nordqvist 2005, Gustafsson et al. 2006, Thur et al. 2007a, b/, the recovery data were modelled using the Advection-Dispersion (AD) equation with retardation due to linear equilibrium sorption on fracture surfaces. This was accomplished by simultaneous fitting of the dispersivity and retardation factors for the non-sorbing tracer uranine and the sorbing tracers Cs^+ and Rb^+, except for borehole KSH02, where no Rb^+ tracer test was performed.

The actual tracer recovery data and the best fit model taken from the simulations are shown in Figure 6-8 for uranine and Cs^+, and in Figure 6-9 for uranine and Rb^+.

Although the simulation results indicate that it is possible to obtain a rough fit to the experimental data using the AD equation with linear sorption, close inspection of the curves indicates that there is consistent under-prediction of the long time tailing of the breakthrough curve for uranine. The results for the sorbing tracers Cs^+ and Rb^+ are mixed; in some cases late time tailing is under-predicted while in other cases it is over predicted.

In a second round of modelling /Nordqvist 2008/, the tracer recovery data were modelled using an advection-dispersion-sorption model coupled with matrix diffusion/sorption (AD-MD) in an attempt to better resolve the long time tailing behaviour. To achieve this, a lumped matrix interaction parameter, A representing the sorptive and diffusive properties of the rock matrix, was introduced /Moreno and Neretnieks 1983/:

$$A = \frac{(\delta_t/2)R_a}{\sqrt{D_e(\theta_m + K_{dm}\rho_{bm})}} \qquad \text{(Eq. 6-2)}$$

Where $\delta_t/2$ is the transport half-aperture, R_a is the retardation factor for equilibrium sorption along the flowpath, and the denominator is the material properties group for the rock matrix. If the depth of solute penetration is very low or the material properties of the fracture surface do not differ significantly from the underlying rock matrix, the R_a term can be neglected and subsumed into the denominator (i.e. as an effective material properties group for the sampled rock).

In the AD-MD modelling approach, an attempt was made to fit the lumped matrix interaction parameter, A as defined in Equation 6-2. The modelling procedure was based upon an extension of the SUTRA model used for the initial modelling efforts, although with the addition of a rock matrix 20 cm in extent. The rock matrix was implemented in the model by defining a zone with very low hydraulic conductivity adjacent to the flow domain. The rock associated with the immobile zone was assigned representative matrix porosity and pore diffusivity values appropriate for the rock matrix. Parameters characterising the transport of solute were estimated by the same inverse modelling technique as described previously for the AD model; i.e. simultaneous fitting of the lumped dispersivity parameter,τ and the matrix interaction parameter, A for all non-sorbing and sorbing tracers simultaneously. The results of the extended evaluation using the AD-MD model for the uranine and Cs^+ tracers are shown in Figure 6-10.

The evaluation using the matrix diffusion model was found to give a much improved fit of the long time tailing behaviour of uranine to the experimental data. However, the model fit of Cs^+ is generally not satisfactory. With the exception of the evaluation made for KSH02, a better fit for Cs^+ was obtained using the advection-dispersion-sorption (AD) model. This is in contrast with the model results for Cs^+ obtained for SWIW tests in Forsmark, where the AD-MD model generally gave an improved fit as compared with the AD model.

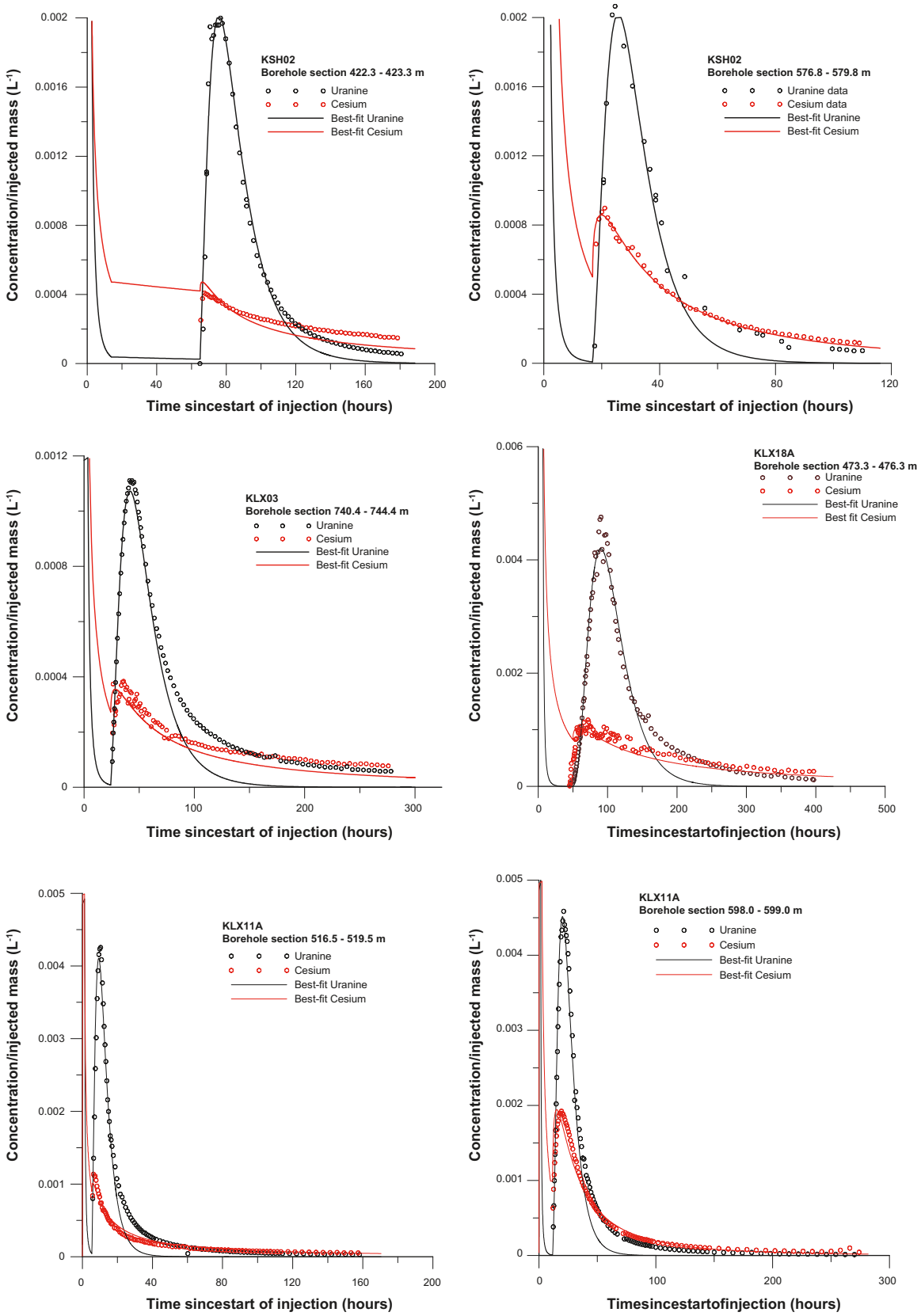

Figure 6-8. *Visualisation of model fit to uranine and Cs^+ recovery data for the radially symmetric, AD model with retardation simulated using SUTRA. Figures taken from /Nordqvist 2008/.*

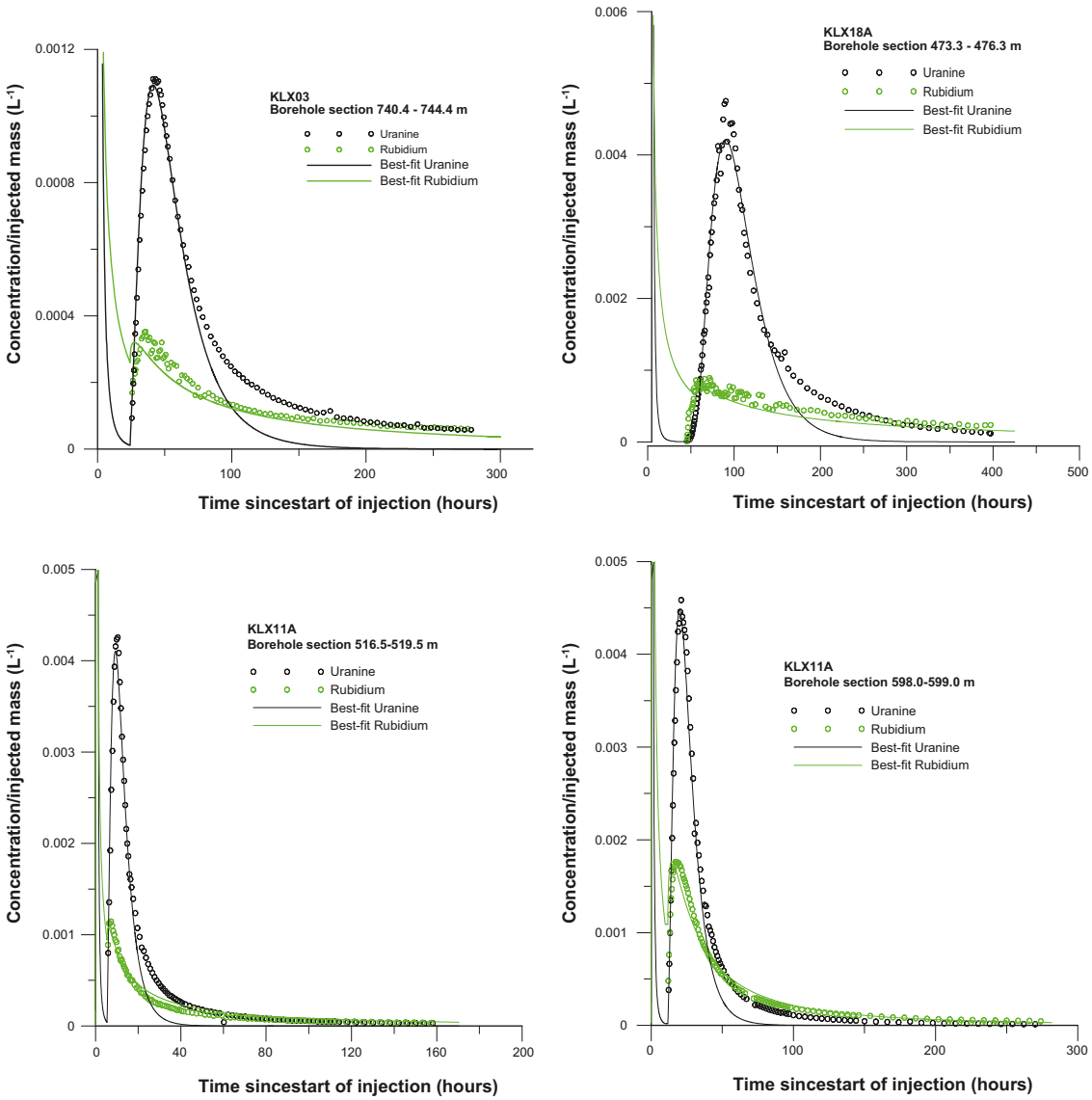

Figure 6-9. *Visualisation of model fit to uranine and Rb^+ recovery data for the radially symmetric, AD model with retardation simulated using SUTRA. Figures taken from /Nordqvist 2008/.*

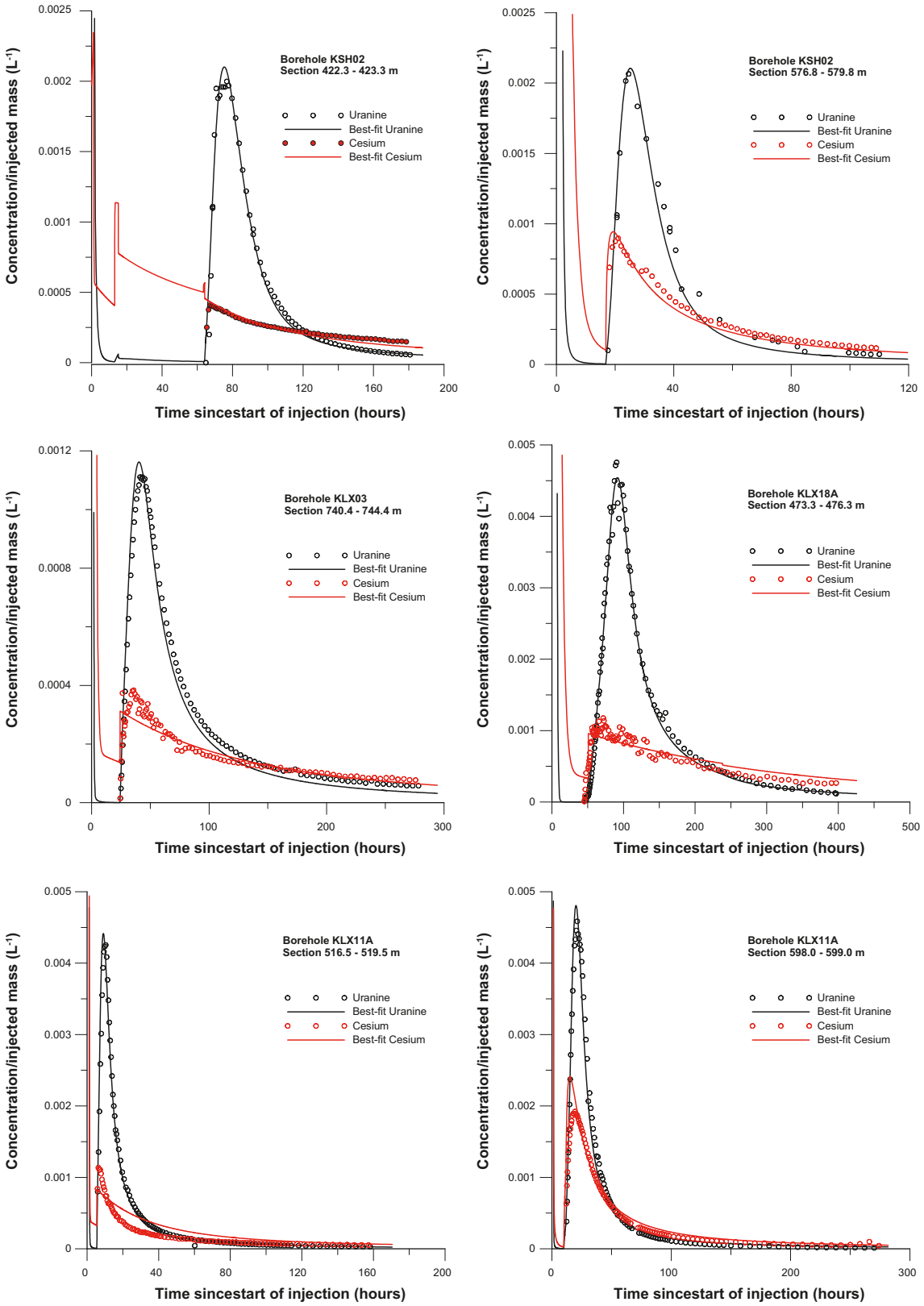

Figure 6-10. *Visualisation of model fit to uranine and Cs^+ recovery data for the radially symmetric, AD-MD model simulated using SUTRA. Figures taken from /Nordqvist 2008/.*

Assuming that the sorbing tracer, on average, "samples" the same rock matrix as the non-sorbing tracer, the effective pore diffusion retardation factor, R_m can be roughly estimated from the A-parameter calculated for each solute and their known free phase diffusivities using the following relation:

$$R_m^{Cs^+} = \frac{D_w^{uranine}}{D_w^{Cs^+}} \left(\frac{A_{uranine}}{A_{Cs^+}} \right)^2 \qquad \text{(Eq. 6-3)}$$

A summary of results from the modelling evaluation using the AD model is given in Table 6-4 and for the AD-MD model in Table 6-5.

Table 6-4. Summary of best fit parameter estimates for the AD model (linear sorption on fracture surfaces).

Borehole	Elevation (m.a.s.l.)	Dimensionless dispersivity, τ (-)	Retardation factor, R_a (-)	
			Cs^+	Rb^+
KSH02	–417	5.7	975	n/a
KSH02	–571	3.8	87	n/a
KLX03	–701	3.9	235	390
KLX18A	–447	1.2	857	2700
KLX11A	–466	3.8	808	622
KLX11A	–542	2.8	66	105

Table 6-5. Summary of best fit parameter estimates for the AD-MD model (matrix diffusion and linear sorption within matrix porosity).

Borehole	Elevation (m.a.s.l.)	Dimensionless dispersivity, τ (-)	Matrix interaction parameter for uranine, A ($s^{-½}$)	Matrix retardation factor for Cs^+, R_m (-)
KSH02	–417	0.4	400	> 10^4
KSH02	–571	0.7	370	118
KLX03	–701	0.04	143	> 10^4
KLX18A	–447	0.1	323	> 10^4
KLX11A	–466	0.1	86	> 10^4
KLX11A	–542	0.09	182	12.8

6.3 Interpretation of modelling results and consequences for safety assessment

There are a number of processes which occur during the transport of solutes that can cause spreading of a tracer pulse injected into a heterogeneous flow system. Although these are customarily lumped together under the general term "dispersion", they may have very different origins and scale very differently depending upon the experimental flow configuration and timescale of a tracer test. Proper understanding of retention processes observed during a tracer test is dependent upon the ability to separate hydrodynamic dispersive effects from the effects of matrix diffusion and sorption upon geologic materials.

One of the major problems encountered when evaluating multiple well tracer tests is the occurrence of advective dispersion which can have a considerable impact upon modelling evaluation. Advective dispersion is the name given to the tracer spreading that occurs by way of the injected mass of tracer being transported along multiple, although mostly independent, flowpaths with differing fluid velocities /e.g. Neretnieks 1983/. Essentially, advective dispersion is a direct consequence of flow-channelling which has already been discussed at length in previous chapters. This is considered separately to "ordinary" hydrodynamic dispersion in that it cannot be described mathematically as a mixing process. Ordinary hydrodynamic dispersion is usually referred to in the literature as Fickian or Gaussian dispersion. Indeed, while ordinary hydrodynamic dispersion is thought to behave in a Gaussian manner with a constant dispersivity as a function of flowpath length, advective dispersion gives a dispersivity that increases with observation distance. The apparent increase in dispersivity with increasing length scales has been discussed by a number of reviewers and is well known in the scientific literature /e.g. Gelhar et al. 1992, Berkowitz and Scher 1995, Neuman 1995/.

This is problematic since the advection-dispersion equation (with or without added matrix diffusion) implicitly assumes dispersion to be Gaussian, meaning that any non-Gaussian effects are typically interpreted to be evidence of diffusive uptake to the rock matrix or stagnant zones adjacent to the flowpath /e.g. Becker and Shapiro 2000, Shapiro 2001, Becker and Shapiro 2003/. The distinction between the effects of advective dispersion and matrix diffusion along flowpaths featuring differing F-factors, however, is difficult to discriminate since advective tailing cannot easily be distinguished from breakthrough tailing arising due to matrix diffusion. The situation is complicated even further if additional consideration is given to possible multiple timescales of mass transfer arising due to heterogeneous material properties and different types of immobile zones /e.g. Haggerty and Gorelick 1995/. Modelling interpretation of data from multiple-well tracer tests therefore remains a contentious issue which has not yet been fully resolved /e.g. Zhou et al. 2005/.

SWIW tests, on the other hand, are thought to be much less sensitive to the effects of advective dispersion and flowpath dimensionality /e.g. Becker and Shapiro 2003, Tsang and Doughty 2007/. If there is no background hydraulic gradient, no matrix diffusion, and no hydrodynamic dispersion in the radiating flow channels, one would expect an injected pulse of solute to be recovered exactly as it was injected /Neretnieks 2007/. This is because solute travelling along fast flowpaths travels further into the formation than solute residing in slow flowpaths, the distance being proportional to the flow velocity and the flow injection time. Under the assumption of purely advective transport it can be shown that the flow reversal exactly counteracts the advective spreading of the pulse regardless of the total injection and pumping flowrates. In practice, however, along a heterogeneous flowpath there is always a residual component of local hydrodynamic dispersion which is irreversible /Becker and Shapiro 2003/.

Given the various dispersive effects which can influence the residence time distribution of a tracer, interpretation of what the results actually represent must be made with care in order to make physically justified assertions concerning the up-scaling of transport properties to safety assessment timescales and flow configurations.

If one accepts, for the moment, the hypothesis of a diffusive sequestering mechanism for the long time tailing observed in a tracer test then the question remains as to what diffusive process or mix of processes this represents. Here, it is implicitly assumed that the hypothesis of Gaussian hydrodynamic dispersion is correct and can therefore be separated from diffusive effects. As discussed previously, the strength of presumed matrix interaction in the modelling evaluations is given in terms of a lumped parameter, A which includes the effects of the effective F-factor for the transport path, the matrix effective diffusivity and sorptivity. If the average matrix porosity of the system is reasonably

well constrained it is possible to estimate the "apparent" formation factor, F_f^{TT}, observed in a tracer test if information is also available concerning the mean transport aperture, δ_t of the system:

$$F_f^{TT} = \frac{1}{4D_w\theta_m}\left(\frac{\delta_t}{A}\right)^2 \qquad \text{(Eq. 6-4)}$$

For a sorbing tracer, the apparent formation factor is instead given by:

$$F_f^{TT} = \frac{1}{4D_w\left(\theta_m + K_{dm}\rho_{bm}\right)}\left(\frac{R_a\delta_t}{A}\right)^2 \qquad \text{(Eq. 6-5)}$$

In this case, additional information is needed for the sorptivity of the tracer in order to constrain the apparent formation factor, since the estimated A-parameter lumps the effects of sorptivity and diffusivity together. It should be noted that the additional retardation term R_a is included in Equation 6-5 only because it is already utilised to obtain fitted values of A as given in /Nordqvist 2008/. If mass transfer is modelled purely as a matrix diffusion process this extra parameter is not necessary.

The transport aperture is usually not well known since it is not necessarily related to the hydraulic aperture of the system in a simple fashion (see /Crawford 2008/). For the SWIW tests, an assumed value for the transport aperture is used throughout the simulations using the SUTRA simulation code /Nordqvist 2008/. Since these values are already internalised in the evaluation of the A-parameter, it is these values which are most appropriate to use for further analysis using Equation 6-4 or 6-5. This is because the ratio δ_t/A negates the effect of the unknown transport aperture if the same aperture is used as that utilised in obtaining the initial fitted estimate of the A-parameter. This, however, does not mean that the assumed fracture aperture gives a correct representation of the flow-wetted surface encountered by tracer during the test and it is not difficult to imagine complex fracture sets that could give larger surface areas for diffusive uptake for the same kinematic porosity.

In the analysis presented here, the SWIW tracer test data for non-sorbing tracers is revisited and a comparison is made of the apparent formation factor derived using Equation 6-4 with the appropriate recommended value obtained from the retardation model. For sorbing tracers, recommended K_d values from the retardation model are used (i.e. for the specific rock type in the borehole interval investigated) in conjunction with Equation 6-5 to estimate an apparent formation factor. This then gives an indication of the amount of apparent diffusive mass transfer enhancement that is observed in the tracer experiment compared to that which would be expected on the basis of data derived from laboratory measurements. It also allows a comparison of the apparent matrix diffusive properties of both sorbing and non-sorbing tracers from the same experiment in a semi quantitative fashion. In making these calculations it is necessary to make some basic assumptions about the rock volume being tested. These assumptions are listed in Table 6-6.

Using the modelling assumptions given above, the ratio of apparent and recommended formation factor can be compared. The apparent diffusive mass transfer enhancement factor calculated in this fashion is shown in Figure 6-11 for the various SWIW tests carried out in the Laxemar-Simpevarp area. Since SWIW tests are not associated with a well-defined observation distance, the results are plotted against the transmissivity of the tested fracture system/zone. It is noted, however, that although there may be correlation with observation scale, there appears to be no meaningful correlation between transmissivity and mass transfer evident in Figure 6-11.

An interesting feature of the tracer test data reinterpretation presented here is that the diffusive mass transfer enhancement factor for the two tests with quantitatively determined retardation factors seems to be larger for non-sorbing tracers than for sorbing tracers. This trend has also been shown to be consistent across all tracer tests evaluated at Forsmark /Crawford 2008/. For KLX11A (–542 m.a.s.l.) and KSH02 (–571 m.a.s.l.), the difference is considerable and cannot readily be explained away as a result of uncertainty concerning the sorption K_d value used in the evaluation since the stronger the sorption effect is at the fracture surface, the larger the apparent discrepancy becomes.

The results of this analysis indicate that there is an apparent enhancement of diffusive mass transfer of the non-sorbing tracer to the immobile zone that is considerably larger than can be justified on the basis of uncertain laboratory derived measurement values. With the exception of the test performed in KLX18A, the apparent formation factor of uranine is sufficiently high as to be nearly commensu-

rate with that for free diffusion in water. Even making allowances for very large increases in formation factors at the fracture surfaces, or in association with fault gouge material, cannot satisfactorily explain the degree of apparently enhanced diffusive uptake of uranine. An alternative explanation is that transport occurs within a complex fracture featuring substantially greater flow-wetted surface than the single fracture plane assumed in the simulations. The increase in flow-wetted surface required, however, is larger than what would seem realistic for the flow structures considered.

One aspect of the data interpretation that should be noted is that the two tests that show the largest difference in apparent diffusive mass transfer enhancement factors between Cs^+ and uranine, namely KSH02 (–571 m.a.s.l.) and KLX11A (–542 m.a.s.l.), are also the only tests with quantitatively determined matrix retardation factors. With the exceptions of these two tests, the matrix retardation factor, R_m, is only qualitatively estimated to be larger than 10^4 (in Figure 6-11 the results are shown

Table 6-6. Additional modelling assumptions used in extended evaluation of SWIW tracer test data.

SWIW tracer	Parameter	Value (min-max)	Comments
KSH02 (–417 m.a.s.l.):			
all tracers	F_f (reference)	3.1×10^{-5}	assumed for rock type 501030
uranine	K_d (m^3/kg)	0	non-sorbing
Cs^+	K_d (m^3/kg)	$(1.0–4.3)\times10^{-2}$	K_d range for fresh rock in saline water[1]
KSH02 (–571 m.a.s.l.):			
all tracers	F_f (reference)	4.4×10^{-5}	assumed for rock type 511058
uranine	K_d (m^3/kg)	0	non-sorbing
Cs^+	K_d (m^3/kg)	$(0.24–3.9)\times10^{-1}$	K_d range for fractures in saline water[2]
KLX03 (–701 m.a.s.l.):			
all tracers	F_f (reference)	9.8×10^{-5}	assumed for rock type 505102
uranine	K_d (m^3/kg)	0	non-sorbing
Cs^+	K_d (m^3/kg)	$(1.6–1.8)\times10^{-2}$	K_d range for DZ in saline water[3]
KLX18A (–447 m.a.s.l.):			
all tracers	F_f (reference)	4.6×10^{-4}	assumed for rock type 501046
uranine	K_d (m^3/kg)	0	non-sorbing
Cs^+	K_d (m^3/kg)	$(2.6–3.2)\times10^{-2}$	K_d range for fresh rock in saline water[1]
KLX11A (–466 m.a.s.l.):			
all tracers	F_f (reference)	6.1×10^{-5}	assumed for rock type 501036
uranine	K_d (m^3/kg)	0	non-sorbing
Cs^+	K_d (m^3/kg)	$(1.1–4.8)\times10^{-2}$	K_d range for fractures in saline water[2]
KLX11A (–542 m.a.s.l.):			
all tracers	F_f (reference)	6.1×10^{-5}	assumed for rock type 501036
uranine	K_d (m^3/kg)	0	non-sorbing
Cs^+	K_d (m3/kg)	$(0.77–4.4)\times10^{-2}$	K_d range for fresh rock in saline water[1]

(1) Value measured in fresh rock in the 1–2 mm size fraction after 180 days contact time in saline Simpevarp groundwater.
(2) Value measured in fracture material in the < 0.125 mm size fraction after 180 days contact time in saline Simpevarp groundwater.
(3) Value measured for Category 2 deformation zone material in the <0.125 mm size fraction after 180 days contact time in saline Simpevarp groundwater.

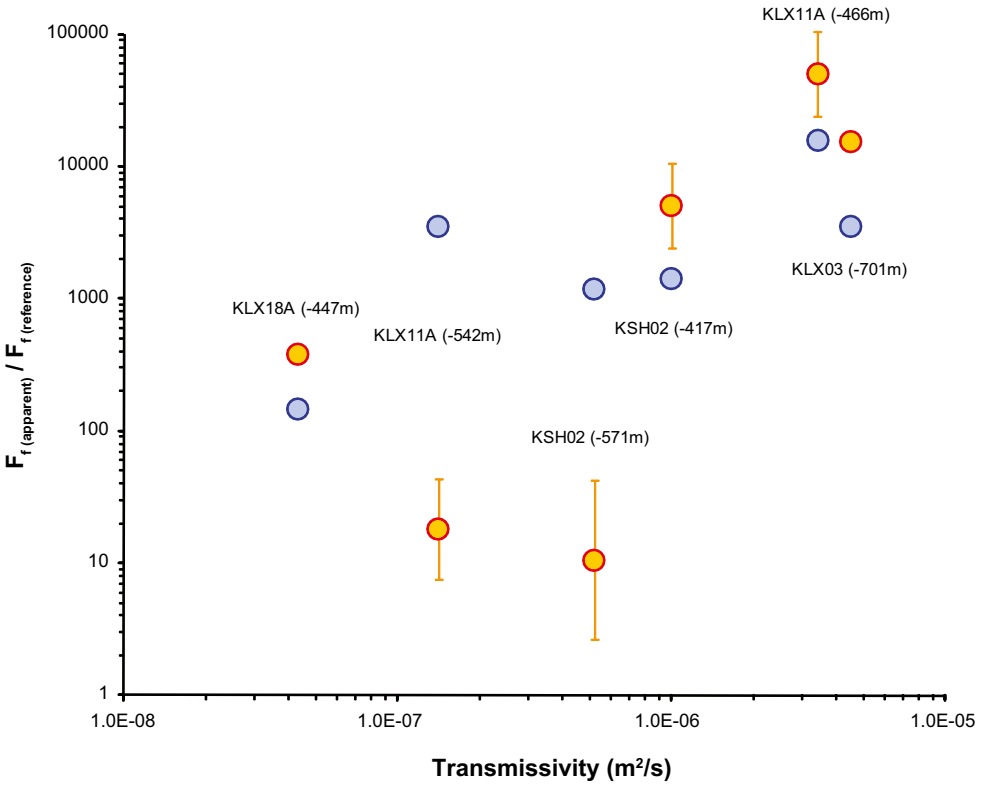

Figure 6-11. *Apparent diffusive mass transfer enhancement factors for SWIW tracer tests carried out in Laxemar and Simpevarp plotted against transmissivity of the tested flow path (assuming reference formation factors typical for the host rock in the test section, based on through diffusion measurements). Data are shown for both Cs^+ (orange shaded symbols) and non-sorbing Uranine tracer (blue shaded symbols). The plotted data are geometric means with error bars where a range of possible K_d values has been considered. It should be noted that in some cases, owing to the small ranges of reported K_d values for specific rock types, the error bars for Cs^+ are not visible against the larger circular markers.*

for $R_m = 10^4$). Since these other tests also exhibit the poorest model fit for Cs^+, it may be reasonable to question the estimated matrix interaction parameters reported in these particular cases for Cs^+.

In Forsmark it was suggested that the apparently enhanced diffusivity of non-sorbing tracers might be related to non-Gaussian dispersion within flow channels featuring tapered apertures (i.e. non-equilibrium diffusion between flow streamlines). If true, this would suggest that tracers with differing sorptive properties probe different parts of the immobile zone, with the mass transfer of non-sorbing tracers dominated by diffusion between neighbouring flow streamlines, whereas the mass transfer of sorbing tracers is dominated by mass transfer directly to the rock matrix or fracture coating along the flow-wetted surface of the advective flow path.

An alternative explanation for the observed effect could be inaccurate accounting for background levels of uranine at the site derived from drilling fluids. As far as can be discerned, however, the background concentrations of uranine have been correctly accounted for in the data evaluations and this does not appear to be an issue. Other concerns related to the presence of background flows in strongly heterogeneous formations which could flush away significant amounts of the non-sorbing tracer do not appear to be a problem either since a very high tracer recovery (> 80%) was obtained in all tests.

Additional modelling work with more detailed consideration of hydrodynamic processes on the timescale of tracer tests may need to be done if these issues are deemed to warrant further resolution.

6.4 Summary of main findings

In summary, the key findings of this chapter include:

- In general, the tracer tests carried out in support of transport property site descriptive modelling give indications of diffusive effects and retardation of sorbing solutes that are consistent with our conceptual model of solute transport within the fractured rock in Laxemar. Furthermore, the lumped parameters obtained from the modelling evaluation allow us to speculate on a range of different physical phenomena that could have influenced the observed tracer transport. It appears that tracer retention is generally enhanced relative to that predicted on the basis of independent laboratory data. Although this may be due in part to enhanced retention in the rim zone of fractures, detailed analysis of the results suggests that there may be other effects at play which are difficult to distinguish from true matrix retention processes, particularly for non-sorbing solutes.
- The various tracer test data obtained from Laxemar can be considered to support level A ("Confirmation of flow connectivity"), B ("Qualitative confirmation of retention"), and C ("Confirmation of process understanding") criteria as described in /Löfgren et al. 2007/ concerning the utility of tracer tests in Site Characterisation. The modelling evaluations also support Level D criteria ("Abstraction of lumped transport parameters") with the caveat that the retardation processes observed may not scale simply to safety assessment timescales. The reason for this is that the matrix depth probed during the duration of the tracer test most likely only reflects the properties of the fracture coatings which are known to have enhanced retention relative to the rock matrix proper;
- Although tracer tests performed in multiple well, dipole configurations exhibit signs of sorptive and diffusive retention, it is difficult to make detailed analyses of their magnitude owing to the presence of advective dispersion which has a similar impact upon the residence time distribution of solute as matrix diffusion (i.e. a tailing effect). In principle it is possible to evaluate the breakthrough of different tracers simultaneously to separate these processes and estimate a probability density function for the distribution of advective pathways /e.g. Cvetkovic et al. 2007/. In these cases too, however, the matrix depth probed during the duration of the tracer test most likely only reflects the properties of the fracture coatings and therefore says very little about the retention processes of most relevance for safety assessment.
- SWIW tracer tests are less sensitive to the impact of advective dispersion owing to the reversal of the flow field which partially reforms the injection pulse. The SWIW tests carried out at Laxemar gave strong indications of sorptive and diffusive retardation of transported solutes. Detailed evaluation of the modelling results also indicates that the enhancement of diffusive mass transfer was possibly greater for non-sorbing solutes than sorbing solutes. This, however, could only be demonstrated for two out of the six SWIW tests where the matrix retardation factor for Cs^+ could be determined quantitatively. Effects that might give rise to this behaviour include non-equilibrium streamline diffusion (giving rise to non-Gaussian dispersion indistinguishable from matrix diffusion), faulty correction for background tracer concentrations, and possibly non-negligible background flows that have not been accounted for. Additional modelling work with more detailed consideration of hydrodynamic processes on the timescale of tracer tests may need to be done if the issue is deemed to warrant further resolution.
- Material property data derived from tracer tests, even if fully corrected for the effects outlined above, should be interpreted with care since the depths of solute penetration typically achieved may not be representative of the rock that is expected to give the bulk of the retardation effect operating at safety assessment timescales. It should be emphasised that there are no observations in the field experiments which would contradict the use of the proposed data set described in Chapter 4 for safety assessment. All field tests show greater retardation than the parameter values proposed for safety assessment would otherwise predict and the main reasons for these differences are relatively well understood even if not quantified.

7 Overall summary and conclusions

In this report, the transport properties of the bedrock at the Laxemar site have been examined with the intention of creating a site descriptive model (SDM) that can function as an input to safety assessment. Since the aim of this work is to give a detailed overview of the properties of the site rather than making specific recommendations for conservatively chosen parameter values to be used in safety assessment, the actual choice of which data to use in safety assessment calculations will be made later in the SR-Site data report for transport properties. This report serves in a supporting role for the final data selection.

The flow-related transport properties modelling described in Chapter 3 indicates a large variability of hydrodynamic transport resistance (F-factor) estimates in the hydraulic rock domains (HRD) and the hydraulic conductor domains (HCD). The variability arises both from the general heterogeneity of flowpaths as well as a number of underlying modelling assumptions implicit in both the flow model formulation and applied boundary conditions. Generally, it is not possible to unequivocally determine whether the bulk of the hydrodynamic transport resistance resides in the HRD or HCD.

Scoping calculations suggest typical F-factors for major flowpaths within the proposed repository volume in Laxemar of 10^3–10^5 yr/m for a reference hydraulic gradient of 1%. For radionuclide release at –500 m elevation within deterministic deformation zones and the same reference hydraulic gradient, typical F-factors for transport to the near surface (assumed –100 m elevation) are estimated to be roughly in the same range as that calculated for the HRD. Additional modelling assumptions in the form of whether deformation zones are represented as 2D planar structures or as a 3D porous media (streamtubes) can give as much as two orders of magnitude variation in the estimated mean F-factor for the HCD. These predictions, however, are dependent upon underlying assumptions in the compartmentalised scoping calculations and deviations from this forecast are likely if full consideration of the integrated flow system is made. Additional hydrodynamic transport resistance will be available if credit is also taken for the poorly transmissive flow paths connecting individual canister positions with the major flowpaths in the repository volume. Since the scoping calculations of F-factors for these initial flowpaths are associated with significant uncertainties owing to underlying assumptions related to repository design, they have not been considered to contribute significantly to the transport retardation of radionuclides.

ECPM simulations of the integrated flow system made using ConnectFlow suggest that local flow streamlines may, in some situations, cause radionuclides to migrate upwards through the HRD rather than horizontally before making contact with HCD structures. Owing to the strong depth dependency of deformation zone hydraulic conductivities, particles making first contact with these structures in close proximity to the surface will not experience large hydrodynamic transport resistance in these structures. In these cases it is possible to say that the hydrodynamic transport resistance encountered in the HRD should be significantly greater than for the HCD. Additionally, the assumption of a 1% local hydraulic gradient for the scoping calculations, although not unreasonable, does not take into consideration the propagation of hydraulic head in the integrated hydrostructural model. When particle tracking is performed in the ECPM simulations, much lower “average” hydraulic gradients are frequently encountered by the transported particles along their migration paths. This can give higher F-factors and advective travel times than those estimated in the scoping calculations.

Six different sub-classes of flow channelling have been considered in this investigation as being relevant for the Laxemar site. It appears that their existence can be at least partially accounted for using information internalised in the geological and hydrogeological site descriptive models. The impact of these phenomena can be reasonably well bounded using scoping calculations of the kind described in this report and /Crawford 2008/. Although there is a risk that extreme flow channelling may lead to censoring of borehole data leading to biases in the hydrogeological properties description, it is thought that the flow space should be sufficiently well-connected hydraulically that most major flow channels hosted in fracture planes should be identifiable from borehole investigations (see /Crawford 2008/ for a more detailed discussion). Here, however, it is assumed that fractures are not excessively filled with mineral precipitates or calcite erosion pipes which would cast some doubt on the conclusions of the simplified analysis.

Full resolution of this issue, however, will not be possible until the construction of an underground tunnel at the site since many aspects of flow channelling cannot be properly quantified from a surface based site investigation. It is emphasised, however, that even in situ observations are subject to substantial bias effects owing to stress redistribution and excavation damage which can have an impact on the distribution and extent of flow channelling observed in a tunnel.

It should also be noted in the context of the solute transport calculations detailed in Chapter 5, that when flow channelling effects are properly considered in the simulation of radionuclide transport they can have an overall positive effect on the retardation of radionuclide migration.

In Chapter 4, a retardation model has been developed which describes the material properties of the rock, various fracture types characteristic of the Laxemar site, and a number of recurring deformation zone structural elements. The retardation model describing the properties of various sub-structures within the rock can be assembled in a modular fashion and combined with hydrogeological models to create integrated models for the prediction of radionuclide transport. The differences in material properties between the different unaltered rock types are, however, very small and it is not possible to discriminate between them statistically given the small sample numbers.

For the transport calculations described in Chapter 5, the depth interval of HRD_C between –400 m and –650 m elevation has been taken to be representative of the target volume for a hypothetical repository for spent nuclear fuel. The calculations made for typical major flowpaths encountered within HRD_C indicate that the transport retardation of solutes is, for the most part, relatively weak although flowpaths featuring F-factors ~10^5 yr/m or greater are generally associated with stronger retardation effects.

The sorptive and diffusive retention properties of fracture coatings and altered wall rock (Chapter 4) are not as well constrained as those for the unaltered rock matrix. Since these materials are thought to have enhanced retention properties relative to the unaltered rock, transport calculations have been made assuming only the retardation effect arising from contact with unaltered rock. The additional impact of fracture coatings has been handled by partially generic calculations in an extended analysis. The calculations indicate that a considerable improvement in the transport retardation of early arriving solute might be achievable for radionuclides characterised as moderately to strongly sorbing if fracture coatings are fully considered in transport calculations. Scoping calculations also indicate that the presence of biofilms should have a negligible effect on radionuclide transport times under safety assessment conditions unless microbial growth is found to obstruct the pores of the rock matrix near the fracture surfaces.

The increased microstructural complexity of the HCD, on balance, is also likely to be associated with an elevated degree of transport retardation than the F-factor for these zones would appear to indicate at face value. The same can be probably be said for flow channels of limited extent hosted within fault stepovers or formed at the intersection of crossing or terminating fracture intersections (referred to in this report as conductive fracture intersection zones, or FIZ). The reason for this is the likely existence of larger amounts of diffusion accessible surface area (DAS) in these structures relative to the less microstructurally complex flow channels hosted in the HRD.

Three different alternative models of radionuclide transport have been considered in this report to study the impact of flow channelling for the transport of solutes representing a broad range of sorption properties from very poorly sorbing in the case of Sr(II) to very strongly sorbing in the case of the trivalent lanthanides or actinides. The base case model is a simple description of advective flow coupled with 1D matrix diffusion and sorption typically used in safety assessment calculations. The second model considers as an additional process, the diffusion of solutes into stagnant zones and subsequent uptake to the rock matrix. The third model assumes 2D radially symmetric matrix uptake from flow channels of very narrow width.

The estimated F-factors obtained from the flow related transport modelling were combined with sorption and effective diffusivity data from the retardation model to make predictions of typical solute transport times. It was found that when transport occurs in highly channelised flow within partially closed fractures containing regions of practically stagnant water, the diffusion of solute into stagnant zones followed by uptake to the rock matrix can give a considerably enhanced retardation effect compared to the base case model where this transport mechanism is not considered. For the

ranges of F-factors and channel widths considered in the simulations, however, the effective solute penetration depth is sufficiently low that the radial matrix diffusion model gives largely identical results to the 1D base case model. It is only for F-factors in excess of 10^5 yr/m and higher that the additional transport retardation arising from a radial matrix diffusion model becomes apparent.

A number of confirmatory tracer tests have been carried out in Laxemar with the aim of studying retention processes in situ. With regard to the transport properties site descriptive modelling, the main purpose of these tests was partial validation of the conceptual models of transport and material property data obtained from laboratory investigations using bore core samples. The results were found to be generally consistent with the conceptual models of solute transport used in safety assessment which consider a coupled sorptive-diffusive retention mechanism and strong retardation effects were also observed for sorbing solutes. While the retardation of sorbing solutes appears to be dominated by sorptive interaction with the rim zone of fracture surfaces, the diffusion mediated retardation of non-sorbing or poorly sorbing solutes seems to be more strongly influenced by what could be transverse diffusion between flow streamlines in variable aperture flow channels featuring tapered edges. This observation, however, is weakly supported since only two out of the six performed SWIW tests gave quantifiable estimates of the apparent matrix retardation factor for Cs^+. Other experimental artefacts and processes could potentially give rise to similar effects during the tracer tests so this is only suggested as a speculative explanation for the enhanced retention of uranine observed in the SWIW tests.

8 Nomenclature

This section contains explanations of the various variable names referred to in this report. Some variable names are reused in different contexts and therefore are defined multiple times in the following list as appropriate (i.e. with separate meanings referenced to different sections, or specific equations where first used in the report). More common variable names that are used consistently with the same meaning throughout the text, however, are not referenced to any specific section or equation.

a	(-)	Empirical parameter in transmissivity distribution function (Table 3-1).
a	(m)	Equivalent flow channel radius for 2D radially symmetric diffusion model (Equation 5-5).
a	(-)	Empirical constant in deformation zone transmissivity model (Equation 3-2 and 3-3).
a	(-)	Empirical constant in deformation zone model for specific flow-wetted surface depth variation (Equation 3-4).
a	(-)	Empirical constant in power law expression for surface conductivity (Equation D-5).
A	($s^{-½}$)	Matrix interaction parameter (Equation 6-2).
A_{BET}	(m^2/g)	Specific surface area measured using the BET method.
$A_{colloid}$	(m^2/g)	Specific surface area of colloidal material.
A_{EXT}	(m^2/g)	Specific external surface area of a crushed rock particle.
A_{INT}	(m^2/g)	Specific surface area of internal microsurfaces within the particle or rock matrix.
a_R	(m^2/m^3)	Specific flow-wetted surface normalised with respect to rock volume.
A_{xs}	(m^2)	Cross-sectional area of a stream tube.
$A_{colloid}$	(m^2/g)	Specific surface area of groundwater colloidal material.
A_0	(m^2/g)	Specific surface area of analogue mineral used to represent natural groundwater colloid.
b	(-)	Empirical parameter in transmissivity distribution function (Table 3-1).
B	(-)	Empirical constant in deformation zone transmissivity model (Equation 3-2 and 3-3).
b	(-)	Empirical constant in deformation zone model for specific flow-wetted surface depth variation (Equation 3-4).
b	(-)	Empirical constant in power law expression for surface conductivity (Equation D-5).
C_f	(mol/m^3)	Free concentration in advective flow channel (Equation E-2).
C_{sc}	(mol/m^3)	Reference concentration of diffusing substance (Equation E-2).
C_0	(mol/m^3)	Reference concentration of diffusing substance.
d_p	(m)	Characteristic particle size of crushed rock.
D_e	(m^2/s)	Effective diffusivity of rock matrix.
D_p	(m^2/s)	Pore diffusivity of rock matrix (Equation 4-2).
d_s	(m)	Disturbed matrix depth (Equation D-3).
D_w	(m^2/s)	Free diffusivity of solute at infinite dilution.
F	(yr/m)	Hydrodynamic transport resistance (F-factor).
F_{app}	(yr/m)	Apparent F-factor for colloidal transport (Equation E-5).
F_{DFF_0}	(yr/m)	F-factor for distant far field (DFF) flow paths under reference hydraulic gradient conditions.
F_f	(-)	True rock matrix formation factor.

F_{fs}	(-)	Formation factor of disturbed rock matrix (Equation D-3).
F_f^{TT}	(-)	Apparent formation factor derived from tracer test interpretation (Equation 6-4 and 6-5).
F_f^*	(-)	Rock matrix formation factor including surface conduction and porewater compositional uncertainty (Equation D-6).
F_f^{app}	(-)	Apparent rock matrix formation factor including surface conduction uncertainty (Equation D-5).
F_{IFF_0}	(yr/m)	F-factor for immediate far field (IFF) flow paths under reference hydraulic gradient conditions.
F_{NNF_0}	(yr/m)	F-factor for non-engineered near field (NNF) flow paths under reference hydraulic gradient conditions.
f_s	(-)	Symmetry parameter for stagnant zone mass transfer (Equation 5-1).
h_a	(m)	Hydraulic head at lower deformation zone boundary (Figure 3-12).
h_b	(m)	Hydraulic head at upper deformation zone boundary (Figure 3-12).
i	(m/m)	Hydraulic gradient.
i_0	(m/m)	Reference hydraulic gradient.
J_m	(mol/m²s)	Diffusive mass flux to rock matrix.
J_s	(mol/m²s)	Diffusive mass flux to stagnant zone.
K_a	(m)	Equilibrium surface sorption coefficient (Equation 4-4).
K_d	(m³/kg)	Equilibrium sorption coefficient.
$K_d^{colloid}$	(m³/kg)	Equilibrium sorption coefficient for colloidal particles (Equation E-2).
K_d^0	(m³/kg)	Equilibrium sorption coefficient for colloidal analogue mineral (Equation E-4).
K_{dm}	(m³/kg)	Equilibrium coefficient for sorption in rock matrix.
K_{ds}	(m³/kg)	Equilibrium coefficient for sorption in fracture coating.
K_{eff}	(m/s)	Effective hydraulic conductivity.
k_r	(-)	Shape parameter in fracture size power law distribution (Table 3-2).
L	(m)	Hydraulic boundary separation distance.
L_p	(m)	Transport distance.
m_c	(kg/m³)	Colloidal mass concentration (Equation E-2).
MPG	(m/s½)	Material properties group.
P_{con}	(-)	Percolation probability.
P_{10}	(m^{-1})	Linear intensity of fractures.
$P_{10,pfl}$	(m^{-1})	Linear intensity of flow-bearing fractures identified using PFL.
$P_{10,cor}$	(m^{-1})	Linear intensity of flow-bearing fractures corrected for borehole orientation bias.
P_{32}	(m²/m³)	Volumetric areal intensity of fractures.
P_{32o}	(m²/m³)	Volumetric areal intensity of open fractures.
P_{32cof}	(m²/m³)	Volumetric areal intensity of hydraulically connected open fractures.
P_{32pfl}	(m²/m³)	Volumetric areal intensity of flow-bearing fractures.
q	(m³/yr)	Flowrate along a flow streamline.
Q	(m³/yr)	Total flowrate.
Q_{bh}	(m³/yr)	Borehole flowrate.
r	(m)	Fracture radius.
r_{bh}	(m)	Borehole radius (Equation D-3).
R_d	(m³/kg)	Apparent sorption partitioning ratio (Equation 4-3).
r_0	(m)	Location parameter in fracture size power law distribution (Table 3-2).

r_0	(m)	Reference distance (Equation D-3).
R_a	(-)	Effective retardation coefficient for instantaneous equilibrium sorption within an advective flow channel.
R_f	(-)	Ratio of F-factors (Equation E-5).
R_g	(m^2/m^2)	Mass transfer surface area ratio for particulate fracture infill (e.g. breccia) to rock matrix mass transfer surface area.
R_m	(-)	Effective pore diffusion retardation factor.
R_s	(m^2/m^2)	Mass transfer surface area ratio for stagnant zone relative to rock matrix mass transfer surface area.
t	(yr)	Time.
T	(m^2/s)	Transmissivity.
T	(K)	Temeperature (Equation A-24)
t_w	(yr)	Advective travel time.
u	(m^3/m^2yr)	Darcy flux.
v	(m/yr)	True advective velocity.
V_p	(m^3)	Water filled volume of an advective flowpath.
w	(m)	Local flow channel width.
W_c	(m)	Average flow channel width.
W_{bh}	(m)	Borehole width.
z	(m)	Elevation.
z_a	(m)	Lower hydraulic boundary elevation in deformation zone analytical model (Figure 3-12).
z_b	(m)	Upper hydraulic boundary elevation in deformation zone analytical model (Figure 3-12).
z_r	(m)	solute release elevation in deformation zone analytical model (Figure 3-12).

Greek symbols:

α_L	(m)	Dispersion length (Equation 6-1).
β_g	(m^3/m^3)	Relative void fraction of fracture occupied by particulate material (Equation 4-6).
δ_{DZ}	(m)	Thickness of deformation zone.
δ_{fs}	(m)	Thickness of fracture coating (Equation 4-4).
δ_m	(m)	Maximum matrix diffusion depth.
δ_s	(m)	Effective aperture of stagnant zone.
δ_t	(m)	Fracture transport aperture.
δ/τ^2	(-)	Tortuosity-constrictivity geometric factor (Equation 4-1).
θ_f	(m^3/m^3)	Kinematic porosity for advective flow.
θ_g	(m^3/m^3)	Water saturation porosity of particulate fracture infill material (Equation 4-6).
θ_m	(m^3/m^3)	Water saturation porosity of rock matrix.
θ_p	(m^3/m^3)	Transport porosity of rock matrix (Equation 4-2).
θ_s	(m^3/m^3)	Water saturation porosity of fracture surface coatings (Equation 4-2).
κ_r	(S/m)	Electrical conductivity of brine saturated rock (Equation D-2).
κ_s	(S/m)	Surface conductivity (Equation D-4).
κ_w	(S/m)	Electrical conductivity of brine porewater (Equation D-2).
λ	(m^2/m^2)	Surface roughness-sphericity factor (Equation 4-7).

μ_w	(Pa.s)	Water viscosity (Equation A-24).
ρ_{bg}	(kg/m^3)	Bulk density of particulate fracture infill material (Equation 4-6).
ρ_{bm}	(kg/m^3)	Bulk density of the rock matrix.
ρ_{bs}	(kg/m^3)	Bulk density of fracture surface coating (Equation 4-5).
ρ_r	(Ωm)	Electrical resistivity of brine saturated rock.
ρ_w	(Ωm)	Brine porewater electrical resistivity.
τ	(-)	Dimensionless hydrodynamic dispersion parameter (Equation 6-1).

Glossary of specific terms used in this report:

CDF	Cumulative distribution function.
CEC	Cation exchange capacity.
DFF	Distant far-field.
EC	Electrical conductivity.
ECPM	Equivalent continuous porous medium.
EDL	Electrical double layer.
Elsterian glaciation	A sequence of three glacial/interglacial periods commencing about 455 ka concluding roughly 300 ka before present.
HCD	Hydraulic conductor domain.
HRD	Hydraulic rock domain.
IFF	Immediate far-field.
KT extinction	Cretaceous-Tertiary extinction event; a large-scale mass extinction of animal (the conclusion of the age of the dinosaurs and the rise of modern mammals) and plant species in a geologically short period of time, approximately 65.5 million years ago, which marked the end of the Mesozoic era and beginning of the Cenozoic era.
Last glacial maximum	Refers to the timing of maximum ice sheet extent, approximately 20 ka before present, during the Weichsel glaciation.
MDZ	Minor deformation zone.
NNF	Non-engineered near-field.
Permian extinction	The Permian-Triassic (PT) extinction event was an extinction event that occurred 251.4 million years ago forming the boundary between the Permian and Triassic geologic periods. It was the Earth's most severe extinction event, with up to 96 percent of all marine species and 70 percent of terrestrial vertebrate species becoming extinct.
Pleistocene	The geological epoch extending from 1.8 Ma to 10 ka before present covering the recent period of repeated glaciations. The end of the Pleistocene corresponds with the retreat of the last continental glacier and the commencement of the current geological epoch referred to as the Holocene.
PMMA	Poly-methyl methacrylate.
SWIW	Single well injection-withdrawal test.
Weichsel glaciation	Most recent glacial period extending from 110 ka to roughly 12 ka before present.

9 References

Abelin H, Birgersson L, Widén H, Ågren T, Moreno L, Neretnieks I, 1990. Channeling experiment. Stripa Project. SKB 90-13, Svensk Kärnbränslehantering AB.

Abelin H, Birgersson L, Moreno L, Widén H, Ågren T, Neretnieks I, 1991. A large-scale flow and tracer experiment in granite. II. Results and interpretation. Water Resources Research 27(12), pp 3119–3135.

Abelin H, Birgersson L, Moreno L, Widén H, Ågren T, Neretnieks I, 1994. Channeling experiments in crystalline fractured rocks. Journal of Contaminant Hydrology 15, pp 129–158.

Alexander W R, Smith P A, McKinley I G, 2003. Modelling radionuclide transport in the geological environment: a case study from the field of radioactive waste disposal. Modelling Radioactivity in the Environment. E. M. Scott (Ed.). Vol 4, 109-145, In: Radioactivity in the Environment, Elsevier B. V. Amsterdam.

Anderson C, Pedersen K, Jacobsson A-M, 2006. Autoradiographic comparisons of radionuclide adsorption between subsurface anaerobic biofilms and granitic host rocks. Geomicrobiology Journal 23(1), pp 15–29.

Anderson C, Jacobsson A-M, Pedersen K, 2007. Influence of in situ biofilm coverage on the radionuclide adsorption capacity of subsurface granite. Environmental Science and Technology 41(3), pp 830–836.

Andersson J, Hermanson J, Elert M, Gylling B, Moreno L, Selroos J-O, 1998. Derivation and treatment of the flow-wetted surface and other geosphere parameters in the transport models FARF31 and COMP23 for use in Safety Assessment. SKB R-98-60, Svensk Kärnbränslehantering AB.

Andersson P, Byegård J, Dershovitz W, Doe T, Hermanson J, Meier P, Tullborg E L, Winberg A, 2002. TRUE Block Scale Project. Final Report. 1. Characterisation and model development. SKB TR-02-19, Svensk Kärnbränslehantering AB.

Atkins P, 1999. Physical Chemistry. 6 ed. Oxford University Press.

Autio J, Kirkkomäti T, Siitari-Kauppi M, Timonen J, Laajalahti M, Aaltonen T, Maaranen J, 1999. Äspö Hard Rock Laboratory. Use of the 14C-PMMA and He-gas methods to characterise excavation disturbance in crystalline rock. SKB IPR-99-18, Svensk Kärnbränslehantering AB.

Axe L, Trivedi P, Anderson P, 2002. Diffusion at oxide and related surfaces. Encyclopedia of Surface and Colloid Science. A. Hubbard (Ed.), pp 1447–1457, Marcel Dekker.

Becker M W, Shapiro A M, 2000. Tracer transport in fractued crystalline rock: evidence of nondiffusive breakthrough tailing. Water Resources Research 36(7), pp 1677–1686.

Becker M W, Shapiro A M, 2003. Interpreting tracer breakthrough tailing from different forced-gradient tracer experiment configurations in fractured bedrock. Water Resources Research 39(1), p 1024.

Berglund S, Selroos J-O, 2004. Transport properties site descriptive model. Guidelines for evaluation and modelling. SKB R-03-09, Svensk Kärnbränslehantering AB.

Berkowitz B, Scher H, 1995. On characterization of anomalous dispersion in porous and fractured media. Water Resources Research 31(6), pp 1461–1466.

Bertetti F, Pabalan R, Turner D, Almedarez M, 1996. Neptunium(V) sorption behaviour on clinoptilolite, quartz and montmorillonite. In: Scientific Basis for Nuclear Waste Management XIX, Materials Research Society Symposium Proceedings Vol 412, pp 631–638.

Bertetti F, Pabalan R, Almedarez M, 1998. Neptunium(V) sorption behaviour on quartz, clinoptilolite, montmorillonite, and α-alumina. Adsorption of Metals by Geomedia – Variables, Mechanisms, and Model Applications. E. Jenne (Ed.), pp 131–148, Academic Press, New York.

Bidaux P, Tsang C F, 1991. Fluid flow patterns around a well bore or an underground drift with complex skin effects. Water Resources Research 27(11), pp 2993–3008.

Bird R B, Stewart W E, Lightfoot E N, 2002. Transport Phenomena. 2 ed. Wiley, New York.

Birgersson L, Neretnieks I, 1990. Diffusion in the Matrix of Granitic Rock: Field Test in the Stripa Mine. Water Resources Research 26(11), pp 2833–2842.

Birgersson L, Widén H, Ågren T, Neretnieks I, 1992. Stripa project. Tracer migration experiments in the Stripa mine 1980–1991. SKB 92-25, Svensk Kärnbränslehantering AB.

Black J, Hodgkinson D, 2005. Äspö Task Force on modelling of groundwater flow and transport of solutes. Review of task 6C. SKB R-05-33, Svensk Kärnbränslehantering AB.

Bonnet E, Bour O, Odling N, Davy P, Main I, Cowie P, Berkowitz B, 2001. Scaling of fracture systems in geological media. Reviews of Geophysics 39(3), pp 347-383.

Brace W, Orange A, Madden T, 1965. The effect of pressure on the electrical resistivity of water-saturated crystalline rocks. Journal of Geophysical Research 70(22), pp 5669–5678.

Brace W, Orange A, 1968. Further studies of the effects of pressure on electrical resistivity of rocks. Journal of Geophysical Research 73(16), pp 5407–5420.

Bradbury M, Green A, 1986. Investigations into the factors influencing long range matrix diffusion rates and pore space accessibility at depth in granite. Journal of Contaminant Hydrology pp 89, 123–139.

Bradbury M H, Baeyens B, 1997. A mechanistic description of Ni and Zn sorption on Na-montmorillonite. Part II: modelling. Journal of Contaminant Hydrology 27, pp 223–248.

Bradbury M H, Baeyens B, 2005. Experimental measurements and modeling of sorption competition on montmorillonite. Geochimica et Cosmochimica Acta 69(17), pp 4187–4197.

Bruines P, 2003. Laminar ground water flow through stochastic channel networks in rock. Ph.D. Thesis, ENAC School of Architecture, Civil and Environmental Engineering, École Polytechnique Fédérale de Lausanne, Switzerland.

Brunauer S, Emmet P, Teller E, 1938. Adsorption of gases in multimolecular layers. Journal of the American Chemical Socitey 60, pp 309-319.

Byegård J, Larsson N-Å, 2004. Metodbeskrivning för batchsorptionmätning. SKB MD 540.002 Version 1.2, Svensk Kärnbränslehantering AB.

Byegård J, Selnert E, Tullborg E L, 2008. Site descriptive modelling of transport properties. Retardation model Forsmark 2.3. SKB R-08-98, Svensk Kärnbränslehantering AB.

Börner F, 2006. Complex conductivity measurements. Groundwater Geophysics. Kirsch (Ed.), pp 119-153, Springer.

Caine J S, Evans J P, Forster C B, 1996. Fault zone architecture and permeability structure. Geology 24(11), pp 1025–1028.

Charbonneau A, Novakowski K, Ross N, 2006. The effect of a biofilm on solute diffusion in fractured porous media. Journal of Contaminant Hydrology 85(3-4), pp 212–228.

Contardi J, Turner D, Ahn T, 2001. Modeling colloid transport for performance assessment. Journal of Contaminant Hydrology 47, pp 323–333.

Coppin F, Berger G, Bauer A, Castet S, Loubet M, 2002. Sorption of lanthanides on smectite and kaolinite. Chemical Geology 182, pp 57–68.

Coppin F, Castet S, Berger G, Loubet M, 2003. Microscopic reversibility of Sm and Yb sorption onto smectite and kaolinite: Experimental evidence. Geochimica et Cosmochimica Acta 67(14), pp 2515–2527.

Cormen T, Leiserson C, Rivest R, Stein C, 2001. Introduction to Algorithms. 2 ed. MIT Press and McGraw Hill.

Cosgrove J, Stanfors R, Röshoff K, 2006. Geological characteristics of deformation zones and a strategy for their detection in a repository. SKB R-06-39, Svensk Kärnbränslehantering AB.

Crank J, 1975. The mathematics of diffusion. 2 ed. Oxford University Press, Oxford.

Crawford J, 2006. Modelling in support of bedrock transport property assessment. Preliminary site description. Laxemar subarea – version 1.2. SKB R-06-28, Svensk Kärnbränslehantering AB.

Crawford J, Neretnieks I, Malmström M, 2006. Data and uncertainty assessment for radionuclide K_d partitioning coefficients in granitic rock for use in SR-Can calculations. SKB R-06-75, Svensk Kärnbränslehantering AB.

Crawford J, 2008. Bedrock transport properties Forsmark. Site descriptive modelling. SDM-Site Forsmark. SKB R-08-48, Svensk Kärnbränslehantering AB.

Cvetkovic V, Painter S, Outters N, Selroos J-O, 2004. Stochastic simulation of radionuclide migration in discretely fractured rock near the Äspö Hard Rock Laboratory. Water Resources Research 40, W02404.

Cvetkovic V, Cheng H, Widestrand H, Byegård J, Winberg A, Andersson P, 2007. Sorbing tracer experiments in a crystalline rock fracture at Äspö (Sweden): 2. Transport model and effective parameter estimation. Water Resources Research 43, W11421.

Degueldre C, Ulrich H, Silby H, 1994. Sorption of Am-241 onto montmorillonite, illite and hematite colloids. Radiochimica Acta 65, pp 173–179.

Dershowitz B, Klise K, 2002. Äspö Hard Rock Laboratory. TRUE Block Scale Project. Evaluation of fracture network transport pathways and processes using the Channel Network approach. SKB IPR-02-34, Svensk Kärnbränslehantering AB.

Dershowitz W, Lee G, Foxford T, 2004. FracWorks XP Discrete Fracture Modeling Software, User Documentation. Golder Associates, Redmond, WA.

Drake H, Tullborg E L, 2009. Fracture mineralogy of the Laxemar site. Final report. SKB R-08-99, Svensk Kärnbränslehantering AB.

Eklund S, Mattsson K-J, 2008. Oskarshamn site investigation. Quantitative mapping of fracture minerals in Laxemar. SKB P-08-38, Svensk Kärnbränslehantering AB.

EPA, 2002. A lexicon of cave and karst terminology with special reference to environmental karst hydrology. EPA7600/R-02/003, US Environmental Protection Agency (EPA), Office of Reserach and Development. Washington DC.

Essén S, Johnsson A, Bylund D, Pedersen K, Lundström U, 2007. Siderophore production by Pseudomonas stutzeri under anaerobic conditions. Applied and Environment Microbiology 73(18), pp 5857–5864.

Fisher R, 1953. Dispersion on a sphere. Proceedings of the Royal Society of London. Series A, Mathematical and Physical Sciences. 217(1130), pp 295–305.

Follin S, Ludvigson J-E, Levén J, 2006. A comparison between standard well test evaluation methods used in SKB's site investigations and the Generalised Radial Flow concept. SKB P-06-54, Svensk Kärnbränslehantering AB.

Follin S, Levén J, Hartley L, Roberts D, Swift B, 2007. Hydrogeological characterisation and modelling of deformation zones and fracture domains, Forsmark modelling stage 2.2. SKB R-07-48, Svensk Kärnbränslehantering AB.

Gelhar L W, Collins M A, 1971. General analysis of longitudinal dispersion in non-uniform flow. Water Resources Research 7(6), pp 1511–1521.

Gelhar L W, Welty C, Rehfeldt K R, 1992. A critical review of data on field-scale dispersion in aquifers. Water Resources Research 28(7), pp 1955–1974.

Gimeno M J, Auqué L F, Gómez J B, Acero P, 2009. Water-rock interaction modelling and uncertainties of mixing modelling SDM–Site Laxemar-Simpevarp SKB R-08-111, Svensk Kärnbränslehantering AB.

Gleich D, 2006. Matlab BGL v2.0 (users guide). Stanford University, Institute for Computational and Mathematical Engineering.

Glover P W J, Matsuki K, Hikima R, Hayashi K, 1998. Fluid flow in synthetic rough fractures and application to the Hachimantai geothermal hot dry rock test site. Journal of Geophysical Research 103(B5), pp 9621–9635.

Gurban I, 2009. M3 modelling of the hydrochemical parameters of Laxemar-Simpevarp groundwaters. SKB R-08-111, Svensk Kärnbränslehantering AB.

Gustafsson E, 2002. Bestämning av grundvattenflödet med utspädningsteknik. Modifiering av utrustning och kompletterande fältmätningar. SKB R-02-31. Svensk Kärnbränslehantering AB.

Gustafson G, Franson Å, 2006. The use of the Pareto distribution for fracture transmissivity assessment. Hydrogeology Journal 14(1-2), pp 15–20.

Gustafsson E, Ludvigson J-E, 2005. Combined interference test and tracer test between KLX02 and HLX10. SKB P-05-20, Svensk Kärnbränslehantering AB.

Gustafsson E, Nordqvist R, 2005. Oskarshamn site investigation. Groundwater flow measurements and SWIW tests in boreholes KLX02 and KSH02. SKB P-05-28, Svensk Kärnbränslehantering AB.

Gustafsson E, Nordqvist R, Thur P, 2006. Groundwater flow measurements and SWIW test in borehole KLX03. SKB P-05-246, Svensk Kärnbränslehantering AB.

Haggerty R, Gorelick S M, 1995. Multiple-rate mass transfer for modeling diffusion and surface reaction in media with pore-scale heterogeneity. Water Resources Research 31(10), pp 2383–2400.

Hakami E, Fredriksson A, Lanaro F, 2008. Rock mechanics Laxemar. Site descriptive modelling. SDM-Site Laxemar. SKB R-08-57, Svensk Kärnbränslehantering AB.

Hallbeck L, Pedersen K, 2008. Explorative analyses of microbes, colloids, and gases together with microbial modelling. Site description model. SDM-Site Laxemar. SKB R-08-109, Svensk Kärnbränslehantering AB.

IUPAC, 1997. Compendium of chemical terminology (the "Gold Book"). 2 ed. Blackwell Scientific Publications, Oxford.

Jacobsson L, 2007. Oskarshamn site investigation. Borehole KLX17A. Microcrack volume measurements and triaxial compression tests on intact rock. SKB P-07-140, Svensk Kärnbränslehantering AB.

Jakobsson A-M, 1999. Measurement and modelling using surface complexation of cation (II to IV) sorption onto mineral oxides. Ph.D. Thesis, Dept. of Nuclear Chemistry, Chalmers University of Technology, Gothenburg.

Johns R A, Roberts P V, 1991. A solute transport model for channelized flow in a fracture. Water Resources Research 27(8), pp 1797–1808.

Johnsson A, Arlinger J, Pedersen K, Ödegaard-Jensen A, Albinsson Y, 2006. Solid-aqueous phase partitioning of radionuclides by complexing compounds excreted by subsurface bacteria. Geomicrobiology Journal 23, pp 621–630.

Jong T, Parry D L, 2004. Adsorption of Pb(II), Cu(II), Cd(II), Zn(II), Ni(II), Fe(II), and As(V) on bacterially produced metal sulfides. Journal of Colloid and Interface Science 275(1), pp 61–71.

La Pointe P, Fox A, Hermanson J, Öhman J, 2008. Geological discrete fracture network model for the Laxemar site. Site descriptive modelling. SDM-Site Laxemar. SKB R-08-55, Svensk Kärnbränslehantering AB.

Laaksoharju M, Smellie J, Tullborg E-L, Wallin B, Drake H, Gascoyne M, Gimeno M, Gurban I, Hallbeck L, Molinero J, Nilsson A-C, Waber N, 2009. Bedrock hydrogeochemistry Laxemar. Site descriptive modelling. SDM-Site Laxemar. SKB R-08-93, Svensk Kärnbränslehantering AB.

Langmuir D, 1997. Aqueous environmental geochemistry. Prentice Hall, New Jeresey.

Li Y-H, Gregory S, 1974. Diffusion of ions in sea water and in deep-sea sediments. Geochimica et Cosmochimica Acta 38 (pp 703–714).

Lichtner P, 1996. Continuum formulation of multicomponent-multiphase reactive transport. Reactive transport in porous media. P Lichtner, C Steefel and E Oelkers (Eds.). Vol 34, pp 1–79, In: Reviews in mineralogy, Mineralogical Society of America.

Lindquist A, Hjerne C, Nordqvist R, Ludvigson J-E, Harrström J, Carlsten S, 2008. Oskarshamn site investigation. Confirmatory hydraulic interference test and tracer test in Laxemar. SKB P-08-96, Svensk Kärnbränslehantering AB.

Lu N, Triay I, Cotter C, Kitten H, Bentley J, 1998. Reversibility of sorption of plutonium-239 onto colloids of hematite, goethite, smectite, and silica. A milestone final report of YMP. LA-UR-98-3057, LANL Los Alamos National Laboratory.

Löfgren M, 2001. Formation factor logging in igneous rock by electrical methods. Licentiate Thesis, Dept. of Chemical Engineering and Technology, Royal Institute of Technology (KTH), Stockhoolm, Sweden.

Löfgren M, Neretnieks I, 2002. Formation factor logging in situ by electrical methods. Background and methodology. Technical Report SKB TR-02-27, Svensk Kärnbränslehantering AB.

Löfgren M, Neretnieks I, 2003. Formation factor logging by electrical methods. Comparison of formation factor logs obtained in situ and in the laboratory. Journal of Contaminant Hydrology 61(1-4), pp 107–115.

Löfgren M, 2004. Diffusive properties of granitic rock as measured by in situ electrical methods. Ph.D. Thesis, Dept. Chemical Engineering and Technology, Royal Institute of Technology, Stockholm, Sweden.

Löfgren M, Neretnieks I, 2005a. Forsmark site investigation. Formation factor logging in situ by electrical methods in KFM01A and KFM02A. Measurements and evaluation of methodology. SKB P-05-29, Svensk Kärnbränslehantering AB.

Löfgren M, Neretnieks I, 2005b. Oskarshamn site investigation. Formation factor logging in situ and in the laboratory by electrical methods in KSH01A and KSH02. Measurements and evaluation of methodology. SKB P-05-27, Svensk Kärnbränslehantering AB.

Löfgren M, Neretnieks I, 2005c. Oskarshamn site investigation. Formation factor logging in situ by electrical methods in KLX03 and KLX04. SKB P-05-105, Svensk Kärnbränslehantering AB.

Löfgren M, Neretnieks I, 2006. Through-electromigration: A new method of investigating pore connectivity and obtaining formation factors. Journal of Contaminant Hydrology 87, pp 273–252.

Löfgren M, Pettersson M, 2006. Oskarshamn site investigation. Formation factor logging in situ by electrical methods in KLX05 and KLX06. SKB P-06-143, Svensk Kärnbränslehantering AB.

Löfgren M, 2007. Oskarshamn site investigation. Formation factor logging in situ by electrical methods in KLX07A, KLX08, KLX10 and KLX12A. SKB P-06-288, Svensk Kärnbränslehantering AB.

Löfgren M, Crawford J, Elert M, 2007. Tracer tests – possibilities and limitations. Experiments from SKB fieldwork: 1977–2007. SKB R-07-39, Svensk Kärnbränslehantering AB.

Mathworks, 2005. Matlab and Simulink (Release 14, SP3). The Mathworks Inc.

McKinley I G, Scholits A, 1993. A comparison of radionuclide sorption databases used in recent performance assessments. Journal of Contaminant Hydrology 13(1–4), pp 347–363.

Missana T, García-Gutiérrez M, Alonso Ú, 2004. Kinetics and irreversibility of cesium and uranium sorption onto bentonite colloids in a deep granitic environment. Applied Clay Science 26, pp 137–150.

Moreno L, Neretnieks I, 1983. Evaluation of some tracer tests in the granitic rock at Finnsjön. SKBF-KBS Technical Report 83-38, Svensk Kärnbränslehantering AB.

Mourzenko V, Thovert J, Adler P, 2004. Macroscopic permeability of three-dimensional fracture networks with a power law size distribution. Physical Review E. 69(6), pp 1–13.

Mourzenko V, Thovert J, Adler P, 2005. Percolation of three-dimensional fracture networks with a power-law size distribution. Physical Review E. 72(3), pp 1–14.

Munier R, Stenberg L, Stanfors R, Geoffrey Milnes A, Hermanson J, Triumf C-A, 2003. Geological site descriptive model. A strategy for the model development during site investigations. SKB R-03-07, Svensk Kärnbränslehantering AB.

Munier R, 2004. Statistical analysis of fracture data, adapted for modelling discrete fracture networks – Version 2. SKB R-04-66, Svensk Kärnbränslehantering AB.

Munier R, Hökmark H, 2004. Respect distances. Rationale and means of computation. SKB R-04-17, Svensk Kärnbränslehantering AB.

Möri A, Mazurek M, Adler M, Schild M, Siegesmund S, Vollbrecht A, Ota K, Ando T, Alexander W R, Smith P A, Haag P, Bühler C, 2003. The Nagra-JNC in situ study of safety relevant radionuclide retardation in fractured crystalline rock – IV: The in situ study of matrix porosity in the vicinity of a water conducting fracture. Technical Report NTB 00-08, Nagra, Wettingen.

NEA, 1999. Confidence in models of radionuclide transport for site-specific assessments. In: Synthesis and Proceedings from the third GEOTRAP Workshop, OECD-NEA Radioactive Waste Management, Carlsbad, New Mexico, USA, 14–17 June 1999.

Neretnieks I, 1980. Diffusion in the rock matrix: an important factor in radionuclide retardation? Journal of Geophysical Research 85(B8), pp 4379–4397.

Neretnieks I, 1983. A note on fracture flow dispersion mechanisms in the ground. Water Resources Research 19(2), pp 364–370.

Neretnieks I, 1993. Solute transport in fractured rock – applications to radionuclide waste repositories. Flow and contaminant transport in fractured rock. J. Bear, C.-F. Tsang and G. De Marsily (Eds.), Academic Press Inc. San Diego.

Neretnieks I, 1994. Nuclear waste repositories in crystalline rock – An overview of nuclide transport mechanisms. In: Scientific Basis for Nuclear Waste Management XVIII, 24–26, Materials Research Society (MRS), Kyoto, Japan.

Neretnieks I, Moreno L, 2003. Prediction of some in situ tracer tests with sorbing tracers using independent data. Journal of Contaminant Hydrology 61(1–4), pp 351–360.

Neretnieks I, 2004. Predicting solute transport in fractured rocks – processes, models and some concerns. Coupled thermo-hydro-mechanical-chemical processes in geo-systems – Fundamentals, modelling, experiments and applications. O. Stephansson, J. A. Hudson and L. Jing (Eds.). Vol 2, pp 19–30, In: Elsevier geo-engineering book series, Elsevier Science B. V.

Neretnieks I, 2006a. Channeling with diffusion into stagnant water and into a matrix in series. Water Resources Research.

Neretnieks I, 2006b. Fast method for simulation of radionuclide chain migration in dual porosity fractured rock. Journal of Contaminant Hydrology 88(3–4), pp 269–288.

Neretnieks I, 2007. Single well injection withdrawal tests (SWIW) in fractured rock. Some aspects on interpretation. SKB R-07-54, Svensk Kärnbränslehantering AB.

Nernst W, 1888. Zur Kinetik der in Lösung befindlichen Körper. Erste Abhandlung. Theorie der Diffusion. Zeitschrift Physikalische Chemie 2(9), pp 613–637.

Neuman S P, 1995. On advective transport in fractal permeability and velocity fields. Water Resources Research 31(6), pp 1455–1460.

Neuman S P, 2005. Trends, prospects and challenges in quantifying flow and transport through fractured rocks. Hydrogeology Journal 13(1), pp 124–147.

Nielsen U T, Ringgaard J, Horn F, 2004. Geophysical borehole logging in borehole KLX04, HLX26, HLX27 and HLX28. SKB P-04-306, Svensk Kärnbränslehantering AB.

Nordqvist R, 1994. Documentation of some analytical flow and transport models implemented for use with PAREST – Users manual. GRAP 94 006, GEOSIGMA, Uppsala.

Nordqvist R, Gustafsson E, 2002. Single-well injection-withdrawal tests (SWIW). Literature review and scoping calculations for homogeneous crystalline bedrock conditions. SKB R-02-34, Svensk Kärnbränslehantering AB.

Nordqvist R, Gustafsson E, 2004. Single-well injection-withdrawal tests (SWIW). Investigation of evaluation aspects under heterogeneous crystalline bedrock conditions. SKB R-04-57, Svensk Kärnbränslehantering AB.

Nordqvist R, 2008. Evaluation and modelling of SWIW tests performed within the SKB site characterisation programme. SKB R-08-104, Svensk Kärnbränslehantering AB.

Nordqvist R, Gustafsson E, Andersson P, Thur P, 2008. Groundwater flow and hydraulic gradients in fractures and fracture zones at Forsmark and Oskarshamn. SKB R-08-103, Svensk Kärnbränslehantering AB.

Nover G, 2005. Electrical properties of crustal and mantle rocks - a review of laboratory measurements and their explanation. Surveys in Geophysics 26, pp 593–651.

NRC, 1996. Rock fractures and fluid flow. Contemporary understanding and applications. Committee on Fracture Characterization and Fluid Flow, National Research Council, National Academy Press, Washington DC.

Ohlsson Y, Neretnieks I, 1998. Some evidence for surface ion mobility in rock. Journal of Contaminant Hydrology 35, pp 91–100.

Ohlsson Y, 2000. Studies of ionic diffusion in crystalline rock. Ph.D. Thesis, Dept. Chemical Enginering and Technology. Royal Institute of Technology, Stockholm, Sweden.

Olin M, Valkiainen M, Aalto H, 1997. Martix diffusion in crystalline rocks: coupling of anion exclusion, surface diffusion and surface complexation. Posiva 96-25, ISBN 951-652-024-3 Posiva OY, Finland.

Outters N, 2003. A generic study of discrete fracture network transport properties using FracMan/MAFIC. SKB R-03-13, Svensk Kärnbränslehantering AB.

Pabalan R, Turner D, Bertetti F, Prikryl J, 1998. Uranium(VI) Sorption onto Selected Mineral Surfaces – Key Geochemical Parameters. Adsorption of Metals by Geomedia – Variables, Mechanisms, and Model Applications. E. Jenne (Ed.), pp 100–128, Academic Press, New York.

Painter S, Cvetkovic V, 2005. Upscaling discrete fracture network simulations: An alternative to continuum transport models. Water Resources Research 41, W02002.

Painter S, 2006. Effect of single-fracture aperture variability on field-scale transport. SKB R-06-25, Svensk Kärnbränslehantering AB.

Painter S, Mancillas J, 2007. MARFA version 3.2 user's manual. Migration analysis of radionuclides in the far field. Center for Nuclear Waste Regulatory Analyses. Southwest Research Insititute (SwRI), San Antonio, Texas.

Pedersen K, Karlsson F, 1995. Investigations of subterranean microorganisms. Their importance for performance assessment of radioactive waste disposal. Technical Report SKB TR-95-10, Svensk Kärnbränslehantering AB.

Penttinen L, Siitari-Kauppi M, Ikonen J, 2006. Oskarshamn site investigation. Determination of porosity and micro fracturing using the ^{14}C-PMMA technique in samples taken from Oskarshamn area. SKB P-06-62, Svensk Kärnbränslehantering AB.

Polak A, Elsworth D, Liu J, Grader A, 2004. Spontaneous switching of permeability changes in a limestone fracture with net dissolution. Water Resources Research 40(W03502), pp 1–10.

Poteri A, Billaux D, Dershovitz W, Gómez-Hernández J J, Cvetkovic V, Hautojärvi A, Holton D, Medina A, Winberg A, 2002. Final report of the TRUE Block Scale project. 3. Modelling of flow and transport. Technical Report SKB TR-02-15, Svensk Kärnbränslehantering AB.

Prikryl J D, Jain A, Turner D R, Pabalan R T, 2001. Uranium(VI) sorption behaviour on silicate mineral mixtures. Journal of Contaminant Hydrology 47(2-4), pp 241–253.

Rabung T, Pierret M, Bauer A, Geckeis H, Bradbury M, Baeyens B, 2005. Sorption of Eu(III)/Cm(III) on Ca-montmorillonite and Na-illite. Part 1: Batch sorption and time resolved laser fluorescence spectroscopy experiments. Geochimica et Cosmochimica Acta 69(23), pp 5393–5402.

Rasmuson A, Neretnieks I, 1986. Radionuclide transport in fast channels in crystalline rock. Water Resources Research 22(8), pp 1247–1256.

Renard F, Gratier J-P, Ortoleva P, Brosse E, Bazin B, 1998. Self-organization during reactive fluid flow in a porous medium. Geophysical Research Letters 25(3), pp 385–388.

RETROCK, 2004. RETROCK Project. Treatment of geosphere retention phenomena in safety assessments. Scientific basis of retention processes and their implementation in safety assessment models (WP2) SKB R-04-48, Svensk Kärnbränslehantering AB.

Revil A, Glover P, 1997. Theory of ionic-surface electrical conduction in porous media. Physical Review B 55(3), pp 1757–1773.

Rhén I, Gustafson G, Stanfors R, Wikberg P, 1997. Äspö HRL – Geoscientific evaluation 1997/5. Models based on site characterization 1986-1995. SKB TR-97-06, Svensk Kärnbränslehantering AB.

Rhén I, Follin S, Hermanson J, 2003. Hydrogeological site descriptive model – a strategy for its development during site investigations. SKB R-03-08, Svensk Kärnbränslehantering AB.

Rhén I, Forsmark T, Hartley L, Jackson P, Roberts D, Swan D, Gylling B, 2008. Hydrogeological conceptualisation and parametrisation. Site descriptive modelling SDM-Site Laxemar. SKB R-08-78, Svensk Kärnbränslehantering AB.

Rhén I, Forsmark T, Hartley L, Joyce S, Roberts D, Gylling B, Marsic N, 2009. Bedrock hydrogeology: model testing and synthesis. Site descriptive modelling. SDM-Site Laxemar. SKB R-08-91, Svensk Kärnbränslehantering AB.

Rouhiainen P, Pöllänen J, Sokolnicki M, 2005. Oskarshamn site investigation. Difference flow logging of borehole KLX03. Subarea Laxemar. SKB P-05-67, Svensk Kärnbränslehantering AB.

Ruffet C, Darot M, Guéguen Y, 1993. Surface conductivity in rocks: A review. Surveys in Geophysics 16, pp 83–105.

Selnert E, Byegård J, Widestrand H, 2009a. Laboratory measurements within the site investigation programme for the transport properties of the rock. Final report. Oskarshamn site investigation. SKB P-07-179, Svensk Kärnbränslehantering AB.

Selnert E, Byegård J, Widestrand H, Carlsten S, Döse C, Tullborg E L, 2009b. Bedrock transport properties. Data evaluation and retardation model. Site descriptive modelling. SDM-Site Laxemar. SKB R-08-100, Svensk Kärnbränslehantering AB.

Serco Assurance, 2007. NAPSAC Release 9.5. Technical summary document. SA/ENV/CONNECTFLOW/12, Serco Ltd.

Shapiro A M, 2001. Effective matrix diffusion in kilometer-scale transport in fractured crystalline rock. Water Resources Research 37(3), pp 507–522.

Siitari-Kauppi M, 2002. Development of ^{14}C-polymethacrylate method for the characterisation of low porosity media. Ph.D. Thesis, Laboratory of Radiochemistry. University of Helsinki, Helsinki, Finland.

Singurindy O, Berkowitz B, Lowell R P, 2004. Carbonate dissolution and precipitation in coastal environments: Laboratory analysis and theoretical consideration. Water Resources Research 40(W04401), pp 1–12.

Skagius K, Neretnieks I, 1982. Diffusion in Crystalline Rocks of Some Sorbing and Nonsorbing Species. KBS Teknisk Rapport, 82-12. , Svensk Kärnbränsleförsörjning AB.

Skagius K, Neretnieks I, 1986. Diffusivity measurements and electrical resistivity measurements in rock samples under mechanical stress. Water Resources Research 22(4), pp 570–580.

SKB, 2004. Preliminary site description. Simpevarp area – version 1.1. SKB R-04-25, Svensk Kärnbränslehantering AB.

SKB, 2005. Preliminary site description. Simpevarp subarea – version 1.2. SKB R-05-08, Svensk Kärnbränslehantering AB.

SKB, 2006a. Geosphere process report for the safety assessment SR-Can. SKB TR-06-19, Svensk Kärnbränslehantering AB.

SKB, 2006b. Preliminary safety evaluation for the Laxemar subarea. Based on data and site descriptions after the initial site investigation stage. SKB TR-06-06, Svensk Kärnbränslehantering AB.

SKB, 2006c. Preliminary site description. Laxemar subarea – version 1.2. SKB R-06-10, Svensk Kärnbränslehantering AB.

SKB, 2007. FUD-program 2007. Program för forskning, utveckling och demonstration av metoder för hantering och slutförvaring av kärnavfall. Report SKB Art745, Svensk Kärnbränslehantering AB.

Slater L, 2007. Near surface electrical characterization of hydraulic conductivity: From petrophysical properties to aquifer geometries – A review. Surveys in Geophysics 28, pp 169–197.

SSI, 2005. Statens strålskyddsinstituts allmänna råd om tillämpning av föreskrifterna (SSI FS 1998:1) om skydd av människors hälsa och miljön vid slutligt omhändertagande av använt kärnbränsle och kärnavfall. SSI FS 2005:5, Statens strålskyddsintituts författningssamling.

Steefel C, Lasaga A, 1994. A coupled model for transport of multiple chemical species and kinetic precipitation/dissolution reactions with application to reactive flow in single phase hydrothermal systems. American Journal of Science 294, pp 529–592.

Stein D, Kruithof M, Dekker C, 2004. Surface-charge-governed ion transport in nanofluidic channels. Physical Review Letters 93(3), pp 1–4.

Stewart P S, 1998. A review of experimental measurements of effective diffusive permeabilities and effective diffusion coefficients in biofilms. Biotechnology and Bioengineering 59(3), pp 261–272.

Stober I, Bucher K, 2007. Hydraulic properties of the crystalline basement. Hydrogeology Journal 15(2), pp 213–224.

Stoessell R K, 1991. Effects of sulfate reduction on CaCO3 dissolution and precipitation in mixing-zone fluids. Journal of Sedimentary Petrology 62(5), pp 873–880.

Stumm W, Morgan J J, 1996. Aquatic Chemistry: Chemical equilibria and rates in natural waters. 3 ed. Wiley, New York.

Sundberg J, Wrafter J, Back P-E, Rosén L, 2008. Thermal properties Laxemar. Site descriptive modelling. SDM-Site Laxemar. SKB R-08-61, Svensk Kärnbränslehantering AB.

Svensson T, Ludvigson J-E, Walger E, Thur P, Gokall-Norman K, Wass E, 2008. Oskarshamn site investigation. Combined hydraulic interference- and tracer test in HLX33, SSM000228, and SSM000229. SKB P-07-187, Svensk Kärnbränslehantering AB.

Terzaghi R, 1965. Sources of error in joint surveys. Geotechnique 15(3), pp 287–304.

Thunehed H, 2005a. Resistivity measurements and determination of formation factors on samples from KLX04 and KSH02. Oskarshamn site investigation. SKB P-05-75, Svensk Kärnbränslehantering AB.

Thunehed H, 2005b. Resistivity measurements on samples from KLX02. Oskarshamn site investigation. SKB P-05-19, Svensk Kärnbränslehantering AB.

Thunehed H, 2007a. Complementary resistivity measurements on samples from KLX03, KLX04, KLX05, KLX10, KLX12A and KLX13A. Oskarshamn site investigation. SKB P-07-203, Svensk Kärnbränslehantering AB.

Thunehed H, 2007b. Forsmark site investigation. Resistivity measurements on samples from KFM01A, KFM01B, KFM02A, KFM06A, KFM08A, KFM08C, and KFM09A. SKB P-07-51, Svensk Kärnbränslehantering AB.

Thunehed H, 2007c. Resistivity measurements on samples from KSH01, KSH02, KLX02, KLX04 and KLX11A. Oskarshamn site investigation. SKB P-06-289, Svensk Kärnbränslehantering AB.

Thur P, Gustafsson E, 2007. Groundwater flow measurements in borehole KLX21B. Oskarshamn site investigation. SKB P-07-199, Svensk Kärnbränslehantering AB.

Thur P, Nordqvist R, Gustafsson E, 2007a. Oskarshamn site investigation. Groundwater flow measurements and SWIW test in borehole KLX11A. SKB P-07-180, Svensk Kärnbränslehantering AB.

Thur P, Nordqvist R, Gustafsson E, 2007b. Oskarshamn site investigation. Groundwater flow measurements and SWIW test in borehole KLX18A . SKB P-06-287, Svensk Kärnbränslehantering AB.

Thur P, 2008. Groundwater flow measurements in permanently installed boreholes. Test campaign no. 3 2007. Oskarshamn site investigation. SKB P-08-31, Svensk Kärnbränslehantering AB.

Torstenfelt B, Ittner T, Allard B, Andersson K, Olofsson U, 1982. Mobilities of radionuclides in fresh and fractured crystalline rock. Technical Report SKB TR-82-26, Svensk Kärnbränslehantering AB.

Triumf C-A, 2007. Oskarshamn site investigation. Assessment of possible dolerite dykes in the Laxemar subarea from magnetic total field data and digital elevation models. SKB P-07-223, Svensk Kärnbränslehantering AB.

Tsang Y W, 1992. Usage of "equivalent apertures" for rock fractures as derived from hydraulic and tracer tests. Water Resources Research 28(5), pp 1451–1455.

Tsang C-F, Doughty C, 2007. Some insights from simulations of SWIW tests on a complex fracture. Technical Report SKI-INSITE TRD-07-06, Strålsäkerhetsmyndigheten (SSM).

Turner D, Pabalan R, 1999. Abstraction of mechanistic sorption model results for performance assessment calculations at Yucca Mountain, Nevada. Waste Management 19(6), pp 375–388.

Uchida M, Doe T, Dershovitz W, Andrev T, Wallmann P, Sawada A, 1994. Discrete fracture modeling of the Äspö LPT-2, large scale pumping and tracer test. SKB ICR-94-09, Svensk Kärnbränslehantering AB.

Vahlund F, Hermansson H, 2004. A direct numerical approach to solving the transport equations for radionuclide transport in fractured rock. SKB R-04-50, Svensk Kärnbränslehantering AB.

Valkiainen M, Aalto H, Lehikoinen J, Uusheimo K, 1996. The effect of thickness in through diffusion experiments. VTT Research notes 1788. ISBN 951-38-4983-X. Technical Research Center of Finland.

Verberg R, Ladd A, 2002. Simulation of chemical erosion in rough fractures. Physical Review E 65(056311), pp 1–6.

Vilks P, Caron F, Haas M, 1998. Potential for the formation and migration of colloidal material from a near-surface waste disposal site. Applied Geochemistry 13, pp 31–42.

Vilks P, Cramer J J, Jensen M, Miller N H, Miller H G, Stanchell F W, 2003. In situ diffusion experiment in granite: Phase I. Journal of Contaminant Hydrology 61(1-4), pp 191–202.

Vilks P, Miller N H, Stanchell F W, 2004. Phase II in situ diffusion experiment. 06819-REP-01200-10128-R00, Atomic Energy of Canada Limited (AECL). Ontario Power Generation, Nuclear Waste Management Division. Toronto, Ontario, Canada.

Vilks P, 2007. Oskarshamn site investigation. Rock matrix permeability measurements on core samples from borehole KLX03. SKB P-07-204, Svensk Kärnbränslehantering AB.

Viola G, Venvik Ganerod G, 2007. Oskarshamn site investigation. Structural analysis of brittle deformation zones in the Simpevarp-Laxemar area, Oskarshamn, southeast Sweden. SKB P-07-41, Svensk Kärnbränslehantering AB.

Voss C I, Provost A M, 2002. SUTRA. A model for saturated-unsaturated, variable-density groundwater flow with solute or energy transport. Water-Resources Investigation Report 02-4231, U.S. Geological Survey, Reston, Va.

Waber H N, Smellie J A T, 2004. Oskarshamn site investigations Borehole KSH02: Characterisation of matrix pore water (Feasibility Study). SKB P-04-249, Svensk Kärnbränslehantering AB.

Waber H N, Smellie J A T, 2006a. Oskarshamn site investigation. Borehole KLX03: Characterisation of pore water. Part 1: Methodology and analytical data. SKB P-06-12, Svensk Kärnbränslehantering AB.

Waber H N, Smellie J A T, 2006b. Oskarshamn site investigation. Borehole KLX03: Characterisation of pore water. Part 2: Rock properties and diffusion experiments. SKB P-06-77, Svensk Kärnbränslehantering AB.

Waber H N, Smellie J A T, 2006c. Oskarshamn site investigation. Borehole KLX08: Characterisation of pore water. Part 1: Methodology and analytical data. SKB P-06-163, Svensk Kärnbränslehantering AB.

Waber H N, Smellie J A T, 2007. Forsmark site investigation. Boreholes KFM01D, KFM08C, KFM09B. Characterisation of pore water. Part 1 Diffusion experiments and pore-water data. SKB P-07-119, Svensk Kärnbränslehantering AB.

Waber H N, Smellie J A T, 2008. Oskarshamn site investigation. Borehole KLX17A: Characterisation of pore water. Part 1: Methodology and analytical data. SKB P-08-43, Svensk Kärnbränslehantering AB.

Waber H N, Gimmi T, Smellie J A T, de Haller A, 2009. Porewater in the rock matrix. Site descriptive modelling. SDM-Site Laxemar. SKB R-08-112, Svensk Kärnbränslehantering AB.

Wahlgren C-H, Curtis P, Hermanson J, Forssberg O, Öhman J, Fox A, La Pointe P, Drake H, Triumf C-A, Mattson H, Tunehed H, Juhlin C, 2008. Geology Laxemar. Site descriptive modelling SDM-Site Laxemar. SKB R-08-54, Svensk Kärnbränslehantering AB.

Widestrand H, Byegård J, Ohlsson Y, Tullborg E L, 2003. Strategy for the use of laboratory methods in the site investigations programme for the transport properties of the rock. SKB R-03-20, Svensk Kärnbränslehantering AB.

Widestrand H, 2009. Äspö Hard Rock Laboratory, Long Term Sorption Diffusion Experiment (LTDE-SD), Supporting laboratory program – Sorption diffusion experiments and rock material characterisation. International Progress Report SKB IPR-09-08, Svensk Kärnbränslehantering AB.

Winberg A, Andersson P, Hermanson J, Byegård J, Cvetkovic V, Birgersson L, 2000. Äspö hard rock laboratory. Final report of the first stage of the tracer retention understanding experiments. Technical Report SKB TR-00-07, Svensk Kärnbränslehantering AB.

Yasuhara H, Elsworth D, Polak A, Liu J, Grader A, Halleck P, 2006. Spontaneous switching between permeability enhancement and degradation in fractures in carbonate: Lumped parameter representation of mechanically- and chemically-mediated dissolution. Transport in Porous Media 65, pp 385–409.

Zhang S, Tullis T E, 1998. The effect of fault slip on permeability and permeability anisotrophy in quartz gouge. Tectonophysics 295(1-2), pp 41–52.

Zhang S, Tullis T E, Scruggs V J, 1999. Permeability anisotrophy and pressure dependency of permeability in experimentally sheared gouge materials. Journal of Structural Geology 21(7), pp 795–806.

Zhou Q, Liu H, Molz F, Zhang Y, Bodvarsson G, 2005. Field-scale effective matrix diffusion coefficient for fractured rock: results from literature survey. Report LBLNL-57368, Lawrence Berkeley National Laboratory (LBL), Berkeley, CA.

Appendix A

On the F-factor, advective travel times, and salt transport

Author: James Crawford

Definition of the F-factor and its estimation

The F-factor can be defined in a number of ways which are interchangeable according to the basic definitions of hydraulic parameters characterising the system. In its most intuitive, although not necessarily most generalised, form the F-factor is defined as the ratio of flow-wetted surface and flowrate. For a single, isolated flow channel featuring homogeneous flow, this can be shown to be equal to twice the product of flowpath width, W_c (m) and length, L_p (m) divided by the flowrate, Q (m³/s):

$$F = \frac{2W_c L_p}{Q} \qquad \text{(Eq. A-1)}$$

In the more general case of a spatially variable flow field hosted in a fracture one might instead choose to consider a flow "packet" or "particle" of constant volume following a streamline (equivalent to a particle in a particle tracking calculation) as illustrated schematically in Figure A-1.

For a fluid particle representing a flow sub-element of constant volume, the analogous equation for flow through a variable cross-sectional area containing that flow could be written as:

$$F = \frac{2}{q}\int_0^{L_p} w(s)\,ds \qquad \text{(Eq. A-2)}$$

Where $w(s)$ is the local width (m) of the flow streamline following a trajectory, $s = f(x, y)$ through the advective pore space and q (m³/s) is the constant flowrate following the traced streamline. This equation also holds for a discrete flow channel of variable physical cross-section. For a discrete fracture network (DFN) simulation, however, a more convenient formulation is obtained using:

$$F = 2\int_0^{L_p} \frac{ds}{v(s)\delta_t(s)} \qquad \text{(Eq. A-3)}$$

Where $v(s)$ and $\delta_t(s)$ represent respectively, the local fluid velocity (m/s) and transport aperture (m) encountered along a particle trajectory. In this formulation, the local fluid velocity is a "true" velocity averaged over the flowpath aperture and should not be confused with the Darcy flux.

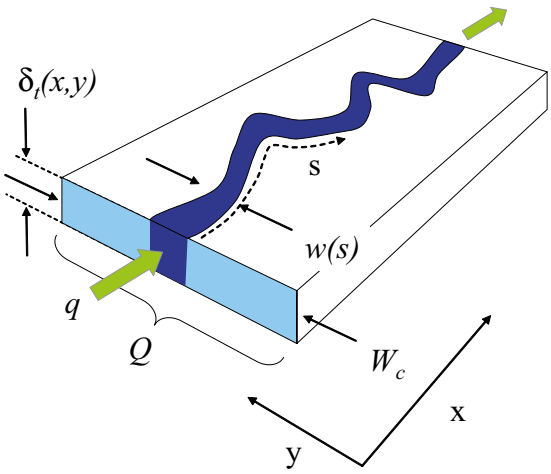

Figure A-1. *Illustration of a flow field hosted within an open or partially open fracture. Here, the F-factor can be defined for a particle representing a constant volume of fluid following a flow streamline (the dark blue band in the centre of the flow field) where the trajectory of the particle is represented by the path length variable s(x,y).*

Equation A-3 is often used in DFN-based particle tracking calculations since the F-factor can be simply integrated along a flow streamline in terms of the local fluid velocity and transport aperture. It is a somewhat more practical approach than Equation A-2 since the width of the flow channel or pathline element does not need to be considered explicitly – a useful simplification when making calculations involving a spatially heterogeneous flow field.

Although Equation A-3 is arguably the most generalised definition of the F-factor, it is not necessarily the most intuitive as it appears at face value to contain a strong dependency on the inverse of the transport aperture. The local fluid velocity, however, is equal to the flowrate divided by cross-sectional area and is, by definition, also inversely proportional to the transport aperture for a given flowrate:

$$v(s) = \frac{q}{w(s)\delta_t(s)} \qquad \text{(Eq. A-4)}$$

When taking the product of flow velocity and transport aperture, the direct transport aperture dependency cancels out and Equation A-3 can be shown to be equivalent to Equation A-2 for a predetermined flowrate:

$$F = 2\int_0^{L_p} \frac{ds}{v(s)\delta_t(s)} = 2\int_0^{L_p} \frac{ds}{\left(\frac{q}{w(s)\delta_t(s)}\right)\delta_t(s)} = \frac{2}{q}\int_0^{L_p} w(s)\,ds \qquad \text{(Eq. A-5)}$$

In a practical sense this means that the same F-factor should be obtained regardless of which transport aperture is assumed in the calculation provided the flow field, via the transmissivity distribution, is regarded as a primitive. In DFN simulations, the transmissivity field is usually assigned without any direct reference to fracture transport apertures. The transmissivity field together with an appropriate boundary condition is all the information necessary to establish both the potential field and flow solution to the hydrologic problem.

The term transport aperture used here is defined in the sense of "mass balance aperture" as defined by /Tsang 1992/ and is not necessarily the same as various definitions of effective hydraulic aperture for heterogeneous flow spaces which, being macroscopic parameters, are to some extent scale dependent. Both the effective hydraulic aperture and transport aperture are considered to be different measures than the local physical aperture of a flowing feature (however this is defined).

Although at very small scales one might expect a functional relation between flowrate and physical aperture by way of the local cubic law, on larger macroscopic length scales there is no strict requirement for this to be the case and the effective hydraulic aperture does not necessarily correlate simply with the transport aperture. It is easy to imagine situations where such a relation might not apply; for example: flow pinch points, particulate filled flowspaces, calcite erosion pipes, etc. On macroscopic scales there appears to be some empirical support for a quadratic or near quadratic relation between estimated transmissivities of flowing features and transport aperture as determined by inverse modelling of tracer tests. It is noted, however, that this is only verifiable in a statistical sense and the absolute value of the transport aperture, as distinct from its functional relation to transmissivity, varies greatly between different investigations.

Since the transmissivity does not need to be related to transport aperture in a simple fashion, it is therefore not unreasonable to regard the flow field (which is directly observable in boreholes) as a primitive and consider transport aperture independently of assigned hydraulic properties. The extent to which the transport aperture then affects the outcome of F-factor calculations therefore depends upon whether one starts with a description of flow and derives transport apertures consistent with those flows (by way of the transmissivity distribution) or whether one starts with a specification of transport apertures and derives transmissivities (and consequently flows) consistent with the aperture distribution. In the SDM-Site for both Laxemar and Forsmark, the spatial distributions of flow anomalies and flow magnitudes (measured using the PFL method) are used directly to condition the properties of the Hydrogeological DFN.

These discussions can also be extended to the porous medium case in a straight-forward manner. The F-factor for transport within a porous medium is given by the product of the flowpath volume and specific flow-wetted surface, divided by the flowrate:

$$F = \frac{V_p a_R}{Q} = \frac{L_p A_{xs} a_R}{Q} \quad \text{(Eq. A-6)}$$

Where V_p (m^3) is the volume of the advective pore space, a_R (m^2/m^3) is the specific flow-wetted surface, and A_{xs} (m^2) is the cross-sectional area of the streamtube. If one considers a streamtube (representing a particle trajectory) with a spatially variable cross-sectional area and specific flow-wetted surface, the F-factor must be integrated along a pathline:

$$F = \frac{1}{q}\int_0^{L_p} A_{xs}(s) a_R(s) ds \quad \text{(Eq. A-7)}$$

Since the flowrate divided by the cross-sectional area for flow is equal to the Darcy flux u (m^3/m^2s), Equation A-7 can be given as:

$$F = \int_0^{L_p} \frac{a_R(s)}{u(s)} ds \quad \text{(Eq. A-8)}$$

The Darcy flux and true fluid velocity are related by way of the kinematic porosity, θ_f (m^3/m^3):

$$u(s) = v(s)\theta_f(s) \quad \text{(Eq. A-9)}$$

In a similar fashion, the specific flow-wetted surface and transport aperture are related by the flow porosity:

$$a_R(s) = 2\theta_f(s)/\delta_t(s) \quad \text{(Eq. A-10)}$$

Substituting Equations A-9 and A-10 into A-8 gives:

$$F = \int_0^{L_p} \frac{\theta_f(s)/\delta_t(s)}{v(s)\theta_f(s)} ds = 2\int_0^{L_p} \frac{ds}{v(s)\delta_t(s)} \quad \text{(Eq. A-11)}$$

As can be seen by comparing Equation A-11 with A-3, in principle it should make no difference whether the particle tracking problem is formulated within a DFN or ECPM framework provided the parameter values used in the simulations are mutually consistent with the above definitions.

The main difference between F-factors calculated by particle tracking in a fully resolved Hydrogeological DFN and that in an ECPM relates to the averaging effect of upscaling. An ECPM representation, for example, typically considers upscaled block elements considerably larger than the individual fractures comprising the block (noting that the ensemble properties of the hydraulically connected fractures are used to derive the permeability tensor for the block). Since the spatially averaged flow within a block is assumed to contact the available flow wetted surface in an uncorrelated manner, the path integrated F-factor may be different to that obtained using a direct DFN approach where individual fractures are considered explicitly in higher spatial resolution. While the F-factors calculated for particle transport through a block in an ECPM model should be adequate for representing the "average" properties of the participating flow bearing fractures, information is lost concerning fast and slow flowpaths deviating from the block averages.

Definition of the advective travel time and its estimation

The advective travel time for a single flow channel of a specified width, length and transport aperture is given by the ratio of flowpath volume and flowrate:

$$t_w = \frac{W_c L_p \delta_t}{Q} \quad \text{(Eq. A-12)}$$

For a fluid particle transported within a heterogeneous flow field hosted in a fracture, one could then write:

$$t_w = \frac{1}{q}\int_0^{L_p} w(s)\delta_t(s) ds \quad \text{(Eq. A-13)}$$

In a Hydrogeological DFN calculation, however, it is easier to use the relation:

$$t_w = \int_0^{L_p} \frac{ds}{v(s)} \qquad \text{(Eq. A-14)}$$

For a porous medium, the advective travel time is given by:

$$t_w = \frac{V_p \theta_f}{Q} \qquad \text{(Eq. A-15)}$$

For a streamtube with spatially variable streamtube cross-sectional area and kinematic porosity (i.e. representing a particle trajectory in an ECPM calculation), the advective travel time is given by the analogous pathline integrated ratio of kinematic porosity and Darcy flux:

$$t_w = \frac{1}{q}\int_0^{L_p} A_{xs}(s)\theta_f(s)ds = \int_0^{L_p} \frac{\theta_f(s)}{u(s)}ds = \int_0^{L_p} \frac{ds}{v(s)} \qquad \text{(Eq. A-16)}$$

As can be seen from the form of Equation A-14 and A-16, uncertainty concerning the transport aperture has a direct impact upon the advective travel time by way of the fluid velocity which, as has been shown previously, is inversely proportional to transport aperture. Here as well, one would expect the advective travel times calculated using the DFN and ECPM approaches to be identical, in principle, provided the parameter values used in the simulations are mutually consistent as discussed previously.

The flowpath integrated, average transport aperture ($\overline{\delta}_t$) for a pathline can be calculated as:

$$\overline{\delta}_t = \frac{\int_0^{L_p} w(s)\delta_t(s)ds}{\int_0^{L_p} w(s)ds} = \frac{2}{F}\int_0^{L_p} w(s)\delta_t(s)ds = \frac{2}{F}t_w \qquad \text{(Eq. A-17)}$$

Or, by rearranging this expression the advective travel time can be given in terms of the F-factor and average transport half-aperture:

$$t_w = \frac{\overline{\delta}_t}{2}F \qquad \text{(Eq. A-18)}$$

Owing to the mutual equivalence of expressions derived for the F-factor and advective travel time (as established above), it is relatively easy to show that Equation A-18 is also valid for the ECPM case. Here, however, the flowpath integrated average transport aperture is given by the expression:

$$\overline{\delta}_t = \frac{2\int_0^{L_p} \frac{\theta_f(s)}{u(s)}ds}{\int_0^{L_p} \frac{a_R(s)}{u(s)}ds} = \frac{2}{F}t_w \qquad \text{(Eq. A-19)}$$

The impact of uncertain transport aperture and advective transport time on salt transport.

In complex 3-dimensional hydrogeological simulations involving density driven flow, it is often difficult to reconcile model predictions of salt transport with simple notions of transport and matrix retardation along a single flowpath. Owing to heterogeneity in the transmissivity of the bedrock and complex regional and local topographic boundary conditions, the flow-related transport properties of groundwater recharge pathways vary considerably. Certain hydrodynamic controls on the transport of environmental tracers (e.g. chloride concentrations, hydrogen and oxygen isotopes, etc.) may dominate along one recharge pathline, while a short distance away, completely different conditions might exist. Pathlines associated with one recharge-discharge flowpath might be short and exhibit very low F-factors and short advective travel times, whereas others may be very long and exhibit very high F-factors and long advective travel times as conceptually illustrated in Figure A-2.

To properly explain the transport of salt in the palaeo-hydrochemical simulations it is important to consider how uncertain transport apertures might impact on the distribution of salt in the system while simultaneously recognising the diversity of hydrodynamic conditions characterising individual transport pathways.

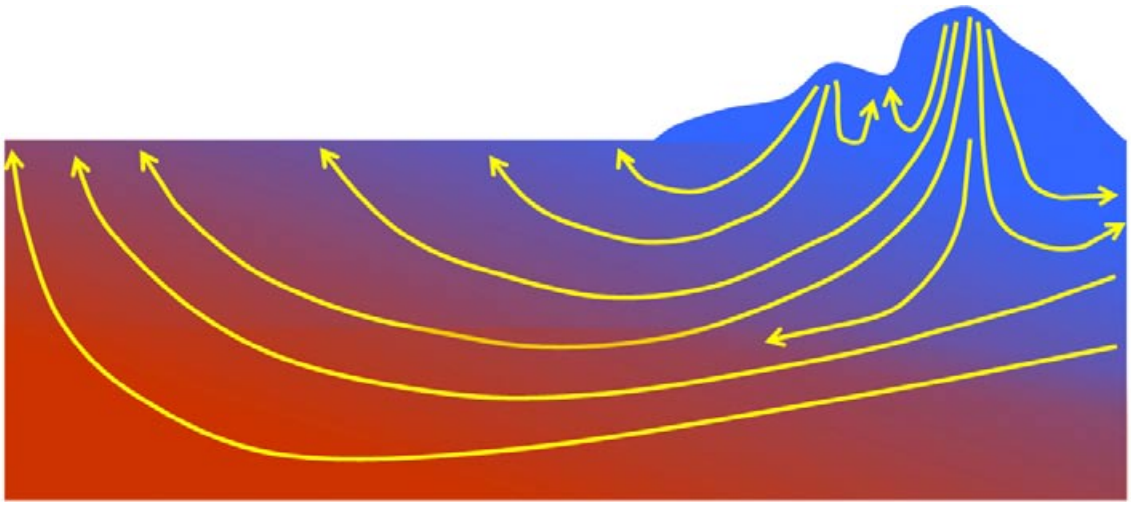

Figure A-2. *Conceptual illustration of hypothetical groundwater recharge pathlines driven by local and regional topographical boundary conditions. The red background shading represents saline water initially present in the system slowly being displaced by the infiltrating meteoric water (blue shading). Heterogeneity of the bedrock hydrological properties coupled with complex boundary conditions give strong variations in typical path lengths and characteristic F-factors thereby influencing hydrodynamic controls on solute transport.*

If one were to consider a single recharge pathway, the travel time for an infiltrating solute can be broken down into contributions from several sub-processes. If sorption on fracture coatings lining the transport path is neglected, the travel time is given by /Löfgren et al. 2007/ as:

$$\begin{pmatrix}\text{total}\\ \text{travel}\\ \text{time, } t\end{pmatrix} = \begin{pmatrix}\text{advective}\\ \text{travel}\\ \text{time, } t_w\end{pmatrix} + \begin{pmatrix}\text{residence time due to diffusion}\\ \text{and sorption/storage in the rock}\\ \text{matrix, } t_m\end{pmatrix} \qquad \text{(Eq. A-20)}$$

If an effectively infinite rock matrix is assumed on the timescale of transport, the analytical solution given by /Neretnieks 1980/ can be rearranged to give Equation A-20 in the form:

$$t = t_w + \frac{D_e\left(\theta_m + K_{dm}\rho_{bm}\right)}{4\left(\text{erfc}^{-1}\left(C/C_0\right)\right)^2}F^2 \qquad \text{(Eq. A-21)}$$

Here, D_e (m^2/s) is the effective diffusivity, θ_m (m^3/m^3) is the matrix porosity, K_{dm} (m^3/kg) is the sorption partitioning ratio, and ρ_{bm} (kg/m^3) is the bulk density of the rock. The concentration ratio, C/C_0 corresponds to a mixing fraction which, in the present analysis, is taken to be the fraction of meteoric water at a given location relative to the fraction at the recharge inlet ($C_0 = 1$). Although environmental tracers such as chloride and water with variable proportions of hydrogen and oxygen isotopes are not normally considered to be sorbing species, it is still necessary to account for the storage of these solutes in the water-filled connected porosity of the rock matrix. Since the advective travel time is given by the product of the flowpath F-factor and transport half-aperture, it is possible to write for a non-sorbing solute:

$$t = \frac{\delta_t}{2}F + \frac{D_e\theta_m}{4\left(\text{erfc}^{-1}\left(C/C_0\right)\right)^2}F^2 \qquad \text{(Eq. A-22)}$$

Transport of salt (here assumed to be NaCl) is slightly more complex since it is actually a 2-component tracer consisting of equimolar quantities of anions (Cl^-) and cations (Na^+). In order to estimate the free diffusivity of the binary mixture, one must consider the mutual electrostatic effects of the diffusing ions of opposite charge. For a simple monovalent ion-pair such as Na^+/Cl^-, the free diffusivity can be shown to be equal to the harmonic mean of the individual components /Nernst 1888/:

$$D_w^{NaCl} = \frac{2\,D_w^{Na^+}D_w^{Cl^-}}{\left(D_w^{Na^+} + D_w^{Cl^-}\right)} \approx 1.6\times10^{-9}\,\text{m}^2/\text{s}\ \ (25°\text{C}) \qquad \text{(Eq. A-23)}$$

At temperatures other than 25ºC, the diffusivity needs to be corrected for intrinsic and viscous temperature effects using the Stokes-Einstein relation /Li and Gregory 1974/:

$$D_w(T) = D_w(T_0) \times \left(\frac{\mu_w^T}{\mu_w^{T_0}} \right) \times \left(\frac{T}{T_0} \right) \qquad \text{(Eq. A-24)}$$

Where T *(K)* is absolute temperature in Kelvin and μ_w (Pa.s) is the viscosity of water at the reference (T_0) and actual temperature (T), respectively. Assuming an in situ average temperature of 12ºC would thereby give a free diffusivity reduced by a factor 0.7 relative to the value at 25ºC.

The situation is further complicated by the possible effects of anion exclusion within the tight pore spaces of the rock matrix (which reduces the effective diffusivity and storage of Cl^-) as well as cation-exchange on mineral surfaces and possibly also surface diffusion in the electrical double layer (which might also have an influence on the effective diffusivity and apparent storage of Na^+). Since the combined impact of these effects has not been adequately studied in granitic rock, they are usually neglected. The storage capacity is therefore assumed to be the same as the water saturation porosity of the rock and the effective diffusivity of salt is assumed to be equal to the free diffusivity of the binary salt mixture multiplied by the estimated geometric formation factor of the rock (see Appendix D).

$$D_e = F_f D_w \qquad \text{(Eq. A-25)}$$

When meteoric water infiltrates fractured bedrock initially equilibrated with saline water, a mixing front is established that propagates along the recharge pathline over time. Since the propagation of the mixing front is retarded by matrix diffusion, Equation A-22 can be used to predict the transport time for the mixing front midpoint (here taken to be the time where the water discharged at the end of a pathline is diluted to a 50% mix of meteoric and saline water). The mixing front breakthrough time calculated in this manner is shown in Figure A-3 assuming the same storage porosity (θ_m = 0.008) and effective diffusivity ($D_e = 1.5\times10^{-13}$ m²/s) as used in the palaeo-hydrogeological simulations described in /Rhén et al. 2009/.

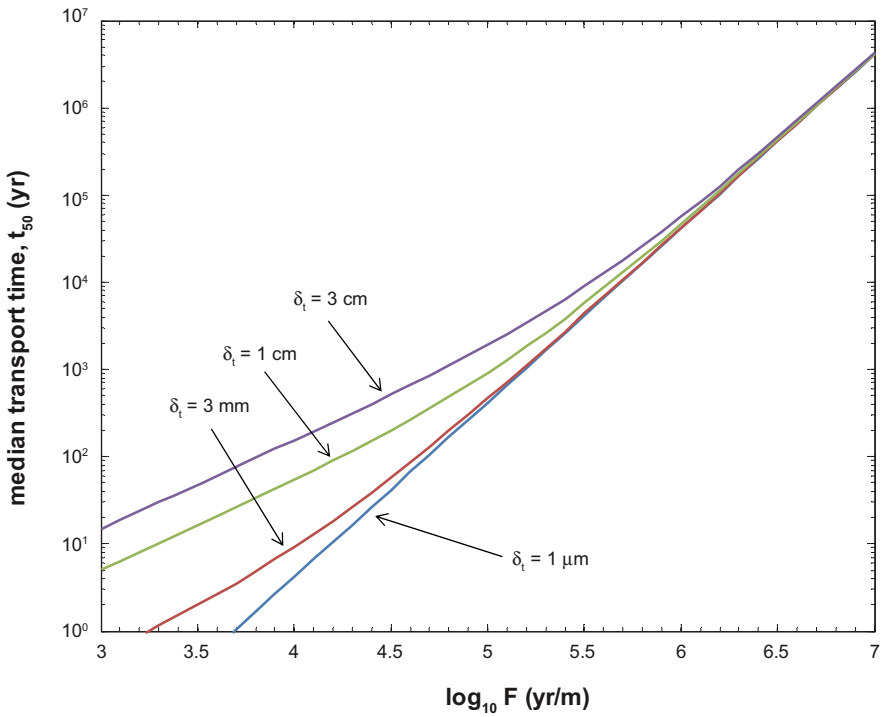

Figure A-3. *Median transport time, t_{50} (yr) versus F-factor (yr/m) for breakthrough of the mixing front for meteoric water infiltrating into a system initially equilibrated with saline water. Curves are given for four different transport apertures as indicated in the figure.*

As can be seen from Figure A-3, the uncertain transport aperture has the largest impact for those flow paths where the F-factor is lowest. The lowermost curve (δ_t = 1 μm) is taken to be a limiting case since the advective travel time has very little impact on the overall transport time for transport apertures of this size or smaller. The curves for transport apertures of 3 mm, 1 cm, and 3 cm cover the range of estimated transport apertures implied by the kinematic porosities used in the palaeo-hydrogeological simulations involving salt transport. These transport apertures are larger than what would normally be encountered in fractured bedrock. The reason for this is that the kinematic porosity used in the palaeosimulations includes fractures smaller than the 5.6 m cut-off used for determining the hydrogeological properties. The rationale behind this is described in more detail in /Rhén et al. 2009/ although is based upon the fact that only the larger fractures will contribute in a meaningful way to the transmissivity of the rock and the overall flow, whereas smaller fractures can still be expected to contribute noticeably towards the advective volume of the system. These apparent transport apertures should therefore not be interpreted as "true" fracture apertures, but rather as twice the ratio of the advective volume and flow-wetted surface in the system.

The overall transport times associated with recharge flowpaths for F-factors much less than 10^5 yr/m are sufficiently low that any impact that the transport aperture makes on the travel time will be barely noticeable over a 10 ka palaeosimulation time span. In a practical sense this means that flushing of salt from such flowpaths occurs very quickly relative to the timescale of the simulation and the additional delay introduced by a large transport aperture will not make much of a difference to this process. For recharge flowpaths featuring very high F-factors (say, F ~ 10^6 yr/m), on the other hand, the retardation of the mixing front is sufficiently strong that the transport aperture should also make very little difference to the distribution of salt along the flowpath at 10 ka. In these cases the matrix retention time is sufficiently long that advective travel time is negligible in comparison. From Figure A-3 it would appear that it is only in a very narrow range of F-factors (say, F ~ 10^5–10^6 yr/m) that the transport aperture will have a noticeable impact on the distribution of salt at 10 ka.

These are flowpaths where the F-factor is such that one would expect the saline content of the flowpath to be displaced approximately on the timescale of the palaeosimulations. The existence of a large transport aperture, however, gives an advective transport time sufficiently large (several thousand years, or more) that the flushing of salt and breakthrough of meteoric water is delayed by a noticeable amount.

It could be contended that the argumentation applied above to the impact of transport aperture does not strictly apply to situations where a rock matrix of limited extent becomes saturated. In this case, equilibrium transport conditions would apply and retardation of salt transport can then be described in terms of a retardation factor describing the delay of solute transport relative to the advective travel time. The extent to which this is true, however, depends on the magnitude of the storage capacity in the rock matrix relative to that in the advective pore space. In the case of equilibrium salt transport, the retarded travel time is given by:

$$t = R_a t_w = \left(1 + \frac{2\theta_m \delta_m}{\delta_t}\right)\frac{\delta_t}{2} F = \frac{\delta_t}{2} F + \theta_m \delta_m F \qquad \text{(Eq. A-26)}$$

In this case, the accessible volume of the rock matrix (matrix storage capacity) is given by the parameter group $2\theta_m\delta_m$ (where δ_m is the depth of rock matrix) and the storage capacity in the advective pore space is δ_t. If the matrix storage capacity is much larger than the advective storage capacity, then the transport aperture makes very little difference to the travel time which is then proportional to the F-factor and matrix storage capacity (i.e. by way of the second term on the right-hand side of Equation A-26 when $2\theta_m\delta_m \ll \delta_t$).

Although this simple analysis gives some clues as to the impact of transport aperture and F-factor in the palaeosimulations, it is also important to consider how the F-factor might influence the apparent width of the mixing front as it progresses along a recharge pathline. Once again, returning to the analytical solution given by /Neretnieks 1980/, it is possible to write:

$$\frac{C}{C_0} = \operatorname{erfc}\left(\frac{F_L x}{2L_p}\sqrt{\frac{D_e\theta_m}{t - t_w(x)}}\right) \qquad \text{(Eq. A-27)}$$

Where, F_L is the F-factor for an entire flowpath of length L_p, the variable x is some distance along that path, and $t_w(x)$ is the advective travel time taken to reach point x. This can be rearranged to give x explicitly in terms of the concentration mixing fraction (i.e. C/C_0):

$$x = \frac{2}{F_L}\sqrt{\frac{t - t_w(x)}{D_e\theta_m}} \cdot \mathrm{erfc}^{-1}\left(C/C_0\right) \qquad \text{(Eq. A-28)}$$

If the characteristic width of the diffusive mixing front is taken to be the distance between the 10% and 90% concentration mixing fractions, the width of the front relative to the mean location of the mixing front (i.e. the location where the mixing fraction is exactly 50%) can be given as:

$$\frac{\Delta x_{10\text{ to }90}}{x_{50}} = \frac{\sqrt{t - t_w\left(x_{0.1}\right)} \cdot \mathrm{erfc}^{-1}\left(0.1\right) - \sqrt{t - t_w\left(x_{0.9}\right)} \cdot \mathrm{erfc}^{-1}\left(0.9\right)}{\sqrt{t - t_w\left(x_{0.5}\right)} \cdot \mathrm{erfc}^{-1}\left(0.5\right)} \qquad \text{(Eq. A-29)}$$

If the advective travel time, $t_w(x)$ is much less than the time of interest as is the case for realistic transport apertures and sufficiently large F-factors, the relative width of the mixing front given by Equation A-29 can be simplified to:

$$\frac{\Delta x_{10\text{ to }90}}{x_{50}} = \frac{\mathrm{erfc}^{-1}\left(0.1\right) - \mathrm{erfc}^{-1}\left(0.9\right)}{\mathrm{erfc}^{-1}\left(0.5\right)} \approx 2.25 \qquad \text{(Eq. A-30)}$$

This means that the relative width of the mixing front is constant as it passes a given location along the flowpath regardless of the overall path F-factor (F_L). The absolute width of the mixing front, however, increases with the square root of time and is proportional to the mixing front penetration depth along the pathline (i.e. x_{50}) as can be appreciated by consideration of Equation A-28 and A-30 together. This means that the mixing front increases in width as it progresses downstream along a recharge path, although its location at any given time, t is proportional to the square root of t and inversely proportional to F_L.

A large F-factor, for example, implies such a large retardation effect that the mixing front may not penetrate very far along the recharge pathline during the palaeosimulation time. This would give a transition from fresh to saline conditions over a relatively short distance. An intermediate range of F-factors, on the other hand, would allow a greater mixing front penetration depth with a mixing front width proportional to this greater distance.

A very low F-factor would give such a small matrix retardation effect as to be negligible and then only the advective travel time influences the transport of salt which is then flushed in an essentially plug-flow manner. It is therefore possible to predict that both very small and very large F-factors result in narrow mixing front widths, while intermediate ranges of F-factors give extended and diffuse mixing fronts if these are compared at exactly the same point in time. If at the conclusion of the palaeosimulations, the mixing front has progressed to approximately half way along the recharge path then the mixing front will, in effect, be larger than the path itself. This is further complicated by rock matrix saturation effects outlined previously which can reduce the retardation effect of matrix diffusion relative to the case of infinite diffusion depth.

On the time scale of an interglacial period, longitudinal molecular diffusion could also have an influence on solute spreading and induce further dispersion in the mixing front width. Furthermore, the mixing front penetration depth along a flowpath ($x_{0.5}$) is sufficiently strongly affected by the F-factor that any non-trivial difference in F-factors between adjacent flowpaths can give very large differences in mixing front propagation distances unless these flowpaths are connected and undergo mixing. When averaging across a larger control volume, the difference between individual pathlines (or streamtubes) making up the flowpath ensemble would give additional dispersion in the apparent width of the halocline.

To fully appreciate the impact of uncertain transport aperture together with limited maximum matrix penetration depths, it is necessary to make numerical calculations for different combinations of F-factors, transport aperture, and matrix penetration depths. Two sets of characteristic curves are useful to consider in this respect: one is the evolution of saline concentration at a downstream check-point at some elevation in the model, while the other is the salt profile along the length of a recharge pathway at a fixed moment in time. The main conceptual differences between these are illustrated in Figure A-4.

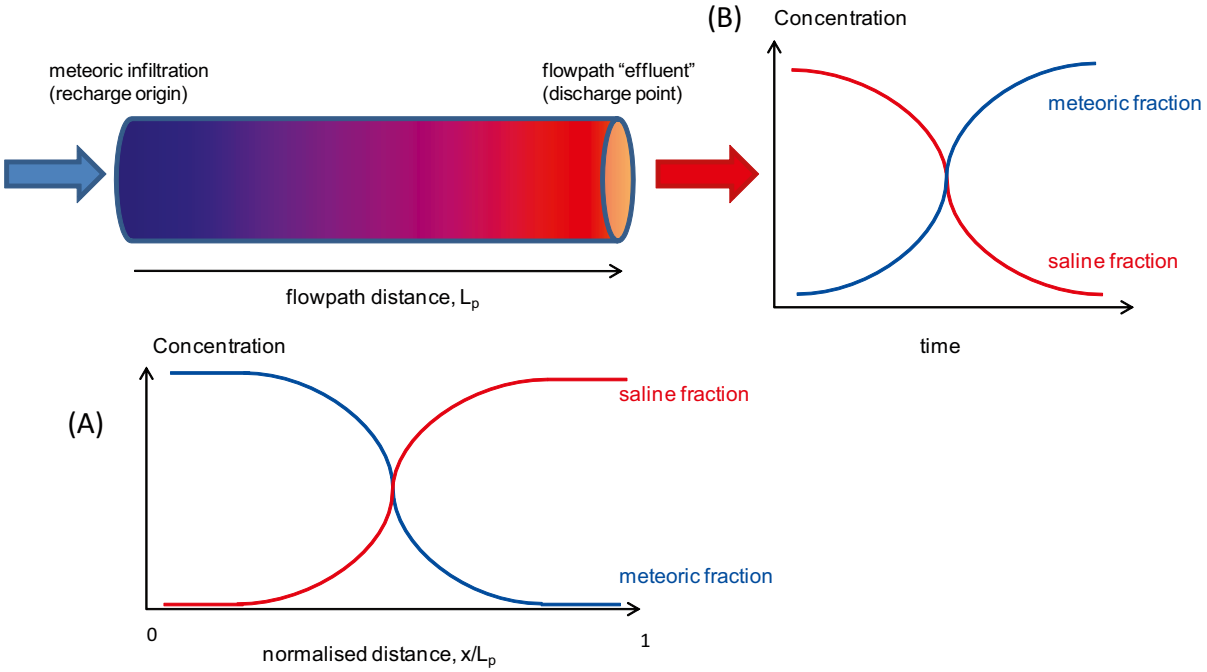

Figure A-4. *Conceptual illustration showing how typical flowpath concentration profiles (concentration vs. distance) for a fixed moment in time (A) and effluent breakthrough curves (concentration vs. time) for a fixed location (B) are physically related to the actual flowpath or streamtube under consideration.*

Generally it is found that although the transport aperture has a definite impact on the breakthrough time of the meteoric-saline mixing front, it is only for a small range of F-factors around 10^6 yr/m that this has a noticeable impact on the distribution of salt at the conclusion of the palaeosimulations after 10 ka of meteoric infiltration. The calculated salt distribution profiles for F-factors equal to 10^5 yr/m or less along a recharge path indicate relatively rapid flushing of salt from the fracture system which is not affected appreciably by the transport aperture. At the other end of the scale for F-factors on the order of 10^7 yr/m, the retardation of the mixing front is sufficiently strong that the saline content of the recharge path is only slightly displaced, also with an almost negligible impact due to transport aperture. Some examples of flowpath effluent breakthrough curves and mixing front profiles are shown in Figure A-5 to Figure A-7 for an F-factor of 10^6 yr/m. This particular choice of F-factor is illustrative since it gives a mixing front penetration depth which corresponds to about half the recharge path length for the smallest transport apertures. As can be seen from the Figures, the time and distance profiles for the saline component are the mirror image of the corresponding profiles for the non-saline component since the individual component fractions, by definition, sum to unity.

It should be noted that a large F-factor, although implying a large retardation effect for an infiltrating meteoric water mixing front, does not imply a large impact on the salt inventory of the rock matrix. In fact, a low F-factor giving relatively fast flushing of the saline content of the advective fractures can be shown to give rise to a greater mobilisation of salt owing to the concentration gradient between the rock matrix and the salt-depleted fracture water. A recharge pathway featuring a large F-factor, on the other hand, will not be depleted of its salt content and therefore there is very little driving force for out-diffusion of salt from the rock matrix. The impact on the overall salt content of the system (i.e. including that stored in the rock matrix), however, depends not only on the F-factors characterising individual recharge pathways, but also the spatial intensity of flow conductors. A high intensity of flow conductors will therefore allow the mobilisation of larger amounts of salt than a low intensity of flow conductors even when the flowpaths have identical F-factors.

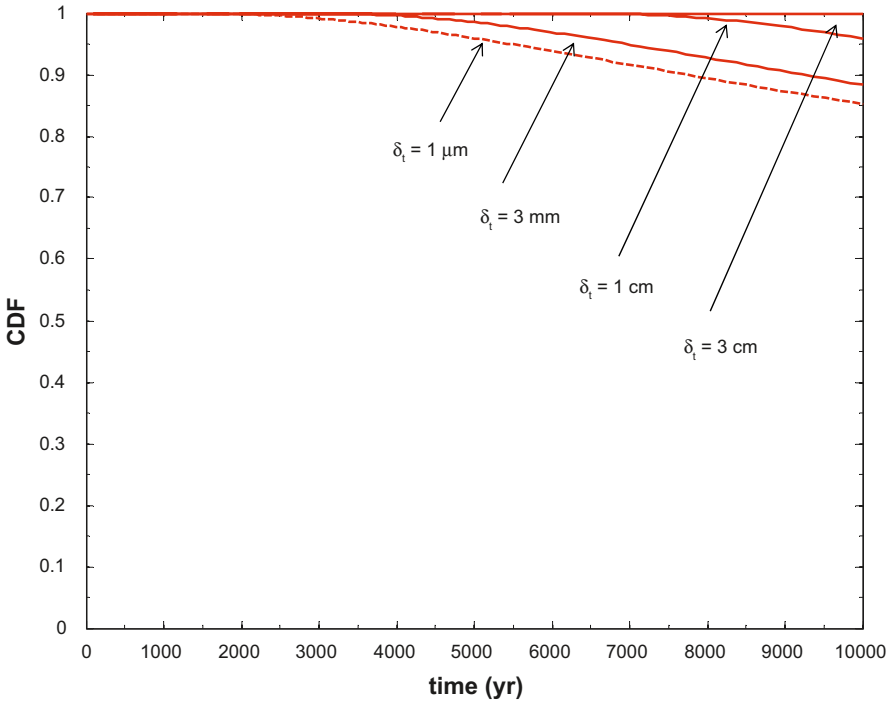

Figure A-5. *Residence time distribution for saline water displacement front. The red curves show the saline concentration fraction of the effluent at the end of a flowpath versus time for an F-factor of 10^6 yr/m, 6 m maximum rock matrix diffusion depth, and a range of transport apertures.*

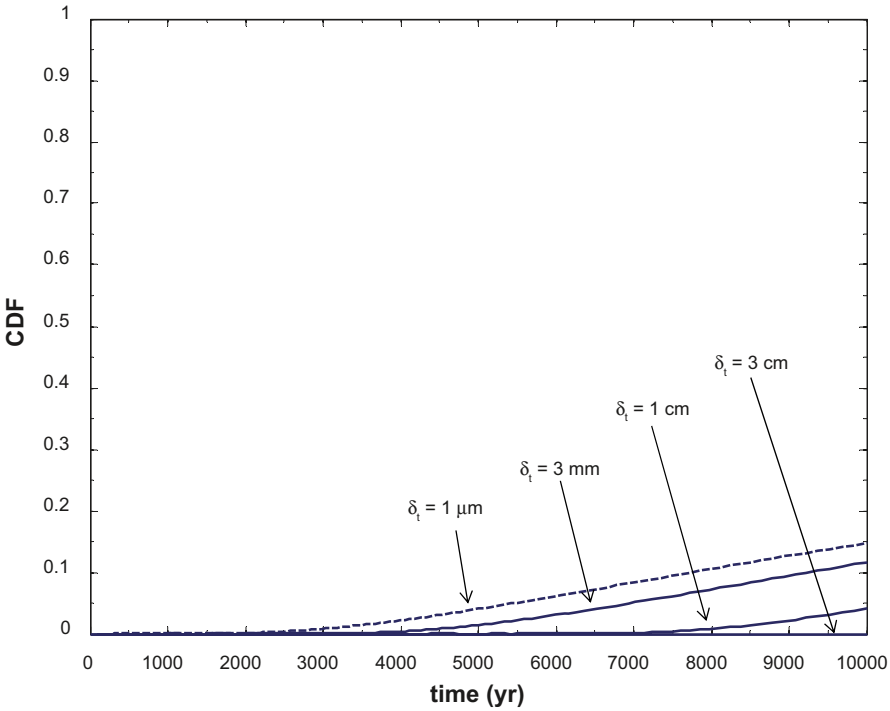

Figure A-6. *Residence time distribution for meteoric water mixing front. The blue curves show the meteoric water concentration fraction of the effluent at the end of a flowpath versus time for an F-factor of 10^6 yr/m, 6 m maximum rock matrix diffusion depth, and a range of transport apertures.*

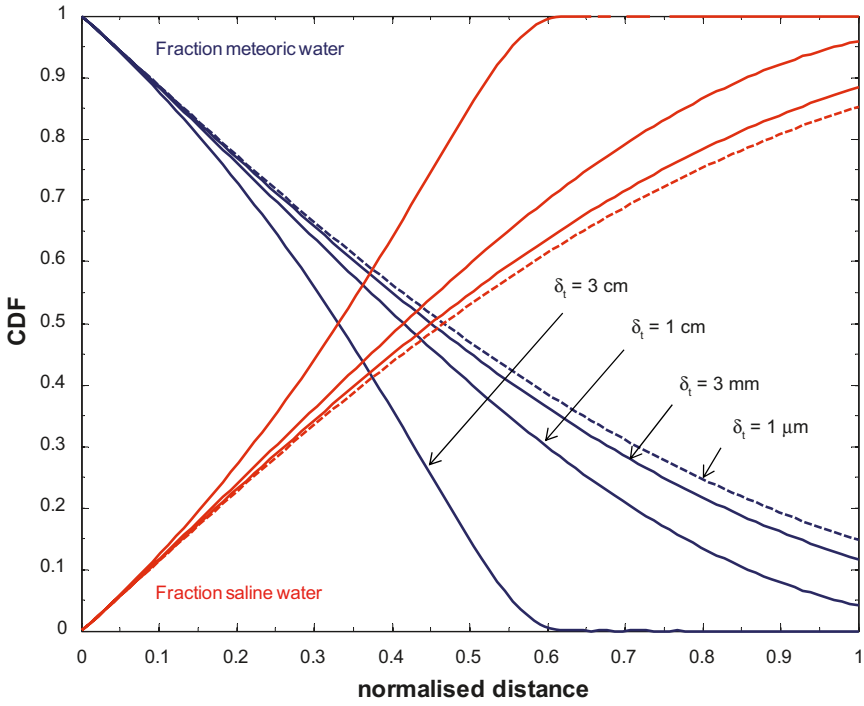

Figure A-7. *Distribution of saline (red curves) and meteoric water (blue curves) along a recharge pathline after 10 ka of meteoric water infiltration for a system initially equilibrated with saline water. Relatively large differences are obtained between calculated salt profiles corresponding to different transport apertures for an F-factor of 10^6 yr/m.*

Appendix B

Flow related transport properties of the HRD

Author: James Crawford

The following sections contain a detailed account of the modelling results for the different hydraulic rock domains that have been studied. As discussed in Section 3.4, the modelling work attempts to identify ranges of F-factors characteristic of typical flowpaths in the immediate far-field (IFF) surrounding a hypothetical repository. Two different modelling strategies have been adopted which utilise the Hydrogeological DFN produced by Hydrogeology /Rhén et al. 2008/ as a basis for calculations.

In the primary modelling strategy, 100 stochastic realisations were made of the Hydrogeological DFN for HRD_C, HRD_W, HRD_EW007, and HRD_N in the elevation interval –400 m to –650 m using a program implemented in Matlab /Mathworks 2005/. As a first step, a connectivity analysis was performed to ascertain how the hydraulic connectivity of the system varies over different boundary plane separation distances and along different principal axes in a cubic simulation volume of side length 100 m. From the connectivity analysis, the percolation probability can be plotted as a function of boundary plane separation over different distances and along different axis directions. The percolation probability is defined to be the fraction of realisations that exhibit at least one hydraulically connected structure spanning the modelled domain for a given number of stochastic realisations of the Hydrogeological DFN. The percolation threshold is operationally defined /Mourzenko et al. 2004, 2005/ as the distance at which the percolation probability is exactly 50% (i.e. half of all realisations exhibit no connectivity). This definition considers the fact that when the largest fractures are of the same size or larger than the system itself, the percolation probability can never completely vanish as there is always a slight probability of a single fracture spanning the entire modelled volume.

Hydraulically connected DFN realisations were then converted to an equivalent pipe network and the path of least transport resistance (PLTR) was calculated for each realisation using graph theory for the case of neutrally conductive fracture intersections as well as highly conductive fracture intersections (fracture intersection zones referred to as FIZ in this report). A full account of the modelling procedure and calculation algorithms is given in /Crawford 2008/.

In the complementary modelling strategy, 20 stochastic realisations of the Hydrogeological DFN were generated in Napsac/ConnectFlow /Serco Assurance 2007/ and subject to particle tracking analysis. These calculations were also made in a cubic simulation volume of similar dimensions to that used for the primary modelling calculations using Matlab.

In both modelling strategies, a semi-correlated fracture length-transmissivity model was assumed as a base case and F-factor calculations were made for a reference hydraulic gradient of 1% (discussed previously in Section 3.3). In the Napsac/ConnectFlow calculations, advective travel times were also calculated using the macroscopic quadratic law (MQL) relating transport aperture and fracture transmissivity (as described in Table 3-8).

Modelling results for HRD_C

Matlab simulation results for the path of least transport resistance (PLTR)

Figure B-1 shows the percolation probability, P_{con} plotted as a function of boundary plane separation distance for hydraulic connectivity along the different principal axes of the simulation volume.

The stochastic analysis indicates anisotropy with considerably lower connectivity along the north-south axis than for west-east or vertical connectivity. For the north-south direction, the percolation threshold appears to occur at roughly 60 m whereas along the west-east and vertical axes the threshold appears to exceed the 100 m length of the simulation volume.

Figure B-2 to Figure B-4 shows plots of F-factor ranges for the path of least transport resistance (PLTR) along typical transport paths within HRD_C assuming a 1% hydraulic gradient applied along each of the three principal axes of the simulation volume and at different boundary plane separation distances. The cumulative F-factor distributions represent the aggregate set of 100 realisations and therefore should be interpreted as the probability distribution for the singular F-factor corresponding to the path of least transport resistance in any given realisation. Summary statistics corresponding to the plotted data are given in Table B-1 to Table B-3.

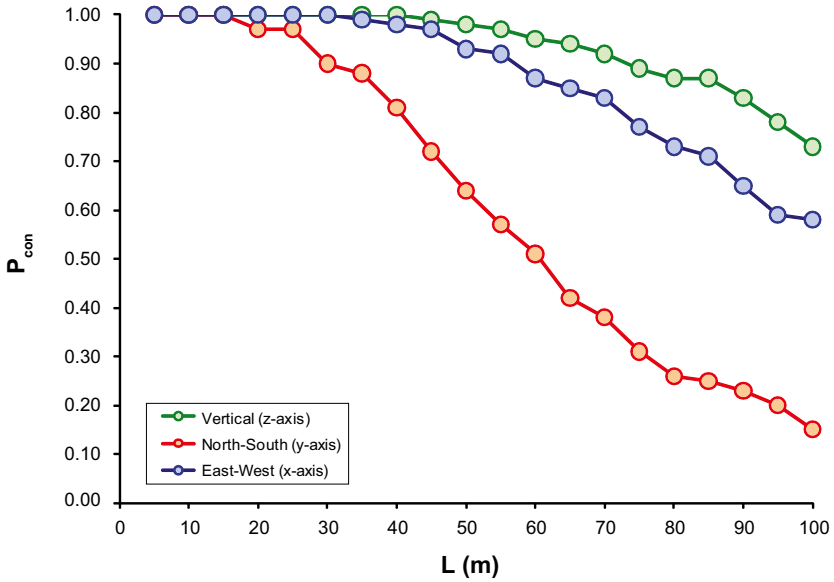

Figure B-1. *Results of connectivity analysis for HRD_C (–400 m to –650 m) based upon 100 stochastic realisations of the Hydrogeological DFN model based on open and partly open fractures (OPO). The percolation probability is plotted as a function of distance for the three principal axes of the model.*

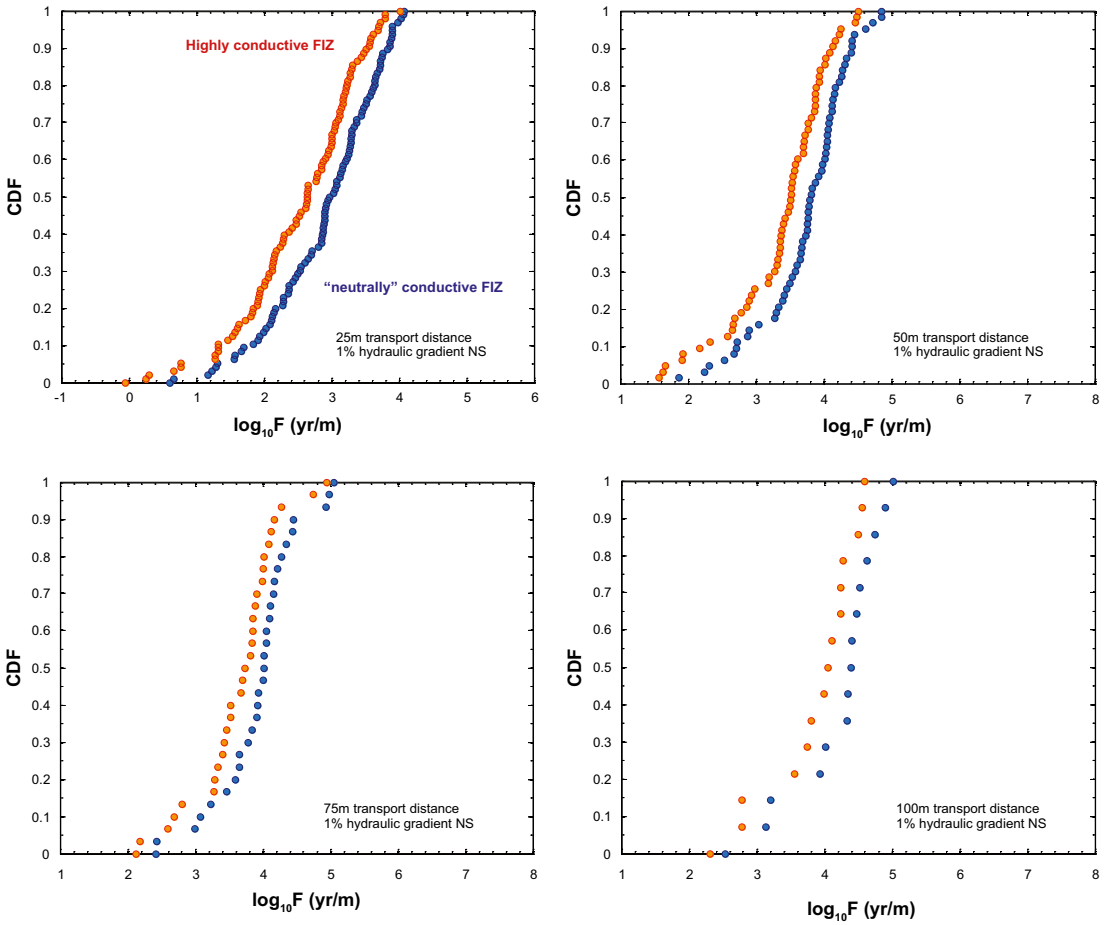

Figure B-2. *Typical F-factor ranges for the path of least resistance, PLTR in HRD_C in the elevation interval –400 m to –650 m based on 100 realisations of the Hydrogeological DFN. The calculations consider boundary plane separation distances of 25 m, 50 m, 75 m and 100 m for a 1% hydraulic gradient applied along the north-south axis of the simulation volume. Results are given for the case of neutrally conductive FIZ (blue markers) and for highly conductive FIZ (red-orange markers) and are plotted as cumulative distribution probability curves.*

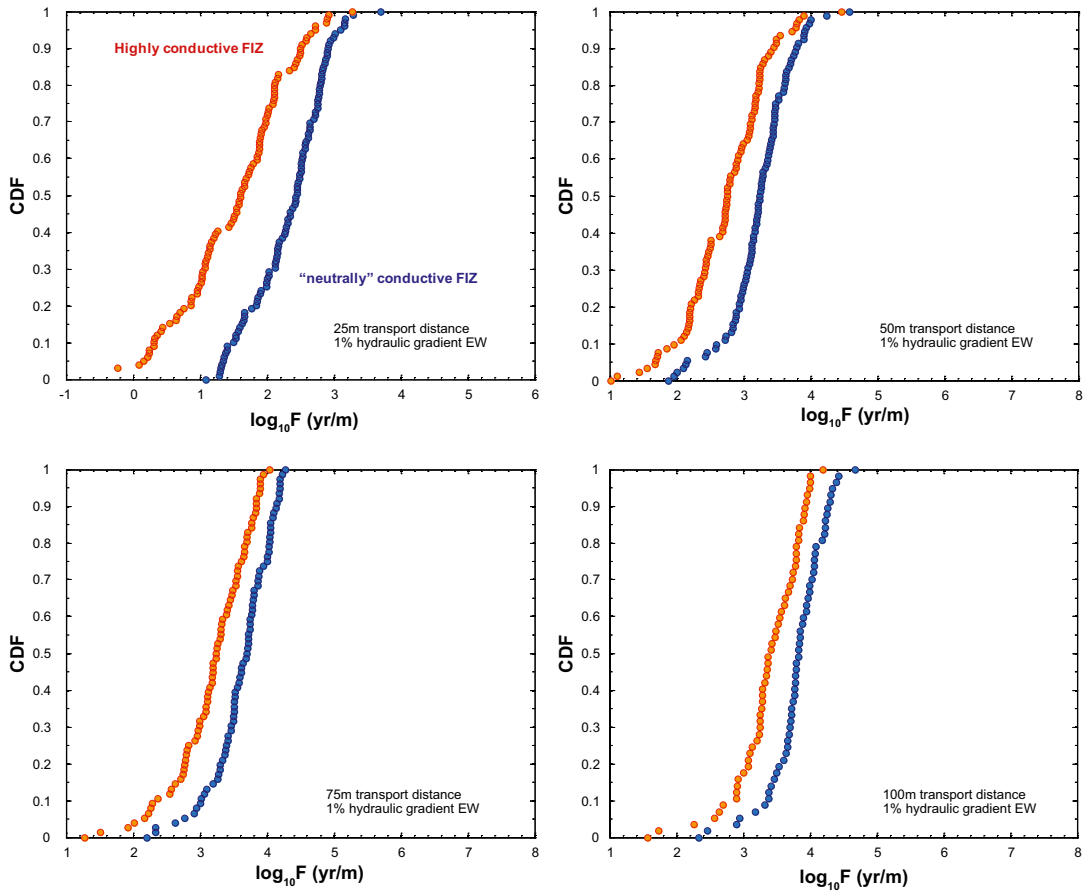

Figure B-3. *Typical F-factor ranges for the path of least resistance, PLTR in HRD_C in the elevation interval –400 m to –650 m based on 100 realisations of the Hydrogeological DFN. The calculations consider boundary plane separation distances of 25 m, 50 m, 75 m and 100 m for a 1% hydraulic gradient applied along the west-east axis of the simulation volume. Results are given for the case of neutrally conductive FIZ (blue markers) and for highly conductive FIZ (red-orange markers) and are plotted as cumulative distribution probability curves.*

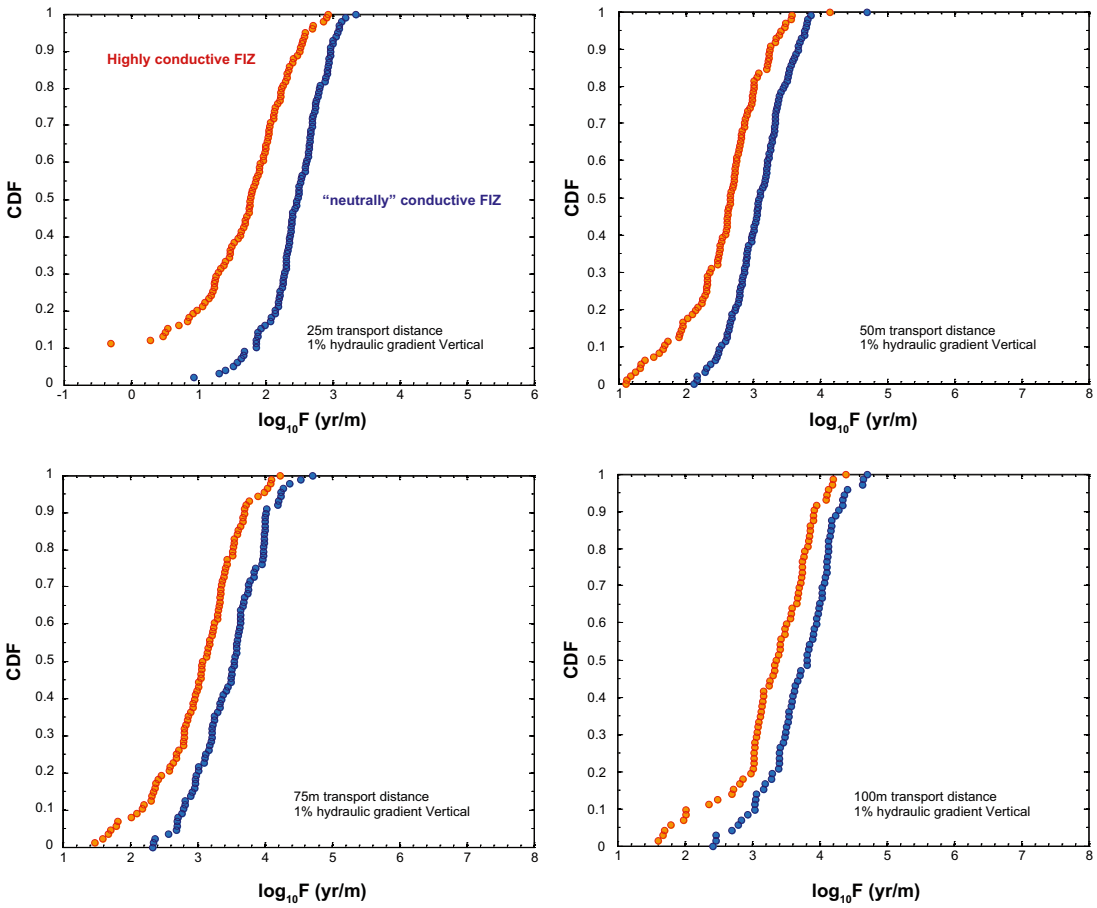

Figure B-4. *Typical F-factor ranges for the path of least resistance, PLTR in HRD_C in the elevation interval –400 m to –650 m based on 100 realisations of the Hydrogeological DFN. The calculations consider boundary plane separation distances of 25 m, 50 m, 75 m and 100 m for a 1% hydraulic gradient applied along the vertical axis of the simulation volume. Results are given for the case of neutrally conductive FIZ (blue markers) and for highly conductive FIZ (red-orange markers) and are plotted as cumulative distribution probability curves.*

Table B-1. Summary statistics for the F-factor (log_{10} units) corresponding to the pooled simulation data for HRD_C in the elevation interval –400 m to –650 m. The data are for the path of least transport resistance (PLTR) over different transport distances assuming a 1% reference hydraulic gradient applied along the north-south axis (100 stochastic DFN realisations). Results are given for both the neutrally conductive FIZ case as well as the highly-conductive FIZ case.

North-South case	log_{10}F (neutrally conductive FIZ)				log_{10}F (highly-conductive FIZ)			
Semi-Correlated (SC)	25 m	50 m	75 m	100 m	25 m	50 m	75 m	100 m
Mean	2.88	3.75	3.91	4.17	2.51	3.39	3.62	3.84
Median	2.97	3.82	4.01	4.40	2.64	3.52	3.74	4.06
5th percentile	1.29	2.46	2.46	2.69	0.77	1.82	2.20	2.43
10th percentile	1.73	2.72	3.04	3.13	1.32	2.29	2.65	2.78
25th percentile	2.37	3.46	3.65	3.96	1.94	3.03	3.36	3.60
75th percentile	3.51	4.13	4.21	4.60	3.17	3.87	4.00	4.27
90th percentile	3.85	4.41	4.65	4.89	3.55	4.14	4.21	4.56
95th percentile	3.90	4.65	4.98	4.98	3.70	4.33	4.72	4.58
Std. deviation	0.80	0.63	0.62	0.70	0.87	0.70	0.64	0.70
Variance	0.64	0.40	0.39	0.49	0.75	0.49	0.41	0.49
Min value	0.61	1.87	2.41	2.54	–0.06	1.58	2.12	2.31
Max value	4.07	4.85	5.05	5.01	4.02	4.51	4.94	4.59
Connected fraction (%)	97	63	31	15	97	63	31	15

Table B-2. Summary statistics for the F-factor (log_{10} units) corresponding to the pooled simulation data for HRD_C in the elevation interval –400 m to –650 m. The data are for the path of least transport resistance (PLTR) over different transport distances assuming a semi-correlated fracture length-transmissivity model and 1% reference hydraulic gradient applied along the west-east axis (100 stochastic DFN realisations). Results are given for both the neutrally conductive FIZ case as well as the highly-conductive FIZ case.

West-East case	log_{10}F (neutrally conductive FIZ)				log_{10}F (highly-conductive FIZ)			
Semi-Correlated (SC)	25 m	50 m	75 m	100 m	25 m	50 m	75 m	100 m
Mean	2.32	3.23	3.61	3.80	1.37	2.73	3.17	3.37
Median	2.44	3.25	3.71	3.83	1.61	2.76	3.24	3.39
5th percentile	1.33	2.14	2.68	2.92	0.12	1.68	2.07	2.39
10th percentile	1.46	2.59	3.01	3.34	0.31	1.93	2.30	2.76
25th percentile	1.95	3.00	3.39	3.66	0.97	2.33	2.82	3.14
75th percentile	2.76	3.49	4.01	4.07	2.10	3.17	3.63	3.79
90th percentile	2.91	3.80	4.15	4.29	2.51	3.46	3.84	3.94
95th percentile	3.13	3.94	4.19	4.37	2.72	3.77	3.90	4.00
Std. deviation	0.55	0.49	0.46	0.44	1.29	0.62	0.58	0.52
Variance	0.30	0.24	0.21	0.19	1.66	0.39	0.33	0.27
Min value	1.09	1.87	2.20	2.33	–4.77	1.02	1.28	1.57
Max value	3.70	4.58	4.28	4.67	3.28	4.46	4.05	4.19
Connected fraction (%)	100	93	77	58	100	93	77	58

Table B-3. Summary statistics for the F-factor (log_{10} units) corresponding to the pooled simulation data for HRD_C in the elevation interval –400 m to –650 m. The data are for the path of least transport resistance (PLTR) over different transport distances assuming a 1% reference hydraulic gradient applied along the vertical axis (100 stochastic DFN realisations). Results are given for both the neutrally conductive FIZ case as well as the highly-conductive FIZ case.

Vertical case	log_{10}F (neutrally conductive FIZ)				log_{10}F (highly-conductive FIZ)			
Semi-Correlated (SC)	25 m	50 m	75 m	100 m	25 m	50 m	75 m	100 m
Mean	2.46	3.10	3.48	3.72	1.20	2.58	3.01	3.26
Median	2.49	3.10	3.55	3.82	1.79	2.67	3.07	3.36
5th percentile	1.61	2.34	2.68	2.72	–4.62	1.33	1.71	1.71
10th percentile	1.87	2.51	2.78	3.02	–0.13	1.67	2.14	2.02
25th percentile	2.25	2.81	3.12	3.41	1.24	2.31	2.69	3.03
75th percentile	2.75	3.37	3.88	4.11	2.18	2.99	3.42	3.75
90th percentile	2.97	3.68	4.02	4.30	2.52	3.26	3.70	3.93
95th percentile	3.09	3.79	4.24	4.41	2.66	3.45	3.99	4.14
Std. deviation	0.45	0.45	0.51	0.52	1.96	0.60	0.64	0.70
Variance	0.20	0.20	0.26	0.27	3.85	0.36	0.41	0.49
Min value	0.94	2.12	2.34	2.42	–4.97	1.12	0.96	0.85
Max value	3.34	4.70	4.72	4.71	2.94	4.15	4.23	4.40
Connected fraction (%)	98	98	89	73	98	98	89	73

Napsac/ConnectFlow simulation results using particle tracking

Figure B-5 shows F-factor distributions calculated using the particle tracking capabilities of Napsac/ConnectFlow for a boundary plane separation distance of 100 m along the different principal axes of the simulation volume. Since it is not possible to simulate highly conductive fracture intersections (FIZ) in any simple manner, only the base case of neutrally conductive FIZ has been considered. The cumulative curves correspond to the ensemble of 1000 particles released in each individual simulation (20 stochastic realisations). The corresponding cumulative distributions of advective travel times are shown in Figure B-6. Summary statistics for the F-factor and advective travel time are given in Table B-4 to Table B-6 for different boundary plane separation distances and for transport along the different principal axis directions. The summary statistics represent a pooling of all particle tracking results from individual realisations.

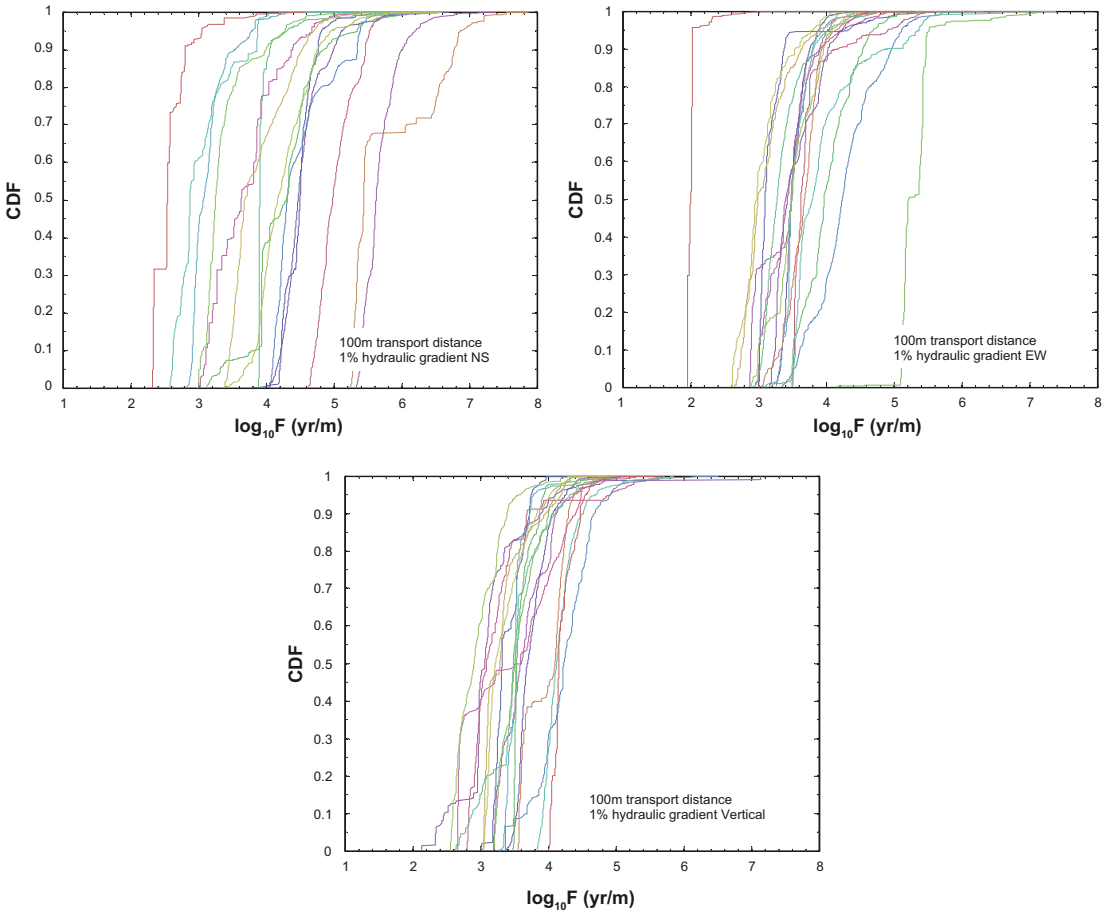

Figure B-5. *Typical F-factor distributions obtained using particle tracking for HRD_C in the elevation interval –400 m to –650 m based on 20 realisations of the Hydrogeological DFN in Napsac/ConnectFlow. The calculations consider a boundary plane separation distance of 100 m for a 1% hydraulic gradient applied along each of the three principal axes of the simulation volume as indicated in the figure. Results are given for the case of neutrally conductive FIZ only and are plotted as cumulative distribution probability curves for each individual realisation.*

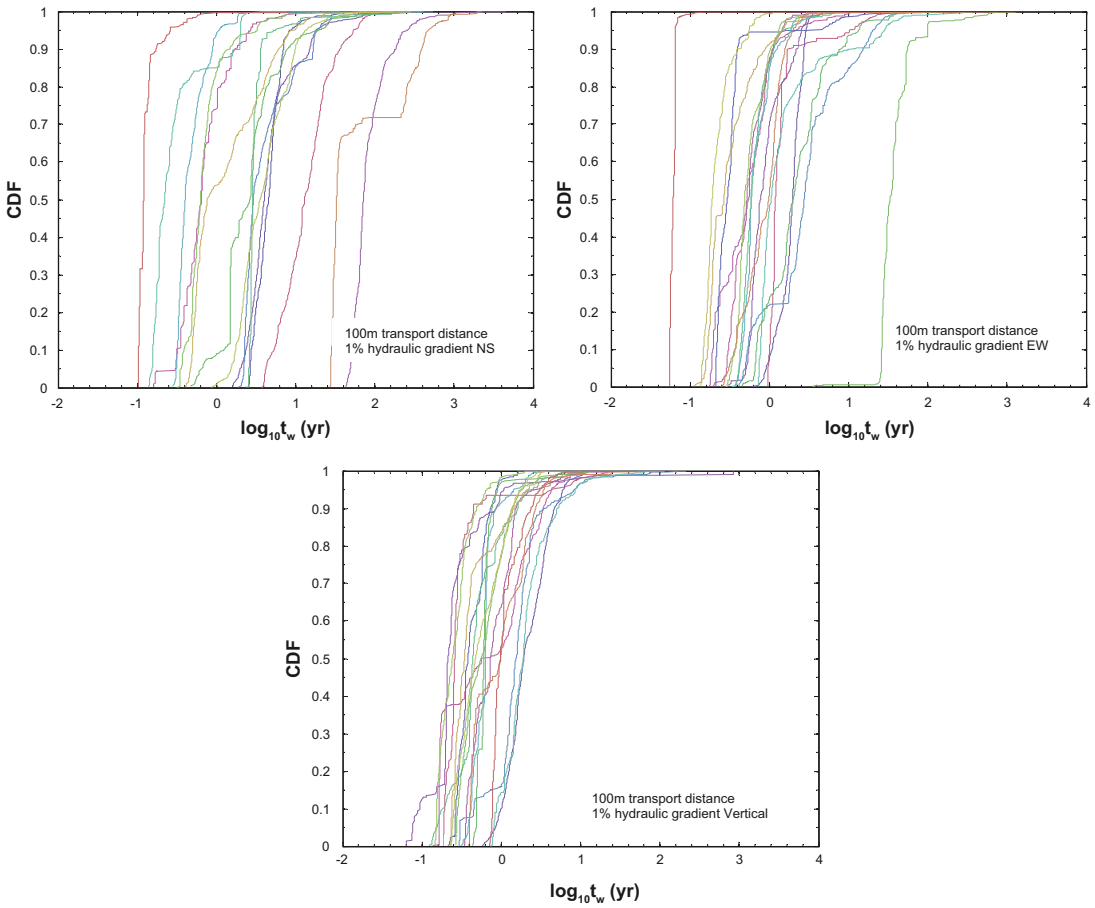

Figure B-6. *Typical advective travel time distributions obtained using particle tracking for HRD_C in the elevation interval –400 m to –650 m based on 20 realisations of the Hydrogeological DFN in Napsac/ConnectFlow. The calculations consider a boundary plane separation distance of 100 m for a 1% hydraulic gradient applied along each of the three principal axes of the simulation volume as indicated in the figure. Results are given for the case of neutrally conductive FIZ only and are plotted as cumulative distribution probability curves for each individual realisation.*

Table B-4. Summary statistics for the F-factor and advective travel time (log_{10} units) corresponding to the pooled particle tracking data for HRD_C in the elevation interval –400 m to –650 m. The data are for different transport distances assuming a 1% reference hydraulic gradient applied along the north-south axis (20 pooled stochastic DFN realisations with 1,000 particles released in each realisation). Results are given for the neutrally conductive FIZ case only.

North-South case	log_{10} F (yr/m)				log_{10} tw (yr)			
Semi-Correlated (SC)	25 m	50 m	75 m	100 m	25 m	50 m	75 m	100 m
Mean	3.28	3.20	4.26	4.16	–0.58	–0.53	0.36	0.43
Median	3.22	3.43	4.29	4.14	–0.58	–0.38	0.35	0.44
5th percentile	1.86	1.38	2.69	2.59	–1.52	–2.17	–0.91	–0.87
10th percentile	2.02	2.11	3.03	2.89	–1.46	–1.26	–0.64	–0.65
25th percentile	2.53	2.61	3.71	3.38	–1.10	–0.97	–0.17	–0.24
75th percentile	3.99	4.15	4.92	4.74	–0.12	0.23	0.78	0.86
90th percentile	4.43	4.51	5.45	5.45	0.25	0.52	1.51	1.61
95th percentile	4.67	4.79	5.64	5.70	0.53	0.70	1.72	1.88
Std. deviation	0.89	1.52	0.91	0.97	0.64	1.27	0.75	0.83
Variance	0.80	2.30	0.83	0.95	0.41	1.61	0.57	0.69
Min value	1.63	–2.57	2.15	2.33	–1.68	–5.52	–1.14	–0.99
Max value	6.20	6.46	8.21	7.87	2.14	2.59	4.12	3.65
Recovered particles	19,546	18,000	18,996	14,970	19,546	18,000	18,996	14,970

Table B-5. Summary statistics for the F-factor and advective travel time (log_{10} units) corresponding to the pooled particle tracking data for HRD_C in the elevation interval –400 m to –650 m. The data are for different transport distances assuming a 1% reference hydraulic gradient applied along the west-east axis (20 pooled stochastic DFN realisations with 1,000 particles released in each realisation). Results are given for the neutrally conductive FIZ case only.

West-East case	log_{10} F (yr/m)				log_{10} tw (yr)			
Semi-Correlated (SC)	25 m	50 m	75 m	100 m	25 m	50 m	75 m	100 m
Mean	2.90	3.14	3.75	3.58	–0.92	–0.52	–0.14	–0.06
Median	2.87	3.13	3.78	3.52	–0.99	–0.51	–0.13	–0.14
5th percentile	2.01	1.94	2.70	2.02	–1.45	–1.38	–0.90	–1.19
10th percentile	2.06	2.32	2.90	2.89	–1.43	–1.18	–0.78	–0.73
25th percentile	2.28	2.67	3.17	3.18	–1.33	–0.92	–0.63	–0.43
75th percentile	3.39	3.67	4.16	3.87	–0.61	–0.16	0.24	0.20
90th percentile	3.82	3.92	4.69	4.53	–0.28	0.09	0.54	0.68
95th percentile	4.03	4.11	4.89	5.17	–0.08	0.26	0.76	1.44
Std. deviation	0.68	0.65	0.68	0.74	0.47	0.51	0.53	0.64
Variance	0.46	0.42	0.46	0.55	0.22	0.26	0.28	0.41
Min value	1.88	1.68	2.57	1.96	–1.59	–1.54	–0.99	–1.25
Max value	6.44	5.83	7.71	7.40	2.23	1.65	3.57	3.12
Recovered particles	20,000	19,972	19,941	17,000	20,000	19,972	19,941	17,000

Table B-6. Summary statistics for the F-factor and advective travel time (log_{10} units) corresponding to the pooled particle tracking data for HRD_C in the elevation interval –400 m to –650 m. The data are for different transport distances assuming a 1% reference hydraulic gradient applied along the vertical axis (20 pooled stochastic DFN realisations with 1,000 particles released in each realisation). Results are given for the neutrally conductive FIZ case only.

Vertical case	log_{10} F (yr/m)				log_{10} tw (yr)			
Semi-Correlated (SC)	25 m	50 m	75 m	100 m	25 m	50 m	75 m	100 m
Mean	2.70	3.51	3.50	3.61	–1.02	–0.40	–0.28	–0.17
Median	2.63	3.50	3.50	3.55	–1.15	–0.47	–0.25	–0.22
5th percentile	1.95	2.37	2.59	2.72	–1.49	–1.16	–0.96	–0.76
10th percentile	2.02	2.49	2.83	2.98	–1.49	–1.11	–0.83	–0.66
25th percentile	2.24	2.97	3.16	3.24	–1.32	–0.80	–0.62	–0.48
75th percentile	3.01	4.00	3.89	4.01	–0.82	–0.11	–0.01	0.11
90th percentile	3.61	4.51	4.15	4.26	–0.36	0.37	0.24	0.37
95th percentile	3.82	4.71	4.34	4.46	–0.08	0.60	0.44	0.55
Std. deviation	0.63	0.73	0.53	0.53	0.47	0.56	0.43	0.42
Variance	0.39	0.53	0.28	0.28	0.22	0.31	0.18	0.18
Min value	0.26	2.18	2.19	2.13	–3.69	–1.29	–1.28	–1.20
Max value	5.27	6.16	7.22	7.14	1.63	2.57	3.01	2.93
Recovered particles	20000	18998	17997	16922	20000	18998	17997	16922

Modelling results for HRD_W

Matlab simulation results for the path of least transport resistance (PLTR)

Figure B-7 shows the percolation probability, P_{con} plotted as a function of boundary plane separation distance for hydraulic connectivity along the different principal axes of the simulation 100 m simulation volume.

The stochastic analysis indicates relatively homogeneous connectivity along all three axes with a percolation threshold occurring at roughly 65–80 m. The hydraulic connectivity in HRD_W is on average lower than in any of the other hydraulic rock domains investigated.

Figure B-8 to Figure B-10 shows plots of F-factor ranges for the path of least transport resistance (PLTR) along typical transport paths within HRD_W assuming a 1% hydraulic gradient applied along each of the three principal axes of the simulation volume and at different boundary plane separation distances. Summary statistics corresponding to the plotted data are given in Table B-7 to Table B-9.

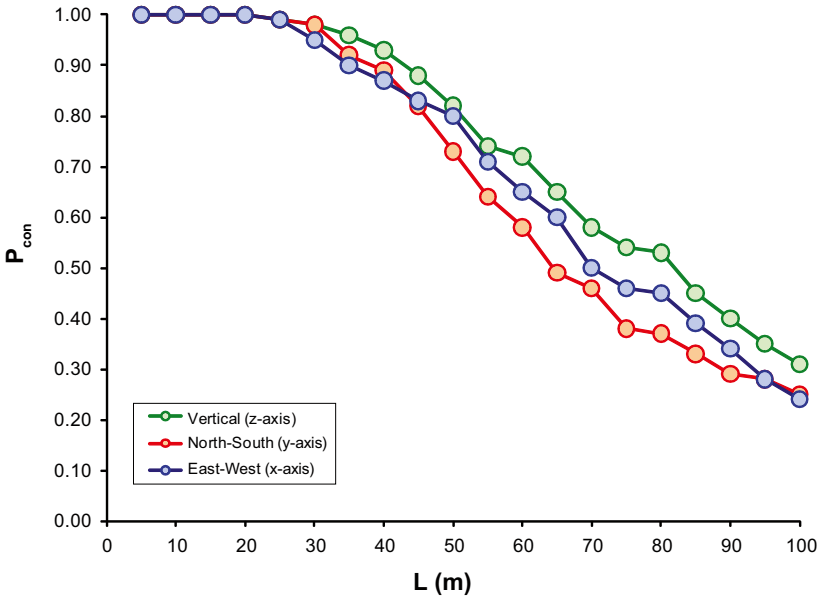

Figure B-7. *Results of connectivity analysis for HRD_W (–400 m to –650 m) based upon 100 stochastic realisations of the Hydrogeological DFN model based on open and partly open fractures (OPO). The percolation probability is plotted as a function of distance for the three principal axes of the model.*

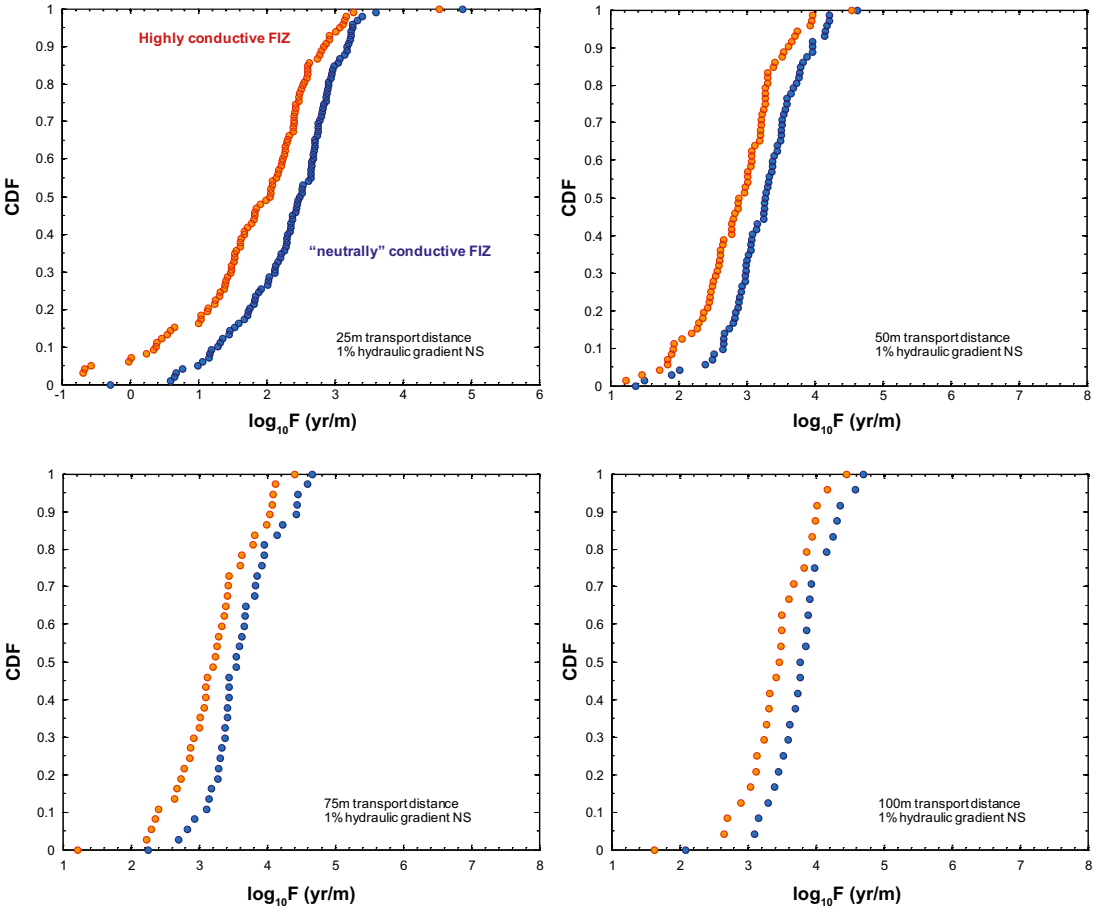

Figure B-8. *Typical F-factor ranges for the path of least resistance, PLTR in HRD_W in the elevation interval –400 m to –650 m based on 100 realisations of the Hydrogeological DFN. The calculations consider boundary plane separation distances of 25 m, 50 m, 75 m and 100 m for a 1% hydraulic gradient applied along the north-south axis of the simulation volume. Results are given for the case of neutrally conductive FIZ (blue markers) and for highly conductive FIZ (red-orange markers) and are plotted as cumulative distribution probability curves.*

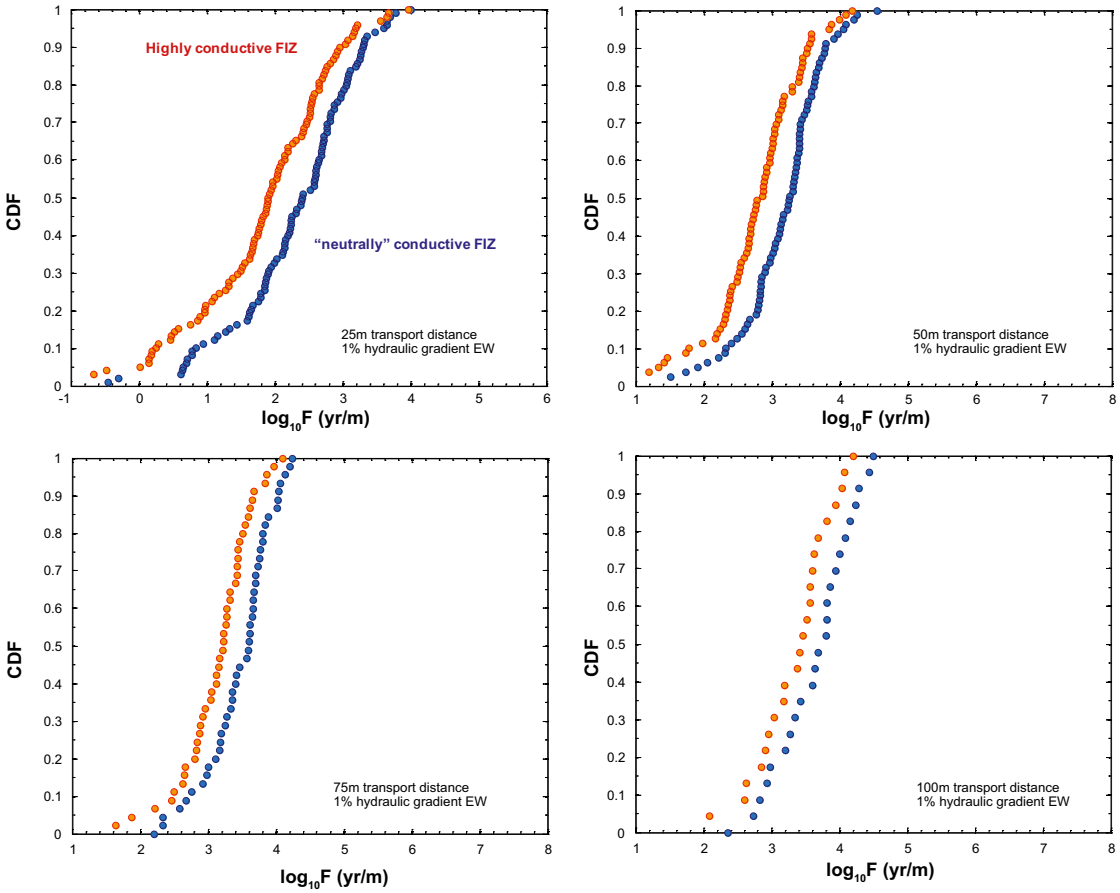

Figure B-9. *Typical F-factor ranges for the path of least resistance, PLTR in HRD_W in the elevation interval –400 m to –650 m based on 100 realisations of the Hydrogeological DFN. The calculations consider boundary plane separation distances of 25 m, 50 m, 75 m and 100 m for a 1% hydraulic gradient applied along the west-east axis of the simulation volume. Results are given for the case of neutrally conductive FIZ (blue markers) and for highly conductive FIZ (red-orange markers) and are plotted as cumulative distribution probability curves.*

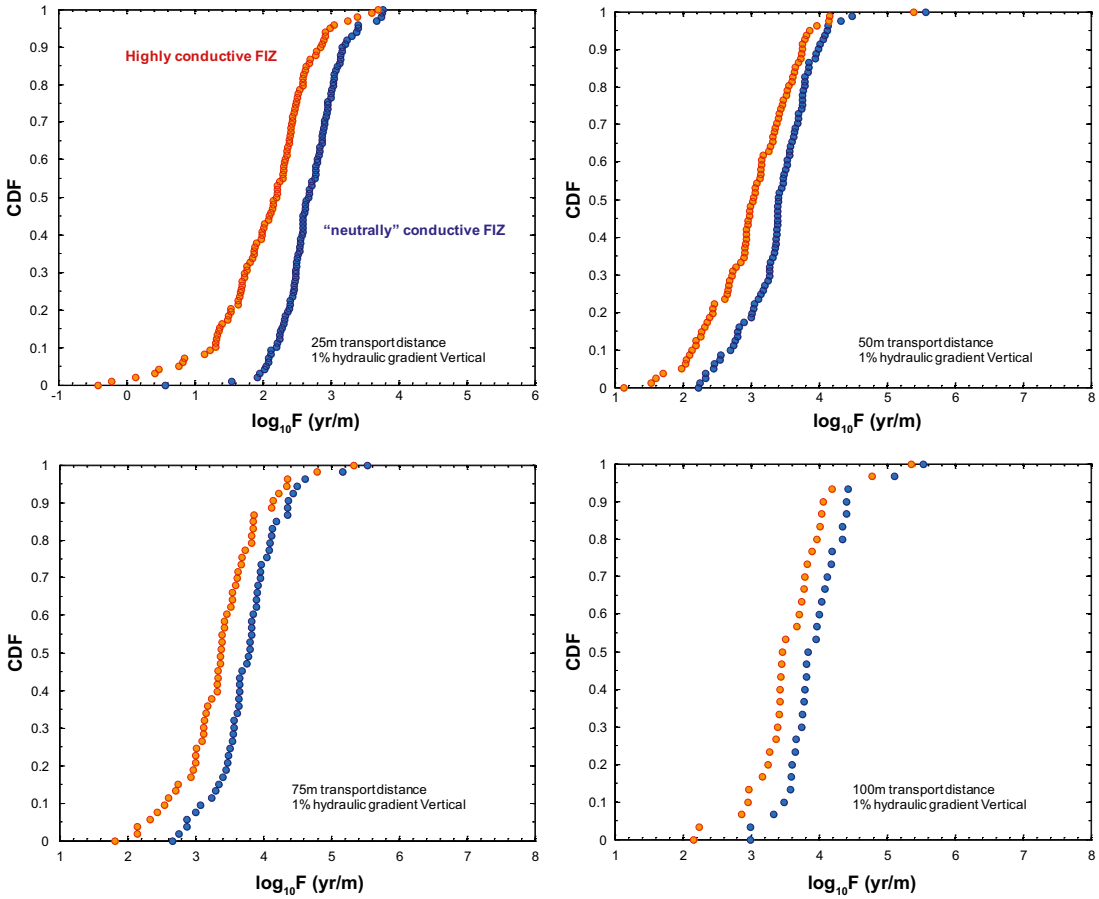

Figure B-10. *Typical F-factor ranges for the path of least resistance, PLTR in HRD_W in the elevation interval –400 m to –650 m based on 100 realisations of the Hydrogeological DFN. The calculations consider boundary plane separation distances of 25 m, 50 m, 75 m and 100 m for a 1% hydraulic gradient applied along the vertical axis of the simulation volume. Results are given for the case of neutrally conductive FIZ (blue markers) and for highly conductive FIZ (red-orange markers) and are plotted as cumulative distribution probability curves.*

Table B-7. Summary statistics for the F-factor (log_{10} units) corresponding to the pooled simulation data for HRD_W in the elevation interval –400 m to –650 m. The data are for the path of least transport resistance (PLTR) over different transport distances assuming a 1% reference hydraulic gradient applied along the north-south axis (100 stochastic DFN realisations). Results are given for both the neutrally conductive FIZ case as well as the highly-conductive FIZ case.

North-South case	log_{10}F (neutrally conductive FIZ)				log_{10}F (highly-conductive FIZ)			
Semi-Correlated (SC)	25 m	50 m	75 m	100 m	25 m	50 m	75 m	100 m
Mean	2.36	3.24	3.60	3.76	1.69	2.85	3.19	3.41
Median	2.48	3.27	3.55	3.77	2.05	2.89	3.22	3.47
5th percentile	0.87	2.08	2.75	2.85	–0.62	1.74	2.26	2.40
10th percentile	1.23	2.63	2.99	3.16	0.36	1.92	2.38	2.70
25th percentile	1.90	2.92	3.31	3.50	1.34	2.47	2.87	3.13
75th percentile	2.86	3.59	3.92	4.02	2.46	3.28	3.61	3.84
90th percentile	3.20	3.98	4.43	4.36	2.86	3.63	4.06	4.02
95th percentile	3.27	4.18	4.53	4.61	3.11	3.91	4.10	4.24
Std. deviation	0.78	0.60	0.53	0.54	1.36	0.66	0.63	0.58
Variance	0.61	0.36	0.28	0.29	1.86	0.43	0.40	0.34
Min value	–0.29	1.37	2.25	2.09	–4.72	0.94	1.22	1.63
Max value	4.88	4.63	4.66	4.69	4.53	4.54	4.41	4.45
Connected fraction (%)	99	73	38	25	99	73	38	25

Table B-8. Summary statistics for the F-factor (log_{10} units) corresponding to the pooled simulation data for HRD_W in the elevation interval –400 m to –650 m. The data are for the path of least transport resistance (PLTR) over different transport distances assuming a semi-correlated fracture length-transmissivity model and 1% reference hydraulic gradient applied along the west-east axis (100 stochastic DFN realisations). Results are given for both the neutrally conductive FIZ case as well as the highly-conductive FIZ case.

West-East case	log_{10}F (neutrally conductive FIZ)				log_{10}F (highly-conductive FIZ)			
Semi-Correlated (SC)	25 m	50 m	75 m	100 m	25 m	50 m	75 m	100 m
Mean	2.31	3.12	3.45	3.63	1.78	2.72	3.08	3.25
Median	2.41	3.26	3.60	3.75	1.91	2.83	3.22	3.44
5th percentile	0.67	1.83	2.34	2.62	0.07	1.26	1.83	1.62
10th percentile	0.87	2.32	2.69	2.82	0.26	1.76	2.47	2.56
25th percentile	1.85	2.83	3.19	3.24	1.28	2.39	2.84	2.93
75th percentile	2.93	3.53	3.77	4.05	2.54	3.16	3.45	3.66
90th percentile	3.31	3.79	4.04	4.31	3.01	3.54	3.67	4.04
95th percentile	3.63	4.07	4.15	4.46	3.21	3.86	3.89	4.11
Std. deviation	0.89	0.71	0.50	0.57	1.22	0.83	0.69	0.77
Variance	0.80	0.50	0.25	0.33	1.49	0.69	0.48	0.60
Min value	–0.45	–0.03	2.21	2.36	–4.69	–0.69	–0.06	0.53
Max value	4.01	4.55	4.24	4.50	3.97	4.18	4.10	4.20
Connected fraction (%)	98	80	46	24	98	80	46	24

Table B-9. Summary statistics for the F-factor (log_{10} units) corresponding to the pooled simulation data for HRD_W in the elevation interval –400 m to –650 m. The data are for the path of least transport resistance (PLTR) over different transport distances assuming a 1% reference hydraulic gradient applied along the vertical axis (100 stochastic DFN realisations). Results are given for both the neutrally conductive FIZ case as well as the highly-conductive FIZ case.

Vertical case	log_{10}F (neutrally conductive FIZ)				log_{10}F (highly-conductive FIZ)			
Semi-Correlated (SC)	25 m	50 m	75 m	100 m	25 m	50 m	75 m	100 m
Mean	2.69	3.41	3.78	3.96	2.05	3.01	3.37	3.57
Median	2.67	3.41	3.79	3.84	2.20	3.04	3.38	3.46
5th percentile	2.04	2.41	2.88	3.02	0.61	1.87	2.19	2.27
10th percentile	2.16	2.66	3.07	3.43	1.26	2.12	2.54	2.93
25th percentile	2.45	3.15	3.51	3.65	1.68	2.66	3.02	3.30
75th percentile	2.96	3.75	4.05	4.19	2.49	3.47	3.69	3.88
90th percentile	3.20	4.00	4.38	4.42	2.87	3.76	4.16	4.12
95th percentile	3.40	4.13	4.59	5.08	3.03	3.91	4.36	4.75
Std. deviation	0.47	0.54	0.53	0.52	0.74	0.68	0.64	0.63
Variance	0.22	0.30	0.29	0.27	0.55	0.46	0.42	0.39
Min value	0.57	2.23	2.67	3.00	–0.42	1.14	1.81	2.16
Max value	3.77	5.57	5.54	5.53	3.70	5.40	5.34	5.36
Connected fraction (%)	99	82	54	31	99	82	54	31

Napsac/ConnectFlow simulation results using particle tracking

Figure B-11 shows F-factor distributions calculated using the particle tracking capabilities of Napsac/ConnectFlow for a boundary plane separation distance of 100 m along the different principal axes of the simulation volume. Since it is not possible to simulate highly conductive fracture intersections (FIZ) in any simple manner, only the base case of neutrally conductive FIZ has been considered. The cumulative curves correspond to the ensemble of 1000 particles released in each individual simulation (20 stochastic realisations). The corresponding cumulative distributions of advective travel times are shown in Figure B-12. Summary statistics for the F-factor and advective travel time are given in Table B-10 to Table B-12 for different boundary plane separation distances and for transport along the different principal axis directions. The summary statistics represent a pooling of all particle tracking results from individual realisations.

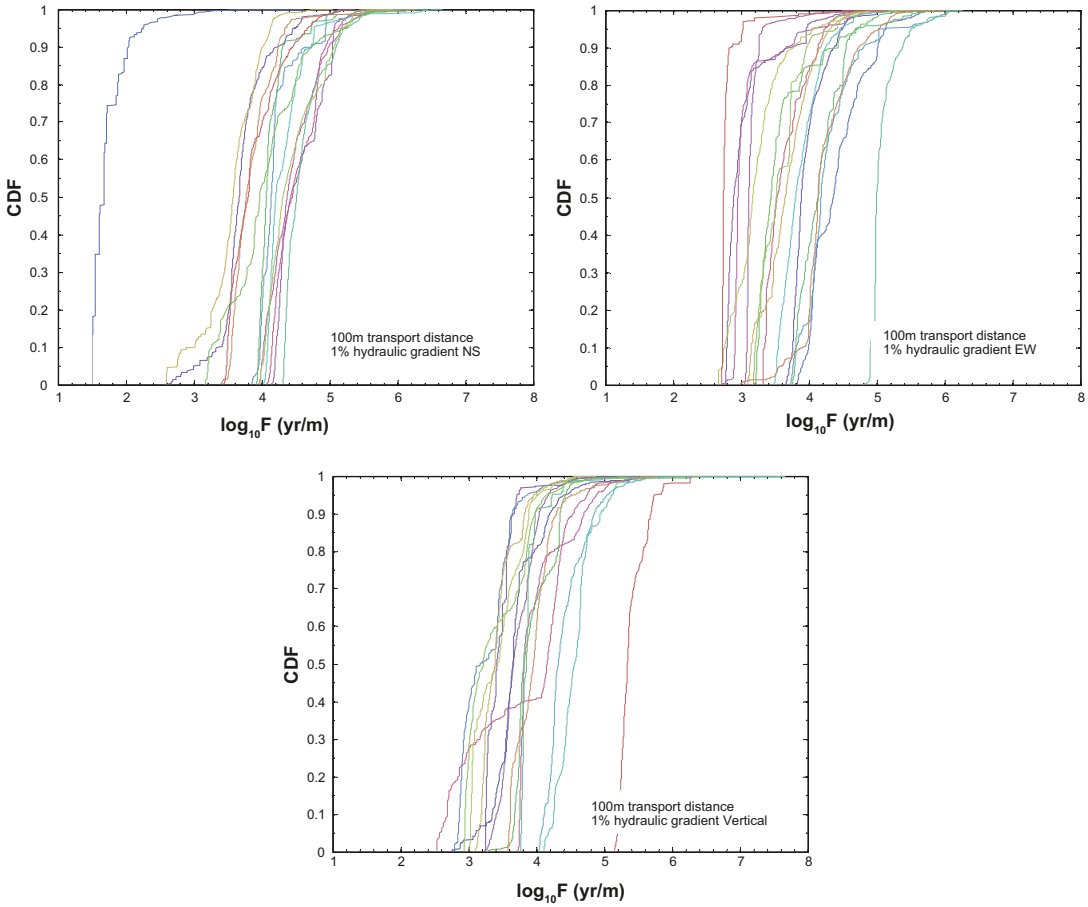

Figure B-11. *Typical F-factor distributions obtained using particle tracking for HRD_W in the elevation interval –400 m to –650 m based on 20 realisations of the Hydrogeological DFN in Napsac/ConnectFlow. The calculations consider a boundary plane separation distance of 100 m for a 1% hydraulic gradient applied along each of the three principal axes of the simulation volume as indicated in the figure. Results are given for the case of neutrally conductive FIZ only and are plotted as cumulative distribution probability curves for each individual realisation.*

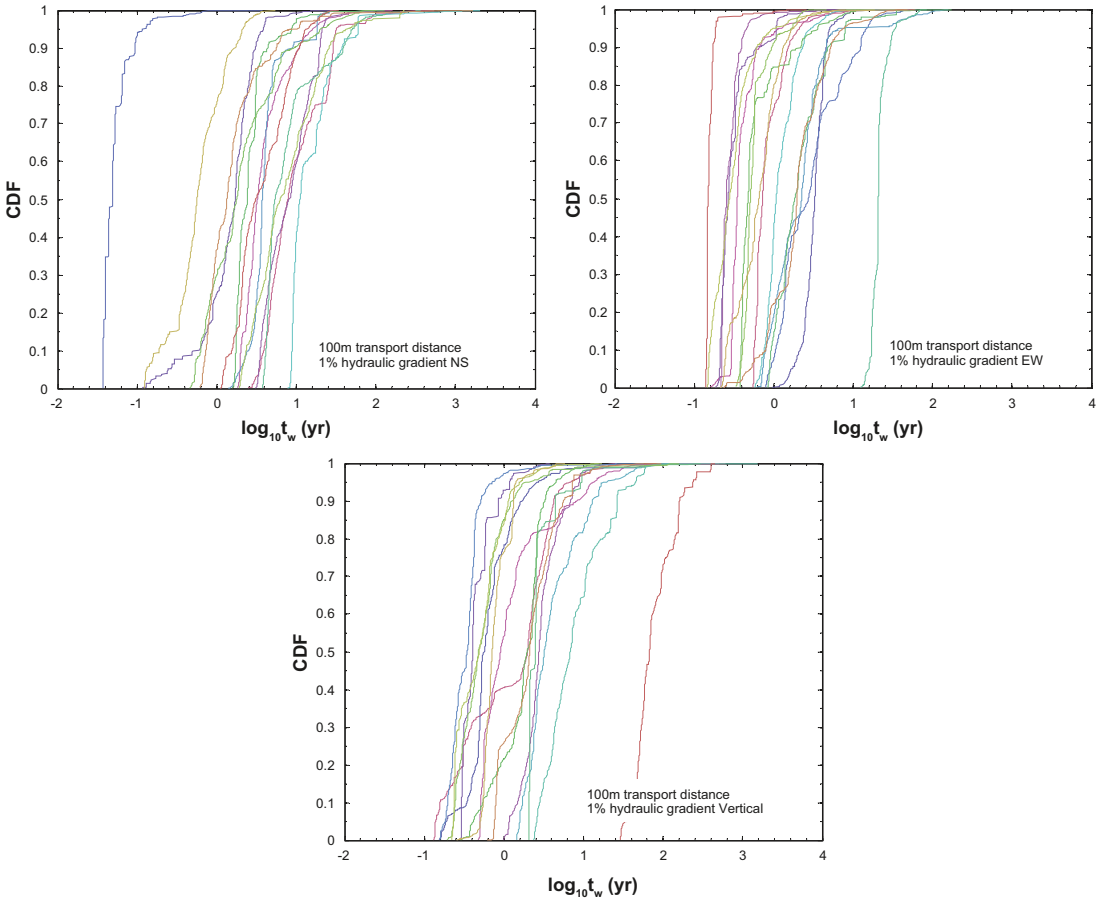

Figure B-12. *Typical advective travel time distributions obtained using particle tracking for HRD_W in the elevation interval –400 m to –650 m based on 20 realisations of the Hydrogeological DFN in Napsac/ConnectFlow. The calculations consider a boundary plane separation distance of 100 m for a 1% hydraulic gradient applied along each of the three principal axes of the simulation volume as indicated in the figure. Results are given for the case of neutrally conductive FIZ only and are plotted as cumulative distribution probability curves for each individual realisation.*

Table B-10. Summary statistics for the F-factor and advective travel time (log_{10} units) corresponding to the pooled particle tracking data for HRD_W in the elevation interval –400 m to –650 m. The data are for different transport distances assuming a 1% reference hydraulic gradient applied along the north-south axis (20 pooled stochastic DFN realisations with 1,000 particles released in each realisation). Results are given for the neutrally conductive FIZ case only.

North-South case	log_{10} F (yr/m)				log_{10} tw (yr)			
Semi-Correlated (SC)	25 m	50 m	75 m	100 m	25 m	50 m	75 m	100 m
Mean	2.15	3.08	3.51	4.01	–1.27	–0.41	–0.03	0.45
Median	2.33	3.35	3.66	4.13	–1.25	–0.26	0.01	0.53
5th percentile	0.09	1.07	1.81	1.72	–2.40	–1.81	–1.28	–1.28
10th percentile	0.34	1.24	2.04	3.29	–2.21	–1.67	–1.01	–0.35
25th percentile	1.45	2.60	3.04	3.73	–1.73	–0.92	–0.44	0.20
75th percentile	2.92	3.75	4.14	4.42	–0.78	0.13	0.45	0.89
90th percentile	3.62	3.98	4.59	4.81	–0.34	0.40	0.84	1.25
95th percentile	3.92	4.23	4.84	5.04	0.04	0.56	0.99	1.42
Std. deviation	1.14	0.99	0.90	0.80	0.71	0.73	0.69	0.69
Variance	1.29	0.98	0.81	0.64	0.50	0.54	0.48	0.48
Min value	–0.02	0.42	1.37	1.49	–2.55	–2.09	–1.55	–1.43
Max value	6.57	7.05	7.14	6.66	2.23	2.97	2.94	3.31
Recovered particles	19,000	16,986	15,000	14,000	19,000	16,986	15,000	14,000

Table B-11. Summary statistics for the F-factor and advective travel time (log_{10} units) corresponding to the pooled particle tracking data for HRD_W in the elevation interval –400 m to –650 m. The data are for different transport distances assuming a 1% reference hydraulic gradient applied along the west-east axis (20 pooled stochastic DFN realisations with 1,000 particles released in each realisation). Results are given for the neutrally conductive FIZ case only.

West-East case	log_{10} F (yr/m)				log_{10} tw (yr)			
Semi-Correlated (SC)	25 m	50 m	75 m	100 m	25 m	50 m	75 m	100 m
Mean	2.34	3.08	3.52	3.74	–1.19	–0.60	–0.16	–0.01
Median	2.36	2.93	3.34	3.73	–1.25	–0.76	–0.41	–0.10
5th percentile	0.98	1.70	2.26	2.76	–1.91	–1.48	–1.20	–0.80
10th percentile	1.27	1.81	2.42	2.89	–1.82	–1.42	–0.97	–0.66
25th percentile	1.48	2.45	2.78	3.16	–1.70	–0.96	–0.70	–0.46
75th percentile	3.06	3.78	4.19	4.15	–0.77	–0.17	0.33	0.35
90th percentile	3.54	4.36	4.86	4.72	–0.47	0.29	0.87	0.73
95th percentile	3.74	4.47	5.36	5.01	–0.23	0.46	1.61	1.30
Std. deviation	0.90	0.92	0.96	0.68	0.57	0.68	0.78	0.58
Variance	0.81	0.85	0.92	0.47	0.32	0.46	0.60	0.34
Min value	0.80	0.33	1.60	2.66	–2.00	–3.10	–1.46	–0.85
Max value	6.74	6.65	6.36	6.27	2.51	2.77	2.46	2.24
Recovered particles	20000	18996	18000	16000	20000	18996	18000	16000

Table B-12. Summary statistics for the F-factor and advective travel time (log_{10} units) corresponding to the pooled particle tracking data for HRD_W in the elevation interval –400 m to –650 m. The data are for different transport distances assuming a 1% reference hydraulic gradient applied along the vertical axis (20 pooled stochastic DFN realisations with 1,000 particles released in each realisation). Results are given for the neutrally conductive FIZ case only.

Vertical case	log_{10} F (yr/m)				log_{10} tw (yr)			
Semi-Correlated (SC)	25 m	50 m	75 m	100 m	25 m	50 m	75 m	100 m
Mean	2.84	3.43	3.59	3.90	–0.91	–0.34	–0.10	0.23
Median	2.71	3.35	3.56	3.80	–1.08	–0.44	–0.15	0.15
5th percentile	1.92	2.49	2.67	2.96	–1.43	–1.05	–0.86	–0.62
10th percentile	2.15	2.72	2.95	3.09	–1.40	–0.92	–0.69	–0.52
25th percentile	2.43	2.97	3.27	3.46	–1.24	–0.78	–0.41	–0.28
75th percentile	3.28	3.85	3.88	4.26	–0.65	0.04	0.18	0.51
90th percentile	3.74	4.27	4.32	4.79	–0.26	0.44	0.57	1.11
95th percentile	4.09	4.44	4.54	5.29	0.01	0.69	0.90	1.74
Std. deviation	0.65	0.61	0.53	0.66	0.48	0.56	0.51	0.67
Variance	0.42	0.37	0.28	0.44	0.23	0.31	0.26	0.45
Min value	1.49	2.16	2.33	2.53	–1.59	–1.27	–1.04	–0.89
Max value	5.35	6.26	7.06	7.66	1.72	2.06	3.39	3.19
Recovered particles	19,000	16,000	13,000	14,899	19,000	16,000	13,000	14,899

Modelling results for HRD_EW007

Matlab simulation results for the path of least transport resistance (PLTR)

Figure B-13 shows the percolation probability, P_{con} plotted as a function of boundary plane separation distance for hydraulic connectivity along the different principal axes of the simulation 100 m simulation volume.

The stochastic analysis indicates relatively homogeneous and strong hydraulic connectivity along all three axes (although slightly lower along the north-south axis) with no identifiable percolation threshold. The hydraulic connectivity in HRD_EW007 is higher than any of the other hydraulic rock domains investigated.

Figure B-14 to Figure B-16 shows plots of F-factor ranges for the path of least transport resistance (PLTR) along typical transport paths within HRD_EW007 assuming a 1% hydraulic gradient applied along each of the three principal axes of the simulation volume and at different boundary plane separation distances. Summary statistics corresponding to the plotted data are given in Table B-13 to Table B-15.

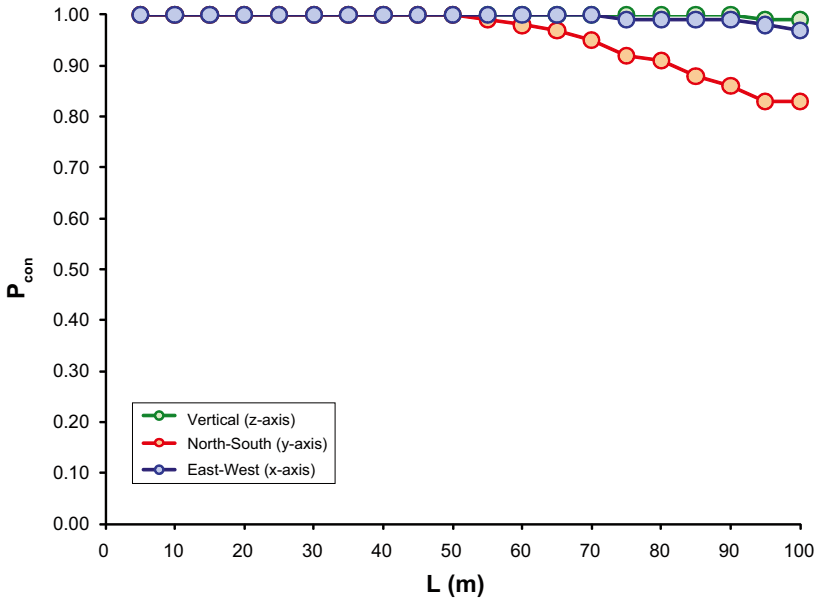

Figure B-13. *Results of connectivity analysis for HRD_EW007 (–400 m to –650 m) based upon 100 stochastic realisations of the Hydrogeological DFN model based on open and partly open fractures (OPO). The percolation probability is plotted as a function of distance for the three principal axes of the model.*

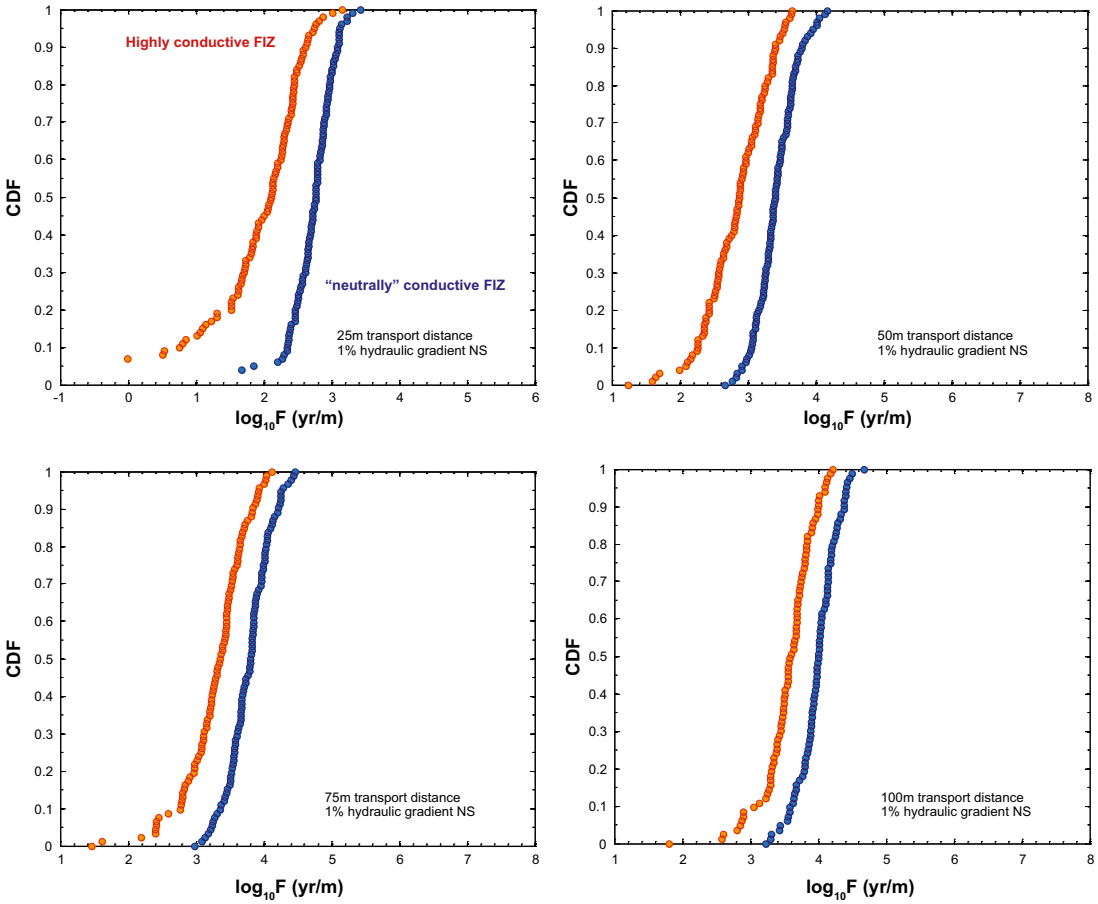

Figure B-14. *Typical F-factor ranges for the path of least resistance, PLTR in HRD_EW007 in the elevation interval –400 m to –650 m based on 100 realisations of the Hydrogeological DFN. The calculations consider boundary plane separation distances of 25 m, 50 m, 75 m and 100 m for a 1% hydraulic gradient applied along the north-south axis of the simulation volume. Results are given for the case of neutrally conductive FIZ (blue markers) and for highly conductive FIZ (red-orange markers) and are plotted as cumulative distribution probability curves.*

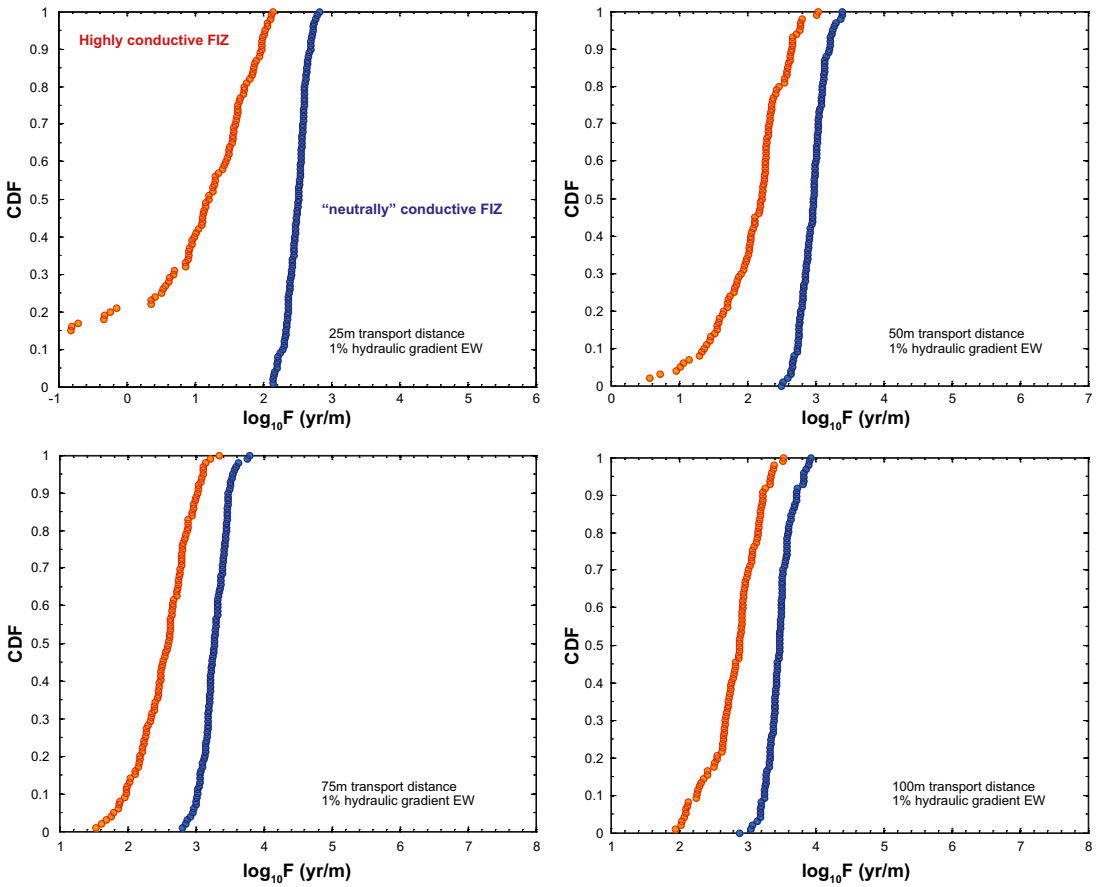

Figure B-15. *Typical F-factor ranges for the path of least resistance, PLTR in HRD_EW007 in the elevation interval –400 m to –650 m based on 100 realisations of the Hydrogeological DFN. The calculations consider boundary plane separation distances of 25 m, 50 m, 75 m and 100 m for a 1% hydraulic gradient applied along the west-east axis of the simulation volume. Results are given for the case of neutrally conductive FIZ (blue markers) and for highly conductive FIZ (red-orange markers) and are plotted as cumulative distribution probability curves.*

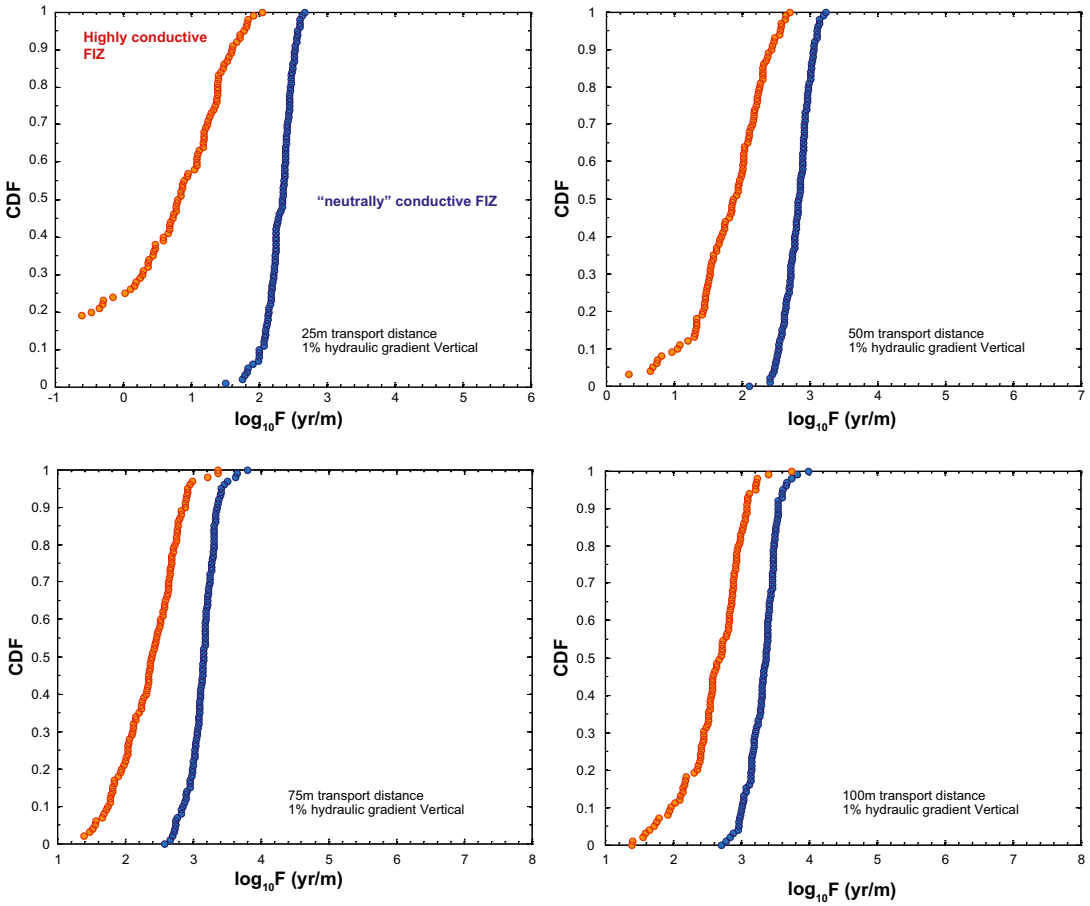

Figure B-16. *Typical F-factor ranges for the path of least resistance, PLTR in HRD_EW007 in the elevation interval –400 m to –650 m based on 100 realisations of the Hydrogeological DFN. The calculations consider boundary plane separation distances of 25 m, 50 m, 75 m and 100 m for a 1% hydraulic gradient applied along the vertical axis of the simulation volume. Results are given for the case of neutrally conductive FIZ (blue markers) and for highly conductive FIZ (red-orange markers) and are plotted as cumulative distribution probability curves.*

Table B-13. Summary statistics for the F-factor (log_{10} units) corresponding to the pooled simulation data for HRD_EW007 in the elevation interval –400 m to –650 m. The data are for the path of least transport resistance (PLTR) over different transport distances assuming a 1% reference hydraulic gradient applied along the north-south axis (100 stochastic DFN realisations). Results are given for both the neutrally conductive FIZ case as well as the highly-conductive FIZ case.

North-South case	log_{10}F (neutrally conductive FIZ)				log_{10}F (highly-conductive FIZ)			
Semi-Correlated (SC)	**25 m**	**50 m**	**75 m**	**100 m**	**25 m**	**50 m**	**75 m**	**100 m**
Mean	2.75	3.42	3.78	3.99	1.83	2.83	3.28	3.55
Median	2.77	3.40	3.81	4.00	2.13	2.87	3.36	3.60
5th percentile	2.32	2.91	3.23	3.44	0.52	2.04	2.41	2.83
10th percentile	2.37	3.05	3.35	3.58	1.03	2.26	2.73	3.04
25th percentile	2.57	3.23	3.56	3.84	1.67	2.52	3.07	3.39
75th percentile	2.95	3.62	4.00	4.18	2.43	3.19	3.60	3.80
90th percentile	3.11	3.80	4.22	4.38	2.64	3.41	3.84	4.00
95th percentile	3.14	3.99	4.29	4.42	2.76	3.54	3.93	4.11
Std. deviation	0.29	0.30	0.32	0.29	1.20	0.49	0.49	0.40
Variance	0.08	0.09	0.10	0.08	1.43	0.24	0.24	0.16
Min value	1.68	2.66	2.98	3.23	–4.20	1.24	1.46	1.80
Max value	3.43	4.17	4.47	4.68	3.15	3.66	4.12	4.22
Connected fraction (%)	97	100	93	84	97	100	93	84

Table B-14. Summary statistics for the F-factor (log_{10} units) corresponding to the pooled simulation data for HRD_EW007 in the elevation interval –400 m to –650 m. The data are for the path of least transport resistance (PLTR) over different transport distances assuming a semi-correlated fracture length-transmissivity model and 1% reference hydraulic gradient applied along the west-east axis (100 stochastic DFN realisations). Results are given for both the neutrally conductive FIZ case as well as the highly-conductive FIZ case.

West-East case	log_{10}F (neutrally conductive FIZ)				log_{10}F (highly-conductive FIZ)			
Semi-Correlated (SC)	25 m	50 m	75 m	100 m	25 m	50 m	75 m	100 m
Mean	2.50	2.96	3.28	3.47	0.45	1.97	2.54	2.81
Median	2.52	2.98	3.28	3.48	1.21	2.21	2.61	2.89
5th percentile	2.20	2.65	2.96	3.19	–4.38	0.99	1.83	2.09
10th percentile	2.30	2.73	3.03	3.25	–4.27	1.36	1.98	2.25
25th percentile	2.39	2.82	3.17	3.35	0.52	1.79	2.26	2.66
75th percentile	2.60	3.09	3.43	3.58	1.64	2.36	2.81	3.08
90th percentile	2.70	3.21	3.49	3.72	1.98	2.65	3.03	3.23
95th percentile	2.74	3.27	3.56	3.83	2.05	2.77	3.11	3.35
Std. deviation	0.15	0.19	0.19	0.19	2.05	0.99	0.39	0.42
Variance	0.02	0.03	0.04	0.04	4.19	0.98	0.15	0.18
Min value	2.15	2.50	2.80	2.89	–4.53	–4.16	1.53	0.65
Max value	2.83	3.40	3.79	3.94	2.14	3.04	3.34	3.53
Connected fraction (%)	100	100	99	98	100	100	99	98

Table B-15. Summary statistics for the F-factor (log_{10} units) corresponding to the pooled simulation data for HRD_EW007 in the elevation interval –400 m to –650 m. The data are for the path of least transport resistance (PLTR) over different transport distances assuming a 1% reference hydraulic gradient applied along the vertical axis (100 stochastic DFN realisations). Results are given for both the neutrally conductive FIZ case as well as the highly-conductive FIZ case.

Vertical case	log_{10}F (neutrally conductive FIZ)				log_{10}F (highly-conductive FIZ)			
Semi-Correlated (SC)	25 m	50 m	75 m	100 m	25 m	50 m	75 m	100 m
Mean	2.30	2.82	3.14	3.33	0.02	1.66	2.34	2.62
Median	2.35	2.84	3.16	3.37	0.83	1.87	2.39	2.70
5th percentile	1.87	2.48	2.74	2.96	–4.51	0.67	1.55	1.69
10th percentile	2.04	2.54	2.85	3.01	–4.36	1.02	1.74	1.96
25th percentile	2.19	2.69	3.03	3.18	0.07	1.48	2.04	2.41
75th percentile	2.45	2.96	3.28	3.47	1.37	2.22	2.69	2.93
90th percentile	2.54	3.06	3.37	3.55	1.61	2.45	2.89	3.09
95th percentile	2.59	3.12	3.44	3.64	1.80	2.58	2.94	3.21
Std. deviation	0.21	0.20	0.21	0.22	2.10	1.11	0.48	0.45
Variance	0.04	0.04	0.05	0.05	4.41	1.24	0.23	0.20
Min value	1.51	2.11	2.59	2.71	–4.63	–4.19	0.54	1.40
Max value	2.68	3.24	3.80	4.00	2.05	2.71	3.37	3.75
Connected fraction (%)	100	100	100	100	100	100	100	100

Napsac/ConnectFlow simulation results using particle tracking

Figure B-17 shows F-factor distributions calculated using the particle tracking capabilities of Napsac/ConnectFlow for a boundary plane separation distance of 100 m along the different principal axes of the simulation volume. Since it is not possible to simulate highly conductive fracture intersections (FIZ) in any simple manner, only the base case of neutrally conductive FIZ has been considered. The cumulative curves correspond to the ensemble of 1,000 particles released in each individual simulation (20 stochastic realisations). The corresponding cumulative distributions of advective travel times are shown in Figure B-18. Summary statistics for the F-factor and advective travel time are given in Table B-16 to Table B-18 for different boundary plane separation distances and for transport along the different principal axis directions. The summary statistics represent a pooling of all particle tracking results from individual realisations.

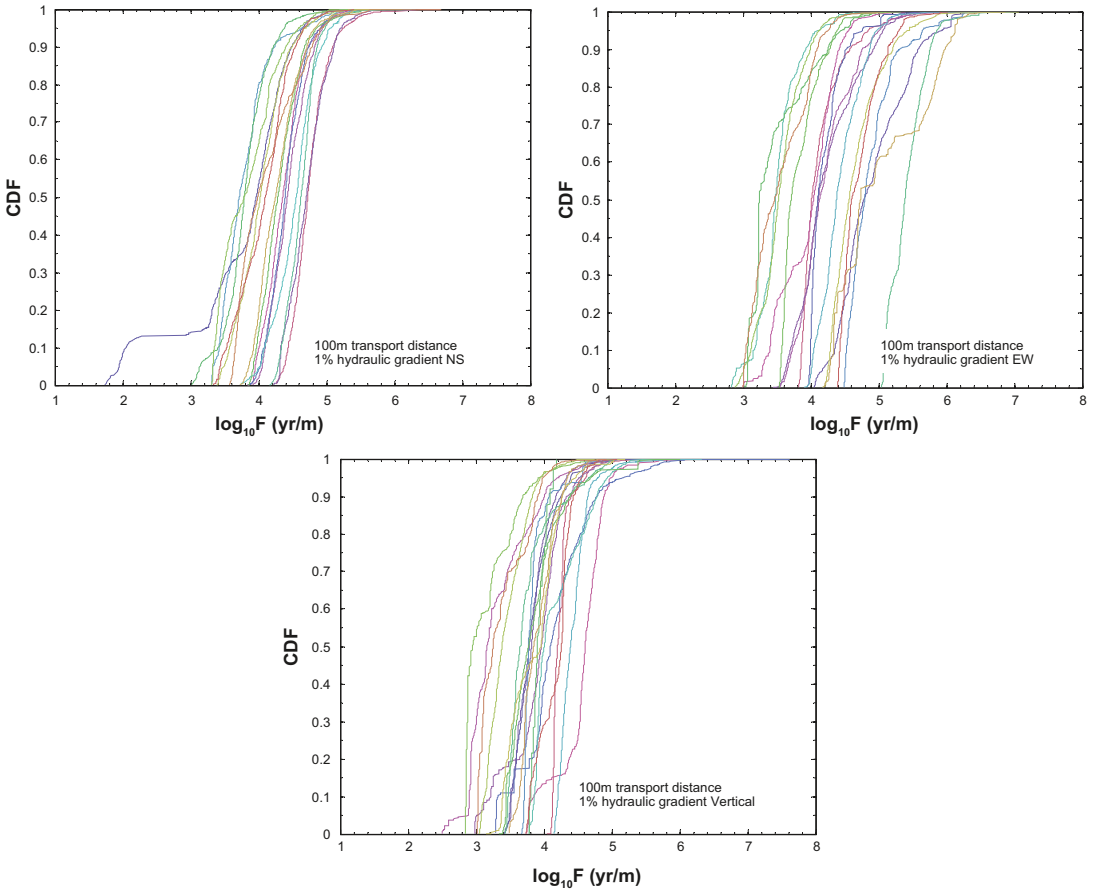

Figure B-17. *Typical F-factor distributions obtained using particle tracking for HRD_EW007 in the elevation interval –400 m to –650 m based on 20 realisations of the Hydrogeological DFN in Napsac/ConnectFlow. The calculations consider a boundary plane separation distance of 100 m for a 1% hydraulic gradient applied along each of the three principal axes of the simulation volume as indicated in the figure. Results are given for the case of neutrally conductive FIZ only and are plotted as cumulative distribution probability curves for each individual realisation.*

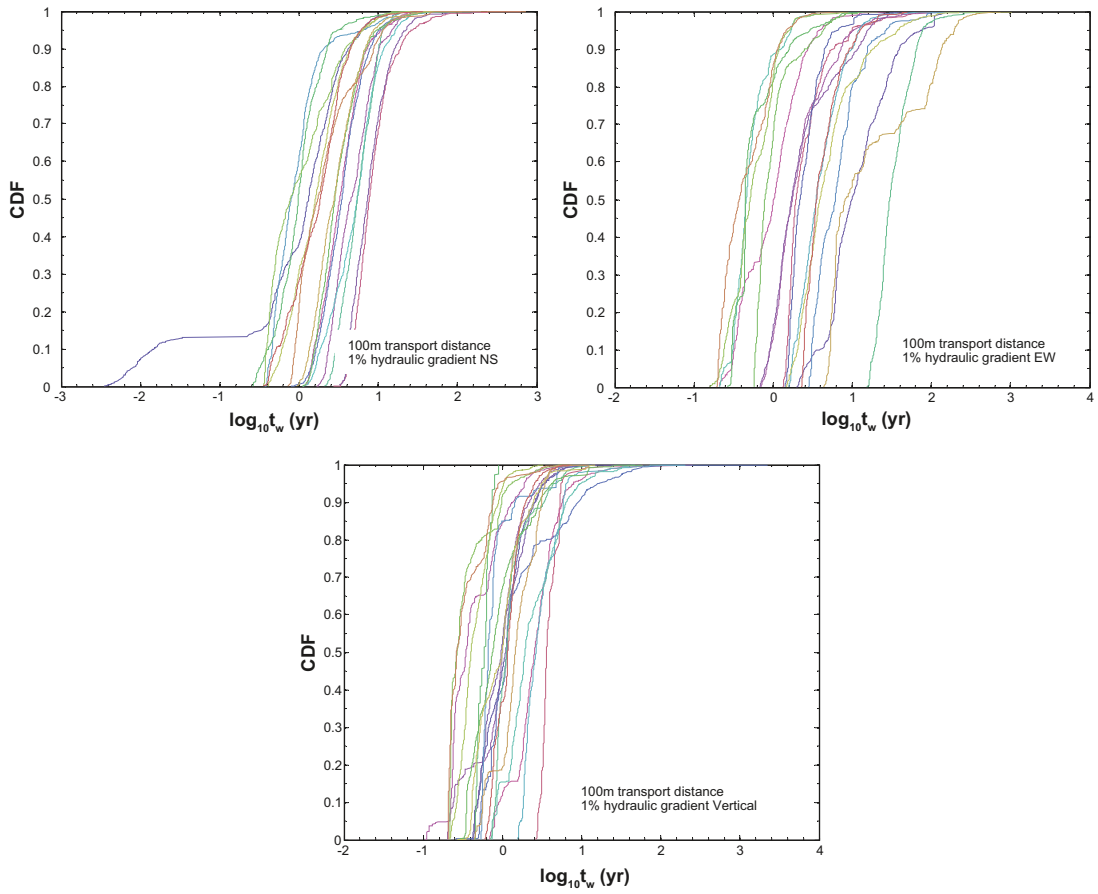

Figure B-18. *Typical advective travel time distributions obtained using particle tracking for HRD_EW007 in the elevation interval –400 m to –650 m based on 20 realisations of the Hydrogeological DFN in Napsac/ConnectFlow. The calculations consider a boundary plane separation distance of 100 m for a 1% hydraulic gradient applied along each of the three principal axes of the simulation volume as indicated in the figure. Results are given for the case of neutrally conductive FIZ only and are plotted as cumulative distribution probability curves for each individual realisation.*

Table B-16. Summary statistics for the F-factor and advective travel time (log_{10} units) corresponding to the pooled particle tracking data for HRD_EW007 in the elevation interval –400 m to –650 m. The data are for different transport distances assuming a 1% reference hydraulic gradient applied along the north-south axis (20 pooled stochastic DFN realisations with 1,000 particles released in each realisation). Results are given for the neutrally conductive FIZ case only.

North-South case	log_{10} F (yr/m)				log_{10} tw (yr)			
Semi-Correlated (SC)	25 m	50 m	75 m	100 m	25 m	50 m	75 m	100 m
Mean	3.16	3.72	4.10	4.24	–0.63	–0.09	0.28	0.42
Median	3.15	3.68	4.10	4.28	–0.68	–0.14	0.27	0.45
5th percentile	2.36	3.04	3.27	3.43	–1.29	–0.70	–0.51	–0.34
10th percentile	2.56	3.13	3.40	3.60	–1.11	–0.61	–0.39	–0.19
25th percentile	2.80	3.38	3.71	3.94	–0.94	–0.40	–0.09	0.13
75th percentile	3.54	4.02	4.48	4.59	–0.35	0.14	0.63	0.75
90th percentile	3.85	4.34	4.76	4.81	–0.02	0.48	0.91	0.97
95th percentile	4.05	4.59	4.93	4.97	0.14	0.71	1.06	1.10
Std. deviation	0.56	0.48	0.52	0.50	0.46	0.43	0.49	0.49
Variance	0.31	0.23	0.27	0.25	0.21	0.19	0.24	0.24
Min value	1.51	2.47	2.69	1.74	–1.75	–1.12	–0.90	–2.46
Max value	6.14	6.59	6.96	6.69	2.18	2.79	3.06	2.86
Recovered particles	19,983	19,981	17,987	15,988	19,983	19,981	17,987	15,988

Table B-17. Summary statistics for the F-factor and advective travel time (log_{10} units) corresponding to the pooled particle tracking data for HRD_EW007 in the elevation interval –400 m to –650 m. The data are for different transport distances assuming a 1% reference hydraulic gradient applied along the west-east axis (20 pooled stochastic DFN realisations with 1,000 particles released in each realisation). Results are given for the neutrally conductive FIZ case only.

West-East case	log_{10} F (yr/m)				log_{10} tw (yr)			
Semi-Correlated (SC)	25 m	50 m	75 m	100 m	25 m	50 m	75 m	100 m
Mean	2.79	3.40	3.87	4.28	–0.99	–0.42	0.01	0.41
Median	2.82	3.39	3.90	4.25	–0.99	–0.46	0.02	0.36
5th percentile	1.92	2.53	2.89	3.20	–1.50	–1.02	–0.75	–0.52
10th percentile	2.02	2.73	3.11	3.37	–1.47	–0.94	–0.59	–0.39
25th percentile	2.33	3.03	3.44	3.77	–1.31	–0.72	–0.36	–0.06
75th percentile	3.14	3.70	4.32	4.70	–0.75	–0.22	0.41	0.79
90th percentile	3.57	4.08	4.72	5.22	–0.51	0.10	0.78	1.32
95th percentile	3.75	4.32	4.96	5.56	–0.29	0.36	1.01	1.60
Std. deviation	0.58	0.54	0.75	0.70	0.40	0.42	0.68	0.64
Variance	0.34	0.29	0.56	0.49	0.16	0.18	0.47	0.41
Min value	1.56	1.40	0.71	2.83	–1.74	–2.41	–3.13	–0.80
Max value	5.65	7.25	7.09	7.06	1.67	2.95	2.79	3.01
Recovered particles	20,000	20,000	18,000	16,997	20,000	20,000	18,000	16,997

Table B-18. Summary statistics for the F-factor and advective travel time (log_{10} units) corresponding to the pooled particle tracking data for HRD_EW007 in the elevation interval –400 m to –650 m. The data are for different transport distances assuming a 1% reference hydraulic gradient applied along the vertical axis (20 pooled stochastic DFN realisations with 1,000 particles released in each realisation). Results are given for the neutrally conductive FIZ case only.

Vertical case	log_{10} F (yr/m)				log_{10} tw (yr)			
Semi-Correlated (SC)	25 m	50 m	75 m	100 m	25 m	50 m	75 m	100 m
Mean	2.65	3.09	3.35	3.88	–1.12	–0.70	–0.45	0.02
Median	2.60	3.08	3.32	3.88	–1.17	–0.75	–0.51	–0.02
5th percentile	2.16	2.46	2.66	3.02	–1.41	–1.12	–0.92	–0.64
10th percentile	2.21	2.50	2.75	3.20	–1.38	–1.09	–0.86	–0.54
25th percentile	2.41	2.81	3.05	3.58	–1.28	–0.91	–0.69	–0.26
75th percentile	2.85	3.36	3.63	4.20	–1.02	–0.52	–0.25	0.29
90th percentile	3.13	3.66	3.92	4.53	–0.79	–0.23	0.04	0.57
95th percentile	3.31	3.84	4.11	4.69	–0.61	–0.02	0.21	0.72
Std. deviation	0.36	0.49	0.45	0.50	0.26	0.41	0.36	0.42
Variance	0.13	0.24	0.20	0.25	0.07	0.17	0.13	0.17
Min value	1.47	0.11	1.25	2.50	–2.42	–3.54	–2.61	–0.97
Max value	4.99	5.34	6.85	7.62	1.30	1.66	2.93	3.35
Recovered particles	20,000	19,980	19,961	18,997	20,000	19,980	19,961	18,997

Modelling results for HRD_N

Matlab simulation results for the path of least transport resistance (PLTR)

Figure B-19 shows the percolation probability, P_{con} plotted as a function of boundary plane separation distance for hydraulic connectivity along the different principal axes of the simulation 100 m simulation volume.

The stochastic analysis gives some indications of anisotropy along the different principal axes with greater connectivity in the vertical direction than along the north-south or west-east axes. The connectivity along the vertical axis is not associated with any well defined percolation threshold, although the percolation threshold for the horizontal directions appears to occur at a boundary plane separation distance on the order of 90–100 m. This hydraulic rock domain has a generally greater degree of hydraulic connectivity than either HRD_C or HRD_W although somewhat less than HRD_EW007.

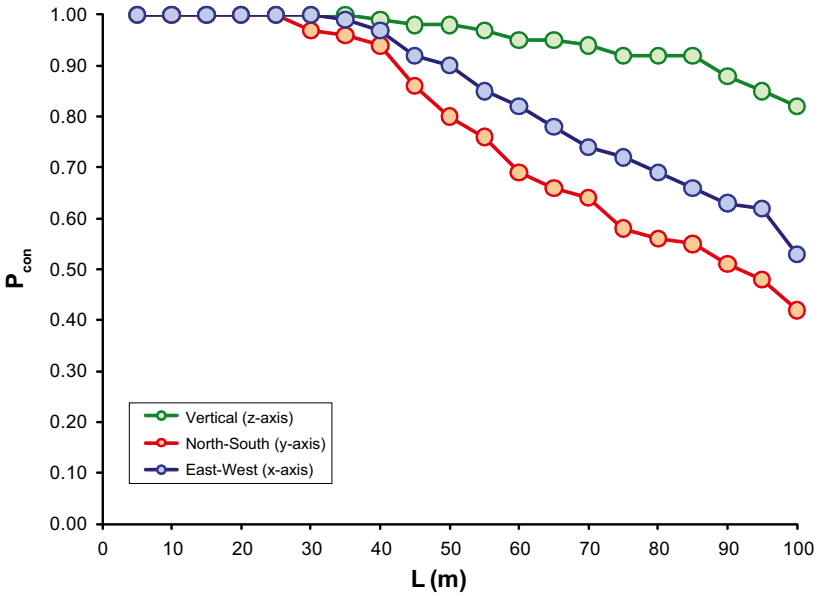

Figure B-19. *Results of connectivity analysis for HRD_N (–400 m to –650 m) based upon 100 stochastic realisations of the Hydrogeological DFN model based on open and partly open fractures (OPO). The percolation probability is plotted as a function of distance for the three principal axes of the model.*

Figure B-20 to Figure B-22 shows plots of F-factor ranges for the path of least transport resistance (PLTR) along typical transport paths within HRD_N assuming a 1% hydraulic gradient applied along each of the three principal axes of the simulation volume and at different boundary plane separation distances. Summary statistics corresponding to the plotted data are given in Table B-19 to Table B-21.

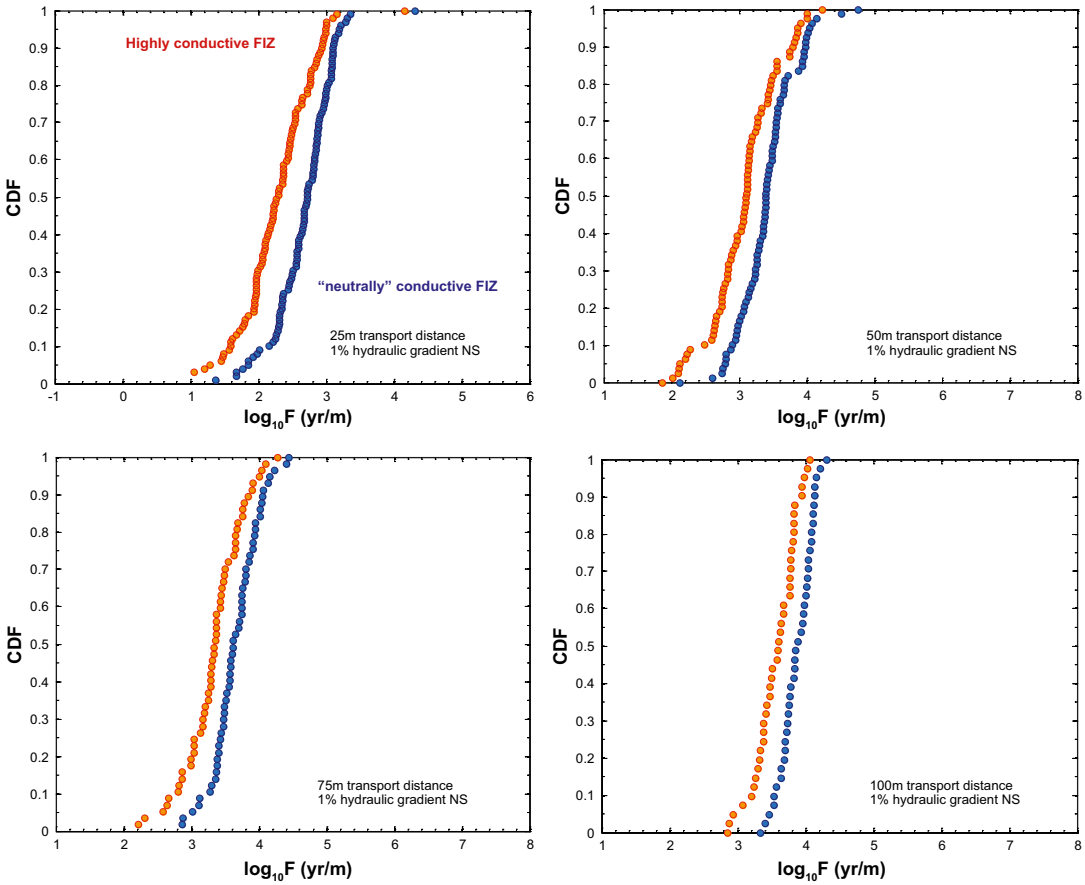

Figure B-20. *Typical F-factor ranges for the path of least resistance, PLTR in HRD_N in the elevation interval –400 m to –650 m based on 100 realisations of the Hydrogeological DFN. The calculations consider boundary plane separation distances of 25 m, 50 m, 75 m and 100 m for a 1% hydraulic gradient applied along the north-south axis of the simulation volume. Results are given for the case of neutrally conductive FIZ (blue markers) and for highly conductive FIZ (red-orange markers) and are plotted as cumulative distribution probability curves.*

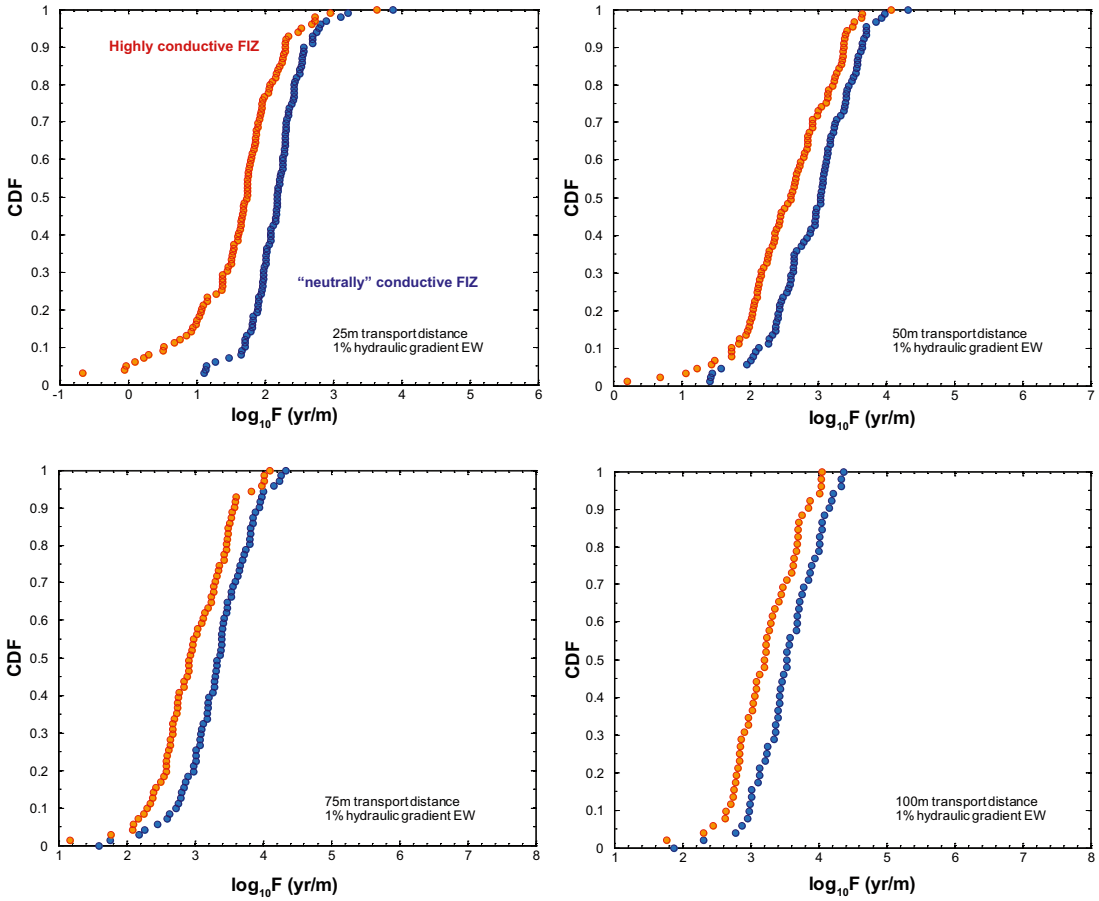

Figure B-21. *Typical F-factor ranges for the path of least resistance, PLTR in HRD_N in the elevation interval –400 m to –650 m based on 100 realisations of the Hydrogeological DFN. The calculations consider boundary plane separation distances of 25 m, 50 m, 75 m and 100 m for a 1% hydraulic gradient applied along the west-east axis of the simulation volume. Results are given for the case of neutrally conductive FIZ (blue markers) and for highly conductive FIZ (red-orange markers) and are plotted as cumulative distribution probability curves.*

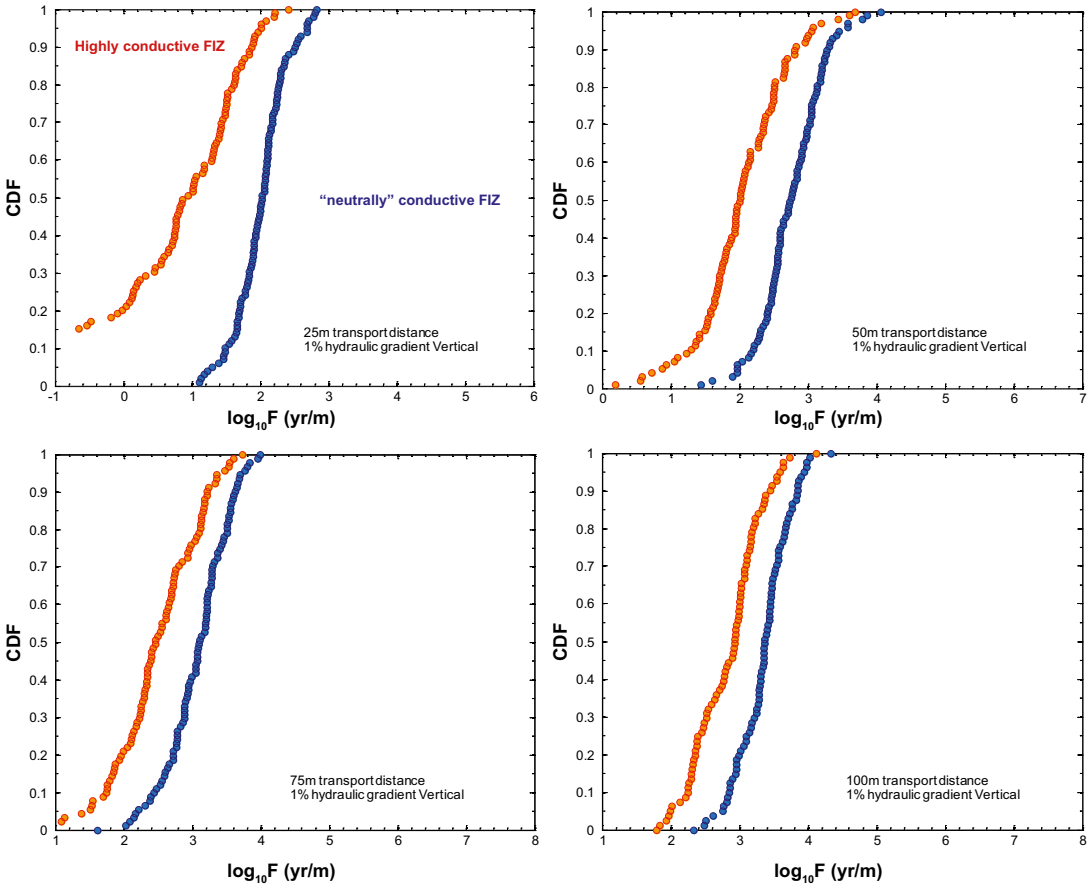

Figure B-22. *Typical F-factor ranges for the path of least resistance, PLTR in HRD_N in the elevation interval –400 m to –650 m based on 100 realisations of the Hydrogeological DFN. The calculations consider boundary plane separation distances of 25 m, 50 m, 75 m and 100 m for a 1% hydraulic gradient applied along the vertical axis of the simulation volume. Results are given for the case of neutrally conductive FIZ (blue markers) and for highly conductive FIZ (red-orange markers) and are plotted as cumulative distribution probability curves.*

Table B-19. Summary statistics for the F-factor (log_{10} units) corresponding to the pooled simulation data for HRD_N in the elevation interval –400 m to –650 m. The data are for the path of least transport resistance (PLTR) over different transport distances assuming a 1% reference hydraulic gradient applied along the north-south axis (100 stochastic DFN realisations). Results are given for both the neutrally conductive FIZ case as well as the highly-conductive FIZ case.

North-South case	log_{10}F (neutrally conductive FIZ)				log_{10}F (highly-conductive FIZ)			
Semi-Correlated (SC)	25 m	50 m	75 m	100 m	25 m	50 m	75 m	100 m
Mean	2.68	3.41	3.66	3.87	2.20	3.08	3.34	3.56
Median	2.72	3.40	3.62	3.87	2.30	3.11	3.36	3.60
5th percentile	1.85	2.77	3.05	3.44	1.36	2.12	2.61	2.92
10th percentile	2.18	2.89	3.29	3.53	1.60	2.38	2.81	3.17
25th percentile	2.45	3.16	3.44	3.70	1.97	2.77	3.11	3.38
75th percentile	2.98	3.61	3.91	4.06	2.64	3.42	3.65	3.80
90th percentile	3.11	3.98	4.06	4.13	2.95	3.80	3.89	3.94
95th percentile	3.21	4.06	4.21	4.18	3.00	3.89	4.03	4.00
Std. deviation	0.43	0.43	0.34	0.24	0.92	0.50	0.42	0.31
Variance	0.19	0.18	0.12	0.06	0.84	0.25	0.18	0.09
Min value	1.37	2.12	2.87	3.34	–4.25	1.86	2.22	2.86
Max value	4.31	4.76	4.44	4.31	4.16	4.24	4.28	4.07
Connected fraction (%)	99	80	57	42	99	80	57	42

Table B-20. Summary statistics for the F-factor (log_{10} units) corresponding to the pooled simulation data for HRD_N in the elevation interval –400 m to –650 m. The data are for the path of least transport resistance (PLTR) over different transport distances assuming a semi-correlated fracture length-transmissivity model and 1% reference hydraulic gradient applied along the west-east axis (100 stochastic DFN realisations). Results are given for both the neutrally conductive FIZ case as well as the highly-conductive FIZ case.

West-East case	log_{10}F (neutrally conductive FIZ)				log_{10}F (highly-conductive FIZ)			
Semi-Correlated (SC)	25 m	50 m	75 m	100 m	25 m	50 m	75 m	100 m
Mean	2.19	2.95	3.31	3.53	1.64	2.57	2.92	3.17
Median	2.19	3.04	3.35	3.54	1.74	2.61	2.92	3.20
5th percentile	1.54	1.94	2.29	2.80	0.25	1.43	2.09	2.33
10th percentile	1.72	2.19	2.70	2.98	0.77	1.78	2.28	2.64
25th percentile	1.97	2.56	3.02	3.24	1.38	2.12	2.60	2.84
75th percentile	2.42	3.40	3.69	3.91	1.98	3.13	3.39	3.64
90th percentile	2.67	3.65	3.95	4.17	2.30	3.38	3.59	3.85
95th percentile	2.81	3.72	4.14	4.32	2.63	3.51	3.97	4.04
Std. deviation	0.42	0.60	0.54	0.50	0.67	0.68	0.68	0.59
Variance	0.17	0.36	0.29	0.25	0.46	0.47	0.47	0.35
Min value	1.12	1.41	1.59	1.88	–0.67	0.21	–0.52	0.74
Max value	3.88	4.33	4.33	4.36	3.64	4.08	4.10	4.05
Connected fraction (%)	97	89	72	53	97	89	72	53

Table B-21. Summary statistics for the F-factor (log_{10} units) corresponding to the pooled simulation data for HRD_N in the elevation interval –400 m to –650 m. The data are for the path of least transport resistance (PLTR) over different transport distances assuming a 1% reference hydraulic gradient applied along the vertical axis (100 stochastic DFN realisations). Results are given for both the neutrally conductive FIZ case as well as the highly-conductive FIZ case.

Vertical case	log_{10}F (neutrally conductive FIZ)				log_{10}F (highly-conductive FIZ)			
Semi-Correlated (SC)	25 m	50 m	75 m	100 m	25 m	50 m	75 m	100 m
Mean	2.02	2.76	3.07	3.36	0.35	2.04	2.48	2.84
Median	2.03	2.76	3.10	3.37	0.95	2.01	2.46	2.93
5th percentile	1.34	1.97	2.17	2.70	–4.50	0.90	1.39	1.98
10th percentile	1.51	2.21	2.43	2.84	–4.37	1.31	1.73	2.24
25th percentile	1.79	2.49	2.78	3.10	0.15	1.67	2.12	2.39
75th percentile	2.24	3.06	3.42	3.60	1.51	2.48	2.97	3.16
90th percentile	2.53	3.30	3.64	3.85	1.89	2.82	3.23	3.46
95th percentile	2.69	3.54	3.76	3.96	2.02	3.07	3.46	3.61
Std. deviation	0.37	0.47	0.47	0.39	1.96	0.65	0.63	0.49
Variance	0.14	0.22	0.22	0.15	3.83	0.42	0.39	0.24
Min value	1.11	1.44	1.62	2.34	–4.77	0.19	0.87	1.80
Max value	2.82	4.06	3.99	4.34	2.42	3.69	3.74	4.12
Connected fraction (%)	99	97	92	82	99	97	92	82

Napsac/ConnectFlow simulation results using particle tracking

Figure B-23 shows F-factor distributions calculated using the particle tracking capabilities of Napsac/ConnectFlow for a boundary plane separation distance of 100 m along the different principal axes of the simulation volume. Since it is not possible to simulate highly conductive fracture intersections (FIZ) in any simple manner, only the base case of neutrally conductive FIZ has been considered. The cumulative curves correspond to the ensemble of 1,000 particles released in each individual simulation (20 stochastic realisations). The corresponding cumulative distributions of advective travel times are shown in Figure B-24. Summary statistics for the F-factor and advective travel time are given in Table B-22 to Table B-24 for different boundary plane separation distances and for transport along the different principal axis directions. The summary statistics represent a pooling of all particle tracking results from individual realisations.

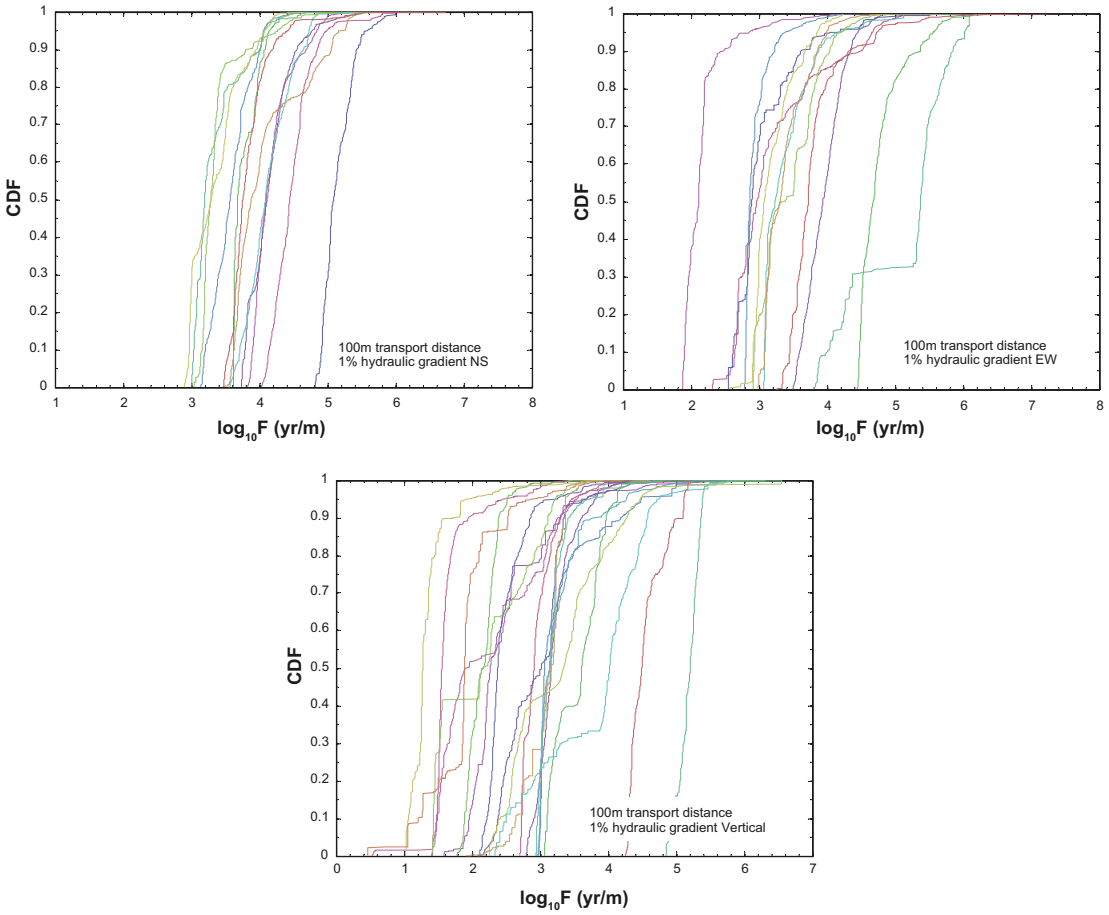

Figure B-23. *Typical F-factor distributions obtained using particle tracking for HRD_N in the elevation interval –400 m to –650 m based on 20 realisations of the Hydrogeological DFN in Napsac/ConnectFlow. The calculations consider a boundary plane separation distance of 100 m for a 1% hydraulic gradient applied along each of the three principal axes of the simulation volume as indicated in the figure. Results are given for the case of neutrally conductive FIZ only and are plotted as cumulative distribution probability curves for each individual realisation.*

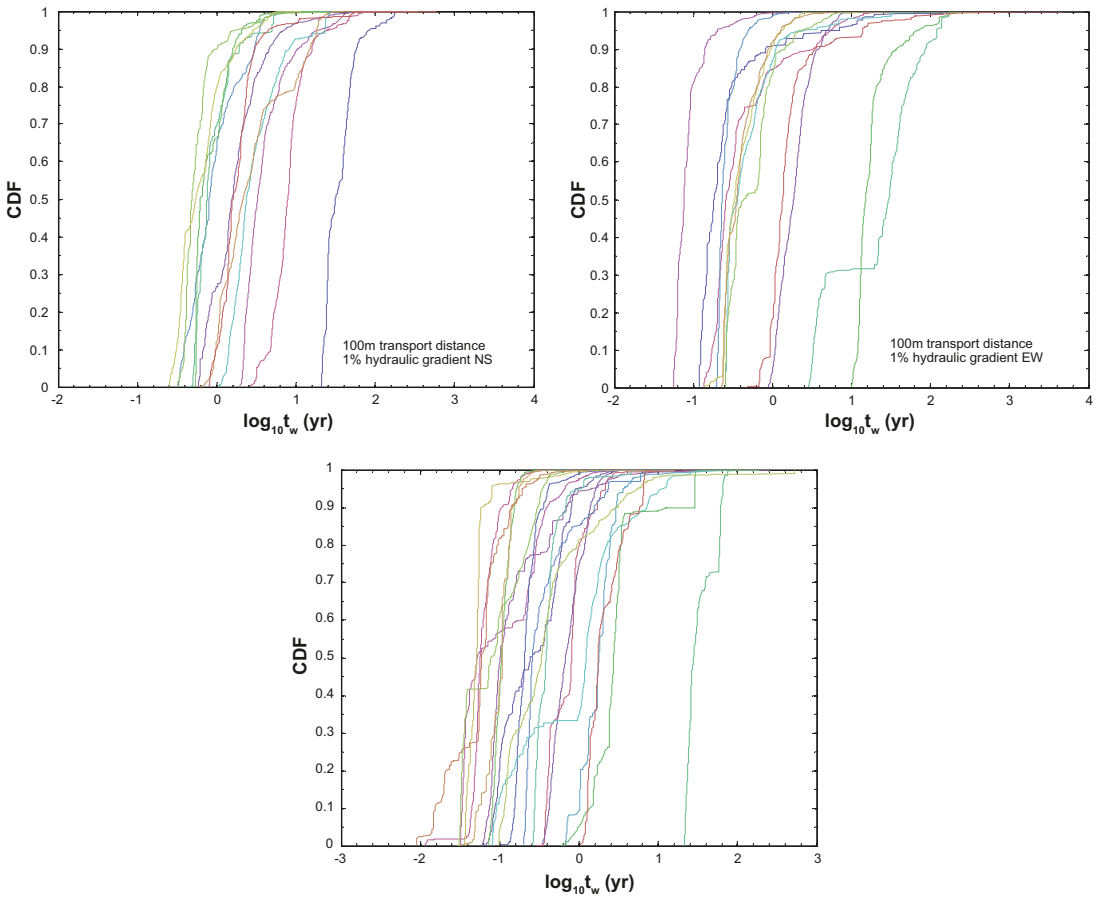

Figure B-24. *Typical advective travel time distributions obtained using particle tracking for HRD_N in the elevation interval –400 m to –650 m based on 20 realisations of the Hydrogeological DFN in Napsac/ConnectFlow. The calculations consider a boundary plane separation distance of 100 m for a 1% hydraulic gradient applied along each of the three principal axes of the simulation volume as indicated in the figure. Results are given for the case of neutrally conductive FIZ only and are plotted as cumulative distribution probability curves for each individual realisation.*

Table B-22. Summary statistics for the F-factor and advective travel time (log_{10} units) corresponding to the pooled particle tracking data for HRD_N in the elevation interval –400 m to –650 m. The data are for different transport distances assuming a 1% reference hydraulic gradient applied along the north-south axis (20 pooled stochastic DFN realisations with 1,000 particles released in each realisation). Results are given for the neutrally conductive FIZ case only.

North-South case	log_{10} F (yr/m)				log_{10} tw (yr)			
Semi-Correlated (SC)	25 m	50 m	75 m	100 m	25 m	50 m	75 m	100 m
Mean	2.84	3.43	3.83	3.96	–0.86	–0.29	0.17	0.33
Median	2.88	3.41	3.69	3.90	–0.90	–0.31	–0.01	0.22
5th percentile	1.77	2.67	2.98	3.08	–1.50	–0.84	–0.57	–0.41
10th percentile	1.88	2.81	3.11	3.19	–1.47	–0.76	–0.47	–0.30
25th percentile	2.50	3.11	3.36	3.55	–1.12	–0.57	–0.25	–0.14
75th percentile	3.22	3.71	4.25	4.28	–0.63	–0.10	0.51	0.64
90th percentile	3.51	4.04	4.87	4.91	–0.29	0.19	1.07	1.33
95th percentile	3.76	4.34	5.15	5.12	–0.04	0.47	1.52	1.50
Std. deviation	0.57	0.50	0.68	0.61	0.42	0.40	0.63	0.58
Variance	0.33	0.25	0.46	0.37	0.18	0.16	0.39	0.34
Min value	1.68	2.11	2.39	2.89	–1.58	–1.13	–0.85	–0.61
Max value	5.36	7.35	6.46	6.73	1.77	3.70	2.50	2.77
Recovered particles	19,000	17,841	14,991	12,000	19,000	17,841	14,991	12,000

Table B-23. Summary statistics for the F-factor and advective travel time (log_{10} units) corresponding to the pooled particle tracking data for HRD_N in the elevation interval –400 m to –650 m. The data are for different transport distances assuming a 1% reference hydraulic gradient applied along the west-east axis (20 pooled stochastic DFN realisations with 1,000 particles released in each realisation). Results are given for the neutrally conductive FIZ case only.

West-East case	log_{10} F (yr/m)				log_{10} tw (yr)			
Semi-Correlated (SC)	25 m	50 m	75 m	100 m	25 m	50 m	75 m	100 m
Mean	2.46	3.08	3.21	3.53	–1.12	–0.57	–0.42	–0.07
Median	2.39	3.03	3.09	3.37	–1.19	–0.71	–0.57	–0.34
5th percentile	1.39	1.81	1.92	2.13	–1.76	–1.42	–1.29	–1.08
10th percentile	1.59	2.12	2.44	2.66	–1.67	–1.25	–1.01	–0.84
25th percentile	1.93	2.42	2.77	2.93	–1.53	–0.97	–0.77	–0.61
75th percentile	2.97	3.65	3.72	3.99	–0.84	–0.20	–0.06	0.29
90th percentile	3.47	4.16	4.05	4.74	–0.43	0.33	0.30	1.22
95th percentile	3.66	4.40	4.42	5.38	–0.18	0.48	0.66	1.50
Std. deviation	0.71	0.78	0.72	0.88	0.50	0.59	0.58	0.78
Variance	0.50	0.61	0.51	0.78	0.25	0.35	0.34	0.61
Min value	1.15	1.14	1.62	1.86	–1.96	–2.66	–1.49	–1.25
Max value	5.48	6.00	6.88	7.26	1.36	1.99	3.17	3.67
Recovered particles	20,000	19,000	13,000	12,000	20,000	19,000	13,000	12,000

Table B-24. Summary statistics for the F-factor and advective travel time (log_{10} units) corresponding to the pooled particle tracking data for HRD_N in the elevation interval –400 m to –650 m. The data are for different transport distances assuming a 1% reference hydraulic gradient applied along the vertical axis (20 pooled stochastic DFN realisations with 1,000 particles released in each realisation). Results are given for the neutrally conductive FIZ case only.

Vertical case	log_{10} F (yr/m)				log_{10} tw (yr)			
Semi-Correlated (SC)	25 m	50 m	75 m	100 m	25 m	50 m	75 m	100 m
Mean	1.19	1.81	2.46	2.94	–1.82	–1.27	–0.82	–0.44
Median	1.26	1.81	2.47	3.00	–1.84	–1.38	–0.88	–0.56
5th percentile	–0.12	0.21	1.03	1.41	–2.59	–2.25	–1.92	–1.43
10th percentile	–0.08	0.62	1.28	1.54	–2.53	–2.04	–1.59	–1.29
25th percentile	0.38	1.16	1.61	2.23	–2.23	–1.70	–1.36	–1.03
75th percentile	1.67	2.66	3.17	3.39	–1.60	–0.91	–0.32	0.08
90th percentile	2.50	3.17	3.91	4.44	–1.15	–0.42	0.28	0.48
95th percentile	2.76	3.47	4.23	5.04	–0.87	0.15	0.47	1.36
Std. deviation	0.92	1.03	1.04	1.03	0.59	0.70	0.73	0.77
Variance	0.84	1.06	1.08	1.06	0.35	0.49	0.53	0.60
Min value	–0.62	–0.32	0.11	0.46	–2.83	–2.53	–2.30	–2.05
Max value	5.43	5.51	5.74	6.56	1.16	1.55	1.75	2.73
Recovered particles	20,000	19,995	19,908	19,966	20,000	19,995	19,908	19,966

Appendix C

Detailed ECPM modelling results

Author: James Crawford

This appendix contains a detailed examination of particle tracking results for a number of particles thought to be representative of potential migration paths within HRD_C from release at an elevation of –500 m (see Section 3.10) to surface discharge locations. The analysis is based upon particle tracking results already presented in /Rhén et al. 2009/. In Section 3.10.2, a detailed examination of the migration path for particle p855 has already been given. In this Appendix, detailed results are given for particle p652, p850, p1202, and p1214. Figure C-1 shows a visualisation of the entire set of particle release locations with individual pathways and surface exit locations highlighted for the 5 particular migration paths described above.

One interesting result derived from the comparison of different particle migration paths is the observation that the transported particles tend to fall into 2 distinct categories. One set of particles follows near-vertical migration paths through HRD_C. These particles only encounter deformation zones comprising the HCD in the upper 200 m of the bedrock. Particles p652, p850, and p1202 are typical examples of this migration path category. In these cases, owing to the strong depth-dependency of deformation zone transmissivity, the HCD makes very little contribution to the hydrodynamic transport resistance and the bulk of the F-factor is accumulated in the HRD.

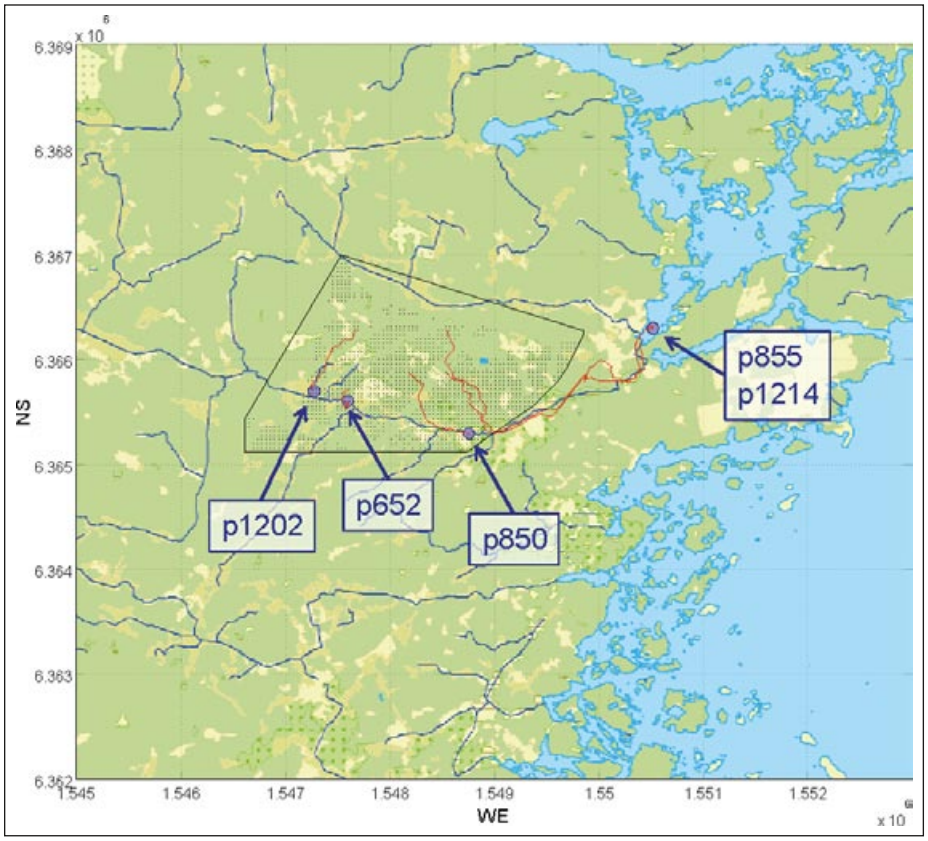

Figure C-1. *Visualisation of particle release locations (small black markers) within HRD_C (polygon outline). Surface exit locations of the particular particles described in detail in this report are indicated by the blue circular markers and accompanying text. Migration paths are indicated by the red pathways drawn in the figure.*

Particles belonging to the second set tend to track eastwards via an initially downwards trajectory before turning upwards and exiting near the Baltic coast, typically via a sequence of subsidiary HRD volumes (i.e. outside of the Laxemar local model volume) and deformation zones. Particles p855 and p1214 are typical examples of this migration path category. In these cases, owing to the long migration pathlines and the fact that the particles come into contact with HCD structures at greater depths where they are less transmissive (at or below an elevation of –500 m), the HCD actually provides most of the hydrodynamic transport resistance and the HRD accounts for only a minor part of the accumulated F-factor.

Detailed profile of particle p652

The migration path for particle p652 is shown in Figure C-2 from an overhead perspective as well as a south and west facing vantage point. This migration path is a good example of the group of particles that follow an essentially vertical trajectory from repository depth to the surface and in this case, the surface exit location is only 110 m displaced horizontally from its start position. The cumulative F-factor is shown in Figure C-3 and the corresponding cumulative advective travel time in Figure C-4.

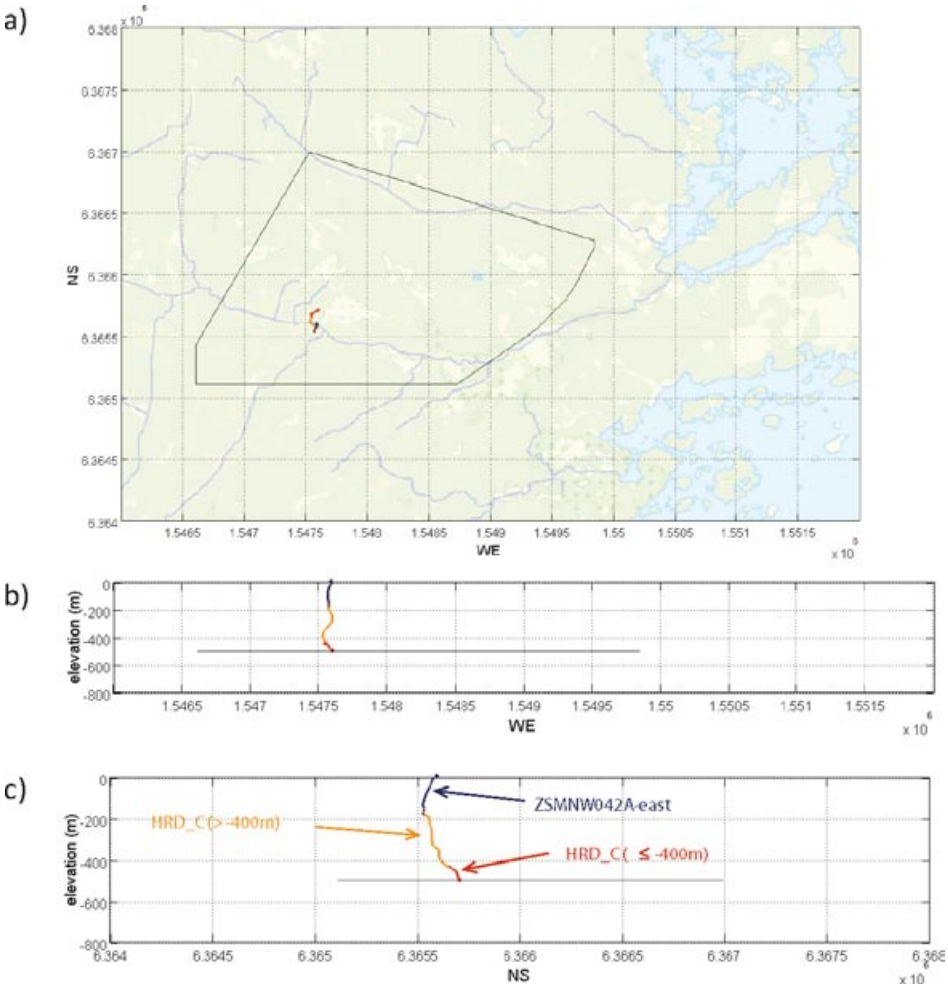

Figure C-2. *The transport path taken by a single particle, p652 seen from above (a) as well as a cross-sectional view from a vantage point facing south (b) and facing west (c). The pathline is coloured with regard to structural elements encountered by the particle on its way to the surface exit location, i.e. red for HRD_C (≤ –400 m), dark blue for deterministic deformation zones, and orange for HRD_C depth zonations above –400 m. The outline of the particle release area is shown as a polygon at –500 m elevation.*

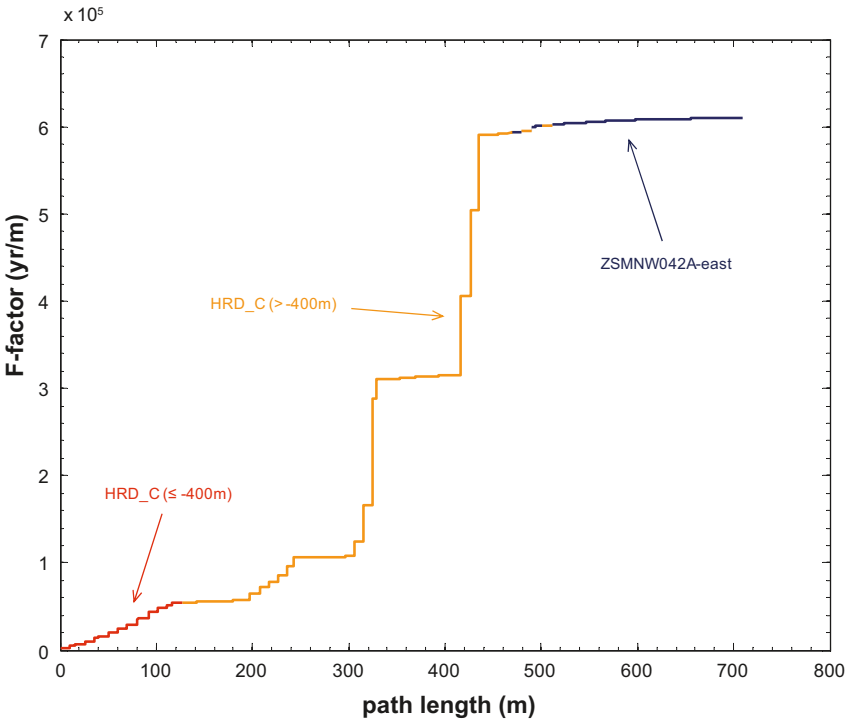

Figure C-3. *Cumulative F-factor (yr/m) as a function of migration path length for particle p652. Different structural elements encountered by the particle along its migration path are colour-coded and labelled in the figure.*

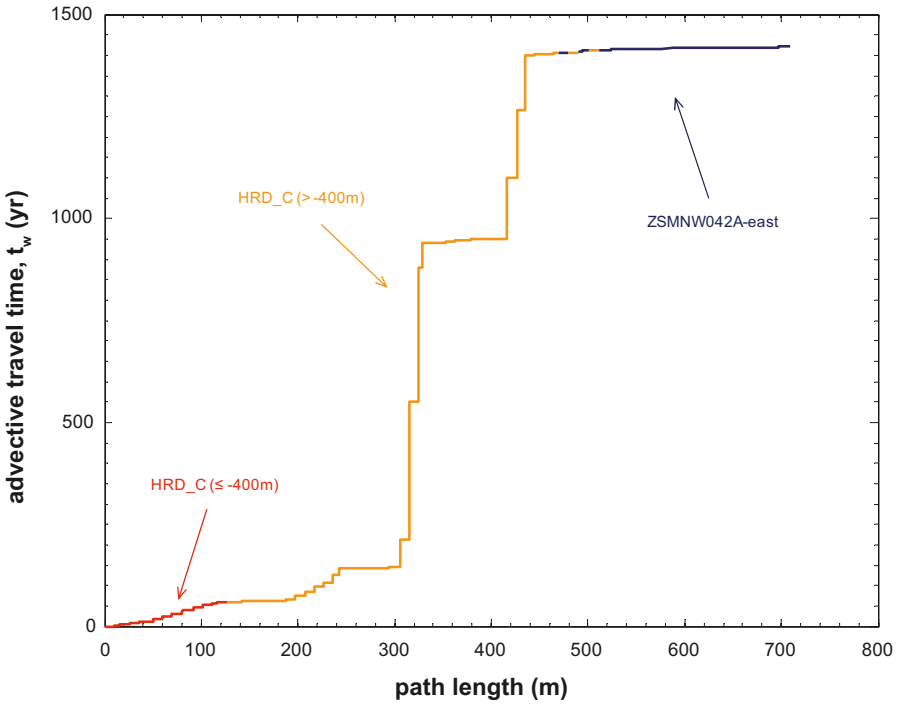

Figure C-4. *Cumulative advective travel time (yr) as a function of migration path length for particle p652. Different structural elements encountered by the particle along its migration path are colour-coded and labelled in the figure.*

For particle p652, roughly 98% of the hydrodynamic transport resistance is encountered in HRD_C, although only about 10% of this is accrued in the depth zonation below –400 m and most is accumulated in the upper reaches of HRD_C (i.e. from –400 m to –200 m). In this case, the hydrodynamic transport resistance provided by the HCD (deformation zone ZSMNW042A-east) near the surface exit location is negligible in comparison. The cumulative advective travel time follows a similar pattern as the F-factor with an essentially negligible residence time in the HCD. It is also interesting to note the two very steep increases in both F-factor and advective travel time over a short distance at roughly 315–325 m and 405–435 m along the migration path length.

Clues as to why these sudden changes occur can be found in the corresponding plots for hydraulic conductivity (Figure C-5) and hydraulic gradient (Figure C-6). For the first discontinuity at 315–325 m it appears that the particle enters a region where the hydraulic conductivity is very low and the hydraulic potential gradient falls away to almost nothing. The second instance at 405–435 m is associated with a slightly greater than average hydraulic potential gradient, although an anomalously low hydraulic conductivity. Neither of the discontinuities appears to be an artefact related to a transition between depth zonations. It is interesting to note that the particle is released in one of the most saline parts of the model (see, for example, Figure 9-13 and Figure 9-14 in /Rhén et al. 2009/). The discharge area is associated with the Laxemarån valley and the relatively high salinity extends up to an elevation of at least –300 m. It is speculated that the sudden rise in hydraulic gradient at 380 m along the particle track (–240 m elevation) might be related to the particle crossing the halocline.

The maximum hydraulic potential gradient experienced by the particle is approximately 1% over a short distance between 360 m and 420 m along the migration path, although the path average is approximately 0.36% which is roughly an order of magnitude less than the site average topographical gradient discussed in Section 3.3. A cross-plot of the hydraulic potential gradient versus mean hydraulic conductivity is shown in Figure C-7 and shows the expected inverse correlation. The specific flow-wetted surface is plotted in Figure C-8 as a function of migration path length.

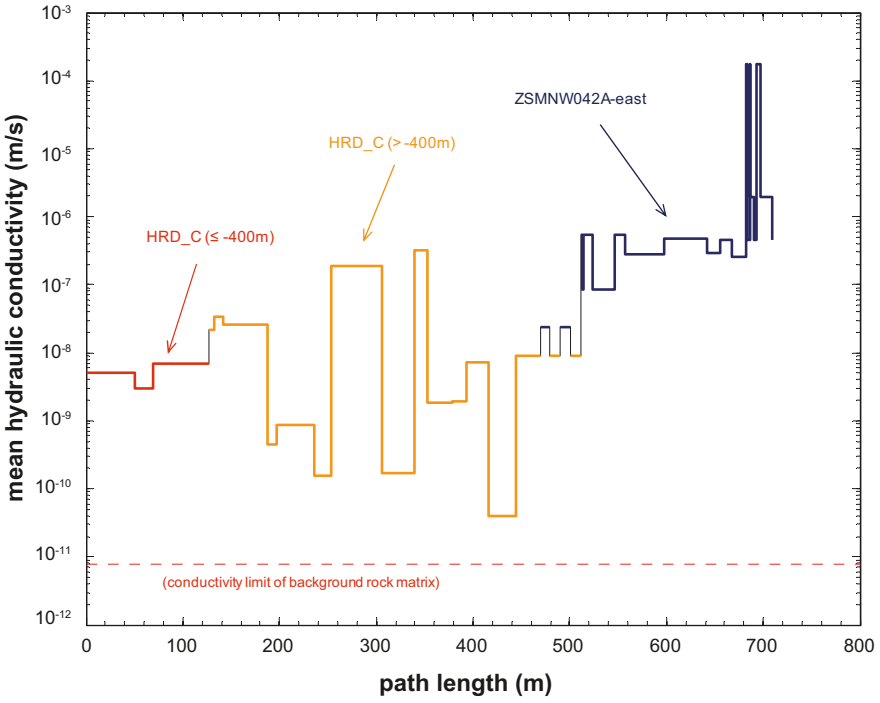

Figure C-5. *Local mean hydraulic conductivity (m/s) as a function of migration path length for particle p652. The broken horizontal line at the bottom of the figure represents the limit of hydraulic conductivity for the rock matrix assuming an in situ temperature of 12°C. Different structural elements encountered by the particle along its migration path are colour-coded and labelled in the figure. Grey coloured segments represent discontinuities in the parameter value when the particle passes from one structural feature to another.*

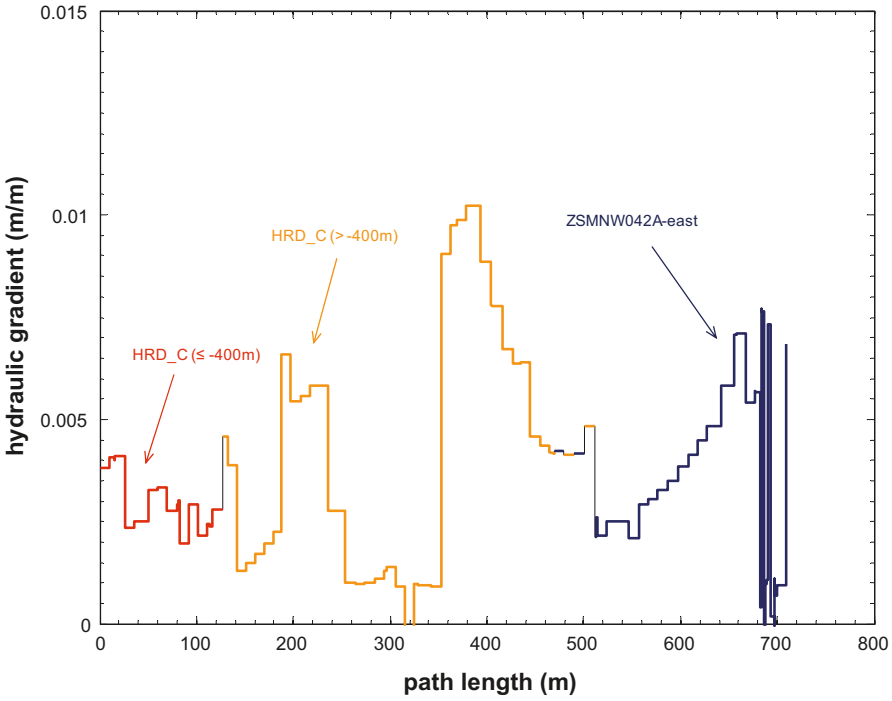

Figure C-6. *Local hydraulic potential gradient (m/m) as a function of migration path length for particle p652. Different structural elements encountered by the particle along its migration path are colour-coded and labelled in the figure as previously.*

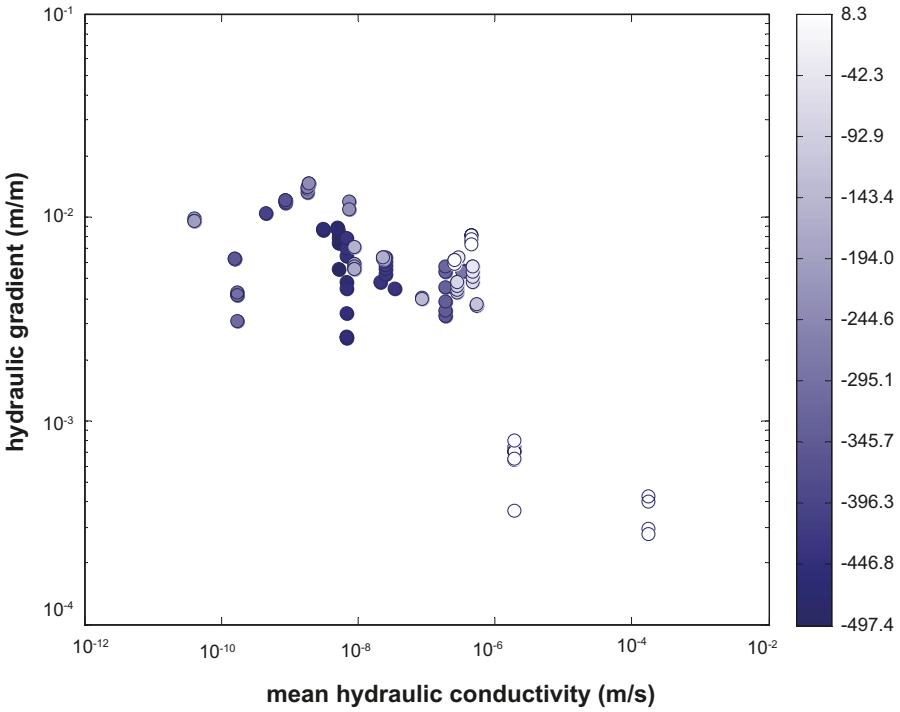

Figure C-7. *A cross-plot of the local hydraulic potential gradient (m/m) encountered by particle p652 along its migration path versus the local mean hydraulic conductivity (m/s) of the rock at that location. The markers are shaded according to elevation (m) as specified by the colour bar on the right-hand side of the figure.*

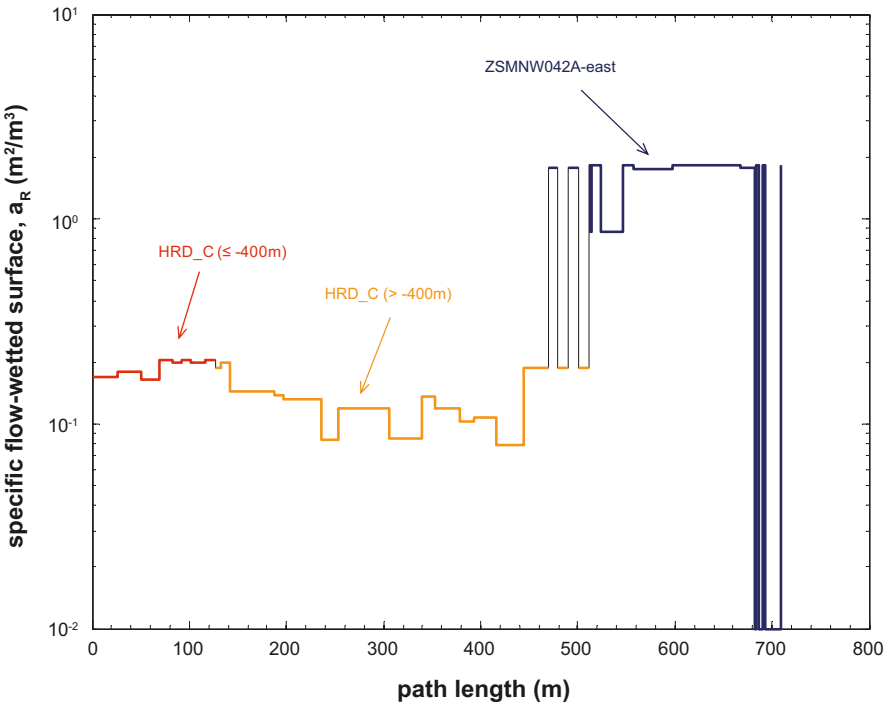

Figure C-8. *Local specific flow-wetted surface (m^2/m^3) encountered by particle p652 and plotted as a function of migration path length. Different structural elements encountered by the particle are colour-coded and labelled in the figure as previously.*

Detailed profile of particle p850

The migration path for particle p850 is shown in Figure C-9 from an overhead perspective as well as a south and west facing vantage point. This migration path is a good example of the group of particles that follow a semi-vertical trajectory from repository depth to the surface with an exit location displaced 640 m horizontally from its start position. The cumulative F-factor is shown in Figure C-10 and the corresponding cumulative advective travel time in Figure C-11.

For particle p850, roughly 76% of the hydrodynamic transport resistance is encountered in HRD_C, although only about 20% of this is accrued in the depth zonation below –400 m and most is accumulated in the upper reaches of HRD_C (i.e. above –400 m). The hydrodynamic transport resistance provided by deformation zone ZSMNE107A corresponds to about 24% of the total for the migration path.

The local mean hydraulic conductivity and hydraulic potential gradient are plotted in Figure C-12 and Figure C-13, respectively. The maximum hydraulic potential gradient experienced by the particle is approximately 1.8% over a short distance between 40 m and 90 m along the migration path, although the path average is approximately 0.7% (excluding anomalous hydraulic potential gradients in the immediate proximity of the exit location). A cross-plot of the hydraulic potential gradient versus mean hydraulic conductivity is shown in Figure C-14 while the specific flow-wetted surface is plotted in Figure C-15 as a function of migration path length. The release location for this particular particle happens to be in a region of low salinity which might explain the initially slightly higher hydraulic gradients than in the case of the previously discussed particle (p652).

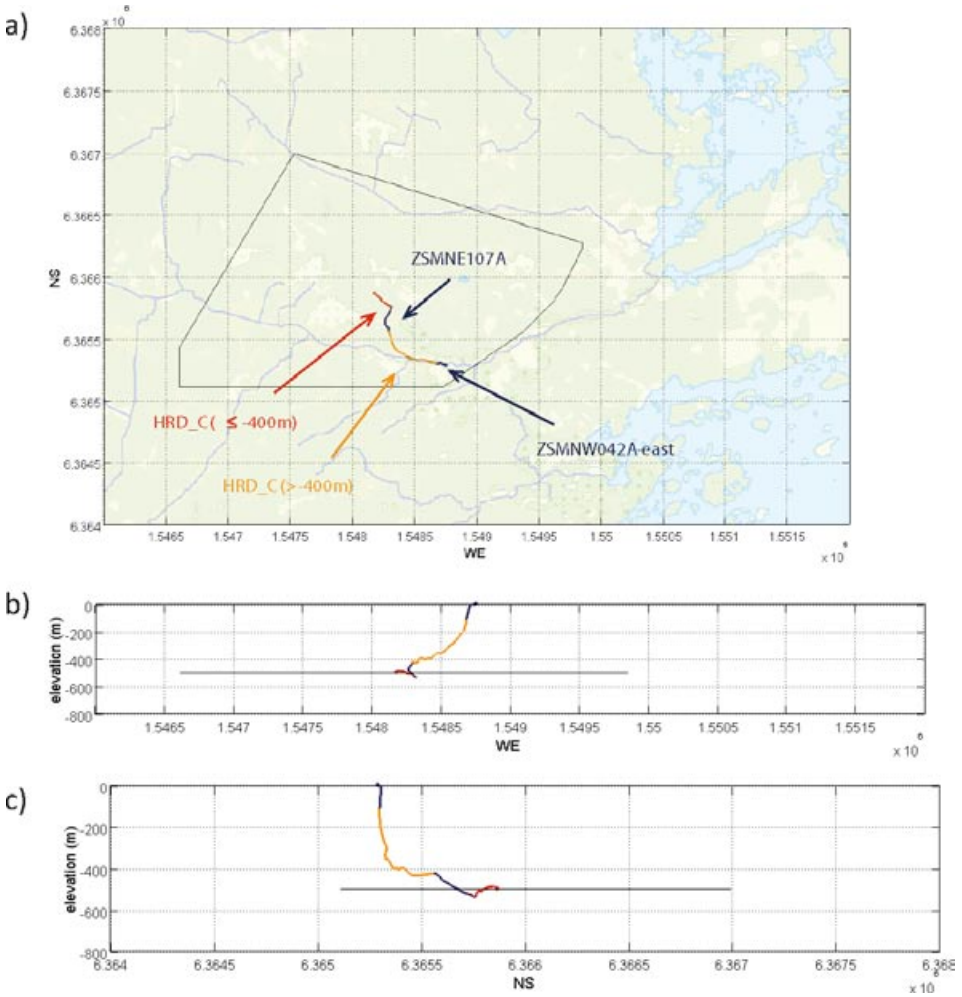

Figure C-9. *The transport path taken by a single particle, p850 seen from above (a) as well as a cross-sectional view from a vantage point facing south (b) and facing west (c). The pathline is coloured with regard to structural elements encountered by the particle on its way to the surface exit location, i.e. red for HRD_C (≤ –400 m), dark blue for deterministic deformation zones, and orange for HRD_C depth zonations above –400 m. The outline of the particle release area is shown as a polygon at –500 m elevation.*

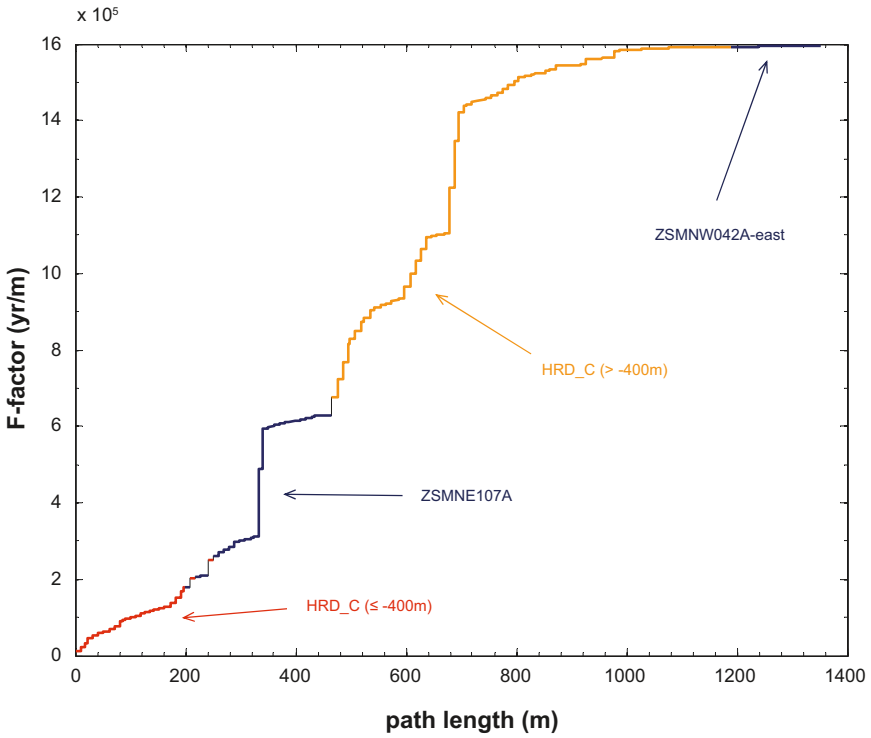

Figure C-10. *Cumulative F-factor as a function of migration path length for particle p850. Different structural elements encountered by the particle along its migration path are colour-coded and labelled in the figure.*

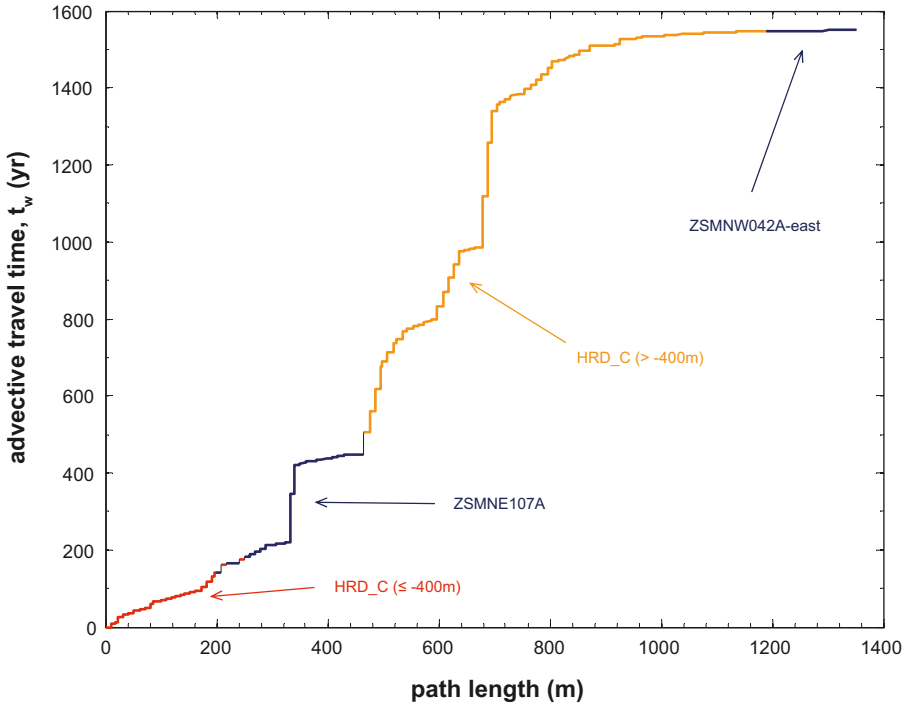

Figure C-11. *Cumulative advective travel time (yr) as a function of migration path length for particle p850. Different structural elements encountered by the particle along its migration path are colour-coded and labelled in the figure.*

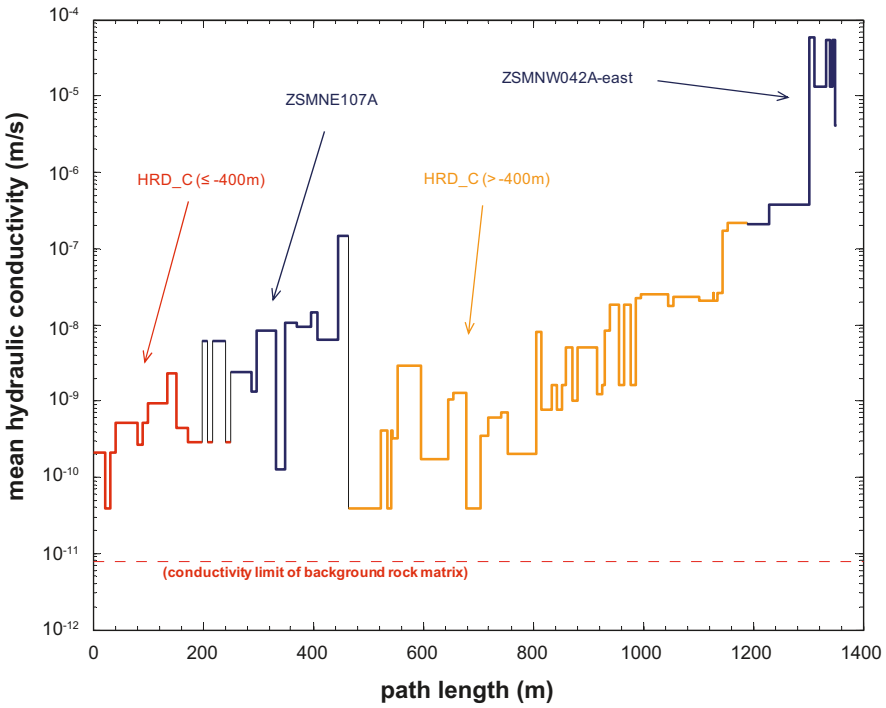

Figure C-12. *Local mean hydraulic conductivity as a function of migration path length for particle p850. The broken horizontal line at the bottom of the figure represents the limit of hydraulic conductivity for the rock matrix assuming an in situ temperature of 12°C. Different structural elements encountered by the particle along its migration path are colour-coded and labelled in the figure. Grey coloured segments represent discontinuities in the parameter value when the particle passes from one structural feature to another.*

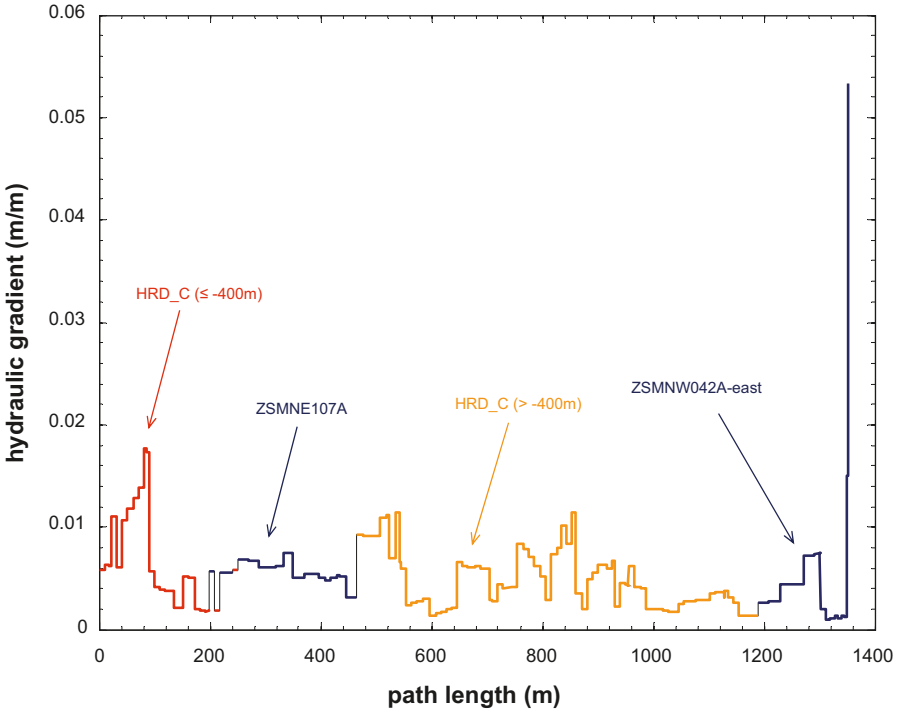

Figure C-13. *Local hydraulic potential gradient as a function of migration path length for particle p850. Different structural elements encountered by the particle along its migration path are colour-coded and labelled in the figure as previously.*

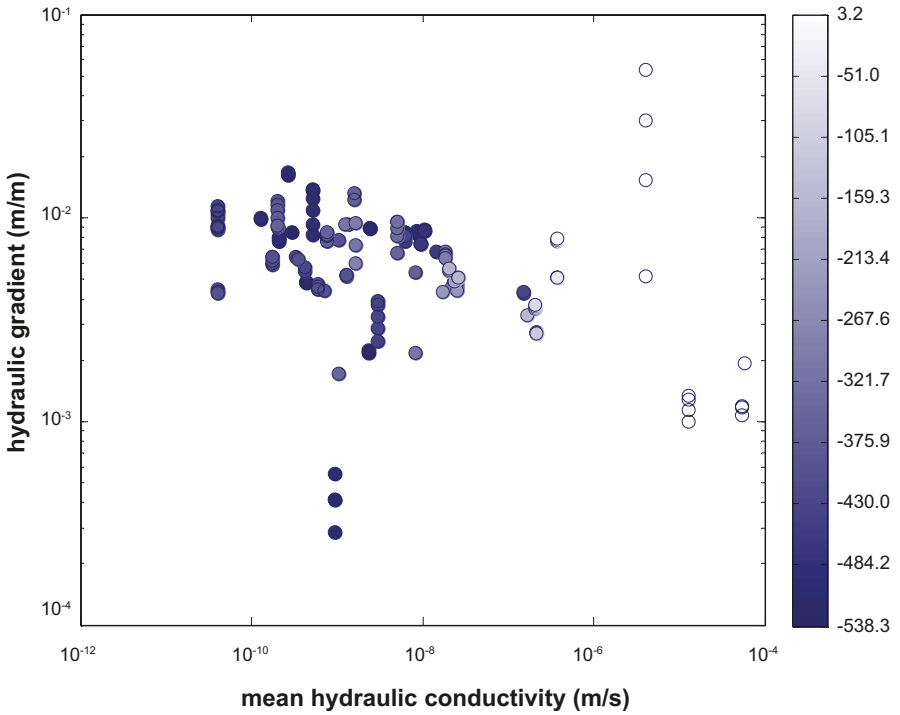

Figure C-14. *A cross-plot of the local hydraulic potential gradient (m/m) encountered by particle p850 along its migration path versus the local mean hydraulic conductivity (m/s) of the rock at that location. The markers are shaded according to elevation (m) as specified by the colour bar on the right-hand side of the figure.*

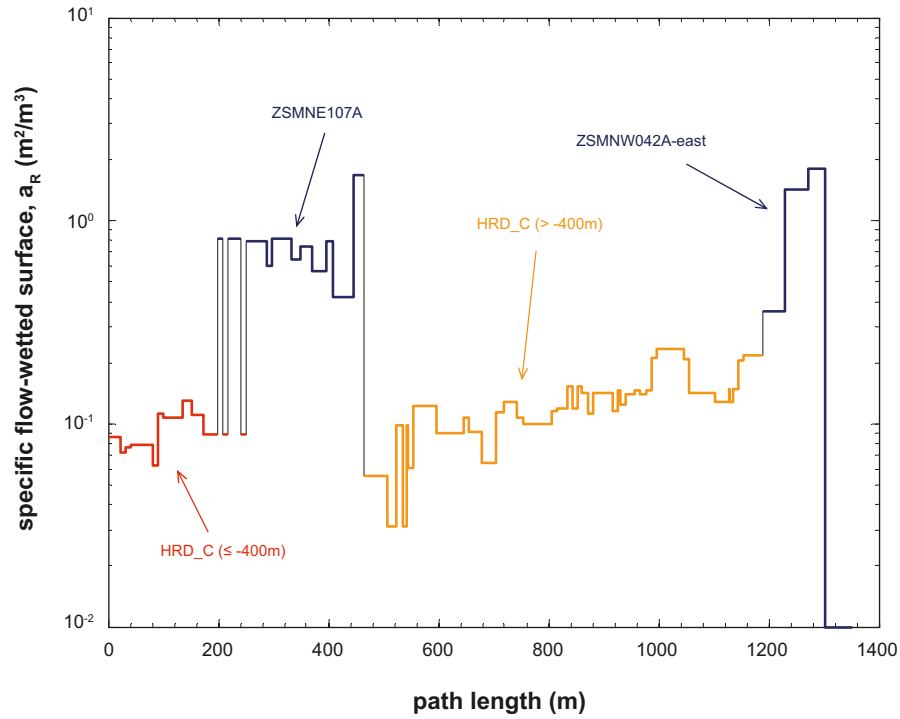

Figure C-15. *Local specific flow-wetted surface (m^2/m^3) encountered by particle p850 and plotted as a function of migration path length. Different structural elements encountered by the particle are colour-coded and labelled in the figure as previously.*

Detailed profile of particle p1202

The migration path for particle p1202 is shown in Figure C-16 from an overhead perspective as well as a south and west facing vantage point. This migration path is a good example of the group of particles that follow a semi-vertical trajectory from repository depth to the surface with an exit location displaced 711 m horizontally from its start position. The cumulative F-factor is shown in Figure C-17 and the corresponding cumulative advective travel time in Figure C-18.

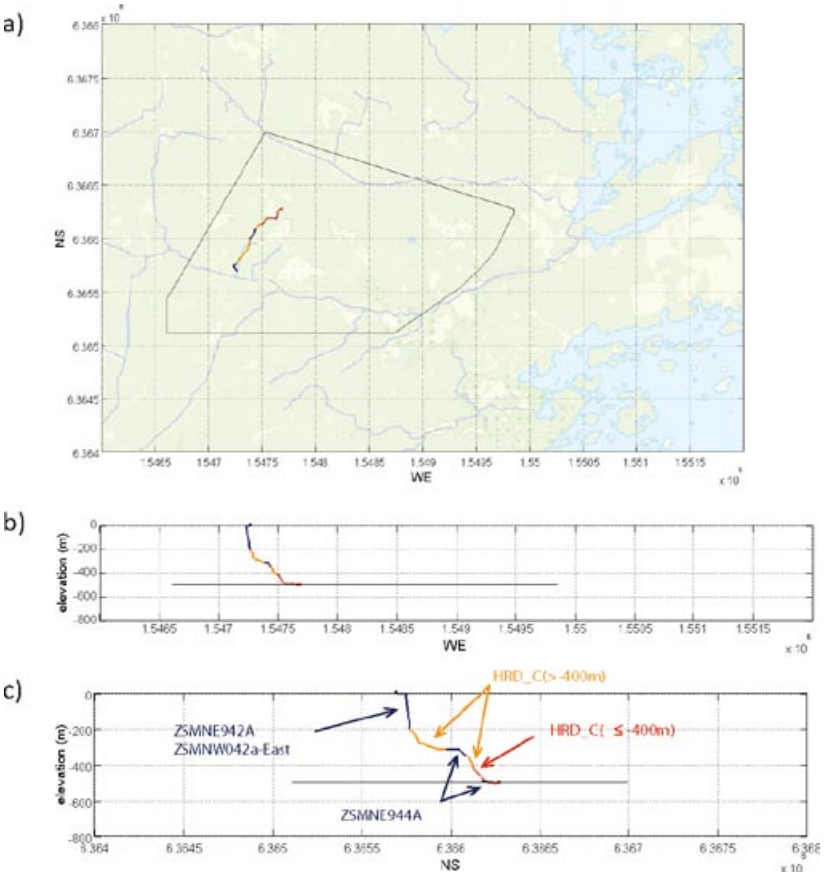

Figure C-16. *The transport path taken by a single particle, p1202 seen from above (a) as well as a cross-sectional view from a vantage point facing south (b) and facing west (c). The pathline is coloured with regard to structural elements encountered by the particle on its way to the surface exit location, i.e. red for HRD_C (≤ –400 m), dark blue for deterministic deformation zones, and orange for HRD_C depth zonations above –400 m. The outline of the particle release area is shown as a polygon at –500 m elevation.*

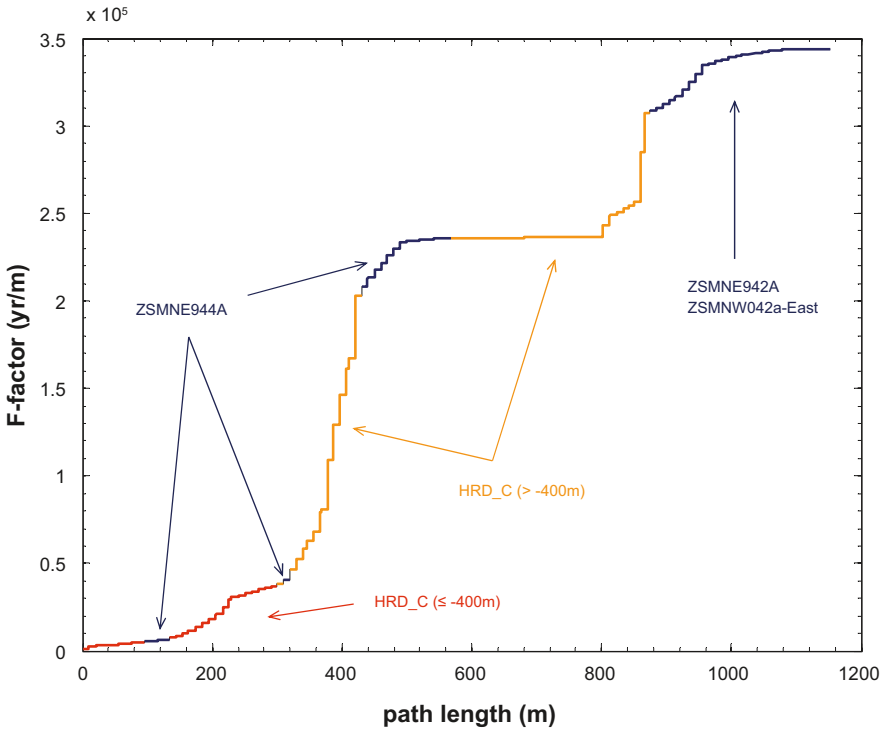

Figure C-17. *Cumulative F-factor as a function of migration path length for particle p1202. Different structural elements encountered by the particle along its migration path are colour-coded and labelled in the figure.*

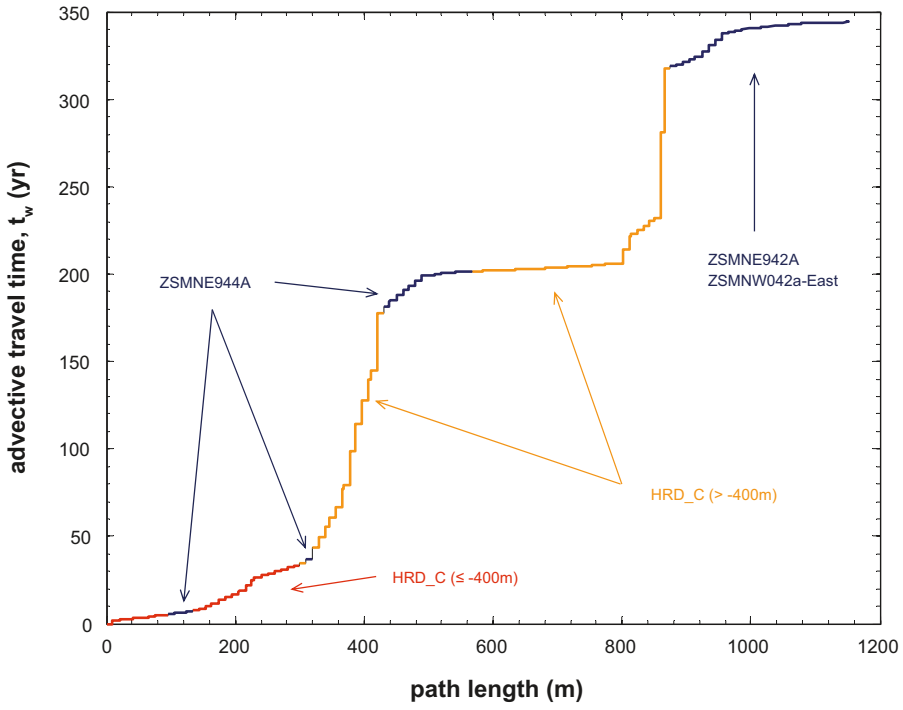

Figure C-18. *Cumulative advective travel time (yr) as a function of migration path length for particle p1202. Different structural elements encountered by the particle along its migration path are colour-coded and labelled in the figure.*

For particle p1202, roughly 79% of the hydrodynamic transport resistance is encountered in HRD_C, although only about 13% of this is accrued in the depth zonation below –400 m and most is accumulated in the upper reaches of HRD_C. The hydrodynamic transport resistance provided by the deformation zones comprising the HCD corresponds to about 21% of the total cumulative F-factor for the migration path. The sudden increase in cumulative F-factor and advective travel time over short distances at –350 m to –450 m path length and –800 m to –900 m relate to the particle encountering rock volumes featuring very low hydraulic conductivity in these locations.

The local mean hydraulic conductivity and hydraulic potential gradient are plotted in Figure C-19 and Figure C-20 respectively. The maximum hydraulic potential gradient experienced by the particle is approximately 2% over a short distance roughly 820 m along the migration path, although the path average is approximately 0.6% (excluding anomalous hydraulic potential gradients in the immediate proximity of the exit location). This particle is released in a relatively saline region of the model which might explain the lower hydraulic gradients than those for particle, p850.A cross-plot of the hydraulic potential gradient versus mean hydraulic conductivity is shown in Figure C-21 while the specific flow-wetted surface is plotted in Figure C-22 as a function of migration path length.

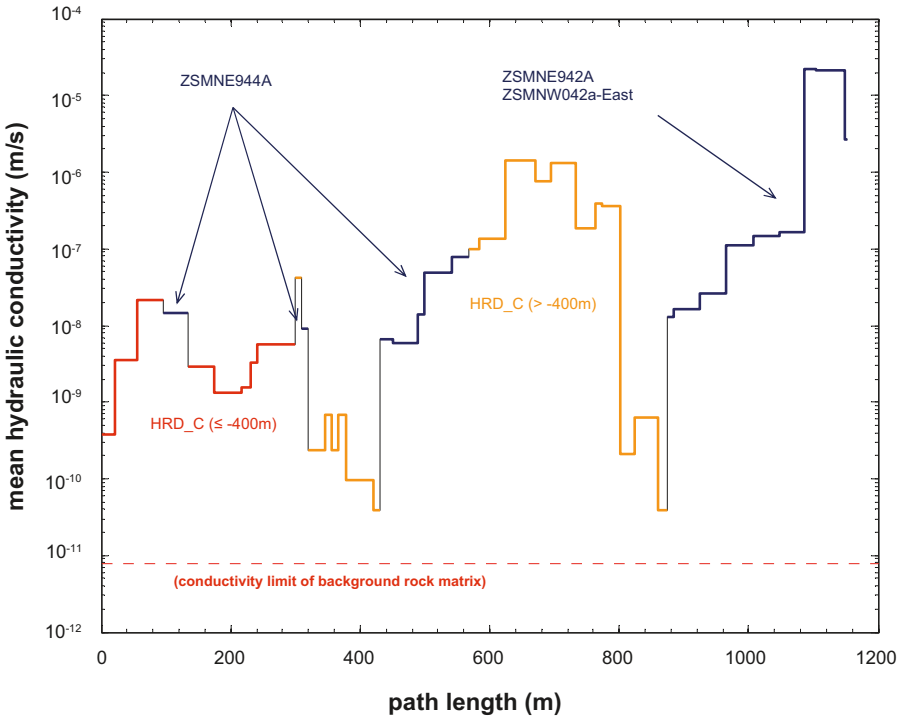

Figure C-19. *Local mean hydraulic conductivity as a function of migration path length for particle p1202. The broken horizontal line at the bottom of the figure represents the limit of hydraulic conductivity for the rock matrix assuming an in situ temperature of 12ºC. Different structural elements encountered by the particle along its migration path are colour-coded and labelled in the figure. Grey coloured segments represent discontinuities in the parameter value when the particle passes from one structural feature to another.*

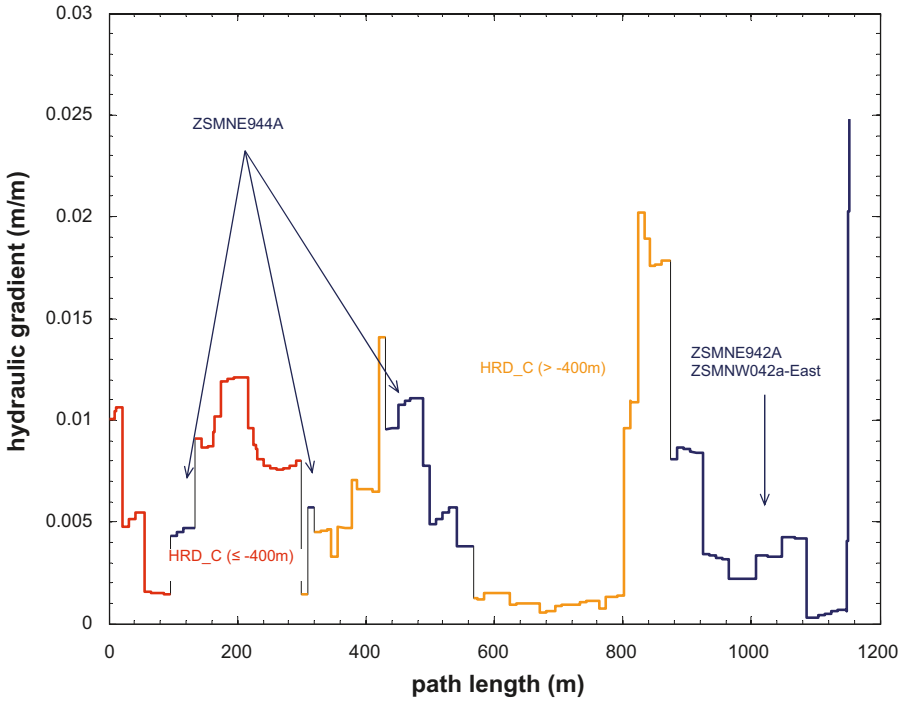

Figure C-20. *Local hydraulic potential gradient as a function of migration path length for particle p1202. Different structural elements encountered by the particle along its migration path are colour-coded and labelled in the figure as previously.*

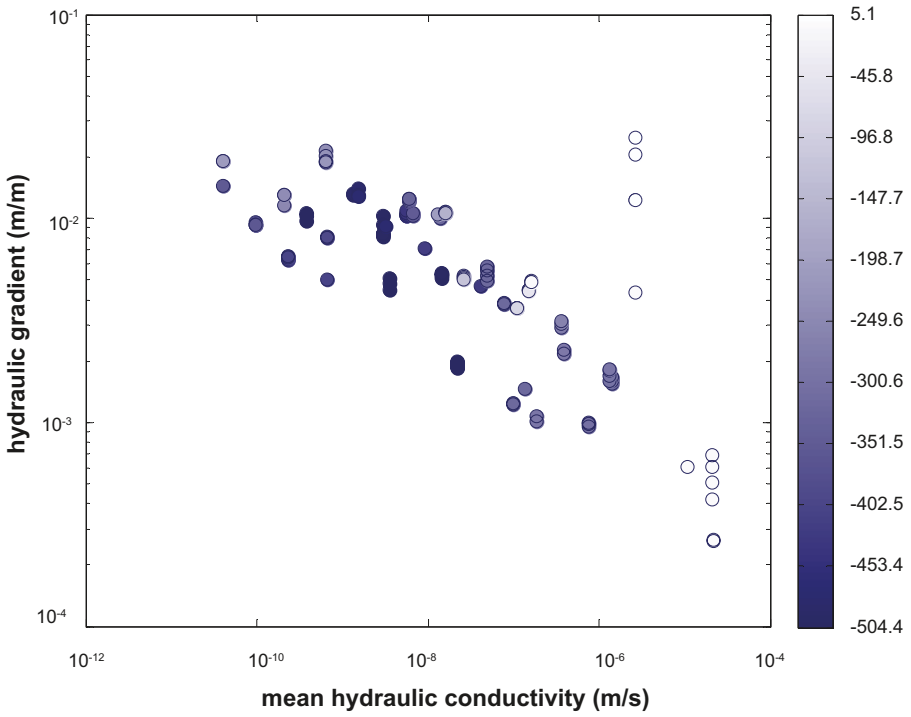

Figure C-21. *A cross-plot of the local hydraulic potential gradient (m/m) encountered by particle p1202 along its migration path versus the local mean hydraulic conductivity (m/s) of the rock at that location. The markers are shaded according to elevation (m) as specified by the colour bar on the right-hand side of the figure.*

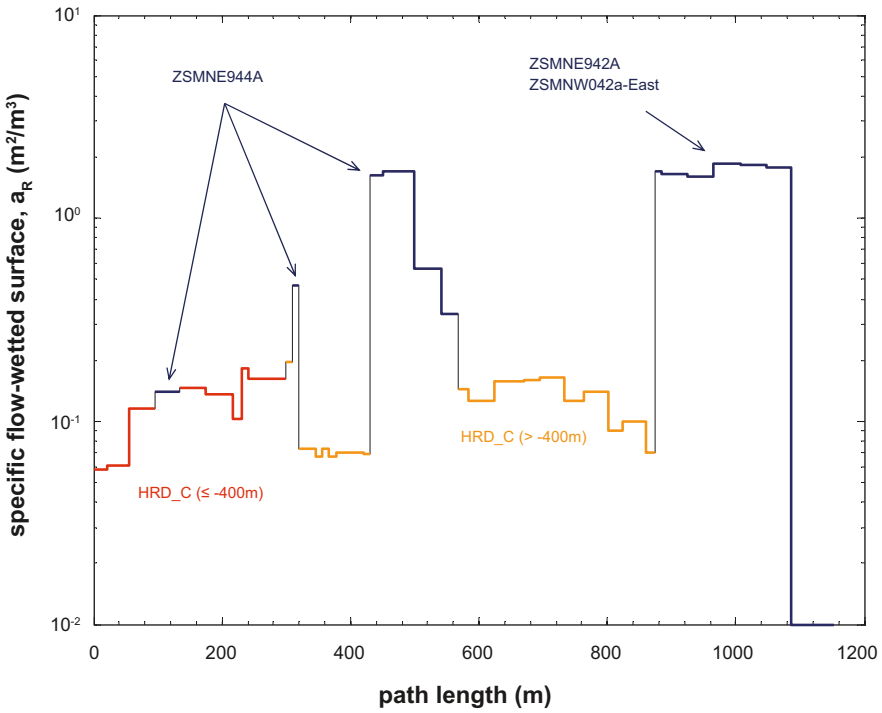

Figure C-22. *Local specific flow-wetted surface (m²/m³) encountered by particle p1202 and plotted as a function of migration path length. Different structural elements encountered by the particle are colour-coded and labelled in the figure as previously.*

Detailed profile of particle p1214

The migration path for particle p1214 is shown in Figure C-23 from an overhead perspective as well as a south and west facing vantage point. This migration path is a good example of the group of particles that follow a trajectory towards the Baltic coast from repository depth to the surface with an exit location displaced 1980 m horizontally from its start position. The cumulative F-factor is shown in Figure C-24 and the corresponding cumulative advective travel time in Figure C-25.

For particle p1214, roughly 9% of the hydrodynamic transport resistance is encountered in HRD_C and 1% in other HRD volumes external to HRD_C. The hydrodynamic transport resistance provided by the deformation zones comprising the HCD corresponds to about 90% of the total cumulative F-factor for the migration path.

The local mean hydraulic conductivity and hydraulic potential gradient are plotted in Figure C-26 and Figure C-27 respectively. The maximum hydraulic potential gradient experienced by the particle is approximately 1.85% over a short distance roughly 1000 m along the migration path, although the path average is approximately 0.3% (excluding anomalous hydraulic potential gradients in the immediate proximity of the exit location). This particle originates in a relatively saline region of the model and migrates towards even higher salinity regions which might explain the very low hydraulic potential gradients over much of the transport path. A cross-plot of the hydraulic potential gradient versus mean hydraulic conductivity is shown in Figure C-28 while the specific flow-wetted surface is plotted in Figure C-29 as a function of migration path length.

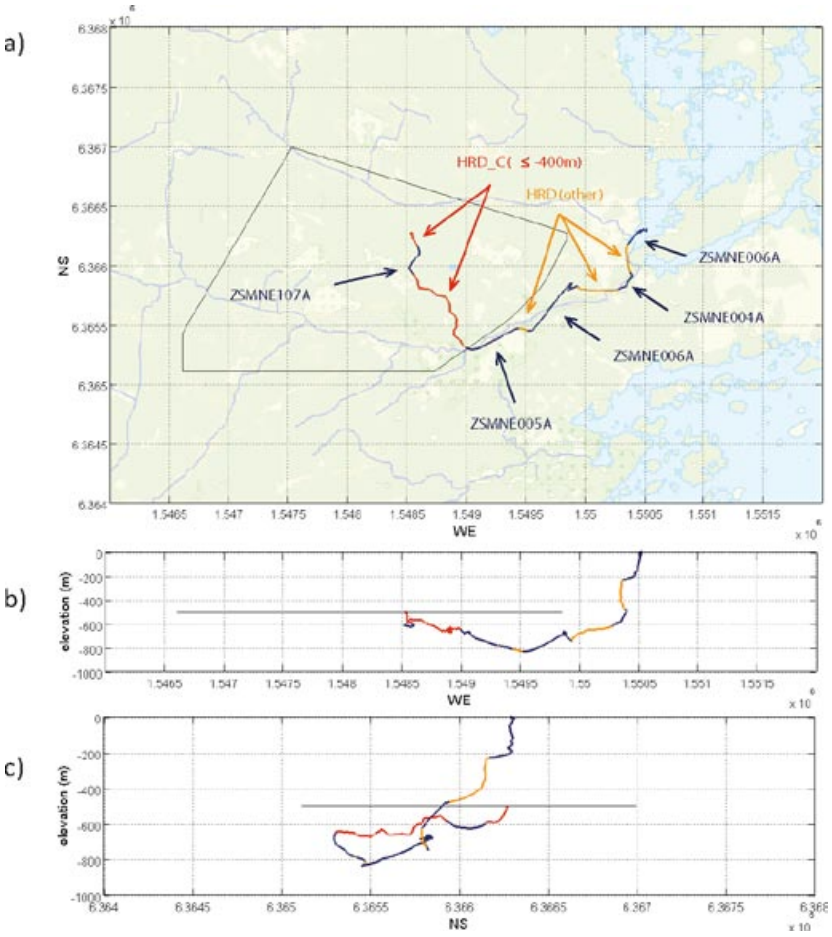

Figure C-23. *The transport path taken by a single particle, p1214 seen from above (a) as well as a cross-sectional view from a vantage point facing south (b) and facing west (c). The pathline is coloured with regard to structural elements encountered by the particle on its way to the surface exit location, i.e. red for HRD_C (≤ –400 m), dark blue for deterministic deformation zones, and orange for HRD_C depth zonations above –400 m. The outline of the particle release area is shown as a polygon at –500 m elevation.*

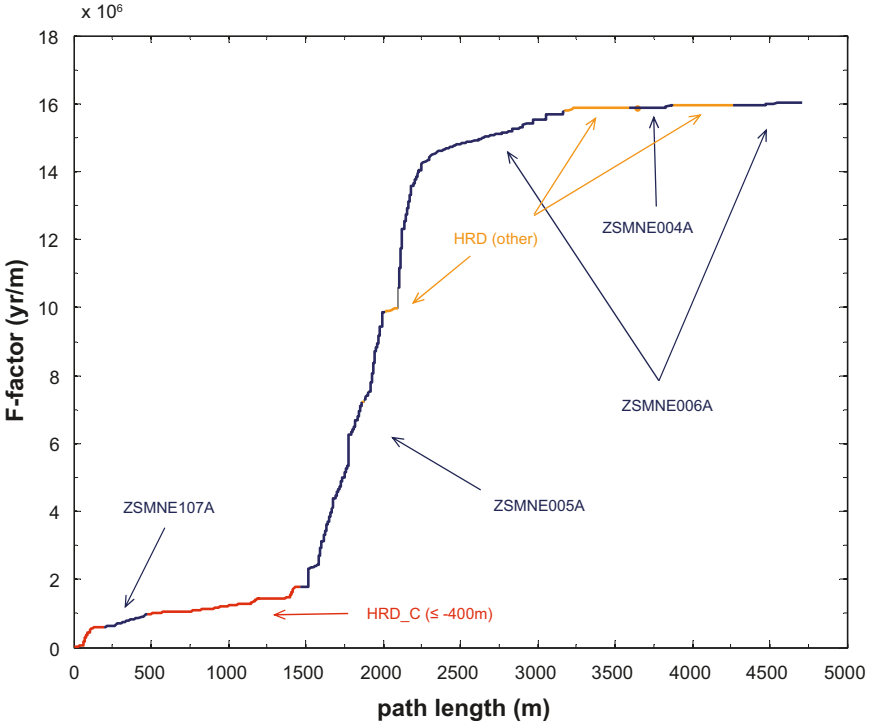

Figure C-24. *Cumulative F-factor as a function of migration path length for particle p1214. Different structural elements encountered by the particle along its migration path are colour-coded and labelled in the figure.*

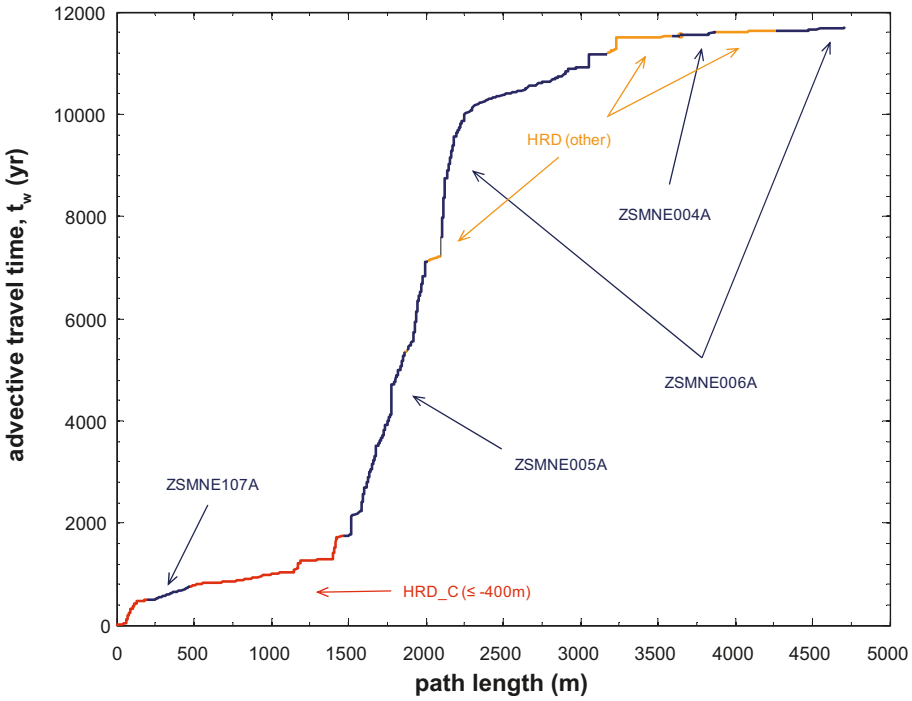

Figure C-25. *Cumulative advective travel time (yr) as a function of migration path length for particle p1214. Different structural elements encountered by the particle along its migration path are colour-coded and labelled in the figure.*

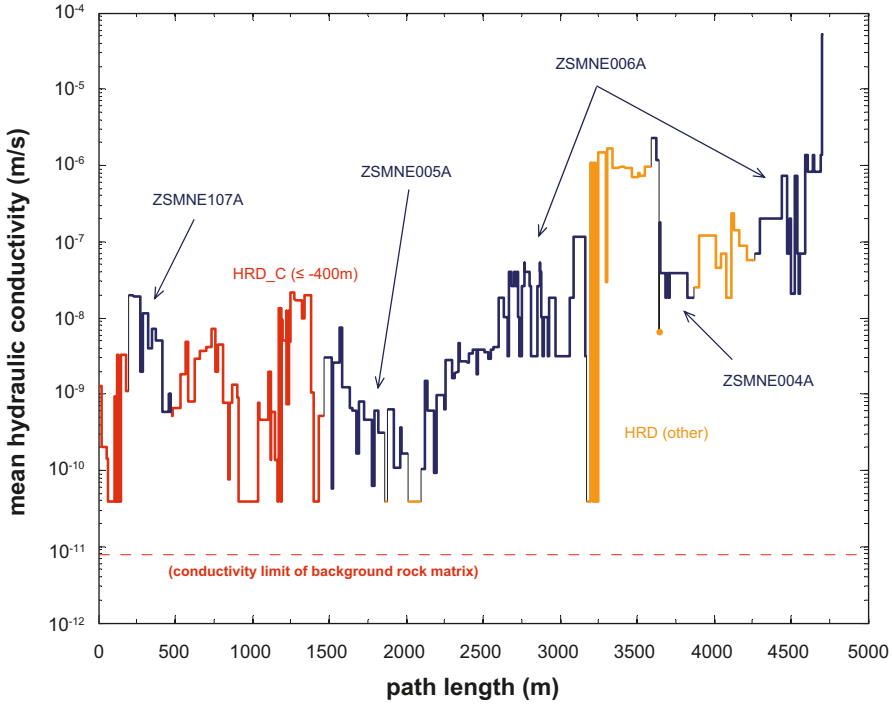

Figure C-26. *Local mean hydraulic conductivity as a function of migration path length for particle p1214. The broken horizontal line at the bottom of the figure represents the limit of hydraulic conductivity for the rock matrix assuming an in situ temperature of 12°C. Different structural elements encountered by the particle along its migration path are colour-coded and labelled in the figure. Grey coloured segments represent discontinuities in the parameter value when the particle passes from one structural feature to another.*

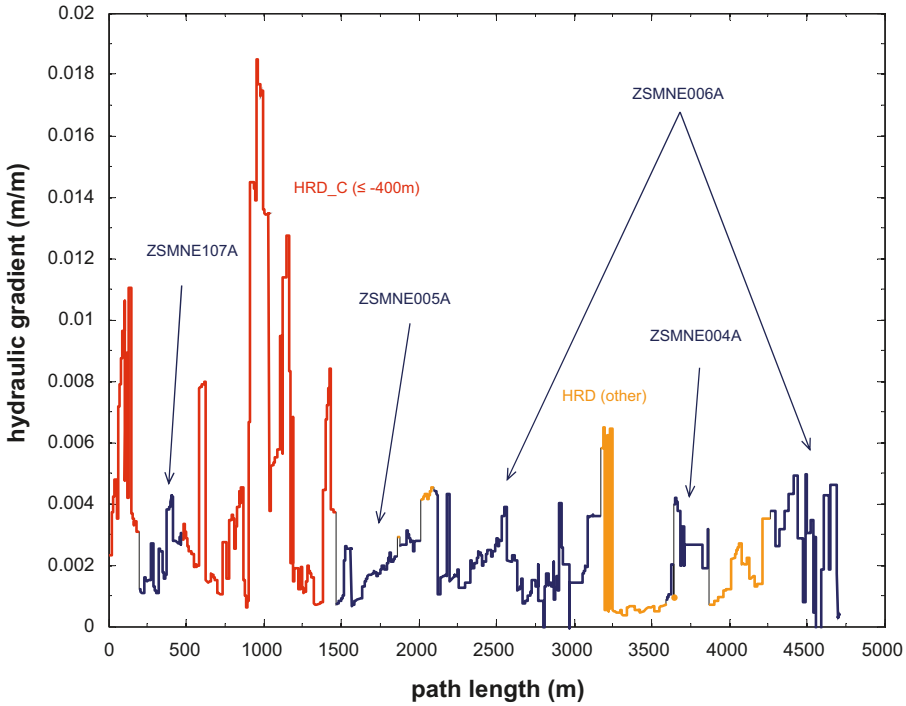

Figure C-27. *Local hydraulic potential gradient as a function of migration path length for particle p1214. Different structural elements encountered by the particle along its migration path are colour-coded and labelled in the figure as previously.*

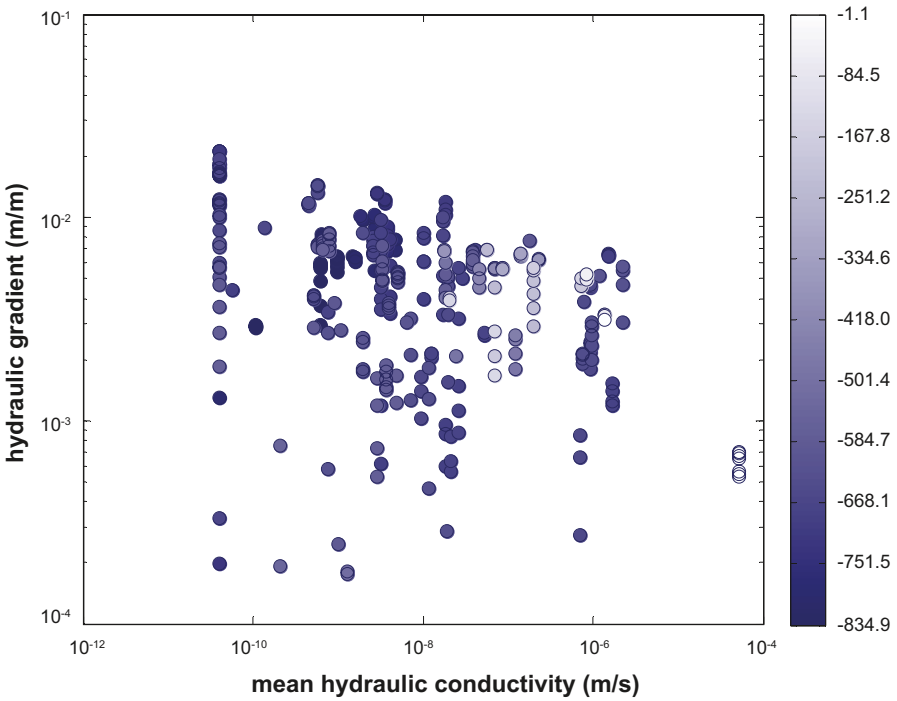

Figure C-28. *A cross-plot of the local hydraulic potential gradient (m/m) encountered by particle p1214 along its migration path versus the local mean hydraulic conductivity (m/s) of the rock at that location. The markers are shaded according to elevation (m) as specified by the colour bar on the right-hand side of the figure.*

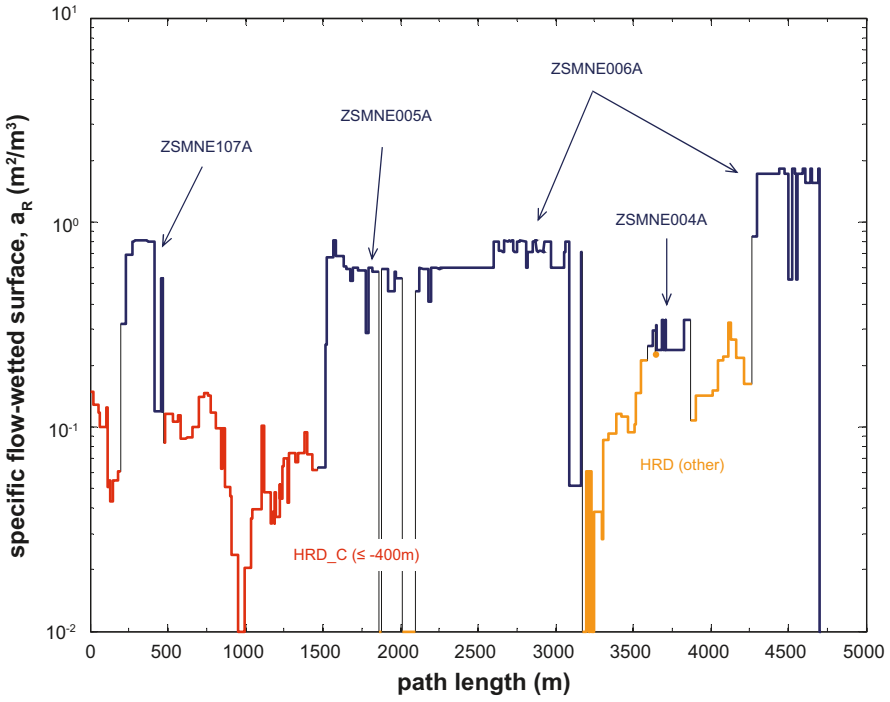

Figure C-29. *Local specific flow-wetted surface (m²/m³) encountered by particle p1214 and plotted as a function of migration path length. Different structural elements encountered by the particle are colour-coded and labelled in the figure as previously.*

Appendix D

On the use of in situ formation factors

Authors: James Crawford and Martin Löfgren

Introduction

In the transport calculations presented in this report, the effective matrix diffusivity used is based upon formation factor data obtained in situ using electrical methods. It is thought that this data may more accurately reflect the properties of the rock matrix at repository depth, compared to data obtained in the laboratory on drill core samples, which could be considerably affected by stress relaxation and mechanical damage. Before using estimated formation factors based upon in situ resistivity data, however, there are a number of issues which need to be considered. These are discussed in this Appendix chapter, which has the following outline:

Theory: A short description of the formation factor and its relation to key parameters underlying the electrical methods.

In situ rock resistivity measurements and data uncertainty: A short description of how the in situ rock resistivity is measured and issues of uncertainty related to such measurements.

Estimates of electrical conductivity of in situ pore water and data uncertainty: A short description of how the electrical conductivity (EC) of the in situ pore water is measured or estimated, and its associated uncertainty.

Evidence of pore connectivity: A discussion of the evidence for large-scale pore connectivity; a much debated issue that is of great importance for radionuclide retention and a prerequisite for the application of electrical methods in situ.

Effect of stress relaxation and mechanical damage: When comparing results from in situ and laboratory measurements the comparison is complicated by the fact that the core samples used in laboratory investigations have been subjected to a different degree of stress relaxation and mechanical damage than the in situ rock in the vicinity of a borehole.

Corrections required to account for differences between measurement methods: When comparing results obtained by electrical methods and traditional diffusion-based methods (whether in the laboratory or in situ) the comparison is complicated by the fact that the two methods do not utilise the same pore water species as a probe of migration. Therefore, corrections are needed to account for inherent mechanistic differences between the two approaches.

Representative results: After having discussed the above issues, which is a requirement for assessing the usefulness of the in situ method in comparison to the laboratory method, some representative results obtained by the in situ method are presented.

Although the above topics have already been dealt with in the SDM-Site Forsmark background report /Crawford 2008/ there are many issues of a site specific nature that need to be assessed independently for Laxemar. Consequently, the discussion of these topics is repeated here, although with details customised for the Laxemar site.

Theory

The effective diffusivity of the rock matrix is often given in terms of the formation factor, F_f as:

$$D_e = F_f D_w \qquad \text{(Eq. D-1)}$$

Where D_w is the diffusivity of the solute in free solution, often approximated by the diffusivity of the solute at infinite dilution. The formation factor is a purely geometric entity that is only dependent on the bulk geometrical properties of the micropore network and is independent of the identity of the diffusing species. Specifically, it accounts for the combined effects of porosity, tortuosity and constrictivity on the effective rate of diffusive transport in the rock.

A prerequisite for the formation factor to be genuinely independent of the identity of a diffusing solute species is firstly that the size of the solute is small compared to that of the pore diameter (or other appropriate characteristic length of the confined pore space). In crystalline rock this is not a major issue for most dissolved species owing to their small size relative to that of the pores. An issue that has not yet been satisfactorily examined and discussed within the scientific community is how to internalise influences of diffusive processes occurring in the vicinity of charged mineral surfaces into the formation factor (or, whether or not it is a good idea to do so). In safety assessment calculations a cautious approach is generally taken whereby effects lowering the effective rate of diffusive transport (anion exclusion) are internalised in the formation factor, whereas effects that may increase this (surface diffusion) are excluded.

Traditionally, the effective diffusivity of crystalline rock has been examined by allowing solutes, often in trace amounts, to diffuse through rock samples and to observe their apparent macroscopic diffusive flux. An alternative method, implemented within the SKB site investigation programme, allows solutes to migrate in the porous system under the influence of an electric potential. The mechanistic analogy between diffusion and electro-migration has been known for about a century with the relation between the diffusivity and ionic mobility being formalised in the Einstein relation /e.g. Atkins 1999/.

A precondition for using the relation between electro-migration and diffusion in a porous system is that the matrix surrounding the water saturated pores (mineral grains in the case of crystalline rock) do not conduct current. This condition is fulfilled at Laxemar, as the principal minerals (e.g. plagioclase, quartz, etc.) of the most common rock types have electrical conductivities orders of magnitude lower than that of the water saturated rock. If, however, there are non-negligible amounts of electronically conductive mineral grains in the rock, resistivity measurements may not accurately reflect charge conduction within the pore spaces and the formation factor may be overestimated.

Phase angles recorded during laboratory alternating current (AC) resistivity measurements can be used to characterise induced polarisation within rock samples. Induced polarisation relates to an accumulation of ionic charge at solid-fluid interfaces that alters the apparent resistivity of a sample during measurement and can introduce bias in the measurement data. The phase angle is a measure of the lag (given in mrad) between applied current and measured voltage for a monochromatic AC current sine wave and is a measure of the dielectric permittivity of the rock. Low AC frequency induced polarisation in rock arises by two principal mechanisms:

Membrane polarisation. This occurs in very narrow pore spaces with a characteristic diameter not much larger than the thickness of the electrical double layer (EDL). Owing to the restricted pore space, the transport of anions is impeded. This results in an accumulation of charge at the openings of these pores thereby altering the apparent resistivity of the sample (basically these can be thought of a bottlenecks for ionic charge transfer).

Electrode polarisation. This occurs where the pore space is blocked by a mineral grain that is electronically conductive (either metallic or a semiconductor). In this case, surface electrochemical reactions which allow electrons to pass through the mineral grain also give rise to electrical double layers on either side of the blocking mineral grain and alter the apparent resistivity of the sample.

Since quantities of electronically conductive minerals (principally pyrite or magnetite) are very low in the rock types investigated, it is thought that the primary effect is likely to be related to membrane polarisation phenomena in the restricted pore space of the rock matrix. According to /Thunehed 2005a, b, 2007a, c/ most samples have small phase angles indicating a limited impact of induced polarisation, although there are a non-negligible fraction of samples from the Laxemar boreholes that have relatively high phase angles. The strong positive correlation between resistivity and phase angle measured in Laxemar rock samples corroborates the hypothesis of a significant population of very narrow pores in some of these samples. Such samples can exhibit anomalous resistivities that may not fully representative of the geometric formation factor.

From the Einstein relation it is relatively straight-forward to deduce the relations between effective diffusivity, electrical current, electrical conductivity (EC), and resistance as has been previously shown in /e.g. Löfgren 2004/ for crystalline rock. The formation factor (F_f) can be defined in terms of either electrical resistivity or EC as:

$$F_f = \frac{\rho_w}{\rho_r} = \frac{\kappa_r}{\kappa_w} \qquad \text{(Eq. D-2)}$$

Here, the terms ρ_w and ρ_r are the electrical resistivity (Ωm) of the pore water and saturated rock respectively, while κ_w and κ_r are the corresponding terms for electrical conductivity (S/m).

By using Equations D-1 and D-2, the effective diffusivity in situ can be assessed if the in situ rock resistivity (which can be measured) and the EC of the in situ pore water (which can be either measured or estimated) are both known.

In situ rock resistivity measurements and data uncertainty

Measuring the in situ rock resistivity by electrically based, geophysical methods has been commonplace for decades even in crystalline rock such as granite. In essence, an alternating electrical current is sent out into the rock matrix from a probe lowered down a borehole. The tool used in the SKB site investigations is a focused tool whereby the current is sent out in an orthogonal direction to the borehole. This minimizes the influence of the borehole itself on the results and also that of an adjacent zone of rock subjected to stress release and mechanical damage. Measurements are made at 10 cm intervals along the borehole which may be as much as 1,000 m in length. The resistivity tool and method used in the SKB site investigations are described in /e.g. Löfgren 2007/.

A problem that can potentially bias the data obtained using in situ measurements is the upper measurement limit of the resistivity probe which, for highly impermeable media, can result in truncation of the lower tail of the formation factor distribution. If not accounted for in the data interpretation, this can result in apparent formation factors higher than in actuality. The sensitivity of the resistivity probe used in the site investigations (Century 9072) varies according to the site specific conditions, although it is known to be quantitatively accurate to a rock resistivity of 50,000 Ωm with an uncertainty of ±5% /Löfgren and Neretnieks 2005b/ and qualitatively accurate to roughly 80,000 Ωm with an uncertainty of ±10% /Löfgren and Neretnieks 2005a/. The bulk of the resistivity data (> 85%) obtained in most boreholes at Laxemar are well within the range of the quantitative measurement limits of the resistivity probe used. The only borehole which deviates from this is KLX05 where roughly 75% of the data are within the quantitative measurement limits /Löfgren and Pettersson 2006/.

Estimates of electrical conductivity of in situ pore water and data uncertainty

A correct estimation of the formation factor requires an accurate knowledge of the EC of the pore water of the rock matrix. Within the SKB site investigation programme for Laxemar the composition of the pore water has for some boreholes been investigated by leaching drill core samples /Waber and Smellie 2004, 2006a, b, c, 2008/. From the assessed concentration of the major groundwater constituent Cl^- and knowledge of the in situ temperature, the in situ EC of the pore water can then be estimated. In addition to estimating the EC of the in situ pore water by leaching of drill core samples, the EC of freely flowing groundwater has been directly measured in situ.

Data from the hydrochemical sampling programme was obtained by isolating short sections around hydraulically conductive fractures, pumping for an extended period of time, and measuring the EC of the groundwater flowing out from the fractures. Other groundwater EC data were also available from measurements made during PFL flow logging campaigns. Not all of these groundwater measurement data sets are thought to be representative of in situ conditions owing to downwards flow of dilute water from shallow depths within the boreholes and other artefacts. A subset of the measurement data, however, have been assessed by /Löfgren 2007/ and judged to be approximately representative of in situ conditions at the relevant depths in a number of different Laxemar boreholes. Data from the pore water characterisation and some selected groundwater EC data from /Löfgren 2007/ are shown in Figure D-1, for some Laxemar boreholes at in situ temperature. It should be noted that EC values calculated at the in situ temperature are used here rather than the customary 25°C reference level since resistivities are also reported at in situ temperature and the same reference temperature must be used for calculating the formation factor.

As can be seen from Figure D-1, there is a significant variation in the data sets for individual boreholes. There is also a need to interpolate between the data points in order to estimate an EC profile for the rock surrounding the borehole. This is further complicated by the possible presence of nearby although undetected water bearing fractures which can have an impact on local EC profiles in the rock. Where there is a lack of data, the interpolation becomes somewhat subjective as can be seen, for example, in the illustrated case of KLX03 (EC trend line).

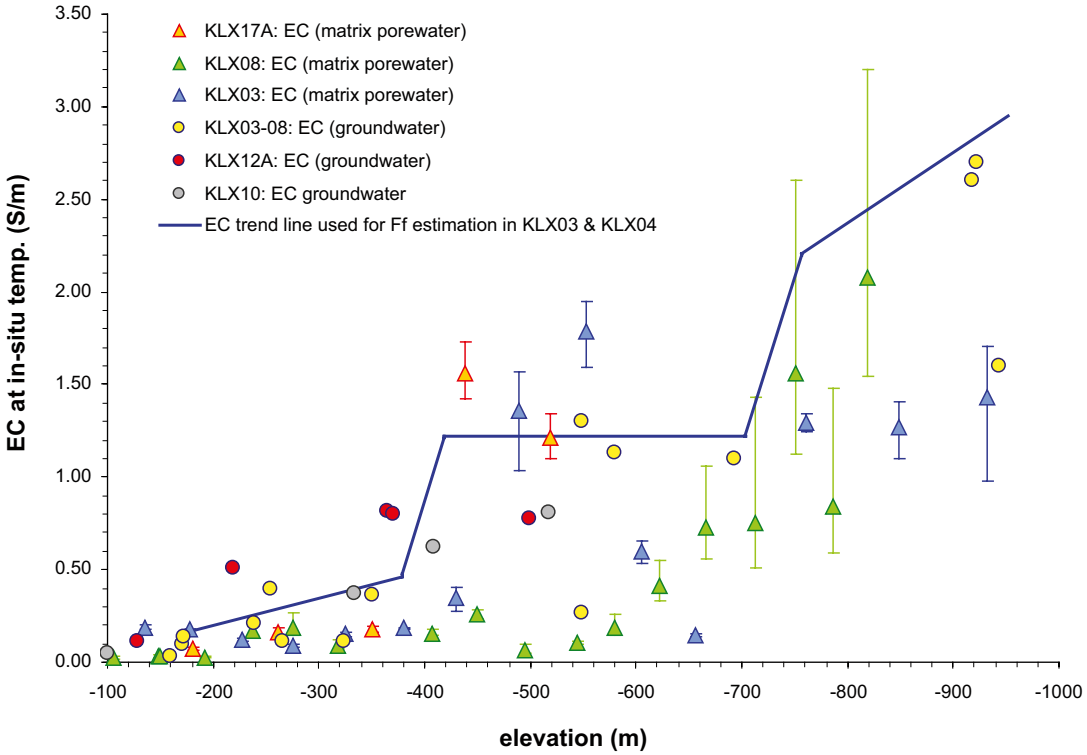

Figure D-1. *Groundwater and matrix porewater EC at in situ temperature in a number of boreholes at the Laxemar site. The trend line assumed for the calculation of formation factors in KLX03 and KLX04 /Löfgren and Neretnieks 2005c/ is also shown.*

There are a number of sources of error that give rise to data uncertainties associated with estimation of the EC from leached core samples. One is sample handling where samples taken to the surface are subject to stress release and mechanical damage. This could potentially result in their original pore water being diluted or altered in other ways. In /Waber and Smellie 2007/, however, it was found that although a certain amount of stress relaxation did occur either during or after bore core retrieval, there was no detectable borehole water contamination and these effects could be accounted for in a rigorous manner.

Another source of data uncertainty is that in order to calculate the original concentration of the pore water from the concentration of the leachate, the porosity of the core sample must be known. In addition to this, there are also data uncertainties associated with sample preparation and analysis. Even so, the estimated total data uncertainty of the pore water chloride concentration is only about 10% in /Waber and Smellie 2007/. A similar magnitude of uncertainty is likely to be introduced when estimating the EC at in situ temperature from this chloride concentration.

Sources of data uncertainty for the EC estimated from measurements of free flowing groundwater are the following:

- Under the influence of pumping, the groundwater may have flowed relatively quickly from another location and may not be representative of the rock matrix porewater in the locality where it is sampled;
- The sampled groundwater may have been diluted by the drilling fluid or other water flowing in the borehole;
- Even if the groundwater is representative for the location, it is not necessarily equilibrated with the pore water at some distance from the fracture within the rock matrix.

It is not an easy task to quantify the data uncertainty of the estimated pore water EC profile. As discussed later, the in situ resistivity data compiled for the site are generally rejected if the matrix porewater is suspected to have an EC below about 0.5 S/m. If one were only to consider data where the EC is above this level it would appear that the error introduced by uncertain EC profiles should

not be more than about a factor of 3–4 in most cases. This, however, assumes that the data are obtained under conditions where the EC is always greater than 0.5 S/m which is not completely assured for a number of boreholes at the Laxemar site.

The EC data obtained from the matrix porewater measurements on samples from KLX08, for example, are such that all resistivity data above an elevation of about –780 m are rejected according to this selection criterion. Since the EC data obtained from KLX04 were judged to be of such poor quality as to be unusable, the same EC profile previously used for interpretation of the resistivity log from KLX03 was assumed for the interpretation of KLX04 /Löfgren and Neretnieks 2005c/. This assumption is not well founded since it could be argued, owing to their close geographic proximity, that the EC data for borehole KLX04 and the KLX08 should be more similar than that of KLX04 and KLX03. If true, this suggests that the formation factors estimated for KLX04 using EC data from KLX03 may not be accurate (i.e. the assumed EC profile for KLX04 is excessively saline). Moreover, this also suggests that a large portion of the in situ formation factor data reported for particularly the upper 600 m of KLX04 may actually fail the abovementioned selection criteria.

An additional uncertainty associated with borehole in situ resistivities logged for Laxemar early-on in the site investigations was due to some electrical conductivities (used for estimating the EC profile) being reported at in situ temperature and some at 25°C. It is possible that the original formation factor data reported for borehole KSH01A and KSH02, for example, /Löfgren and Neretnieks 2005b/ may be biased downwards by a factor of as much as 50%, partly due to this reason.

Evidence of pore connectivity

The connectivity of the microporous system of crystalline rock is an issue that has been hotly debated within the scientific community for decades. The in situ rock resistivity tool used by SKB in the site investigations is claimed to emit a current many meters into the rock matrix. As the mineral grain resistivity of the rock is so large, the current should be propagated predominantly in the interstitial water of the microporous system. The fact that very reasonable formation factors are obtained with the in situ method indicates that the current indeed penetrates the rock matrix on the scale of many metres. If only small scale connectivity existed, say on the scale of centimetres to a few decimetres, the rock resistivity would be much larger than what is actually measured and consequently, the obtained formation factors would be unreasonably low.

It has been questioned whether the concept of large-scale pore connectivity can be justified on the basis of the propagation of an alternating current, where the current-bearing ions only migrate over minute distances. In order to investigate this, the through-electromigration method was developed, where direct current is used to propagate ionic tracers through the rock /Löfgren and Neretnieks 2006/. In that investigation it was shown that the alternating current and direct current methods gave comparable results on drill core samples (from the Laxemar site) up to 12 cm in length.

Large-scale pore connectivity can also be inferred from in situ migration experiments where diffusion has been the only significant transport mechanism. An important example is the in-diffusion experiment performed at the Stripa mine /Birgersson et al. 1992/ where tracers were shown to have migrated to a depth of at least 40 cm into the undisturbed rock matrix; a distance consistent with the expected penetration depth on the time scale of the experiment. As mentioned previously in this report, the characterisation of porewater many metres distant from known fractures shows relict indications of past climatic conditions and groundwater compositions /Laaksoharju et al. 2009/ that differ significantly from what would be expected if the porewater originated purely from initially existing fluid inclusions of formation water. This observation, in itself, is strong corroborating evidence for the existence of a connected microporosity in the rock.

It should be noted that dissolved species migrating in the microporous network, whether driven by a concentration gradient or an electrical potential gradient, do not discriminate pores based on their origin. Migration occurs in all connected porosity, including grain boundary pores, micro-fractures and sometimes sheet silicate pores. It is therefore not strictly necessary to make pronouncements on the relative proportions and distribution of micro-fracture versus grain boundary porosity in situ as discussed in 2.2.1 to justify the use of in situ data derived from electrical resistivity measurements.

Effect of stress relaxation and drilling induced mechanical damage

Within the SKB site investigations, much effort has been spent on obtaining formation factors by using three different, although complementary methods. One is the traditional through-diffusion method using a concentration gradient as the driving force for migration, which is performed in the laboratory on short drill core samples /e.g. Widestrand et al. 2003/. The other is the in situ electrical resistivity method that is the focus of attention for this Appendix chapter. The third is a similar electrical method applied to drill core samples in the laboratory. All three methods are associated with their own specific data uncertainty issues, but there is one issue that deserves extra attention. This issue concerns drill core samples that are subjected to stress relaxation and drilling induced mechanical damage. In addition to this, short drill core samples of, say 10 mm length may also be significantly affected by sawing induced mechanical damage.

When a drill core sample is excavated and taken to the surface, the confining pressure it has been subjected to in situ is released. As a result, tension in the mineral grains may be released and different minerals may expand to different degrees, depending on their bulk moduli of expansion. This generally gives rise to increased porosity, which in turn gives rise to an increased formation factor. The increase in porosity may to some extent be reversed, by re-confining the rock sample in triaxial compression tests /e.g. Jacobsson 2007/, as discussed in Section 2.2.1.

Within the site investigation programme, formation factor measurements in the laboratory have not been performed on re-confined samples. However, such measurements have been performed elsewhere and a reduction in the formation factor for crystalline rock samples under increasing applied confining stress is well known in the literature /Brace et al. 1965, Brace and Orange 1968, Skagius and Neretnieks 1986/. As already discussed in Section 2.2.1 there is strong corroborating evidence that suggests a possible compression of pore spaces under in situ stress conditions. Specifically, porosity measurements made in triaxial compression tests /Jacobsson 2007/ give indications of this.

A very weak although consistent depth trend for the in situ formation factor is perceptible at the Laxemar site as can be clearly from Figure D-2. It is inconclusive, however, whether this apparent variation can be credited to the increasing in situ stresses at greater depths or whether it is an artefact of uncertainty in the assumed matrix porewater EC profiles. If, for example, the depth trend for the EC of the matrix porewater is overestimated (i.e. it increases more rapidly with depth than in actuality) then the estimated formation factor might show a decreasing depth trend even where there is none. Since it is not possible to ascertain whether the depth trend is real or an artefact, the trend is neglected in the data recommendations given in chapter 4 and considered to be part of the overall data uncertainty.

There is no clear tendency towards increasing or decreasing formation factors with increasing depth in the laboratory formation factor data. On the other hand, the non-linear portion of the pressure versus volumetric strain curves reported by /Jacobsson 2007/ in triaxial compression tests (attributed to closure of microcracks and grain boundary pores) is found to increase with core sampling depth which could be the result of a drilling induced damage effect.

Partially corroborating evidence for the impact of the confining stress on the microporous system is available in the form of laboratory measurements of flow permeability. Permeability and effective diffusivity are very closely related since they are both highly dependent upon the geometry of the microporous structure in the rock. In /Siitari-Kauppi 2002/, for example, a near perfect linear correlation is found between the permeability of crystalline rock samples and effective diffusivity. As part of the site investigations, the permeability of drill core samples from KLX03 was measured at different confining pressures /Vilks 2007/. Although there are some additional issues associated with bore core damage and the creation of new micro-fractures in the small samples used in these experiments, a weak tendency for decreased permeability with increasing confining pressure is apparent in some of the data sets (see Figure D-3).

Reductions in effective diffusivity under increasing stress have also been reported by /Skagius and Neretnieks 1986/ in re-confined samples at pressures up to 35 MPa. Similar results were obtained by /Bradbury and Green 1986/ at confining pressures up to 16 MPa. Results from in situ diffusion experiments reported by /Birgersson and Neretnieks 1990/ in the Stripa project, however, were inconclusive with regard to compression of pore spaces under in situ stress conditions (estimated to be ~15 MPa at the 360 m level in the Stripa mine). In situ diffusion experiments reported by /Vilks et al. 2003, Vilks et al. 2004/ at the (Canadian) AECL Underground Research Laboratory showed no

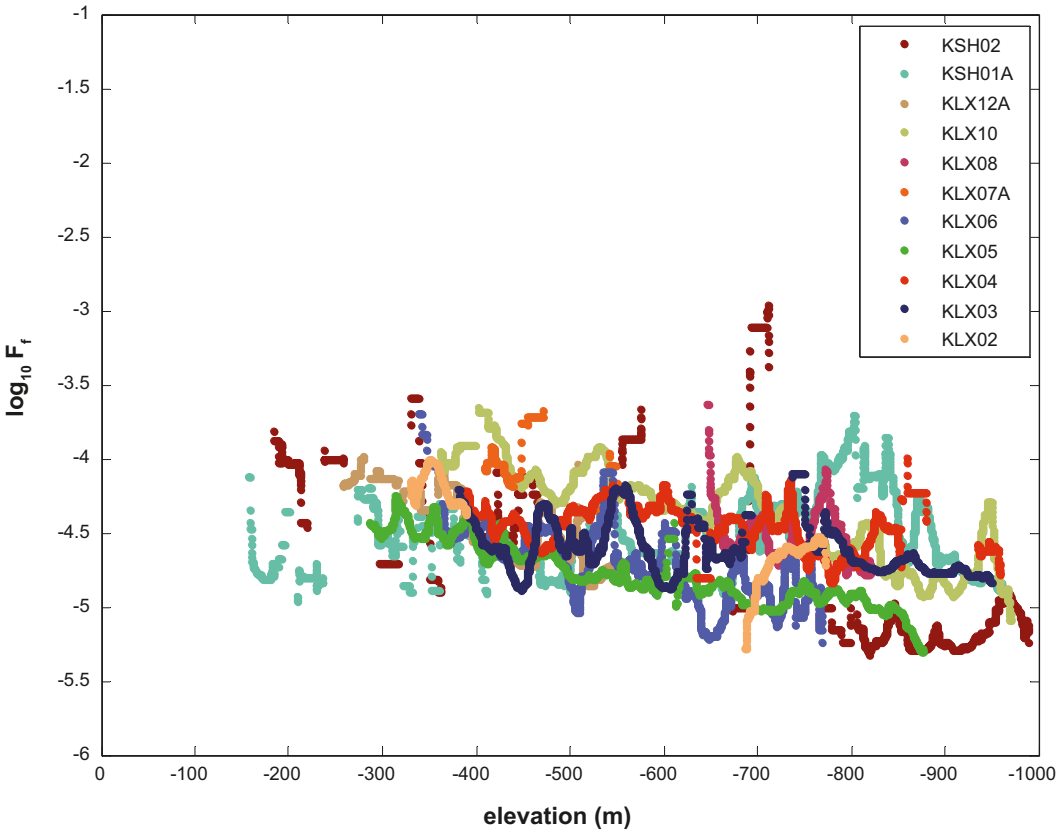

Figure D-2. *Variation of the in situ formation factor (10 m running averages) plotted as a function of elevation for all reported boreholes from the Laxemar-Simpevarp area. Measurement points less than 0.5 m distant from mapped open fractures are excluded.*

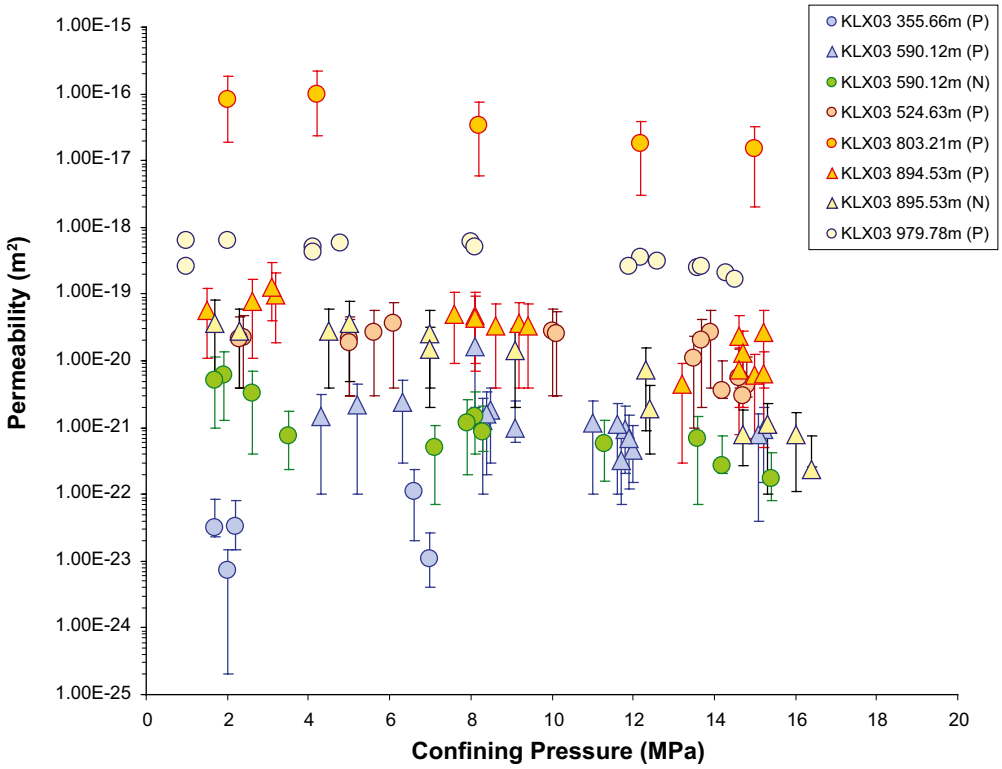

Figure D-3. *Results of laboratory permeability measurements on core samples from borehole KLX03 /Vilks 2007/. Data series are labelled with regard to borehole length and an indication whether permeability was measured parallel (P) or normal (N) to the core axis.*

evidence for a decreasing effective diffusivity with increasing depth. The experiments were carried out at different depth levels (240 m, 300 m, 420 m) corresponding to an interval of 30–60 MPa maximum stress. Stress redistribution in the nearest centimetre adjacent to the borehole wall, giving a locally decreased effective diffusivity, was identified as a confounding factor complicating the interpretation of the results. For the shallowest depth (30 MPa), however, the *in situ* results were found to be identical to effective diffusivities measured in the laboratory in re-confined samples subjected to the same stress magnitude. This may suggest that borehole wall damage effects might not be prevalent in boreholes drilled in Laxemar owing to the generally lower *in situ* stresses encountered in the bedrock.

Mechanical damage due to drilling or other sample preparation is an issue that should not be confused with the issue of stress relaxation. The degree of mechanical damage inflicted on the excavated sample depends on numerous factors such as the rock type, properties of the drill bit and sawing blade, the power applied in the drilling and sawing, percussive vibration, etc. The porosity induced as result of mechanical damage during the excavation process would most likely be best characterised as a tendency to increased intensity of micro-fracturing. One would expect this damage to increase slightly with depth as the mechanical force which needs to be applied during core drilling often tends to increase with depth. When excavating a sample and taking it to the laboratory, the increased porosity is due to both stress relaxation and mechanical damage. Predicted trends of increased porosity or formation factor in the laboratory compared to in situ values at different depths may also be masked by mechanical damage effects that are not directly related to the drilling process itself (i.e. sample sawing).

Stress relaxation most likely affects the entire core sample, whereas damage effects may be concentrated near the periphery of the sample. Since the damaged zone in situ forms a series resistance with outlying undamaged rock during resistivity logging, the in situ data will be only marginally affected by damage in the immediate vicinity of the borehole. Resistivity and through diffusion measurements performed on core samples in the laboratory, on the other hand, are typically made parallel to the core sample axis. In this configuration, the damaged zone will most likely form a parallel resistance which could have a larger impact upon laboratory based measurement results.

It is difficult to say exactly by how much in situ measurements might be affected by drilling induced damage to the borehole walls, although it is possible to make a simple scoping calculation assuming approximately cylindrical current propagation over a limited distance, r_0 into the rock (this is probably not an unreasonable assumption for at least the first 3 m, or so away from the borehole when using a focussed resistivity probe). For a disturbed zone of thickness d_s surrounding a borehole of radius r_{bh}, the measured in situ formation factor, $\overline{F}_f$ can then be given in terms of the formation factor of the damaged rock and that of the undisturbed matrix as (by analogy with the corresponding problem in heat transfer):

$$\overline{F}_f \approx \frac{\log\left(r_0/r_{bh}\right)}{\dfrac{\log\left(\left(r_{bh}+d_s\right)/r_{bh}\right)}{F_{fs}}+\dfrac{\log\left(r_0/\left(r_{bh}+d_s\right)\right)}{F_f}} \qquad \text{(Eq. D-3)}$$

Figure D-4 shows the impact of a damaged zone of 1 cm thickness surrounding a borehole of radius 4 cm and a measurement support scale, r_0 of 3 m. Here, the formation factor of the damaged zone has been varied relative to that of the undisturbed rock. As can be seen from the figure, a damaged zone giving an increased formation factor has negligible impact on the measurement results. If, on the other hand, the drilling induced damage results in a decreased formation factor the impact is larger. For moderate amounts of induced damage, however, the impact is likely to be very small as indicated by the broken lines corresponding (respectively) to a 10 times increased and 10 times decreased formation factor in the first 1 cm surrounding the borehole. Although it is not possible rule out the existence of a decreased formation factor, the combined effect of drilling induced microfracturing, tangential shear stress during drilling, and inwards acting stress redistribution is thought to most likely result in an increased formation factor in the damaged zone.

More detailed discussions concerning the impact of a damaged zone surrounding the borehole can be found in /Löfgren 2001/ and /Autio et al. 1999/. If it were not for the disturbance in porosity arising due to sample excavation, the formation factors obtained in the laboratory by electrical methods should be comparable to those obtained in situ for the same pore water EC. A prerequisite for this, of course, is that the in situ pore water EC is correctly estimated.

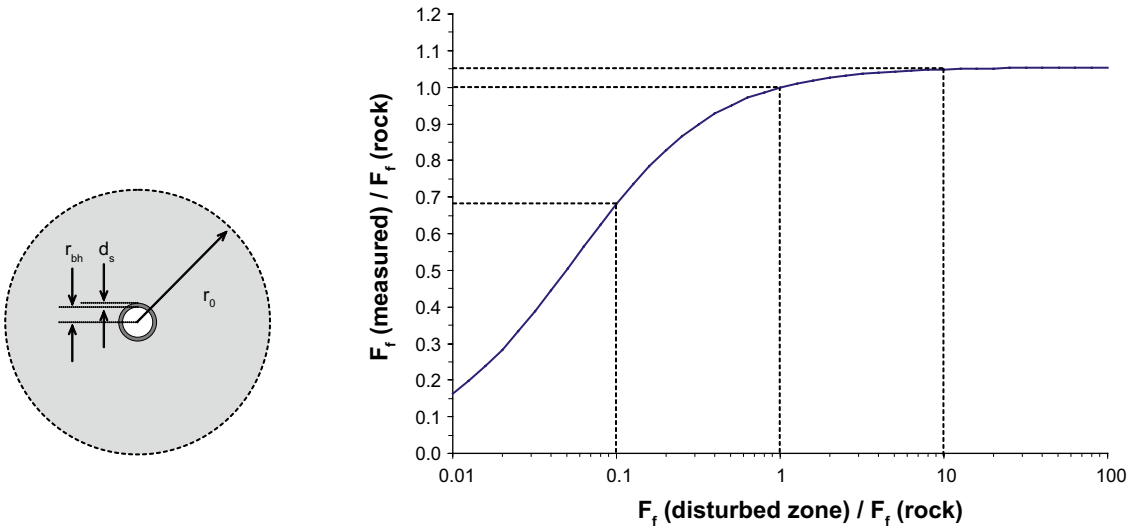

Figure D-4. *Scoping calculation made using Equation D-3 showing the impact of a 1 cm thick disturbed zone surrounding a borehole. The ratio of the measured and actual formation factor is given on the vertical axis (right-hand image) as a function of the formation factor ratio of the disturbed and undisturbed rock on the horizontal axis. The left-hand image is an illustration of a borehole of radius r_{bh} in relation to the damaged zone of thickness d_s and the support scale of the measurement, r_0.*

Corrections required to account for differences between measurement methods

As discussed in the theory part of this Appendix chapter, the formation factor by definition should only depend on the geometry of the porous system and not on the identity of the migrating solute. Also, by definition, the formation factor should be the ratio of the effective diffusivity D_e and the diffusivity in free solution D_w. However, for ionic solutes in crystalline rock, both of these requirements cannot be fulfilled, as the mineral surfaces surrounding the pores are generally negatively charged and can be expected to interact with the ionic solutes, thereby affecting their rate of migration.

As it is not yet settled within the scientific community how to handle this inconsistency, in the site description a pragmatic decision has been taken to avoid internalising processes as part of the formation factor that lead to an increase in the effective rate of diffusion. In practice, this means that enhanced migration at the mineral surfaces (by surface diffusion or surface conduction) is not internalised in the formation factor. Although this could well be considered to be an inconsistency in the data evaluation, it is motivated by the wish to avoid the possibility of overestimating the effective diffusivity of matrix diffusing solutes.

When comparing formation factors obtained by electrical methods and traditional diffusion methods, the comparison is complicated by the fact that the two methods do not utilise the same pore water species as a probe of migration. In through-diffusion measurements, a single tracer (or a defined set of tracers) diffuses through the porous system under a concentration gradient. The tracer being used within the site investigation is the non-charged, and hypothetically non-interacting molecule, tritiated water (HTO) /Byegård et al. 2008/. In supporting studies, the anionic tracers uranine and iodide have also be used /Ohlsson 2000, Löfgren and Neretnieks 2006/. In the electrical methods, all anionic and cationic solutes dissolved within the pore water propagate the current. In the laboratory programme of the site investigation, the solution used as pore water is 1 M NaCl. Rock resistivity measurements in situ are, by necessity, performed at the naturally existing pore water (with an ionic strength comparable to 0.1 M NaCl or higher).

A number of comparative studies have been performed in the laboratory using both electrical and through diffusion methods on the same samples /Ohlsson 2000, Löfgren and Neretnieks 2006, Byegård et al. 2008/. As expected, some deviation in the formation factors obtained by the different methods is found. Probable explanations for this deviation are that the methods do not utilise the same pore water species as a probe of migration, that they utilise analogue but not identical transport mechanisms, and that the different methods invoke different data uncertainties. The deviations found are generally a factor of about two in magnitude, where the electrical method gives enhanced formation factors compared to the through-diffusion method. Three processes have been identified as candidates for being responsible for (part) of this deviating factor of about two. These are surface conduction, anion exclusion, and capacitance effects.

Surface conduction

A process postulated to occur that would give a theoretically increased effective rate of diffusive transport (and therefore should not be internalised in formation factors recommended for safety assessment calculations) is diffusion in the electrical double layer (EDL). This process is also referred to as surface diffusion in the scientific literature /Olin et al. 1997/. Since cations are concentrated in the EDL due to electrostatic attraction, this could potentially lead to higher concentration gradients close to the mineral surfaces and thus an enhanced rate of cation diffusion /Ohlsson and Neretnieks 1998/. Although the existence or non-existence of surface diffusion is a hotly debated topic in the field of transport modelling in fractured crystalline rock, no such controversy exists in the field of geophysics where the existence of charge conduction in the EDL has been used as a basis of petrophysical methods for many years /Ruffet et al. 1993, Nover 2005, Börner 2006, Slater 2007/. It should be noted that the conduction of electric charge in the EDL is primarily mediated by the movement of principal cations of the pore water, which are only loosely bound to the mineral surfaces, such as Na^+ or Ca^{2+}. This should be considered distinct from notions of surface diffusion involving more strongly bound, sorbing solutes which may have very different mobilities in the EDL /Axe et al. 2002/. An overview of the theory of surface conduction in porous media is given in /Revil and Glover 1997/.

When measuring the formation factor by electrical methods, surface conduction is a process that, if not corrected for, gives rise to enhanced formation factors. It has been noted in laboratory experiments that even at relatively high salinities (~1 M NaCl) the apparent formation factors are roughly a factor of two times higher than those measured by through-diffusion using non-sorbing tracers on the same samples. This has been found to be the case for Laxemar specific rocks using the non-charged tracer HTO /Byegård et al. 2008/. At present, however, it is not entirely clear how much of this deviation is actually related to surface conduction how much depends on other mechanisms that are not fully understood.

The transmission of charge in the layer of enhanced cation concentration at the mineral surfaces in the electrical methods could be responsible for at least part of the observed deviation. However, it could be questioned whether the effect of surface conduction is that significant at salinities as high as 1 M NaCl. In a study by /Ohlsson and Neretnieks 1998/ measurements of rock conductivity were made for a number of samples that were first saturated with low ionic strength pore water (~0.001 M NaCl) and thereafter with high ionic strength pore water (1 M NaCl). The measured rock conductivity corresponding to the low ionic strength pore water can be assumed to represent the surface conductivity, in agreement with /Revil and Glover 1997/. Furthermore, it can also be assumed that the surface conductivity does not significantly change with the pore water's ionic strength, in agreement with /Olin et al. 1997/. By comparing the measured rock conductivities at high and low ionic strength pore water, one can surmise that surface conduction should only contribute towards about 5–10% of the overall rock conductivity if the sample is saturated with 1 M NaCl.

The surface conductivities obtained in /Ohlsson and Neretnieks 1998/ and later on in /Ohlsson 2000/ and /Löfgren 2004/ range between 6×10^{-6} and 6×10^{-5} S/m. After accounting for differences in porosity and tortuosity-constrictivity between the different investigations, this is in excellent agreement with the detailed experimental and theoretical results reported by /Stein et al. 2004/ in studies of surface charge transport in nanofluidic channels (0.07–1.0 μm) fabricated on fused silica substrates. The results obtained by /Ohlsson 2000/ and /Löfgren 2004/ (based upon earlier work in /Löfgren 2001/) are shown in Figure D-5.

It should be noted that since the (apparent) formation factor, F_f^{app} was measured using core samples saturated with 1 M NaCl electrolyte, a correction needs to be made to give the surface conductivity in terms of the "true" formation factor, F_f. The horizontal axis of Figure D-5 is therefore recalculated using the following equation to correct for the contribution of surface conductivity, κ_s (S/m) to the measured formation factor:

$$F_f = F_f^{app} - \frac{\kappa_s}{\kappa_w} \qquad \text{(Eq. D-4)}$$

An interesting result obtained in the investigation was that the surface conductivity appears to be strongly correlated with the formation factor. This stands to reason since it is easy to imagine that compact pore spaces are likely to be more strongly affected by the presence of the electrical double layer than larger, less constricted pore spaces. Furthermore, the choice of a power law fit to the data

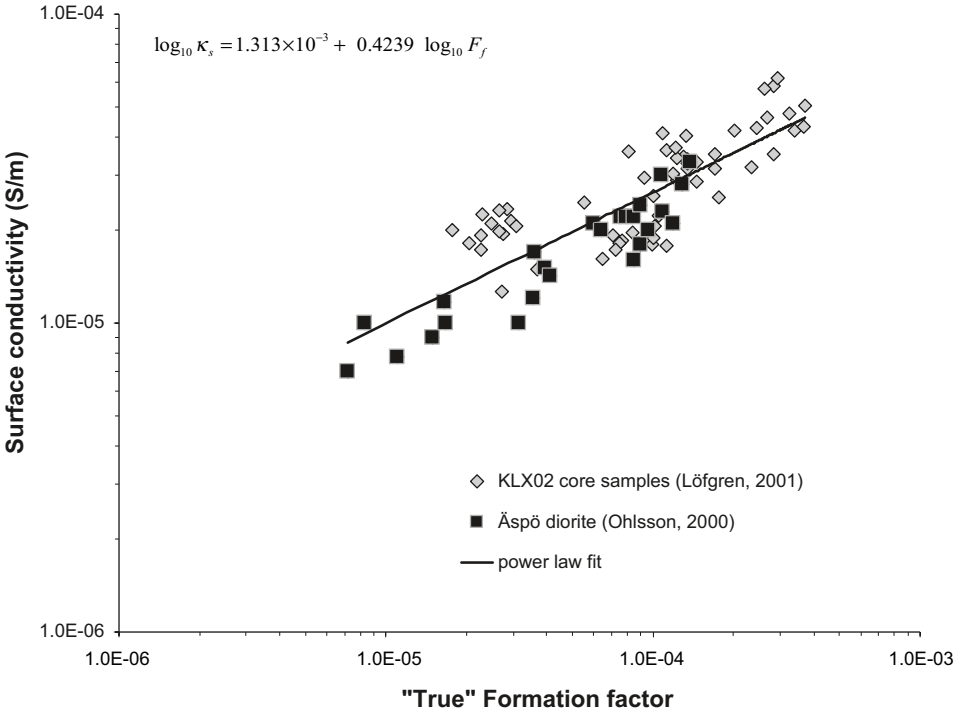

Figure D-5. *Estimated surface conductivity vs. "true" formation factor for a number of core samples investigated by /Ohlsson 2000/ and /Löfgren 2001/. The power law fit is based upon linear regression of the joint data set.*

is phenomenologically consistent with the fact that one would expect the surface conductivity to approach zero for a formation factor also approaching zero (i.e. since a non-conductive sample, by definition should not exhibit any surface conduction either). Using the regression equation given in Figure D-5 allows us to approximately correct in situ measured (apparent) formation factors for the effect of surface conduction. The apparent formation factor is then given by:

$$F_f^{app} = \frac{\kappa_s + \kappa_r}{\kappa_w} \approx \frac{a F_f^b}{\kappa_w} + F_f \qquad \text{(Eq. D-5)}$$

With regard to the consequences of surface conduction effects for the interpretation of in situ resistivity data, it is possible to predict a significant biasing effect for the lower end of the formation factor distribution measured for rock, particularly for porewater of low ionic strength. Figure D-6 shows the theoretical impact that different porewater conductivities should have upon the apparent formation factor (i.e. including surface conduction effects) for a range of assumed "true" formation factors.

This analysis assumes, however, that one has full knowledge of the actual matrix porewater conductivity since the analysis given in Figure D-6 represents a correction for surface conductivity effects at a specified porewater composition. While this assumption may be defensible for laboratory measurements where samples have been equilibrated with a known porewater composition, the applicability of the correction implied by the data in Figure D-6 may not be accurate for in situ derived data.

In reality, what one has estimated with regard to in situ data is an apparent formation factor evaluated for an assumed porewater conductivity that may not even be correct. If one considers the additional uncertainty introduced by uncertain or incorrectly determined porewater conductivity, the relation between the estimated formation factor derived from uncertain measurement data, F_f^* and the true formation factor, F_f would then be given by:

$$F_f^* = \left(\frac{\kappa_s + \kappa_r}{\kappa_w} \right) \frac{\kappa_w}{\kappa_w^*} \approx \frac{a F_f^b}{\kappa_w^*} + F_f \left(\frac{\kappa_w}{\kappa_w^*} \right) \qquad \text{(Eq. D-6)}$$

Where, κ_w represents the true porewater conductivity and κ_w^* is the estimated (uncertain/incorrect) porewater conductivity. Essentially this amounts to an additional correction factor over and above that specified by the correction for surface conduction effects (as illustrated in Figure D-6).

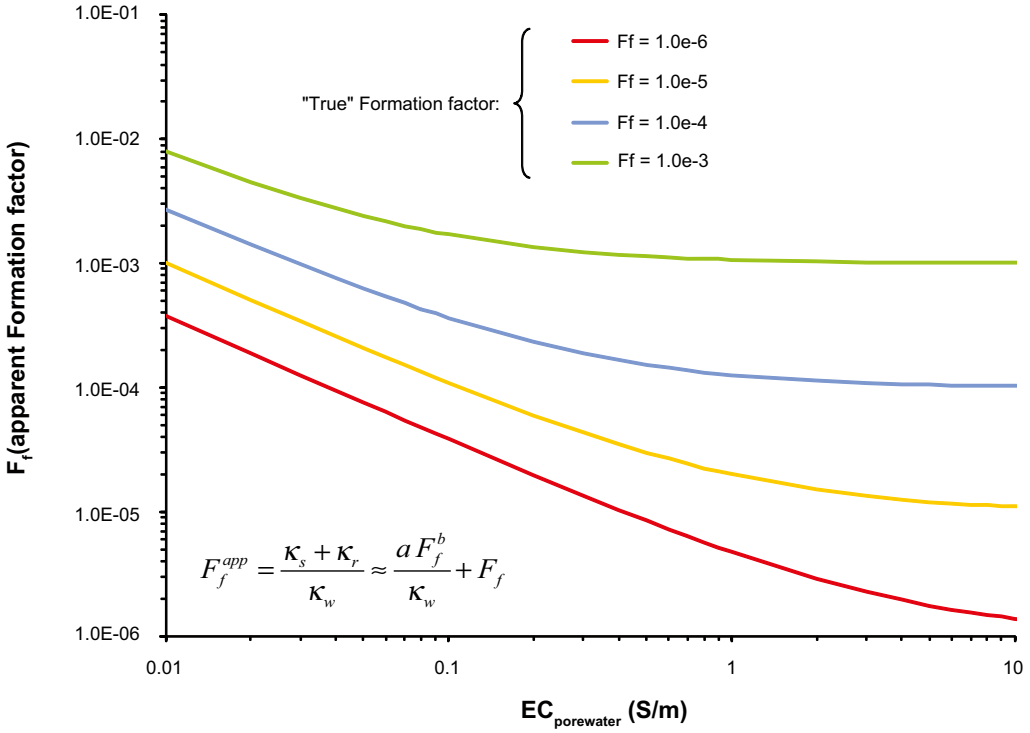

Figure D-6. *Theoretical apparent formation factor as derived from electrical resistivity measurement vs. matrix porewater electrical conductivity for a range of "true" formation factors using the power law relation for surface conductivity given in Figure D-6. For low porewater EC values, one would expect a systematic bias leading to overestimation of formation factors towards the lower end of the formation factor distribution.*

Since Equation D-6 is non-linear function of the "true" formation factor, one would expect uncertainty in the porewater conductivity to have a variable impact across the distribution of values derived from in situ measurements. Figure D-7 shows an example of how an uncertainty in the true porewater conductivity of ±0.5 S/m might impact upon the magnitude of the formation factor measured in situ as estimated using Equation D-6. The choice of ±0.5 S/m as a calculation example here is arbitrary, although not unreasonable in light of the data presented in Figure D-1.

For formation factors greater than about 10^{-4}, the data in Figure D-7 indicates that the surface conduction bias is less significant and the error in the estimated formation factor is roughly proportional to the error in the porewater conductivity estimate. For lower formation factors, however, the direct impact of uncertainty in the assumed porewater conductivity (i.e. by way of the second term on the right hand side of Equation D-6) is insignificant and the surface conductivity bias dominates. The analysis therefore suggests that one would generally expect formation factors derived from in situ measurement data to almost always overestimate the true formation factor (at least for the lower end of the distribution) even in the presence of considerable uncertainty concerning the actual porewater conductivity.

Anion exclusion

Due to the presence of negatively charged mineral surfaces (which is counteracted by the cations in the EDL), part of the pore volume will be excluded for anionic migration. Such anion exclusion can be studied by comparing the matrix diffusion of anions and the non-charged tracer HTO. However, no such measurements have been performed within the site investigation programme or in supporting studies on Swedish rock. In studies on Finnish granite, through diffusion measurements utilising the tracers HTO and ^{36}Cl have been performed on the same samples, with the aim of investigating the effect of anion exclusion /Valkiainen et al. 1996, Olin et al. 1997/. In /Olin et al. 1997/ it was concluded that about one third of the pore space is restricted for anionic movement and that ion exclusion is not a (clear) function of the pore water's ionic strength. A number of different pore water salt solutions in the interval 0.001 M–0.5 M were used. In /Valkiainen et al. 1996/, effective diffusivity measurements were performed on three granite samples 2–6 cm in length. By comparing the D_e

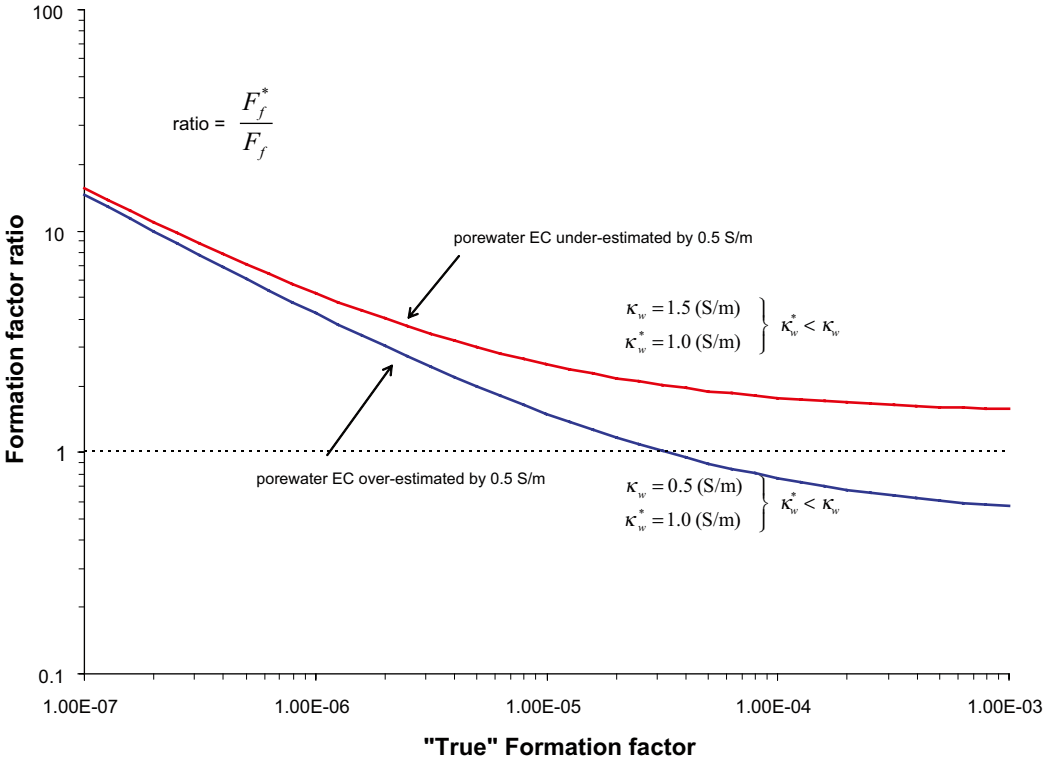

Figure D-7. *Estimated formation factor ratio indicating by how much the formation factor based upon interpretation of in situ measurements might be overestimated or underestimated relative to the "true" formation factor for an actual in situ porewater conductivity ±0.5 S/m relative to an assumed porewater conductivity of 1.0 S/m (~0.1 M NaCl).*

obtained by HTO and ^{36}Cl for each sample, it was found that the D_e obtained by HTO was on average six times larger. It should be noted that D_w for both ^{36}Cl and HTO is about the same (~2×10^{-9} m^2/s).

Anion exclusion may greatly contribute to the deviating factor of about two between formation factors obtained by electric methods and through diffusion measurements using uranine /Ohlsson 2000/ and iodide /Löfgren and Neretnieks 2006/ as tracers. It does not explain, however, the deviation in formation factors obtained with electrical methods and through diffusion measurements using HTO /Byegård et al. 2008/. Other possible reasons therefore need to be considered to explain this deviation.

Capacitance effects

It is well known within the field of geophysics that if the rock resistivity is measured with alternating current at too high frequency, the obtained apparent resistivity will be underestimated due to capacitance effects. For this reason the rock resistivity has been measured at different frequencies, ranging from 0.1 – 10^6 Hz /Löfgren 2001, Thunehed 2007b/. In addition, the rock resistivity has been measured using direct current /Löfgren and Neretnieks 2006/. What can be concluded is that measurement of the rock resistivity with alternating current at frequencies of a few Hz up to a few hundred Hz, the formation factor is overestimated by not more than a few (< 5%) percent.

Handling of correction factors in site investigations and the site descriptive model

As has been found within the site investigation and supporting studies, formation factors obtained from electrical methods are roughly a factor of two times larger than those obtained in laboratory tracer tests. A factor of two is a small deviation compared to the formation factor variability and uncertainties in other transport parameters. Therefore, only very limited data uncertainty is introduced if, without further consideration, the formation factors obtained from electrical methods are (cautiously) decreased by a factor of two. An additional prerequisite for applying this correction

to formation factors obtained in situ is that the deviating factor does not increase under conditions other than those used in the laboratory. Two conditions that may differ significantly are the sample size and the pore water ionic strength.

Concerning the sample size, /Löfgren and Neretnieks 2006/ compared formation factors obtained with the electrical resistivity methods and a tracer test method (the through-electromigration method) on samples from 1.5 cm up to 12 cm in length. It was concluded that the deviating factor of about two does not appear to change with increasing sample length. Also the fact that in situ formation factor measurements, where the effective sample size is on the scale of metres, gives reasonable formation factors lends weight to the notion that the factor is not dependant on sample size (as long as the sample length is significantly larger than the size of individual pores or microfractures). There are measurements made on very thin samples ($\leq$ 1 cm) that indicate larger formation factors /Byegård et al. 2008/. For samples larger than a few centimetres, however, the formation factor seems unaffected by sample size /Skagius and Neretnieks 1982, Bradbury and Green 1986, Ohlsson 2000/.

Concerning the porewater ionic strength, the observations of the deviating factor of about two are all made for porewaters of high ionic strength (typically 1 M NaCl). It would be very valuable to observe that the factor does not increase significantly at pore waters relevant for the site (~0.1 M NaCl at repository depth) using site specific rock samples. The situation is further complicated by the observed correlation between surface conductivity and formation factor which was touched upon in the preceding section where surface conduction effects were discussed. A supporting study has been initiated and is currently underway to better address this data uncertainty in SR-Site.

It should be noted that the suggested correction factor of two is based purely upon empirical observation and is not quantitatively related to any detailed theoretical reasoning. Indeed, the laboratory data obtained during the site investigations suggests a large uncertainty concerning the deviation between formation factors determined by resistivity measurements and the through-diffusion technique. Figure D-8 shows the relative deviation between measurements using the same rock core samples. The average deviation (i.e. ratio of resistivity and through diffusion formation factors) is found to be 2.6±2.4 with an apparently larger variance towards the lower end of the formation factor range as determined by the through-diffusion measurements. A theoretical curve is also shown in Figure D-8 based upon Equation D-5 and assuming that surface conduction bias is the only source of the discrepancy.

As can be seen from Figure D-8, the effect of surface conduction bias appears to be far too small to account for the observed deviation between through-diffusion measurements and laboratory resistivities measured at 1 M NaCl porewater concentration. The samples used in the electrical measurements were all immersed for a period of approximately 8 weeks in 1 M NaCl which should be sufficient time for equilibration of the porewater. It is therefore currently not understood why the deviation between methods is so much larger than that predicted by the data used to construct the surface conductivity correction in Figure D-5.

Figure D-9 shows the same data as in Figure D-8 although with the measurement data grouped according to core sample length rather than rock type. As can be seen from the plotted data, sample length does not seem to be able to explain the large uncertainty in the measurement deviation between the electrical and through diffusion methods. A histogram of the comparative data for the resistivity and through-diffusion methods is shown in Figure D-10 and indicates a strong positive skew in the data which appears to be related to the non-constant variance across the formation factor range.

As discussed in previous sections, however, the importance of surface conductivity relative to the overall rock matrix conductivity increases with decreasing ionic strength of the pore water /Skagius and Neretnieks 1982, Ohlsson and Neretnieks 1998/. When obtaining in situ formation factors within the site investigation programme, this has been handled by rejecting resistivity data where the EC of the pore water is thought to be lower than 0.5 S/m. Above this EC, the majority of the current propagated through the rock should be carried by ions in the bulk pore water. This lower EC limit of 0.5 S/m is based on interpretation of Figure 3-8 in /Löfgren 2004/ for rock with an "average" formation factor typical for the site.

It is expected on the basis of the data contained in Figure D-5 that electrical resistivity measurements performed on rock with low formation factors should be associated with a relatively large positive bias due to surface conduction effects, although more particularly at the lower ionic strengths possibly encountered in situ. It is possible that this leads to a considerable overestimation of the formation

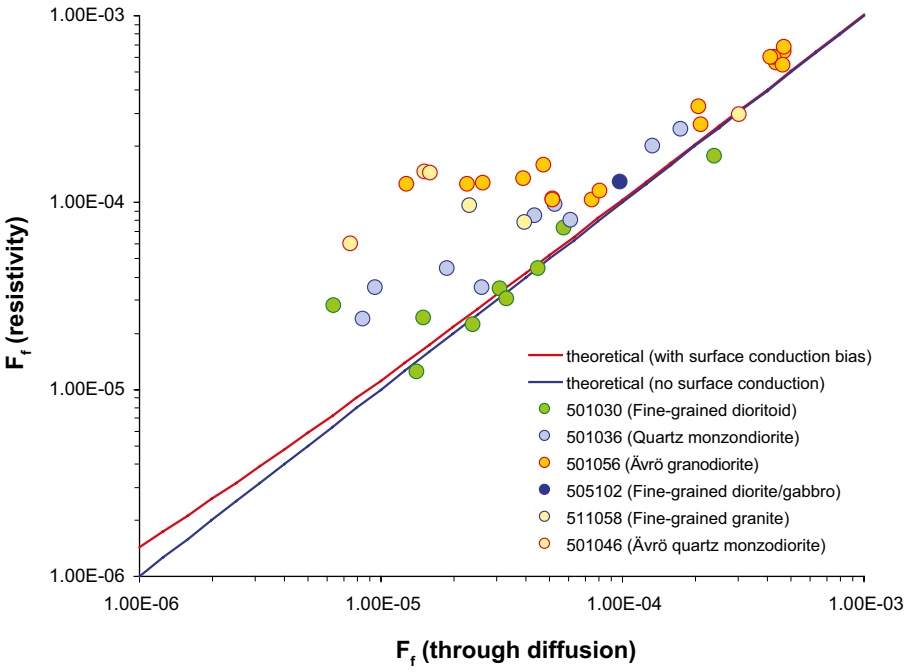

Figure D-8. *Cross-plot comparison of formation factors derived from resistivity measurements with formation factors obtained from through-diffusion measurements performed on the same rock samples (grouped according to rock type). The theoretical trend (red curve) indicates the estimated magnitude of the surface conduction bias for the 1M NaCl (EC = 8.5 S/m) solution with which the rock samples were equilibrated with for 8–10 weeks prior to the resistivity measurements.*

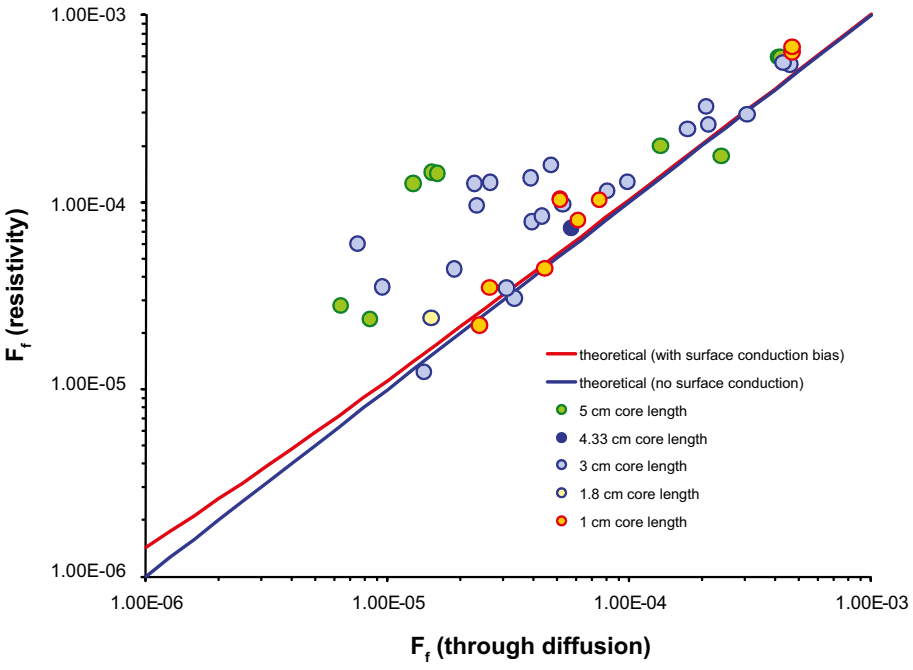

Figure D-9. *Cross-plot comparison of formation factors derived from resistivity measurements with formation factors obtained from through-diffusion measurements performed on the same rock samples (grouped according to core sample length). The theoretical trend (red curve) indicates the estimated magnitude of the surface conduction bias for the 1 M NaCl (EC = 8.5 S/m) solution with which the rock samples were equilibrated with for 8–10 weeks prior to the resistivity measurements.*

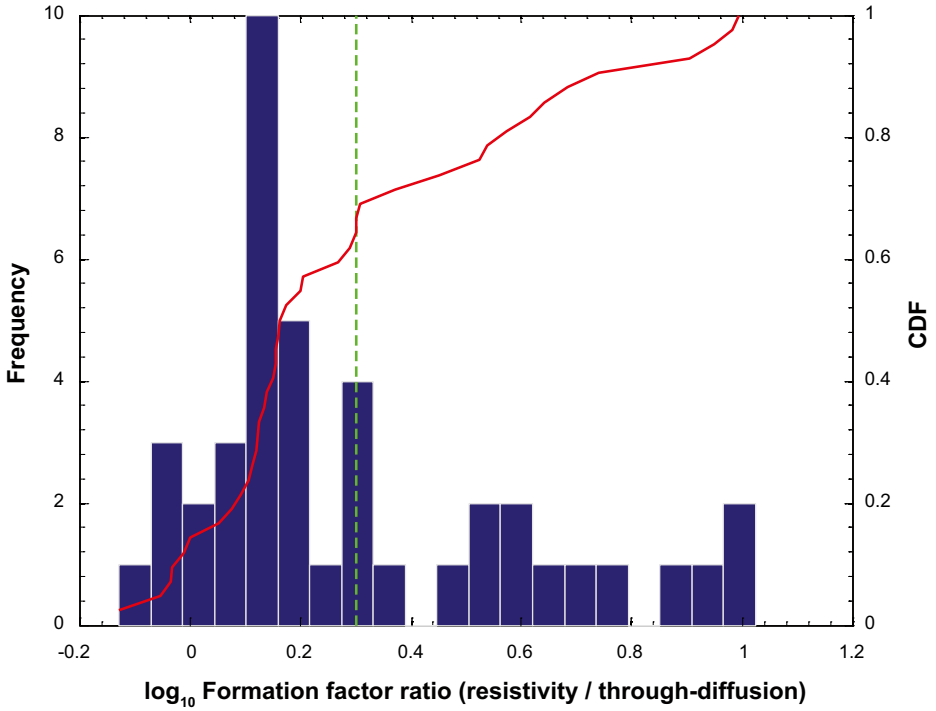

Figure D-10. *Histogram showing ratio of formation factors derived from resistivity measurements with formation factors obtained from through-diffusion measurements performed on the same rock samples (log_{10}-units). The red curve shows the cumulative distribution function, CDF and the vertical broken line indicates a ratio of 2.*

factors comprising the lower end of the range. This, together with the limited measurement range of the in situ rock resistivity tool, may result in a significant uncertainty in the lower tail of the formation factor distribution. It is noted, however, that the uncertainty due to surface conduction at low in situ ionic strength should be considered in addition to that presented in Figure D-8 which indicates a further uncertainty of currently unknown origin.

When averaged over a flowpath, however, the solute transport time can be shown to be proportional to the effective diffusivity of the rock matrix and sorptivity of the transported solute /Löfgren et al. 2007/. One can therefore expect that the arithmetic mean of the formation factor distribution is probably the most appropriate measure for calculating the effective matrix diffusivity for the flowpath. Uncertainties in the lower tail of the formation factor distribution (assumed to be lognormally distributed) should only make a small contribution to the overall uncertainty of the arithmetic mean calculated for the flowpath depending upon how much of the distribution is affected by the bias.

Further reflections on surface diffusion and surface conduction

It appears that the existence of increased concentrations of mobile cations in the EDL and the ability of these ions to conduct electrical current is non-controversial. On the other hand, the existence of increased concentration gradients in the EDL sufficiently large that they can significantly enhance the total diffusive flux through the porous system is still not entirely resolved.

Although part of a continuum of behaviour, the relative mobility of loosely bound cations in the EDL should be considered distinct to surface diffusion involving more strongly bound solutes. The diffusion of sorbing solutes is strongly influenced by the magnitude of the potentiometric energy well in which the solute sits when occupying sorption sites. Movement by surface diffusion in such cases is associated with a considerably greater activation energy for site transition and results in markedly different surface diffusivities for different solutes /Axe et al. 2002/. Experimentally derived results for surface diffusion of particular solutes therefore cannot be generally extrapolated to other solutes without specifically accounting for this effect.

Representative results

If one accepts the arguments in favour of using formation factors derived from in situ electrical resistivity measurements, it is possible to begin discussing the likely distribution of formation factors under in situ conditions provided the caveats and possible errors inherent in the reported data sets are kept in mind (at least qualitatively).

Unfortunately, the Laxemar borehole from which the best estimates of porewater chemistry are available (KLX08) is also the borehole where most of the measurements above –780 m elevation have been rejected on the grounds that the porewater is too dilute (< 0.5 S/m) while the measurements below the elevation are associated with considerably greater porewater compositional uncertainty. None of the other boreholes have particularly well-characterised porewater chemistry and are therefore associated with considerable uncertainty. The Laxemar site in general is characterised by a relatively low porewater salinity down to repository depth /Laaksoharju et al. 2009/ which makes it difficult to give accurate estimates for the in situ formation factor at these elevations.

One borehole where there is a particularly good agreement between formation factor measured in situ and laboratory based methods, however, is KLX04. A plot showing the variation of the formation factor with borehole elevation can be seen in Figure D-11 which is dominated by Ävrö granite (although mostly Ävrö quartz monzodiorite in the elevation interval from about –410 m to –650 m). Also shown in the same Figure is a comparison with formation factors determined in the laboratory by way of the through-diffusion technique as well as electrical resistivity measurements.

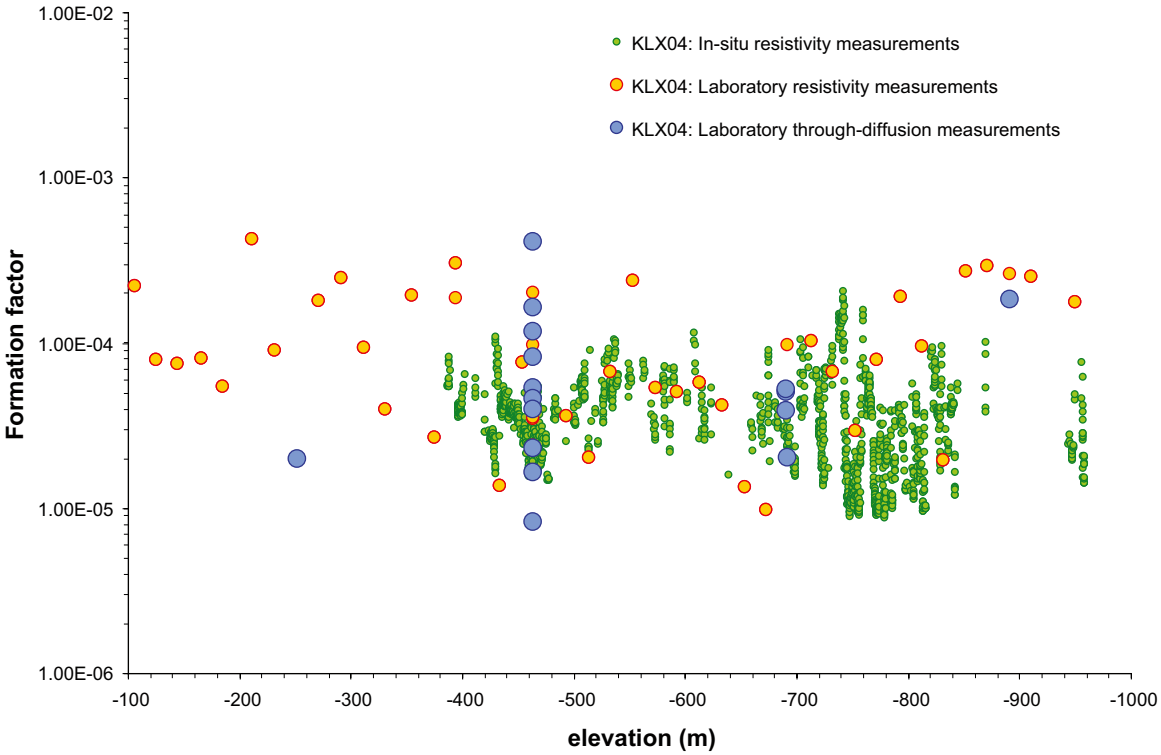

Figure D-11. *Comparison of formation factors derived from in situ resistivity measurements in KLX04 (green markers) with corresponding data measured on core samples in the laboratory (orange makers) also based upon electrical resistivity measurements. Laboratory measurements based upon the through-diffusion method using tritiated water are also shown for comparison (blue markers). In situ measurement points less than 0.5 m distant from mapped open fractures are excluded. Laboratory based data are plotted in accordance with borehole sampling elevation from where the cores were obtained.*

Although there appears to be very good correspondence between the laboratory and in situ data, it is not clear whether the in situ data are accurately estimated owing to uncertainty concerning the porewater composition and the agreement could be purely accidental. At the time in situ formation factor data were reported for KLX04 /Löfgren and Neretnieks 2005c/, there was insufficient information to make an accurate determination of the porewater composition. Furthermore, the groundwater EC profile as determined during the geophysical logging programme /Nielsen et al. 2004/ was deemed to be not suitable owing to a suspected downward flow of surface water in the borehole. For this reason, groundwater EC data obtained during PFL logging in KLX03 was used as a proxy since this was deemed to be relatively accurate. In doing so, it is assumed that the matrix porewater in the rock hosting KLX03 is broadly similar to that for KLX04. In a later investigation /Waber and Smellie 2006c/, the porewater composition of core samples taken from KLX08 was determined. Since KLX08 is in much closer proximity to KLX04 than KLX03, it is possible that the porewater EC profile for KLX08 is a better proxy for the estimation of in situ formation factors in KLX04.

The matrix porewater EC trend line used in the original analysis (based upon groundwater EC measurements) is shown as the blue curve in Figure D-12 together with actual matrix porewater data from /Waber and Smellie 2006a/ for KLX03. Also shown is an alternative trendline based upon data from /Waber and Smellie 2006c/ for KLX08.

In principle it should be possible to use the correction given by Equation D-6 to give a possibly more accurate estimate of the in situ formation factor in KLX04 using the piecewise linear, EC profile shown in Figure D-12 (green curve). Unfortunately, the low EC in the borehole for elevations above about –650 m means that much of the data is likely to be so strongly influenced by surface conduction effects that the results would be to uncertain to be of any use.

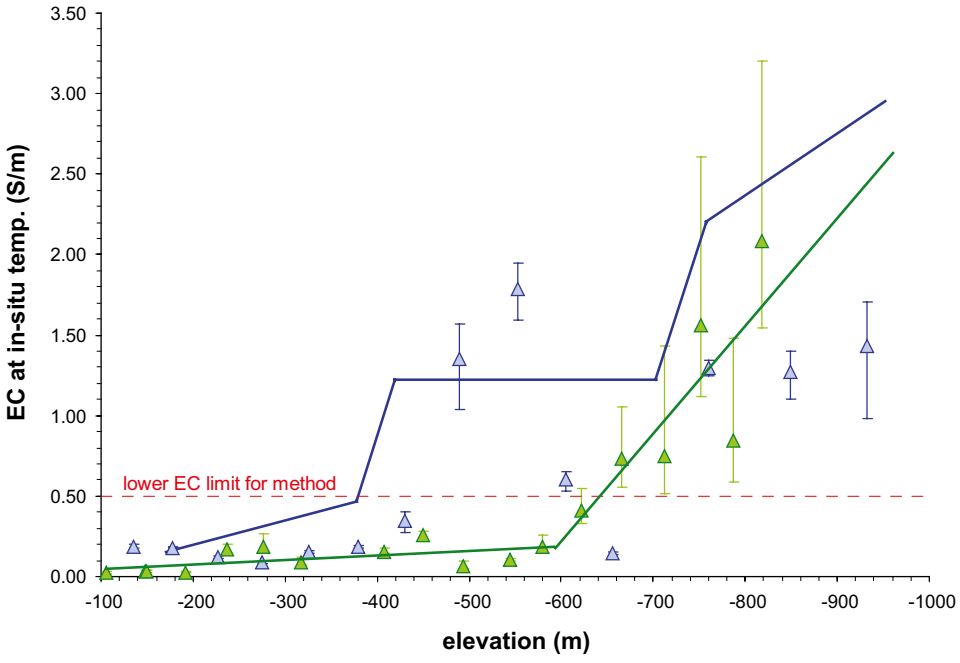

Figure D-12. *Comparison of alternative matrix porewater profiles for KLX04. The original matrix porewater EC profile (blue curve) was used to interpret borehole resistivity logs in KLX03 and KLX04 and reported in SICADA. Blue symbols with error bars are porewater compositions reported by /Waber and Smellie 2006a/ for core samples taken from KLX03. Green symbols with error bars are porewater compositions reported by /Waber and Smellie 2006c/ for KLX08. A possible alternative matrix porewater EC profile for KLX04 is shown (green curve) based upon piecewise linear regression of the porewater data for KLX08.*

Although it is possible to estimate the surface conductivity contribution for a known "true" formation factor and porewater EC, the back-calculation of the true formation factor from an apparent formation factor measured in situ is very uncertain (possibly meaningless) if the surface conduction component is substantially larger than true pore conduction component. For this reason it is only really possible to justify a calculation for data below –650 m elevation. The back-calculation of the corrected formation factor from the data reported in SICADA requires a numerical treatment owing to the non-linearity of Equation D-6. The necessary calculations were performed using Matlab and are plotted in Figure D-13.

It is interesting to note that in some cases the correction implies an increase in the formation factor, while in other cases a decrease in the formation factor although generally the corrected data do not differ significantly from the original data set. This is partly due to the relatively small differences between the original and new EC profiles at greater depths and also related to the fact that since the porewater EC was initially overestimated, the direct porewater compositional correction and that for the surface conduction effects partly cancel out for middle part of the formation factor distribution.

As can be seen from the error bars for the porewater composition, however, even the new EC trend line for KLX08 is subject to a large degree of uncertainty and the accuracy of the corrected data is therefore questionable.

A comparison of in situ formation factor data and laboratory measured values is given in Figure D-14 for borehole KLX03. The data from –380 m to –700 m are mostly dominated by Ävrö quartz monzodiorite with small patches of Ävrö granodiorite, while the data below –750 m are mostly quartz monzodiorite. In this case there appears to be a substantially greater discrepancy between the laboratory and in situ data although the in situ data for KLX03 are approximately in the same range as those reported for KLX04. The distribution of in situ data also appears to have a significant positive skew possibly indicating a large influence of surface conduction for the lower end of the data distribution.

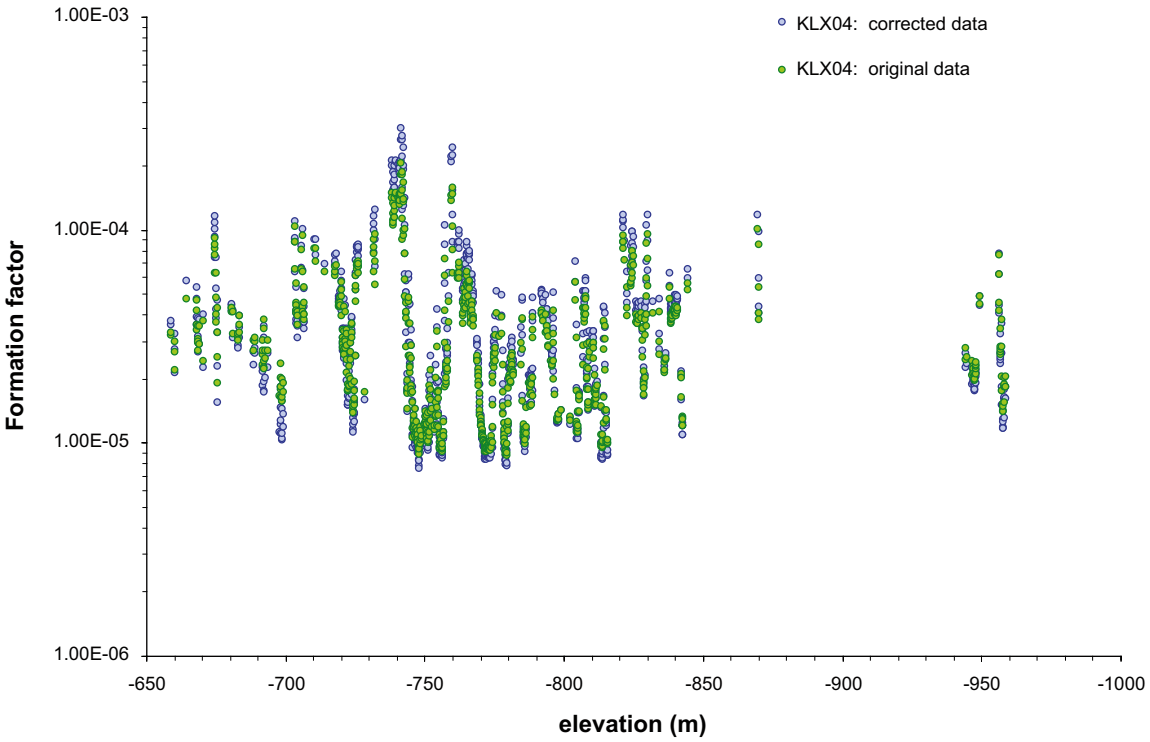

Figure D-13. *Original in situ resistivity data (green markers) reported for KLX04 in SICADA and "corrected" data (blue markers) based upon the proxy porewater EC profile determined for KLX08 and Equation D-6. It should be noted here that the correction only considers the theoretical impact of uncertain porewater composition and surface conduction and not the deviation of unknown origin apparent in Figure D-8.*

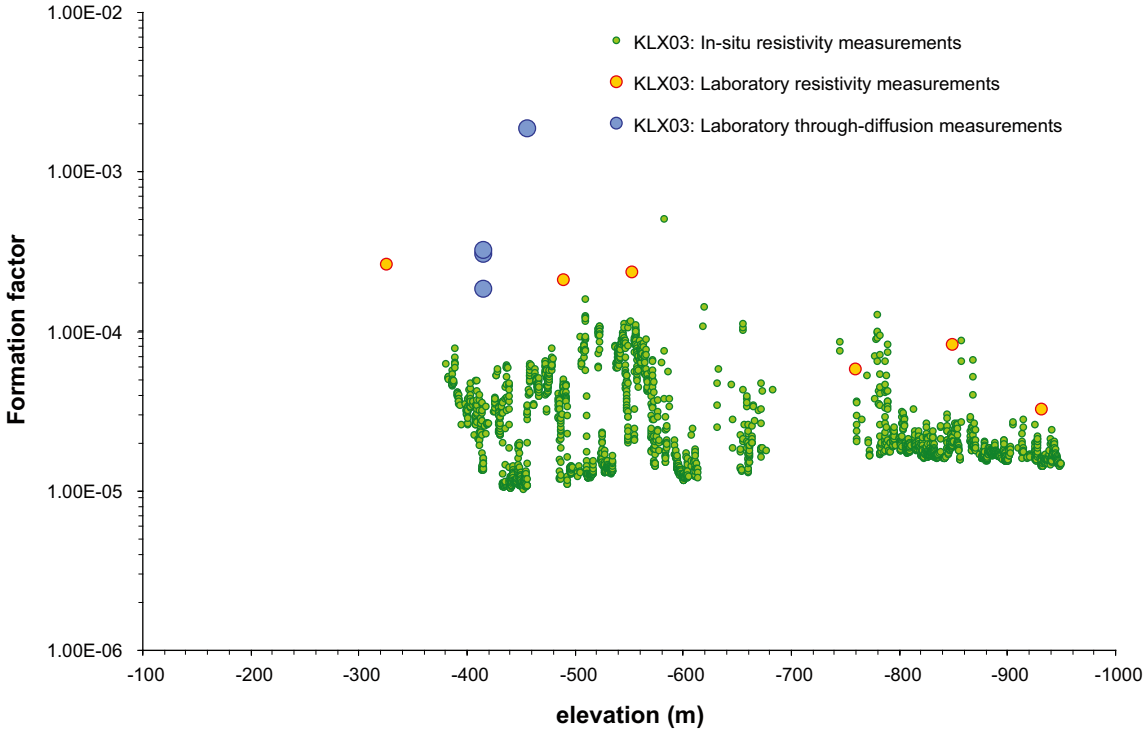

Figure D-14. *Comparison of formation factors derived from in situ resistivity measurements in KLX03 (green markers) with corresponding data measured on core samples in the laboratory (orange makers) also based upon electrical resistivity measurements. Laboratory measurements based upon the through-diffusion method using tritiated water are also shown for comparison (blue markers). In situ measurement points less than 0.5 m distant from mapped open fractures are excluded.*

The first borehole in which the in situ measurement method was adopted was KLX02. Consequently, the data from this borehole are possibly less reliable since the method was still under development. One notable difference between this data set, plotted in Figure D-15, and subsequent measurement campaigns is that no distinction was made between the rock matrix formation factor (i.e. all measurement points ≥0.5 m distant from the nearest mapped open fracture) and so-called "fractured rock" formation factors including fractures.

The comparison between laboratory and in situ formation factors is quite interesting in the case of KSH01A (Figure D-16) and KSH02 (Figure D-17). Here, the spread of values obtained in the laboratory measurements is considerable with formation factors both substantially lower and higher than the average in situ data range. Part of the reason for this might be related to core damage since a less gentle drilling technique might have been used in these earlier boreholes. The sparsity of rock matrix data points as compared to fractured rock data points suggests a modality of fracturing that is different in these two Simpevarp boreholes to the boreholes at Laxemar. The rock above an elevation of –700 m in KSH01A is dominated by fine-grained dioritoid with small patches of quartz monzodiorite while below this elevation the rock is a mix of quartz monzodiorite, Ävrö quartz monzodiorite, and Ävrö granodiorite. Borehole KSH02, on the other hand, is largely dominated by fine-grained dioritoid throughout its entire length. Since both boreholes have a predominance of fine-grained rock types, one would expect low formation factors. Once again, a very strong positive skew is identifiable in the data set as is clearly apparent in the data histograms shown in Figure D-18. This suggests a considerable surface conduction bias for the lower tail of the distribution giving the appearance of data truncation or censoring for formation factors below about 10^{-5}.

The lower regions of KSH01A are more sparsely fractured than elevations above –850 m and there are a number of stretches of rock between –850 m and –1000 m where the resistivity of the rock exceeded the quantitative limit of the borehole probe (Century 9072). Very low formation factors in these regions therefore may be inaccurately measured by the probe resulting in a degree of data censoring. The fact that the laboratory measurement data increases greatly in this range is a possible indicator of core damage incurred in this part of the borehole.

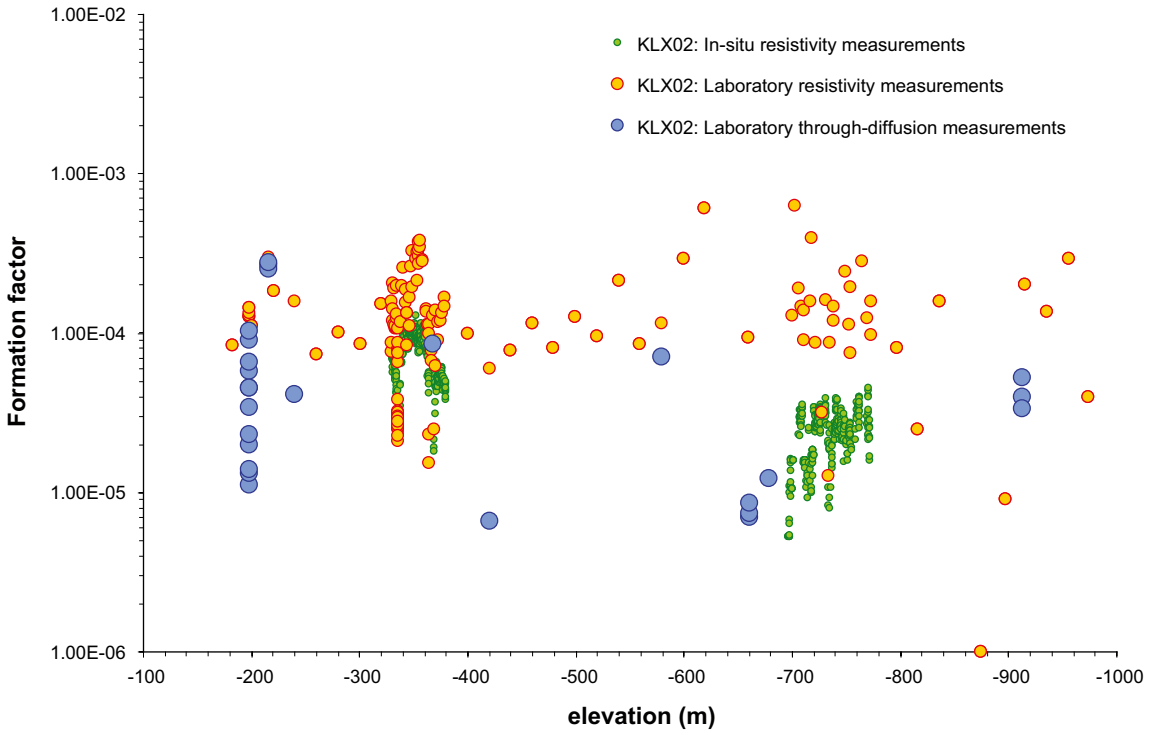

Figure D-15. *Comparison of formation factors derived from in situ resistivity measurements in KLX02 (green markers) with corresponding data measured on core samples in the laboratory (orange makers) also based upon electrical resistivity measurements. Laboratory measurements based upon the through-diffusion method using tritiated water are also shown for comparison (blue markers). It should be noted that this was an early campaign and the in situ data were not classified according to open fracture proximity in this particular borehole.*

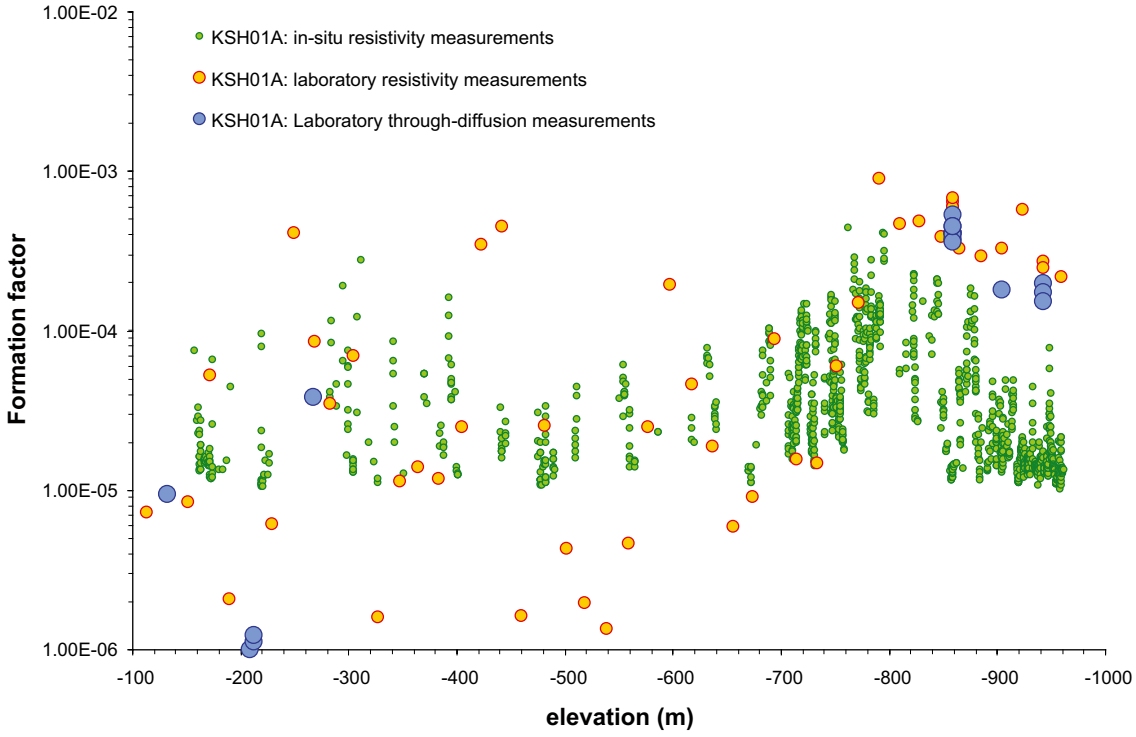

Figure D-16. *Comparison of formation factors derived from in situ resistivity measurements in KSH01 (green markers) with corresponding data measured on core samples in the laboratory (orange makers) also based upon electrical resistivity measurements. Laboratory measurements based upon the through-diffusion method using tritiated water are also shown for comparison (blue markers). In situ measurement points less than 0.5 m distant from mapped open fractures are excluded.*

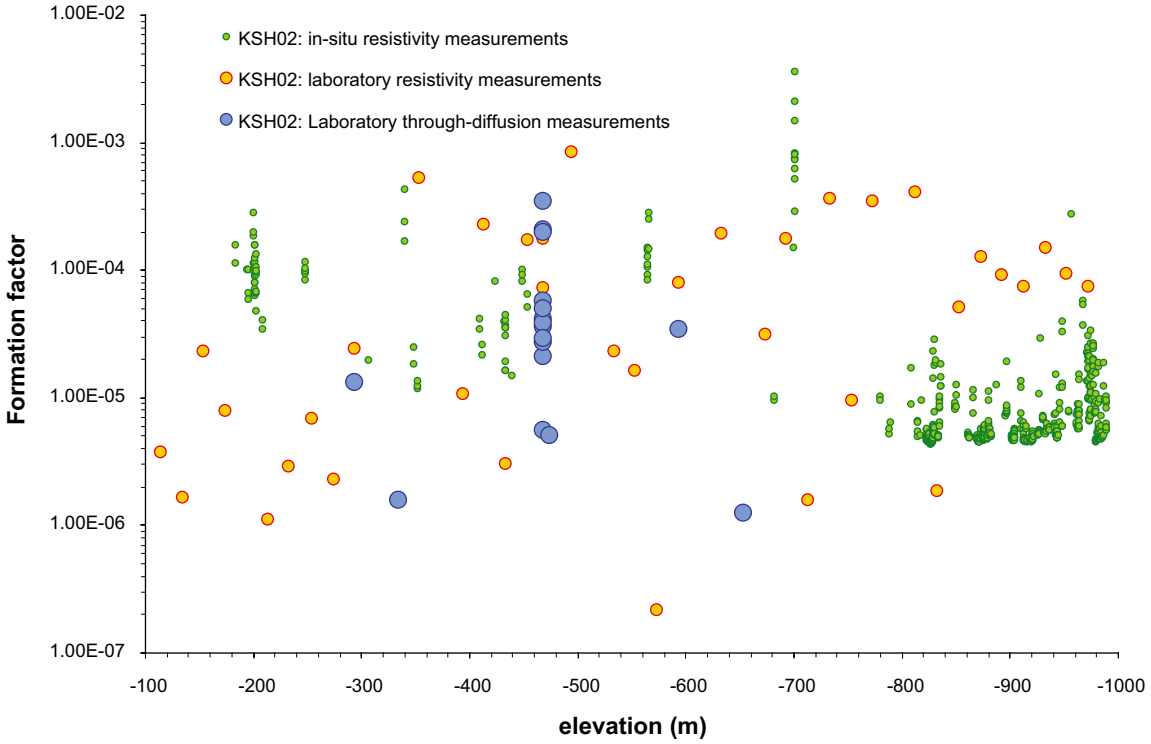

Figure D-17. *Comparison of formation factors derived from in situ resistivity measurements in KSH02 (green markers) with corresponding data measured on core samples in the laboratory (orange makers) also based upon electrical resistivity measurements. Laboratory measurements based upon the through-diffusion method using tritiated water are also shown for comparison (blue markers). In situ measurement points less than 0.5 m distant from mapped open fractures are excluded.*

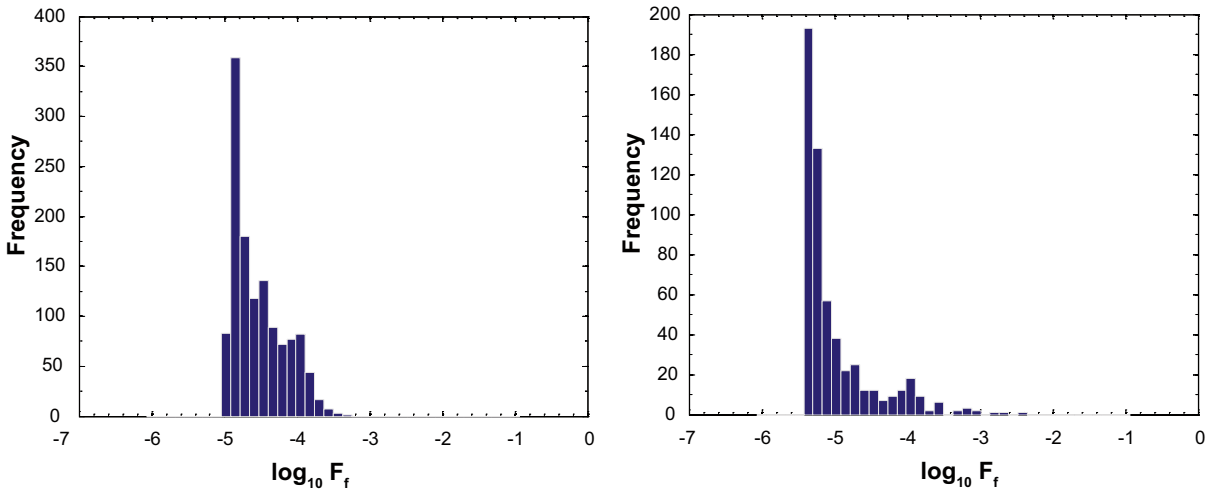

Figure D-18. *Histogram of formation factors derived from in situ resistivity measurements in KSH01A (left) and KSH02 (right). The very strong positive skew is qualitatively consistent with a significant surface conduction biasing effect for the lower tail of the formation factor distribution. In situ measurement points less than 0.5 m distant from mapped open fractures are excluded.*

Owing to the relatively intense fracturing apparent in KSH01A and KSH02 it was judged in /Löfgren and Neretnieks 2005b/ that the groundwater EC as determined during PFL logging should be reasonably well equilibrated with the rock matrix. The modelled EC profiles, however, were very different in each borehole with KSH01A exhibiting a weak decreasing trend with depth and KSH02 exhibiting a much stronger increasing EC trend with depth.

Statistical distributions of in situ formation factors for different rock types

Although there are considerable uncertainties inherent in the in situ formation factor data sets obtained for Laxemar, a cursory examination of the raw in situ data reported in the SICADA database can give us a rough indication of the relative properties of the different rock types to be found at the site. Some representative data (uncorrected) are plotted in Figure D-19 for all boreholes at the Simpevarp-Laxemar site for matrix rock classified as unaltered. Data for matrix rock classified as altered are plotted in Figure D-20.

As can be seen from the plotted data, there does not appear to be very large systematic differences between the different rock types and the spread of data points within individual rock types tends to be greater than the differences between rock types. It is possible that the lower end of some of the data distributions are biased due to surface conduction effects. This might possibly explain the unusual form of the distribution for fine-grained dioritoid (501030) in Figure D-19.

Data is given in the following tables for the individual rock types represented in Figure D-19 further broken down by alteration status as reported in SICADA. Values for rock matrix (≥0.5 m distant from open fractures) and fractured rock (including fractures) are specified separately.

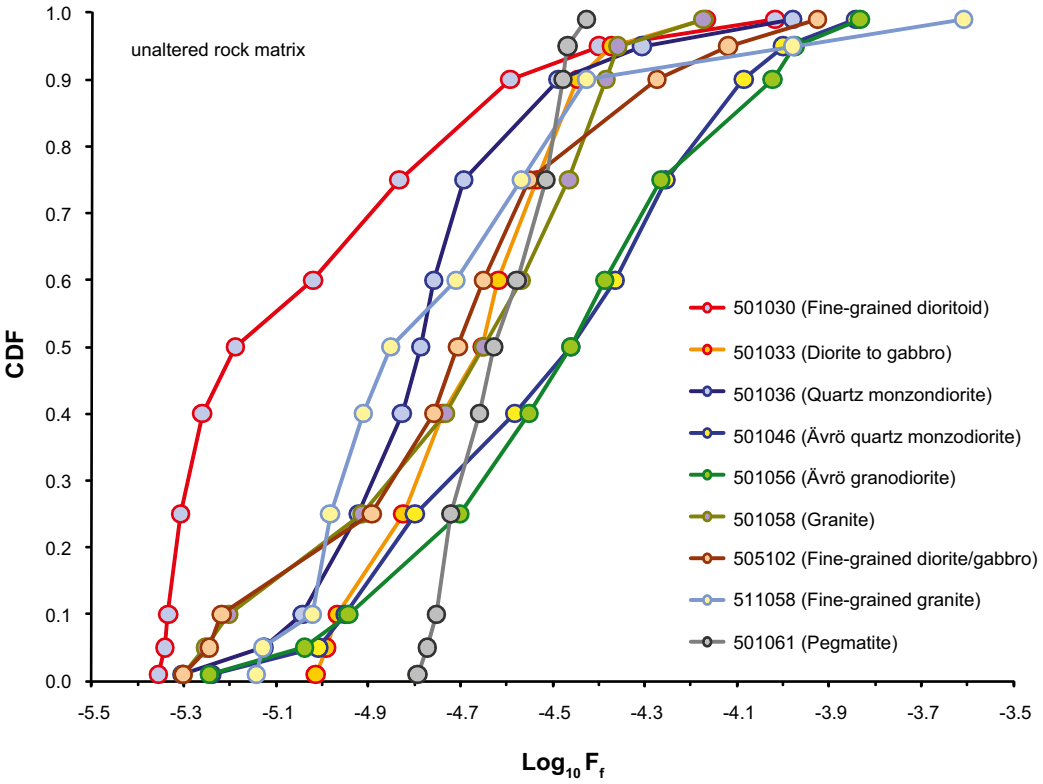

Figure D-19. *Empirical percentiles for in situ rock matrix formation factors (uncorrected data), specified according to rock type for all boreholes and plotted as a cumulative distribution function, CDF. The data are for rock matrix (measurement points less than 0.5 m distant from open fractures not included) classified as unaltered.*

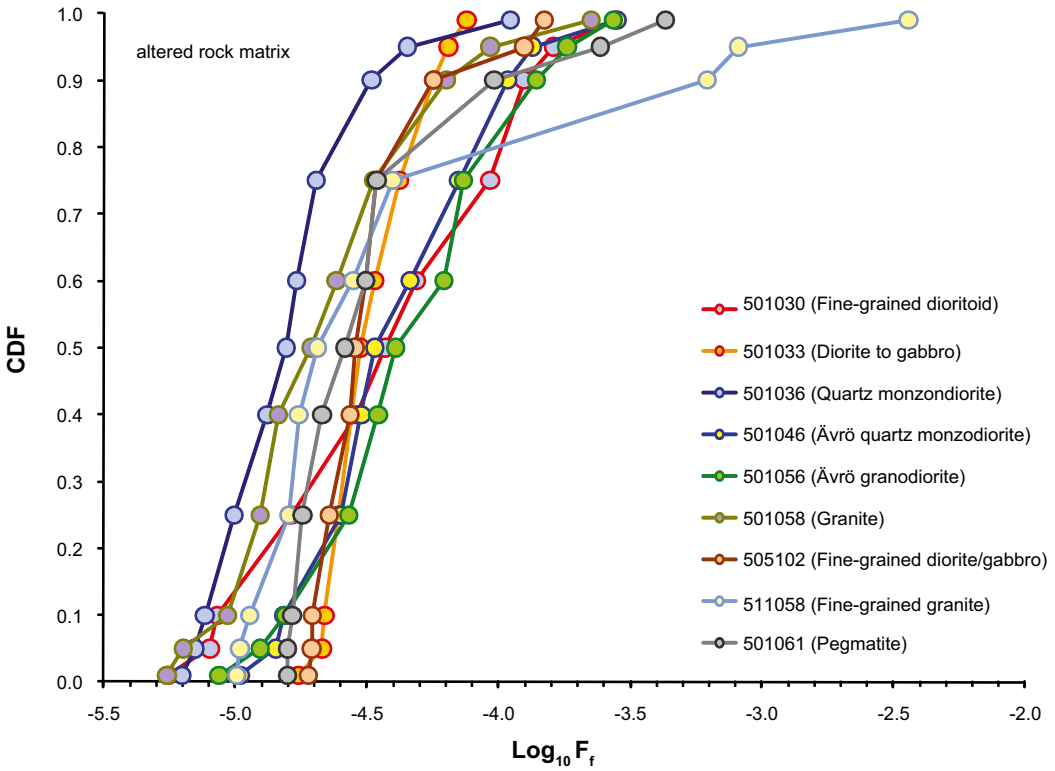

Figure D-20. *Empirical percentiles for in situ rock matrix formation factors (uncorrected data), specified according to rock type for all boreholes and plotted as a cumulative distribution function, CDF. The data are for rock matrix (measurement points less than 0.5 m distant from open fractures not included) classified as altered.*

Table D-1. Empirical percentiles for in situ rock matrix formation factors for different rock types. Data set is for rock matrix classified as unaltered (measurement points less than 0.5 m distant from open fractures not included). Median and interquartile range are highlighted with red and blue text. Numbers of measurements comprising each data set are given in the top row of the table.

Unaltered rock matrix									
# samples	643	554	3,668	4,454	1335	324	154	172	42
Quantiles	**501030**	**501033**	**501036**	**501046**	**501056**	**501058**	**505102**	**511058**	**501061**
0.01	–5.36	–5.01	–5.30	–5.24	–5.25	–5.30	–5.30	–5.14	–4.79
0.05	–5.34	–4.99	–5.13	–5.01	–5.04	–5.25	–5.24	–5.13	–4.77
0.10	–5.33	–4.97	–5.04	–4.95	–4.94	–5.20	–5.22	–5.02	–4.75
0.25	**–5.31**	**–4.82**	**–4.92**	**–4.80**	**–4.70**	**–4.91**	**–4.89**	**–4.98**	**–4.72**
0.40	–5.26	–4.74	–4.83	–4.58	–4.55	–4.73	–4.76	–4.91	–4.66
0.50	**–5.19**	**–4.65**	**–4.79**	**–4.46**	**–4.46**	**–4.65**	**–4.71**	**–4.85**	**–4.63**
0.60	–5.02	–4.62	–4.76	–4.36	–4.39	–4.57	–4.65	–4.71	–4.58
0.75	**–4.83**	**–4.53**	**–4.69**	**–4.25**	**–4.27**	**–4.46**	**–4.55**	**–4.57**	**–4.51**
0.90	–4.59	–4.44	–4.49	–4.09	–4.02	–4.38	–4.27	–4.43	–4.48
0.95	–4.40	–4.37	–4.31	–4.00	–3.97	–4.36	–4.12	–3.98	–4.47
0.99	–4.02	–4.17	–3.98	–3.84	–3.83	–4.17	–3.92	–3.61	–4.43

Table D-2. Empirical percentiles for in situ rock matrix formation factors for different rock types. Data set is for rock matrix classified as altered (measurement points less than 0.5 m distant from open fractures not included). Median and interquartile range are highlighted with red and blue text. Numbers of measurements comprising each data set are given in the top row of the table.

Altered rock matrix									
# samples	85	55	754	359	195	75	37	77	29
Quantiles	**501030**	**501033**	**501036**	**501046**	**501056**	**501058**	**505102**	**511058**	**501061**
0.01	–5.26	–4.76	–5.20	–4.98	–5.06	–5.26	–4.72	–5.00	–4.80
0.05	–5.10	–4.67	–5.15	–4.85	–4.91	–5.20	–4.71	–4.98	–4.80
0.10	–5.07	–4.66	–5.12	–4.82	–4.81	–5.03	–4.71	–4.95	–4.78
0.25	**–4.79**	**–4.61**	**–5.00**	**–4.60**	**–4.57**	**–4.91**	**–4.64**	**–4.80**	**–4.75**
0.40	–4.54	–4.56	–4.88	–4.52	–4.46	–4.84	–4.57	–4.76	–4.67
0.50	**–4.43**	**–4.53**	**–4.81**	**–4.47**	**–4.39**	**–4.71**	**–4.55**	**–4.69**	**–4.58**
0.60	–4.31	–4.47	–4.77	–4.34	–4.21	–4.62	–4.50	–4.55	–4.51
0.75	**–4.03**	**–4.37**	**–4.69**	**–4.15**	**–4.13**	**–4.47**	**–4.46**	**–4.40**	**–4.46**
0.90	–3.90	–4.25	–4.48	–3.97	–3.86	–4.20	–4.25	–3.21	–4.02
0.95	–3.79	–4.19	–4.35	–3.87	–3.74	–4.03	–3.90	–3.09	–3.61
0.99	–3.55	–4.12	–3.95	–3.55	–3.57	–3.65	–3.83	–2.44	–3.37

Table D-3. Empirical percentiles for in situ fractured rock formation factors for different rock types. Data set is for fractured rock classified as unaltered (measurement points in proximity to open fractures included, with exception of PFL features and crush). Median and interquartile range are highlighted with red and blue text. Numbers of measurements comprising each data set are given in the top row of the table.

Unaltered "fractured" rock									
# samples	6,130	2418	8,295	11,421	3,382	982	1,462	971	150
Quantiles	**501030**	**501033**	**501036**	**501046**	**501056**	**501058**	**505102**	**511058**	**501061**
0.01	–5.34	–5.00	–5.19	–5.21	–5.22	–5.28	–5.25	–5.16	–4.88
0.05	–5.30	–4.89	–5.06	–4.99	–5.00	–5.19	–5.10	–5.10	–4.79
0.10	–5.25	–4.79	–4.99	–4.89	–4.86	–4.97	–4.90	–5.00	–4.75
0.25	**–4.91**	**–4.64**	**–4.84**	**–4.64**	**–4.60**	**–4.71**	**–4.69**	**–4.86**	**–4.69**
0.40	–4.72	–4.56	–4.77	–4.43	–4.43	–4.58	–4.52	–4.67	–4.66
0.50	**–4.58**	**–4.49**	**–4.73**	**–4.33**	**–4.34**	**–4.50**	**–4.41**	**–4.57**	**–4.62**
0.60	–4.42	–4.42	–4.66	–4.25	–4.25	–4.43	–4.28	–4.45	–4.59
0.75	**–4.18**	**–4.25**	**–4.47**	**–4.13**	**–4.08**	**–4.30**	**–4.04**	**–4.19**	**–4.50**
0.90	–3.88	–4.00	–4.17	–3.95	–3.85	–4.01	–3.67	–3.84	–4.16
0.95	–3.69	–3.84	–4.00	–3.83	–3.72	–3.77	–3.34	–3.62	–3.38
0.99	–3.42	–3.56	–3.67	–3.57	–3.42	–3.31	–2.56	–3.26	–3.05

Table D-4. Empirical percentiles for in situ fractured rock formation factors for different rock types. Data set is for fractured rock classified as altered (measurement points in proximity to open fractures included, with exception of PFL features and crush). Median and interquartile range are highlighted with red and blue text. Numbers of measurements comprising each data set are given in the top row of the table.

Altered "fractured" rock									
# samples	4,110	196	3,749	2,536	3,033	645	473	1,237	190
Quantiles	**501030**	**501033**	**501036**	**501046**	**501056**	**501058**	**505102**	**511058**	**501061**
0.01	–5.10	–4.88	–5.19	–4.94	–4.80	–5.11	–5.06	–5.13	–4.80
0.05	–4.77	–4.83	–5.06	–4.74	–4.58	–4.91	–4.76	–4.99	–4.76
0.10	–4.62	–4.74	–4.97	–4.61	–4.44	–4.72	–4.67	–4.94	–4.73
0.25	**–4.35**	**–4.59**	**–4.77**	**–4.43**	**–4.17**	**–4.49**	**–4.43**	**–4.75**	**–4.63**
0.40	–4.16	–4.49	–4.63	–4.22	–3.97	–4.36	–4.20	–4.60	–4.47
0.50	**–4.05**	**–4.44**	**–4.52**	**–4.11**	**–3.86**	**–4.26**	**–4.05**	**–4.51**	**–4.38**
0.60	–3.94	–4.35	–4.37	–4.01	–3.73	–4.20	–3.90	–4.42	–4.24
0.75	**–3.74**	**–4.20**	**–4.09**	**–3.83**	**–3.45**	**–4.03**	**–3.63**	**–4.29**	**–4.02**
0.90	–3.47	–3.33	–3.58	–3.56	–2.98	–3.69	–3.04	–4.08	–3.75
0.95	–3.28	–2.90	–3.28	–3.34	–2.76	–3.36	–2.52	–3.87	–3.63
0.99	–2.91	–2.32	–2.84	–2.72	–2.09	–2.34	–2.06	–3.52	–3.25

Statistical distributions of in situ formation factors for hydrogeologic domains

Data for hydraulic rock domains and deformation zones corresponding to the hydraulic conductor domains are plotted in Figure D-21 for rock matrix classified as unaltered and in Figure D-22 for rock matrix classified as altered.

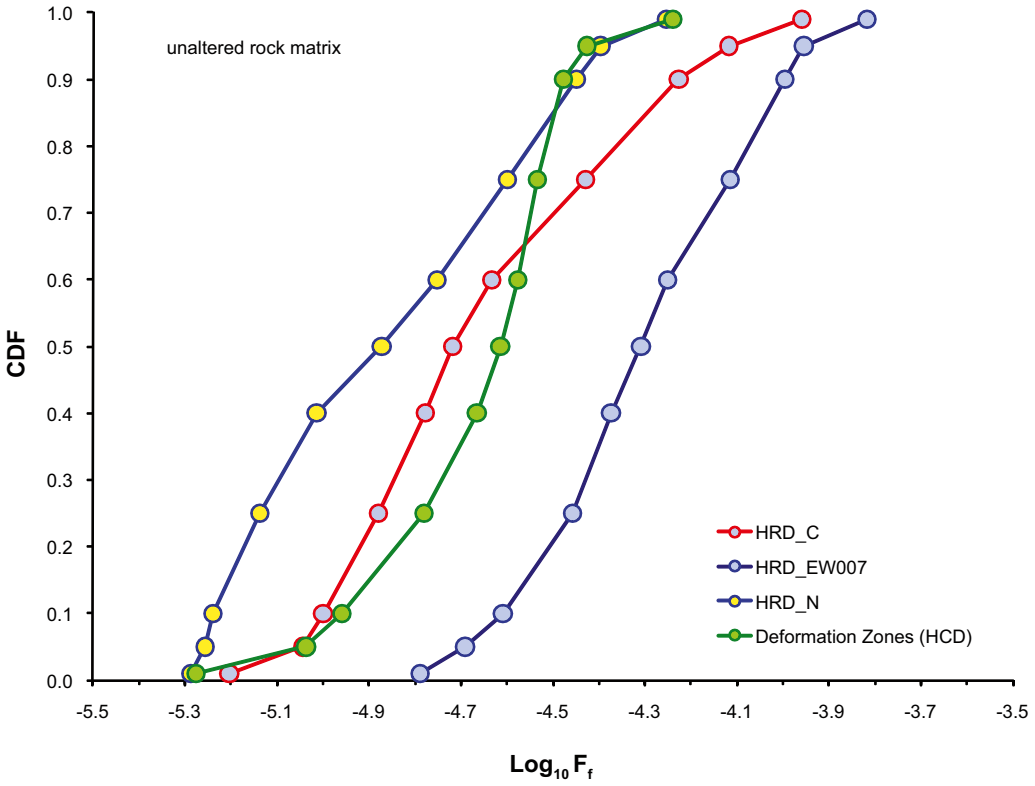

Figure D-21. *Empirical percentiles for in situ rock matrix formation factors (uncorrected data), specified according to hydraulic domain for all boreholes and plotted as a cumulative distribution function, CDF. The data are for rock matrix (measurement points less than 0.5 m distant from open fractures not included) classified as unaltered.*

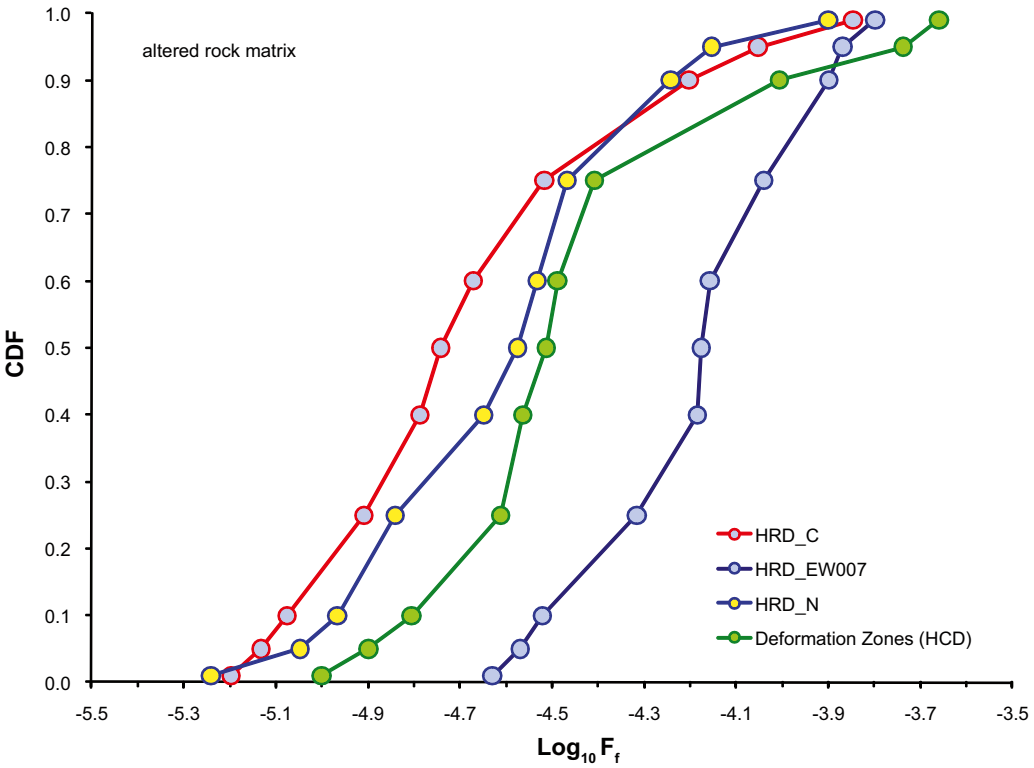

Figure D-22. *Empirical percentiles for in situ rock matrix formation factors (uncorrected data), specified according to hydraulic domain for all boreholes and plotted as a cumulative distribution function, CDF. The data are for rock matrix (measurement points less than 0.5 m distant from open fractures not included) classified as altered.*

Data is given in the following tables for the rock broken down by hydraulic rock domain (HRD) and hydraulic conductor domain (HCD) where available. The data are given for the indicated structural and hydrogeologic units with additional classification according to alteration status. Values for rock matrix (measurements ≥0.5 m distant from open fractures) and fractured rock (including measurements in proximity to fractures, with exception of PFL features and crush) are specified separately.

Table D-5. Empirical percentiles for in situ formation factors for different hydraulic rock domains (HRD) where available. Data set is for the ensemble of all rock types classified as unaltered. Median and interquartile range are highlighted with red and blue text. Numbers of measurements comprising each data set are given in the top row of the table.

Unaltered rock						
	HRD_C		**HRD_EW007**		**HRD_N**	
# samples	7,362	17,918	1,207	3,010	855	3,344
Quantiles	**matrix**	**fractured**	**matrix**	**fractured**	**matrix**	**fractured**
0.01	–5.20	–5.14	–4.79	–4.77	–5.29	–5.27
0.05	–5.04	–5.01	–4.69	–4.66	–5.26	–5.23
0.10	–5.00	–4.94	–4.61	–4.58	–5.24	–5.16
0.25	**–4.88**	**–4.78**	**–4.46**	**–4.44**	**–5.14**	**–4.98**
0.40	–4.78	–4.65	–4.37	–4.34	–5.01	–4.78
0.50	**–4.72**	**–4.53**	**–4.31**	**–4.27**	**–4.87**	**–4.68**
0.60	–4.63	–4.41	–4.25	–4.20	–4.75	–4.58
0.75	**–4.43**	**–4.24**	**–4.11**	**–4.08**	**–4.60**	**–4.43**
0.90	–4.23	–4.05	–4.00	–3.83	–4.45	–4.25
0.95	–4.12	–3.93	–3.95	–3.71	–4.40	–4.08
0.99	–3.96	–3.73	–3.82	–3.47	–4.25	–3.77

Table D-6. Empirical percentiles for in situ formation factors for different hydraulic rock domains (HRD) where available. Data set is for the ensemble of all rock types classified as altered. Median and interquartile range are highlighted with red and blue text. Numbers of measurements comprising each data set are given in the top row of the table.

Altered rock						
	HRD_C		HRD_EW007		HRD_N	
# samples	1,132	5,489	87	1,329	208	1,773
Quantiles	**matrix**	**fractured**	**matrix**	**fractured**	**matrix**	**fractured**
0.01	–5.20	–5.17	–4.63	–5.17	–5.24	–5.17
0.05	–5.13	–5.01	–4.57	–5.01	–5.05	–5.01
0.10	–5.08	–4.90	–4.52	–4.90	–4.97	–4.90
0.25	**–4.91**	**–4.73**	**–4.32**	**–4.73**	**–4.84**	**–4.73**
0.40	–4.79	–4.57	–4.19	–4.57	–4.65	–4.57
0.50	**–4.74**	**–4.45**	**–4.18**	**–4.45**	**–4.57**	**–4.45**
0.60	–4.67	–4.32	–4.16	–4.32	–4.53	–4.32
0.75	**–4.52**	**–4.09**	**–4.04**	**–4.09**	**–4.47**	**–4.09**
0.90	–4.20	–3.81	–3.90	–3.81	–4.24	–3.81
0.95	–4.05	–3.60	–3.87	–3.60	–4.15	–3.60
0.99	–3.85	–3.13	–3.80	–3.13	–3.90	–3.13

Table D-7. Empirical percentiles for in situ formation factors for deformation zones (i.e. corresponding to hydraulic conductor domains, HCD). Data set is for the ensemble of all rock types classified as either unaltered or altered. Median and interquartile range are highlighted with red and blue text. Numbers of measurements comprising each data set are given in the top row of the table.

	Unaltered rock (DZ)		Altered rock (DZ)	
# samples	234	752	94	2,282
Quantiles	**matrix**	**fractured**	**matrix**	**fractured**
0.01	–5.28	–4.71	–5.00	–4.65
0.05	–5.04	–4.50	–4.90	–4.36
0.10	–4.96	–4.33	–4.81	–4.20
0.25	**–4.78**	**–4.08**	**–4.61**	**–3.95**
0.40	–4.67	–3.93	–4.56	–3.71
0.50	**–4.61**	**–3.85**	**–4.51**	**–3.57**
0.60	–4.58	–3.76	–4.49	–3.42
0.75	**–4.53**	**–3.56**	**–4.41**	**–3.12**
0.90	–4.48	–3.11	–4.01	–2.75
0.95	–4.43	–2.70	–3.74	–2.53
0.99	–4.24	–2.27	–3.66	–2.05

Statistical distributions of in situ formation factors for geologic rock domains

Data for geologic rock domains (RSM) are plotted in Figure D-23 for rock matrix classified as unaltered and in Figure D-24 for rock matrix classified as altered.

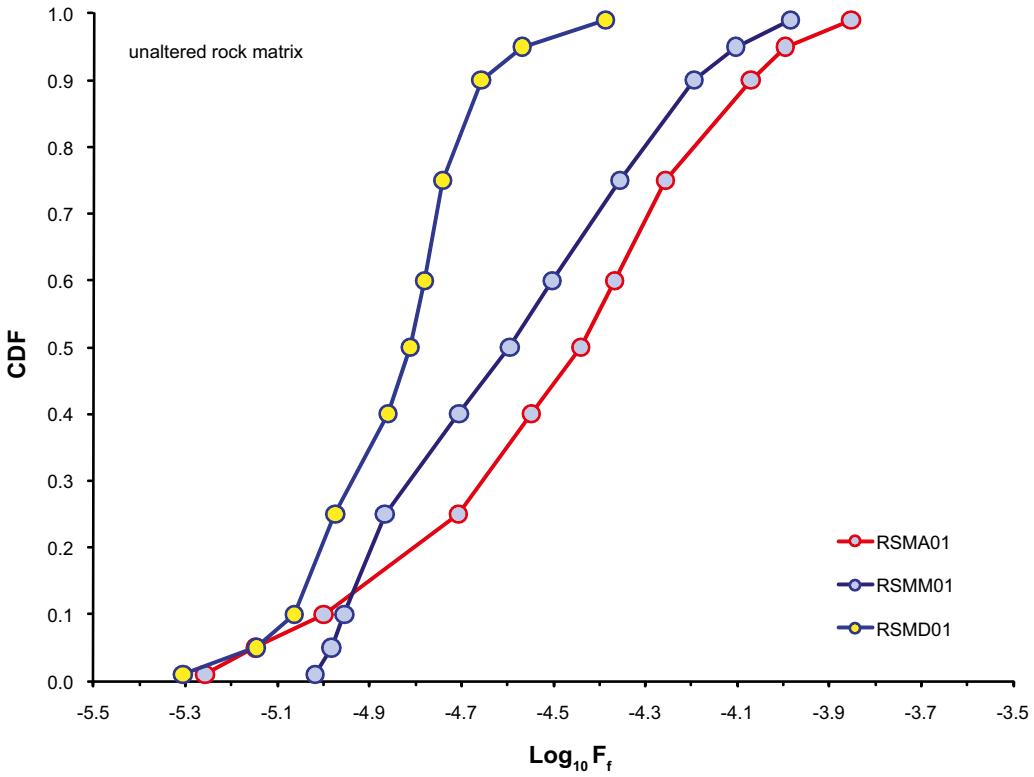

Figure D-23. *Empirical percentiles for in situ rock matrix formation factors (uncorrected data), specified according to geologic rock domain for all boreholes and plotted as a cumulative distribution function, CDF. The data are for rock matrix (measurement points less than 0.5 m distant from open fractures not included) classified as unaltered.*

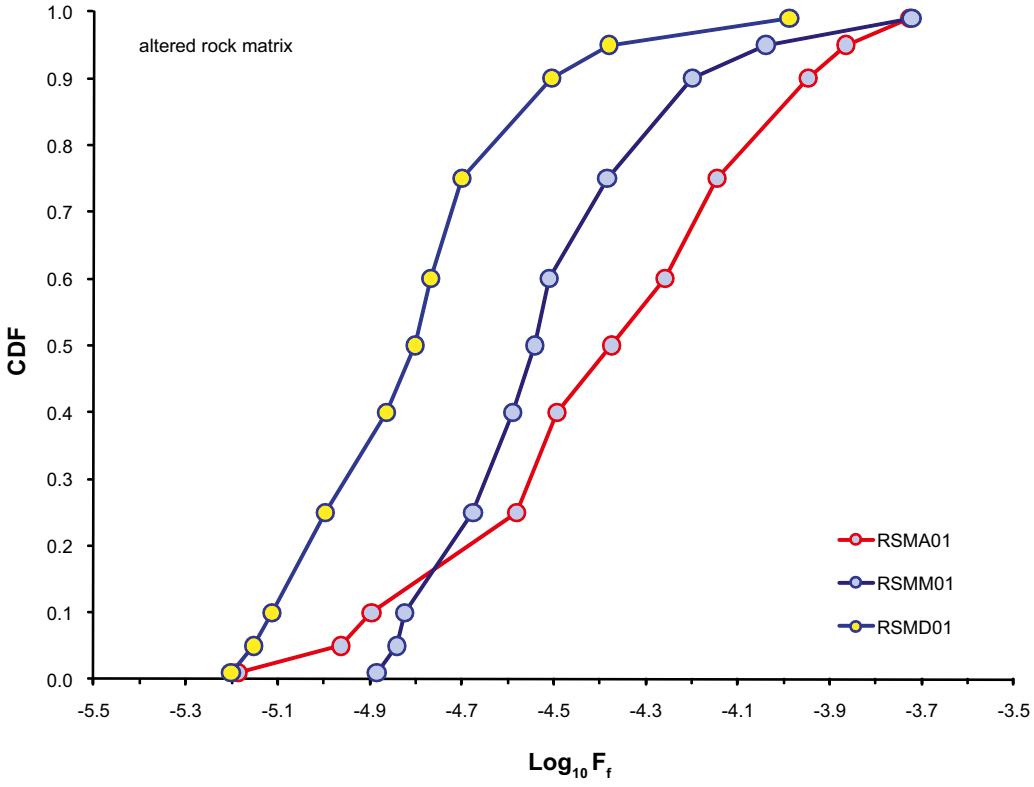

Figure D-24. *Empirical percentiles for in situ rock matrix formation factors (uncorrected data), specified according to geologic rock domain for all boreholes and plotted as a cumulative distribution function, CDF. The data are for rock matrix (measurement points less than 0.5 m distant from open fractures not included) classified as altered.*

Table D-8. Empirical percentiles for in situ formation factors for different geologic rock domains (RSM) where available. Data set is for the ensemble of all rock types classified as unaltered (data for rock matrix and fractured rock specified separately). Median and interquartile range are highlighted with red and blue text. Numbers of measurements comprising each data set are given in the top row of the table.

	RSMA01		RSMD01		RSMM01	
# samples	4,000	11,445	2,963	6,180	2,467	7,399
Quantiles	**matrix**	**fractured**	**matrix**	**fractured**	**matrix**	**fractured**
0.01	–5.26	–5.24	–5.31	–5.23	–5.02	–5.01
0.05	–5.15	–5.08	–5.15	–5.08	–4.98	–4.95
0.10	–5.00	–4.91	–5.06	–5.02	–4.95	–4.88
0.25	**–4.71**	**–4.62**	**–4.97**	**–4.89**	**–4.87**	**–4.64**
0.40	–4.55	–4.45	–4.86	–4.80	–4.71	–4.49
0.50	**–4.44**	**–4.36**	**–4.81**	**–4.77**	**–4.60**	**–4.40**
0.60	–4.37	–4.28	–4.78	–4.74	–4.50	–4.30
0.75	**–4.26**	**–4.13**	**–4.74**	**–4.65**	**–4.36**	**–4.17**
0.90	–4.07	–3.90	–4.66	–4.43	–4.19	–4.00
0.95	–4.00	–3.76	–4.57	–4.27	–4.10	–3.90
0.99	–3.85	–3.36	–4.39	–3.84	–3.98	–3.68

Table D-9. Empirical percentiles for in situ formation factors for different geologic rock domains (RSM) where available. Data set is for the ensemble of all rock types classified as altered (data for rock matrix and fractured rock specified separately). Median and interquartile range are highlighted with red and blue text. Numbers of measurements comprising each data set are given in the top row of the table.

	RSMA01		RSMD01		RSMM01	
# samples	455	5,958	802	3,917	190	998
Quantiles	**matrix**	**fractured**	**matrix**	**fractured**	**matrix**	**fractured**
0.01	–5.19	–5.02	–5.20	–5.19	–4.88	–4.88
0.05	–4.96	–4.75	–5.15	–5.06	–4.84	–4.81
0.10	–4.90	–4.60	–5.11	–4.97	–4.82	–4.69
0.25	**–4.58**	**–4.37**	**–5.00**	**–4.77**	**–4.68**	**–4.52**
0.40	–4.49	–4.16	–4.86	–4.67	–4.59	–4.37
0.50	**–4.37**	**–4.02**	**–4.80**	**–4.58**	**–4.54**	**–4.27**
0.60	–4.26	–3.88	–4.77	–4.45	–4.51	–4.15
0.75	**–4.15**	**–3.64**	**–4.70**	**–4.22**	**–4.38**	**–4.03**
0.90	–3.95	–3.15	–4.50	–3.87	–4.20	–3.79
0.95	–3.86	–2.85	–4.38	–3.58	–4.04	–3.58
0.99	–3.73	–2.17	–3.99	–3.05	–3.72	–2.89

Appendix E

Scoping calculations of the impact of natural colloids

Author: James Crawford

The unsteady, differential mass balance for advective transport of (both dissolved and colloidal bound) solute in a flow channel with diffusive uptake of solute can be written as:

$$R_a \frac{\partial C_f}{\partial t} + v\left(\frac{\partial C_f}{\partial x} + \frac{\partial C_{sc}}{\partial x}\right) = \frac{2J_m}{\delta_t} \qquad \text{(Eq. E-1)}$$

Where, C_f (mol/m^3) is the free aqueous concentration of solute, C_{sc} (mol/m^3) is the colloid bound concentration of solute, R_a (-) is the equilibrium retardation coefficient for equilibrium sorption on fracture outer surfaces, v (m/s) is the advective velocity, δ_t (m) is the flow channel transport aperture, and J_m (mol/m^{2}s) is the diffusive flux to the rock matrix.

Since colloids[3] are generally thought to be too large to participate in matrix diffusion, only their carrying capacity is considered as part of the advective transport term on the left-hand side of the Equation E-1. If one furthermore assumes that sorption of solutes upon suspended colloids is an instantaneous and reversible equilibrium process, the concentration of solute bound to colloidal particles, C_{sc} (mol/m^3) can be given as:

$$C_{sc} = m_c K_d^{colloid} C_f \qquad \text{(Eq. E-2)}$$

Where, m_c (kg/m^3) is the suspended colloidal mass concentration which is assumed to be constant, and $K_d^{colloid}$ (kg/m^3) is the coefficient for sorption on the colloidal particles. For a constant colloid loading, the mass balance can be rewritten as:

$$R_a \frac{\partial C_f}{\partial t} + v\left(1 + m_c K_d^{colloid}\right)\frac{\partial C_f}{\partial x} = \frac{2J_m}{\delta_t} \qquad \text{(Eq. E-3)}$$

In /Hallbeck and Pedersen 2008/ it was concluded that the natural colloidal particles identified in Laxemar groundwater sampled at repository depth are composed predominantly of iron and sulphur although with a minor fraction in the form of clay minerals (characterised as K-Mg-illite).

Provided the composition of the colloids is known, an approximate sorption K_d value for the colloidal particles can be estimated by scaling the K_d for an appropriate mineral analogue by the specific surface area ratio ($A_{colloid}/A_0$) of the colloidal material and analogue mineral:

$$K_d^{colloid} \approx \left(\frac{A_{colloid}}{A_0}\right) K_d^0 \qquad \text{(Eq. E-4)}$$

The form of Equation E-3 suggests that the impact of suspended colloidal material enters the transport equations by way of reducing the "apparent" F-factor for a transport flowpath. Here, the assumption that the load of colloids is constant along a transport path and there is no adhesion to, or remobilisation from fracture surfaces is also made. The ratio of the apparent and actual F-factor for a transport path including the effects of equilibrium sorption on colloids can then be given as:

$$R_F = \frac{F_{app}}{F} = \frac{1}{1 + m_c K_d^{colloid}} \approx \frac{1}{1 + m_c\left(\frac{A_{colloid}}{A_0}\right) K_d^0} \qquad \text{(Eq. E-5)}$$

It should be noted that this definition of the impact of colloids on radionuclide transport is different to the analyses presented by /Vilks et al. 1998/ and /Contardi et al. 2001/ since matrix diffusion effects were not considered in those studies. To the best knowledge of the author, scoping calculations equivalent to Equation E-5 (i.e. including matrix diffusion) have not been previously described in the literature.

[3] It should be noted that in this discussion the term colloid is used exclusively to refer to so-called "pseudocolloids" formed where solute is reversibly adsorbed to naturally existing colloidal particles, rather than "eigencolloids" formed by agglomeration of strongly hydrolysed solute species in the groundwater.

In /Hallbeck and Pedersen 2008/ the average natural colloid concentration in Laxemar groundwater at repository depth was estimated to be roughly 24±27 µg/L.

In the kind of scoping calculation implied by Equation E-5 it is probably most relevant to chose the most strongly sorbing radionuclides as this would give the largest impact upon transport. Of all the analogue minerals that one could choose to calculate an order of magnitude estimate for R_F using Equation E-5, the assumption of colloidal ferric oxyhydroxide or hematite would probably give the largest effect since K_d values are typically very high for these sorbents.

In /Degueldre et al. 1994/, for example, the K_d for Am(III) sorption on hematite colloids was found to be in the range 345–9,330 m^3/kg at pH 8. Taking the upper limit of this range, R_F is calculated to be on the order of 0.82–0.99 depending upon the colloid concentration (and assuming $A_{colloid} \sim A_0$). This means that in the worst case scenario for the most strongly sorbing radionuclides one would expect a reduction in retardation equivalent to decreasing the F-factor by roughly 20%.

For other possible analogue minerals such as smectite clay, far smaller impacts upon radionuclide transport are calculated. The sorption K_d of trivalent lanthanides on smectite has been measured by /Coppin et al. 2002/ to be approximately in the range 0.5–100 m^3/kg. Taking the upper limit of this K_d range would give R_F values of 0.997 or greater.

In /Hallbeck and Pedersen 2008/, a significant fraction of the total colloid loading of certain groundwater samples was found to contain sulphur, although this was found to vary considerably amongst different boreholes and sampling depths. It was also not possible to fully ascertain whether the sampled sulphide colloids were in the form of pyrite (FeS_2), or a polymeric, free sulphide form. Provided the concentration of transported radionuclides is low, one would not necessarily expect surface precipitation of metal sulfide, radionuclide forms on the surface of such colloids although there is still the possibility of inner sphere surface complexation as a binding mechanism. The sorption of a number of divalent transition metals (Cu, Pb, Zn, Ni, Fe) on mixed metal sulphide colloids of microbial origin were studied by /Jong and Parry 2004/. Based upon the ranges of Langmuir isotherm parameters reported by these authors, limiting K_d values in the range 30–120 m^3/kg can be estimated for these metals. On the basis of this data and assuming approximate geochemical analogy with the groundwater sulphide colloids at Laxemar (not a particularly well-supported assumption), one can predict approximate R_F values in excess of 0.997.

As the calculations above indicate, the impact of a given concentration of natural colloids depends upon which proxy mineral is used to represent their properties and the sorptivity of the transported solute under consideration. Since the trivalent lanthanides, exemplified here by Am(III), are among the most strongly sorbing of the solutes of interest in safety assessment, these calculations give an upper limit to the impact of colloidal transport mechanisms under the prevailing groundwater conditions measured at Laxemar. For less strongly sorbing solutes featuring K_d values less than about 10–100 m^3/kg the impact is likely to be negligible.

The crucial assumption in this analysis is, of course, that the sorption of radionuclides on the colloids is macroscopically reversible over the timescale of transport. The status of sorption reversibility for key radionuclides on colloids is not conclusively established at present and there are conflicting pronouncements on this issue in the scientific literature.

Generally it is thought that the sorption of ion-exchanging solutes (and solutes that form outer sphere complexes) should be largely reversible owing to the absence of covalent chemical bonding /Coppin et al. 2003/. For solutes that form inner-sphere surface complexes, however, partial irreversibility and hysteresis effects are frequently observed /Lu et al. 1998, Coppin et al. 2003, Jong and Parry 2004, Missana et al. 2004/. This is typically due to a slow rate of desorption as compared to the adsorptive uptake step and the limited observational timescale of experiments. Such behaviour could occur where there is a slow redistribution of solute sorbed initially in the form of outer sphere surface complexes to more stable inner-sphere surface complexes. Given sufficient time, however, the sorption should be reversible provided there is an absence of chemical reactions which might lead to incorporation of radionuclides in the structure of the colloids /Rabung et al. 2005/. Given the uncertainty associated with the reversibility of radionuclide sorption on colloids, however, further analysis of this will need to be undertaken within safety assessment.

Appendix F

Detailed solute transport modelling results

Author: James Crawford.

In this section, detailed simulation results are given for the transport times of different solutes for the different representative groundwater compositions defined within the laboratory programme. Here results are given for Fresh, Marine, Saline, Brine, and Type V (a mixed interglacial, saline non-marine) groundwater types. The results for Saline conditions have already been presented in Section 5.3.1 although are included again here to aid comparisons between the results for different groundwater types.

As discussed previously in chapter 5, the simulation results are presented for the three transport model variants (BM, MA1, MA2) considering a range of sorption K_d values representing the spectrum of sorptivity from weakly sorbing ($K_d = 10^{-5}$ m^3/kg) to strongly sorbing ($K_d = 1$ m^3/kg). It should be noted that only the K_d values for specific nuclides change between the different groundwater examples (i.e. the coloured polygons representing recovery times for specific nuclides) while the underlying generic curves representing the entire K_d range remain constant. The three model variants are:

A. (BM) Advective flow coupled with 1D diffusion/sorption within the rock matrix;

B. (MA1) Advective flow in a narrow channel coupled with 1D diffusion/sorption in the rock matrix plus diffusion into a stagnant zone of limited extent and subsequent 1D diffusion/sorption within the rock matrix;

C. (MA2) Advective flow in a narrow channel coupled with 2D radial diffusion/sorption in the rock matrix.

Transport times for each model variant are plotted against sorption K_d for assumed F-factors in the range 10^3–10^5 yr/m and a formation factor of 1.1×10^{-5}. The Formation factor is approximately the site average for HRD_C, as derived from in situ resistivity measurements (see Appendix D). The plots are made for a solute recovery fraction of 50% (i.e. the transport time for the first 50% of arriving solute), neglecting radioactive decay and assuming a maximum matrix depth of 2 m. Calculations based upon the MA1 model variant consider a single stagnant zone of width 10 times greater than the main advective flow channel (this is referred to as a 10:1 stagnant zone in the present report).

To illustrate the combined impact of K_d uncertainty and model uncertainty for specific solutes, the span of transport times vs. K_d is plotted as a rectangular polygon in the figures. The lower left hand vertex is the transport time for the model giving the fastest breakthrough using the lowest reported K_d value, while the upper right hand vertex corresponds to the transport time for the model giving the slowest breakthrough time using the maximum reported K_d value. Since there are too few measurements of sorption on individual rock types to give a sufficiently reliable span of K_d uncertainty, the depicted K_d ranges consider a pooling of data for all the main rock types (501030, 501036, 501046, 501056, and 511058) compiled in /Selnert et al. 2009b/ (see Table 4-1 for applicable rock codes).

To set the results in a proper perspective, time limits for quantitative and qualitative Safety assessment are indicated by the red broken and unbroken lines in the figure (loosely based upon guidelines in /SSI 2005/). Transport times longer than 10^7 years are considered to be of only academic interest and are included with the sole purpose of illustrating the relative scaling of transport times. In addition, to give an appreciation of the time scales involved, some significant events in Earth's geological past are indicated on the time axis. Since these events have already taken place in the past, they are intended to be interpreted in a relative sense with regard to the estimated transport times.

It should be noted that although the upper end of the time axis, $\geq 10^7$ years is largely meaningless for safety assessment, the extrapolation to these timescales is a logical consequence of the physics of the simplified system as it is modelled without any additional consideration of geosphere stability. What this might mean in a safety assessment perspective is that the postulated retardation mechanism (i.e. transport of dissolved solute) may not be the major transport mechanism for very strongly sorbing solutes and alternative transport mechanisms such as pseudocolloid transport may be more important (i.e. transport of solute sorbed to naturally existing groundwater colloids).

Typical transport times for solutes under fresh (Type I) groundwater conditions

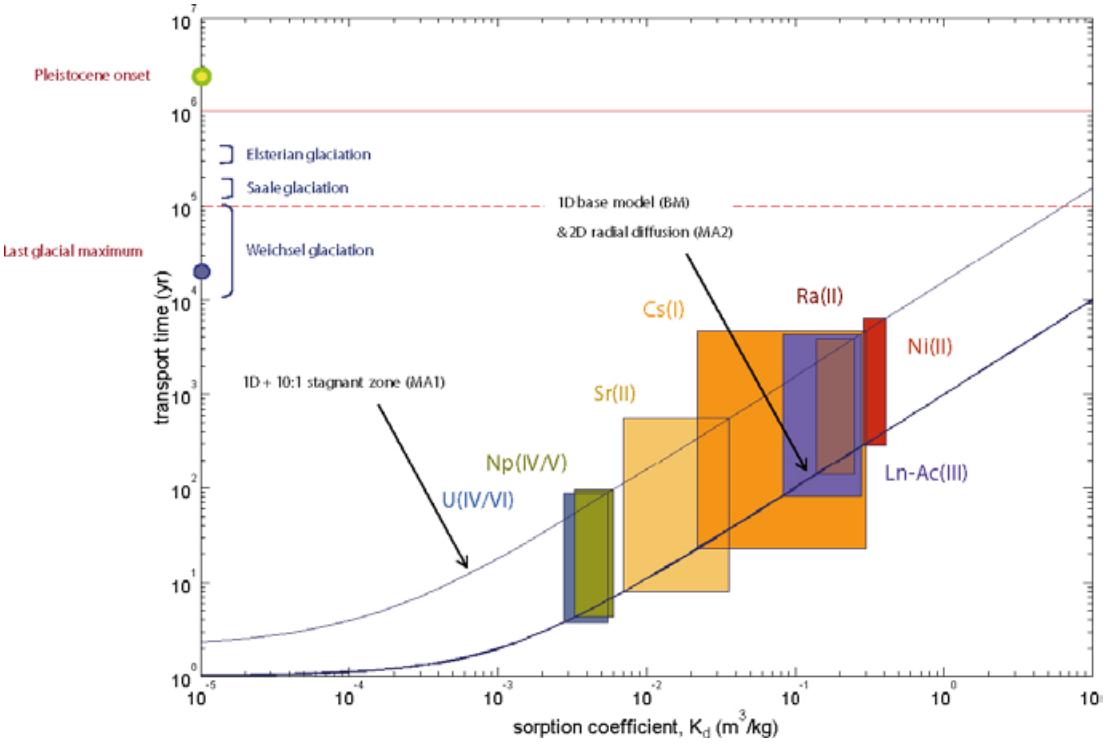

Figure F-1. *Recovery times for solutes as a function of K_d for a recovery fraction of 50%, a fixed* ***F-factor of 10^3 yr/m****, and formation factor of 1.1×10^{-5}. Polygons represent approximate ranges of behaviour for indicated solutes under fresh (Type I) groundwater conditions.*

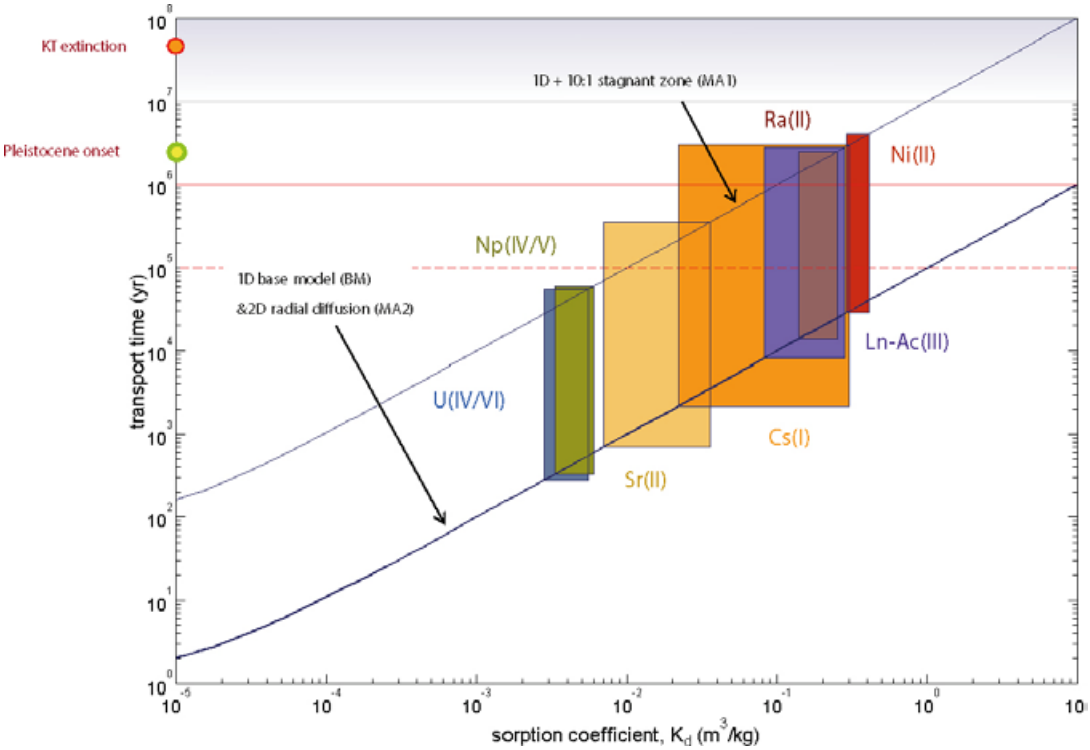

Figure F-2. *Recovery times for solutes as a function of K_d for a recovery fraction of 50%, a fixed* ***F-factor of 10^4 yr/m****, and formation factor of 1.1×10^{-5}. Polygons represent approximate ranges of behaviour for indicated solutes under fresh (Type I) groundwater conditions.*

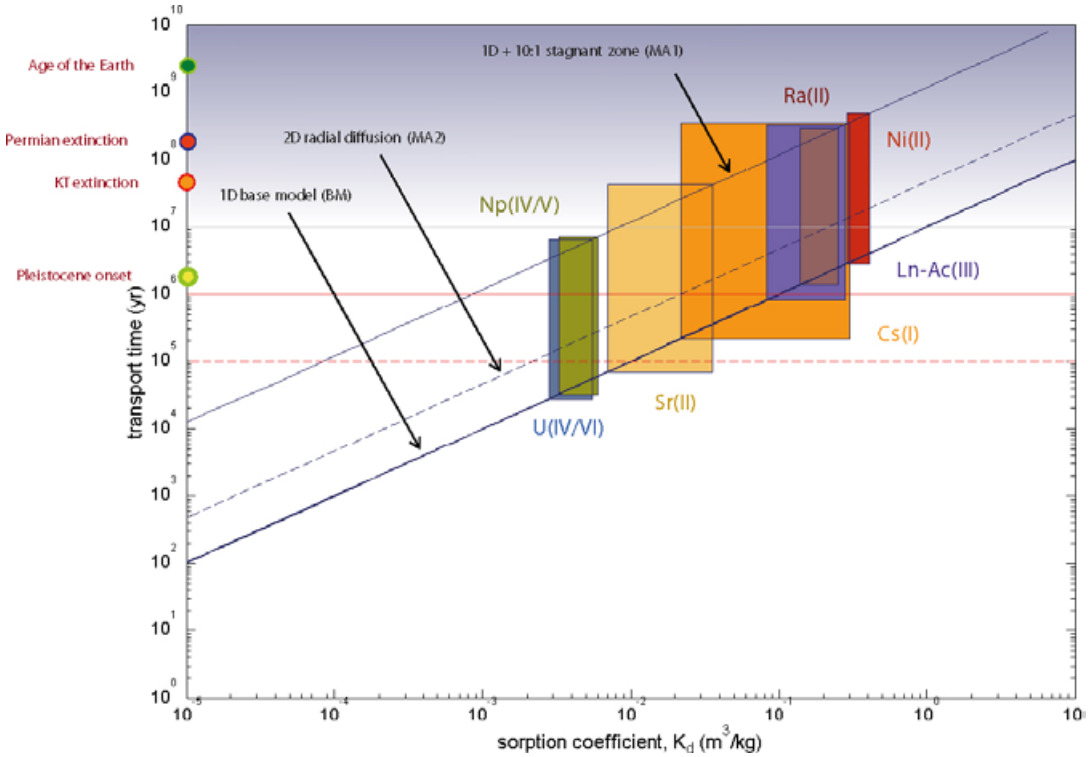

Figure F-3. *Recovery times for solutes as a function of K_d for a recovery fraction of 50%, a fixed* ***F-factor of 10^5 yr/m****, and formation factor of 1.1×10^{-5}. Polygons represent approximate ranges of behaviour for indicated solutes under fresh (Type I) groundwater conditions.*

Typical transport times for solutes under marine (Type II) groundwater conditions

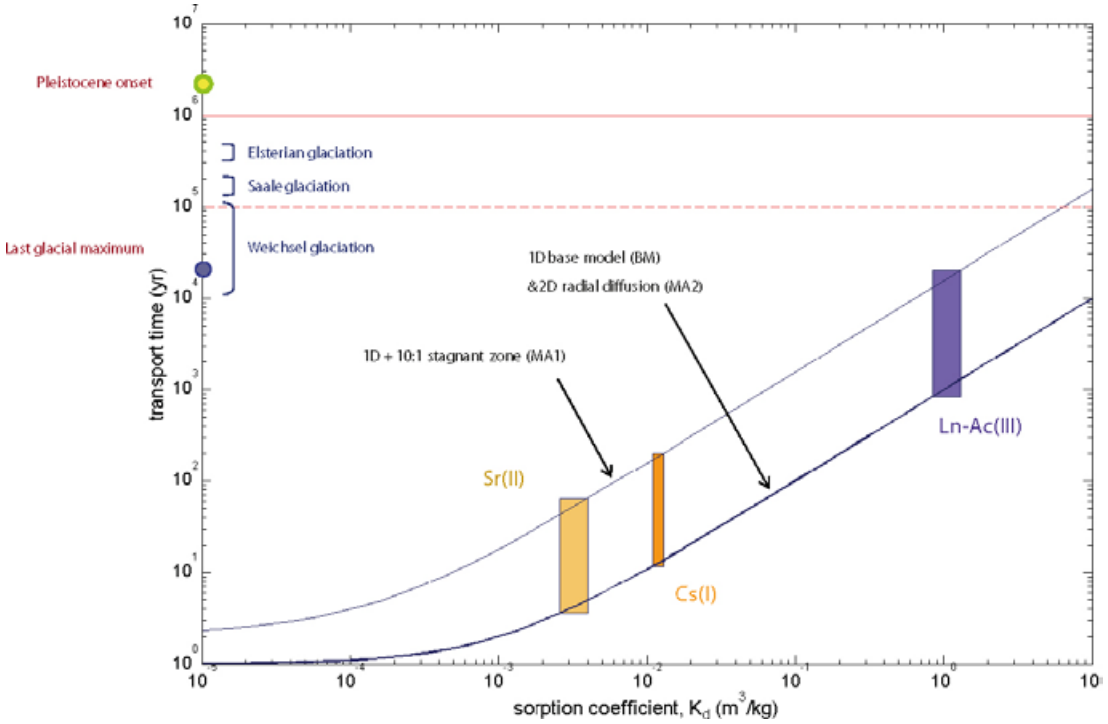

Figure F-4. *Recovery times for solutes as a function of K_d for a recovery fraction of 50%, a fixed* ***F-factor of 10^3 yr/m****, and formation factor of 1.1×10^{-5}. Polygons represent approximate ranges of behaviour for indicated solutes under marine (Type II) groundwater conditions.*

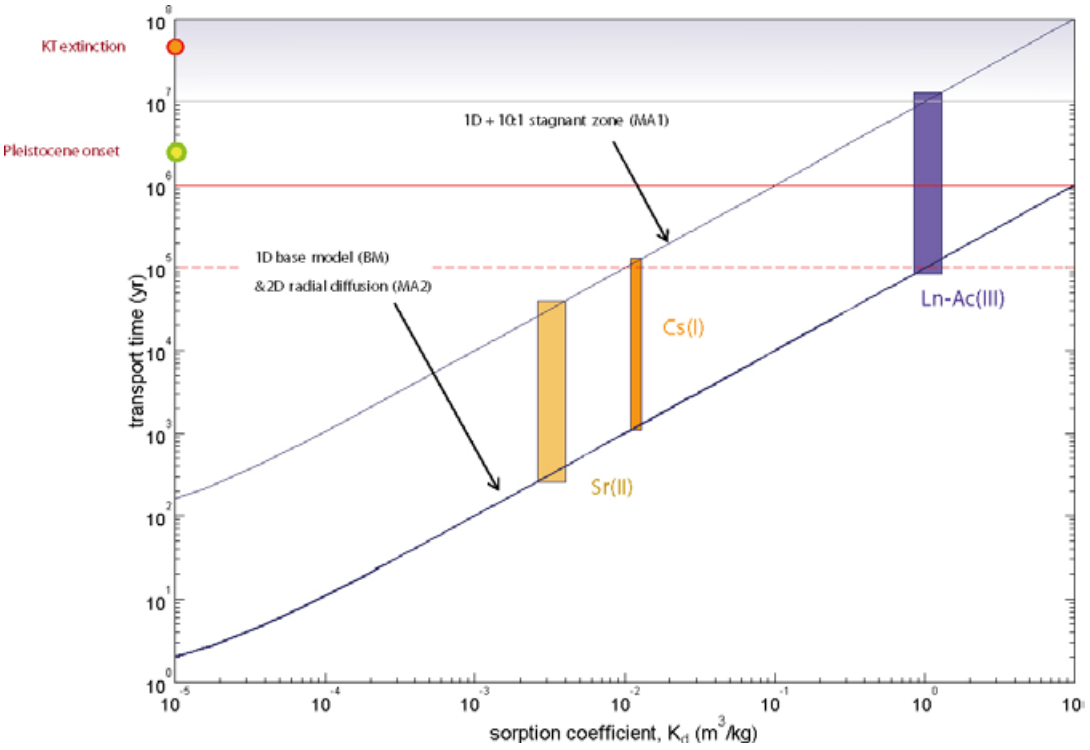

Figure F-5. *Recovery times for solutes as a function of K_d for a recovery fraction of 50%, a fixed* ***F-factor of 10^4 yr/m****, and formation factor of 1.1×10^{-5}. Polygons represent approximate ranges of behaviour for indicated solutes under marine (Type II) groundwater conditions.*

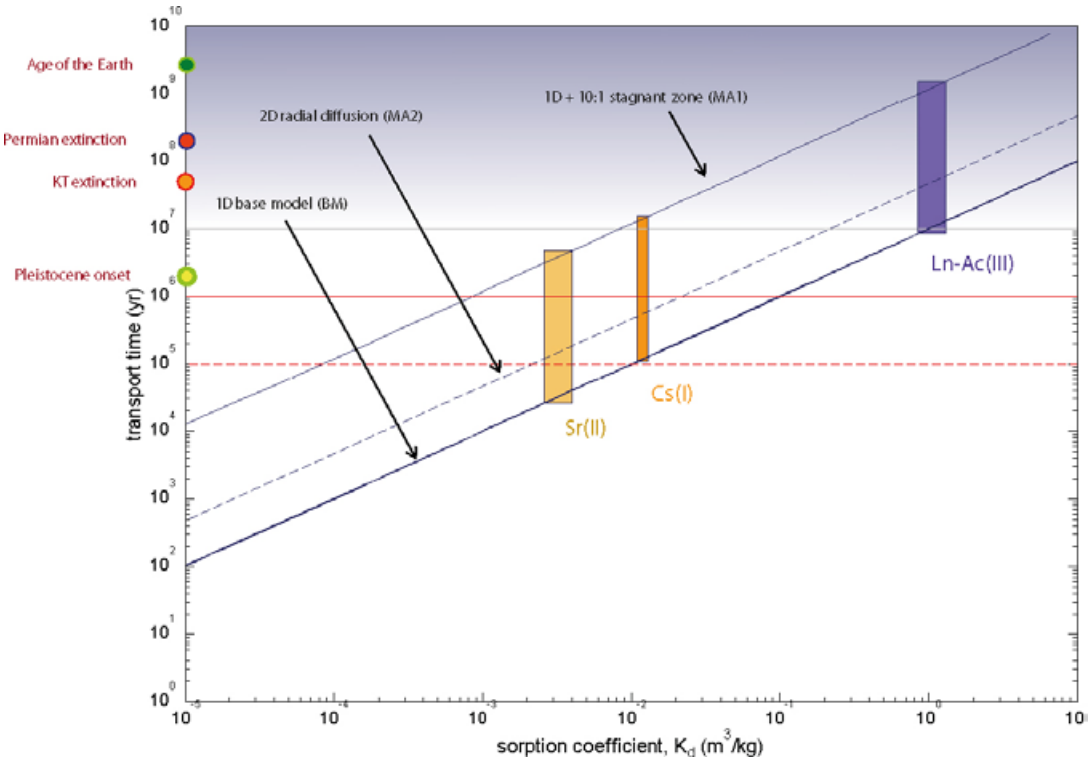

Figure F-6. *Recovery times for solutes as a function of K_d for a recovery fraction of 50%, a fixed* ***F-factor of 10^5 yr/m****, and formation factor of 1.1×10^{-5}. Polygons represent approximate ranges of behaviour for indicated solutes under marine (Type II) groundwater conditions.*

Typical transport times for solutes under saline (Type III) groundwater conditions

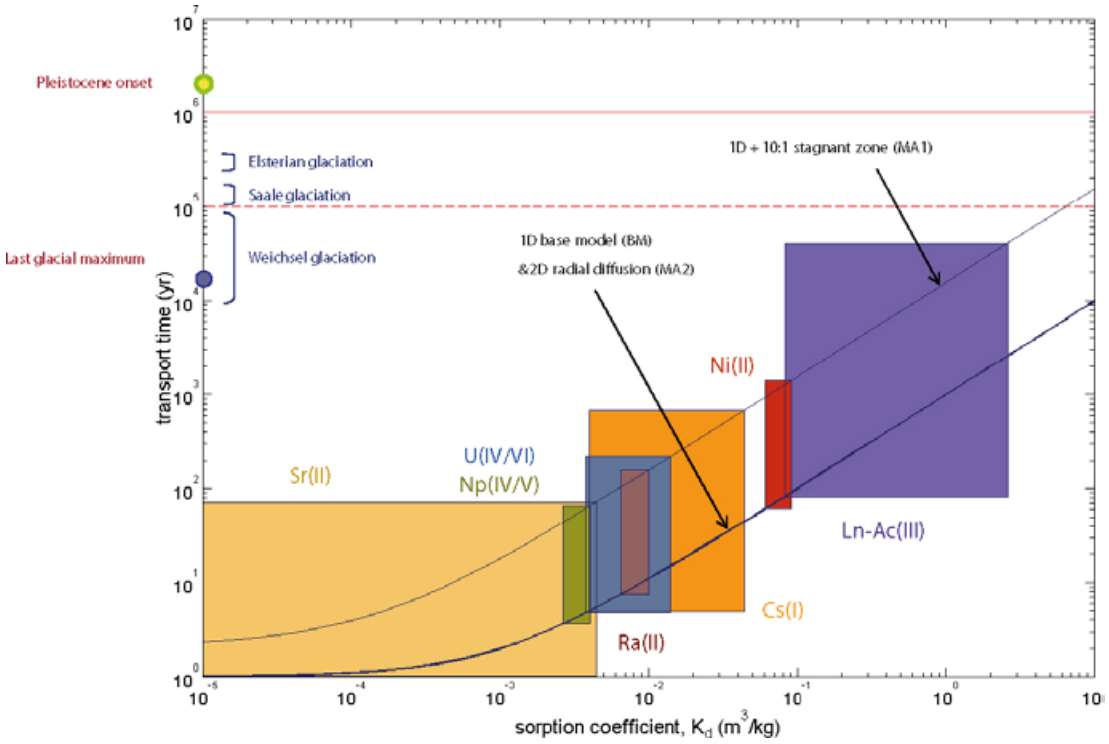

Figure F-7. *Recovery times for solutes as a function of K_d for a recovery fraction of 50%, a fixed* ***F-factor of 10^3 yr/m****, and formation factor of 1.1×10^{-5}. Polygons represent approximate ranges of behaviour for indicated solutes under saline (Type III) groundwater conditions.*

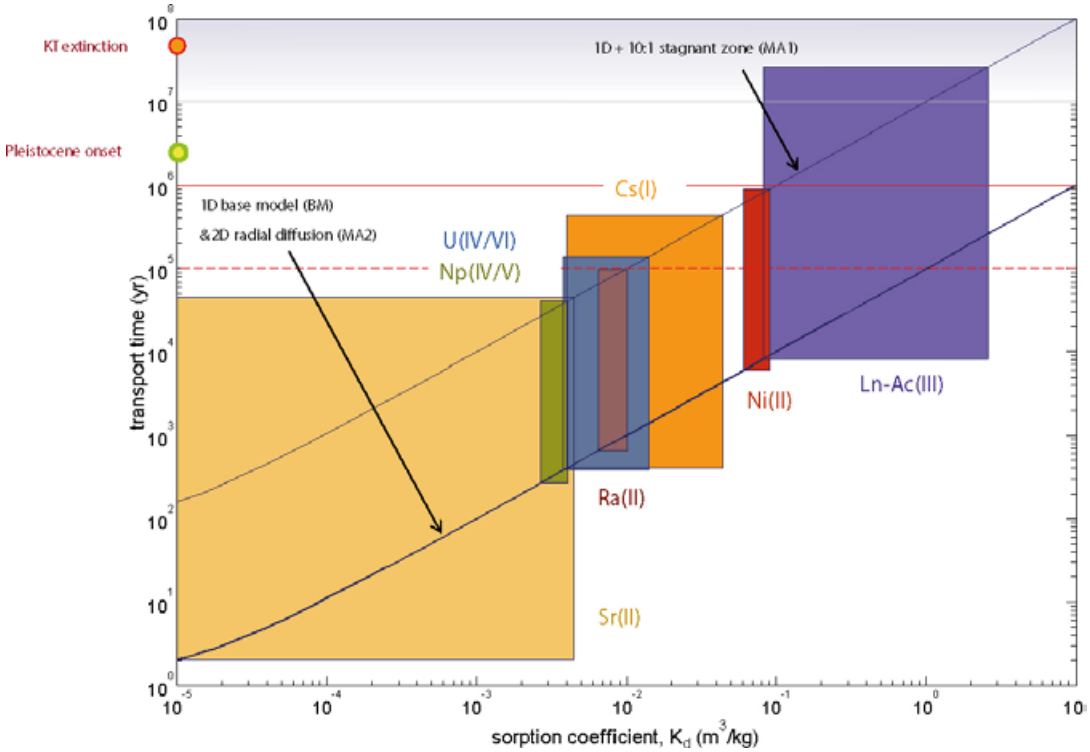

Figure F-8. *Recovery times for solutes as a function of K_d for a recovery fraction of 50%, a fixed* ***F-factor of 10^4 yr/m****, and formation factor of 1.1×10^{-5}. Polygons represent approximate ranges of behaviour for indicated solutes under saline (Type III) groundwater conditions.*

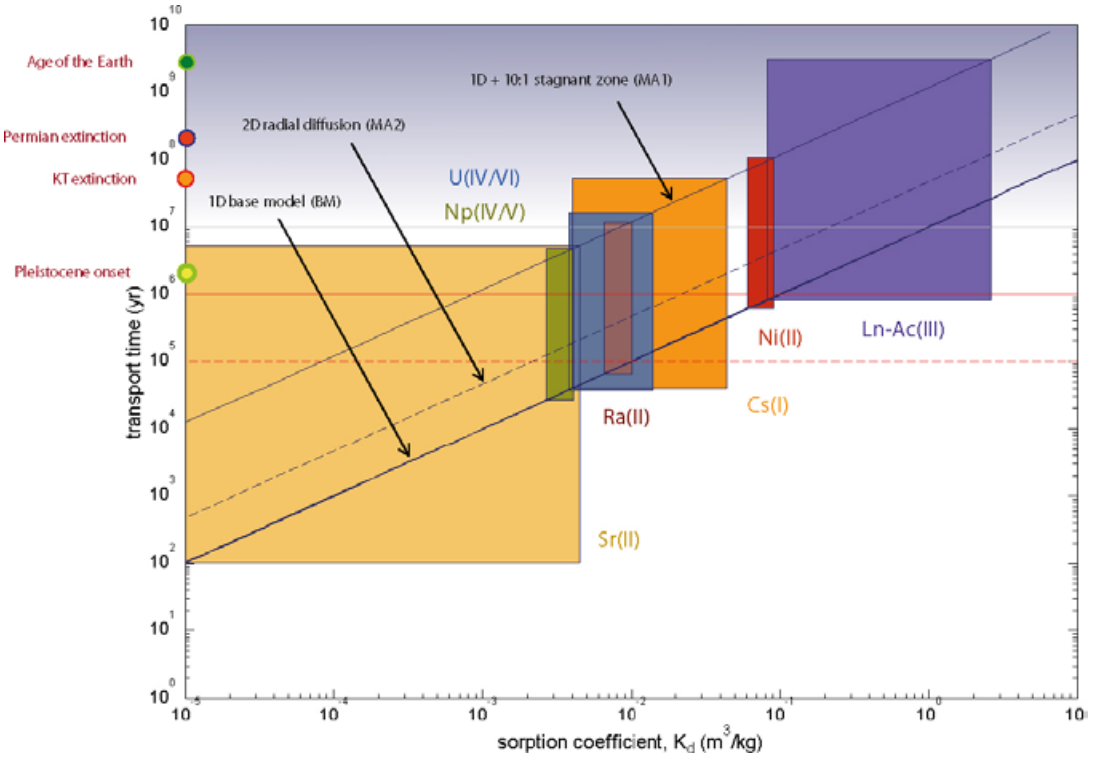

Figure F-9. *Recovery times for solutes as a function of K_d for a recovery fraction of 50%, a fixed* ***F-factor of 10^5 yr/m****, and formation factor of 1.1×10^{-5}. Polygons represent approximate ranges of behaviour for indicated solutes under saline (Type III) groundwater conditions.*

Typical transport times for solutes under brine (Type IV) groundwater conditions

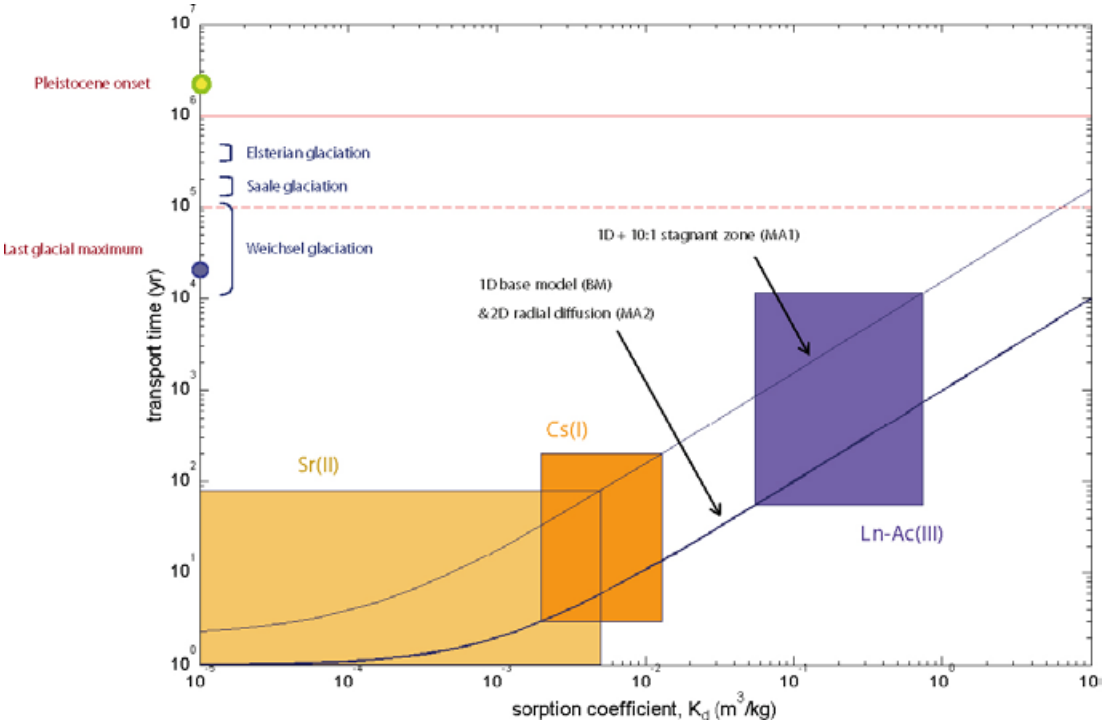

Figure F-10. *Recovery times for solutes as a function of K_d for a recovery fraction of 50%, a fixed* ***F-factor of 10^3 yr/m****, and formation factor of 1.1×10^{-5}. Polygons represent approximate ranges of behaviour for indicated solutes under brine (Type IV) groundwater conditions.*

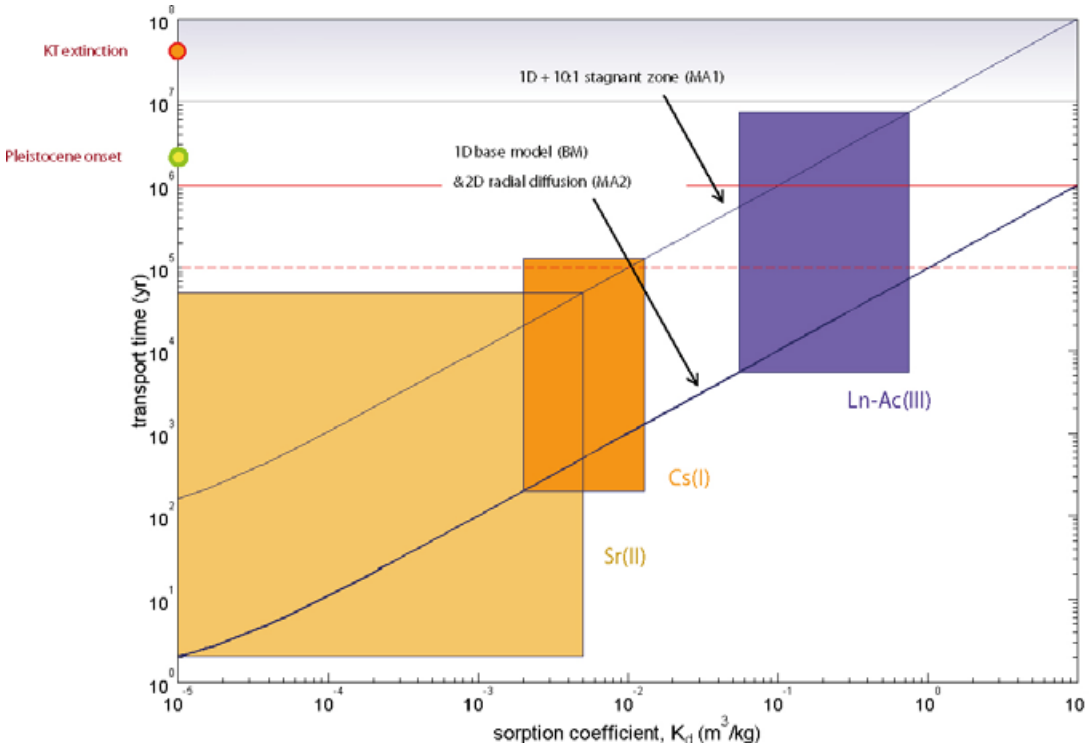

Figure F-11. *Recovery times for solutes as a function of K_d for a recovery fraction of 50%, a fixed F-factor of 10^4 yr/m, and formation factor of 1.1×10^{-5}. Polygons represent approximate ranges of behaviour for indicated solutes under brine (Type IV) groundwater conditions.*

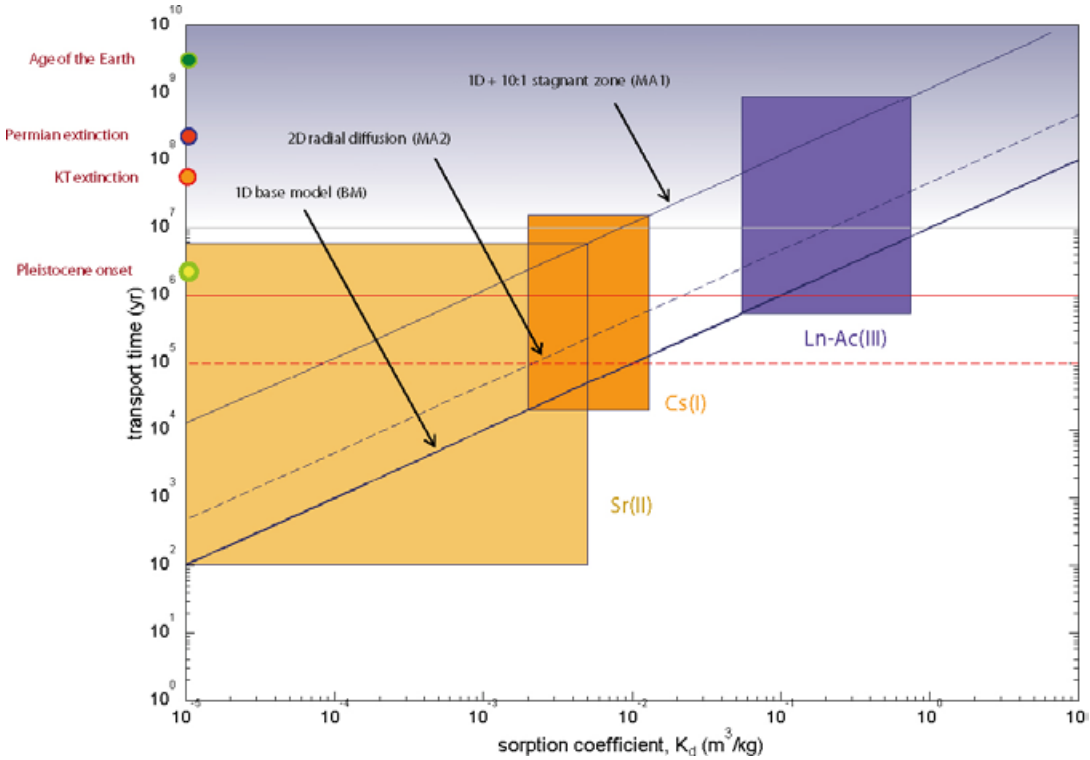

Figure F-12. *Recovery times for solutes as a function of K_d for a recovery fraction of 50%, a fixed* ***F-factor of 10^5 yr/m****, and formation factor of 1.1×10^{-5}. Polygons represent approximate ranges of behaviour for indicated solutes under brine (Type IV) groundwater conditions.*

Typical transport times for solutes under mixed interglacial (Type V) groundwater conditions

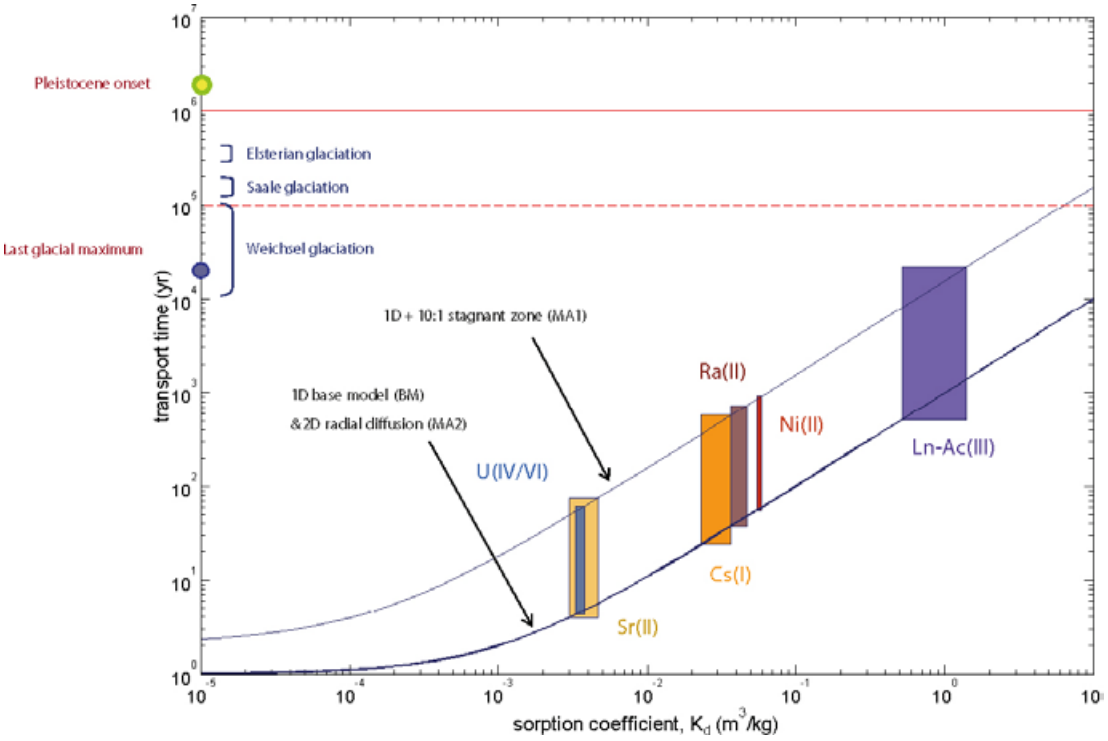

Figure F-13. *Recovery times for solutes as a function of K_d for a recovery fraction of 50%, a fixed* ***F-factor of 10^3 yr/m****, and formation factor of 1.1×10^{-5}. Polygons represent approximate ranges of behaviour for indicated solutes under mixed interglacial (Type V) groundwater conditions.*

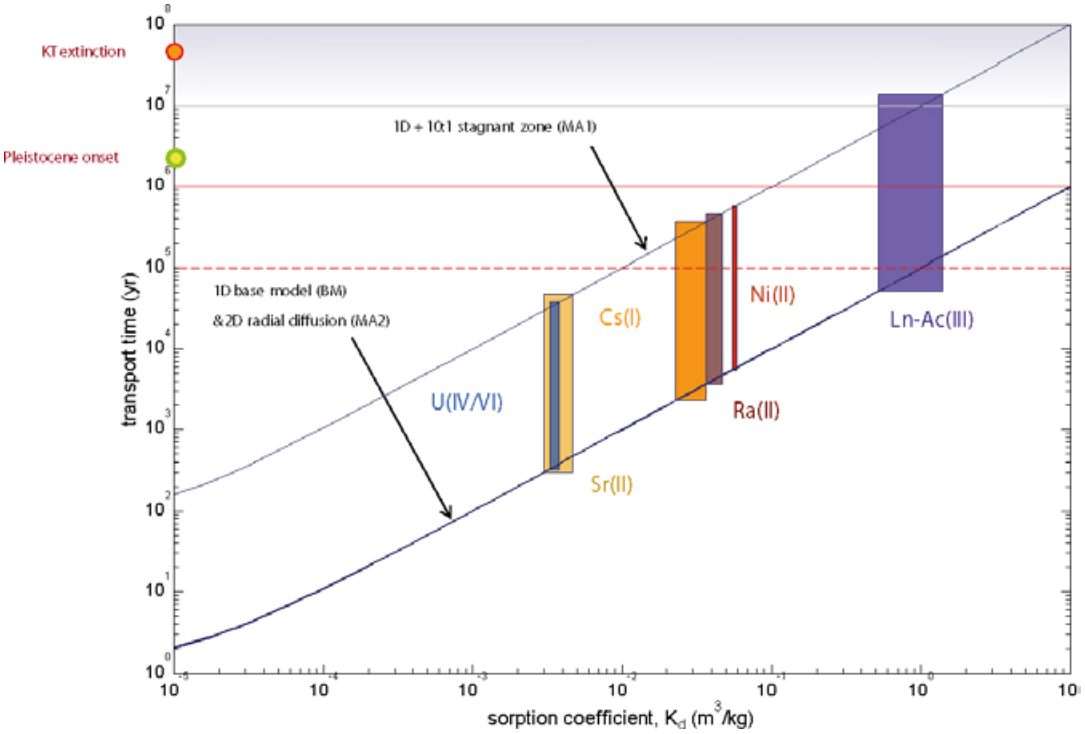

Figure F-14. *Recovery times for solutes as a function of K_d for a recovery fraction of 50%, a fixed* ***F-factor of 10^4 yr/m****, and formation factor of 1.1×10^{-5}. Polygons represent approximate ranges of behaviour for indicated solutes under mixed interglacial (Type V) groundwater conditions.*

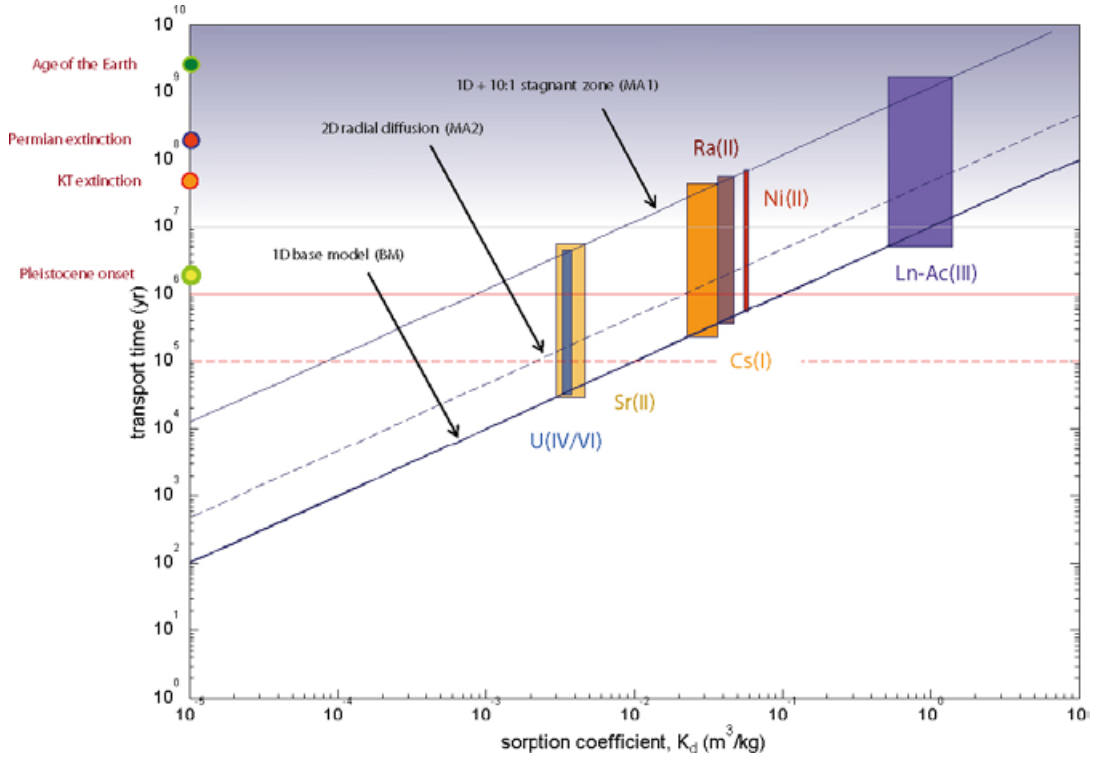

Figure F-15. *Recovery times for solutes as a function of K_d for a recovery fraction of 50%, a fixed* ***F-factor of 10^5 yr/m****, and formation factor of 1.1×10^{-5}. Polygons represent approximate ranges of behaviour for indicated solutes under mixed interglacial (Type V) groundwater conditions.*